MAPPING THE GALAXY and NEARBY GALAXIES

ASTROPHYSICS AND
SPACE SCIENCE PROCEEDINGS

Keiichi Wada
Françoise Combes

Editors

Mapping the Galaxy and Nearby Galaxies

With 203 Illustrations

Springer

Editors

Keiichi Wada
Center for Computational Astrophysics
National Astronomical Observatory of Japan
Mitaka, Tokyo 181-8588
wada.keiichi@nao.ac.jp

Françoise Combes
Observatoire de Paris
LERMA
61 Av. de l'Observatoire, 75014
Paris, France
francoise.combes@obspm.fr

ISBN: 978-0-387-72767-7 e-ISBN: 978-0-387-72768-4

Library of Congress Control Number: 2007933034

Printed on acid-free paper.

9 8 7 6 5 4 3 2 1

springer.com

Preface

In our quest to elucidate the origin of the universe and the formation of galaxies, particularly that of the Milky Way in which we live, astounding progress has been made in recent years through observational and theoretical studies. Not only have gigantic surveys covering a large fraction of the sky brought statistics enlightening evolutionary paths of galaxies, but powerful instruments, such as radio interferometers and ground- and space-based optical/infrared telescopes, have been able to map individual objects with high sensitivity and spatial resolution. Yet we do not fully understand the physics behind the observational results, and a number of unsolved problems need to be discussed, such as: What is the origin of disks and spheroids and which form first? What determines the global star formation rate in galaxies? How influential are the environment and interactions for nearby galaxies? What causes starburst and AGN activity in galaxies?

In order to discuss and make progress on these important questions, aided by recent observational and theoretical work, we organized a symposium entitled "Mapping the Galaxy and Nearby Galaxies", on 26 June - 30 June, 2006, at Ishigaki island. Ishigaki is a tropical resort island located about 1000 km south-west from the main island of Japan and surrounded by a coral reef and beautiful white sand beaches. Ishigaki is also the site of one of the 20 m radio telescopes in the VLBI Exploration of Radio Astrometry (VERA) network, which is operated by National Astronomical Observatory of Japan.

The symposium was also planned in celebration of Professor Yoshiaki Sofue's 63rd birthday and his retirement from the University of Tokyo. Although Prof. Sofue has worked mainly in the domain of radio astronomy, he has been active over the past four decades in a large number of different fields in galactic and extra-galactic astronomy. The wide range of topics discussed in this symposium were all related to some of his numerous works.

After very long flights (even for most Japanese attendees!), and a friendly welcome at the airport from the local authorities, a total of 160 people participated to the symposium, about half from outside Japan. During the week, 24 invited talks, 28 contributed talks, and 94 poster papers were presented in

four sessions: (1) Basic Components of the Galaxy and Spiral Galaxies, (2) The Galactic Center and Central Region of Galaxies, (3) Nearby Galaxies, and (4) Galactic Evolution and Environment.

In Session I, the discussion focused on results on stellar and interstellar matter in spiral galaxies from recent observational surveys at optical through radio wavelengths, such as those carried out with NANTEN, Spitzer, or maser techniques. Theoretical studies on the evolution of barred spiral galaxies and the Milky Way halo were also presented. The structure of galactic magnetic fields was discussed from both an observational point of view and that of three-dimensional magneto-hydrodynamic simulations.

In Session II, observational results were presented on the central region of our Galaxy and active galactic nuclei from the X-ray satellite SUZAKU, as well as from optical, infrared, and radio studies. CO line surveys of nearby spiral galaxies obtained by NMA, the NRO45 m, the IRAM30m and the IRAM interferometer were discussed, along with 3D kinematics of the central parts of nearby spiral galaxies. Initial results of ASTE were also presented in talks and poster papers. The strong influence of barred potentials on the gas dynamics was discussed from a theoretical point of view.

Session III continued with invited talks and contributions on observational studies of nearby galaxies, or the outer part of spiral galaxies and extra-galactic magnetic field.

Galactic evolution and environment were discussed in Session IV. Environmental effects in clusters of galaxies and local groups, results from the COSMOS survey, and observations of rotation curves in $z \sim 2$ spiral galaxies from the VLT were presented, as well as recent theoretical studies on the co-evolution of supermassive black holes and bulges.

During a free afternoon, participants visited the VERA observatory and took a tour of the 20 m telescope with its unique dual-beam system. In the observatory, the 4D2U (Four-dimensional Digital Universe) project of NAOJ presented 3-D movies of numerical simulations and a virtual trip from the solar system to the horizon of the universe. Astronomers also enjoyed beautiful tropical beaches and another "universe" with colorful fish and many kinds of coral from glass-bottom boats, at the emerald blue Kabira bay. They had also the opportunity to visit the nearby island Taketomi, and some of them made a complete bicycle tour of the island, famous for its ancient typical houses decorated with "Seasers" (talismanic lions).

The conference banquet close to the sea was the climax of the meeting. After a beautiful sunset tinted the beach, participants enjoyed local cuisine and magnificent performances of traditional dancing and music by students of Yaeyama Shoko High School.

In the next decade, further progress will be possible with new-generation instruments, such as ALMA, JWST, ELTs, Herschel, SPICA, and SKA. With these telescopes, complete multi-wavelength data at high resolution will become available on structures in our Galaxy, nearby galaxies and the more distant universe. The present symposium was a good opportunity to have a

comprehensive discussion on what has been learned so far, what are the major outstanding problems, and how we can physically tackle them. We were impressed by recent progress in numerical modeling of galaxies, which will be an essential tool in understanding and testing physical interpretations of "mapping observations" at high resolution.

We wish to express our thanks to the members of the scientific organizing committee for their valuable advice. On behalf of the SOC, we would like to thank Mareki Honma and his team for their collaborative and assiduous effort for almost two years to organize this successful symposium. We are also grateful to Ishigaki City and NPO Yaeyama Hoshino-kai (Star Watching Club) for their warm hospitality and help in various aspects not only during the conference but also in the phases of preparation. We also thank the 4D2U project (Eiichiro Kokubo, Takaaki Takeda, and Sorahiko Nukatani) for their impressive demonstration in VERA observatory. We should also thank Shioko Izumi, Toshiko Tachibana, Tomoka Tosakaki, Haruhiko Takahashi, Takeshi Hashiguchi, and Mayumi Handa for the help they provided to the LOC.

The symposium was financially supported by the Foundation for Promotion of Astronomy, the National Astronomical Observatory of Japan, NEC Corporation, Mitsubishi Electric Corporation, Okinawa Prefecture, the Inoue Foundation for Science, the Japanese Society for the Promotion of Science, Japan Communication Equipment Corporation, and Oshima Prototype Engineering Corporation.

Keiichi Wada (*National Astronomical Observatory of Japan*)
and Françoise Combes (*Observatoire de Paris*)

Prof. Yoshiaki Sofue, Hiromi Sofue, and Françoise Combes

Yoshiaki Sofue, Mareki Honma, Masaki Morimoto, Naomasa Nakai, Keiichi Wada, Nick Scoville, Nagateru Ohama (City Mayor), Françoise Combes, Reinhard Genzel

The Organizing Committee

Scientific

Keiichi **Wada** (NAOJ, Chair)
Nobuo **Arimoto** (NAOJ)
Françoise **Combes** (Paris observatory, France)
Reinhard **Genzel** (MPE, Germany)
Naomasa **Nakai** (Tsukuba, Japan)
Nick **Scoville** (Caltech, USA)
Masato **Tsuboi** (Nobeyama, NAOJ, Japan)

Local

Mareki **Honma** (NAOJ, Chair)
Fumi **Egusa** (University of Tokyo)
Toshihiro **Handa** (University of Tokyo)
Jin **Koda** (Caltech)
Kotaro **Kohno** (University of Tokyo)
Shinya **Komugi** (University of Tokyo)
Hiroyuki **Nakanishi** (Nobeyama, NAOJ, Japan)
Takayuki **Saitoh** (NAOJ)
Sachiko **Onodera** (University of Tokyo)

NAOJ: National Astronomical Observatory of Japan

Reinhard Genzel gives a speech for a warm welcome by Ishigaki-City at the airport.

List of Participants

Amram Philipe, Laboratoire d'Astrophysique de Marseille, OAMP, Université de Provence, CNRS, France Philippe.Amram@oamp.fr
Arimoto, Nobuo, NAOJ, arimoto@optik.mtk.nao.ac.jp
Athanassoula, Evangelia, Observatoire de Marseille, lia@oamp.fr
Azzollini, Ruyman, Instituto de Astrofisica de Canarias, ruyman@iac.es
Baker, Andrew, NRAO/University of Maryland, ajb@astro.umd.edu
Beckman, John, Insitituto de Astrofisica de Canarias, jeb@iac.es
Beletsky, Yuri, ESO, ybialets@eso.org
Benjamin, Robert, U of Wisconsin-Whitewater, benjamir@uww.edu
Bettoni, Daniela, INAF - Osservatorio Astronomico di Padova, bettoni@pd.astro.it
Bot, Caroline, California Institute of Technology, USA, bot@caltech.edu
Braine, Jonathan, Obs. de Bordeaux, France, braine@obs.u-bordeaux1.fr
Bureau, Martin, University of Oxford, bureau@astro.ox.ac.uk
Carretero, Conrado, Instituto de Astrofisica de Canarias, cch@iac.es
Carretti, Ettore, INAF - Istituto di Radioastronomia, carretti@ira.inaf.it
Cervantes-Sodi, Bernardo, Intituto de Astronomia, UNAM, bcervant@astroscu.unam.mx
Chiba, Masashi, Tohoku University, chiba@astr.tohoku.ac.jp
Chilingarian, Igor, Sternberg Astronomical Institute of the Moscow State University/CRAL Observatoire de Lyon, chil@sai.msu.su
Combes, Françoise, Astronomel l'Observatoire de Paris (Observatoire de Paris, LERMA), Francoise.Combes@obspm.fr
Cortes, Juan, ASTE/Departamento de Astronomia, Universidad de Chile, jcortes@das.uchile.cl
Davies, Richard, Max Planck Institute for Extraterrestrial Physics, davies@mpe.mpg.de
Dedes, Leonidas, Argelander-Institut foe Astronomy of the University Bonn, ldedes@astro.uni-bonn.de
Deguchi, Shuji, Nobeyama Radio Observatory, NAOJ, deguchi@nro.nao.ac.jp

Dobashi, Kazuhito, Tokyo Gakugei University, dobashi@u-gakugei.ac.jp
Dumas, Gaelle, CRAL Observatoire de Lyon, gdumas@obs.univ-lyon1.fr
Egusa, Fumi, IoA, University of Tokyo, fegusa@ioa.s.u-tokyo.ac.jp
Emsellem, Eric, Centre de Recherche Astrophysique de Lyon, emsellem@obs.univ-lyon1.fr
Garcia-Appadoo, Diego Alex, Argelander-Institut für Astronomie, dgarcia@astro.uni-bonn.de
Garcia-Burillo, Santiago, Observatorio Astronomico de Madrid, s.gburillo@oan.es
Genzel, Reinhard, Max Planck Institute for Extraterrestrial Physics, genzel@mpe.mpg.de
Giveon, Uriel, University of California, Davis, giveon@physics.ucdavis.edu
Goldston, Joshua, University of California, Berkeley, goldston@astro.berkeley.edu
Gonzalez Fernandez, Carlos, Instituto de Astrofisica de Canarias, carlos.gonzalez@iac.es
Grosbol, Preben, European Southern Observatory, pgrosbol@eso.org
Habe, Asao, Graduate School of Science, Hokkaido University, habe@astro1.sci.hokudai.ac.jp
Hachisuka, Kazuya, Max-Planck-Institut fuer Radioastronomie, hkazuya@mpifr-bonn.mpg.de
Handa, Toshihiro, IoA, University of Tokyo, handa@ioa.s.u-tokyo.ac.jp
Hatsukade, Bunyo, IoA, University of Tokyo, hatsukade@ioa.s.u-tokyo.ac.jp
Haverkorn, Marijke, NRAO/UC-Berkeley, marijke@astro.berkeley.edu
Hirashita, Hiroyuki, Center for Computational Sciences, University of Tsukuba, hirasita@ccs.tsukuba.ac.jp
Hirota, Akihiko, The University of Tokyo/NRO, hirota_a@nro.nao.ac.jp
Hirota, Tomoya, VERA, NAOJ, tomoya.hirota@nao.ac.jp
Honma, Mareki, NAOJ/VERA Observatory, honmamr@cc.nao.ac.jp
Hu, Jingyao, National Astronomical Observatories of China, hjy@bao.ac.cn
Hyodo, Yoshiaki, Kyoto University, hyodo@cr.scphys.kyoto-u.ac.jp
Imanishi, Masatoshi, NAOJ, masa.imanishi@nao.ac.jp
Inoue, Akio, Osaka Sangyo University, akinoue@las.osaka-sandai.ac.jp
Inoue, Makoto, NAOJ, inoue@nro.nao.ac.jp
Ishizuki, Sumio, Nobeyama Radio Observatory, NAOJ, ishizksm@cc.nao.ac.jp
Jiang, Biwei, Department of Astronomy, Beijing Normal University, bjiang@bnu.edu.cn
Jin, Shoko, Cambridge, shoko@ast.cam.ac.uk
Kamegai, Kazuhisa, IoA, University of Tokyo, kamegai@ioa.s.u-tokyo.ac.jp
Kameya, Osamu, NAOJ, kameya@miz.nao.ac.jp
Kawakatu, Nozomu, NAOJ, kawakatu@th.nao.ac.jp
Kawamura, Akiko, Nagoya University, kawamura@a.phys.nagoya-u.ac.jp
Kenney, Jeffrey, Yale University, kenney@astro.yale.edu

Kerins, Eamonn, Liverpool John Moores University, ejk@astro.livjm.ac.uk
Knapen, Johan, University of Hertfordshire, UK, j.knapen@star.herts.ac.uk
Kobayashi, Chiaki, NAOJ, chiaki@th.nao.ac.jp
Koda, Jin, California Insititute of Technology/NAOJ, koda@astro.caltech.edu
Kodama, Tadayuki, NAOJ, kodama@optik.mtk.nao.ac.jp
Kohno, Kotaro, IoA, University of Tokyo, kkohno@ioa.s.u-tokyo.ac.jp
Kokubo, Eiichiro, NAOJ, kokubo@th.nao.ac.jp
Komugi, Shinya, IoA, University of Tokyo, skomugi@ioa.s.u-tokyo.ac.jp
Kramer, Carsten, KOSMA, I.Physikalisches Institut, Universitaet zu Koeln, kramer@ph1.uni-koeln.de
Kuno, Nario, Nobeyama Radio Observatory, NAOJ, kuno@nro.nao.ac.jp
Lee, Youngung, Korea Astronomy and Space Science Institute/ University of Science and Technology, yulee@kasi.re.kr
Levine, Evan, UC Berkeley, elevine@astron.berkeley.edu
Lin, Lien-Hsuan, ASIAA, Taiwan, lhlin@asiaa.sinica.edu.tw
Lundgren, Andreas, APEX Project, ESO, Chile, alundgre@eso.org
de Lorenzo-Cáceres, Adriana, Instituto de Astrofísica de Canarias, adlcr@iac.es
Maciejewski, Witold, Astrophysics, University of Oxford, witold@astro.ox.ac.uk
Mahoney, Terry (Terence), Instituto de Astrofisica de Canarias, tjm@iac.es
Marshall, Douglas, Observatoire de Besançcon, doug.marshall@ias.fr
Martini, Paul, The Ohio State University, martini@astronomy.ohio-state.edu
Matsui, Hidenori, Hokkaido University, hidenori@astro1.sci.hokudai.ac.jp
Matsumoto, Ryoji, Chiba University, matumoto@astro.s.chiba-u.ac.jp
Matsunaga, Noriyuki, IoA, University of Tokyo, matsunaga@ioa.s.u-tokyo.ac.jp
Matsushita, Satoki, ASIAA, Taiwan, satoki@asiaa.sinica.edu.tw
Meurer, Gerhardt, The Johns Hopkins University, meurer@pha.jhu.edu
Miura, Rie, University of Tokyo/NAOJ, rie.miura@nao.ac.jp
Miyazaki, Atsushi, Shanghai Astronomical Observatory, amiya@shao.ac.cn
Muehle, Stefanie, University of Toronto, muehle@astro.utoronto.ca
Muller, Sebastien, ASIAA, Taiwan, muller@asiaa.sinica.edu.tw
Muraoka, Kazuyuki, IoA, University of Tokyo, kmuraoka@ioa.s.u-tokyo.ac.jp
Nagai, Hiroshi, The Graduate University for Advanced Studies, nagai@hotaka.mtk.nao.ac.jp
Nagai, Makoto, University of Tokyo, nagai@taurus.phys.s.u-tokyo.ac.jp
Nagashima, Masahiro, Nagasaki University, masahiro@nagasaki-u.ac.jp
Nagayama, Takumi, Kagoshima University, nagayama@astro.sci.kagoshima-u.ac.jp
Nakada, Yoshikazu, University of Tokyo, nakada@kiso.ioa.s.u-tokyo.ac.jp
Nakai, Naomasa, Tsukuba University, nakai@physics.px.tsukuba.ac.jp
Nakanishi, Hiroyuki, Nobeyama Radio Observatory, NAOJ, hnakanis@nro.nao.ac.jp

Nakanishi, Kouichiro, Nobeyama Radio Observatory, NAOJ, nakanisi@nro.nao.ac.jp
Nikola, Thomas Cornell, University, tn46@cornell.edu
Nishiyama, Shogo, Nagoya University, shogo@z.phys.nagoya-u.ac.jp
Novak, Giles, Northwestern University, Dept. of Physics and Astronomy, g-novak@northwestern.edu
Ohnishi, Kouji, Nagano National College of Technology, ohnishi@ge.nagano-nct.ac.jp
Oka, Tomoharu, Department of Physics, Graduate School of Science, The University of Tokyo, tomo@phys.s.u-tokyo.ac.jp
Okada, Yoko, Department of Astronomy, University of Tokyo, okada@ir.isas.jaxa.jp
Okamoto, Takashi, NAOJ, okamoto@th.nao.ac.jp
Okuda, Takeshi, Institute of Astronomy, University of Tokyo, okuda@ioa.s.u-tokyo.ac.jp
Onishi, Toshikazu, Nagoya University, ohnishi@a.phys.nagoya-u.ac.jp
Peeples, Molly, The Ohio State University, molly@astronomy.ohio-state.edu
Pfenniger, Daniel, Geneva Observatory, daniel.pfenniger@obs.unige.ch
Preben, Grosbol, European Southern Observatory, pgrosbol@eso.org
Ranalli, Piero, RIKEN, piero@crab.riken.jp
Regan, Michael, STScI, mregan@stsci.edu
Reich, Wolfgang, Max-Planck-Institut fuer Radioastronomie, wreich@mpifr-bonn.mpg.de
Reid, Mark, Harvard-Smithsonian CfA, reid@cfa.harvard.edu
Rodriguez, Monica, STScI, CRyA-UNAM, monica@stsci.edu
Saitoh, Takayuki, NAOJ, saitoh.takayuki@nao.ac.jp
Sawa, Takeyasu, Aichi University of Education, tsawa@auecc.aichi-edu.ac.jp
Sawada, Tsuyoshi, Nobeyama Radio Observatory, NAOJ, sawada@nro.nao.ac.jp
Sawada-Satoh, Satoko, ASIAA, Taiwan, satoko@asiaa.sinica.edu.tw
Schinnerer, Eva, MPI for Astronomy, schinner@mpia-hd.mpg.de
Schultheis, Mathias, Observatoire de Besançon, mathias@obs-besancon.fr
Scoville, Nick, California Insititute of Technology, nzs@astro.caltech.edu
Sofue, Yoshiaki, IoA, Univ. Tokyo, sofue@ioa.s.u-tokyo.ac.jp
Sorai, Kazuo, Graduate School of Science, Hokkaido University, sorai@astro1.sci.hokudai.ac.jp
Sugitani, Koji, Graduate School of Natural Sciences, Nagoya City University, sugitani@nsc.nagoya-cu.ac.jp
Tacconi, Linda, Max-Planck-Inst. f. ext. Physik, linda@mpe.mpg.de
Tamaki, Teppei, YAMAGUCHI UNIVERSITY, c054dc@yamaguchi-u.ac.jp
Tamura, Yoichi, University of Tokyo/NAOJ, yoichi.tamura@nao.ac.jp
Tanaka, Kunihiko, IoA, University of Tokyo, tanaka@ioa.s.u-tokyo.ac.jp
Tanaka, Mikito, NAOJ, miki@optik.mtk.nao.ac.jp
Tosaki, Tomoka, Nobeyama Radio Observatory, NAOJ, tomoka@nro.nao.ac.jp
Tsuboi, Masato, Nobeyama Radio Observatory, NAOJ, tsuboi@nro.nao.ac.jp
Umemura, Masayuki, Center for Computational Sciences, University of Tsukuba, umemura@ccs.tsukuba.ac.jp

Veilleux, Sylvain, University of Maryland, veilleux@astro.umd.edu
Vlahakis, Catherine, Argelander Institut for Astronomy,
Bonn University, vlahakis@astro.uni-bonn.de
Vollmer, Bernd, Observatoire astronomique de Strasbourg,
bvollmer@astro.u-strasbg.fr
Wada, Keiichi, NAOJ, wada.keiichi@nao.ac.jp
Walter, Fabian, Max Planck Institute for Astronomy, Heidelberg, walter@mpia.de
Watabe, Yasuyuki, Center for Computational Sciences,
University of Tsukuba, watabe@ccs.tsukuba.ac.jp
Wielebinski, Richard, Max-Planck-Institute for radio astronomy, Bonn,
rwielebinski@mpifr-bonn.mpg.de
Wong, Tony, CSIRO ATNF & UNSW, Tony.Wong@csiro.au
Yamauchi, Aya, Institute of Physics, University of Tsukuba,
yamauchi@physics.px.tsukuba.ac.jp
Yen, Chien-Chang, Department of Mathematics,
Fu Jen Catholic University, Taipei, yen@asiaa.sinica.edu.tw
Yoshida, Naoki, Nagoya University, nyoshida@a.phys.nagoya-u.ac.jp

VERA and "Seaser"

Something new in another "universe"?

Masashi Chiba and dancing astronomers!

Contents

Mareki Honma, LOC chair

Nick Scoville and young Japanese astronomers: Hiroyuki Nakanishi, Shinya Komugi, Sachiko Onodera, Kazuhisa Kamegai, Jin Koda (from left to right)

Part I

BASIC COMPONENTS OF THE GALAXY AND SPIRAL GALAXIES

This page intentionally blank

Mayumi Sato, Masahiro Samejima, Makoto Inoue, Mark Reid, Bernd Vollmer, Jeff Kenney, Joanna Kenney

Mike Regan, Eva Schinnere, Lia Athanassoula, Keiichi Wada, Paul Martini, Bob Benjamin, John Beckman, Johan Knapen, Witold Maciejewski, Andreas Lundgren

1

Atlas and Catalog of Dark Clouds Based on Digitized Sky Survey I

Kazuhito Dobashi

Department of Astronomy and Earth Sciences, Tokyo Gakugei University
dobashi@u-gakugei.ac.jp

Summary. We introduce our quantitative atlas and catalog of dark clouds derived by using the optical database "Digitized Sky Survey I". Applying a traditional star-count technique to 1043 plates contained in the database, we produced an A_V map covering the entire region in the galactic latitude range $|b| \leq 40^\circ$. Based on the A_V map drawn at the two different angular resolutions $6'$ and $18'$, we identified 2448 dark clouds and 2840 clumps located inside them. Some physical parameters, such as the position, extent, and optical extinction, were measured for each of the clouds and clumps. We also searched for counterparts among already known dark clouds in the literature. The A_V map and a list of the identified clouds and clumps were summarized as an atlas and catalog of dark clouds. Printed version of the data is already published in a special issue of the Publications of the Astronomical Society of Japan (Dobashi et al. 2005, PASJ, Vol. 57, No. SP1, pp. S1–S386). Digital version of the data, i.e., a FITS file for the A_V map and an ASCII file for the catalog, is also available at URL http://astro.u-gakugei.ac.jp/~tenmon/Atlas/index.html.

1 Introduction

Dark clouds play an important role in the Galaxy as sites of star formation, and their precise distribution on the sky has been of great interest. In the past a few decades, general catalogs of dark clouds were published by several authors, for instance, Khavtassi in 1955 [1], Lynds in 1962 [2], and Feitzinger and Stüwe in 1984 [3]. These pioneer researchers surveyed for dark clouds over a great portion of the sky, and recorded the positions and extents of opaque regions. Although these catalogs were published mostly more than ~ 20 years ago, they are still very useful for various studies of dark clouds. These catalogs, however, have remained rather qualitative, and have suffered from a lack of some basic parameters, including the visual extinction (A_V) of individual dark clouds. Furthermore, some clouds must have escaped detection in these catalogs, because searches of dark clouds were carried out by eye inspections. These demerits of the catalogs apparently arose from difficulty in analysing a large amount of data (e.g., optical photographic plates) covering a vast region

at the age when the catalogs were organized, although a fundamental method, such as a star-count technique, to measure the optical extinction had already been established.

The Digitized Sky Survey I (hereafter, DSS) [4] is a useful database to complete such surveys for dark clouds more quantitatively. The recent development of computers has made it possible to analyse the huge dataset contained in DSS within a reasonable amount of time and cost. In 1998, we started a systematic survey for dark clouds by applying a traditional star-count technique to DSS, and in 2002, we completed the measurement of A_V all over the galactic plane within the latitude range $|b| \leq 40^\circ$ [5]. Based on the A_V map, we further attempted to identify individual dark clouds to compile a quantitative atlas and catalog of dark clouds. Resulting atlas and catalog are presented in a special issue of the Publications of the Astronomical Society of Japan [6] (Dobashi et al. 2005, PASJ, Vol. 57, No. SP1, pp. S1–S386) where the methods to derive the extinction map and then to identify the clouds are fully described. In the following sections of this paper, we will briefly summarize the procedure to derive the extinction map and will introduce our atlas and catalog of dark clouds.

2 Data Reduction to Derive the Extinction Map

DSS comprises mainly 3 types of plates obtained with different filters, which are named S, XV, and XE plates, obtained at the B, V, and R bands, respectively. XE and S plates cover the northern and southern hemisphere, respectively, while XV plates cover mainly the regions at low galactic latitudes. Coverage of the individual DSS plates is $\sim 6^\circ \times 6^\circ$, and the pixel size is $\sim 1.7" \times 1.7"$ on the sky. We show an example of DSS plates in Fig.1.

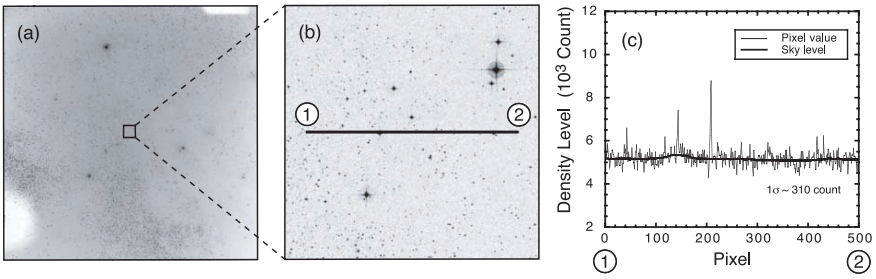

Fig. 1. An example of the DSS plates. (a) The entire image of the plate No. S879 covering the $6.^\circ5 \times 6.^\circ5$ region on the sky. (b) Small region with 600×600 pixels ($\sim 17' \times 17'$) near the center of the plate. (c) Profile of density taken along the line 1–2 in panel (b). The thin solid line indicates the raw data, and the thick solid line indicates the sky background.

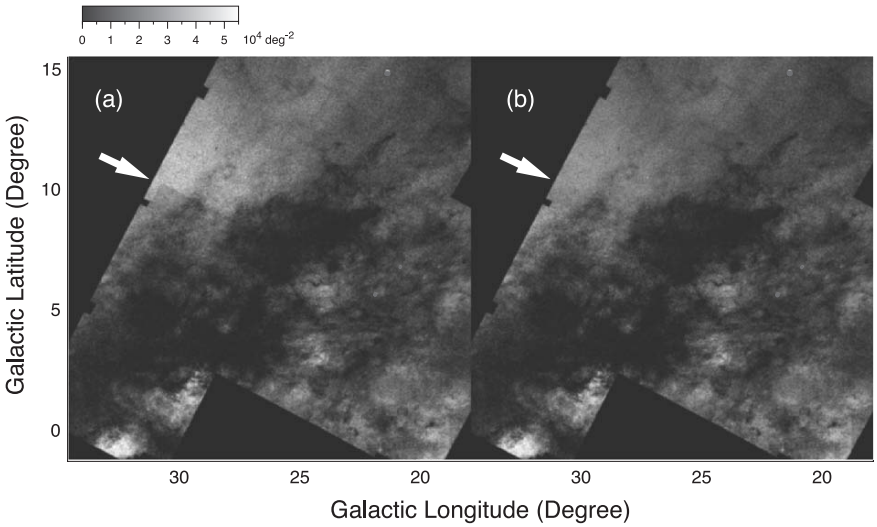

Fig. 2. Sample of the star density maps produced from DSS plates. (a) Composed star density map for S plates around the Serpens region. The threshold magnitude is set to 19 mag. A slight inconsistency due to the ambiguity in the photometric calibration is seen at the boundary of two adjacent plates pointed by the arrow. (b) Star density map corrected for the inconsistency by scaling some star density maps, typically by $\sim 10\%$.

In order to identify stars on the individual DSS plates, we developed software using the Interactive Data Language (IDL). We first identified stars as a set of continuous pixels having $\geq 5\sigma$ noise level above the sky background (Fig.1c), and then performed the photometric calibration by comparing the density of the detected stars with magnitudes listed in other star catalogs such as the Tycho-2 catalog [7], the Guide Star Photometric Catalog I [8] , and the USNO-Precision Measuring Machine A2.0 catalog [9]. The accuracy of the calibration is better than ~ 0.5 mag. We applied the above procedure to 1043 DSS plates located within the galactic latitude range $|b| \leq 40°$, and compiled a list of $\sim 6.94 \times 10^8$ stars in total.

Using the list of stars, we produced a star density map (i.e. number of stars found in a unit solid angle) for individual DSS plates by counting stars falling in a $2' \times 2'$ mesh set along the galactic coordinates, and then synthesized neighboring maps to compose a large star density map for each of the 3 bands. When producing the individual star density maps, we used only stars brighter than 19 mag for the S (B band) and XE (R band) plates, and 16 mag for the XV (V band) plates. An example of the composition is shown in Fig.2. As seen in the figure, the ambiguity in the magnitude calibration results in a slight inconsistency among the neighboring star density maps (Fig.2a). Such inconsistencies are corrected by scaling some star density maps, typically by

$\sim 10\%$ (Fig.2b). Large–scale star density maps composed in this manner are show in the upper panels of Fig.3.

On the basis of the composed density maps, we attempted to measure the background star density level N_0 as a function of the galactic coordinates. We set a strip along galactic latitude b at a certain longitude l with a width of $\Delta l = 2^\circ$, and then averaged the star density within Δl to obtain the actual star density N as a function of b. We determined the background star density level N_0 by fitting $N(b)$ with an exponential function in cloud-free regions showing no apparent extinction. We interpolated the background data obtained at every 1° in l to produce background star density maps, $N_0(l, b)$, having the same size as the actual star density maps. We display the background star density maps in the middle panels of Fig.3.

In order to reduce the noise in the final extinction maps, we performed Gaussian smoothing to both the actual and the background star density maps. Because the noise level in the extinction map depends on the logarithmic number of stars counted in a mesh, Gaussian smoothing is useful to avoid quantization errors, especially in the most opaque regions in the galactic plane, where only one or a few stars are found in the $2' \times 2'$ mesh. For the width of the two-dimensional Gaussian function used for smoothing, we selected $6'$ and $18'$ (FWHM). The former is to find well-defined dark clouds along the galactic plane at a high angular resolution, and the latter was to search for diffuse and extended dark clouds.

Based on the actual and background star density maps for each band, we derived an extinction map using the well-known formula,

$$A_\lambda(l, b) = [\log N_0(l, b) - \log N(l, b)]/a_\lambda, \tag{1}$$

where N and N_0 are the actual and the background star densities, respectively, λ is the band of the map (i.e., B, V, or R), and a_λ is the slope of the $m_\lambda - \log N$

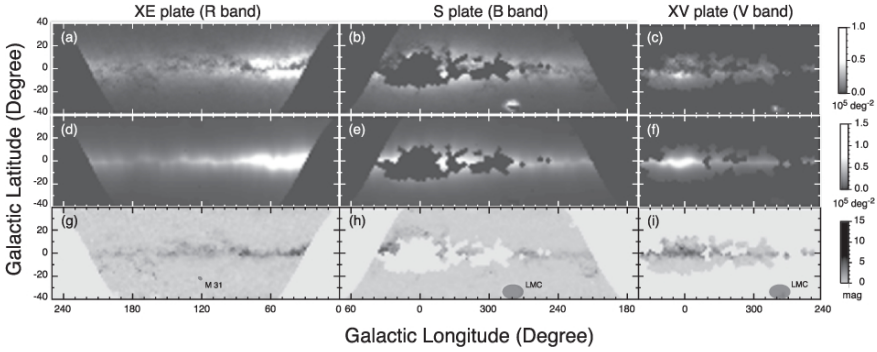

Fig. 3. Distributions of the actual star density, the fitted background star density, and the resulting extinction, displayed in the upper, middle, and lower panels, respectively, for each type of the DSS plates.

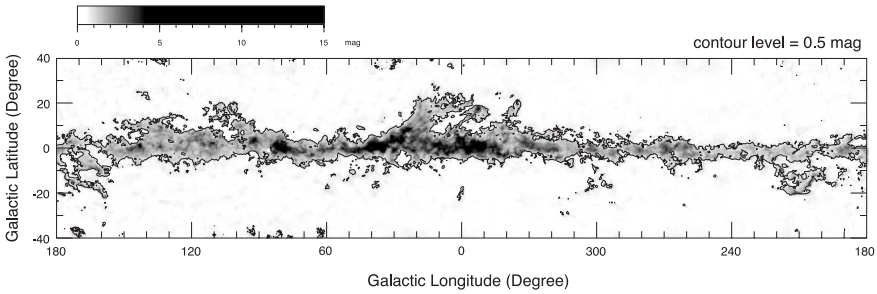

Fig. 4. Composed A_V map covering the entire region at $|b| \leq 40°$. The resolution of the map is $6'$. The contour is drawn at $A_V = 0.5$ mag.

diagram (i.e., the Wolf diagram [10]) taken to be 0.3 all over the galactic plane. Resulting extinction maps (A_B, A_V, and A_R) are displayed in the lower panels of Fig.3.

We converted A_R and A_B to A_V using the relation $A_V = C_{VR}A_R = C_{VB}A_B$ where the conversion factors, C_{VR} and C_{VB}, are assumed to be 1.21 and 0.76 [11], respectively, and then we synthesized the 3 large extinction maps into one large A_V map covering the entire galactic plane at $|b| \leq 40°$. We composed the large-scale A_V map in this manner using the two star density maps smoothed at the different angular resolutions (i.e., $6'$ and $18'$). These A_V maps are referred to as the high- and low-resolution A_V maps, respectively. Noise level of the high-resolution map arising from the $\sqrt{N}$ counting uncertainty is $\Delta A_V \sim 0.5$ mag, and that of the low-resolution map is $\Delta A_V \sim 0.3$ mag. We show the high-resolution A_V map in Fig.4.

3 Atlas and Catalog of Dark Clouds

The extinction map derived in this work reveals the dust distribution in detail over the entire region at $|b| \leq 40°$. In Fig.5, we demonstrate a close-up view of dark clouds in the Taurus and Ophiuchus regions.

Based on the high- and low- resolution maps, we searched for dark clouds as well as the clumps inside them, which are defined as a small scale structure in the extinction maps surrounded by a certain contour level in the map. In total, we identified 2448 dark clouds and 2840 clumps, and derived some physical parameters, such as the position, extent, and optical extinction for each of the clouds and clumps. We also searched for counterparts among already known dark clouds in the literature [12]. We summarized the A_V map and the list of the identified dark clouds and clumps as well as their counterparts as a quantitative atlas and catalog of dark clouds, and presented them in a special issue of the Publications of the Astronomical Society of Japan [6] where precise definition of the clouds and clumps as well as an estimate for the errors in the A_V map are described in detail.

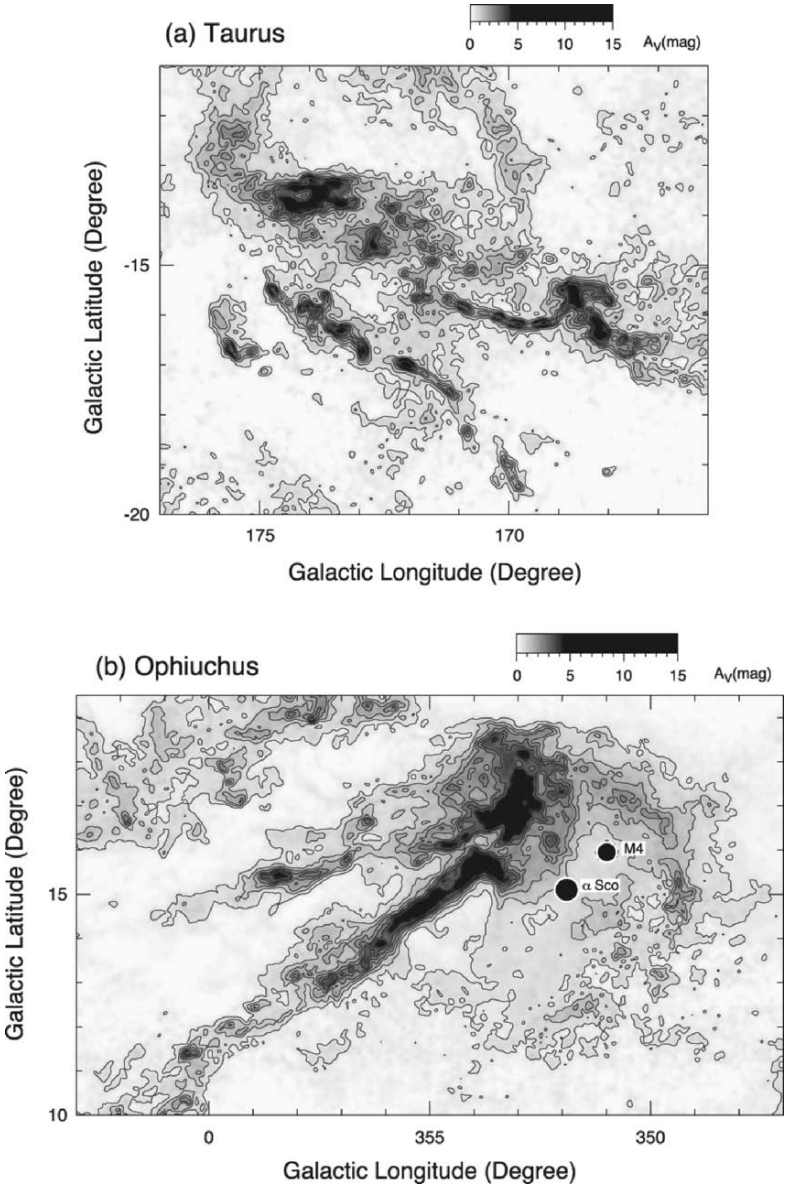

Fig. 5. An example of our atlas of dark clouds derived from DSS. Panels (a) and (b) show the distribution of A_V in the Taurus and Ophiuchus regions, respectively. The resolution of the map is $6'$. The lowest contours are drawn at $A_V = 0.5$ mag, and the contour intervals are 0.5 mag and 1.0 mag for the ranges $A_V \leq 3$ and $A_V > 3$ mag, respectively.

We also prepared a web site for researchers to access to the digital version of the data at URL http://astro.u-gakugei.ac.jp/~tenmon/Atlas/index.html where FITS files of the A_V map and ASCII files of the catalog are available.

4 Comparison with the FIR Dust Emission

We compare our extinction map with the "dust map" composed by Schlegel et al. [13]. They derived a map of color excess $E(B-V)$ based on the far-infrared (FIR) data provided by COBE/DIRBE and IRAS/ISSA. The dust map covers the entire sky with an angular resolution of $6'$, and is now widely used for various purposes.

Assuming a relation $A_V = R_V E(B-V)$ with $R_V = 3.1$, we converted their $E(B-V)$ map into A_V, and compared it with our high-resolution A_V map. Results of the comparison indicate that the A_V value derived from the FIR dust map is always higher by a factor of ~ 3 than that in our A_V map measured directly in the optical wavelengths. It is noteworthy that this trend is clearly seen not only toward the low galactic latitude regions where assumption on the dust temperature of Schlegel et al. can suffer from a large error due to enormous contamination along the line of sight, but also toward isolated clouds at high latitudes. An example of such a large-scale inconsistency is demonstrated in Fig.6.

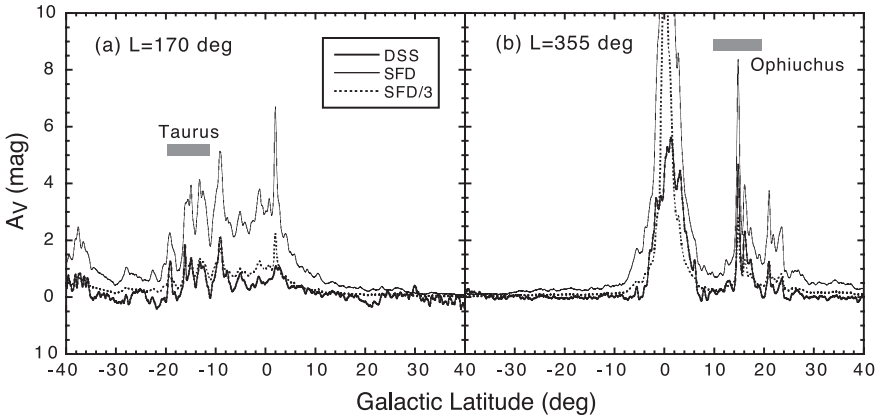

Fig. 6. Profiles of extinction shown as a function of the galactic latitude. The values of A_V derived from DSS in this paper are denoted by the thick solid lines, and those derived from the far-infrared dust emission by Schlegel et al. [13] are indicated by the thin solid lines. One third level of the latter extinction is shown by the broken lines for a comparison. The profiles shown in panels (a) and (b) are taken across the Taurus and Ophiuchus regions, respectively. The gray hatches in the panels denote the latitude ranges displayed in Fig.5.

There are two major possible sources to account for the global overestimation of A_V derived from the FIR dust emission. One is the low resolution ($\sim 1^\circ$) of the temperature map adopted by Schlegel et al. As stated by Schlegel et al., a small change in the dust temperature can modify their estimate of the dust column density by a large factor. However, the large difference between the two A_V is extensively observed even in the extended regions with low extinction, indicating that the poor resolution of the temperature map may not be a major source of the inconsistency. The other possible source is an underestimation of the actual dust emissivity in the FIR wavelengths. For example, fluffy aggregates that can form through grain–grain coagulation are known to have a far-infrared emissivity a few times higher than that of normal dust grains, while their absorptivity at optical wavelengths is insensitive to the fluffiness. Such aggregates have been actually detected in some dense dark clouds [14]. Because the overestimation of A_V is largely seen along the galactic plane, we suggest that such enhancement of dust emissivity, probably due to the formation of fluffy aggregates, is common not only in dense dark clouds, but also in the diffuse interstellar medium.

Acknowledgement. The printed version of the atlas and catalog of dark clouds appeared in the PASJ special issue was compiled by K. D. and several collaborators. They are H. Uehara, R. Kandori, M. Kaiden, S. Sakurai, T. Umemoto, and S. Sato. K.D. thanks S. Nishiura, T. Kaneko, and I. Kato for their help to maintain the web server. This work was financially supported by Tokyo Gakugei University, and by the Grant-in-Aid for Scientific Research provided by Ministry of Education, Culture, Sports, Science and Technology (18026003) as well as by Japan Society for the Promotion of Science (17540214, 178059, and 188065).

References

1. D. Sh. Khavtasi: Bull. Abastumani Obs. 18, 29 (1955)
2. B. T. Lynds: ApJS 7, 1 (1962)
3. J. V. Feitzinger, J. A. & Stüwe: A&AS 58, 365 (1984)
4. B. M. Lasker: BAAS 26, 914 (1994)
5. K. Dobashi, H. Uehara, R. Kandori, T. Umemoto, F. Sato: in Proc. IAU 8th Asian Pacific Regional Meeting (Vol. II), ed. S. Ikeuchi, J. Hearnshaw, & T. Hanawa (Tokyo: Astronomical Society of Japan), pp.67–68 (2002)
6. K. Dobashi, H. Uehara, R. Kandori, T. Sakurai, M. Kaiden, T. Umemoto, F. Sato: PASJ 57, S1 (2005)
7. E. Høg, et al.: A&A 355, L27 (2000)
8. B. M. Lasker, et al.: AJ 99, 2019 (1990)
9. D. Monet: BAAS 30, 1427 (1998)
10. M. Wolf: Astron. Nachr. 219, 109, (1923)
11. R. L. Dickman: AJ 83, 363 (1978)
12. C. M. Dutra, Bica, E.: A&A 383, 631 (2002)
13. D. J. Schlegel, D. P. Finkbeiner, M. Davis: ApJ 500, 525 (1998)
14. J. P. Bernard, et al.: A&A 347, 640 (1999)

2

New Views of Molecular Gas Distribution and Star Formation of the Southern Sky with NANTEN

Toshikazu Onishi

Department of Astrophysics, Nagoya University, Chikusa-ku, Nagoya 464-8602
ohnishi@a.phys.nagoya-u.ac.jp

1 Introduction

Star formation is a fundamental process that dominates the cycling of various matters in galaxies. Stars are formed in molecular clouds, and the formed stars often affect the parent body of the molecular gas strongly via their UV photons, stellar winds, and supernova explosions. It is therefore of vital importance to reveal the distribution of molecular gas in a galaxy in order to investigate the galaxy history. Recent progress in developing (sub-)millimeter wave receiver systems has enabled us to rapidly increase our knowledge on molecular clouds. The "NANTEN" telescope has an angular resolution of 2′.6 at 115 GHz and has rapidly revealed the molecular view of the Galaxy, LMC, and SMC with its relatively high spatial resolution. The spatial coverage of the NANTEN is comparable or larger than that by CfA 1.2m telescopes[1] in the southern sky. In this presentaion, I shall introduce some of the results obtained from the NANTEN CO surveys in the Galaxy. I will also mention the "NANTEN2" project, which is an upgrade of NANTEN to achieve an extensive survey in sub-mm wavelength at Atacama.

2 NANTEN Telescope

The 4-m radio telescope of Nagoya University equipped with the highest sensitivity SIS receiver at 115 GHz allowed us to cover a large area within a reasonable time at an angular resolution high enough to resolve dense cores in nearby (within 1 kpc) dark clouds and also to resolve distant (up to 30kpc from the sun) giant molecular clouds. In 1996, the 4-m telescope "NANTEN" was installed at Las Campanas observatory in Chile under mutual collaboration with the Carnegie Institution of Washington, and we started a CO survey toward the southern sky. Two major works with the NANTEN telescope were

the Galactic plane CO survey and the Magellanic Clouds molecular cloud survey (see Kawamura et al. in this conference). The other projects are to observe various objects including high mass star forming regions (Carina, Centaurus, Orion, Bright-Rimmed Clouds), SNRs/Supershells (Vela SNR, Gum Nebula, Carina Flare), Galactic center, Low-mass star forming regions (Ophuichus, Lupus, Chamaeleon, Pipe nebula), Galactic high-latitude molecular clouds (Aquila, infrared-excess clouds), and so on. Many of the results are presented in two special issues of **PASJ 1999 vol. 51 No. 6 and 2001 vol. 53 No. 6**.

3 Results from Surveys by NANTEN

3.1 Galactic Plane Survey

Figure 1 shows the CO total intensity map of a part of the southern Galactic plane obtained with the NANTEN telescope. This map consists of more than 1,100,000 spectra. The observing grid spacings are $4'$ between 5 degrees from the galactic plane and $8'$ for the area above 5 degrees in the galactic latitude with a $2.'6$ beam. In the longitudinal direction almost 200 degrees, i.e., L=220° to 60° have been covered. The velocity resolution and coverage are 0.65 km s^{-1} and ∼500 km s^{-1}, respectively. Typical rms noise fluctuations are ∼0.4 K at a velocity resolution of 0.65 km s^{-1}. We are trying to re-identify Giant Molecular Clouds in the Galaxy by using this new data set. One of the notable features seen especially in this survey is the existence of a number of vertical features perpendicular to the galactic plane. I will focus here on two of such features, CO supershells and high galactic latitude clouds.

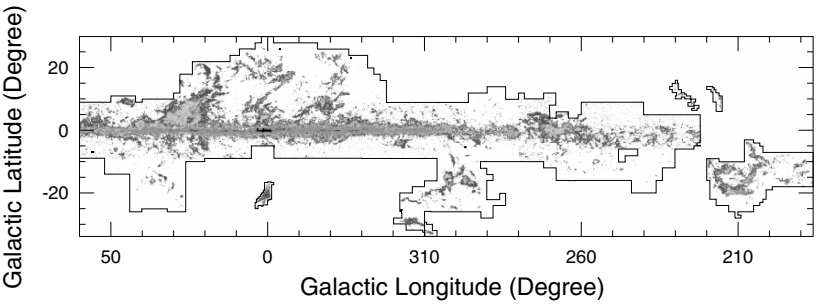

Fig. 1. A grayscale map of the ^{12}CO (J =1–0) velocity integrated intensity shown in galactic coordinate for the galactic plane survey with NANTEN.

3.2 Molecular Supershells

Supershells are large cavities created by multiple supernovae, having a size greater than $\sim$ 100 pc in the interstellar space mostly identified in the HI emission in the past. Some of the supershells exhibit expansion at a velocity greater than 10 km s^{-1}, and their kinetic energies are more than 10^{52} erg. So far, more than a few hundred HI shells including galactic worms have been identified in the galaxy (e.g., [5, 6]). On the other hand, the number of CO supershells, large shell structure identified in CO emission, are quite few because of the lack of systematic CO searches out of the plane to date.

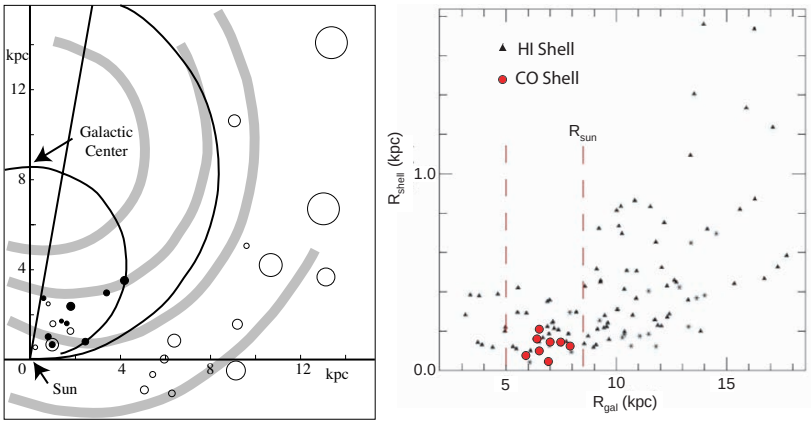

Fig. 2. (Left) Distribution of the CO shells (filled circles, [9]) and the HI shells (open circles, [10]) in the 4th quadrant. The gray thick lines indicate the location of spiral arms. (Right) Galacto-centric radius vs. size distribution of the CO and HI shells.

We discovered a CO supershell in the Carina region, named "Carina flare", from sensitive observations with NANTEN [2], demonstrating that there actually exist molecular clouds associated with supershells. More detailed analysis is carrying out by using high resolution HI data toward the Carina flare (Dawson et al. in preparation). Subsequently, we started a systematic search for CO supershells with NANTEN. [9] completed the search for CO supershells in the 4th galactic quadrant between 300° and 350° in the galactic longitude. Eight CO supershell candidates have been additionally identified by them. In Figure 2a, we show the face-on view of the distribution of CO [9] and HI [10] supershells. It is notable that the coincidence between the CO and HI shells is fairly poor. Only one shell is detected in both CO and HI.

We summarize the characteristics of CO shells along with a comparison with those of HI shells: (1) CO shells are located along the galactic arms, but many HI shells are located in the inter-arm regions (see Figure 2a). (2) CO shells are smaller in size than most of the HI shells (see Figure 2b). (3) The

dynamical timescales ($=R_{\rm shell}$ / $V_{\rm exp}$) of CO shells ($(0.2-1)\times10^7$ yr) are smaller than those of HI shells ($(0.5-3)\times10^7$ yr). These three characteristics are interpreted in terms of the evolution of supershells as follows. It is likely that a supershell is formed in an OB association that is located in the spiral arm. In the spiral arm, the shell accumulates the ambient gas as it expands, and molecular clouds are formed in the shell. In this phase, the supershell tends to be observable as a CO shell rather than a HI shell because the cavity of the shell is embedded in and contaminated by the HI gas. After a typical crossing time, a few $\times\ 10^7$ yr, the shell should gradually move to the inter-arm region due to the galactic rotation, and the galactic shear may distort the shell. Then the expanding shell cannot collect the ambient gas efficiently any longer. Separation between the CO clouds in the shell becomes sparse, and the CO clouds themselves may dissipate due to the expansion or by forming stars. Thus, the shell-like feature of CO clouds is not significant in this phase. In the inter-arm region, the HI contamination becomes less significant, and the shell becomes more obvious in HI than in CO. In this scenario, the HI and CO shell corresponds to different evolutionary stages of a single shell, and this may explain the cause for the poor coincidence between the CO and HI shells.

3.3 High Latitude Clouds

We have carried out high galactic latitude molecular clouds observations with the NANTEN telescope in order to reveal the molecular gas distribution around the solar system and the physical properties of low-density molecular clouds. Three types of observations have been made at the region.

A survey for high galactic latitude molecular clouds was carried out toward the 68 of far-infrared excess clouds of [12] by using ^{12}CO (J=1–0) line [11]. The CO emissions were detected in the 32 infrared excess clouds, corresponding to the detection rate of 47%. The CO detection rates for the cold and warm infrared excess clouds whose dust temperature are lower and higher than 17 K are 72% and 33%, respectively. This indicates that the cold clouds are well shielded from external UV radiation, resulting in a high CO abundance and a low temperature of the clouds. The infrared-excess clouds with no CO emission are most likely to be molecular hydrogen clouds because the temperature is similar to, or lower than, that of the surrounding H I gas. Even in far-infrared excess clouds with CO emission, molecular gas without CO emission seems to occupy more than 90% of the area of the clouds.

We then carried out a CO survey of high galactic latitude molecular clouds toward an H I filament including MBM 53, 54, and 55 [13]. We covered the whole area of the H I filament in ^{12}CO (J=1–0) with a $4'$ grid spacing (Figure 3a). Many clumpy molecular clouds are found to form the filament. We identified 110 ^{12}CO clouds and the total mass is estimated to be $\sim1200M_\odot$. ^{13}CO (J=1–0) observations were carried out toward the region of strong ^{12}CO intensities in order to measure the optical depth of molecular gas. There is

no detection in $C^{18}O$ (J=1–0) line in the observed region. This indicates that there are no clouds dense enough to have star formation in the near future. These observations spatially resolved the entire gas distribution of MBM 53, 54, and 55 for the first time, and we have found a massive cloud, HLCG 92−35 whose mass is ∼330 $M_\odot$, corresponding to 1/4 of the total mass. This CO cloud occupies the galactic western half of a circular H I cloud toward (L, B) ∼ (92°, −35°), and the H I to CO mass ratio is estimated to be the largest in the observed region. Far-infrared excess clouds toward HLCG 92−35 are the largest in the observed region. The ratio of the luminosity of the infrared excess to CO mass is also significantly larger than those of the other clouds, by a factor of ∼5. These facts indicate that HLCG 92−35 is a CO-forming molecular cloud, which is younger than the MBM clouds in terms of molecular cloud formation. A past explosive event has been suggested by [3] toward the H I filament. Toward HLCG 92−35, molecular gas is distributed along the western edge of the H I cloud, which implies that the molecular gas may be formed by a compression of expanding H I shell.

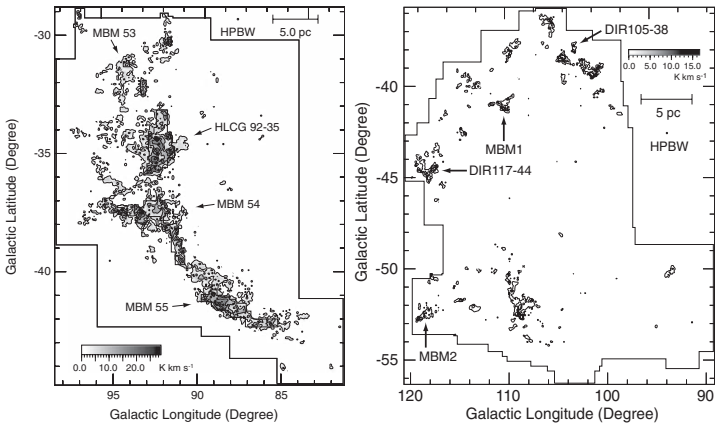

Fig. 3. (Left) a: Total velocity integrated intensity map of ^{12}CO (J = 1–0) toward MBM53, 54, and 55 region in the galactic coordinate[13]. The lowest contour is 1.50 K km s^{-1}, and the separation between the contours is 6.0 K km s^{-1}. The observed area of ^{12}CO is denoted by a thin solid line and the one of ^{13}CO is denoted by thick solid lines. (Right) b: Total velocity integrated intensity map of ^{12}CO (J = 1–0) shown in the galactic coordinate[14]. The lowest contour and the separation between contours are 0.77 and 3.08 K km s^{-1}, respectively. The solid line represents the observed area. The locations of DIR clouds in [12] and MBM clouds in [8] are shown in the figure.

Finally, we carried out large scale CO observations toward a loop-like structure in far infrared whose angular extent is about 20×20 degrees around (L, B) ∼ (109°, −45°) in Pegasus whose diameter corresponds to ∼26 pc assuming a distance of 100 pc, which is a distance of a star HD886 (B2IV) at

the center of the loop. We covered the loop-like structure in the ^{12}CO (J=1–0) emission at 4′–8′ grid spacing and in the ^{13}CO (J=1–0) emission at 2′ grid spacing for the ^{12}CO emitting regions [14]. The ^{12}CO distribution is found to consist of 78 small clumpy clouds whose mass ranges from 0.04 $M_{\odot}$ to 11 $M_{\odot}$. Interestingly, about 83% of the ^{12}CO clouds have very small masses of less than 1.0 $M_{\odot}$. ^{13}CO observations revealed that 19 of the 78 ^{12}CO clouds show significant ^{13}CO emission. ^{13}CO emission was detected the region where the molecular column density of ^{12}CO clouds is greater than 5×10^{20} cm^{-2}, corresponding to Av of ∼1 mag. We find no indication of star formation in these clouds in IRAS Point Source Catalog and 2MASS Point Source Catalog. The very low mass clouds identified are unusual in the sense that they have very weak ^{12}CO $T_{\rm peak}$ of 0.5 K–2.7 K and that they aggregate in a region of a few pc with no main massive clouds; contrarily to this, similar low mass clouds less than 1 $M_{\odot}$ previously observed in the other regions including at high galactic latitude region are all associated with more massive main clouds of $\gtrsim$100 $M_{\odot}$. A comparison with a theoretical work on molecular cloud formation [7] suggests that such small clouds may have been formed in the shocked layer through the thermal instability. The star HD886 (B2IV) at the center of the shell may be the source of the mechanical luminosity via stellar winds to create shocks, forming the loop-like structure with very small clouds delineated.

4 NANTEN2 Projects

The "NANTEN2" is an upgrade of the 4-m mm telescope, NANTEN, which was operated at Las Campanas Observatory, Chile. The upgrade started by moving NANTEN from Las Campanas to Atacama in Northern Chile at an altitude of 4,800m in 2004 to realize a large-scale survey at sub-mm wavelengths. In this new project, we will make large-scale surveys toward the Galaxy and the nearby galaxies including the Magellanic Clouds. We will reveal the physical and chemical states of interstellar gas in various density regions with the highly excited CO (carbon-monoxide) and CI (neutral carbon) spectra in the millimeter to sub-millimeter wavelength (86–810 GHz). With thorough extensive surveys, we will make studies of star formation process in the Local Group and investigate the dynamical effects of energetic explosive events like supernovae and supershells on the interstellar matter.

We installed a new main dish to achieve the sub-mm observations for NANTEN2. It consists of 33 aluminum panels that are adjustable with actuators (3 for each panel), and a light-weight carbon fiber back structure. After adjustment of the main reflector using photogarmmetry and holography, the expected surface accuracy is 15 micron rms. The new telescope is enclosed in a dome with a shiftable GoreTex membrane to prevent perturbations such as strong wind and sunlight. The installation started at the beginning of 2004. The highest observing frequencies will be covered by KOSMA SMART

(Sub-Millimeter Array Receivers for Two frequencies) receiver [4], a new multi-beam receiver capable of observing both 490 GHz and 810 GHz radiation simultaneously and effectively.

Fig. 4. NANTEN2 telescope

NANTEN2 is equipped with such low-noise superconducting receivers and the field of view of NANTEN2 is larger than those of ASTE, APEX, and ALMA. NANTEN2 will be suitable to cover a large sky area within a short observation time while the resolution is coarser than those of ASTE, APEX, and ALMA. In this sense NANTEN2 and other telescopes in Atacama are complementary relationship. The NANTEN2 observations provide a large database of interstellar matter in the Galaxy and the Magellanic Clouds. This database must be a useful guide for the future science with ALMA.

NANTEN2 Project is a collaboration between universities in Japan (Nagoya University and Osaka Prefecture University), in Germany (University of Cologne and University of Bonn), in South Korea (Seoul National University), and in Chile (University of Chile). Two groups are joining, University of New South Wales (Australia) and ETH Zurich (Switzerland), making a NANTEN2 Consortium with 8 Universities.

5 Summary

The NANTEN CO survey has provided a new view of the molecular distribution in the southern sky, from the galactic center to the outer edge of the galaxy. Its larger coverage in the galactic latitude than the previous surveys

and high sensitivity have allowed us to identify previously unknown weak features such as CO supershells. Detailed searches for weak CO emission toward the galactic center and the warp regions have revealed physical properties of CO clouds in peculiar environments in the galaxy. NANTEN telescope was moved to Atacama area in 2004 with an upgraded main reflector having three times better surface accuracy. This project, NANTEN2, is motivated to explore the large-scale molecular distribution for the first time in the sub-mm region.

Acknowledgements
The NANTEN project is based on the mutual agreement between Nagoya University and the Carnegie Institution of Washington. We acknowledge that this project was able to be realized by contributions from many Japanese public donators and companies. This work is financially supported in part by a Grant-in-Aid for Scientific Research from the Ministry of Education, Culture, Sports, Science and Technology of Japan (No. 15071203) and from JSPS (No. 14102003, core-to-core program 17004 and No. 18684003).

References

1. T. M. Dame, D. Hartmann, P. Thaddeus: ApJ 547, 792 (2001)
2. Y. Fukui, T. Onishi, R. Abe, A. Kawamura, K. Tachihara, R. Yamaguchi, A. Mizuno, H. Ogawa: PASJ 51, 751 (1999)
3. B. Y. Gir, L. Blitz, L. Magnani: ApJ 434, 162 (1994)
4. U. U. Graf, et al.: Millimeter and Submillimeter Detectors for Astronomy. Edited by Phillips, Thomas G.; Zmuidzinas, Jonas. Proceedings of the SPIE 4855, 322 (2003)
5. C. Heiles: APJS 229, 533 (1979)
6. B. -C. Koo , C. Heiles, W. T. Reach: ApJ 390, 108 (1992)
7. H. Koyama, S. Inutsuka: ApJ 564, 97 (2002)
8. L. Magnani, L. Blitz, L. Mundy: ApJ 295, 402, (1985)
9. K. Matsunaga, N. Mizuno, Y. Moriguchi, T. Onishi, A. Mizuno, Y. Fukui: PASJ 53, 1003 (2001)
10. N. M. McClure-Griffiths, J. M. Dickey, B. M. Gaensler, A. J. Green: ApJ 578, 176 (2002)
11. T. Onishi, N. Yoshikawa, H. Yamamoto, A. Kawamura, A. Mizuno, Y. Fukui: PASJ, 53, 1017 (2001)
12. W. T. Reach, W. F. Wall, N. Odegard: ApJ 507, 507 (1998)
13. H. Yamamoto, T. Onishi, A. Mizuno, Y. Fukui: ApJ 592, 217 (2003)
14. H. Yamamoto, A. Kawamura, K. Tachihara, N. Mizuno, T. Onishi, Y. Fukui: ApJ 642, 307 (2006)

3

Mapping the Milky Way and the Local Group

Mark Reid[1], Andreas Brunthaler[2,3], Xu Ye[3,4], Zheng Xing-Wu[5], Karl Menten[3], Lincoln Greenhill[1], and Luca Moscadelli[6]

[1] Harvard-Smithsonian CfA, USA
[2] Joint Institute for VLBI in Europe, The Netherlands
[3] Max-Planck-Insitut für Radioastronomie, Germany
[4] Shanghai University, China
[5] Nanjing University, China
[6] Arcetri Observatory, Italy

Summary. Over the past decade, the astrometric accuracy of Very Long Baseline Inteferometry has improved dramatically. Currently relative positions between sources separated by about 1° are being measured with accuracies of $\sim$ 10 μas. With this accuracy, trigonometric parallaxes throughout the Milky Way and proper motions of Local Group galaxies are now being measured. These observations will lead to direct mapping of the structure of the Milky Way, testing of the spiral density wave paradigm, measuring the dark matter halos of Local Group galaxies, and better understanding of the past history and future fate of these galaxies.

1 Advances in VLBI Astrometric Accuracy

Very Long Baseline Interferometry has always held the promise for near microarcsecond (μas) astrometry. In some cases such accuracy has been achieved, for example, for relative positions of maser spots within a source [1, 2]. Also, there are some pairs of continuum sources (eg, QSOs) very close together on the sky for which μas relative positions have been determined [3]. However, such accuracies have not been routine until recently.

Routine astrometric accuracy for VLBI observations of pairs of sources separated by about 1° has advanced from about 1 mas in 1995 to about 20–50 μas in 2005. One example of high astrometric accuracy is the measurement of the proper motion of Sgr A*. Observations originally started in the late 1970s, but not successful until the VLBA came on-line in the 1990s, have been used to track the apparent position of Sgr A*. Fig. 1 displays the position of Sgr A*, relative to a distant "QSO" J1745-283, from 1995 currently through 2003 [4].

The apparent motion of Sgr A* is dominated by the orbit of the Sun about the center of the Milky Way. The Sun travels in a nearly circular ($e < 0.1$) orbit at a speed of about 220 km s^{-1} at a radius of 8 kpc [5]. The small

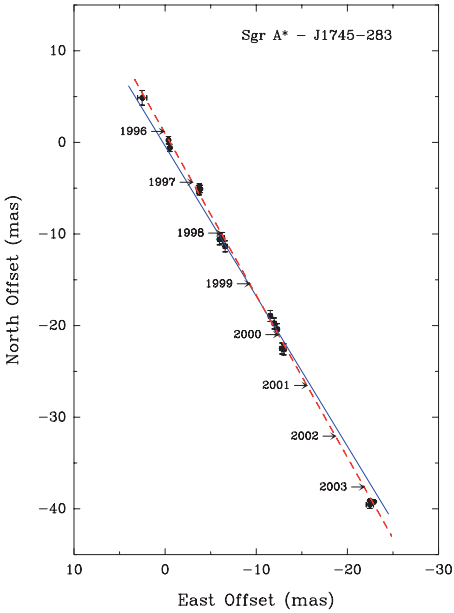

Fig. 1. Apparent proper motion of Sgr A* on plane of the sky. Position residuals of Sgr A* relative to J1745–283 on the plane of the sky are plotted. Each measurement is indicated with an ellipse, approximating the scatter-broadened size of Sgr A* at 43 GHz, and 1σ error bars. The dashed line is the variance-weighted best-fit proper motion, and the solid line gives the orientation of the IAU Galactic plane. The different slopes of the two lines corresponds to the motion of the Sun perpendicular to the Galactic Plane.

component of motion out of the Plane is caused by the 7.2 km s^{-1} component of the peculiar motion of the Sun. After accounting for the motion of the Sun, the residual motion of Sgr A* out of the Plane is less than about 1 km s^{-1} [4]. Were Sgr A* a stellar object and not a super-massive black hole, it would be moving at speeds of $\sim 10^{3-4}$ km s^{-1}, as observed for stars near its position.

2 Trigonometric Parallax Measurements

With relative positional accuracy of $\sim$ 10 μas, one can obtain trigonometric parallaxes to sources as far away as the Galactic Center with accuracies of better than 10%. By comparison, the very successful astrometric satellite *Hipparcos* [6], which determined $\sim 10^5$ parallaxes, only achieved an accuracy of $\sim$ 1 mas – a factor of nearly 100 poorer than from VLBI techniques.

A trigonometric parallax is the "gold standard" for astronomical distance measurements, involving simple triangulation with the Earth's orbit about the Sun as one leg of a triangle. The parallax signatures for three representative

Galactic sources are shown in Fig. 2. From the vantage point of a source at Galactic longitude 134° (eg, W3OH), the Earth's orbit appears nearly face-on and the sinusoidal excursions observed in the R.A. and Dec. directions are nearly the same magnitude. For sources closer to the Galactic Center, the orbital plane of the Earth tilts and the Declination parallax amplitude decreases. At the Galactic Center, the Earth's orbit appears nearly edge-on and the R.A. parallax sinusoid completely dominates.

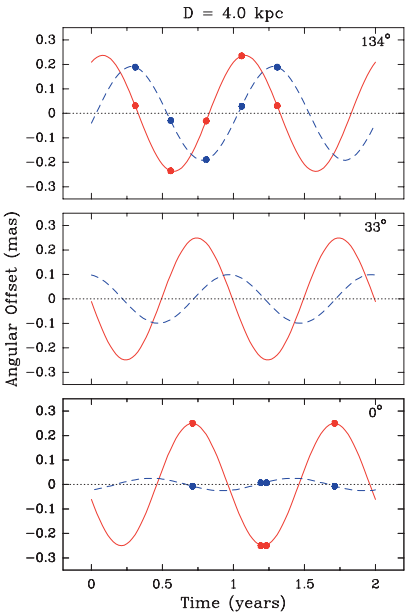

Fig. 2. Example trigonometric parallax signatures for sources in the Galactic Plane at three Galactic longitudes (indicated in each panel). The effect of the Earth's orbit around the Sun in the East-West (*solid lines*) and North-South (*dashed lines*) directions are shown. Sample data, which are nearly optimum for parallax measurement, are shown on the top and bottom panels. A distance of 4 kpc is assumed.

When determining a trigonometric parallax, one must also solve for a proper motion. Parallax accuracy is improved by minimizing correlations between the parallax and proper motion parameters. Symmetric sampling of the parallax signature near the maximum position excursions is optimal. The top panel of Fig. 2 shows a case where the R.A. and Dec. parallax excursions are comparable and a near optimum time sampling every 3 months is indicated. However, in the bottom panel, when the R.A. parallax excursion is significantly greater than the Dec. excursion, the time sampling shown every 6 months is a better strategy.

3 Trigonometric Parallax for W3OH

Recently the parallax of W3OH, a massive newly-formed star in the Perseus spiral arm of the Milky Way, has been measured by two groups, using CH_3OH [7] and H_2O [8] masers as astrometric targets. In general, CH_3OH masers, whose lifetimes are $\gg 1$ year, are better suited for parallax measurements than H_2O masers, whose typical lifetimes are < 1 year. (However, H_2O masers are generally stronger and more numerous in the Milky Way.) Fig. 3 demonstrates the stability of CH_3OH masers by showing a portion of the W3OH source at two epochs spaced by one year.

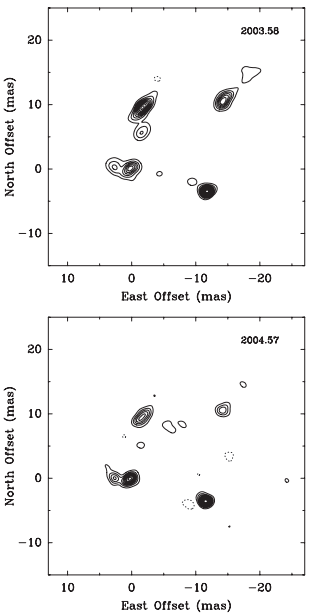

Fig. 3. A cluster of 12 GHz methanol maser spots in W3OH. These masers change only slightly over the 1 year between observations, making them excellent astrometric targets.

Positions of a single CH_3OH maser spot in W3OH, relative to three QSOs, are shown in Fig. 4. The parallax signature plus the source proper motion results in the "tilted" sinusoids. Combining parallax data from 9 maser spots and 3 background QSOs yields a parallax of 0.512 ± 0.010 mas (1.95 ± 0.04 kpc) [7]. This parallax resolves a long-standing problem of a discrepancy of a factor of 2 between kinematic (4.3 kpc) and luminosity (2.2 kpc) distances to star forming regions in this portion of the Perseus spiral arm. The kinematic distances are a factor of 2 too large, while the luminosity distances are correct to within 15%.

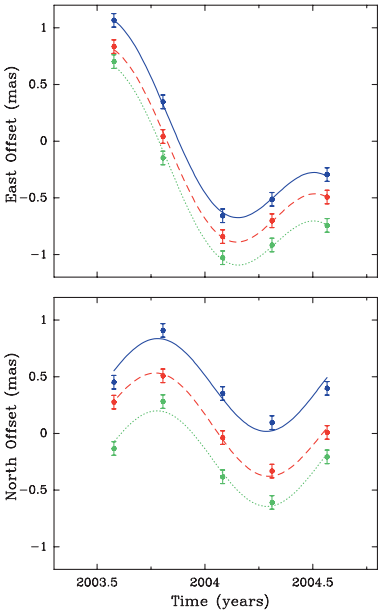

Fig. 4. Positions for one 12 GHz maser spot in W3OH relative to 3 background sources (offset from each other for clarity). The data show the sinusoidal parallax signature superposed on the proper motions.

The proper motion of W3OH, measured with an accuracy of better than 1 km s^{-1}, indicates the reason for the kinematic distance anomaly. W3OH has a very large peculiar motion of 22 km s^{-1}, with respect to circular motion in the Milky Way. Essentially all of this peculiar motion is toward the Sun, resulting in a very large kinematic distance error. While spiral density wave theories allow for such a peculiar motion [9], the magnitude of the motion is larger than most models predict. Parallax and proper motion measurements with the VLBA and VERA for large numbers of massive star forming regions can be used to determine the spiral structure of the Milky Way and to test critically the spiral density wave paradigm.

4 Proper Motions in the Local Group

With near μas relative position accuracy, there are many interesting applications of VLBI astrometry to extragalactic astronomy. In the 1920s, van Maanen claimed to have measured the angular rotation of nearby spiral galaxies. Fig. 5 reproduces a plate from his 1923 paper [10], purporting to show large rotation, which was offered as evidence against the extragalactic nature of "spiral nebulae."

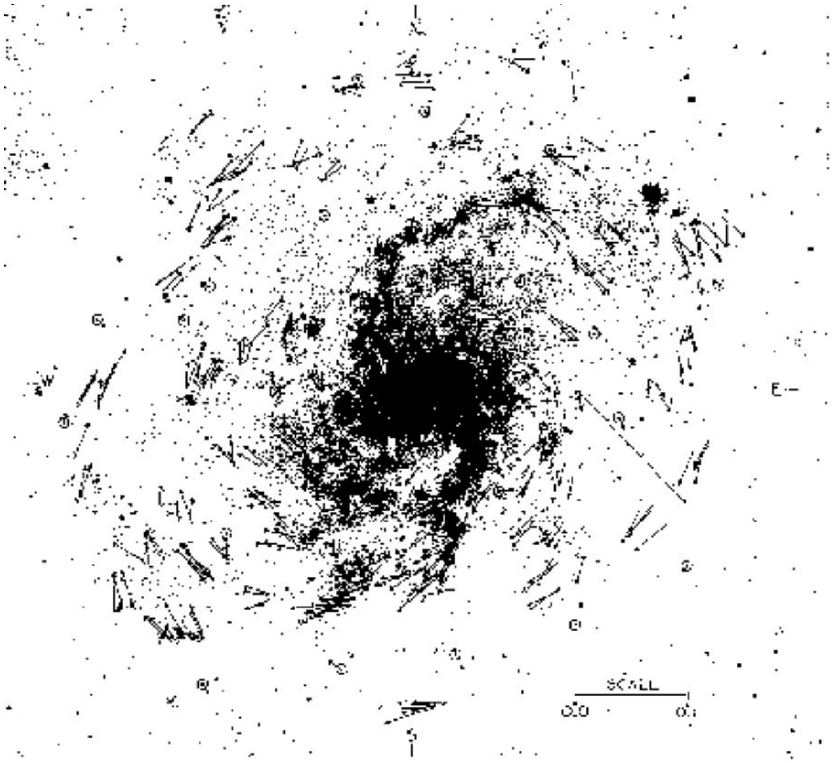

Fig. 5. The van Maanen Experiment [10]: relative proper motions in M33 obtained from optical plates in the 1920s. The proper motions are far larger than possible for an external galaxy; the reason for the exaggerated motions have never been determined.

Andreas Brunthaler, as part of he PhD thesis work, was able to accomplish the "van Maanen experiment" and measure the angular rotation of M33 [11]. Fig. 6 shows schematically the location and expected motion of two H_2O maser sources relative to the center of M33. The measured motions are close to the expected motions. Combining the measured angular rotation with a model of the rotation speed and inclination of M33 (from HI observations) gives a distance of 730 ± 168 kpc. Since proper motion accuracies improve rapidly with increased observing time span (as $t^{3/2}$), continued VLBA observations will soon yield a very accurate distance to M33.

Brunthaler's observations were phase-referenced to distant QSOs. This allows the proper motion of the entire galaxy to be estimated. Galaxy proper motions are key to understanding the past history and future fate of galaxies in groups. Fig. 7 shows the measured motions of M31 (radial velocity only) and M33 (3-D velocity), relative to the Milky Way. Were M31 to have a near zero proper motion, as might be expected since M31 and the Milky Way are

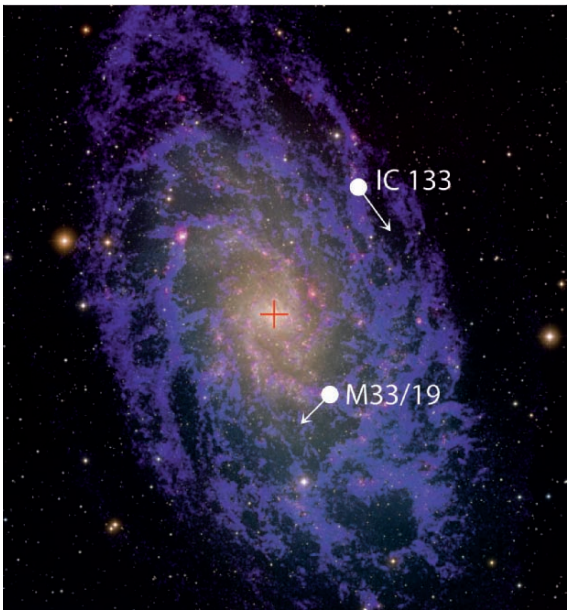

Fig. 6. The locations and expected proper motions of two sites of H_2O masers in M33. These motions (the "van Maanen experiment") have been measured by VLBI observations [11].

the dominant galaxies in the Local Group, one could calculate the "orbits" of M33, M31, and the Milky Way.

Loeb et al. [12] calculated Local Group orbits for different trial proper motions of M31. Over large ranges of trial proper motions, M33 was found to have interacted strongly with M31. Such interactions would have tidally heated and stripped stars in M33, which seems inconsistent with M33's undisturbed disk. In this manner, M31's proper motion is strongly constrained.

Calculations of "orbits" of Local Group galaxies are sensitive to the mass of dark matter halos. Reducing dark matter halos masses can avoid having strong tidal interactions between M33 and M31, as well as close encounters between M31 and the Milky Way in the past [12]. Clearly, proper motions of Local Group galaxies provide powerful information on dark matter.

5 The Future Today

Recently, Sofue & Rubin [13] reviewed progress on understanding rotation curves of spiral galaxies. They also made predictions of where significant advances could be expected. Three of these predictions are already close to fruition: 1) "Rotation of the Galaxy...will be directly measured from proper motions and parallaxes...using microarcsecond radio interferometry; 2) "Radio

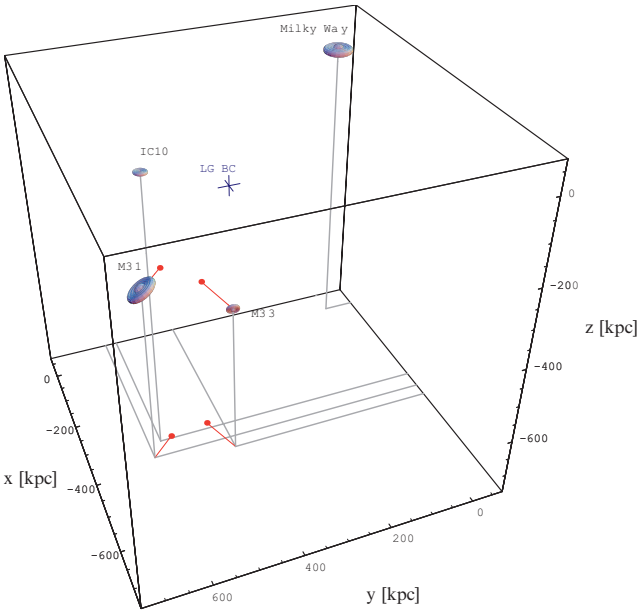

Fig. 7. Motions of M33 and M31 relative to the Milky Way [11]. M33's radial and proper motion has been measured, however, only the radial component if M31's motion has been measured.

interferometry of maser stars will be used to directly measure rotation on the sky of the nearest galaxies; and 3) "Dark halos...Will we learn if our halo brushes the halo of M31?"

We can certainly look forward to the fantastic results that the VLBA and VERA will provide.

References

1. M. J. Reid et al: ApJ, 330, 809 (1988)
2. C. Gwinn, J. M. Moran & M. J. Reid: ApJ, 393, 149 (1992)
3. M. J. Rioja et al: A&A, 325, 383 (1997)
4. M. J. Reid & A. Brunthaler: ApJ, 616, 872 (2004)
5. M. J. Reid: ARA&A, 31, 345 (1993)
6. M. A. C. Perryman et al: A&A, 323, 49P (1997)
7. Y. Xu, M. J. Reid, X. W. Zheng & K. M. Menten: Science, 311, 54 (2005)
8. K. Hachisuka et al: ApJ, 645, 337 (2006)
9. W. W. Roberts: ApJ, 259, 283 (1972)
10. A. van Maanen: ApJ, 57, 264 (1923)
11. A. Brunthaler et al: Science, 307, 1440 (2005)
12. A. Loeb, M. J. Reid, A. Brunthaler & H. Falcke: ApJ, 633, 894 (2005)
13. Y. Sofue & V. Rubin: ARA&A, 39, 137 (2001)

4

VERA Project

Mareki Honma[1,2], Takeshi Bushimata[1,3], Yoon Kyung Choi[1,4], Tomoya Hirota[1], Hiroshi Imai[5], Kenzaburo Iwadate[1], Takaaki Jike[1], Osamu Kameya[1,2], Ryuichi Kamohara[1], Yukitoshi Kan-ya[1], Noriyuki Kawaguchi[1,2], Masachika Kijima[1,2], Hideyuki Kobayashi[1,3,4], Seisuke Kuji[1], Tomoharu Kurayama[1], Seiji Manabe[1,2], Takeshi Miyaji[1,3], Takumi Nagayama[5], Akiharu Nakagawa[5], Chung Sik Oh[1,4], Toshihiro Omodaka[5], Tomoaki Oyama[1], Satoshi Sakai[1], Katsuhisa Sato[1], Tetsuo Sasao[6], Katsunori M. Shibata[1,3], Motonobu Shintani[5], Hiroshi Suda[1,4], Yoshiaki Tamura[1,2], Miyuki Tsushima[5] and Kazuyoshi Yamashita[1,2]

[1] Mizusawa VERA Observatory, NAOJ, Mitaka, Tokyo, 181-8588, Japan
[2] Graduate University for Advanced Studies, Mitaka, Tokyo, 181-8588, Japan
[3] Space VLBI Project, NAOJ, Mitaka, Tokyo, 181-8588, Japan
[4] Department of Astronomy, University of Tokyo, Bunkyo, Tokyo, 113-8654, Japan
[5] Faculty of Science, Kagoshima University, Kagoshima, 890-0065, Japan
[6] Ajou University, Suwon 442-749, Republic of Korea

In this paper we review the current status of VERA (VLBI Exploration of Radio Astrometry) project. First, we present an overview of VERA, and then we report on recent results from VERA, particularly the parallax measurement of Galactic star forming region S269 at the distance of 5.3 kpc.

1 Introduction

VERA (VLBI Exploration of Radio Astrometry) is Japanese VLBI array dedicated to VLBI astrometry (Honma et al. 2000; Kobayashi et al. 2003 and references therein). The main objective of VERA is to study the 3-D structure and dynamics of the Galaxy through the high-precision astrometry of Galactic maser sources. In order to achieve astrometric accuracy that is required for Galaxy-scale astrometry ($\sim 10\mu$as), VERA utilize the phase-referencing VLBI technic. As an optimized system for phase-referencing, VERA is the only existing VLBI array that is installed with dual-beam system, which allows us to observe simultaneously a target and a reference to effectively cancel out the tropospheric fluctuations. Thus, VERA can be regarded as an ultimate array for phase-referencing VLBI astrometry. In the present paper, we introduce the VERA project and report on the recent results of astrometric measurements.

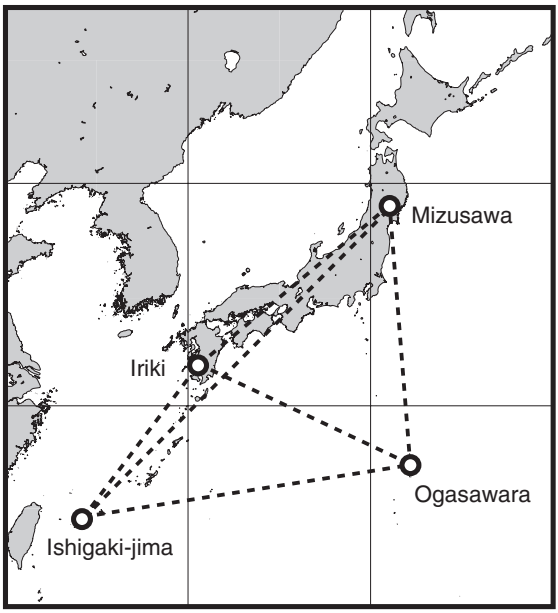

Fig. 1. Array map of VERA showing the location of 4 stations. Ishigaki-jima station (the south-west one) is located on Ishigaki island, where this conference was held.

2 Project Overview

The VERA array consists of four radio telescopes with 20 m diameter spread over Japan. VERA stations are located at Mizusawa, Iriki, Ogasawara, and Ishigaki-jima, with north latitudes ranging from 24° to 39°, and east longitude ranging from 124° to 141° (see figure 1). The lengths of six baselines range from 1000 km to 2300 km. Each antenna is installed with dual-beam receiving system shown in figure 2 (Kawaguchi et al. 2000). The dual-beam system is composed of two steerable receivers which are installed on Steward-mount platform. This dual-beam system enables us to observe a target maser source and a extra-galactic position reference (QSO and radio galaxies) at the same time in order to cancel out tropospheric fluctuations more effectively than switching VLBI observations with normal single-beam telescopes. The major observing bands of VERA are K band (22 GHz) and Q band (43 GHz). K-band is for H_2O maser sources (mainly star forming regions and AGB stars), and Q-band is for SiO maser sources (mainly AGB stars). In these two bands, VERA will observe $\sim$1000 of H_2O and SiO maser sources and measure their parallaxes and proper motions to reveal 3D structure and dynamics of the Galaxy.

In 1999 the project was funded by the Japanese government and the constructions of stations were started in 2000. In April 2001 three stations (Mizusawa, Iriki, Ogasawara) were completed, and in April 2002 construction of

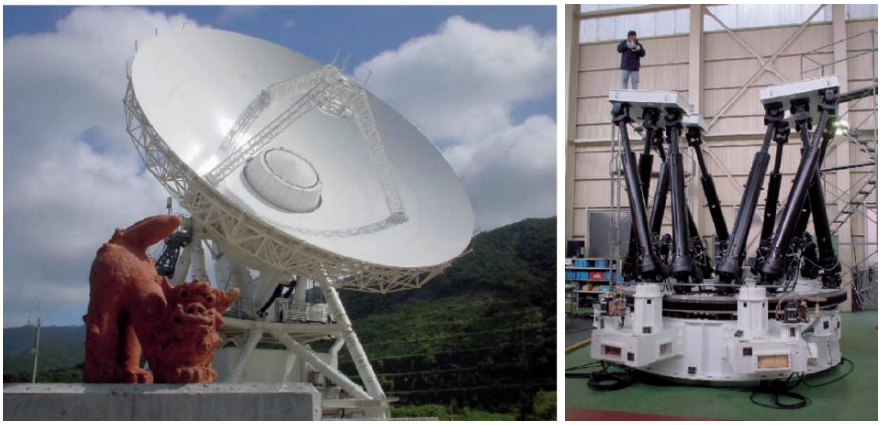

Fig. 2. (left) View of Ishigaki-jima station. (right) Steward-mount dual-beam plat form.

full array was finished when the fourth station, Ishigaki-jima, was completed. After the completion of constructions and installations of instruments, test observations have been started to evaluate system performance. In particular phase-referencing test observations with dual-beam system showed its high capability, demonstrating that the atmospheric phase fluctuations were effectively cancelled out based on the dual-beam observations (Honma et al. 2003). Since the fall of 2003, we started astrometric monitoring observations of Galactic maser sources, and recently parallax and proper motions have been successfully measured for some sources.

3 Recent Results : Parallax Measurement of S269

3.1 Observations

As an example of recent astrometric results, here we report on the parallax measurements of a Galactic star forming region S269. S269 is a massive star forming regions toward anti-center region located at (l, b)=(196.45°, −1.67°), with an estimated distance of 4 kpc (Moffat et al. 1979). At the center of YSO cluster of S269, there are two bright infrared sources named as IRS 2e and IRS 2w, and H_2O maser is associated with the star IRS 2w, which is though to be a young O-type star deeply embedded in a surrounding gas and dust (Jiang et al. 2003). VERA observations of S269 H_2O maser were regularly performed since November of 2004 with a typical interval of 1 to 2 months. Here we present the data of 6 epochs that were obtained with the full 4-station array under relatively good conditions, which are day of year (DOY) 323 in 2004, DOY 026, 073, 134, 266 and 326 in 2005 (Nov. 18 in 2004, Jan. 26,

Mar. 14, May. 14, Sep. 23 and Nov. 21 in 2005), spanning 1 year. At each epoch, S269 H_2O maser (rest frequency of 22.235080 GHz, H_2O 6_{16}-5_{23} transition) and a position reference source J0613+1306, which is one of the ICRF sources (Ma et al. 1998), were simultaneously observed in dual-beam mode for 9 hours. The separation angle between the maser and the reference sources is 0.73 degree. Left-hand circular polarization signals were received and digitally recorded onto magnetic tapes with the VERA-terminal system. Correlation processing was done with the Mitaka FX correlator, with frequency and velocity resolutions of 15.625 kHz and 0.21 km s^{-1}, respectively. Re-calculations of precise delay were made after the correlation, and correlated visibilities were corrected for the difference between the initial (rather crude) apriori delay model and second (more accurate) delay model. When these calibrations were made, tropospheric zenith delays estimated from GPS data taken at each station were applied to correct for the residuals of tropospheric delay model. Also, ionospheric delays were calibrated based on the global ionosphere map (GIM) provide by University of Bern. In the phase-referencing analysis, phase solutions for J0613+1306 were converted into phases at observed H_2O maser frequency, and applied to visibilities of S269 together with dual-beam phase calibration data. After those calibrations, visibilities of S269 H_2O masers were Fourier transformed to produce synthesized images, and the positions of the brightness peaks were determined. In order to calibrate possibly-remaining residuals in tropospheric delay, zenith delay offsets were re-estimated as constants through 9-hour observations so that the coherence of the phase-referenced map is maximized.

3.2 Results

Basically S269 H_2O maser show only one feature at $V_{\rm LSR}$ of 19 to 20 km s^{-1}. In this maser feature, 5 to 6 maser spots were detected at each epoch, and these maser spots are aligned in the east-west direction with a scale of 0.4 mas. The thickness of the feature (spots distribution in the north-south direction) is $\sim$ 50 μas, 10 times smaller than the width in the east-west direction. The maser distribution also shows a velocity gradient from the east to the west. Assuming the position of J0613+1306 as (α_{J2000}, δ_{J2000}) = (06h13m57.692764s, +13d06'45.40116"), the absolute position of the brightest spot at $V_{\rm LSR}$ = 19.5 km s^{-1} is obtained as (06h14m37.0793s, +13d49'36.694") with an uncertainty of 1 mas, which mainly comes from the uncertainty of absolute position of the calibrator J0613+1306. The absolute position of the H_2O maser in S269 agrees well with the position of IRS2w, which is the most luminous infrared source in the S269 regions (Jiang et al. 2003).

Figure 3 shows the position variation of the brightest spot at 19.5 km s^{-1} in both X and Y directions for monitoring span of 1 yr. As clearly seen from the X component plot, the spot motion shows systematic sinusoidal variation with a period of 1 yr, which is certainly from the parallax of S269. Here we use only X component to determine the parallax of S269, because 1) the

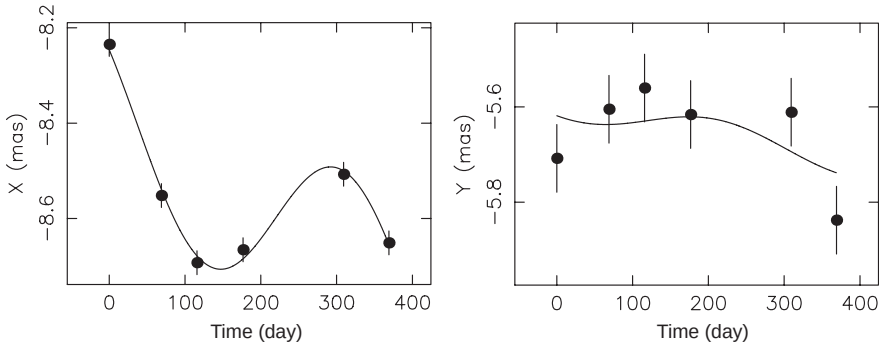

Fig. 3. Motions of the brightest maser spot in S269. Left is for X component (the east-west direction), and right is for Y component (the north-south direction). X component clearly shows annual modulation, that is the parallax of S269. Note that positions are relative values to the tracking center position of S269, which is (06h14m37.08s, +13d49'36.7") in the J2000 coordinate system.

Y-direction error is large and 2) S269 is near the ecliptic and parallax ellipse is highly elongate in the X direction, making the contribution of Y to parallax determination small. Based on the brightest three spots at the radial velocity of 19.4 to 19.8 km s^{-1}, the parallax of S269 is determined to be 189 ± 16 μas (12 σ). This corresponds to the source distance of $5.30^{+0.48}_{-0.41}$ kpc, which is slightly larger than previous estimates, which claimed a distance of ∼4 kpc (e.g., Moffat et al. 1979). This is the smallest parallax ever measured, and this results demonstrate the high capability of VERA to perform the Galactic-scale astrometry. In addition to parallax, we also obtained average proper motion as ($\dot{X} = -0.428 \pm 0.027$, $\dot{Y} = -0.121 \pm 0.038$) mas yr^{-1}, respectively. At the distance of 5.30 kpc, these corresponds to heliocentric velocities of 10.7 km s^{-1} and 3.0 km s^{-1}, which are remarkably smaller that the galactic rotation velocity (∼ 200 km s^{-1}). The small relative velocities indicate that the galactic rotation velocity at S269 ($l = 196.45°$) is similar to that at the Sun and relative proper motions are mostly cancelled out.

In figure 3, we also show error bars estimated as the standard deviation from the best fit curve. The error bar sizes are 25 μas for X and 75 μas for Y. It is remarkable that error in Y is three times larger than that in X. This can be explained if one assumes that the uncertainty in the tropospheric zenith delay is the dominant error source. For instance, if we assume an uncertainty of 3 cm of the the tropospheric zenith delay, then it causes an path length difference of 0.4 mm (∼ 30 mm/0.7°, where 0.7° is the separation between S269 and the calibrator) between the two sources. This uncertainty in path length difference roughly corresponds to 40 μas (=$0.4/2.3\times10^9$, where 2.3 $\times10^9$ mm is the maximum baseline length of the VERA array). In practical observations, the effect of zenith delay error is multiplied by a factor of 1 to

2 depending on source declinations and observing elevations. If this factor is taken into account, one can expect an astrometric error of 60 to 80 μas in Y direction, which agrees with the estimated error in the present study. On the other hand, astrometric error in the X direction can be suppressed for two reasons: first, the source pair considered here has smaller separation in X direction compared to Y (i.e., north-south pair), and second, the observational track of UVW coverage of each epoch are roughly symmetric with respect to the meridian transit, and this symmetry can help to reduce the astrometric error in the X direction caused by the tropospheric zenith delay offset. Therefore, if the dominant error source is troposphere as we discussed above, calibration of tropospheric delays are important for obtaining better astrometric accuracy in future observations (particularly in Y component). This can be solved by additional measurements of tropospheric delays, for instance by GPS receivers, water vapor radio meter and/or geodetic mode observations (e.g., Brunthaler et al. 2005).

4 Concluding Remarks

As we have described above, we have successfully measured parallax beyond 5 kpc, and now VERA seems ready to perform Galactic-scale astrometry. In fact, from regular observations of several maser sources, and we have also detected parallax of star forming regions such as Orion-KL and NGC 1333 (Hirota et al. 2006). In near future, we will observe 60 to 70 maser sources every year, and in 15 years we will observe nearly 1000 maser sources in the Galaxy, and finally provide accurate 3D map of the Galaxy's disk.

References

1. Brunthaler A., et al.: in ASP Conf. Ser. 340, Future Directions in High Resolution Astronomy, eds. J. Romney & M. Reid, 455 (2005)
2. Honma M., Kawaguchi N., Sasao T.: in Proc. SPIE 4015, Radio Telescope, ed. H. R. Buthcer, 624 (2000)
3. Honma, M., et al.: PASJ 55, L57 (2003)
4. Hirota, T., et al.: in this proceeding volume.
5. Jiang, Z., et al.: ApJ 596, 1064 (2003)
6. Kawaguchi N., Sasao T., Manabe S: in Proc. SPIE 4015, Radio Telescope, ed. H. R. Buthcer, 544 (2000)
7. Kobayashi, H., et al.: in ASP Conf. Ser. 306, New Technologies in VLBI, ed. Y. C. Minh, 367 (2003)
8. Ma, C., Arias, E.F., Eubanks, T.M., Fey, A.L., Gontier, A.M., Jacobs, C.S., Sovers, O.J., Archinal, B.A., & Charlot, P.: AJ 116, 516 (1998)
9. Moffat, A. F. J., Jackson, P. D., & Fitzgerald, M. P.: A&AS 38, 197 (1979)

5

Dynamics of Stars in the Inner Galactic Bulge Revealed from SiO Maser Surveys

Shuji Deguchi[1], Takahiro Fujii[2,3], Yoshifusa Ita[4,5], Hideyuki Izumiura[6], Osamu Kameya[2,7] Atsushi Miyazaki[1,8],Yoshikazu Nakada[4,9] and Makoto Ideta[10]

[1] Nobeyama Radio Observatory, National Astronomical Observatory, Minamimaki, Minamisaku, Nagano 384-1305, Japan
[2] VERA Project Office, National Astronomical Observatory, 2-21-1 Osawa, Mitaka, Tokyo 181-8588, Japan
[3] Faculty of Science, Kagoshima University, 1-21-35 Korimoto, Kagoshima, Kagoshima 890-0065, Japan
[4] Institute of Astronomy, School of Science, The University of Tokyo, 2-21-1 Osawa, Mitaka, Tokyo 181-001, Japan
[5] Institute of Space and Astronautical Science, Japan Aerospace Exploration Agency, Yoshinodai 3-1-1, Sagamihara, Kanagawa 229-8510, Japan
[6] Okayama Astrophysical Observatory, National Astronomical Observatory, Kamogata, Asakuchi, Okayama 719-0232, Japan
[7] Mizusawa Astrogeodynamics Observatory, National Astronomical Observatory, 2-12 Hoshigaoka, Mizusawa, Iwate 023-0861, Japan
[8] Shanghai Astronomical Observatory, Chinese Academy of Sciences, 80 Nandan Road, Shanghai, 200030, P.R. China
[9] Kiso Observatory, School of Science, The University of Tokyo, Mitake, Kiso, Nagano 397-0101
[10] Center for Computational Astrophysics, National Astronomical Observatory, 2-21-1 Osawa, Mitaka, Tokyo 181-8588, Japan

Abstract: We surveyed $\sim$ 300 MSX/2MASS infrared objects in the $7^\circ \times 2^\circ$ area of the Galactic center in the $\sim$43 GHz SiO maser lines, obtaining accurate radial velocities of $\sim$ 160 detected objects. The longitude–velocity diagram of these objects reveals two conspicuous features: one indicating a linear velocity increase with longitude with $|l| < 1.5^\circ$, which is likely to be associated with the inner bar, and the other having eccentric velocities with $|V_{\rm lsr}| > 250$ km s^{-1}. Based on numerical simulations of stellar orbits in the Galactic bulge, we conclude that the latter feature is created as a result of a past star formation in the bulge, when the intersecting point of the x_1 and x_2 orbits was considerably outside of the present position.

1 Introduction

Though a considerable amount of theoretical and observational works have been made for understanding the central part of the Galaxy, it is still not very clear how the stars revolve around the Galactic center, and how they are reincarnated through star-forming gas clouds to the bar structure. Mass-losing Asymptotic Giant Branch (AGB) stars in the Galactic bulge supply a large amount of gases to the Galactic nuclear disk. The bar structure of the bulge is responsible for infalling gases to the central nuclear cluster, throwing newly formed stars into inner bulge orbits, changing the bar potential gradually.

Stellar orbits in the bar-like bulges are mainly composed of the x_1 and x_2 families, which fabricate the bar with two elongated features along and perpendicular to the bar (Athanassoula 1992). Past photometric studies revealed the bulge bar in our Galaxy with ∼3:1 elongation making an angle of $\sim 30^\circ$ from the Sun-GC direction (Nakada et al. 1991; Dwek et al. 1995; Lôpez-Corredoira et al. 2001; Benjamin et al. 2005). Position–velocity diagrams of the CO, ^{13}CO, and HI gas distributions clearly indicate the presence of inner-bar structure (Binney et al. 1991). Recently, Alard (2001) and Nishiyama et al. (2005) analyzed the NIR photometric data of stars toward the inner Galactic bulge, finding a presence of the small-scale feature ($|l| < 2^\circ$) which is possibly elongated perpendicularly to the large-scale bar structure.

This paper discuss the features revealed by the SiO maser survey of ∼ 300 MSX/2MASS objects in the area $|l| < 3.5^\circ$, and $|b| < 1^\circ$ (Fujii et al. 2006), based on the obtained longitud–velocity diagram. We integrated equations of motions of bulge stars embedded in the bar potential. Comparing the observed longitude–velocity diagram with simulated ones, we conclude that the extremely high velocity stars in the bulge are remnants of the star formation occurring at the past crossing point between the x_1 and x_2 orbits.

2 Observational Data

Source sampling for the present SiO survey (Fujii et al. 2006) was made based on the MSX and 2MASS catalogs: the MSX catalog provided a large number ($\gg 1000$) of middle-infrared sources in the above area, except very near to the Galactic center ($< 15'$). With 2MASS identifications, the AGB stars under mass loss were easily picked up effectively excluding young stellar objects from the sample. These objects were used as dynamical tracers in the inner bar region of the Galaxy. Because the SiO survey of the very central area ($|l|$ and $|b| < 15'$; inner ∼30 pc) was already published (Deguchi et al. 2004), we excluded the central $15'$ area from the present survey. The longitude–velocity diagram of 163 detected objects is shown in Figure 1.

One notable feature in figure 1 is a rough alignment of objects along the line $V_{\rm lsr} \sim 100 \times (l/{\rm deg})$ km s^{-1} at the range $|l| < 1.5^\circ$, which roughly coincides with the x_2 orbit trajectories. This feature was not seen in the l–v map of

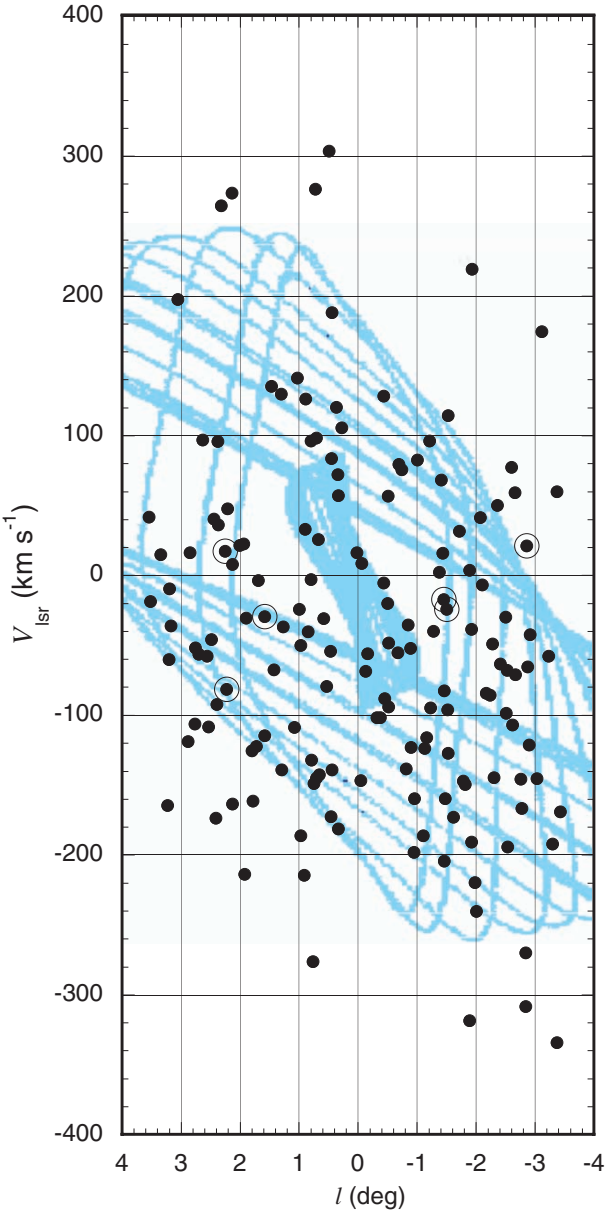

Fig. 1. SiO longitude–velocity diagram overlaid on the x_1 and x_2 orbit trajectories [taken from figure 11 of Bissantz et al. (2003). The large circle indicates a foreground object. Thin outer curves spreading between $V_{\rm lsr} = \pm 240$ km s^{-1} are trajectories for the x_1 orbit family, and inner curves concentrating between $V_{\rm lsr} = \pm 85$ km s^{-1} and between $l = \pm 1.2^{\circ}$ are those for x_2 orbit family.

IRAS/SiO objects in $|l| < 3^\circ$ and $|b| < 3^\circ$ (figure 6 of Deguchi et al. 2000), in which the survey based on IRAS catalog was quite incomplete in $|b| < 1^\circ$. Therefore, it is highly likely that these are objects in the x_2 orbits.

Another notable feature in the SiO l–v diagram is a group of stars with extreme high-velocities, which are located beyond the maximum velocities of the x_1 orbits in figure 1. In fact, these velocities are beyond the upper and lower limits of the radial velocity of the CO gas. In addition, no strong feature in the SiO distribution is found for the velocities corresponding the 240 pc molecular ring (e.g., Sawada et al. 2004), which is represented approximately by the innermost x_1 orbit in figure 1. These facts must be understood in terms of periodic and non-periodic orbital families under condition of a steady gravitational bar potential (or otherwise, chaotic orbital motions in non-steady state conditions).

In fact, Fujii et al. (2006) found a difference in color-corrected K-magnitude between two subsamples: the inner-bar masering stars and other masing stars outside. Also, there is a significant K-magnitude difference between high-velocity stars with $V_{lsr} > 250$ km s^{-1}, and stars with $V_{lsr} < -250$ km s^{-1} near the Galactic center (Deguchi et al. 2004). These facts support that this is due to a geometrical effect (difference in distance) of stars in x_1 orbit family; the brighter stars (located closer to the Sun) tend to have negative radial velocities and faint stars tend to have positive radial velocities.

3 Numerical Simulations

We performed the 3-D numerical simulations of the bulge star motions using the bulge gravitational potential derived by Zhao (1996). In this model, the bulge bar with $2 \times 10^{10} M_\odot$ rotates with the pattern speed of 60 km s^{-1} kpc^{-1}. Because the off-plane motions of the stars do not seem to change the result within a limitation of our investigated parameter range, we present here only the result of simulations of stellar orbits in the Galactic plane. A test particle (star) was ejected from several points on the bar minor axis at the various distances and velocities in the direction parallel to the bar major axis. Trajectories of the test particles are calculated for a time length of 1.7 Gyr, which is comparable with the ages of bulge AGB stars.

The radial velocities (seen from the Sun) were calculated and plotted on the l–v diagrams. Note that the escape velocity of stars from the bulge is approximately 450 km s^{-1} (at around 100 pc from the Galactic center). In fact, the maximum radial velocities obtained are within this limit. Obtained l–v diagrams were compared with the observational ones. Figure 2 shows the best-fit l–v diagram to the observations. The right panel of figure 2 is the face-on view of the orbit (in a frame corotating with the bar). In these panels, the particle positions were plotted in every 3.3 Myr with "+" ($D < 8$ kpc) and "×" ($D > 8$ kpc), so that the densities of these marks are proportional to the observed density of stars (if the selection effect by distance D is ignored).

In fact, the trajectory is close to the resonant orbits (similar to the x_1 orbit family), and is somewhat lopsided. It is amazing that the whole inner bulge star l–v diagram is represented by one trajectory of the test particle ejected at a single velocity at one location.

This orbit resembles somewhat to the x_1 orbit family, but it reaches very near the Galactic center ($\sim$ 10 pc) to the outside (1 kpc). It also reaches near to the x_2 orbits so that the linear feature, which was assigned to the x_2 orbits, was reproduced in this simulation. Furthermore, the source sparse regions which are near (l, v)=($-0.5°$, -200 km s^{-1}), and ($0.3°$, 0 km s^{-1}), were also reproduced in some degree in Figure 2. These facts indicate that one trajectory of a single test particle can explain most of the observed features of the inner bulge stars.

Because the stellar motion is collisionless, these stars must be born at one position on this trajectory. Considering that these AGB stars were born in a few Giga years ago and they circulated in the bulge already many times, it is possible that these stars were born in molecular clouds in a Gyr time span in the bulge history, and relatively minor velocity dispersion at the the time of birth makes these stars distributed all over the inner bulge. The stellar trajectory is close to the x_1 orbit with an apocenter distance of 1 kpc. The star burst must occur at the crossing points of the x_1 and x_2 orbits. However, the present innermost crossing points are considerably inside ($\sim$ 100 pc from the GC). We infer the position of the crossing point to be at approximately 400 pc away from the GC on the minor axis of the bar ellipsoid, where stars can have enough large gravitational potential energy, being accelerated up to the velocity of 300 km s^{-1} if it approaches to the central region of the Galaxy.

4 Conclusion

We have obtained the accurate radial velocities of 163 stars by observing the $\sim$ 300 MSX/2MASS objects in the $7° \times 2°$ area of the Galactic center. The longitude–velocity diagram of these objects were compared with those of the numerical simulations of stars moving in the bar potential. We found that the main features appearing in the observed l–v diagram can be simulated well by one test-particle trajectory, which is slightly lopsided, reaching from 1 kpc to 10 pc from the GC. We conclude that the inner bulge AGB stars were born a few Gyr ago in a relatively short time span at one point on this trajectory, preferably near the crossing point of x_1 and x_2 orbits.[1]

References

1. Alard, C., 2001, A&Ap, 379, L44
2. Athanassoula, E., 1992, MNRAS, 259, 328

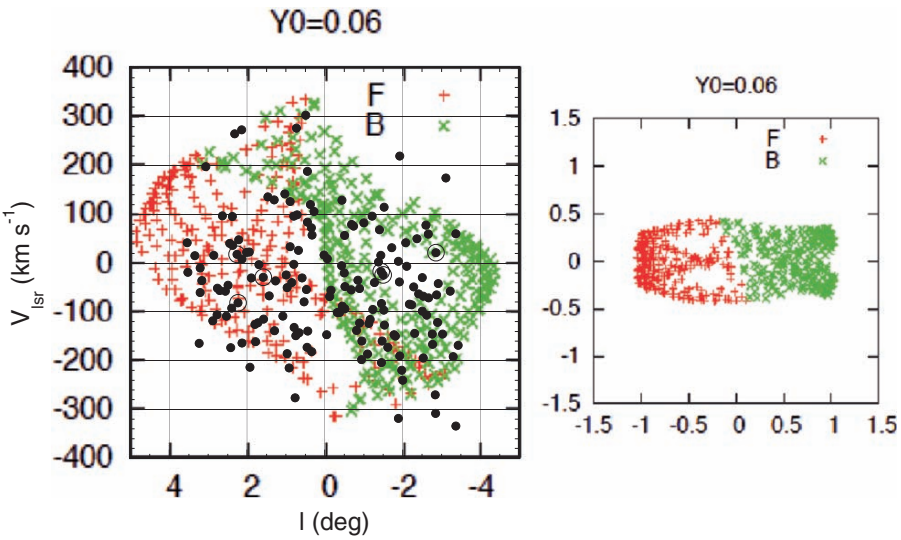

Fig. 2. Model trajectory in the position-velocity diagram (left panel) and the corresponding spatial orbit in the corotating system (right panel). The positions of a test particle were plotted in every 3.3 Myr with "+" ($D < 8$ kpc) and "×" ($D > 8$ kpc) during a period of 1.7 Gyr. Note that the observational data (filled circles) were limited within $|l| < 3.5°$.

3. Benjamin, R. A., Churchwell, E., Babler, B. L., Indebetouw, R., Meade, M. R., Whitney, B. A., et al. 2005, ApJ, 630, L149
4. Binney, J., Gerhard, O. E., Stark, A. A., Bally, J., & Uchida, K. I. 1991, MNRAS, 252, 210
5. Bissantz, N., Englmaier, P., & Gerhard, O. 2003, MNRAS, 340, 949
6. Deguchii, S., Fujii, T., Izumiura, H., Kameya, O., Nakada, Y., Nakashima, J., Otsubo, T., & Ukita, N. 2000, ApJS, 128, 571
7. Deguchi, S., Imai, H., Fujii, T., Glass, I., Ita, Y., Izumiura, H., Kameya, O., Miyazaki, A., Nakada, Y., & Nakashima, J. 2004, PASJ, 56, 261
8. Dwek, E., et al. 1995, ApJ, 445, 716
9. Fujii, T., Deguchi, S., Ita, Y., Izumiura, H., Kameya, O., Miyazaki, A., & Nakada, Y. 2006, PASJ, 58, 529
10. Lôpez-Corredoira, M., Hammersley, P. L., Garzon, F., Cabrera-Lavers, A., Castro-Rodriguez, N., Schultheis, M., Mahoney, T. J. 2001, A&A, 373, 139
11. Nakada et al. 1991, Nature, 353, 140
12. Nishiyama, S., Nagata, T., Baba, D., Haba, Y., Kadowaki, R., et al. 2005, ApJ, 621, L105
13. Sawada, T., Hasegawa, T., Handa, T., & Cohen, R. J. 2004, MNRAS, 349, 1167
14. Zhao, H. S., 1996, MNRAS, 283, 149

6

The Physics of Cold Gas in Galaxy Low Excitation Regions

Daniel Pfenniger

Geneva Observatory, University of Geneva, Switzerland
daniel.pfenniger@obs.unige.ch

1 Introduction

After decades of investigations, the interstellar medium (ISM) still appears as extraordinarily complex. Therefore, as a sound strategy, it is appropriate to return considering the simplest situations. The low excitation regions in or around galaxies, such as the galaxy outer disks, the inter-arm regions, the well shielded starless cores in molecular clouds, or the high velocity clouds (HVC's), appear as ideally suited to test our understanding of gas in simple conditions. A priori, regions far from star formation regions should be much less perturbed by their associated energetic effects, like supernovae explosions and subsequent cosmic rays, or protostellar jets. Another good reason to be interested by low excitation regions is that almost all the matter that shines today in galaxies is thought to have spend some time in a very cold form around 10 K. Therefore the processes that occur during this cold phase are important since they determine the fate of almost everything we can observe.

But precisely because the lack of excitation prevents various radiative emissions to occur, cold gas is difficult to observe. Most matter is then neutral and at the lowest energy levels. The restricted choice of observables that we have, mainly emissions in the spectral domain from the far-infrared (FIR), sub-mm to cm radio waves (CO and HI), or absorptions from bright sources also in shorter wavelengths, have deeply challenged our effective physical understanding of cold gas. Namely, what has been collected up to now are features that strongly contradict the bold prediction of physics about a non-self-gravitating cold gas in vacuum: such an unconfined gas has a positive energy and therefore should expand indefinitively until it meets a larger scale confiner, such as a galaxy potential. Some basic questions remain wide open about cold gas:

- the origin of the ubiquitous supersonic turbulence,
- the apparent lack of energy sources able to sustain supersonic turbulence,
- the molecular cloud fractal-like density inhomogeneities,

- the still unclear rules that determine star formation, which clearly follow a cold gas phase,
- the amount of cold gas in galaxies, can it be significant in regard of the still large amount of dark baryons expected from the Big-Bang theory?

In a situation where unsettled problems stagnate over decades, legitimate doubts may be raised about the commonly adopted assumptions.

2 Types of ISM Models

The first ISM gas models, starting in the 1950's, were often based on spherical clouds in pressure equilibrium and in local thermal equilibrium (LTE). Field's (1965) paper on thermal instability was the seed for multi-phased models of the ISM (Field et al. 1969; McKee & Ostriker 1977) where the local pressure and thermal equilibrium assumptions were also adopted.

It is only around the 1990's that the concepts of fractals or hierarchical systems were applied to the ISM (e.g., Houlahan & Scalo 1990), where fractal dimensions around $d = 2$ or lower were found representing well the molecular clouds. Fractal systems challenge the physics to be used in numerical models because the predicted observables, especially for fractal dimension below 2, depend on the smallest scale that is effectively possible to represent in computers. They also challenge the way observations are interpreted, because most of the time the available instruments are unable to resolve well the expected smallest scales, of the order of a few AU (Pfenniger & Combes 1994).

In the recent years computer simulations have reached a level where the very high dynamical range required by gravitational instability, leading to fractal distributions, can be simulated in 3D with some confidence (e.g., Klessen et al. 2000; Bate et al. 2003). The picture that comes out of such works is that a fractal like ISM is indeed produced by gravitational instability, as least temporary, and that the ISM is a fully dynamical medium at almost all scales, enlarging much the diversity of possible ISM local states in regard of those contemplated up to now.

3 Overcoming Incoherences

In retrospect, we see better which incoherences need to be overcome. A fully dynamical and supersonic turbulent medium is contradicting the often assumed local thermal equilibrium. Indeed, in a supersonic turbulent medium multi-scale density perturbations propagate faster than pressure perturbations. A basic requirement for using thermodynamics, that the system is in dynamical and chemical equilibrium is not fulfilled. But without thermodynamics the concepts of temperature and pressure loose their precise meaning. Predictions based on equilibrium thermodynamics may be wrong by order of magnitudes.

The fundamental reason which makes usual fluids smooth is that the fluctuations are damped by molecular chaos. Fluctuations are erased as long as the molecular relaxation time is much shorter than all the macroscopic timescales. In a supersonic turbulent medium the non-linear convective term of fluid equations on the contrary exacerbates discontinuities, that is, shocks. Since turbulence is multi-scale, these shocks occur and interact with each other at all scales. The medium has all the grounds to constantly grow discontinuities. Then the justification of using differential equations for smooth flows in hydrodynamics is lost.

In other words, supersonic turbulence is a self invalidating characterization of the state of the cold ISM. The very mention of "sound" supposes that a pressure like quantity exists. A localized strong shock, inside which no thermodynamics can be used, makes still sense as long as the shock region is small with respect to the surrounding medium otherwise smooth and in local thermal equilibrium. But if shocks become generalized as result of a strong turbulence, then the irregular regions become the rule, and the validity of local thermal equilibrium is challenged almost everywhere.

Nowadays the most promising way to describe supersonic turbulence are numerical simulations. Like for the Hugoniot-Rankine shock conditions which allow to describe shocks by respecting conservation laws, state of the art numerical techniques strive to do the same at all the scales down to the smallest possible one. In technical terms modern numerical methods strive to solve for the more general so-called "weak solutions" of the conservation laws, which are solutions allowing discontinuities (see, e.g., LeVeque 2002).

4 Non-Extensive Thermodynamics

A very important feature of the ISM is, in too many studies, often completely neglected, namely gravity. This is most likely the physical ingredient that makes the interstellar gas different from laboratory gas. Gravity is the container of the hot or cold ISM at the galactic scale, is also responsible of the spiral density waves that drive gas at the kpc scale. Then gravity is certainly non-negligible in molecular clouds, otherwise their mass derivation using the virial theorem would be non-sense. At smaller scale gravity does play a role throughout the star and planet formation process.

Now what is special with self-gravitating systems is that their thermodynamics lies outside the traditional frame of extensive thermodynamics, in which average quantities like pressure and entropy are assumed either intensive or extensive, i.e., scaling as a power 0 or 1 of the volume. Mainly, the gravitational energy scales as a system dependent power of the volume, for example 5/3 in constant density systems.

Antonov and Lynden-Bell showed in the 60's that gravitational physics leads to a statistical mechanics in contradiction with standard thermodynamics. The negative specific heat of bound gravitational systems prevent them to

be stable when in contact with a heat bath. Without heat bath and container the gravo-thermal instability leads isolated systems to evolve forever.

Until the late 90's the chemo-physics community showed little interest for non-extensive thermodynamics, but this has changed in the recent years, resulting in several conferences and books on the topic. My personal view is that classical extensive thermodynamics is only a subset of more general statistical mechanics still to be worked out, so is not universal and not directly applicable to gravitating systems (Pfenniger 2006).

In other words for practical considerations in many situations of astrophysical interest self-gravity induces a thermally and dynamically unstable state unable to evolve towards any statistical equilibrium. Obviously the gravo-thermal catastrophe, that may have appeared as a paradox in the 60's since the expectations were focused on equilibrium states, appears today as consistent with the fully dynamical and evolving states suggested by numerical experiments, and with the observed fractally structured cold ISM.

Following Lynden-Bell (1999), who argued that negative specific heat systems correspond in usual systems to a phase transition, the ISM may be seen as a system in phase transition. Phases transitions are typically characterized by scaling properties and "giant fluctuations", properties shared by the ISM when viewed globally.

The important consequence is that we must be ready to consider much broader ISM conditions than those predicted by quasi equilibrium states. Effects that have been "proved" to be impossible in equilibrium conditions should not be a priori rejected, because the equilibrium assumptions seem too much restrictive, and non-linearities associated with gravity and turbulence are known in other contexts to lead to surprises.

5 Hierarchical Systems

Many properties mentioned above about the ISM, such as supersonic motion, can be captured by a very simple gravitating hierarchical system of point particles arranged in a hierarchical way and assumed to be in virial equilibrium at every level of the hierarchy (Pfenniger & Combes 1994).

First, the system is decomposed in levels numbered by l, starting at the lowest one $l = 0$. At each level $l + 1$ the mass m_{l+1} is made of n_l clumps of mass m_l, and thus recursively down to $l = 0$,

$$m_{l+1} = n_l \, m_l, \qquad l \geq 0. \tag{1}$$

Second, the mass is supposed to scale as a power law of the size r_l:

$$\frac{m_{l+1}}{m_l} = \left(\frac{r_{l+1}}{r_l} \right)^d, \qquad l \geq 0. \tag{2}$$

The exponent d must be positive since mass is positive, and not larger than the space dimension, 3. The size ratio between adjacent levels is linked to the

mass ratio by $\frac{r_{l+1}}{r_l} = n_l^{1/d}$. It follows immediately that if such as system is in detailed virial balance, the typical velocity v_l, or "sound speed" at this level, scales as,

$$\frac{v_{l+1}^2}{v_l^2} = \frac{Gm_{l+1}/r_{l+1}}{Gm_l/r_l} = \left(\frac{r_{l+1}}{r_l}\right)^{d-1}, \qquad l \geq 0. \tag{3}$$

Interestingly, $d = 1$ is a critical exponent. Velocity, or "temperature" becomes smaller at smaller scale when $d > 1$, like in molecular clouds, but the opposite behavior occurs when $d < 1$. In term of Mach numbers, when $d > 1$ the upper scale is always supersonic with respect to the considered level.

With velocities and sizes one can define crossing or dynamical time-scale at each level.

$$\frac{t_{l+1}}{t_l} = \frac{r_{l+1}/v_{l+1}}{r_l/v_l} = \left(\frac{r_{l+1}}{r_l}\right)^{(3-d)/2}, \qquad l \geq 0. \tag{4}$$

This allows to derive the scaling of the specific power:

$$\frac{v_{l+1}^2/t_{l+1}}{v_l^2/t_l} = \left(\frac{r_{l+1}}{r_l}\right)^{(3d-5)/2}, \qquad l \geq 0. \tag{5}$$

The critical dimension $d_c = 5/3 \approx 1.67$ has the same property as the famous Kolmogorov critical exponent in homogeneous turbulence, for which energy flow is constant throughout the scales. When $d > d_c$ energy flows from small to large scale, and vice versa when $d < d_c$. For $d = d_c$ velocity scales as $v \propto r^{1/3}$ and the Mach number $\mathcal{M} \equiv v_{l+1}/v_l \sim 1.2 - 1.8$ for $2 \leq n_l < 10$, numbers that match quite well those observed in molecular clouds (Larson 1981).

To summarize, this above simple hierarchical model of ISM captures many of the observed features, such as the fractal morphology, the velocity-size scaling, and the supersonic cloud motion. Obviously it cannot describe much more due to its lack of physical ingredients, in particular the ones determining the bottom scale of the hierarchy.

6 AU-Sized Globules Based on Condensed H_2 Cores

We thus expect that a fully dynamical and fractal ISM must explore a much wider range of conditions than the quasi-equilibrium states almost exclusively contemplated in star formation studies. Supersonic turbulence means than dynamical compression and dilatation comparable with the average "temperature" must occur frequently, which justify to consider states up to now neglected, especially the ones that are the least observable states, like cold, dense and small clouds.

A very general trend of self-gravitating central systems is to evolve toward increasing their core density while rejecting much mass in an expanding envelope. Stars evolve toward red-giants, and globular clusters evolve by successive

core collapses and envelope evaporation. In gaseous bodies, if the perfect gas equation of state changes toward incompressibility at some high density, then the core collapse can be halted, and a much longer lived body emerges. Fermi degeneracy, molecular and atomic forces are well known factors stiffening the equation of state and stabilizing known bodies like neutron stars, white dwarfs, giant and rocky planets.

Little discussed so far is the phase transition of molecular hydrogen from gaseous to liquid and solid states. Liquid or solid molecular hydrogen is familiar in industrial cryogenic applications like rockets. Molecular hydrogen becomes liquid or solid, i.e., almost incompressible, already below 33 K at sufficient pressure. The H_2 critical point occurs at $T_c = 33\,\mathrm{K}$, $P_c = 13\,\mathrm{bar}$, while the triple point at $T_3 = 14\,\mathrm{K}$, $P_3 = 0.07\,\mathrm{bar}$. At low T, the saturation pressure and gas density drops to interstellar values. Between 1 and 14 K the sublimation curve is well approximated by (Pfenniger & Combes 1994):

$$P_{\mathrm{solid-gas}} \approx 5.7 \cdot 10^{20}\, T^{5/2}\, \mathrm{e}^{-91.75/T}\, [\mathrm{K\,cm^{-3}}]\,. \tag{6}$$

Now the obvious question is, can a collapsing cloud keep a sufficiently cold core to allow to reach the gas-liquid or gas-solid H_2 transition? In classical spherical collapse studies (e.g., Larson 1969), one learns that a spherical collapse of an initial cold ($T \approx 10\,\mathrm{K}$) gas cloud increases its central density almost isothermally towards infinity in a finite time. Isothermality follows from the large transparency of the cold ISM to its own thermally generated photons, such that the cooling time remains much shorter than the free-fall time. However in the growing density collapsing core, an optical depth exceeding unity is finally reached, allowing the core to keep thermal photons longer. Temperature and pressure increase, stopping the density growth.

Let us estimate the central density at which the center of a pseudo isothermal sphere, $\rho(r) = \rho_0/\left[1 + (r^2/r_c^2)\right]$, becomes opaque for constant opacity κ. Requiring that the optical depth $\tau_\infty = 1$ and virial equilibrium, $\lim_{r\to\infty} GM(r)/r = 3kT/\mu m_p$, leads to a simple expression for the core radius and the critical central density above which the center begins to be opaque:

$$r_c = \frac{3\kappa kT}{8G\mu m_p}\,, \quad \rho_0 = \frac{16 G\mu m_p}{3\pi\kappa^2 kT} \approx \frac{5.5\cdot 10^{-10}\,(\mu/2)}{(\kappa/10^{-3})^2\,(T/5)}\ \left[\mathrm{g\,cm^{-3}}\right]\,. \tag{7}$$

This critical density is independent of the mass or size of the cloud.

The H_2 gas density ρ at the critical pressure is almost the perfect gas density for the partial pressure $P_{\mathrm{solid-gas}}$. Equating this density ρ to the critically opaque density ρ_0 above provides the critical opacity κ_{crit} below which H_2 becomes incompressible *before becoming opaque to its thermal radiation*:

$$\kappa_{\mathrm{crit}} \approx 1.5\cdot 10^{-3}\ (T/5)^{-5/4}\ \mathrm{e}^{9.175(\frac{5}{T}-1))}\,[\mathrm{cm^2 g^{-1}}]\,. \tag{8}$$

Since the ISM sub-mm opacities typical of low metallicity cold clouds can be as low as $\sim 10^{-3}\,[\mathrm{cm^2/g}]$ or less (see Draine 2004, [Fig. 12]), at least below $\sim 5\,\mathrm{K}$

a collapsing cloud is able to condense H_2 in the core before becoming opaque. The condensed core thus is able to stop a collapse without becoming hot. Somewhat warmer or more opaque initial gas can still reach H_2 condensation despite a temporary temperature increase.

We arrive thus at the surprising possibility that gravitational collapses in very cold conditions may lead not necessarily to a body with a hot center, such as planets or stars, but to a temperature inverted gas globule with a condensed cold core. The core would consist of solid H_2 below 14 K, or liquid H_2 above, up to 33 K. Around the core an H_2-He gaseous atmosphere may extend to much larger distances and contain most of the globule mass.

We have calculated the typical properties of such cold gas condensations by integrating the equilibrium equations for isothermal gravitating spheres for which the accurate H_2 equation of state is used (Pfenniger, in preparation). Summarizing, their main properties are:

- The central density is determined by the solid or liquid H_2 density: $0.07 - 0.09\,\mathrm{g\,cm^{-3}}$. This is much lower, by a factor $20 - 50$, than for planets.
- The maximum core radius able to keep an extended atmosphere is about $2 \cdot 10^4$ km, which corresponds to a core mass similar to the Earth mass. At this radius the gravitational and molecular binding energies are similar.
- The cold globules have a relatively weak gravitational binding energy: about 0.001 eV/nucleon, which means that such globules can be rapidly evaporated by sufficient radiative or cosmic ray excitation, but the most dense parts, especially the cores, can survive several Gyr in low excitation regions. In other terms, over time repeated cycles of collapse/evaporation trap an increasingly fraction of the gas mass in condensed cores.
- An extended atmosphere, extending up to $3 - 30$ AU for a Jupiter mass, has rapidly an isothermal profile $\propto r^{-2}$, independently of the central core pressure. The atmosphere is expected to be transparent to sub-mm-FIR radiation, but opaque to visible/UV radiation (Combes & Pfenniger 1997).

It should be noted that the external "heating" of cold globules by penetrating radiation (FIR, cosmic rays) does not increase their apparent temperature due to the negative specific capacity of self-gravitating objects. Such "heating" expands and evaporate the atmosphere without increasing temperature, i.e., without particular emission signature.

The best observational candidates for cold globules are the cometary knots directly observed in nearby planetary nebulae such as in the Helix Nebula (NGC 7293), but not satisfactorily explained (e.g., O'Dell et al. 2002). Their sizes (≈ 100 AU), their temperature ($\sim< 5$ K), and *their centrally concentrated profiles* (Burkert & O'Dell 1998) indicate that they are gravitationally bound around a dense center, not pressure confined clouds. They illustrate how fast cosmic gas cools and produces clumps, and suggest that such a condensation process must occur even more frequently and generally in colder conditions, such as in the outer galactic disks.

7 Conclusions

Supersonic turbulence in the low excitation ISM appears much more natural once one assumes that gravity plays a major role throughout the scales, from galactic to stellar. The ISM should be seen as a fully dynamical medium, like a phase transition, in which a much wider range of physical conditions are explored than the quasi-equilibrium ones assumed in the past. Usual thermodynamics is poorly suited to describe such as medium, and its associated predictions should not be followed too far.

We have described possible cold gas globules stabilized by solid/liquid H_2 cores that may constitute the cold side of the star formation process. The described effect should be general and may explain the inefficiency of usual star formation. Stars should form in higher fractions in hotter and metal rich (opaque) regions, and conversely for cold globules.

The ISM fast cooling problem is removed if the outcome of collapses can be cold globules instead of stars: the ISM appears then as a very active medium constantly recycling gas from large to small scales. Cold globules are in some way the IMF low mass end. Their low binding energy allows them to play the role of a gas reservoir easily accessible via excitation. At different galactic radii an equilibrium distribution of globules sizes can be reached balancing the local excitation and gas cooling rates.

Acknowledgments: I thank the organizers for the stimulating conference. This work was supported by the Swiss National Science Foundation.

References

1. Bate M.R., Bonnell I.A., & Bromm V.: MNRAS, 339, 577 (2003)
2. Burkert A., & O'Dell, C.R.: ApJ, 503, 792 (1998)
3. Combes F., & Pfenniger D.: A&A, 327, 453 (1997)
4. Draine B.T.: in "The Cold Universe", Saas Fee Advanced Course 32, D. Pfenniger & Y. Revaz (eds.), Springer, Berlin, p. 213 (2004)
5. Field G.B.: ApJ, 142, 531 (1965)
6. Field G.B., Goldsmith D.W., & Habing H.J.: ApJ, 155, L149 (1969)
7. Henriksen R.N., & Widrow L.M.: A&A, 441, 70 (1995)
8. Houlahan P., & Scalo J.: ApJS, 72, 133 (1990)
9. Klessen R.S., Heitsch F., & Mac Low M.-M.: ApJ, 535, 887 (2000)
10. Larson R.B.: MNRAS, 194, 809 (1981)
11. LeVeque R.J.: Finite Volume Methods for Hyperbolic Problems, Cambridge Univ. Press, Cambridge (2002)
12. Lynden-Bell D.: Physica A, 263, 293 (1999)
13. McKee C.F., & Ostriker J.P.: ApJ, 218, 148 (1977)
14. O'Dell C.R., Balick B., Hajian A.R., et al.: AJ, 123, 3329 (2002)
15. Pfenniger D.: Comptes Rendus Physique, 7, 360 (2006) (cond-mat/0605665)
16. Pfenniger D., & Combes F.: A&A, 285, 93 (1994) (PC94)
17. Walker M., & Wardle M.: ApJL, 498, L125 (1998)

7

Secular Evolution of Disc Galaxies and of their Components

Evangelia Athanassoula

LAM, Observatoire Astronomique de Marseille Provence, 2 Place Le Verrier, 13248 Marseille cedex 04, France. lia@oamp.fr

Summary. I discuss several aspects of secular evolution linked to bars and to boxy/peanut bulges, based on a very large number of high resolution, fully self-consistent N-body simulations. When the bar forms, it is as thin as the disc. Its three-dimensional shape, however, evolves, so that, at later times, it has a thick inner part and a thin, more extended outer part. The former, when viewed edge-on, is called a boxy/peanut bulge, because of its shape. The strength of the box/peanut correlates with the bar strength, the strongest cases having formed after two buckling episodes. The extent of the box/peanut is considerably shorter than the bar length, in good agreement with orbital structure studies and with observations. Viewed at an angle near to, but not quite edge-on, barred galaxies show specific isodensity/isophotal shapes, which are different in the thick and in the thin part of the bar. The isophotes of M31 also have such shapes. This, taken together with radial photometric profiles and kinematics, argue that M31 is a barred galaxy. Thus, the pseudo-ring seen at roughly 50' could be an outer ring formed at the outer Lindblad resonance of the bar.

1 Introduction

After a short and often violent phase of formation, galaxies undergo a long, quiet phase of evolution, called secular evolution (e.g. Kormendy & Kennicutt 2004). Given its duration, this can have very important effects on the galaxy properties. For barred galaxies, secular evolution is driven by the bar which grows as the angular momentum is exchanged within the galaxy. This is emitted by near-resonant material in the bar region and absorbed by near-resonant material in the halo and, to a much lesser extent, in the outer disc (Athanassoula 2002, 2003). Here we will discuss specific aspects of this secular evolution, linked to the bar and to the boxy/peanut bulge.

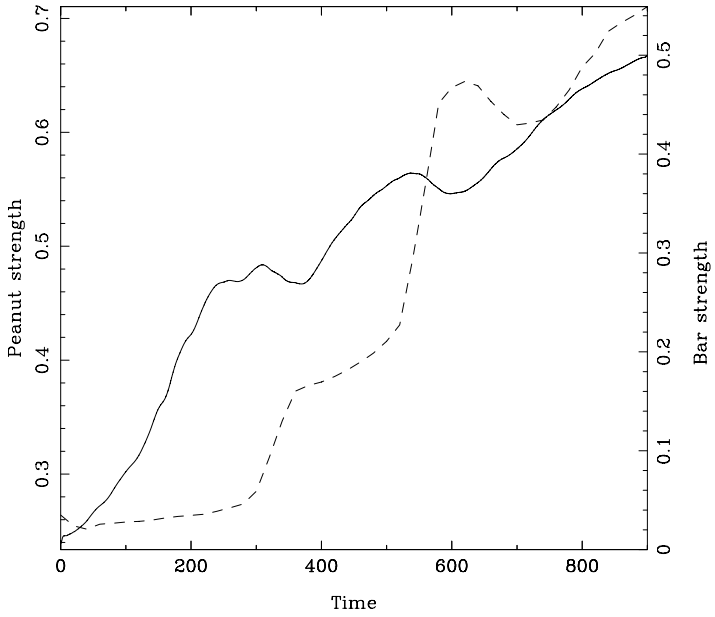

Fig. 1. Formation and evolution of the bar and peanut. The solid line gives the bar strength (scale on the right) and the dashed one the peanut strength (scale on the left), both as a function of time for an N-body simulation of a disc galaxy forming a strong bar. Time is given in computer units, with a 100 computer units being roughly equivalent to 1.4 Gyrs.

2 Box and Peanut Bulges

The backbone of two-dimensional (or very thin) bars consists of a family of periodic orbits elongated along the bar and closing after one revolution around the center and two radial oscillations (Contopoulos & Papayannopoulos 1980; Athanassoula et al. 1983). These orbits are called x_1 and, when stable, they trap around them regular orbits of roughly the same orientation and shape. The orbital structure in three dimensions is similar, but richer and more complicated (Pfenniger 1984; Skokos, Patsis & Athanassoula 2002a,b; Patsis, Skokos & Athanassoula 2002). The backbone of three-dimensional bars is the x_1 tree, i.e. the x_1 family plus a number of two- and three-dimensional families bifurcating from it (Skokos, Patsis & Athanassoula 2002a). The three-dimensional families, together with the regular orbits trapped around them, make an edge-on box or peanut shape (Patsis, Skokos & Athanassoula 2002), such as observed in some edge-on disc galaxies and referred to as a boxy or peanut bulge. Thus, boxy/peanut bulges are *parts* of bars seen edge-on. The interpretation of slit spectra of such structures link them to bars (Kuijken & Merrifield 1995; Bureau & Freeman 1999; Merrifield & Kuijken 1999; Chung & Bureau 2004) as was established by the exhaustive modeling of Athanassoula

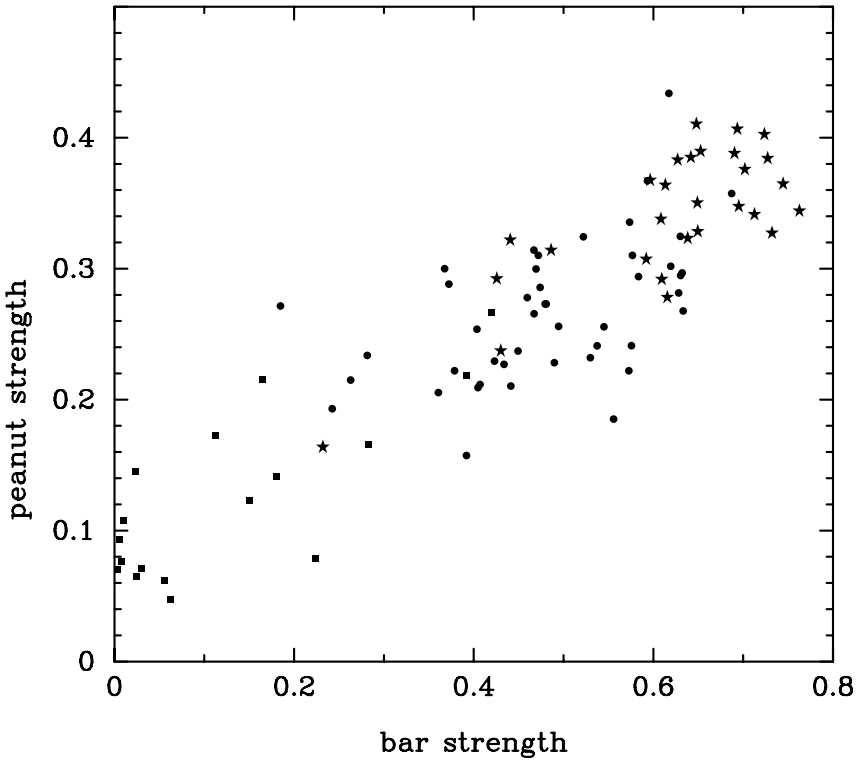

Fig. 2. Correlation between bar and peanut strength. Every point shows the result from one simulation. Simulations which underwent 0, 1, or 2 bucklings are shown with a square, a circle, or a star, respectively.

& Bureau (1999) and Bureau & Athanassoula (2005). This link was reinforced by a study of the NIR photometry of a sample of edge-on disc galaxies (Bureau et al. 2006).

The formation and evolution of boxy/peanut bulges is witnessed in many N-body simulations (e.g. Combes & Sanders 1981; Combes et al. 1990; Pfenniger & Friedli 1991; Raha et al. 1991; Berentzen et al. 1998; Athanassoula & Misiriotis 2002; Athanassoula 2002, 2003, 2005a,b,c; O'Neill & Dubinski 2003; Debattista et al. 2004; Martinez-Valpuesta & Shlosman 2004; Debattista et al. 2006; Martinez-Valpuesta, Shlosman & Heller 2006). As shown Fig. 1, they form rather abruptly, roughly at the same rate as bars, but after some delay (Combes et al. 1990; Martinez-Valpuesta & Shlosman 2004). The formation, often referred to as buckling, is accompanied by a decrease of the bar strength (Raha et al. 1991; Martinez-Valpuesta & Shlosman 2004; Athanassoula 2005c; Martinez-Valpuesta et al. 2006; Debattista et al. 2006). Several cases with more than one buckling episode have been reported in the literature (Athanassoula 2005c; Martinez-Valpuesta et al. 2006). Athanassoula &

Misiriotis (2002), based on a few simulations, showed that the strongest bars have, when viewed edge on, the strongest peanuts, or 'X' shapes. This was further established, on the basis of a very large number of simulations, by Athanassoula & Martinez-Valpuesta (in prep.) who find a strong correlation between bar and peanut strength (Fig. 2). Thus, the trend between bar and peanut strengths, initially found in observations (Lütticke, Dettmar & Pohlen 2000), is well reproduced by simulations. Fig. 2 also shows that simulations in which two bucklings occurred tend to have stronger bars and peanuts than simulations with only one buckling (Athanassoula & Martinez-Valpuesta, in prep.).

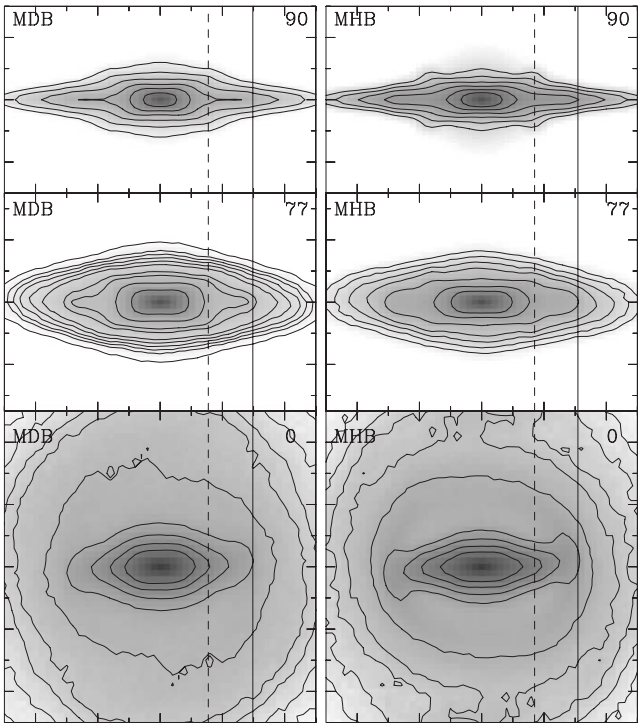

Fig. 3. Three views of two simulations with a halo, a disc and a classical bulge. Only the two latter components are shown. In all cases, the bar major axis is along the x axis. The upper panels give a side-on view (i.e. edge-on, with the line of sight along the bar minor axis), the lower ones a face-on view and the middle ones a view at 77°. The length of the bar, as estimated from the face-on view, is given by a solid vertical line. The length of the box/peanut, as estimated by the edge-on view, is given by a vertical dashed line. It is clear that the extent of the boxy/peanut feature is much shorter than the extent of the bar.

Orbital structure studies, as well as N-body simulations, have shown that boxy/peanut bulges, being a *part* of the bar, should have a shorter extent than that of the bar (for a discussion see Athanassoula 2005 and references therein). This is clearly seen in Fig. 3, which shows the disc and classical bulge components of two simulations at a time after the bar and peanut have grown. The length of the bar is estimated from the face-on view and the length of the box/peanut from the side-on one. I extend the vertical lines in all three panels and this makes it evident that the bar is considerably longer than the boxy/peanut feature. Thus, both orbital structure studies and N-body simulations conclude that the bar, being a three-dimensional object, has a thick inner part of shorter extent and a thin outer part, of longer extent. This view of the bar structure is in good agreement with observations (see Athanassoula 2005a for a compilation). Thus, it is necessary to be careful when comparing observations to simulations, or when comparing observations of galaxies seen at different orientations, because a different part of the bar is seen in face-on and in edge-on views (Fig. 3). Further evidence that boxy/peanut bulges are just *parts* of bars seen edge-on has been presented and discussed by Athanassoula (2005a). This is based on detailed comparisons of N-body simulations to observations and includes morphology, photometry (density/light profiles along horizontal and vertical cuts, results from median filtering) and kinematics (cylindrical rotation, gaseous and stellar position velocity diagrams).

3 M31 : A Disc Galaxy with a Fair Sized Bar

Fig. 3 displays also the disc and classical bulge at an intermediate inclination of 77°, the bar major axis being again along the galaxy major axis (x axis). One can distinguish three regions with different isodensity shapes. In the inner region, ending roughly where the thick part of the bar ends, the isophotes have a rectangular-like shape. This is due to the shape of the thick part of the bar. The outermost region has elliptical isophotes, due to the disc. The intermediate region has isophotes of a more complex shape, with two clear protuberances (elongations) along the bar major axis on either side of the center. This is, in fact, due to the projected shape of the thin outer part of the bar. This intermediate region extends, as expected, from the end of the thick part of the bar to the end of the thin part (Fig. 3).

Let us now compare the isodensity structure of the simulations, discussed above, to the isophotes of M31 in the NIR, shown in Fig. 4. Such a comparison was done initially by Athanassoula and Beaton (2006), while the NIR data from the 2MASS "6X survey" are presented and discussed by Beaton et al. (2006). Similar structures are seen on the 3.6 μm image from the Infrared Array Camera on the Spitzer Space Telescope (Barmby et al. 2006). It is clear that the M31 isophotes have the same three regions as presented above. An inner region with boxy isophotes, an outer region with elliptical isophotes and an intermediate region with protuberances (elongations) pointing to a

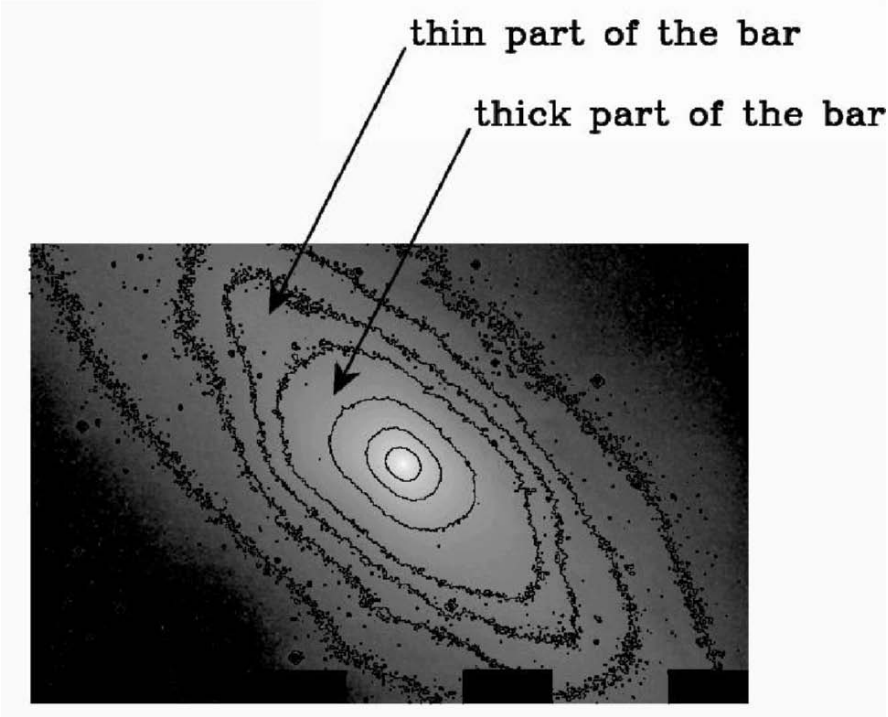

Fig. 4. Greyscale representation and isophotes of M31 in J. North is at the top and East to the left.

direction not far from that of the galaxy major axis. This argues that M31 has a bar with the standard three dimensional shape, i.e a thick inner part and a thin outer part. Such isophotal shapes are also found in other disc galaxies observed at similar intermediate orientations, as NGC 7582 (Quillen et al. 1997) and NGC 4442 (Bettoni & Galletta 1994), again revealing the existence of a bar. Athanassoula & Beaton (2006) made a comparison of M31 to fiducial N-body barred galaxy models, including isophotal/isodensity shapes, light/mass profiles along cuts parallel to the galaxy major axis and kinematics. They argue that M31 has a bar, whose length can be estimated to be roughly 22' and whose major axis is at a small angle with respect to the galaxy major axis. They also present arguments that M31 has both a classical and a boxy/peanut bulge. This model accounts for the pseudo-ring at roughly 50' as an outer ring due to the bar, as observed in a large fraction of barred galaxies (e.g. Buta 1995). Indeed, 50' is compatible with the radius of the outer Lindblad resonance of the bar, where outer rings form (Schwarz 1981; Athanassoula et al. 1982; Buta 1995).

A similar bar structure, with a thick inner part (consisting of the boxy/-peanut feature) and a thin outer part of longer extent, has been found by a number of studies of our own Galaxy (e.g. Hammersley et al. 1994; Lòpez-Corredoira et al. 1999; Hammersley et al. 2000; Benjamin 2005 and in this volume; Lòpez-Corredoira et al. 2006).

Acknowledgments. I thank A. Bosma, M. Bureau, I. Martinez-Valpuesta, A. Misiriotis and I. Shlosman for interesting and motivating discussions on secular evolution and peanut formation. This publication makes use of data products from the Two Micron All Sky Survey, which is a joint project of the University of Massachusetts and the Infrared Processing and Analysis Center/California Institute of Technology, funded by the National Aeronautics and Space Administration and the National Science Foundation.

References

1. E. Athanassoula: MNRAS, ApJL, 569, 83 (2002)
2. E. Athanassoula: MNRAS, 341, 1179 (2003)
3. E. Athanassoula: MNRAS, 358, 1477 (2005a)
4. E. Athanassoula: Celestial Mechanics and Dynamical Astronomy, 91, 9 (2005b)
5. E. Athanassoula: In *Planetary Nebulae as Astronomical Tools*, eds. R. Szczerba, G. Stasińska and S. K. Górny, AIP Conference Proceedings 804, Melville, New York, 333, (2005c)
6. E. Athanassoula, R. L. Beaton: MNRAS, 370, 1499 (2006)
7. E. Athanassoula, O. Bienaymé, L. Martinet, D. Pfenniger: A&A, 127, 349 (1983)
8. E. Athanassoula, A. Bosma, M. Crézé, M. P. Schwarz: A&A, 107, 101 (1982)
9. E. Athanassoula, M. Bureau: ApJ, 522, 699 (1999)
10. E. Athanassoula, A. Misiriotis: MNRAS, 330, 35 (2002)
11. P. Barmby, M. L. N. Ashby, L. Bianchi et al.: ApJL in press and astro-ph/0608593 (2006)
12. R. L. Beaton, S. R. Majewski, P. Guhathakurta, M. F. Skrutskie, R. M. Cutri, J. Good, R. J. Patterson, E. Athanassoula, M. Bureau: ApJ, submitted and astro-ph/0605239 (2006)
13. R. Benjamin, E. Churchwell, B. L. Babler et al.: ApJL, 630, 149 (2005)
14. I. Berentzen, C. Heller, I. Shlosman, K. J. Fricke: MNRAS, 300, 49 (1998)
15. D. Bettoni, G. Galletta: A&A, 281, 1 (1994)
16. M. Bureau, G. Aronica, E. Athanassoula, R.-J. Dettmar, A. Bosma, K. C. Freeman: AJ, 370, 753 (2006)
17. M. Bureau, E. Athanassoula: ApJ, 626, 159 (2005)
18. M. Bureau, K. C. Freeman: AJ, 118, 2158 (1999)
19. R. J. Buta: ApJS, 96, 39 (1995)
20. F. Combes, R. H. Sanders: A&A, 96, 164 (1981)
21. F. Combes, F. Debbasch, D. Friedli, D. Pfenniger: A&A, 233, 82 (1990)
22. A. Chung, M. Bureau: AJ, 127, 3192 (2004)
23. G. Contopoulos, T. Papayannopoulos: A&A, 92, 33 (1980)
24. V. Debattista, M. Carollo, L. Mayer, B. Moore: ApJ, 628, 678 (2005)

25. V. Debattista, L. Mayer, M. Carollo, B. Moore, J. Wadsley, T. Quinn: ApJ, 645, 209 (2006)
26. D. Pfenniger, D. Friedli: A&A, 252, 75 (1991)
27. P. L. Hammersley, F. Garzòn, T. Mahoney, X. Calbet: MNRAS, 269, 753 (1994)
28. P. L. Hammersley, F. Garzòn, T. Mahoney, M. López-Corredoira, M. A. P. Torres: MNRAS, 317, L45 (2000)
29. J. Kormendy, R. C. Jr. Kennicutt: ARA&A, 42, 603 (2004)
30. K. Kuijken, M. R. Merrifield: ApJ, 443, L13 (1995)
31. M. López-Corredoira, F. Garzòn, J. E. Beckman, T. Mahoney, P. L. Hammersley, X. Calbet: AJ, 118, 381 (1999)
32. M. López-Corredoira, A. Cabrera-Lavers, T. J. Mahoney, P. L. Hammersley, F. Garzòn, C. Gonzalez-Fernandez: AJ, in press and astro-ph/0606201 (2006)
33. R. Lütticke, R.-J. Dettmar, M. Pohlen: A&A, 362, 435 (2000)
34. I. Martinez-Valpuesta, I. Shlosman: ApJL, 613, 29 (2004)
35. I. Martinez-Valpuesta, I. Shlosman, C. Heller: ApJ, 637, 214 (2006)
36. M. R. Merrifield, K. Kuijken: A&A, 345, L47 (1999)
37. J. K. O'Neill, J. Dubinski: MNRAS, 346, 251 (2003)
38. P. Patsis, Ch. Skokos, E. Athanassoula: MNRAS, 337, 578 (2002)
39. D. Pfenniger: A&A, 134, 373 (1984)
40. A. C. Quillen, L. E. Kuchinski, J. A. Frogel, D. L. DePoy: ApJ, 481, 179 (1997)
41. N. Raha, J. A. Sellwood, R. A. James, F. D. Kahn: Nature, 352, 411 (1991)
42. M. P. Schwarz: ApJ, 247, 77 (1981)
43. Ch. Skokos, P. Patsis, E. Athanassoula: MNRAS, 333, 847 (2002)
44. Ch. Skokos, P. Patsis, E. Athanassoula: MNRAS, 333, 861 (2002)

8

Structure and Dynamics of the Old Galactic Components

Masashi Chiba, Hirohito Hayashi, and Motoko Yamada

Astronomical Institute, Tohoku University, Sendai 980-8578, Japan
chiba@astr.tohoku.ac.jp

Summary. We present here the recent progress in our understanding of the old stellar components of the Milky Way as fossil records of galaxy formation. Special attention will be paid to if the Cold Dark Matter (CDM) theory as a current theoretical paradigm is able to reproduce recently accumulated data sets of Galactic stars as provided by extensive surveys such as SDSS. We show our recent studies in this regard. First, we have simulated the dynamical interaction between a stellar disk and numerous CDM subhalos to get insights into the origin of the thin and thick disks. Second, we have analyzed the global dynamics of more than 1600 field horizontal branch stars as halo tracers to probe their velocity distribution inside the dark halo of the Milky Way. A detailed comparison with the CDM predictions has been made and key issues are addressed for understanding the formation of the Milky Way.

1 Introduction

Our understanding of how disk galaxies like the Milky Way have formed is still enigmatic. In addition to distant young galaxies at high redshifts, detailed studies of the old Galactic components, including the thick disk and the stellar halo, offer us invaluable information on early dynamical evolution of a typical disk galaxy at epoch earlier than 10 billion years ago. In particular, structure and dynamics of the old stellar populations in conjunction with their metal abundances reflect chemo-dynamical process of galaxy formation.

The Milky Way is composed of the separate stellar components, including the thin disk, bulge, thick disk, and metal-weak halo. The most luminous component is the thin disk with a scale height of ~ 300 pc, where the oldest stars are as old as 10 Gyr. In contrast, the thick disk and halo components are older than 10 Gyr. The stars in these old components are generally metal-poor and distributed in a wide spatial region. The bulge is also an old component, where the majority of the system may have formed about 10 Gyr ago[16]. As a reference for studying the formation of these Galactic components in cosmological context, Figure 1 shows a look back time as a function of redshift

for a currently standard set of cosmological parameters. A characteristic look back time of 10 Gyr is equal to a redshift of about 2, thereby suggesting that studying the thick disk and halo components in the Milky Way corresponds to studying young galaxies at redshift higher than 2. Thus, such old Galactic components provide us with invaluable insights on galaxy formation.

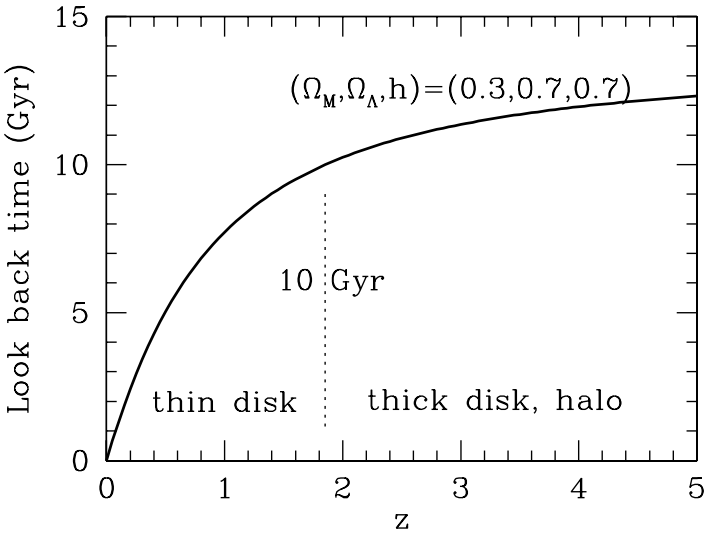

Fig. 1. Look back time as a function of redshift for a standard set of cosmological parameters of $(\Omega_M, \Omega_\Lambda, h) = (0.3, 0.7, 0.7)$.

According to currently standard CDM models, galaxy formation process is a series of hierarchical mergings of small building blocks. Two different approaches exist for the studies of galaxy formation. One is to look at distant, high redshift universe, where we see a number of snapshots for different young galaxies. The other is to look at an old stellar system in a nearby galaxy, especially in the Milky Way, where we can trace back the evolution of a single galaxy based on the studies of stars. These two approaches are of course complementary.

Then, what are the fossil records of galaxy formation imprinted in the old components? First, the spatial and kinematical substructures in the distribution of stars reflect the motion of galaxy collapse or merging of small building blocks during galaxy formation. Second, the chemical abundance distributions of stars reflect star formation and chemical evolution activities. In particular, abundance ratios provide us with where metals come from, such as Type II or Type Ia SN.

Basic characteristics of the old components are summarized as follows. Such components are spatially extended: the halo shows a power-law density distribution with an index of about -3 to -3.5, and the thick disk shows

an exponential radial profile, as seen in the thin disk, but the scale height is of order of 1 kpc. These components are metal-poor, i.e., the halo is more metal-poor than [Fe/H]$= -1$, whereas the metallicity of the thick disk is in the range of $-1 <$[Fe/H]< -0.4. The ages of these components are older than 10 Gyr. It is also known that the [α/Fe] ratio in the thick disk and halo stars is larger than that in the thin disk stars.

The old Galactic components show distinct rotational properties[6]. The mean azimuthal velocity of the nearby stars $\langle V_\phi \rangle$ (where proper motion data are available) as a function of metallicity reveals that the stars with metallicity below [Fe/H]$\simeq -1.7$ show a slightly prograde rotation but no systematic variation with metallicity, whereas for [Fe/H]> -1.7, $\langle V_\phi \rangle$ increases with increasing [Fe/H]. This clearly indicates that the halo formation is totally distinct from the disk formation. Also, the galaxy collapse is not monolithic, unless otherwise we would have seen a continuous increase of $\langle V_\phi \rangle$ from the halo to disk component.

In the following, we summarize some recent progress in our understanding of the thick disk and halo components.

2 Thick Disk

Very important insights on the thick disk component have been drawn from the SDSS catalog, which is one of the biggest sources for stellar data, including magnitude, abundance, and l-o-s velocity. Allende Prieto et al. (2006)[1] utilized F- and G-type stars in SDSS DR3 for deducing the chemo-dynamics of the thick disk stars. Based on l-o-s velocities projected onto the direction of galactic rotation, i.e., rotational velocity components $V_{\rm rot}$, plotted as a function of the distance $|z|$ away from the galactic plane, they found that in the metallicity range for the thick disk, there exists a finite vertical gradient in $V_{\rm rot}$, i.e., $V_{\rm rot}$ decreases with increasing $|z|$. This confirms the earlier results derived from the nearby stars with proper motion data[6]. Allende Prieto et al. also considered the metallicity distribution of thick disk stars as a function of $|z|$ and found no metallicity gradient. These two basic properties give us important hints for the thick-disk formation.

Thick disks are also visible in external disk galaxies. Yoahim & Dalcanton (2006)[15] made a systematic search of thick disks in external galaxies. Based on image decompositions, they derived the luminosity ratio, the ratio between the luminosity of a thick disk and that of a thin disk, as a function of circular velocity $V_{\rm c}$ of observed disks: the luminosity fraction of a thick disk is larger for smaller $V_{\rm c}$ disks. This again gives us an important hint for the thick-disk formation.

So far, many different scenarios for the thick-disk formation have been proposed. These include a monolithic collapse scenario, where the formation of a disk was once stopped by energy feedback, leaving a thick disk, then after metal enrichment the efficient cooling of gas may lead to the formation of a

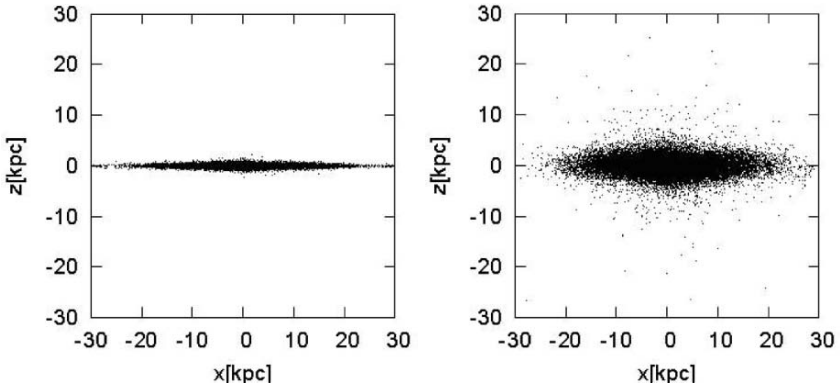

Fig. 2. An example of the disk thickening by CDM subhalos. Left and right panels show the edge-on view of the disk at the beginning ($t = 0$) and the end ($t = 4.9$ Gyr) of the simulation, respectively[8].

thin disk[5]. Chaotic merging of building blocks during galaxy formation may form a thick disk[4]. However, some or many of these models have difficulties in explaining the above kinematical and chemical properties of a thick disk. We present here yet an alternative model for the formation of a thick disk induced by so-called CDM subhalos (Hayashi & Chiba 2006[8]).

Recent high-resolution cosmological N-body simulations have revealed a hundred of CDM subhalos in a galaxy-sized dark halo. Then, one expects the dynamical interaction between a central stellar disk and CDM subhalos, which may give rise to a thick disk by disk heating. Based on this idea, we have conducted a series of numerical simulations for disk heating, using a pre-existing disk with a scale length R_d, mass M_d, and scale height z_d. This disk is subject to dynamical heating due to interaction of subhalos with individual masses $M_{\rm sub}$ (See Figure 2). We have considered a number of subhalo models, including spatial distribution and velocity anisotropy, and found a well-defined linear relation between the increase of a scale height Δz_d and squared total mass of subhalos, as plotted in Figure 3. This is expressed as

$$\frac{\Delta z_d}{R_d} \simeq 8 \sum_{j=1}^{N} \left(\frac{M_{{\rm sub},j}}{M_d} \right)^2 , \qquad (1)$$

where N is the total number of accretion events of subhalos inside a disk region ($\leq 3R_d$). We have found that this relation is naturally explained in the framework of the energy transfer from a subhalo to a disk via dynamical friction. An observed thin disk[10] shows the ratio z_d/R_d smaller than 0.2. Thus, applying equation (1), it follows that a thin disk has not ever interacted with CDM subhalos with the total mass of more than 15 % disk mass.

It is interesting to remark that heated disks resemble an observed thick disk. Heated disks show a vertical gradient in the mean rotation of stars in the

azimuthal direction. Also, the disk heating causes the mixing of stars, thereby erasing any metallicity gradient. Furthermore, the relation we derive implies larger effect of disk heating for smaller V_c, in agreement with observation. This suggests that CDM subhalos can induce the formation of a thick disk.

As yet another dynamical role of CDM subhalos in a disk, such subhalos can also give important impacts on an extended H I disk[2], showing a number of holes or asymmetries as obtained by recent high-resolution radio observations. Dynamical impacts of CDM subhalos on an H I disk also yield a local enhancement of gas density, which may lead to the star formation activity, even though such an outer gas disk is not gravitationally unstable.

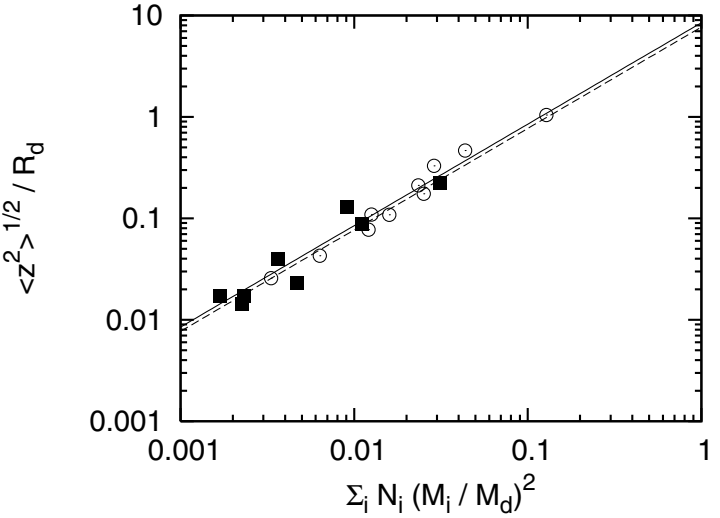

Fig. 3. Relation between the growth of the disk scale height at $R = 3R_d$ (normalized by R_d) and the squared total mass of accreted subhalos at $R \leq 3R_d$ (normalized by M_d^2). A well-defined linear relation is evident[8].

3 Halo

The famous paper by Eggen, Lynden-Bell, & Sandage in 1962[7] offered basically the first picture for the formation of the Galactic halo, based on the correlation between orbital eccentricity e and metal abundance [Fe/H] of both the disk and halo stars. They proposed a monolithic, rapid collapse scenario of Galaxy formation following such a correlation. However, after about 40 years, modern stellar data show no more correlation between e and [Fe/H], and there exist many nearly circular orbits in the metal-poor range[6]. An

important concern is if it is consistent with CDM-based galaxy formation models based on hierarchical merging of small building blocks.

Perhaps, most straightforward evidence of hierarchical merging comes from lots of halo substructures. The presence of a satellite galaxy like Sgr dwarf suggests that such a merging process is still on going. The 2MASS catalog revealing late-type giant stars shows that the stream-like features of star distribution originated from Sgr dwarf are extended in the larger area of the sky. Sgr stream and other streams are also visible in the SDSS catalog. Belokurov et al. (2006)[3] have found, in the map of the SDSS stars in the specific area of the sky, many halo substructures, including Sgr stream, Monoceros ring, and others, which they called "Field of Streams". It is also evident that Sgr stream is found to be confined to a specific orbital plane, which suggests that the gravitational potential of a dark halo is nearly spherically symmetric. The SDSS catalog has also revealed yet further substructures near the Sun, based on the calibration of the nearby stars[9].

A general question is if these properties of the halo component are consistent with the predictions of CDM models. This question was examined by Moore et al.[11] using high-resolution cosmological N-body simulations of CDM particles. They considered the current ($z = 0$) spatial distributions of once high-σ density peaks at high z embedded in a galaxy-sized halo and showed that 2.5 σ density peaks well reproduce the observed power-law distribution of the stellar halo. What about the velocity field of such high-σ peaks? Moore et al. made a plot for the velocity anisotropy parameter $\beta \equiv 1 - \sigma_t^2/\sigma_r^2$ (where σ_r and σ_t are the radial and tangential velocity dispersions, respectively) as a function of the distance r from the halo center. It turns out that $\beta \simeq 0$ near the halo center, i.e., isotropic velocity field, and β is increasing with r, i.e., radially anisotropic in the outer parts. In other words, the orbits of halo objects are expected to be largely radial in the outer parts of the halo. Thus, the stellar kinematics of the halo is a key for assessing such model predictions.

For this purpose, we have investigated the published catalog of field horizontal branch (FHB) stars as halo tracers[14]. FHB stars are excellent targets for our purpose, as they are bright and abundant. Also, accurate distances to the stars are available from the HB morphology, so FHB stars probe the global kinematics of halo stars and mass distribution of a dark halo. We adopt the sample calibrated by Wilhelm et al. (1999)[13] and Sirko et al. (2004)[12], where the latter is based on the SDSS catalog. Most FHB stars in this sample are at distance less than 50 to 60 kpc (sampling limit) and some small number of FHB stars reach $r \sim 100$ kpc.

Upper panel in Figure 4 shows the l-o-s velocities of sample stars, corrected for the Local Standard of Rest and solar motion, against r. There exists a notable change of the velocity distribution at $r \sim 20$ kpc. It is worth noting that at such a distance and beyond, the l-o-s velocity basically corresponds to the radial velocity, V_r, in spherical coordinates. Lower panel shows the velocity dispersion against r, showing a notable decrease at and beyond $r \sim 20$ kpc.

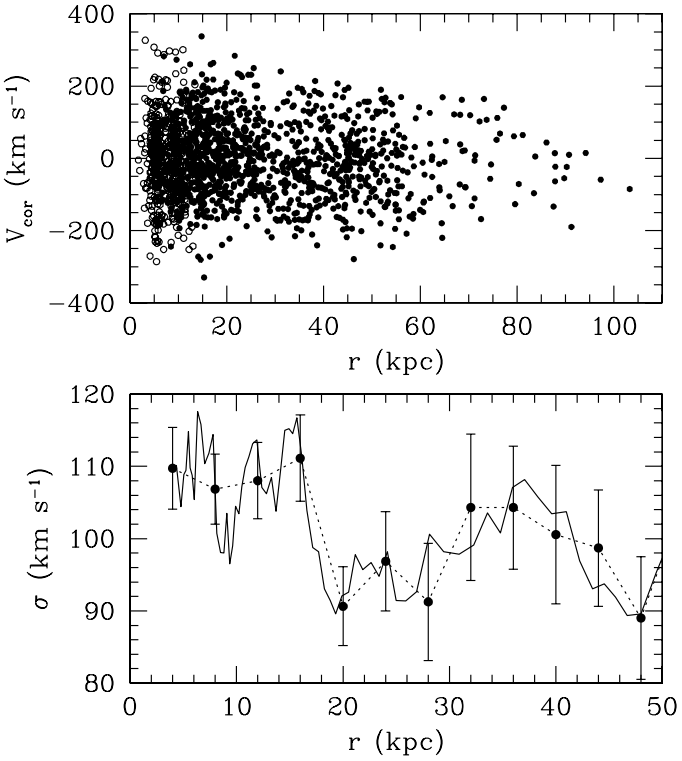

Fig. 4. Upper panel: line-of-sight velocities of the sample FHB stars, $V_{\rm cor}$, corrected for the Local Standard of Rest and solar motion, against r. Lower panel: velocity dispersions in $V_{\rm cor}$ against r (for the range of $r \leq 50$ kpc)[14].

To understand what this profile implies, we have applied Jeans equations to deduce the velocity anisotropy parameter $\beta(r)$ and found that the velocity field is radially anisotropic ($\beta > 0$) in the inner part of $r < 20$ kpc, but mostly tangentially anisotropic ($\beta < 0$) in the outer part. Actually, based on several fittings to the observed profile, we derive such a profile of $\beta(r)$ (See Figure 5). This is in sharp contrast to the profile predicted by CDM models.

We have also investigated the vertical distribution of star velocities. It turns out that the velocity dispersion shows some kind of discontinuous change at $|z| \sim 20$ kpc. Also, mean rotational velocities derived from l-o-s velocity data show asymmetries, being retrograde at $z < -20$ kpc and prograde $z > 20$ kpc. Whatever anomalous signatures of velocity fields appear always at $r \sim 20$ kpc and/or $|z| \sim 20$ kpc.

It is very interesting to note that this number, 20 kpc, also appears in the properties of the globular cluster (GC) system. It is well known that the HB morphology of stars in GCs is not only a function of the metallicity but also of the age of clusters. Specifically, halo clusters are divided into two subgroups:

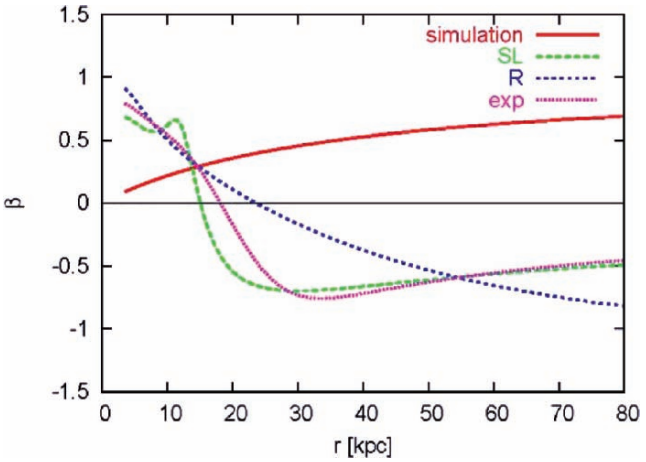

Fig. 5. Comparison between the velocity anisotropy parameter $\beta(r)$ observed in the stellar halo and the corresponding model prediction[14]. Dashed and dotted lines: $\beta(r)$ as derived from the observed l-o-s velocities of FHB stars. Different lines correspond to different functional fittings to $\sigma(r)$. Solid line: CDM-model prediction for $\beta(r)$[11].

old and young halo clusters. The latter clusters distribute in the inner parts of the halo and the boundary distinguishing these two different types of GCs is at $r \sim 20$ kpc. This region is where the field halo stars change their kinematic properties as well. What causes such characteristic distributions of both GCs and field halo stars remains yet unclear and should be clarified.

References

1. C. Allende Prieto, et al.: ApJ 636, 804 (2006)
2. K. Bekki, M. Chiba: ApJ 637, L97 (2006)
3. V. Belokurov, et al.: ApJ 642, L137 (2006)
4. C. B. Brook, D. Kawata, B. K. Gibson, K. C. Freeman: ApJ 612, 894 (2004)
5. A. Burkert, J. W. Truran, G. Hensler: ApJ 391, 651 (1992)
6. M. Chiba, T. C. Beers: ApJ 119, 2843 (2000)
7. O. J. Eggen, D. Lynden-Bell, A. R. Sandage: ApJ 136 748 (1962)
8. H. Hayashi, M. Chiba: PASJ 58, in press (2006) (astro-ph/0609096)
9. M. Juric, et al.: ApJ, submitted (2005) (astro-ph/0510520)
10. M. Kregel, P. C. van der Kruit, R. de Grijs: MNRAS 334, 646 (2002)
11. B. Moore, et al.: MNRAS 368, 563(2006)
12. E. Sirko, et al.: AJ 127, 899 (2004)
13. R. Wilhelm, et al.: AJ 117, 2329 (1999)
14. M. Yamada: Master Thesis, Tohoku University (2006)
15. P. Yoachim, & J. J. Dalcanton: ApJ 131, 226 (2006)
16. M. Zoccali, et al.: A&A 399, 931 (2003)

9

Galactic Magnetic Fields

Wolfgang Reich

Max-Planck-Institut für Radioastronomie
Auf dem Hügel 69, 53121 Bonn, Germany
wreich@mpifr-bonn.mpg.de

Magnetic fields are a major constituent of the interstellar medium. The strength of the Galactic magnetic field ranges from μGauss to mGauss and they exist on many scales. Various radio observing techniques were used to trace small- and large-scale magnetic fields in the Galaxy, where the spatial resolution is on sub-parsec scales. Recent large-scale radio surveys of the linearly polarized emission from the Galaxy reveal a highly structured magneto-ionic interstellar medium. Especially at low frequencies Faraday rotation effects are large and depolarization is significant. Well ordered regular magnetic fields were detected in low density regions by Faraday rotating polarized background emission. The nature of these Faraday screens, which host an excessive regular magnetic field on parsec scales, is not yet clear. Rotation measure (RM) surveys of pulsars and extragalactic sources reveal the large-scale magnetic fields in the Galaxy and their direction. 'Cosmic magnetismn' is one of the key-science projects for the planned Sqare Kilometre Array (SKA), which is based on a sensitive RM sky survey with an unprecedented high source density. The analysis of these data will provide magnetic field information on Galactic structures on all scales, but also on far distant extragalactic magnetic fields.

1 Tracing Galactic Magnetic Fields by Radio Observations

Synchrotron radiation dominates the radio sky at low frequiencies. Relativistic electrons, mostly accelerated in the shock fronts of supernova remnants, convert their kinetic energy into radiation when being deflected in Galactic magnetic fields. The strength of the observed synchrotron intensity depends on the magnetic field component perpendicular to the line of sight. Synchrotron radiation is highly polarized. Depending on the energy spectrum of the relativistic electrons up to 75% of linear polarization are expected for a perfectly regular magnetic field. This is, however, not observed due to irregular magnetic field components, the effect of Faraday depolarization and beam averaging.

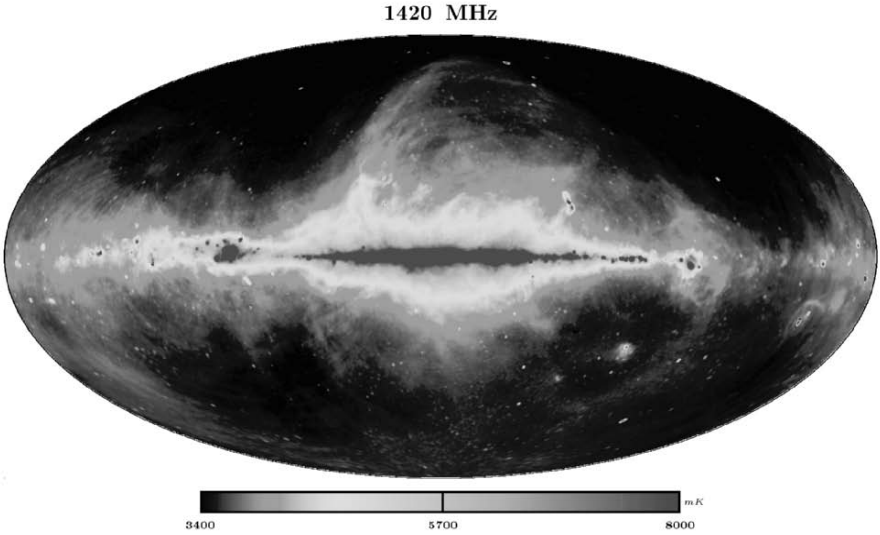

Fig. 1. All-sky 1.4 GHz survey shown in Galactic coordinates combined from data of the northern sky observed with the Stockert 25 m telescope ([11], [7]) and the southern sky observed with the Argentine Villa Elisa 30 m telescope ([9]). The angular resolution is 36'. Intensities are absolute temperatures including the 2.7 K contribution from the cosmic microwave background.

Faraday rotation traces the magnetic field component along the line of sight. Combining total intensity and multi-frequency polarization data in principle openthe possibility of a 3D-reconstruction of the magnetic field direction and its degree of regularity. However, observations sum up the emission components along the line of sight and methods have to be found to reconstruct the magnetic field as a function of distance.

2 Radio Surveys of the Galaxy

Radio surveys of the entire sky are available for a wide range of frequencies at moderate angular resolutions up to 1.4 GHz. Fig. 1 shows the 1.4 GHz all-sky survey, which is combined from data of the northern and southern sky. Out of the Galactic plane steep spectrum synchrotron emission is the dominating emission component, while in the Galactic plane flat spectrum thermal emission becomes more important with increasing frequencies. The local giant radio loops stick out of the Galactic plane with diameters of typically 100°, believed to be old local supernova remnants with steep synchrotron spectra. At lower frequencies the synchrotron spectra are flatter (Roger et al. [14])

than at higher frequencies (Reich et al. [8],[10]) reflecting the steepening of the relativistic electron spectrum.

Strong et al. [15] derived the average radial magnetic field strength of the Galaxy by fitting the 408 MHz survey data by Haslam et al. ([3]) using an electron distribution model. The magnetic field decreases with distance from the Galactic centre, where exceptional high magnetic fields are known to exist. According to Strong et al. about 16 μGauss are derived close to the Galactic centre and the local value is around 6 μGauss. This model assumed a ratio of the regular to the total field strength of 0.6. However, the most recent determination of the regular magnetic field strength within a few kpc by Han et al. [4], which is based on pulsar RM data, indicates a ratio of about 0.3 to 0.4.

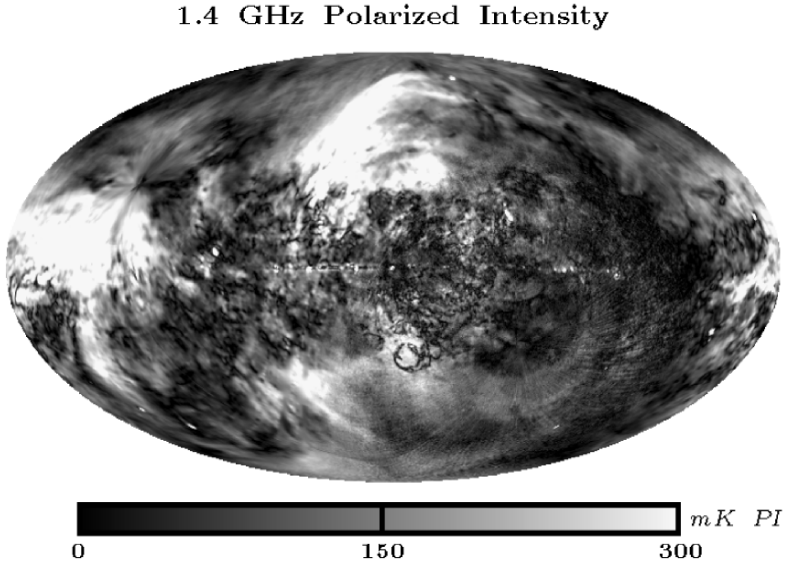

Fig. 2. All-sky 1.4 GHz linear polarization survey shown in Galactic coordinates (W. Reich et al., in prep.). The data are combined from observations of the northern sky with the DRAO 26-m telescope (Wolleben et al. [18]) and a southern sky survey as described by Testori et al. [17]). The polarization zero-level is adjusted to absolutely calibrated 1.4 GHz Dwingeloo polarization data ([2]). The angular resolution is 36'.

Recently an all-sky survey of linear polarization survey at 1.4 GHz was completed (Fig. 2), which differs largely from the corresponding 1.4 GHz total intensity survey (Fig. 1). Two local regions called the "Fan region" centered at about longitude 140° slightly above the Galactic plane and the high latitude

section of the North polar spur show strong emission. Below about $\pm 30^\circ$ latitude the polarization intensity is rather patchy towards the inner Galaxy and does not show an increase of polarized intensity towards the Galactic plane indicating strong depolarization along the line of sight. From the recent "three year" data release of the WMAP satellite (Page et al. [6]) a view of the intrinsic Galactic polarization is obtained. For WMAP's frequency range above 23 GHz Faraday rotation originating in the interstellar medium even in the Galactic plane in general has a negligible effect.

3 Analysis of Polarization Data

Polarization survey images show a impressive variety of large- and small-scale structures, which at most have no correspondance in total intensity. Exceptions are synchrotron sources like supernova remnants or pulsar wind nebula. Analysis of Faraday rotation along the line of sight is needed for the interpretation of polarization maps. Distant polarization suffers more from Faraday rotation in the interstellar medium than local emission, while the sum of both is observed. A relevant analysis of polarization data requires to include large-scale emission, which are often filtered out by the instrument or by data processing steps (see review by Reich [12]). This correction is sometimes difficult to achieve, but unavoidable, because polarization components add as vectors and not as scalar quantities, as it is the case for total intensity measurements. Thus missing large-scale polarization components influence the polarized intensity level and the morphology, which can be rather dramatic as in the case of high latitude fields, where the ratio of small-scale to large-scale emission components is small (Reich et al. [13]).

Distinct Faraday screens (FSs) were identified in the interstellar medium by their strong rotation and/or depolarization of background polarization. The observed undisturbed foreground adds with the modified background emission (see Fig. 3), which contrasts with the polarization seen offset from the FS. The observed data can be modelled to derive the physical parameters of the FS (Wolleben & Reich [19], Sun et al. [16]). In addition foreground and background polarization components can be separated. In the case that the distance of the FS is known information of the distribution of Galactic emission along the line of sight can be obtained. Examples of a FS analysis with known distances are discussed by Wolleben & Reich [19] and by Sun et al. [16].

Faint HII-regions act as FSs, while more dense HII-regions may entirely depolarize the background polarization. Of particular interest are FSs with very low thermal electron density, which host large regular magnetic fields. These objects do not show up in available Hα surveys and their thermal emission is too weak to be seen in radio total intensity maps. Based on an upper limit for the electron density lower limits for the regular magnetic field along the line of sight are calculated from the derived RM for the FS. For

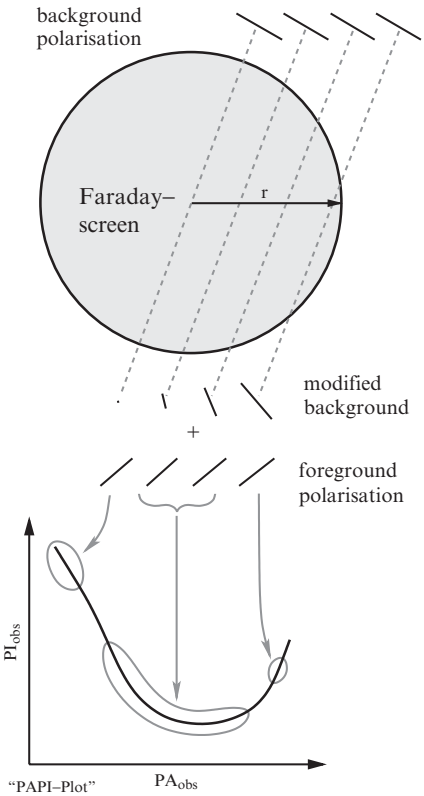

Fig. 3. Effect of a discrete, passive Faraday screen in the interstellar medium, where the polarized background emission is Faraday rotated and depolarized assumed to be proportional to the pathlength through the object. The modified background polarization adds with the undisturbed foreground polarization and shows a characteristic variation when plotting polarization intensity (PI) versus polarization angle (PA) (for details see Wolleben & Reich [19]).

faint HII-regions magnetic fields of a few μGauss are derived (Sun et al. [16]), which are in agreement with field strength estimates by extragalactic RM observations (Heiles et al. [5]). For FSs with very low thermal electron densities excessive magnetic field strength are obtained. ([19], [16]). In particular the running Sino-German λ6 cm Galactic plane polarization survey carried out with the Urumqi 25 m telescope ([16]) shows numerous previously unknown FSs with RMs in the range of 200 rad m^{-2}.

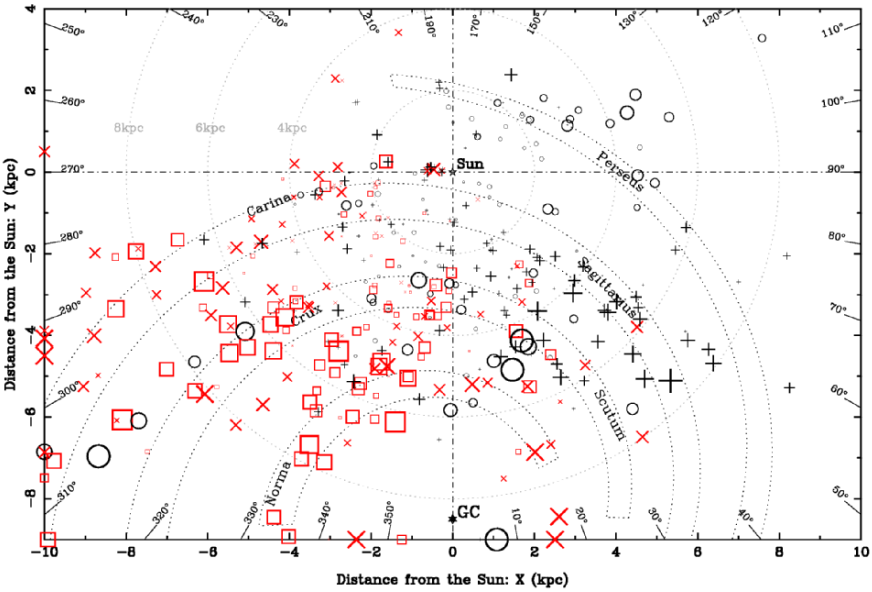

Fig. 4. RM distribution of 388 pulsars as compiled by Han et al. [4]. Plus signs and crosses represent positive RMs, while circles and squares represent negative RMs. For details of the figure see the paper by Han et al. [4].

4 Large-scale Magnetic Fields

Our position inside the Galactic disk makes it difficult to determine the large-scale magnetic field structure of the Galaxy. This is more easy to obtain by observations of nearby galaxies (see recent review by Beck [1]). The large-scale magnetic field structure and the field orientation are of particular interest to test predictions made from the dynamo theory.

The grand design magnetic field of the Milky Way can best be traced by observing the RM from distant pulsars and to some extent also from extra-galactic sources. Distances of pulsars can be determined by measuring their dispersion measure, which is proportional to the amont of thermal electrons along the line of sight. The most recent compilation of pulsar RM was made by Han et al. [4] and is displayed in Fig. 4. Groups of pulsars with different RM signs can be identified. While locally the magnetic field runs clockwise (viewed from the north Galactic pole), there is clear evidence for a large-scale counterclockwise field direction. More field reversals seem possible, but need more RM data to be established. The final answer on the large-scale Galactic magnetic field is expected to be given by the SKA, where about 20,000 pulsars will provide the ultimate data base.

5 Perspectives of the SKA

"Cosmic Magnetismn" is one of the Key Science Projects identified for the future SKA, which is a international telescope project with a collection area of one square kilometre collection area (see Gaensler et al., this volume). RM values from extragalactic sources with a mean distance of 30" will be obtained across the sky, which will allow the determination of the line of sight magnetic field component with unprecedented accuracy in Galactic and extragalactic objects. Fig. 5 shows a simulation of the expected number of extragalactic RM values towards M31. The analysis of such a database will provide detailed information on the magnetic field structure, direction and intensity in M31 on small scales.

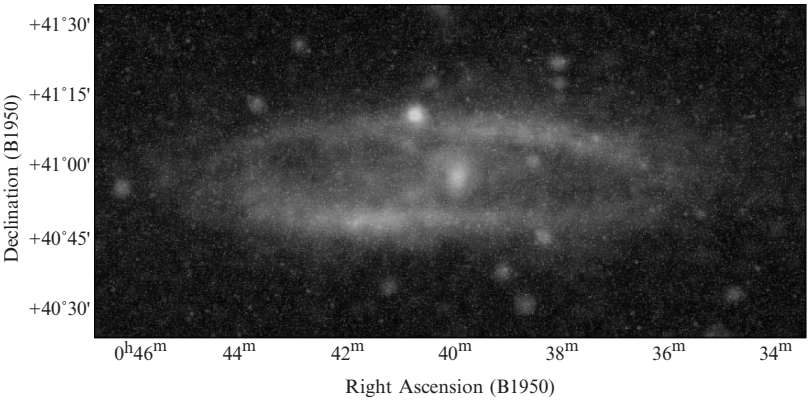

Fig. 5. Simulation by Bryan Gaensler (priv. communication) of the distribution of RM values from extragalactic sources in the area of M31 as seen by the future SKA telescope.

6 Concluding Remarks

Sensitive polarization measurements provide an important input for studies of the properties of the magnetized interstellar medium. Unexpected local enhancement of magnetic fields on parsec scales have been found acting as FSs. The origin of these objects is not known. At present it is unclear to what extent discrete FSs are responsible for the highly structured polarized emission and what contribution is due to the turbulent interstellar medium. High-frequency observations are important to trace distant high magnetic field structures in the Galaxy, while at low frequency details of the local interstellar medium are traced. In the case that the distance of the FS is known its background and

foreground polarization can be separated. This way the spatial distribution of Galactic emission can be obtained. Large-scale field directions are best being traced by a large number of pulsar RMs, where data from the planned SKA will provide a final answer.

References

1. R. Beck, In: *'Cosmic Magnetic Fields'*, ed by R. Wielebinski, R. Beck (Lecture Notes Phys. Spinger 2005), p 41
2. W.N. Brouw, T.A.Th. Spoelstra: Astron. & Astrophys. Suppl. 26, 129 (1976)
3. C.G.T. Haslam, H. Stoffel, C.J. Salter, W.E. Wilson: Astron. & Astrophys. Suppl. 47, 1 (1982)
4. J.L. Han, R.N. Manchester, A.G. Lyne et al.: ApJ 642, 868 (2006)
5. C. Heiles, Y.-H. Chu, T.H. Troland: ApJ 247, L77 (1981)
6. L. Page, G. Hinshaw, E. Komatsu et al.: submitted to ApJ, astro-ph/0603450
7. P. Reich, W. Reich: Astron. & Astrophys. Suppl. 63, 205 (1986)
8. P. Reich, W. Reich: Astron. & Astrophys. Suppl. 74, 7 (1988)
9. P. Reich, J.C. Testori, W. Reich: Astron. & Astrophys. 376, 861 (2001)
10. P. Reich, W. Reich, J.C. Testori, In: *'The Magnetized Interstellar Medium'*, ed by B. Uyanıker, W. Reich, R. Wielebinski (Copernicus GmbH 2004), p 63
11. W. Reich: Astron. & Astrophys. Suppl. 48, 219 (1982)
12. W. Reich: In: *'Cosmic Polarization'*, ed by R. Fabbri (Research Signpost 2006), in press, astro-ph/0603465
13. W. Reich, E. Fürst, P. Reich et al., In:*Astrophysical Polarized Backgrounds'*, vol 609, ed by S. Cecchini et al. (AIP 2006), p 3
14. R.S. Roger, C.H. Costain, T.L. Landecker, C.M. Swerdlyk: Astron. & Astrophys. Suppl. 137, 7 (1999)
15. A.W. Strong, I.V. Moskalenko, O. Reimer: ApJ 537, 763 (2000)
16. X.H. Sun, J.L. Han, W. Reich et al., Astron. & Astrophys. in press
17. J.C. Testori, P. Reich, W. Reich, In: *'The Magnetized Interstellar Medium'*, ed by B. Uyanıker, W. Reich R. Wielebinski (Copernicus GmbH 2004), p 57
18. M. Wolleben, T.L. Landecker, W. Reich, R. Wielebinski: Astron. & Astrophys. 448, 411 (2006)
19. M. Wolleben, W. Reich: Astron. & Astrophys. 427, 537 (2004)

10

Global MHD Simulations of Galactic Gas Disks

Ryoji Matsumoto[1], Hiromitsu Nishikori[2], Minoru Tanaka[2], and Mami Machida[3]

[1] Department of Physics, Faculty of Science, Chiba University, 1-33 Yayoi-Cho, Inage-ku, Chiba 263-8522, Japan matumoto@astro.s.chiba-u.ac.jp
[2] Graduate School of Science and Technology, Chiba University, 1-33 Yayoi-Cho, Inage-ku, Chiba 263-8522, Japan
[3] Division of Theoretical Astronomy, National Astronomical Observatory of Japan, 2-21-1 Osawa, Mitaka, Tokyo 181-8588, Japan

Summary. We present the results of global three-dimensional magnetohydrodynamic simulations of galactic gas disks. Numerical results indicate that magneto-rotational instability amplifies magnetic fields. The growth of magnetic fields saturates when $B \sim 1.5\mu$G. This saturation level is almost independent of the strength of the initial magnetic field. The magnetic loops buoyantly rising from the disk supply azimuthal magnetic flux to the halo. We found that mean azimuthal magnetic fields inside the disk reverse their direction with interval about 1Gyr. The field reversal takes place following the buoyant escape of azimuthal magnetic flux amplified in the disk. The quasi-periodic reversals of azimuthal magnetic fields create a magnetically striped halo, in which azimuthal magnetic fields reverse their direction with height.

1 Introduction

Spiral galaxies have large scale mean magnetic fields [1]. The origin and evolution of large-scale galactic magnetic fields have been studied extensively in the context of the dynamo theory [2]. In conventional dynamo theory, time evolution of magnetic fields is studied by prescribing velocity fields. In differentially rotating gas disks, however, the back reaction of magnetic fields to gas motion drives the magneto-rotational instability (MRI) [3], which amplifies internal magnetic fields of the disk in dynamical time-scale. Since galactic gas disks rotate differentially, they subject to MRI.

Figure 1 schematically shows how MRI grows in differentially rotating gas disks. When the magnetic field threading the disk is perturbed in the radial direction (figure 1a), angular momentum is transported outward by Maxwell stress. The perturbed gas element infalls when the difference between the radial gravity and the centrifugal force exceeds the restoring magnetic tension. This condition is satisfied for long wavelength perturbations along the magnetic field lines. MRI grows even when the initial magnetic field is purely

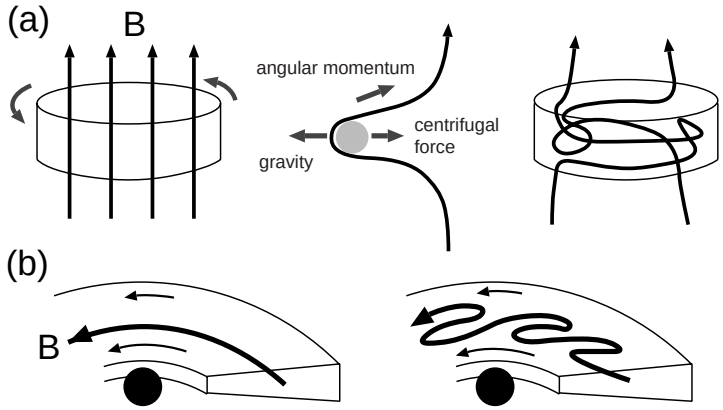

Fig. 1. (a) Magneto-rotational instability in differentially rotating disks. (b) Azimuthal magnetic field subjecting to the magneto-rotational instability.

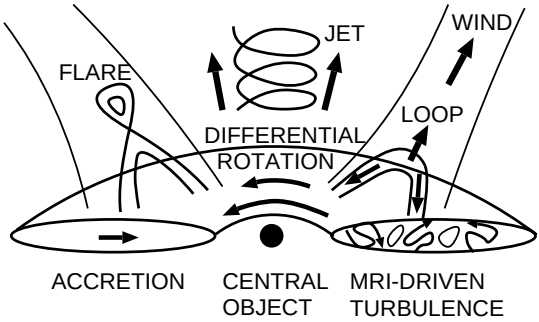

Fig. 2. A schematic picture showing magnetic activities in rotating gas disks.

azimuthal (figure 1b). MRI creates radial fields by deforming the azimuthal magnetic field. Gas elements infalling along the wiggled magnetic channels amplify azimuthal magnetic fields.

Figure 2 schematically shows magnetic activities in differentially rotating gas disks. MRI drives magnetic turbulence inside the disk and transports angular momentum. Magnetic fields amplified inside the disk buoyantly rise and create magnetic loops similar to those observed in the solar corona. In convectively stable, gravitationally stratified atmosphere, the buoyant rise of magnetic loops takes place when the buoyancy force created by sliding the gas along the magnetic field lines exceeds the restoring magnetic tension. This instability is called the Parker instability [4]. Parker instability grows for long wavelength perturbations along horizontal magnetic fields. When such magnetic loops are formed, they are twisted by the Coriolis force and create radial

fields. The radial fields are converted to the azimuthal field by differential rotation.

Since the importance of MRI was recognized for differentially rotating gas disks [3], the evolution of magnetic fields in accretion disks has been studied by three-dimensional magnetohydrodynamic (MHD) simulations. Several authors reported the results of global 3D MHD simulations of accretion disks (e.g., [5],[6],[7]). Dziourkevitch et al. [8] carried out global 3D MHD simulations of galactic gaseous disks and showed that interstellar turbulence is generated. Nishikori, Machida & Matsumoto [9] studied the effects of buoyant escape of magnetic flux from the galactic gaseous disk by 3D global MHD simulations using large simulation area ($0 < z < 10$kpc) in vertical direction. In the following, we summarize the results of such simulations and present new results studying the dependence of field amplification on the initial strength of magnetic fields and external pressure.

2 Simulation Models for Galactic Gas Disks

We assumed an axisymmetric gravitational potential created by stars and dark matter [10], which reproduces the rotation curve of our galaxy. Self-gravity of the gas is neglected. The initial state is a rotating gas torus whose density maximum is at $r_{\rm b} = 10$kpc from the Galactic center. The thermal energy of the torus is parameterized by $E_{\rm th} = c_{\rm s}^2/(\gamma v_0^2)$, where $c_{\rm s}$ is the sound speed at the density maximum, γ is the specific heat ratio, and $v_0 = 255$km/s. We adopted $\gamma = 5/3$ and $E_{\rm th} = 0.05$. The initial density and gas pressure of the torus at $(\varpi, z) = (r_{\rm b}, 0)$ are $\rho_{\rm b} = 3 \times 10^{-25}{\rm g/cm^3}$ and $P_{\rm b} = 10^{-11}{\rm dyne/cm^2}$, respectively. The torus is assumed to be surrounded by an isothermal spherical halo with pressure $P_{\rm c} = 3 \times 10^{-3} P_{\rm b}$ at $r = (\varpi^2 + z^2)^{1/2} = r_{\rm b}$. The torus is assumed to be threaded by weak toroidal magnetic fields at the initial state. The strength of the magnetic field is parameterized by the initial ratio of gas pressure to magnetic pressure, $\beta_0 = P_{\rm gas}/P_{\rm mag}$ at the density maximum of the torus.

We studied the evolution of the gas torus by using a 3D resistive MHD code in cylindrical coordinates based on a modified Lax-Wendroff scheme with artificial viscosity. The number of mesh points is $(N_\varpi, N_\varphi, N_z) = (250, 64, 319)$. We used non-uniform mesh to concentrate meshes near the galactic plane and near the galactic center. The size of the simulation box is $0{\rm kpc} < \varpi < 56{\rm kpc}$, and $0{\rm kpc} < z < 10{\rm kpc}$. We used this large simulation box in order to simulate the buoyant rise of magnetic flux from the disk to the galactic halo. We imposed free boundary conditions at $\varpi = 56$kpc and $z = 10$kpc. Symmetric boundary condition is imposed at the equatorial plane ($z = 0$). For azimuthal direction, we included a full circle ($0 < \varphi < 2\pi$). We imposed absorbing boundary condition at $r = 0.8$kpc. To initiate the evolution, we applied random perturbation for the azimuthal velocity with maximum amplitude $0.01 v_0$.

3 Results of Global 3D MHD Simulations

The left panel of figure 3 shows the distribution of density (gray scale) and magnetic field lines (gray curves) at $t = 2.3$Gyr for a model with $\beta_0 = 100$. Owing to the efficient angular momentum transport by the growth of the magneto-rotational instability, the initial gas torus deforms itself into a disk. The right panel of figure 3 shows magnetic field lines at $t = 3.8$Gyr projected onto the equatorial plane. The magnetic field lines show global spiral pattern with small scale turbulent structures. The strength of the turbulent magnetic field is comparable to the mean azimuthal magnetic field.

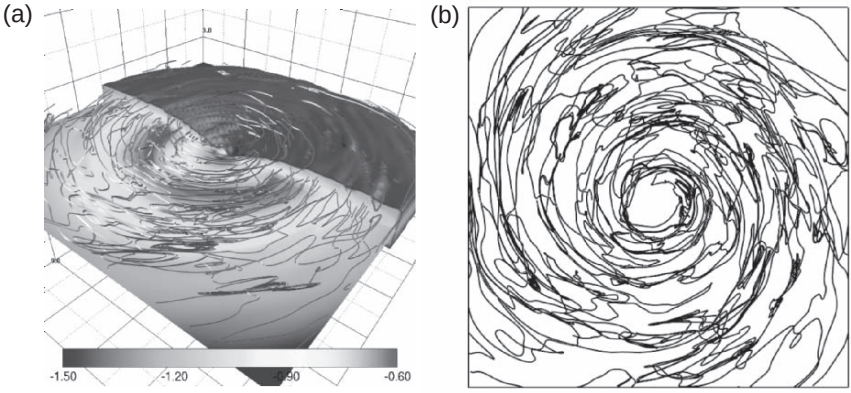

Fig. 3. Numerical results for a model with $\beta_0 = 100$. (a) Density distribution and magnetic field lines at $t = 2.3$Gyr. The isosurface $\rho/\rho_{\rm b} = 10^{-1.5}$ is plotted. The box size is 30kpc × 30kpc × 30kpc. (b) Magnetic field lines at $t = 3.8$Gyr projected onto the equatorial plane.

The left panel of figure 4 shows the time evolution of magnetic energy normalized by the initial maximum pressure of the disk for models starting from azimuthal magnetic fields with $\beta_0 = 100, 1000$ and 10000. The magnetic energy is averaged in $2\text{kpc} < \varpi < 5\text{kpc}$ and $0 < z < 1\text{kpc}$. The magnetic energy begins to increase when the disk gas accretes to this region and saturates when $P_{\rm mag} \sim 0.05 P_{\rm b}$. Numerical results are consistent with the results of global 3D MHD simulations of accretion disks, in which amplification of disk magnetic fields saturates when $\beta \sim 10$ [5]. The right panel of figure 4 shows the radial distribution of azimuthal magnetic fields for a model with $\beta_0 = 10000$. The dashed curve and the dotted curve show the mean azimuthal field averaged in the disk ($0.1\text{kpc} < z < 1\text{kpc}$), and in the halo ($1\text{kpc} < z < 3\text{kpc}$), respectively. The dash-dotted curve shows the distribution at the initial state. The

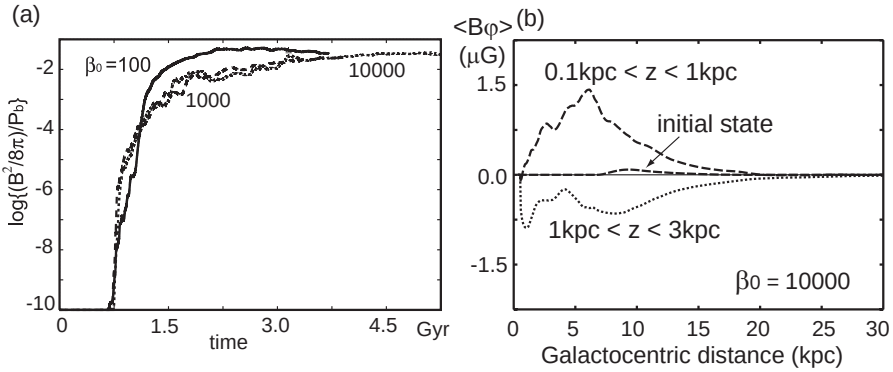

Fig. 4. (a) Growth of magnetic energy for models with $\beta_0 = 100, 1000$ and 10000. (b) Radial distribution of mean azimuthal magnetic field in the disk (dashed curve) and in the halo (dotted curve) at $t = 5.3$Gyr for a model with $\beta_0 = 10000$.

initial weak magnetic field is amplified up to $B_\varphi \sim 1.5\mu$G. The azimuthal magnetic field inside the disk is opposite to that in the halo. Therefore, the total azimuthal magnetic flux integrated in $0 < z < 10$kpc is nearly zero. Although the total azimuthal magnetic flux is conserved, the azimuthal magnetic flux inside the disk can be amplified because magnetic flux having opposite azimuthal direction buoyantly escapes from the disk to the galactic halo.

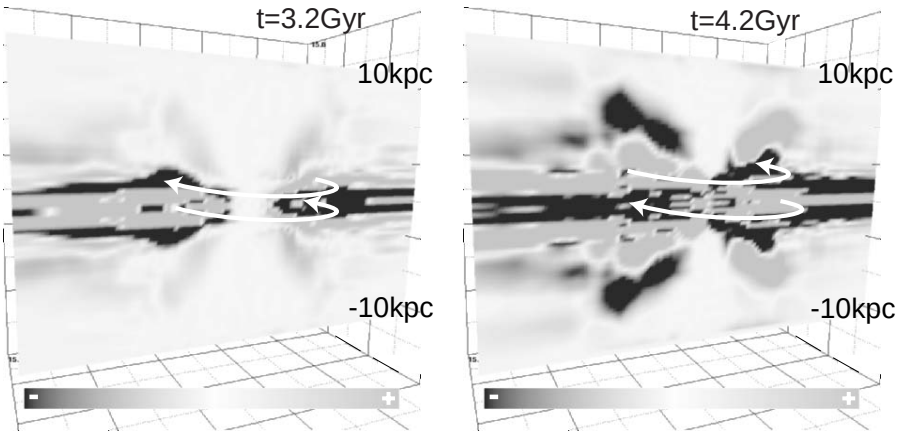

Fig. 5. Distribution of mean azimuthal magnetic fields at $t = 3.2$Gyr (left panel) and $t = 4.2$Gyr (right panel) for a model starting from azimuthal magnetic fields with $\beta_0 = 1000$. Light gray region and dark region correspond to the region where the mean azimuthal magnetic field is positive or negative, respectively.

Figure 5 shows the distribution of mean azimuthal magnetic fields and their time evolution for a model starting from weak azimuthal magnetic fields with $\beta_0 = 1000$. In the early stage (left panel), striped distribution of azimuthal magnetic field appears due to the growth of MRI. Subsequently, The magnetic fields buoyantly rise from the disk to the galactic halo due to the growth of the Parker instability [4]. Such coronal magnetic fields extend up to 10kpc from the equatorial plane. White arrows show the direction of mean azimuthal magnetic fields. The mean azimuthal fields change their direction with height. They also change direction with time.

The reversal of the direction of equatorial azimuthal magnetic fields takes place as the azimuthal magnetic flux escapes from the disk by buoyancy. Similar field reversals are observed in the Sun. The mean azimuthal magnetic fields buoyantly rising to the surface of the Sun change their direction in every 11years. According to our simulation, the galactic magnetic field reverses their direction with interval about 1Gyr.

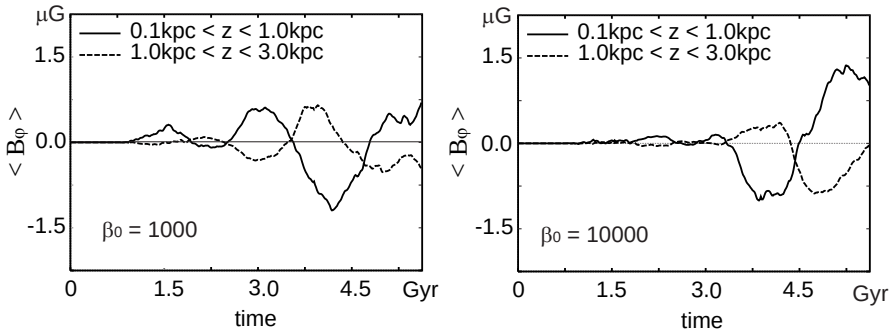

Fig. 6. Time evolution of mean azimuthal magnetic fields averaged in 5kpc $< \varpi <$ 6kpc for a model with $\beta_0 = 1000$ (left panel) and $\beta_0 = 10000$ (right panel). The solid curves and dashed curves show the mean azimuthal magnetic fields averaged in 0.1kpc $< z <$ 1kpc and 1kpc $< z <$ 3kpc, respectively.

Figure 6 shows the time evolution of azimuthal magnetic fields averaged in 5kpc $< \varpi <$ 6kpc for a model with $\beta_0 = 1000$ (left panel) and $\beta_0 = 10000$ (right panel). The solid curves and dashed curves show mean azimuthal fields averaged in the equatorial region ($0 < z <$ 1kpc) and in the halo (1kpc $< z <$ 3kpc), respectively. In both models, the mean azimuthal magnetic fields are amplified up to 1.5μG and reverse their direction with period of 2Gyr. The direction of mean azimuthal magnetic fields in the coronal region is opposite to that in the equatorial region. This field reversal takes place because the total azimuthal magnetic flux is conserved. When such magnetic fields buoyantly rise into the galactic halo, they produce striped distribution of magnetic fields.

The left panel of figure 7 shows magnetic field lines (solid curves) and the direction of azimuthal magnetic fields (gray scale) for our fiducial model ($\beta_0 = 100$). Azimuthal magnetic fields change direction with radius. When the gas pressure is large in the halo, it suppresses the buoyant rise of magnetic flux. The right panel of figure 7 shows the result for a model having halo pressure 10 times higher than that in the fiducial model. In this model, the azimuthal magnetic fields change direction more frequently in radial direction than the model with lower halo pressure. Similar frequent field reversals appear in the global 3D MHD simulation by Dziourkevitch et al. [8], in which the vertical simulation region is limited to $|z| < 1$kpc.

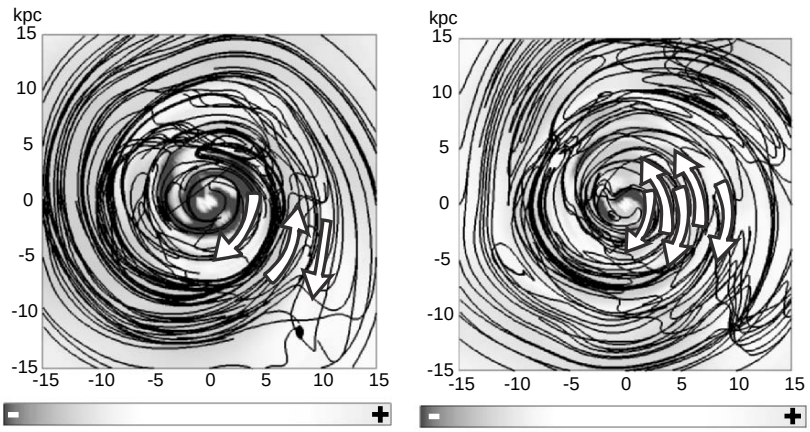

Fig. 7. Magnetic field lines (solid curves) and the direction of azimuthal magnetic fields (gray scale) for our fiducial model ($\beta_0 = 100$, $P_c = 10^{-3}P_b$) and a high halo pressure model with $\beta_0 = 100$ and $P_c = 10^{-2}P_b$ (right panel). The azimuthal magnetic field is negative in the dark region and positive in the light gray region.

4 Summary and Discussion

We carried out global 3D MHD simulations of a galactic gas disk by assuming axisymmetric gravitational potential. We showed that initially weak magnetic fields are amplified as the magneto-rotational instability grows inside the gas disk. The field amplification saturates when $\beta = P_{\rm gas}/P_{\rm mag} \sim 10$. The mean magnetic fields are amplified up to 1–2 μG and maintained. The strength of this mean magnetic field is almost independent of the initial strength of magnetic fields. The magnetic fields inside the disk is mainly azimuthal but has fluctuating poloidal components. The strength of turbulent magnetic field is comparable to the mean magnetic field.

In conventional theory of galactic dynamos, the evolution of magnetic fields is studied by solving the induction equation including the dynamo term $\nabla \times (\alpha \bar{\mathbf{B}})$ where $\bar{\mathbf{B}}$ is the mean magnetic field, which represents the regeneration of mean magnetic fields (α-effect). In galactic gas disks, buoyantly rising magnetic loops are twisted by Coriolis force, and subsequently stretched by differential rotation. In conventional dynamo theory, the detailed physics of this process is implicitly included in the parameter α. In MHD approach, the dynamical evolution of gas and magnetic fields is simulated by numerically solving the MHD equations instead of introducing the phenomenological parameter α.

We found that azimuthal mean magnetic fields reverse their direction both in space and in time. The interval of field reversal is about 1Gyr. This time scale is comparable to the timescale of the buoyant escape of azimuthal magnetic flux from the disk to the galactic halo. Since the total azimuthal magnetic flux is conserved when the resistivity is small enough, the amplification of azimuthal magnetic flux in galactic gas disks is enabled by the buoyant escape of the magnetic flux. Buoyantly escaping magnetic flux creates striped galactic halo which memorizes the previous field reversals of our Galaxy. Numerical results also indicate that the direction of mean azimuthal magnetic field inside the disk reverses with radius. It is consistent with the observations of Galactic magnetic fields by using the rotation measure [11].

We are now carrying out simulations without assuming equatorial symmetry, and extending our simulation models by including cooling, heating, and non-axisymmetric gravitational potential. We would like to report the results of such simulations in near future.

This work is supported in part by Grants-in-Aid for Scientific Research of Japan Society for the Promotion of Science (16340052). Numerical computations were carried out on VPP5000 at the National Astronomical Observatory, Japan.

References

1. Y. Sofue, M. Fujimoto, & R. Wielebinski: ARA&A 24, 459 (1986)
2. E.N. Parker: ApJ 163, 255 (1971)
3. S.A. Balbus, & J.F. Hawley: ApJ 376, 214 (1991)
4. E.N. Parker: ApJ 145, 811 (1966)
5. R. Matsumoto: *Numerical Astrophysics* ed. by S.M. Miyama, K. Tomisaka and T. Hanawa (Kluwer, Dordrecht 1999) pp.195
6. J.F. Hawley: ApJ 528, 462 (2000)
7. M. Machida, M.R. Hayashi, & R. Matsumoto: ApJ 532, L67 (2000)
8. N. Dziourkevitch, D. Elstner, & G. Rüdiger: A&A 423, L29 (2004)
9. H. Nishikori, M. Machida, & R. Matsumoto: ApJ 641, 862 (2006)
10. M. Miyamoto, C. Satoh, & M. Ohashi: A&A 90, 215 (1980)
11. J.L. Han, R.N. Manchester, A.G. Lyne, & G.J. Qiao: ApJ 570, L17 (2002)

11

Numerical Modeling of the ISM in the Galactic Center and Disks

Keiichi Wada[1] and Colin A. Norman[2]

[1] National Astronomical Observatory of Japan wada.keiichi@nao.ac.jp
[2] Johns Hopkins University norman@stsci.edu

Summary. The probability distribution functions (PDF) of density of the interstellar medium (ISM) in galactic disks and global star formation rate (SFR) are discussed. 3-D hydrodynamic simulations show that the PDFs in globally stable, inhomogeneous ISM in galactic disks are well fitted by a single log-normal function over a wide density range. The dispersion of the log-normal PDF (LN-PDF) is larger for more gas-rich systems, whereas the characteristic density of LN-PDF, for which the volume fraction becomes the maximum, is not sensitive for the gas mass. Using the LN-PDF, we give a generalized version of Schmidt-Kennicutt law, i.e. SFR as a function of average gas density, a critical local density for star formation, and star formation efficiency. We find that the observed SFR in normal and starburst galaxies are well-fitted by the theoretical SFR in a wide range of the global gas density ($10 - 10^4 M_\odot$ pc^{-2}). Star formation efficiency (SFE) for high density gas ($n > 10^3$ cm^{-3}) may be intrinsically different between starburst and normal galaxies.

1 Introduction

Observations suggest that there is a positive correlation between global star formation rate (SFR) and the average gas density: $\dot{\Sigma}_\star \propto \Sigma_{gas}^{1.4}$ in nearby galaxies [4]. Since star formation process itself is a local phenomenon on a sub-parsec scale, the observed correlation between the structure of the ISM on a local scale and the global quantities, such as the average gas density, implies that the ISM on different scales are physically related. In fact, 2D and 3D hydrodynamic and MHD simulations show that density structure of turbulent ISM is described by a log-normal density PDF [1, 2, 7, 10]. Elmegreen (2002) first noticed that if the density PDF is log-normal and star formation occurs in dense gases above a critical density, the Schmidt-Kennicutt law is reproduced. This provides a new insight on the origin of the scaling relation. In these theoretical predictions, dispersion of the LN-PDF, σ, is a key parameter. Elmegreen (2002) used $\sigma = 2.4$, which is taken from 2-D hydrodynamic simulations of the ISM [12]. Therefore, it is essential to know whether the LN-PDF in galactic dicks is universal, and what determines σ.

However, most previous simulations, in which LN-PDF or power-law PDF are reported, are 'local' simulations: a patch of the galactic disk is simulated with a periodic boundary condition. Apparently, such local simulations are not suitable to discuss statistical nature of the ISM in galactic disks. On the other hand, global hydrodynamic simulations for 2-D galactic disks or 3-D circumnuclear gas disks suggested that the density PDF, especially a high-density part is well fitted by a single log-normal function over 4-5 decades [11, 12]. Nevertheless universality of LN-PDF and how it is related to global quantities are still unclear. Here we verify the log-normal nature of the ISM in galactic disks, using three-dimensional, global hydrodynamic simulations.

2 The PDF in a galactic disk

Evolution of rotationally supported gas disks in a fixed (i.e. time-independent), spherical galactic potential is investigated using 3-D hydrodynamic simulations. We take into account self-gravity of the gas, radiative cooling and heating processes. The numerical scheme is an Euler method with a uniform Cartesian grid [12]. In order to focus on a intrinsic inhomogeneity in the ISM due to gravitational and thermal instability, first we do not include energy feedback from supernovae. The hydrodynamic part of the basic equations is solved by AUSM [6] with a uniform Cartesian grid. We use $512 \times 512 \times 64$ grid points covering a $2.56 \times 2.56 \times 0.32$ kpc^3 region (i.e. the spatial resolution is 5 pc). The Poisson equation is solved to calculate self-gravity of the gas using FFT.

The initial condition is an axisymmetric and rotationally supported thin disk with a uniform density ρ_i. Random density and temperature fluctuations are added to the initial disk. These fluctuations are less than 1% of the unperturbed values and have an approximately white noise distribution. The initial temperature is set to 10^4 K over the whole region. Figure 1 is snapshots of density distribution at a quasi-stable state for models A, B and D on the x-y plane and x-z plane. Depending on the initial density ($\rho_i = 5, 10$, and 50 $M_\odot$ pc^{-3}), distribution of the gas in a quasi-equilibrium is different. In the most massive disk (Fig. 1c, model D), the disk is fragmented into clumps and filaments, on the other hand, the less massive disk (Fig. 1a, model A) shows more axi-symmetric distribution with tightly winding spirals and filaments.

In Figure 2, we plot the mass-weighted PDFs for the four models. For the log-normal fit, we use σ expected from the argument in §3. The dispersion of the PDF is larger for more massive system. Nevertheless, the characteristic density of the LN-PDF is almost the same (i.e. $\rho_0 \simeq 10^{-1.5} M_\odot$ pc^{-3}). These results are not affected by the numerical resolution.

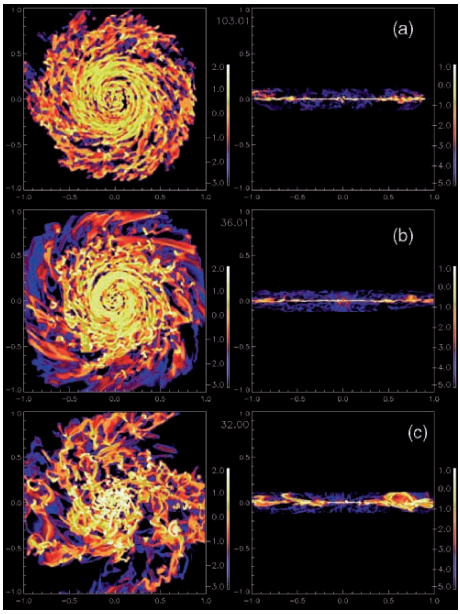

Fig. 1. Surface sections of the density distribution of the gas in models with different initial density (model A, B, and D). x-y and z-x planes are shown. Unit of length is kpc. (a) model A ($\rho_i = 5M_\odot$ pc^{-3}), (b) model B ($\rho_i = 10M_\odot$ pc^{-3}), and (c) model D ($\rho_i = 50M_\odot$ pc^{-3}).

3 Log-normal PDF and Star Formation Rate

Based on the numerical results in §2, we here propose a simple statistical model of the star formation on a kpc-scale. We assume that the multi-phase ISM in a galactic disk, in which stars are formed, is inhomogeneous in a wide density range, but the density structure is universal in a sense that the density PDF, $f(\rho)$ in the galactic disk is described by a single log-normal function:

$$f(\rho)d\rho = \frac{1}{\sqrt{2\pi}\sigma} \exp\left[-\frac{\ln(\rho/\rho_0)^2}{2\sigma^2}\right] d\ln\rho, \tag{1}$$

where ρ_0 is the characteristic density and σ is the dispersion. The volume average density $\langle\rho\rangle_V$ for the gas described by a the LN-PDF is then

$$\langle\rho\rangle_V = \rho_0\, e^{\sigma^2/2}. \tag{2}$$

The mass-average density is $\langle\rho\rangle_M = \rho_0 e^{2\sigma^2}$. The dispersion is therefore determined from volume average density, $\bar{\rho} \equiv \langle\rho\rangle_V$, and the characteristic density ρ_0,

$$\sigma^2 = 2\ln\left(\frac{\bar{\rho}}{\rho_0}\right). \tag{3}$$

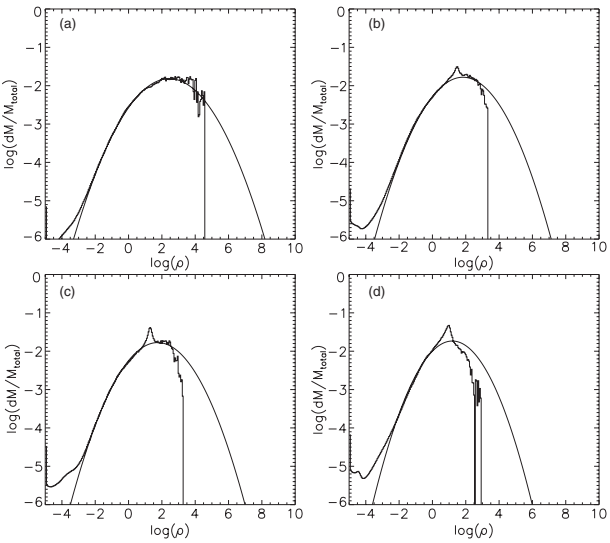

Fig. 2. Mass-weighted PDF of density (ρ) for (a) model D, (b) model C, (c) model B, and (d) model A. In the log-normal fit, a predicted dispersion σ (eq. (3)) is assumed. The cut-off at high density in each plot is caused by the resolution limit.

If the characteristic density is nearly constant as suggested by the numerical results, eq. (3) tells that the dispersion σ is larger for more massive systems, which is also consistent with the numerical results. For a stable, uniform system, in which $\bar{\rho} = \rho_0$, σ should be zero. In another extreme case, namely $\bar{\rho} \to \infty$, $\sigma \to \infty$, but this is not the case, because the system itself is no longer stable. Therefore, σ should take a number in an appropriate range in a globally stable, inhomogeneous systems, like galactic disks.

If we know the total gas mass and volume of the system, in which the ISM is highly inhomogeneous, therefore it is characterized by the LN-pdf, we can simply estimate the dispersion σ using eq. (3). Interestingly, even if the density contrast is extremely large (e.g. $10^6 - 10^8$), the numerical results show that the characteristic density ρ_0 is nearly constant ($\rho_0 = 0.025 - 0.04 M_\odot$ pc^{-3}) among the models with different total gas mass.

In a high-density region ($\rho > \rho_{crit} \approx \rho_0$), stochastic nature of the system, which is the origin of the log-normality, is caused in the gravity-driven turbulence in dense regions and gravitational collapse, and for low density regions its density field is randomized by thermal motion in hot gases. For the gases around ρ_0, the random motion is relatively quiet, therefore probability of the density change is small. As a result, the density PDF takes the maximum around ρ_0.

Suppose the volume average density is $\bar{\rho} = 3 M_\odot$ pc^{-3}, we can estimate the dispersion σ is $\sigma \simeq 3$ for $\rho_0 = 1$ cm^{-3}. For less massive system, e.g.

$\bar{\rho} = 0.3 M_\odot$ pc^{-3}, $\sigma \simeq 2.1$. Using this dependence of σ on the average gas density, we evaluate global star formation rate as follows.

A relation between the fraction of high density gas and global SFR assuming a LN-PDF [3]. If star formation is led by gravitational collapse of high-density clumps with density ρ_c, The star formation rate per unit volume is $\dot{\rho_\star} = \epsilon_c (G\rho_c)^{1/2} f_c \bar{\rho}$, where $f_c(\rho_c, \sigma)$ is a mass fraction of the gas whose density is higher than a critical density for star formation ($\rho > \rho_c$), and ϵ_c is the efficiency of the star formation. Assuming the LN-PDF, f_c is $f_c(\delta_c, \sigma) = 1/2(1 - \mathrm{Erf}[z(\delta_c, \sigma)])$, where $\delta_c \equiv \rho_c/\rho_0$, and $z(\delta_c, \sigma) \equiv (\ln \delta_c - \sigma^2)/\sqrt{2}\sigma$. The fraction of dense gas, f_c is a monotonic function of δ_c and σ, and it decreases rapidly for decreasing σ. Suppose $\delta_c = 10^5$, $f_c \sim 10^{-2}$ for $\sigma = 3$, and $f_c \sim 10^{-6}$ for $\sigma = 2$. SFR per unit volume then can be rewrite as a function of ϵ, δ_c, and σ:

$$\dot{\rho}_\star(\epsilon, \delta_c, \sigma) = \epsilon_c (G\delta_c)^{1/2} f_c \rho_0^{1/2} \bar{\rho} \tag{4}$$

Using eq. (3), we can write SFR as a function of average density $\bar{\rho}$,

$$\dot{\rho}_\star \left[\epsilon_c, \left(\frac{\bar{\rho}}{1 M_\odot \mathrm{pc}^{-3}} \right), \left(\frac{\rho_0}{1\,\mathrm{cm}^{-3}} \right), \left(\frac{\rho_c}{10^5\,\mathrm{cm}^{-3}} \right) \right] = \tag{5}$$
$$3.6 \times 10^{-7} \epsilon_c \, M_\odot \mathrm{yr}^{-1} \mathrm{pc}^{-3} \left[1 - \mathrm{Erf} \left(\frac{\ln(\rho_c \rho_0 / \bar{\rho}_V^2)}{2[\ln(\bar{\rho}/\rho_0)]^{1/2}} \right) \right] \rho_c^{1/2} \bar{\rho}.$$

In Figure 3, we compare surface star formation rate $\dot{\Sigma}_\star$ ($M_\odot$ yr^{-1} pc^{-3}) with observed SFR in normal and starburst galaxies [4, 5]. In the model, the scale height of the disk is 100 pc, and the reference density $\rho_0 = 1$ cm^{-1} and $\delta_c = 10^3$ (i.e. $\rho_c = 10^3$ cm^{-3}) are assumed. Each curve corresponds to SFR with efficiency, $\epsilon = 0.5, 0.1$, 0.01, and 0.001, respectively. The model slope approaches to SFR $\propto \Sigma_g^{1.0}$ for large density, which is shallower than the Kennicutt law (i.e. SFR $\propto \Sigma_g^{1.41}$). For smaller density, the curves are more steep, and it well fits the SFRs observed in normal galaxies (gray dots). Almost all the observed SFRs are distributed between the model curves with $\epsilon = 0.1$ and 10^{-3}. The starburst galaxies are distributed in $\epsilon = 0.1 - 0.01$, on the other hand, the normal galaxies show systematically smaller SFR [5], which is consistent with smaller efficiency (i.e $\epsilon = 0.1 - 0.001$) than those in starburst galaxies. This suggests that the large SFR in starburst galaxies is achieved by both high average gas density and large (several %) star formation efficiency in dense clouds($>10^3$ cm^{-3}).

4 Conclusion

The log-normal nature of the density field should be intrinsic in an inhomogeneous, multi-phase ISM, if 1) the whole system is globally quasi-stable in a

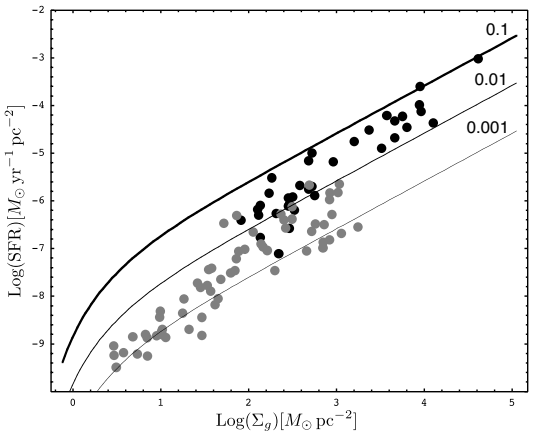

Fig. 3. Comparison between our models and observed surface star formation rate in terms of surface gas density. Black dots are starburst galaxies in Kennicutt (1998) and gray dots are normal galaxies in [5]. Model SFR is plotted for efficiency, $\epsilon_c = 0.1, 0.01$ and 0.001.

long enough period (for a galactic disk, it is at least a few rotational periods), 2) the system is consisted of many sub-structures, and 3) density in such sub-structure is determined by random, non-linear, and independent processes. If these conditions are satisfied, any random and nonlinear processes that change local densities should cause the log-normal PDF. In this sense, most physical processes expected in realistic galactic disks, such as nonlinear development of magneto-rotational instability, interactions between the ISM and stellar wind, and heating due to non-uniform radiation field originated in OB associations should also generate the log-normal PDF. These effects on the PDF can be verified in more realistic numerical simulations near future.

References

1. de Avillez, M. A. 2000, MNRAS, 315, 479 M. 1985, A&Ap, 150, 327
2. Bania, T. M. & Lyon, J. G., 1980, ApJ, 239, 173
3. Elmegreen, B. G. 2002, ApJ, 577, 206
4. Kennicutt, R., 1998, ApJ, 498, 541
5. Komugi, S., Sofue, Y., Nakanishi, H., Onodera, S., & Egusa, F., 2005, PASJ, 57, 733
6. Liou, M., Steffen, C., 1993, J.Comp.Phys., 107, 23
7. Rosen, A., Bregman, J.N., 1995, ApJ, 440, 634
8. Scalo, J., Vázquez-Semadeni, E., Chappell, D., Passot, T., 1998, ApJ, 504, 835
9. Slyz, A. D., Devriendt, J. E. G., Bryan, G., & Silk, J. 2005, MNRAS, 356, 737
10. Vázquez-Semadeni, E., Gazol, A. & Scalo, J. 2000, ApJ, 540, 271 98
11. Wada, K. & Norman, C. A. 1999, ApJL, 516, L13
12. Wada, K. & Norman, C. A. 2001, ApJ, 547, 172

12

The Warp and Spiral Arms of the Milky Way

Evan S. Levine[1], Leo Blitz[1], Carl Heiles[1], and Martin Weinberg[2]

[1] UC Berkeley Astronomy Dept, 601 Campbell Hall, Berkeley CA 94720 USA
elevine@astron.berkeley.edu
[2] University of Massachusetts Amherst Astronomy Dept, LGRT-B 619E, 710 North Pleasant Street, Amherst MA 01003 USA

We examine the outer Galactic HI disk for deviations from the $b = 0°$ plane by constructing maps of disk surface density, mean height, and thickness. We find that the Galactic warp is well described by a vertical offset plus two Fourier modes of frequency 1 and 2, all of which grow with Galactocentric radius. A perturbation theory calculation demonstrates that the tidal influence of the Magellanic Clouds creates distortions in the dark matter halo, which combine to produce disk warp amplitudes comparable to the observations. We also construct a detailed map of the perturbed surface density of HI in the outer disk demonstrating that the Galaxy is a non-axisymmetric multi-armed spiral. Overdensities in the surface density are coincident with regions of reduced gas thickness.

1 Method

We use the 21cm Leiden/Argentine/Bonn (LAB) data [1, 2, 3, 4] to conduct a quantitative study of the warp and spiral structure. We used the Hanning smoothed data, which have a velocity resolution of 1.9 km s^{-1}, and restricted our sample to $|b| \leq 30°$. We apply a median filter to the data to remove angularly small, bright features that are clearly not associated with the disk. To create a map of the Galaxy from the data, we must assume a rotation structure for the disk. Using a flat rotation curve with circular orbits results in a large asymmetry between the surface densities at Galactic longitudes on either side of $\ell = 0°$ and $\ell = 180°$. To eliminate this discontinuity, we assume that the gas is traveling on elliptical streamlines configured such that the surface densities are smooth across the $\ell = 180°$ line (see [5]). We exclude all points that lie within $345° \leq \ell \leq 15°$ or $165° \leq \ell \leq 195°$. Points in these two wedges have velocities along the line of sight that are too small with respect to their random velocities to establish reliable distances.

With this rotation structure, we transform the data to a three dimensional density grid, $\rho(R, \phi, z)$, where R is Galactocentric radius and z is height off

the plane. The Galactocentric azimuth ϕ is defined such that it converges with Galactic longitude ℓ at large R. We use a dispersion filter on ρ to remove extended clouds near the disk or spurs that have split off from the disk. Finally, we calculate the surface density Σ and mean height h as a function of position (R, ϕ) in the disk. The half-thickness T_h is calculated from ρ before the dispersion filter is applied, following the procedure described in [6].

2 Warping

2.1 Modes

A Lomb periodogram analysis of each radius ring reveals that the power in each of the frequency $m = 0$, 1, and 2 modes is consistently larger than that in any other mode for $R > 20$ kpc. Accordingly, we characterize the warp by an offset in the z direction, plus two Fourier modes with frequency $m = 1$ and 2. We fit each ring with the function

$$W(\phi) = W_0 + W_1 \sin(\phi - \phi_1) + W_2 \sin(2\phi - \phi_2); \quad (1)$$

this is similar to a fit described in [7]. Each of the three amplitudes W_i and two phases ϕ_i in this fit is a function of radius, because we fit each radius ring independently. This three component fit does a good job of reproducing the large-scale features in the mean height map (Fig. 1).

The three amplitude parameters each increase monotonically, with the $m = 0$ mode possibly reaching an asymptotic value near the far end of our radius range. At $R \approx 11$ kpc, the $m = 1$ mode dominates the shape of the warp; the other two modes do not become important until $R \approx 15$ kpc. There is little evidence for precession in the lines of maxima for the $m = 1$ and 2 modes, and the line of maxima for the $m = 1$ mode is roughly aligned with one of the lines of maxima of the $m = 2$ mode.

2.2 Mechanism

Many efforts have been directed toward understanding the warp on a theoretical basis. Bending modes have long been suspected as the mechanism creating and maintaining the warp [8, 9, 10, and many others], but several other mechanisms have been suggested [11]. Gravitational interaction with satellites such as the Magellanic Clouds has been a long-standing possibility [12, 13], but there is a debate over whether tidal effects are strong enough to produce the observed effect [14].

We perform a linear perturbation analysis to model the disk's response to the Clouds [15]. We allow the disk to feel the tidal field from the Clouds directly as well as the force from the dark-matter halo wake excited by the Clouds. We adopted the LMC mass from [16], the radial velocity and

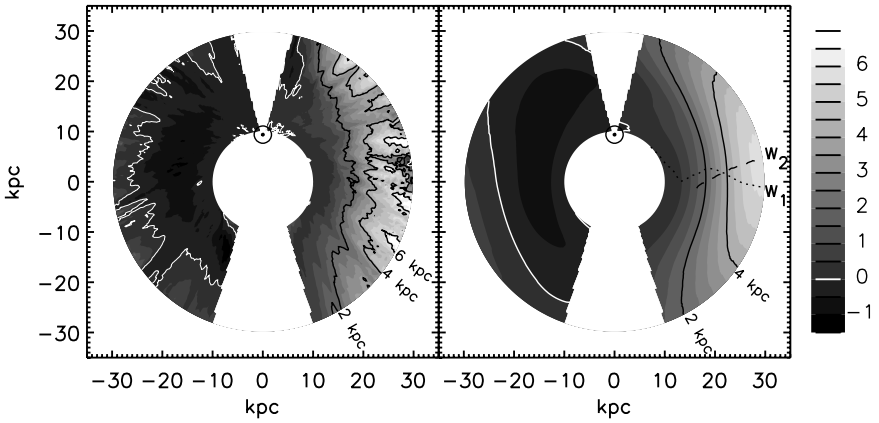

Fig. 1. Left panel: $h(R, \phi)$. Right panel: The fit to the warp is plotted, along with the lines of maximum amplitude for the m=1 (dotted) and m=2 (dashed) modes. These lines are marked W_1 and W_2 respectively. The white contour line denotes a height of 0 kpc; black lines mark the 2, 4, and 6 kpc elevations. The colorbar is marked in kpc.

proper motion from [17], and the distance modulus from [18]. The warp is a very dynamic structure based on the temporal evolution of the model. This can be seen in the AVI file of the simulations which can be found at **http://www.astro.umass.edu/∼weinberg/lmc**. Rather than a static structure that might be expected for a warp in response to a triaxial halo, a warp that results from the Clouds is continuously changing shape because of the varying amplitudes and phases of the various modes. As in the data, the $m = 1$ mode in the calculations is the strongest and increases nearly linearly out to the edge of the disk. The calculations also show a weak response of $m = 0, 2$ modes out to about 15 kpc, and then increasing nearly linearly, but with approximately the same amplitude for both. All of the major features of the warp are reproduced by the calculations, though there are some relatively minor differences which are likely to be due to uncertainties in the modeling.

3 Spiral Structure

Mapping the Milky Way's spiral structure is traditionally difficult because the Sun is imbedded in the Galactic disk; absorption by dust renders optical methods ineffective at distances larger than a few kpc. Radio lines like the 21 cm transition are not affected by this absorption, and are therefore well-suited to looking through the disk. In §1, we described the calculation of $\Sigma(R, \phi)$; we now perform a modified unsharp masking procedure on this map [19]. By

subtracting a blurred copy from the original image, this technique emphasizes low contrast features in both bright and dim regions. In previous maps [6] spiral arms were difficult to pick out on top of the global falloff of surface density with radius.

We construct a ratio $\Pi(R, \phi)$ between the surface density and the local median surface density. This is a dimensionless quantity, and therefore is a direct measure of the strength of the surface density perturbations (Fig. 2). The vast majority of points have values in the range 0.6 to 1.8, implying that the arm-to-interarm surface density ratio is about 3. Several long spiral arms appear clearly on the map, but the overall structure does not have the origin reflection symmetry of a "grand-design" spiral. Easily identified spiral arms cover a larger area in the south than in the north; there are three arms in the southern half of the diagram. Each of these arms has already been detected in previous maps out to 17 kpc for the two arms closer to the anticenter [6] and out to 24 kpc for the 'outer' arm [20].

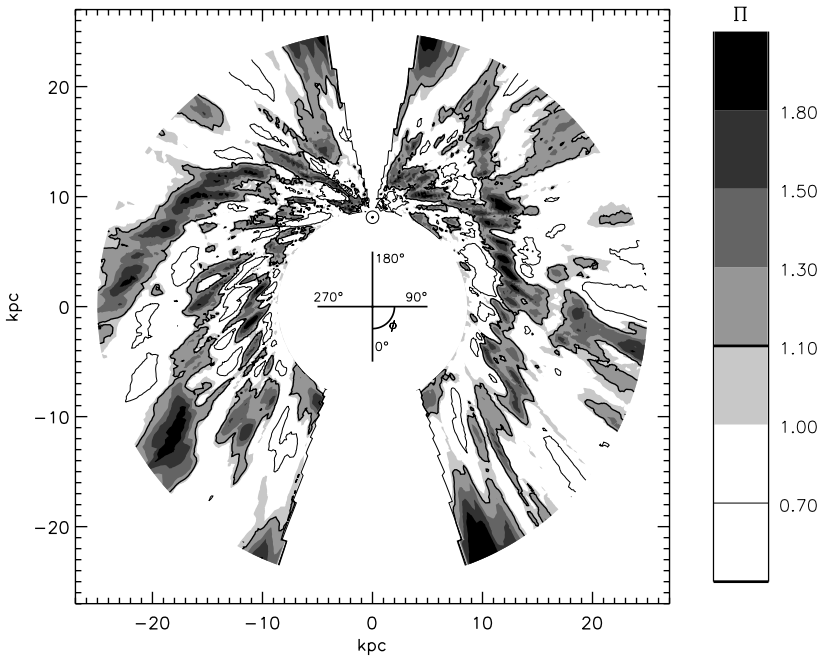

Fig. 2. A contour plot of the ratio of the surface density to the local median surface density $\Pi(R, \phi)$. Shaded regions are overdense compared to the local median. The thick solid contour marks the line $\Pi = 1.1$, while the thinner contour marks the line $\Pi = 0.7$. The values of Π for the different contour levels are given by the colorbar.

We also perform the modified unsharp masking on the thickness $T_h(R, \phi)$; spiral structure is evident in this map as well. We plot the $\Pi = 1.1$ overdensity contour from the surface density perturbation map on top of the thickness perturbation map (Fig. 3), showing that there is a good match between the arm positions as calculated from the surface density and the thickness; the thickness of the HI layer is smaller in the arms than in the rest of the disk, as suggested previously [6].

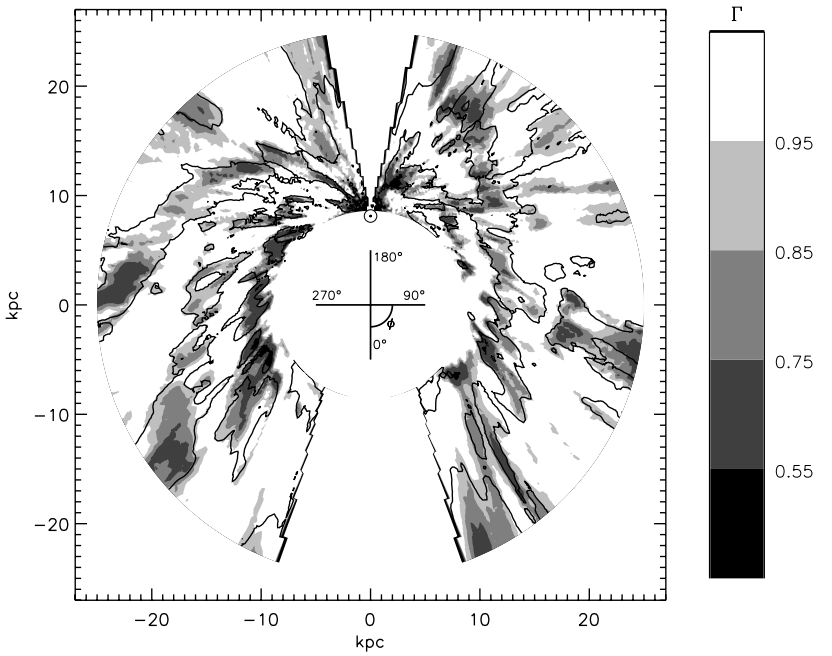

Fig. 3. A contour plot of the perturbations in the gas thickness, $\Gamma(R, \phi)$. Shaded regions have reduced thickness compared to the local median. The perturbation levels for the different contour levels are given by the colorbar. The solid contour marks the line $\Pi = 1.1$, the same as in Fig. 2, to show the alignment of the overdense surface densities with the thinner gas regions.

References

1. P.M.W. Kalberla, W.B. Burton, D. Hartmann, E.M. Arnal, E. Bajaja, R. Morras, & W.G.L. Pöppel: A&A 440, 775 (2005)
2. D. Hartmann, & W.B. Burton: *Atlas of Galactic Neutral Hydrogen* (Cambridge Univ. Press, Cambridge 1997)

3. E. Bajaja, E.M. Arnal, J.J. Larrarte, R. Morras, W.G.L. Pöppel, & P.M.W. Kalberla: A&A 440, 767 (2005)
4. E.M. Arnal, E. Bajaja, J.J. Larrarte, R. Morras, & W.G.L. Pöppel: A&AS 142, 35 (2000)
5. E.S. Levine, L. Blitz, & C. Heiles: ApJ 643, 881 (2006)
6. A.P. Henderson, P.D. Jackson, & F.J. Kerr: ApJ 263, 116 (1982)
7. J. Binney, & M. Merrifield: *Galactic Astronomy* (Princeton University Press, Princeton 1998)
8. C. Hunter & A. Toomre: ApJ 155, 747 (1969)
9. L.S. Sparke & S. Casertano: MNRAS 234, 873 (1988)
10. L.S. Sparke: ApJ 439, 42 (1995)
11. K. Kuijken & I. García-Ruiz: Galactic Disk Warps. In: ASP Conf. Ser. 230, Galaxy Disks and Disk Galaxies, ed. by J. G. Funes & E. M. Corsini (Sheridan Books, Ann Arbor 2001) pp 401–408
12. B.F. Burke: AJ 62, 90 (1957)
13. M.D. Weinberg: MNRAS 299, 499 (1998)
14. F.J. Kerr: AJ 62, 93 (1957)
15. M.D. Weinberg & L. Blitz: ApJ 641, L33 (2006)
16. B.E. Westerlund: *The Magellanic Clouds* (Cambridge Univ. Press, Cambridge 1997)
17. N. Kallivayalil, R.P. van der Marel, C. Alcock, T. Axelrod, K.H. Cook, A.J. Drake, & M. Geha: ApJ 638, 772 (2006)
18. W.L. Freedman, B.F. Madore, B.K. Gibson, L. Ferrarese, D.D. Kelson, S. Sakai, J.R. Mould, R.C. Kennicutt, Jr., H.C. Ford, J.A. Graham, J.P. Huchra, S.M.G. Hughes, G.D. Illingworth, L.M. Macri, & P.B. Stetson: ApJ 553, 47 (2001)
19. E.S. Levine, L. Blitz, & C. Heiles: Science 312, 1773 (2006)
20. N.M. McClure-Griffiths, J.M. Dickey, B.M. Gaensler, & A.J. Green: ApJ 607, L127 (2004)

This page intentionally blank

Part II

THE GALACTIC CENTER AND CENTRAL REGION OF GALAXIES

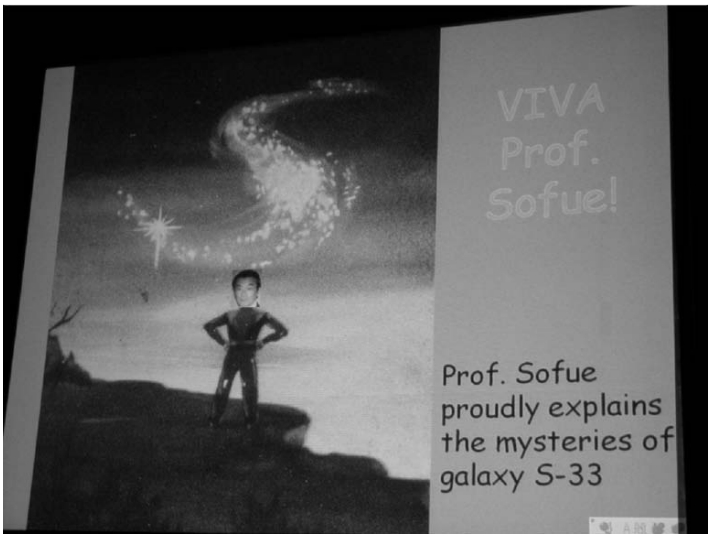

From the presentation by Jeff Kenney

Yoshiaki Sofue. The conference originated from his insatiable curiosity.

13

The Parkes Galactic Meridian Survey (PGMS)

Ettore Carretti[1], D. McConnell[2], M. Haverkorn[3,4], G. Bernardi[5], N.M. McClure-Griffiths[2], S. Cortiglioni[6], and S. Poppi[7]

[1] INAF – Istituto di Radioastronomia, Via Gobetti 101, I-40129 Bologna, Italy carretti@ira.inaf.it
[2] CSIRO – ATNF, PO Box 76, Epping NSW 1710, Australia david.mcconnell@csiro.au, naomi.mcclure-griffiths@csiro.au
[3] Jansky Fellow, National Radio Astronomy Observatory
[4] Astronomy Department University of California–Berkeley, 601 Campbell Hall, Berkeley CA 94720 marijke@astro.berkeley.edu
[5] Kapteyn Astronomical Institute, University of Groningen, PO Box 800, 9700 AV Groningen, The Netherlands bernardi@astro.rug.nl
[6] INAF – IASF Bologna, Via Gobetti 101, I-40129 Bologna, Italy cortiglioni@iasfbo.inaf.it
[7] INAF–Osservatorio Astronomico di Cagliari, Poggio dei Pini, Strada 54, I-09012 Capoterra (CA) spoppi@ca.astro.it

Summary. The Parkes Galactic Meridian Survey (PGMS) is aimed at mapping the polarized diffuse emission at 2.3-GHz along a Galactic meridian to study its behaviour from the Galactic plane to the south Galactic pole. One of the aims is to study the Galactic magnetic field at medium and high Galactic latitudes and at the transition with the Galactic disc. In combination with 1.4-GHz data, Rotation Measures (*RM*s) can be measured with a sensitivity of $\sim$ 2-rad/m^2, allowing exploration of the component of the Galactic magnetic field parallel to the line of sight even at high latitudes. Moreover, position angles corrected for *RM* give information about the direction of the Galactic magnetic field perpendicular to the line of sight. Finally, the properties of the polarized synchrotron emission can be also investigated. This will be crucial for CMB Polarization observations, for which such Galactic emission acts as foreground noise. Here we present the survey together with some preliminary results.

1 The Parkes Galactic Meridian Survey

The Parkes Galactic Meridian Survey (PGMS) is a project carried out at the Parkes telescope to survey a 5° wide strip centred on the Galactic meridian $l = 254°$ at 2.3-GHz. It covers all the Galactic latitudes from the Galactic plane down to the south pole with the goal to study the polarized diffuse emission behaviour as a function of the latitude (Fig. 1). It also includes a 10° enlargement between $b = -30°$ and $b = -40°$ to study a target region

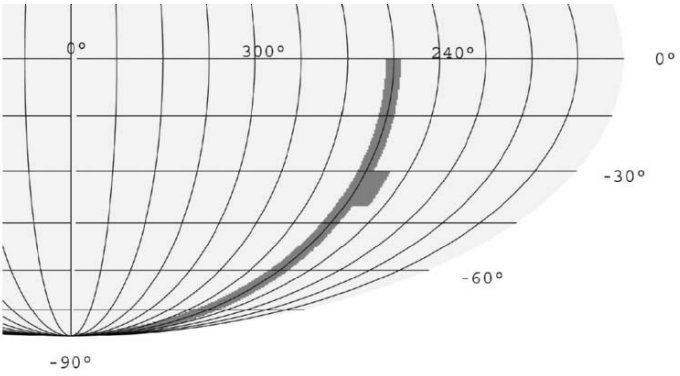

Fig. 1. The PGMS survey coverage in Galactic coordinates.

Table 1. Main parameters of the PGMS survey: ν is the central frequency, BW the bandwidth, N_ν the number of frequency channels, FWHM the beam size, l_0 the central meridian of the strip, and $\sigma_{Q,U}$ the sensitivity of Stokes Q and U in a beam-sized pixel. The area size is also reported.

ν	BW	N_ν	FWHM	l_0	Area size	$\sigma_{Q,U}$
2332-MHz	208-MHz	26	8.8'	254°	$5.0° \times 90.0°$	0.5-mK

of Cosmic Microwave Background Polarization (CMBP) experiments [1]. The main survey parameters are reported in Table 1.

The polarized diffuse emission at radio wavelengths is dominated by the Galactic synchrotron background, which allows the study of the magnetic field **B** of the Galaxy [2]. The component along the line of sight can be investigated through mapping of the Rotation Measure[8] (*RM*), which is determined by the variation of the synchrotron polarization angles as a function of frequency. The expected performance is:

– In the disc the signal and the *RM* values are sufficiently high that *RM* can be measured with PGMS data alone using its 26 frequency channels. The expected sensitivity is 10-rad/m^2, on a $\sim 9'$ scale, sufficient for disc *RM* values of the order of hundreds of rad/m^2.
– In the halo *RM* can be measured in combination with the recent 1.4-GHz polarization survey of the southern sky [3]. The expected sensitivity is 2-rad/m^2 at the $36'$ resolution of the 1.4-GHz survey.

[8] Polarization angles ϕ rotate as $\phi = \phi_0 + RM\lambda^2$, where ϕ_0 is the intrinsic polarization angle and λ the wavelength. The Rotation Measure *RM* is defined as $RM = 0.81 \int n_e[\mathrm{cm}^{-3}] B_\parallel [\mu\mathrm{G}] dl[\mathrm{pc}]$, where n_e is the thermal electron density, $B_\parallel$ the magnetic field strength parallel to the line of sight and dl the path length.

Furthermore, position angles corrected for *RM* represent the direction of the Galactic magnetic field tangential to the plane of the sky.

In addition, the Galactic synchrotron emission is one of the major contaminants of the CMBP. The determination of its strength and angular and frequency behaviour allows estimating the capability of CMBP to study early Universe events like inflation (e.g. [4, 5, 6]).

2 PGMS Goals

2.1 Galactic Magnetic Field

The Galactic magnetic field can be described by two components: a random field related to turbulent phenomena in the ISM, and a component which is coherent on Galactic scales and believed to be generated by dynamo processes [7].

After the 1960s and 1970s pioneering studies (e.g. [8]), there is a renewed interest to study Galactic magnetism. The Galactic plane is increasingly well studied due to new high signal-to-noise (S/N) *RM* data (e.g. the Canadian Galactic Plane Survey [10] and Southern Galactic Plane Survey [11]).

However, considerably less is known about the disc and halo at medium and high Galactic latitudes. The halo magnetic field probably varies mainly on large scales, while in the disc the field is turbulent on much smaller scales. Therefore, a transition ought to occur, likely close to Galactic latitude $|b| = 30°$. Although this picture is supported by *RM*s of extragalactic sources (e.g. see [12]), these data are too sparsely sampled and allow us to see only the design at very large angular scales ($> 10°$). Study of the **B** structure in the halo, e.g. related to superbubbles or Galactic fountains, requires higher resolution. The 1.4-GHz DRAO polarization survey [13] clearly shows a sudden transition between an almost depolarized area across the Galactic plane at $|b| < 30°$ and a smooth emission area above this limit. This sharp change indicates that high resolution data are also necessary to probe the disc–to–halo transition.

Observations at higher frequencies and finer resolution are required both to pick up the signal in the disc area and to sample *RM* on a finer grid. New data covering high Galactic latitudes are becoming available. The aforementioned 1.4-GHz DRAO survey in combination with a southern survey by Testori et al. [3] cover all the sky with a resolution of $36'$. Although these data are a significant step ahead, spectral information is not available so that *RM* cannot be derived. Polarization angles are still strongly rotated by Faraday rotation (expected RM = 10-20-rad/m^2) and therefore are not representative of the magnetic field direction on the plane of the sky.

With the WMAP experiment, the first polarization all-sky map at microwave wavelengths, viz. at 22.8-GHz, has become available [14]. *RM* effects are negligible at this frequency, so that polarization angles track the magnetic

field orientation. However, the weak signal out of the Galactic plane is detected only in large local structures like the radio loops [9]. The rest of the halo region has a low sensitivity ($S/N < 3$ in about 55% of the sky, using 2° pixels – see Fig. 2) which does not allow us to study **B** in the areas uncontaminated by local structures. Meaningful information can be extracted by smoothing to larger scales, again obtaining only information on large scales.

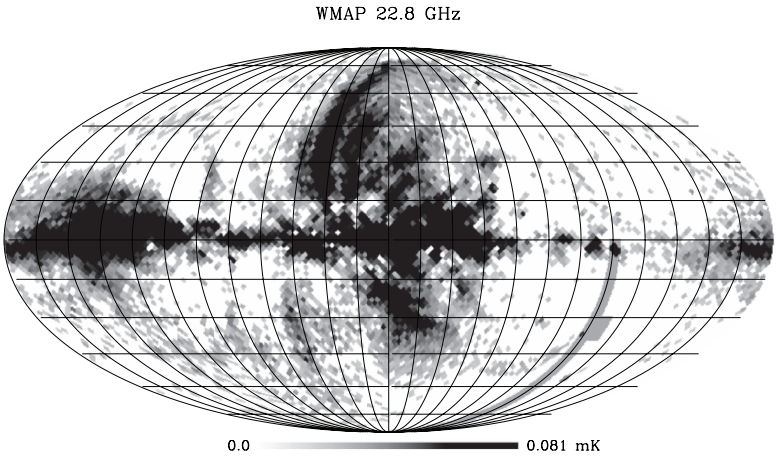

Fig. 2. WMAP polarized intensity map at 22.8-GHz with 2° pixelation (r5 HEALPix resolution). Pixels with signal-to-noise ratio $S/N < 3$ are blanked (white). The PGMS area is also shown (gray strip).

The PGMS is designed to begin to study these insufficiently known regions. Surveying all the Galactic latitudes, PGMS is ideally fit to tackle open issues like:

– the structure and strength of **B** in the halo;
– the structure of **B** in the disc-halo transition, to monitor the transition of both the coherent and the turbulent field;
– **B** in the disc, where 1.4-GHz data are mostly depolarized.

Although the survey is not all-sky, the selected meridian goes through the low emission region and samples the halo magnetic field without any contamination by local structures (Fig. 2). The expected performance in terms of *RM* (Sect. 1) allows a significant improvement of **B** mapping both in resolution and sensitivity, at medium and high Galactic latitudes.

2.2 CMBP Foreground

The early Universe of the inflation can be investigated through one of the two components of the CMB Polarization, the so-called B-Mode [4]. Its emission is

faint (of the order of 10–100 nK), however, and can be affected by the Galaxy in the foreground. One of the main contaminants is the diffuse synchrotron emission, which is best studied at radio wavelengths. The CMBP B-mode level is related to the gravitational wave amount generated by the inflation, which is still unknown and depends on inflation models (e.g. [15]). Estimating the synchrotron emission, thus, helps set the detection limit of the CMBP and which part of the Inflationary model space can be investigated by the CMBP.

The best conditions for this investigation are at high latitude, where the Galactic emission is lowest. First analyses of such areas have been reported recently, both using devoted observations or data of the recent DRAO and WMAP surveys (see [5] for a review). Although the results are promising, the areas investigated so far are either too small or do not have enough sensitivity to draw final conclusions.

One of the aims of the PGMS is to measure and analyse the synchrotron emission behaviour as a function of Galactic latitude to estimate its contamination, especially in the high latitude fields. The survey's strip is positioned through one of the regions with lowest emission (Fig. 2), so that PGMS can study the Galactic contribution even in those areas of the sky most promising for CMBP B–mode detection. The observing frequency of 2.3-GHz seems to be high enough to limit Faraday rotation effects (while 1.4-GHz is probably still too much modified [16]).

3 Status and Preliminary Results

PGMS observations started in January 2006 and are expected to last through 2007. The Galactic plane end between $b = 0°$ and $b = -15°$ has been completed, as well as the first of two coverages for the 10° enlargement (for half of the total integration time). Figure 3 shows the polarized intensity $L = \sqrt{Q^2 + U^2}$ of some of the completed fields. The diffuse component dominates the emission and is structured up to area-size scales with rms signal $L_{\rm rms} \sim 15$-mK. Small-scale modulations and depolarization are visible, indicating a structured magnetized medium, and a few point sources are present. The achieved sensitivity matches our expectations and along with the rms polarization signal found here provides us with high S/N ratios, which promise sensitive *RM* measurements in the disc.

Observations of more fields are in progress (September 2006) and time has been allocated at the Parkes radio telescope to complete most of the survey by January 2007.

Acknowledgments. We acknowledge the use of the HEALPix package [17], WMAP data, and the Legacy Archive for Microwave Background Data Analysis (LAMBDA). Support for LAMBDA is provided by the NASA Office of Space Science. Parkes is part of the Australia Telescope, which is funded by the Commonwealth of Australia for operation as a National Facility managed

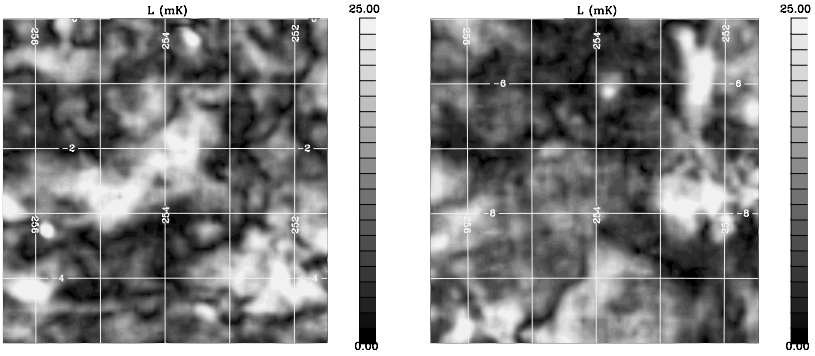

Fig. 3. Polarized intensity emission of two PGMS fields centred at $b = -2.5°$ (left) and $b = -7.5°$ (right).

by CSIRO. M.H. acknowledges support from the National Radio Astronomy Observatory (NRAO), which is operated by Associated Universities Inc., under cooperative agreement with the National Science Foundation.

References

1. S. Masi, et al., A&A, submitted, astro-ph/0507509 (2005)
2. R. Beck, A. Brandenburg, D. Moss, A. Shukurov, D. Sokoloff, AARA, 34, 155 (1996)
3. J.C. Testori, P. Reich, W. Reich, In: *The Magnetized Interstellar Medium*, ed by B. Uyanıker, W. Reich, R. Wielebinski, (Copernicus GmbH, Katleburg-Lindau 2004) p. 57
4. M. Kamionkowski, A. Kosowsky, PRD, 57, 685 (1998)
5. E. Carretti, G. Bernardi, S. Cortiglioni, MNRAS Letters, in press, astro-ph/0609288 (2006)
6. L. Verde, H.V. Peiris, R. Jimenez, JCAP, 1, 19 (2006)
7. R. Beck, SSR, 99, 243 (2001)
8. W.N. Brouw, T.A.Th. Spoelstra, A&AS, 26, 129 (1976)
9. E.M. Berkhuijsen, C.G.T. Haslam, C.J. Salter, A&A, 14, 252 (1971)
10. J.C. Brown, A.R. Taylor, B.J. Jackel, ApJS, 145, 213 (2003)
11. M. Haverkorn, B.M. Gaensler, N.M. McClure-Griffiths, J.M. Dickey, A.J. Green, ApJS, in press, astro-ph/0609010 (2006)
12. M. Johnston-Hollitt, C.P. Hollitt, R.D. Ekers, In: *The Magnetized Interstellar Medium*, ed by B. Uyanıker, W. Reich, R. Wielebinski, (Copernicus GmbH, Katleburg-Lindau 2004) p. 13 (astro-ph/0410659)
13. M. Wolleben, T.L. Landecker, W. Reich, R. Wielebinski, A&A, 448, 411 (2006)
14. L. Page, et al., ApJ, submitted, astro-ph/0603450 (2006)
15. J. Martin, C. Ringeval, JCAP, in press, astro-ph/0605367 (2006)
16. E. Carretti, G. Bernardi, R.J. Sault, S. Cortiglioni, S. Poppi, MNRAS, 358, 1 (2005)
17. K.M. Górski, et al., 2005, ApJ, 622, 759

14

Mapping Large-scale Magnetic Fields in Giant Molecular Clouds

Giles Novak[1], M. Krejny[1], H. Li[1], D. T. Chuss[2] and P. G. Calisse[3]

[1] Northwestern University, Evanston, Illinois, U.S.A. g-novak@northwestern.edu
[2] NASA Goddard Space Flight Center, Greenbelt, Maryland, U.S.A.
[3] Cardiff University, Cardiff, Wales, U.K.

1 The SPARO Experiment

We report observations of magnetic fields in Giant Molecular Clouds (GMCs), obtained using the technique of submillimeter polarimetry. We used a polarimeter called SPARO [1, 2] that we built at Northwestern U. and that we use together with a 2-meter telescope at South Pole station. In comparison with submillimeter polarimeters that have been operated from larger telescopes on Mauna Kea, SPARO obtains relatively coarse angular resolution but much better sensitivity to fainter, more extended emission. We have also discussed these recent SPARO observations in a paper in the Astrophysical Journal [3].

2 Are B-Fields in GMCs Correlated with Galactic B-Fields?

The question that we address here is whether magnetic field directions in GMCs are correlated with the direction of the large-scale magnetic field of the Galaxy. Another way to ask this question is to consider the unknown physical process that causes a large volume of diffuse interstellar matter to come together and form a GMC, and to ask whether this process preserves the memory of the original magnetic field direction, or whether instead the field gets scrambled. The question has been addressed via observations of OH masers in molecular clouds [4, 5, 6] with some investigators finding evidence for a correlation.

The question can also be addressed using submillimeter polarimetry. A collection of measured field directions that were mostly obtained using a polarimeter operated at the Caltech Submillimeter Observatory on Mauna Kea has been studied [7] in order to determine if the field directions are correlated with the direction of the Galactic plane. No correlation was found. The

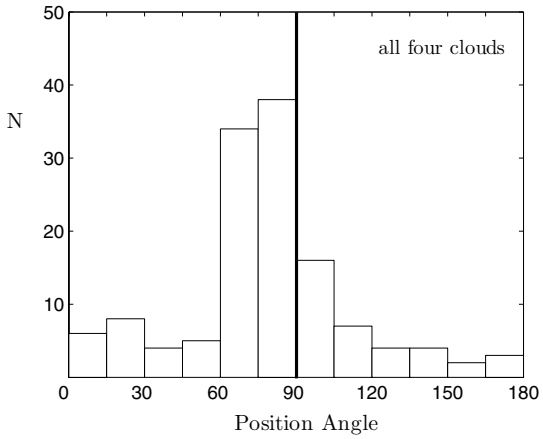

Fig. 1. Histogram of the 131 magnetic field directions measured by SPARO in the four GMCs [3]. The horizontal axis gives the field angle in Galactic coordinates, measured from Galactic North. Ninety degrees corresponds to magnetic fields parallel to the Galactic plane.

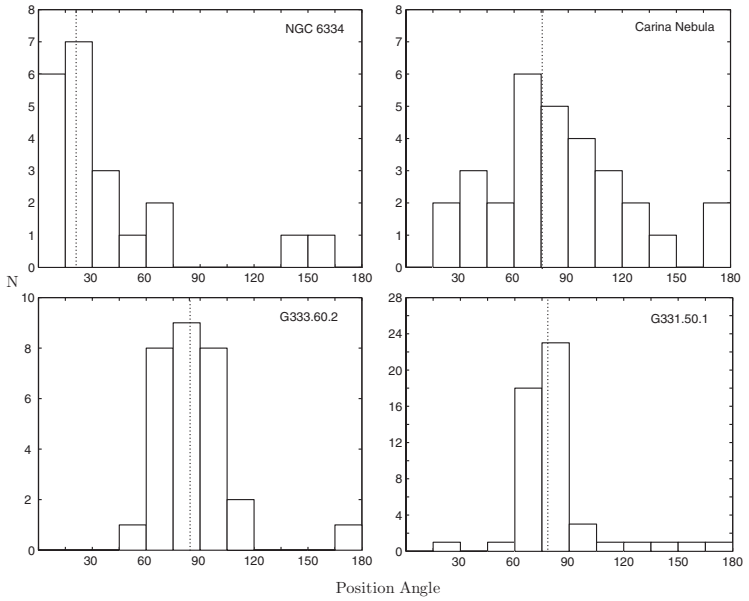

Fig. 2. Same as Figure 1, but broken up into four histograms, one for each GMC. The vertical dotted lines show the mean magnetic field direction for each cloud [3].

SPARO data set consists of magnetic field maps for four GMCs in the Galactic disk, at distances ranging from about two to about five kpc [3]. For each of the four clouds, we measured polarization along a few dozen sight lines, and we obtained a total of 131 measurements. Figure 1 shows a histogram of the 131 measured field directions. The dark vertical line in the middle of the histogram corresponds to having magnetic fields parallel to the Galactic plane. We see that the fields are preferentially parallel to the Galactic plane and thus also preferentially parallel to the large scale field of the Galaxy. The earlier submillimeter study [7] did not see this because it was based on small scale maps of fields near flux peaks in GMCs, whereas our maps cover much more sky area [3] and thus truly sample the global magnetic fields of GMCs.

Figure 2 shows another way to look at the data, with four individual histograms, one for each GMC. Each cloud has a well defined peak in the distribution of field angles, and in three cases the mean field angle is within 15 degrees of the plane. One cloud, NGC 6334, has its field rotated away from the plane by a large angle. This cloud presents a bit of a puzzle, but note that the distribution of mean field angles for the four clouds is not consistent with a random distribution. If one were to chose mean field angles at random, then the probability for finding three out of the four angles to be within 15 degrees of the plane would be less than 2% [3]. Thus, our data show a statistically significant correlation of GMC fields with Galactic plane orientation.

3 Using Optical Polarimetry to Probe the Galactic Field

Note that even if GMC formation does preserve mean field direction, we should not expect to see all GMCs having fields exactly parallel to the Galactic plane, because the Galactic field itself has large scale fluctuations. If NGC 6334 were to have formed in a region of the Galaxy where, due to these fluctuations, the Galactic field was rotated away from the plane by a large angle, then the cloud would end up with its field rotated away from the plane, as we observe. In principle, we can check this hypothesis by using optical polarimetry to sample the Galactic field in the vicinity of each of our four GMCs. Before doing this we need to decide how big a volume of space around each GMC we should sample. A natural size to use is a cube 400 pc on a side, corresponding to a volume of diffuse ISM that contains enough mass to form a GMC [8].

We have carried out a study based on the stellar polarimetry database assembled by Carl Heiles [9]. First we examined how the selective extinction for these stars depends on distance. We found [3] that the extinction vs. distance curve rises linearly at first, as expected for stars chosen at random, but then it flattens. This flattening suggests that the Heiles database contains a selection effect whereby a star at a great distance (say, 3 kpc) has a better chance of making it into the database if the sight-line toward that star is relatively dust-free. Because of this possibility for bias, we decided to avoid using data from the flat part of the curve. The closest of the four GMCs

mapped by SPARO is NGC 6334, the discrepant cloud, at 1.7 kpc. The other three are at distances well into the flat part of the extinction vs. distance curve, so we have not attempted to study the Galactic fields for these three. But we did carry out a study of the field in the region surrounding NGC 6334, as well as in other nearby regions for comparison purposes [3].

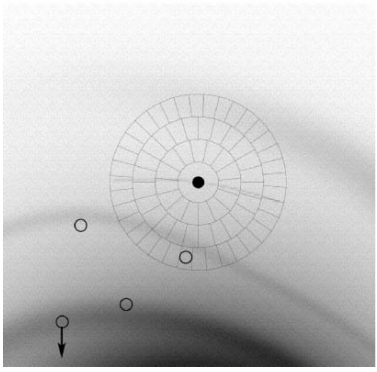

Fig. 3. "Cells" used to analyze optical polarimetry data. View is looking down on the Galaxy's disk from Galactic North. A filled circle indicates the Sun's location, with the Galactic center well off the bottom of the image. Approximate locations of spiral arms are shown using a gray scale image from a model [10]. Open circles show locations of SPARO GMCs. (One is slightly off the bottom of the image, as indicated). The local region of the Galaxy is divided up using three rings of three-dimensional cells [3], shown here in projection.

As shown in Figure 3, we divided the nearby regions of the Galaxy into "cells", one of which is centered on the NGC 6334 cloud, with the goal of using the optical polarimetry data to estimate the mean field direction for each cell. The cell dimensions (300 by 120 by 500 pc) deviate somewhat from the ideal of 400 pc for practical reasons [3]. To estimate the field angle for any given cell, we used "background stars", chosen to be near the back face of the cell, and "foreground stars", chosen to be near the front face. We then estimated the portion of the polarization of a given background star that is due specifically to dust in the cell, by taking differences between Stokes parameters of that background star and the Stokes parameters of a selection of foreground stars chosen to be near in the sky to the background star [3].

The stars in the database are not evenly distributed in the sky, and many of our cells have very few or no stars. We implemented cuts designed to eliminate cells with too few stars, or with too much disorder in the derived magnetic field directions [3]. Only 11 cells survived these cuts (the NGC 6334 cell is one of them) and the histogram at the upper left of Figure 4 shows the distribution of mean field angles. Even though we excluded the most distant stars, the background stars for the third ring of cells (Fig. 3) are still sufficiently

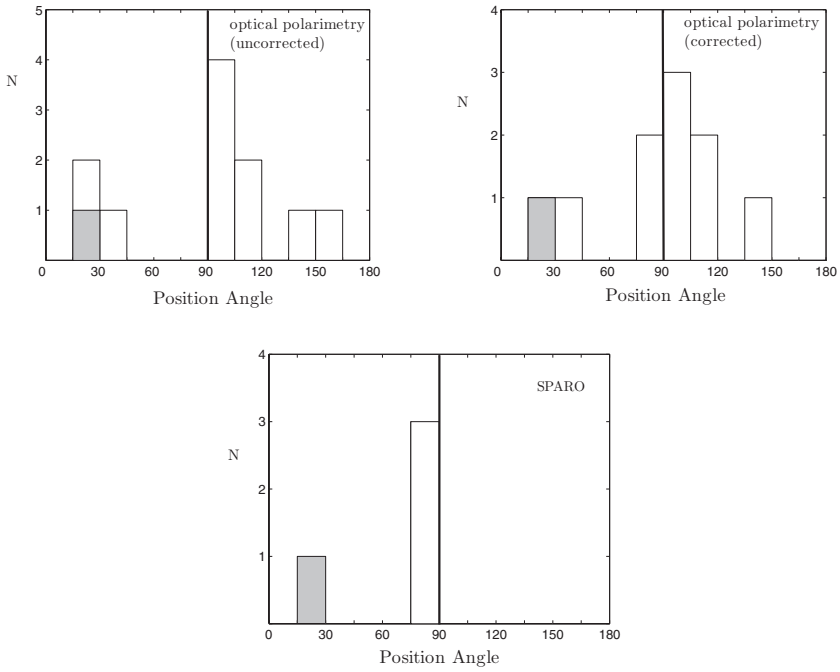

Fig. 4. Histograms from optical polarimetry analysis (upper left and right) and SPARO data (bottom). For all three histograms, the horizontal axis shows the field angle, and the direction corresponding to the Galactic plane is indicated with a dark vertical line. At upper left we show the distribution of mean field angles for 11 optical polarimetry cells, and to the right of this we show the result when the analysis is repeated with bias correction applied (see discussion in text). The bottom plot shows the distribution of the four mean field angles determined by SPARO for the four GMCs we observed. In all three histograms, the box corresponding to NGC 6334 is shaded.

far to put them in the part of the extinction vs. distance curve where the above-mentioned flattening is starting to become evident. We were concerned about the effects of the above-mentioned bias, and as a way to gage this we devised a crude way to correct for the bias [3]. First we made a rough estimate for how badly the extinction is being underestimated at any given distance, based on the observed flattening of the extinction vs. distance curve. Then, under the assumption that the Stokes parameters are being underestimated by the same factor, we corrected them upward. Finally we repeated our entire analysis using these corrected Stokes parameters, and the result is shown in the upper right of Figure 4. Despite the differences, the two optical polarimetry histograms (upper left and upper right of Fig. 4) both show an apparent peak corresponding to cells having mean field parallel to the plane, and both also show significant disorder.

Next we compare our optical polarimetry results to the SPARO results for the mean fields of the four GMCs, shown in the bottom histogram of Figure 4. Recall (Sect. 2) that three of the GMCs have their mean fields well aligned with the Galactic plane, while NGC 6334 is an outlier. In the bottom histogram of Figure 4, the NGC 6334 cloud is shaded. In the upper histograms of Figure 4, the cell corresponding to NGC 6334 is shaded. We see from the position of the shaded box in these upper histograms that the region where NGC 6334 formed has a projected field direction that is unusual in that it is rotated far away from the Galactic plane. In terms of agreement of cell field direction with Galactic plane, it is the worst of 10 cells (upper right histogram) or one of the worst 3 of 11 (upper left histogram). The fact that the NGC 6334 cell is unusual may explain why the NGC 6334 cloud is unusual. The results of our optical polarimetry study are thus consistent with the idea that GMC formation preserves the memory of the large-scale field (measured on $\sim$ 400 pc scales).

This result and the statistically significant correlation we see between GMC fields and the Galactic plane (Sect. 2) can both be naturally understood if the GMC formation process does indeed preserve the mean field direction. This work was supported by a grant to Northwestern U. from the NSF's Office of Polar Programs.

References

1. G. Novak, D. T. Chuss, T. Renbarger, G. S. Griffin, M. G. Newcomb, J. B. Peterson, R. F. Loewenstein, D. Pernic, and J. L. Dotson: Ap. J. Lett. 583, L83 (2003)
2. T. Renbarger, D. T. Chuss, J. L. Dotson, G. S. Griffin, J. L. Hanna, R. F. Loewenstein, P. S. Malhotra, J. L. Marshall, G. Novak, and R. J. Pernic: P.A.S.P 116, 415 (2004)
3. H. Li, G. S. Griffin, M. Krejny, G. Novak, R. F. Loewenstein, M. G. Newcomb, P. G. Calisse, and D. T. Chuss: Ap. J. 648, 340 (2006)
4. M. J. Reid and E. M. Silverstein: Ap. J. 361, 483 (1990)
5. A. Baudry, J. F. Desmurs, T. L. Wilson, and R. J. Cohen: A. & A. 325, 255 (1997)
6. V. L. Fish, M. J. Reid, A. L. Argon, and K. M. Menten: Ap. J. 596, 328 (2003)
7. R. H. Hildebrand: In *Astrophysical Spectropolarimetry*, edited by J. Trujillo-Bueno, F. Moreno-Insertis, & F. Sanchez (Cambridge University Press, Cambridge, 2002) p 265
8. J. P. Williams, L. Blitz, and C. F. McKee: In *Protostars and Planets IV*, edited by V. Mannings, A. P. Boss, & S. S. Russel (University of Arizona Press, Tucson, 2000), p 97
9. C. Heiles: Astron. J. 119, 923 (2000)
10. R. Drimmel and D. N. Spergel: Ap. J. 556, 181 (2001)

15

The Shapes and Supersonic Motions of Molecular Clouds

Jin Koda[1]

California Institute of Technology koda@astro.caltech.edu

Summary. The energy source and mechanism for driving the supersonic motions in molecular clouds remain unknown. The unknown driving mechanism must exert an influence on the shape of molecular clouds [5]. We analyzed a sample of more than 500 molecular clouds identified with the BU-FCRAO Galactic Ring Survey (YRS) data, and found that they are preferentially elongated along the Galactic plane. Their spin axes are randomly oriented; therefore, we conclude that the elongation is supported by internal velocity anisotropy, but not by spin. The mechanism for driving the supersonic velocity dispersion must also account for the preferred elongation. This excludes some suggested mechanism, such as stellar winds and supernovae, because they do not produce the systemic elongation. Driving energy is more likely to come from large-scale motions, such as Galactic rotation.

1 Introduction

The nature, origin, and maintenance of the supersonic motions or turbulence in molecular clouds remain unresolved. These motions must be 'continuously' driven, since otherwise they decay on a cloud crossing timescale $\sim 3\times10^6$yr. In fact, the free-fall collapse timescale of dense molecular clouds and presumably the timescale for the decay of supersonic motions are substantially shorter than the likely cloud lifetimes. Such driving mechanisms must exert influence on the shape of molecular clouds. Larson [6] argued that molecular clouds are only converging regions in interstellar turbulence, and thus, only transient structures. Even in this case, the shape of structures on scales similar to the cloud sizes will reflect the mechanisms inputing energy at the top of the turbulent cascade. Using new data from the BU-FCRAO ^{13}CO survey [3], we statistically investigate the shape of more than 500 molecular clouds found in the inner Galaxy. Their average parameters are in Table 1.

Possible energy sources for the interstellar turbulence have recently been discussed on a theoretical basis [2, 7]. The sources may include stellar feedback (i.e. local events) and galactic rotation (i.e. large-scale motions). The physical

mechanism converting these energies into turbulence has not been well understood. We expect that it affects the morphology of the gas structure as well as the turbulent motions. In particular, the shape of molecular clouds may indicate the possible energy source and physical mechanism. We will discuss the origin of the velocity dispersions as well as the shape of molecular clouds.

Table 1. Properties of ^{13}CO Molecular Cloud

Parameter	Unit	mass-weighted mean	mean
Diameter	pc	38	15
Vel. width	$\mathrm{km\,s^{-1}}$	11.5	5.1
Vel. disp.	$\mathrm{km\,s^{-1}}$	2.2	1.0
T_{peak}	K	11	8.9
M_{VT}	Msun	1.2×10^5	1.3×10^4

2 Elongation

The position angles and axis ratios of molecular clouds are calculated by diagonalizing the moment of inertia matrix as,

$$R_{-\theta} \begin{pmatrix} \Sigma T_{ij}\alpha_{ij}^2 & -\Sigma T_{ij}\alpha_{ij}\beta_{ij} \\ -\Sigma T_{ij}\alpha_{ij}\beta_{jj} & \Sigma T_{ij}\beta_{ij}^2 \end{pmatrix} R_\theta = \begin{pmatrix} I_{xx} & 0 \\ 0 & I_{yy} \end{pmatrix},$$

where T_{ij} is the brightness temperature at a pixel (i,j), and α_{ij} and β_{ij} are the distances from the emission centroid to the pixel in the l- and b-directions. R_θ is a rotation matrix with the rotation angle θ. The axis ratio and position angle of clouds correspond to $(I_{xx}/I_{yy})^{1/2}$ and θ, respectively. The position angle is defined from the positive b-direction going counterclockwise to the positive l. The direction along the Galactic plane is $\theta = 90\,\mathrm{deg}$.

Figure 1 shows the histograms of axis ratio and position angle. The axis ratio has the peak at about 1.8, indicating that the molecular clouds are significantly elongated. The population of round clouds, having the axis ratio of 1, is small. The position angle peaks at $\theta \sim 90\,\mathrm{deg}$ (i.e. along the Galactic plane). Clouds with $\theta \sim 90\,\mathrm{deg}$ is about two times more populated than those with $\theta \sim 0\,\mathrm{deg}$ or $180\,\mathrm{deg}$. *Therefore, molecular clouds are elongated predominantly in the direction of the Galactic plane.* We separate small clouds ($D < 15\,\mathrm{pc}$) from large clouds ($D > 15\,\mathrm{pc}$) in Figure 1. As well as the large clouds, the small clouds are elongated along the Galactic plane. These clouds are much smaller than the thickness of the gas disk (about 100 pc) and stellar disk (about 600 pc), and thus, suffer little from the disk potential.

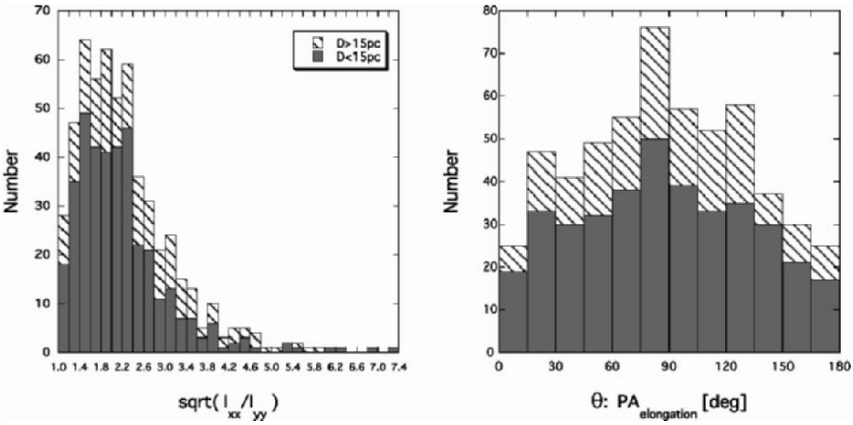

Fig. 1. Distribution of axis ratios (*left*) and position angles (*right*) of molecular clouds. The values are calculated using the moments of inertia. Position angle θ is defined from the $+b$ direction going to positive l. Hence $\theta = 90$deg is the direction along the Galactic plane. Large ($D > 15\,\mathrm{pc}$) and small ($D < 15\,\mathrm{pc}$) clouds are indicated with different patterns and illustrated cumulatively.

3 Spin

It is possible that the elongation is supported by the spin of molecular clouds. In order to evaluate this, we measured the velocity gradient in molecular clouds (projection on the sky) and the position angle perpendicular to the maximum velocity gradient, i. e. parallel to the axis of possible spin (Figure 2). The velocity gradient is estimated from the observed velocity field by fitting a plane. The position angle ψ is oriented with 0 deg at $+b$, increasing toward $+l$. Typical velocity gradients dv/dr projected on the sky are about 0.15 $\mathrm{km\,s^{-1}\ pc^{-1}}$. We did not correct for the apparent velocity gradient due to the projected LSR velocity over the diameter of the clouds, since this gradient is at most $\sim 0.04\,\mathrm{km\,s^{-1}\ pc^{-1}}$, assuming a Galactic rotation velocity of $220\,\mathrm{km\,s^{-1}}$. Prograde and retrograde spins with respect to the Galactic rotation are indicated with different patterns, and are equally populated.

Figure 2 *right* can be directly compared to Figure 1 *right*. If spin supports the elongation, the ψ should be distributed similarly to the θ; their peaks should be related as $\psi_{\mathrm{peak}} \sim \theta_{\mathrm{peak}} - 90\,\mathrm{deg}$. The figures, however, show that the spin is randomly oriented and has no dominant peak. *Therefore, the cloud elongations are not supported by internal spins, but should be related to the internal velocity dispersions (supersonic motions).*

It is noteworthy that confusion (blending) in cloud identification is likely to align the apparent spin axis perpendicular to an elongation – it is most likely that two clouds are slightly offset in space and velocity. The opposing result strongly indicates that the blending is not critical in our sample.

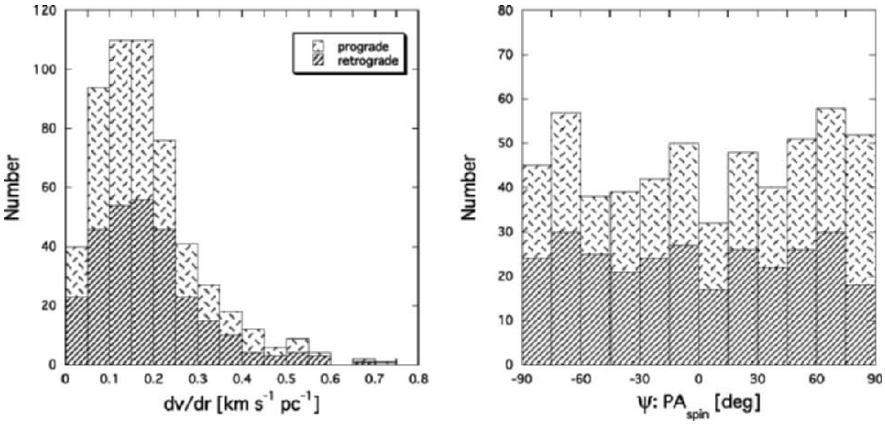

Fig. 2. Distribution of velocity gradients (*left*) and position angles of spin (*right*) of molecular clouds. Position angle pc$i$ is defined as in Figure 1 (*right*), but ranges between -90 deg and 90 arcdeg. Hence, pc$i = 0$ deg is the direction perpendicular to the Galactic plane. The right figure can be compared directly with Figure 1 (*right*). Prograde and retrograde spins are indicated with different patterns.

4 Discussion

4.1 Energy Source

Among several suggested energy sources [2], two sources, i.e. stellar feedback and galactic rotation, are most often considered. Most other sources extract their intrinsic energies from these two.

Stellar feedback includes protostellar outflows, stellar winds, ionizing radiation, and supernova explosions. These feedback mechanisms, however, release energy isotropically or in random directions. Such processes are unlikely to cause the preferential orientation of molecular clouds. They would cause a random orientation.

Supernovae are the most energetic feedback mechanism [9, 7]. There are some arguments for supernovae-induced dense gas formation and supersonic turbulence. If supernova blastwaves, however, compress surrounding material and induce molecular cloud formation, their round expansion will produce *no* preferential orientation. The blastwaves would escape from the Galactic disk predominantly in the direction normal to the Galactic plane. In such case, most molecular clouds would be elongated perpendicular to the plane. The stellar feedback is unlikely to be the dominant cause of the elongation of molecular clouds.

Evidence has been accumulated for the presence of molecular clouds without star formation activity [8, 11, 15]. Stellar feedback cannot supply energy to such clouds. High mass star-forming regions are localized around spiral arms in the Galaxy [1, 10] and in external galaxies [12]. It is also unlikely

that the energy supply from stellar feedback suffices to maintain supersonic motions in interarm molecular clouds.

Since the cloud elongation has the preferential direction, the energy source is likely to have a similar preferred direction. Galactic rotation has an rotation axis, and is a likely energy source. Galactic rotation provides an enormous reservoir of energy; it can maintain the elongations and supersonic motions over the Galactic age.

Even if molecular clouds are only transient structures in large-scale interstellar turbulence, the anisotropic shapes should indicate the origin of the turbulence. It is still likely that the Galactic rotation is the main source of the turbulent energy.

4.2 Driving Mechanism

How might the rotation energy be transferred to random motion in molecular clouds? Energy transfer from rotation to random motions generally occurs in a differentially rotating disk, if mass elements orbiting at slightly different radii pull on each other [13]. Selwood & Balbus [13] pointed out that many types of viscous stress, including Reynolds, Maxwell, and gravitational stresses, can cause the energy transfer from rotation to random motion.

For example, Jog & Ostriker [4] found with an analytic calculation that cloud-cloud gravitational interactions (gravitational stress) can transfer the orbital energy of clouds into random motions *between* clouds [but they did not discuss internal motions]. Wada et al. [14] used hydrodynamical simulations and showed that the rotational energy could cascade into smaller scales (down to their resolution limit, i.e. the size of giant molecular clouds), owing to local tidal force among clouds, filaments, and voids. Perhaps, this cascade proceeds down to the internal motions of the clouds.

If tidal gravitational torques exerted by passing clouds is the cause of the velocity dispersions, the preferred elongation of molecular clouds would be produced naturally. The mean separation of molecular clouds is about $1/n_{\rm MC}^{1/3} \sim 200\,{\rm pc}$ [5]. This is larger than the thickness of the Galactic molecular disk 100 pc. Tidal radius of molecular clouds should be at least a few times larger than their diameter, and thus is not negligible compared with the disk thickness. Tidal interaction should occur predominantly in the Galactic plane; it may generate asymmetric velocity dispersions which cause the elongation along the Galactic disk.

A slight exchange of angular momentum may occur during tidal interaction and spin up clouds. The spin axis might become perpendicular to the elongation, however, this effect should be little. In case that two clouds pass by at the distance $d = 100\,{\rm pc}$ and velocity $v = 6\,{\rm km\,s^{-1}}$ (typical cloud-cloud velocity dispersion), the tidal interaction would increase the velocity gradient within a cloud by at most $v/2\pi d \sim 0.01\,{\rm km\,s^{-1}\,pc^{-1}}$ if the two clouds are strongly coupled. This is negligible compared with the observed velocity gradient. In addition, random encounters would suppress the increase of angular

momentum. The spin-up is not significant even if the tidal interaction is the cause of supersonic motions.

We discussed only gravitational interactions between molecular clouds. Some other density fluctuations, such as filamentary structure in gas, would also strengthen the tidal field around clouds. There are, of course, some other possible mechanisms introduced by magnetic field, surrounding diffuse gas (HI and H_2), and gradients in stellar potential. Further discussions would require theoretical researches.

References

1. Downes, D., Wilson, T. L., Bieging, J. & Wink, J.: A&A 40, 397 (1980)
2. Elmegreen, B. G. & Scalo, J.: ARA&A 42, 211 (2004)
3. Jackson, J. M., Rathborne, J. M., Shah, R. Y., et al.: ApJS 163, 145 (2006)
4. Jog, C. J. & Ostriker, J. P.: ApJ 328, 404 (1988)
5. Koda, J., Sawada, T., Hasegawa, T., Scoville, N. Z.: ApJ 638, 191 (2006)
6. Larson, B. R.: MNRAS 194, 809 (1981)
7. Mac Low, M. -M. & Klessen, R. S.: Reviews of Modern Physics 76, 125 (2004)
8. Mooney, T. J. & Solomon, P. M.: ApJ 334, L51 (1988)
9. Norman, C. A. & Ferrara, A.: ApJ 467, 280 (1996)
10. Sanders, D. B., Scoville, N. Z. & Solomon, P. M.: ApJ 289, 373 (1985)
11. Scoville, N. Z. & Good, J. C.: ApJ 339, 149 (1989)
12. Scoville, N. Z., Polletta, M., Ewald, S. Stolovy, S. R., Thompson, R. & Rieke, M.: AJ 122, 3017 (2001)
13. Sellwood, J. A. & Balbus, S. A.: ApJ 511, 660 (1999)
14. Wada, K., Meurer, G. & Norman, C. A.: ApJ 577, 197 (2002)
15. Williams, J. P. & Blitz, L.: 494, 657 (1998)

16

Millimeter Dust Continuum Emission as a Tracer of Molecular Gas in Galaxies

Caroline Bot[1], F. Boulanger[2], M. Rubio[3], and F. Rantakyro[4]

[1] California Institute of Technology, USA bot@caltech.edu
[2] Institut d'Astrophysique Spatiale (IAS), France
[3] Universidad de Chile, Chile
[4] European Southern Observatory, Chile

Summary. Molecular gas in galaxies is the primary fuel of star formation but the exact amount of molecular gas remains unknown since H_2 is not observed directly in cold interstellar regions. CO observations have been so far the best way to trace molecular gas in external galaxies, but in low metallicity environments the gas mass deduced could be largely underestimated due to enhanced photodissociation of CO. In this context, using millimeter dust emission as a dense gas tracer could unveil large H_2 enveloppes in molecular clouds.
Mass estimates from millimeter dust emission are compared to virial masses in two giant molecular clouds samples: the local clouds in our Galaxy, and equivalents in the Small Magellanic Cloud. In our Galaxy, virial masses are systematically larger than mass estimates from millimeter emission, confirming previous studies. This is not the case for SMC clouds: molecular gas masses deduced from millimeter observations are systematically higher than the virial masses from CO observations. We show that an additional magnetic field support of the SMC clouds could explain the difference observed.

Molecular clouds are of particular importance as beeing the place where star formation occurs in a galaxy. Most of this gas is located in Giant Molecular Clouds (GMCs), but the exact amount of gas contained remains unknown since H_2 is quite impossible to observe directly in cold interstellar regions. CO is the most widely used tracer of molecular gas. However, it could be present only in the densest part of molecular clouds, leaving H_2 enveloppes unseen. This effect has been clearly observed in Solar Neighborhood GMCs [3] and tends to underestimate molecular masses estimated from CO observations. This bias could be important in low metallicity environments where CO will be restrained to tiny dense structures [5] while most of the mass may lie in the cloud molecular envelopes.

In this context, millimeter (mm) dust emission could bring to light the total mass of such clouds. It traces interstellar matter in the densest and most shielded regions in star forming molecular clouds. The advent of sensitive bolometer arrays on sub-mm/mm telescopes makes long wavelength dust

emission as an alternative to CO to compute molecular masses. Dust emission at mm wavelengths is optically thin, scales linearly with dust temperature and complements the HI and CO observations to provide a complete view of the interstellar matter in molecular clouds.

We propose to use mm dust continuum emission to compute masses for two samples of GMCs: the molecular clouds of the Solar neighbourhood, and their size equivalents in the Small Magellanic Cloud (SMC). The SMC is a nearby irregular dwarf galaxy (D$\approx$ 61kpc) with a low metallicity (Z$\approx$Z$_\odot$/10) and giant star forming regions. These point out the SMC as a good candidate to detect extended enveloppes of H_2 gas. A precursor study was done in the SMC by [8] on the molecular cloud SMCB1#1, with SIMBA/SEST 1.2 mm and CO observations. They found an unexpected result: the gas mass traced by mm emission is much larger than the virial mass derived from CO observations. This study follows and continues the work of [8] by analysing a larger number of molecular clouds in the SMC and by analysing these clouds together with a reference sample that we build in our Galaxy.

1 The Data

This study follows the detection of several molecular clouds at 1.2 mm in the SMC with the SIMBA bolometer.

1.1 SEST Observations in the SMC

The SIMBA bolometer was mounted at the Swedish ESO Submillimeter Telescope (SEST). SIMBA operated at a central frequency of 250 GHz (1.2 mm) with a spatial resolution of 24" on the sky. The observed mm dust emission in the SMC is faint and the regions unambigously detected are giant molecular clouds (GMCs). The detected regions correspond to different evolution stages – from quiescent molecular clouds to evolved massive star forming regions–, enabling us to compare mass estimates in different physical conditions. The emission measured at 1.2 mm consists of several components: thermal dust emission, free-free radiation and the ^{12}CO(2-1) line emission. Since our interest is only for cold dust emission, we estimate the other contributions that have to be removed. We find that CO(2-1) emission is negligible in all cases. We removed an upper limit of the free-free emission contribution to each SIMBA flux, estimated from radio observations.

The SIMBA observations are compared to CO observations observed as part of the ESO/SEST Key Programme on CO in the Magellanic Clouds [4]. The beam FWHM is 43" and 22" at the CO(1-0) and the CO(2-1) frequencies respectively. Since CO(2-1) line data has a better resolution, gas masses computed for the CO(2-1) emitting regions will be favored when CO(2-1) observations were performed. In the following, we will use the spatial (radius) and kinematic (velocity dispersion) characteristics of the clouds that were computed in the litterature for each cloud.

1.2 FIRAS and CO Data in Our Galaxy

To complement and help the analysis of SMC clouds, we use FIRAS spectra and the CO (1-0) sky survey [2], for a sample of Local GMCs. The 7^o FIRAS beam for these clouds at a few hundreds of parsecs and the SIMBA beam at the distance of the SMC, correspond to similar linear spatial resolutions. As for the SIMBA observations, the different contributions to the 1.2mm flux are estimated. The CO(2-1) line emission contribution as well as the contribution from free-free emission (estimated from extinction corrected Hα emission) are negligible. We also used HI data to remove the fraction of mm emission associated to neutral gas.

We use a CO(1-0) survey [2] of our Galaxy to compute the size and velocity dispersion of each cloud. We were careful to apply the same method to deduce virial masses for the Galactic clouds as for the SMC sample.

2 Estimates of Molecular Cloud Masses

2.1 Molecular Gas Mass from Millimeter Continuum Emission

The far-infrared/mm emission from dust can be expressed as:

$$I_\lambda = N_H \epsilon_H(\lambda) B_\lambda(T_{dust}) \quad (1)$$

where N_H is the hydrogen column density of the cloud, $\epsilon_H(\lambda)$ is the emissivity of dust per hydrogen atom at the wavelength λ and T_{dust} is the dust temperature. We fixed the dust temperature for both samples at 15 K (the minimum temperature, representative of Galactic molecular clouds without H II regions). Knowing the SMC dust-to-gas ratio and the Galactic dust emissivity per hydrogen atom in the SMC, the mm emission can therefore be translated into a gas amount. The Galactic emissivity per hydrogen atoms for dust in molecular clouds was computed using the correlation between dust mm emission and CO emission in the molecular ring. This dust emissivity is twice larger than in the diffuse medium and is interpreted as due to grain coagulation effects. We also recomputed the SMC dust abundances and found a dust-to-gas mass ratio difference between the SMC and the Solar Neighborhood of one sixth. For the computation of SMC clouds masses in the SMC, we therefore used an emissivity six time lower than the Galactic one. Using these parameters, the measured mm fluxes in each clouds are converted into molecular cloud masses.

2.2 Comparison to Virial Masses

In both data sets, we computed virial masses using the simplified formulation from [6]: $M_{vir} = 190 \Delta V^2 R$, where ΔV is the observed velocity dispersion from the CO linewidth (FWHM) and R is the radius of the cloud. These parameters were obtained in consistent ways in the SMC and the Galactic sample.

3 Results

We obtained two molecular gas mass estimates for the clouds in our Galaxy and in the SMC: masses from the mm dust emission and virial masses. These two estimates are compared through the ratio of these masses, $f = \frac{M_{1.2mm}}{M_{vir}}$. We observe a systematic difference between the two samples: in our Galaxy, the molecular cloud masses deduced from mm emission are systematically lower than the virial masses obtained from CO observations, while in the SMC the mass deduced from mm emission are systematically larger. This difference is best seen in Fig.1.

3.1 In the Galaxy

In the local Galactic clouds, the virial mass is always larger than the mass from mm emission, with a mean f factor of 0.5. Our cloud masses deduced from mm emission are likely to represent the total molecular gas mass of the clouds since they are fully compatible with the "dark gas" masses (interpreted as H_2 without CO) from [3]. Note however that for our Galactic regions the fraction of "dark gas" with respect to the total molecular gas is low. The masses of our Galactic sample are consistent with the relation observed by [9] between the virial mass of the clouds to their CO luminosity, for a large sample of GMCs in our Galaxy (see Fig. 1). Virial mass overestimations of the real mass of the clouds is then a general trend in Galactic GMCs and this overestimation decreases with the mass of the cloud. The interpretation of this effect is that the weight of the overlying material in the cloud could provide a significant binding pressure for the clumps[1].

3.2 In the SMC

In the SMC, masses deduced from the mm emission are systematically higher (1.8 times on average) than the virial masses. The mm excess observed in SMCB1#1 [8] is then a general trend that has to be understood. For the computation of masses from the mm flux, we used a dust temperature of 15 K for all the clouds. A larger dust temperature in SMC GMCs could explain the mass difference but would be in disagreement with the far-infrared Spitzer observations. The cloud masses deduced from dust mm emission rely also on our knowledge of the dust to gas ratio and the emissivity of dust grains in the SMC molecular clouds. However, the values we used for these parameters were chosen to limit the mass of the clouds: (i) We used a dust to gas ratio for the clouds in the SMC, 6 times lower than in the Solar Neighborhood, whereas the canonical metallicity is one tenth solar. (ii) We used a reference emissivity taken in the Galactic molecular gas that is twice that of the diffuse medium and could be due to grain coagulations. It is not clear if such an effect applies on large scale in the harsh environment of the SMC. Using these ranges of possible dust-to-gas ratio and dust emissivities, we estimated the range of

values where the mass deduced from mm emission could lie (represented by a straight line for each cloud in Fig. 1).

This shows that, taking into account the uncertainties on the mass deduced from mm dust emission emphasize the segregation between the SMC and the Galactic sample. The virial mass deduced for the SMC clouds clearly underestimates the true mass of the molecular clouds.

4 Magnetic Field Support in Clouds

In the SMC, GMC masses from mm dust emission are systematically larger than the virial masses and uncertainties on the mass estimates from dust emission can not explain such differences. Since we were careful to apply the same methods and observational bias on the Galactic and the SMC sample, so we are confident that the virial mass underestimation trend in the SMC does not arise from observational uncertainties.

This difference might indicate that the CO line width underestimates the amplitude of the cloud turbulent motions. In the SMC clouds, the CO emission is expected to come from dense clumps embedded in lower density gas where CO is photo-dissociated [5] . The bulk of the cloud mass is in the lower density gas but the CO line width only measures the velocity dispersion of the clumps. In the less massive high Galactic latitude clouds, CO line widths are observed to be systematically lower than the HI line widths. It is not clear to us whether this observed difference can be simply extrapolated to the more massive SMC clouds that are gravitationally bound. But theory suggests that in gravitationally bound clouds the gas velocity dispersion should increase as the density decreases [7]. In the following, we present an alternative interpretation.

In this study, virial mass were determined using the simplified form from [6]. This form neglects among others the surface pressure and the magnetic field terms. We inspected the assumptions made for the virial mass calculations, searching for those which could cause a systematic underestimation of the mass. In particular, the presence of a magnetic field in the molecular clouds could help to balance gravity. We computed the strength of the magnetic field that is necessary to account for the f values. The magnetic field strength obtained range from ~ 10 to ~ 30 μG, with a mean value of ≈ 15 μG. Such strengths are similar to the values reported for some Galactic clouds but the clumps surveyed are much smaller and confined by the pressure, not by their self-gravity [1]. Recently, a magnetic field with a similar strength ($\sim 20\mu$G) has been observed in the outer part of the Taurus molecular cloud (W. Reich, this volume).

A magnetic field support of the molecular clouds could then explain the mass difference observed in the SMC. Further studies and magnetic field observations would be needed to confirm this assumption. But why would the magnetic field support be important for the SMC GMCs only? Molecular

clouds formation could be different in the SMC. Another possibility is that magnetic field support is important also in the Local GMCs and virial masses could have to be re-examined taking into account a magnetic field support on large scales. This study emphasis the interest of mm emission as a dense matter tracer. The large amount of mm data coming will enable interesting follow up studies with a better resolution and sensitivity and the extension of the comparison to other galaxies.

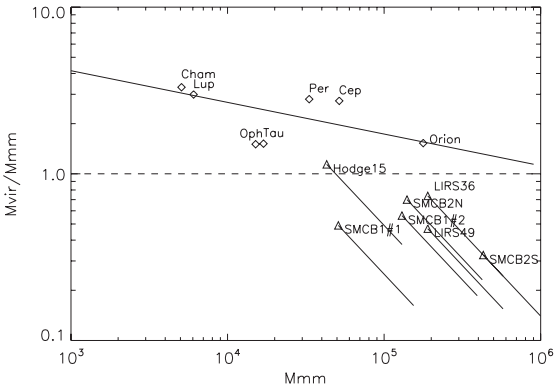

Fig. 1. Evolution of the ratio of the virial mass and the mass deduced from mm emission with respect to the mass deduced from the mm dust emission.The Galactic clouds (rhombs) are compared with the law of [9]. For the SMC (triangles) clouds, the uncertainties on masses deduced from mm emission are represented by a straigth line for each cloud.

References

1. Bertoldi, F., & McKee, C. F., ApJ, 395, 140, (1992)
2. Dame, T. M., Hartmann, D., & Thaddeus, P., ApJ, 547, 792, (2001)
3. Grenier, I. A., Casandjian, J., & Terrier, R., Science, 307, 1292, (2005)
4. Israel, F. P., Johansson, L. E. B., Lequeux, J., et al., A&A, 276, 25, (1993)
5. Lequeux, J., Le Bourlot, J., Des Forets, G. P., et al., A&A, 292, 371, (1994)
6. MacLaren, I., Richardson, K. M., & Wolfendale, A. W., ApJ, 333, 821, (1988)
7. McKee, C., 1999, The origin of Stars and Planetary Systems Ed. Lada et al.
8. Rubio, M., Boulanger, F., Rantakyro, F., & Contursi, A., A&A, 425, L1, (2004)
9. Solomon, P. M., Rivolo, A. R., Barrett, J., & Yahil, A., ApJ, 319, 730, (1987)

17

Mapping Circumnuclear Dust in Nearby Galaxies

Paul Martini

Department of Astronomy, Ohio State University, 140 West 18th Avenue, Columbus, OH 43210, USA martini@astronomy.ohio-state.edu

Summary. Hubble Space Telescope observations have revealed a wealth of dust structure in the circumnuclear regions of galaxies and provide the highest-resolution maps of their cold ISM. These circumnuclear dust structures are of substantial interest for the study of mass transport in galaxies, particular secular evolution, fueling central starbursts, and nuclear accretion onto supermassive black holes. In this review I concentrate on several instances where feedback processes in galaxies appear to have substantially affected the morphology and kinematics of the circumnuclear ISM and discuss the implications of this work for future studies, particularly with ALMA.

1 Introduction

The distribution of cold, molecular gas in the central hundreds of parsecs of galaxies is a valuable probe of the gravitational potential and mass transport mechanisms that fuel central star formation, secular evolution, and accretion onto the central, supermassive black hole. This cold component of the ISM, as revealed in high-resolution CO maps[12, 1], is also well-traced by dust lanes viewed in absorption in visible-wavelength images and therefore the superb angular resolution of HST can produce the highest spatial resolution maps of the cold ISM in nearby galaxies.

These observations have shown that nuclear dust spirals are a common feature of the central regions of disk galaxies and that the morphology of the circumnuclear dust is correlated with larger-scale properties, most notably the presence or absence of a large-scale bar[7, 8]. The kinematics of this cold component have been traced with sensitive CO observations to derive rotation curves and study the mass distribution of many nearby galaxies [13]. Future, higher-resolution CO kinematics with ALMA should obtain vastly improved measurements of the mass distribution and impact of many feedback processes in the cold ISM.

2 Effect of AGN on the Cold ISM in Early-Type Galaxies

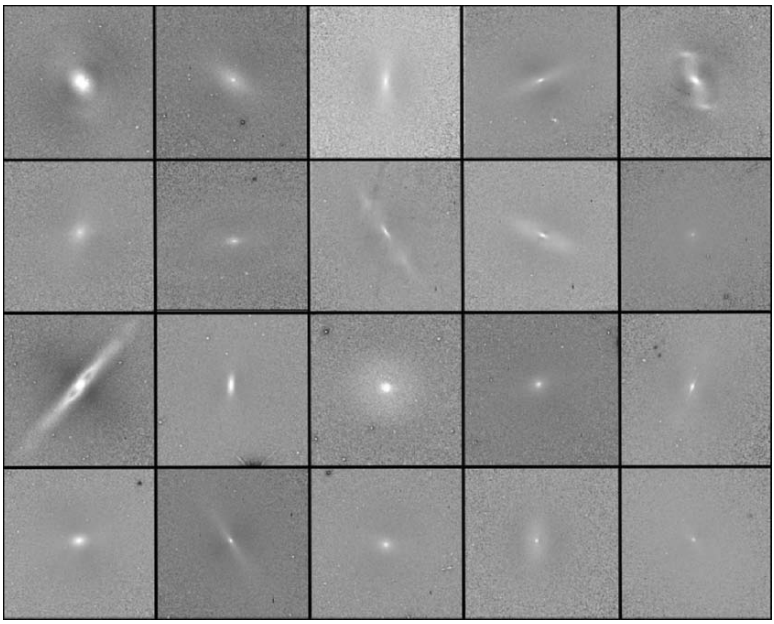

Fig. 1. Structure maps of the centers of nearby inactive early-type galaxies. Each panel shows the central 10″ in their orientation on the HST WFPC2 PC chip. Data are from Lopes et al. (2006).

Early-type galaxies are well known to be deficient in cold gas relative to later-type disk galaxies, yet many HST observations demonstrate that they frequently possess disks of dust within their central kiloparsec[14, 9]. Many of these studies also noted that these dust disks are more common in early-type galaxies that host AGN than those that do not, which implies the presence of dust is required to fuel AGN in many cases.

Recently, Lopes et al. (2006) performed a detailed study[6] of dust in the centers of early-type galaxies and found that *all* of the AGN hosts had circumnuclear dust, while only 25% of the early-type, inactive galaxies showed evidence for circumnuclear dust (see Figures 1 and 2). Unlike previous studies, here we carefully selected only early-type galaxies with high SNR spectroscopy from the Palomar Survey[2] and could determine with high confidence if an early-type galaxy was an AGN or was inactive. In addition, each AGN host was carefully matched to an inactive, control galaxy with the same luminosity, distance, and morphological type. This comparison thus eliminates potential systematics that may have affected previous studies, such as comparison to

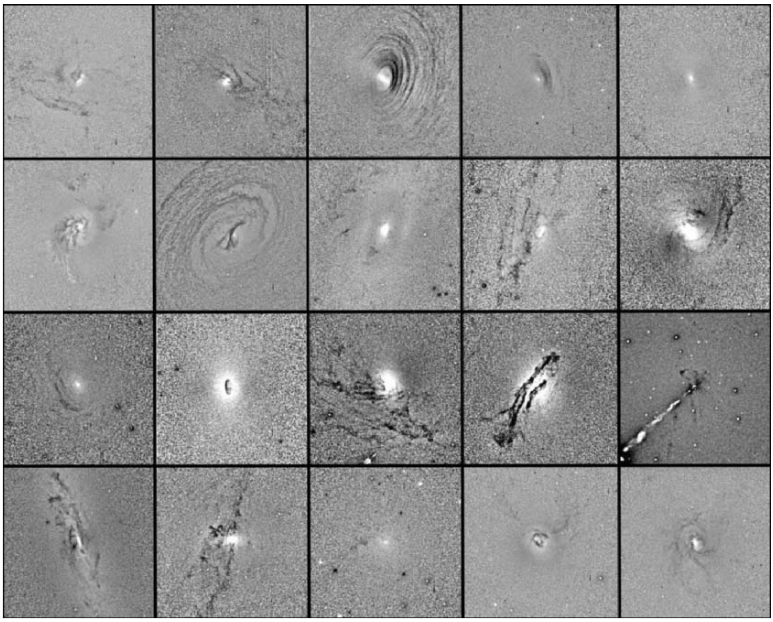

Fig. 2. As in Figure 1 for the centers of active early-type galaxies. The galaxy in each panel is matched in host galaxy type, luminosity, and distance to the inactive galaxy in the corresponding panel in the previous figure.

galaxies with undetected AGN, consideration of only radio-luminous AGN, or comparisons between high and low luminosity galaxy samples,

While these data demonstrate a clear connection between dust and AGN in early-type galaxies, the origin of the dust remains unclear. Stellar mass loss almost certainly produces some dust in early-type galaxies, yet this mechanism alone appears to be inconsistent with the absence of dust in nearly 50% of all early-type galaxies. An external origin, in contrast, appears to require relatively frequent mergers of small gas and dust-rich galaxies, although the required frequency depends strongly on the dust settling and destruction time. Regardless of the origin of the dust, there remains a clear connection between the presence of dust and accretion onto the central black hole. Improved models of gas clumping, settling, and destruction in early-type galaxies could provide new insights into how black holes are fueled in these galaxies, and if the accretion process liberates sufficient energy to destroy the circumnuclear dust and produce the inactive, dust-free early-type hosts.

3 Circumnuclear Morphology and Feedback

While there is not a clear connection between the presence or morphology of circumnuclear dust and nuclear activity in later-type disk galaxies, there

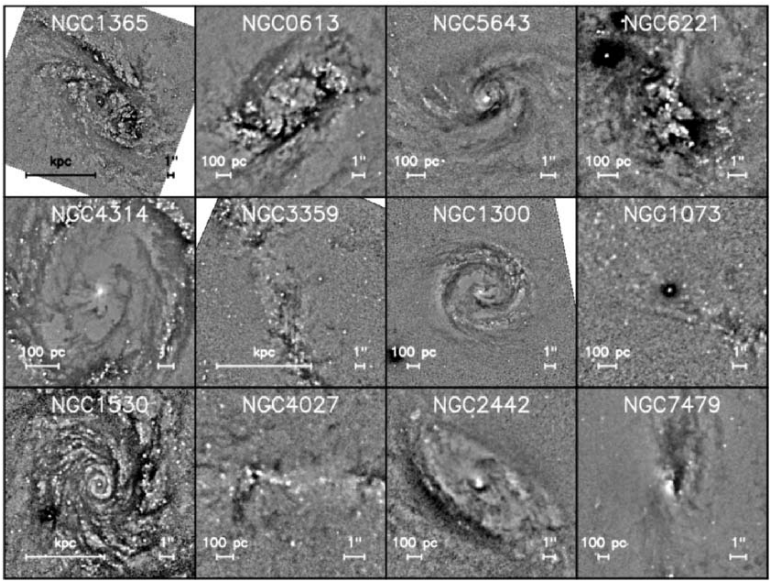

Fig. 3. Circumnuclear regions of the twelve most strongly barred galaxies from Peeples & Martini (2006).

is evidence of a correlation between large-scale bars and both circumnuclear dust morphology[7] and molecular gas content[11] in barred galaxies. Peeples and Martini (2006) recently investigated this further with a sample of galaxies with measured bar strengths[4] from the Ohio State Bright Galaxy Survey and archival HST data[8]. This investigation showed that small pitch angle dust spirals are preferentially found in galaxies with lower bar strengths, while the most strongly barred galaxies exhibit a wide range in circumnuclear morphology (see Figure 3). These morphologies include two symmetric, larger-scale dust lanes that lose coherence before they reach the nucleus or end in a circumnuclear starburst ring, and the most strongly barred galaxies tend to have a chaotic circumnuclear morphology.

Many of these strongly barred galaxies include galaxies with substantial central star formation, and in fact a large fraction of the known nuclear starburst galaxies, rather than starburst rings, have chaotic circumnuclear dust morphologies (see Figure 4). Hydrodynamic models of the multiphase ISM have shown that feedback effects from supernovae and stellar winds may affect the shape of the ISM[15]. In galaxies with substantial nuclear star formation, there may be sufficient mechanical feedback from starformation to disrupt the morphology of the dust and produce a chaotic morphology. For example, the mechanical energy injection from 1 $M_\odot$ yr^{-1} of star formation over 10^7 years is $\sim 10^{55}$ ergs[5], which may suffice to disrupt circumnuclear dust structures

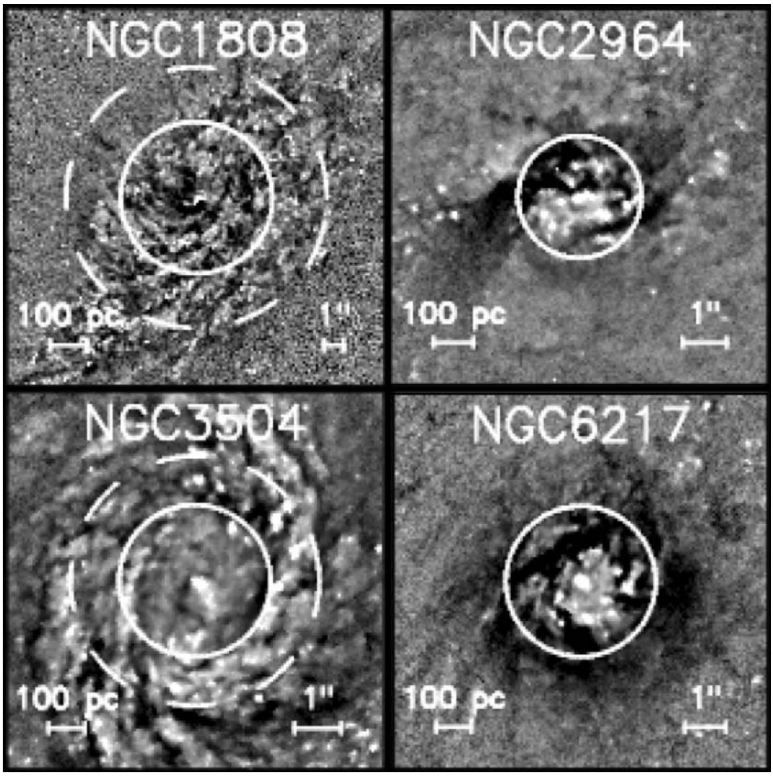

Fig. 4. Centers of four starburst or nuclear starburst galaxies from Peeples & Martini (2006). Most galaxies with substantial circumnuclear star formation have chaotic dust lane morphologies.

composed of $10^2 - 10^4$ $M_\odot$ molecular clouds in the potential wells of typical galaxies.

4 NLR Gas Kinematics

STIS spectroscopy can spatially resolve the NLR on tens to hundreds of parsecs in nearby active galaxies and directly probe the kinematics of the ionized gas. In a recent study of HST archival data on 24 AGN, Rice et al. (2006) studied the line widths and profiles from $0.1'' - 0.2''$ wide slits and compared them to ground-based measurements of the line shapes and the stellar kinematics (see Figure 5). The goal of this investigation was to determine if there was an optimum spatial scale to connect NLR gas kinematics σ_g to stellar kinematics σ_*, which in turn is related to the central black hole mass through the $M - \sigma_*$ relation.

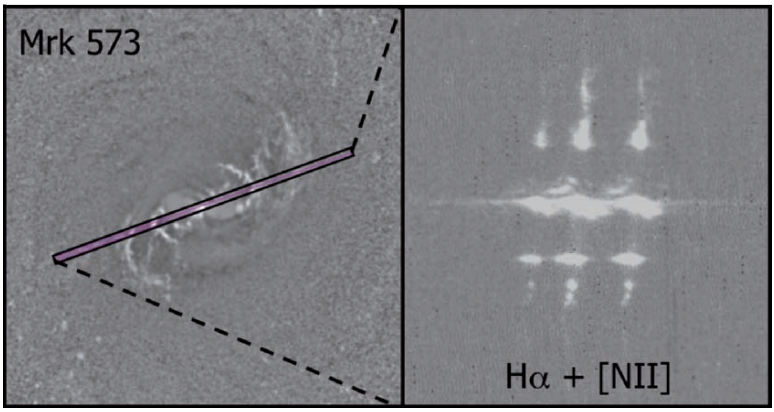

Fig. 5. Central image and 2-D STIS spectra of Mrk 573. (*Left*) Map of the dust and ionized gas distribution along with the 50″ STIS slit. (*Right*) Two-dimensional velocity field of the Hα and [NII] emission lines, demonstrating that the ionized gas kinematics are quite complex and are not an excellent probe of the potential.

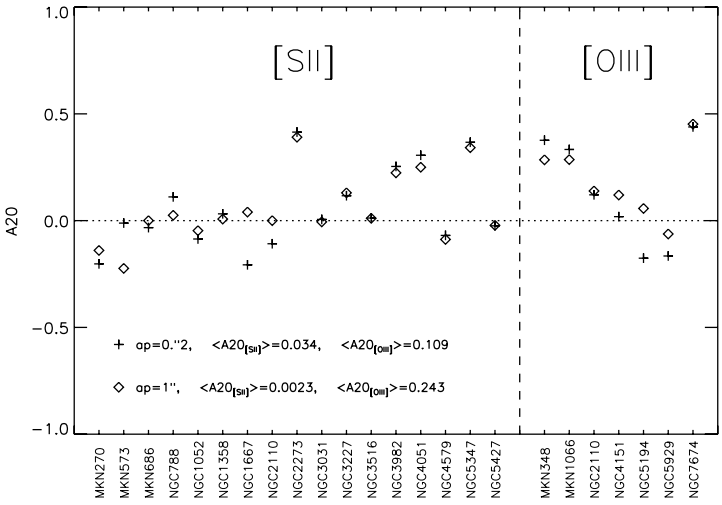

Fig. 6. Asymmetries from NLR emission-line profiles from Rice et al. (2006). The asymmetry measure A20 is a measure of line asymmetry based on the wavelengths that exclude 20% of the total area in the red and blue wings[16]. Positive A20 values indicate blue asymmetries and negative values indicate red asymmetries. These measurements are from STIS spectra measured with an 0.2″ (*crosses*) and 1″ (*diamonds*) aperture sizes.

While this study showed that the substantial (0.3 dex) scatter between stellar and gas kinematics is present on all scales and an empirical improvement in the relationship is not likely, it also provided new data on the shapes of line profiles in the very nuclear region that further demonstrate the complexity of the gas motions in the centers of galaxies. In particular, a surprising number of the AGN showed red asymmetries in their line profiles (see Figure 6). These red asymmetries can not be explained with the radial outflow models that explain blue asymmetries through invocation of a dusty screen in front of the far side of the galaxy. Instead, these red asymmetries may be due to the patchy nature of the ISM on very small scales, which would produce uneven illumination of the NLR clouds and a patchy line-of-sight velocity distribution for the NLR clouds.

5 Future Prospects

The recent observational results reviewed here all demonstrate that the morphology of the cold, molecular gas in the centers of galaxies is an extraordinarily sensitive probe of the gravitational potential and energy feedback mechanisms. Due to the loss of STIS, kinematic data are difficult or impossible to obtain on the same angular scales as these morphological studies and no facilities have been able to achieve $0.1''$ resolution kinematics of the cold ISM. This situation will change remarkably in several years with ALMA, which will measure molecular line kinematics on scales comparable to those achieved with HST.

ALMA will undoubtedly revolutionize the fields mentioned in this review. Observations of early-type galaxies will reveal the kinematics of the dust and cold ISM observed with HST and determine if they are consistent with internal production or an external origin, as well as reveal the details of dust settling and eventual fueling of the central black hole. In later-type disk galaxies, kinematics will reveal mass inflow rates from large-scale bars and other secular processes to the smallest spatial scales, as well as elucidate the extent to which star formation impacts the morphology of the circumnuclear ISM. Finally, ALMA observations of the nuclei of nearby AGN may reveal the extent to which AGN feedback, such as radiation-driven winds, displaces or destroys the cold component of the ISM.

These morphological results and measurements of ionized gas kinematics do demonstrate that feedback processes, whether from star formation or AGN, can have a substantial impact on the morphology of the cold ISM on the smallest spatial scales. Efforts to use ALMA to directly probe the gravitational potential on these scales may therefore be hampered by these feedback processes for galaxies with substantial star formation or AGN. However, as has been noted for black hole mass measurements with ionized gas kinematics[3], the most fruitful kinematic studies may be obtained for galaxies with the most regular circumnuclear dust morphology.

6 Acknowledgments

I would like to thank the organizers for their invitation to speak, some travel support, and for organizing an interesting meeting. Support for this work was also provided by NASA through grants AR-9547 and AR-10677 from the Space Telescope Science Institute, which is operated by the Association of Universities for Research in Astronomy, Inc., under NASA contract NAS5-26555.

References

1. S. García-Burillo, F. Combes, E. Schinnerer, & L.K. Hunt: A&A, 441, 1011 (2005)
2. L.C. Ho, A.V. Filippenko, & W.L.W. Sargent: ApJS, 112, 315 (1997)
3. L.C. Ho et al: PASP, 114, 137 (2002)
4. E. Laurikainen et al: MNRAS, 355, 1251 (2004)
5. C. Leitherer et al: ApJS, 123, 3 (1999)
6. R. Simões Lopes, T. Storchi-Bergmann, M.O. Saraiva, & P. Martini: ApJ, *submitted* (2006)
7. P. Martini, M.W. Regan, J.S. Mulchaey, & R.W. Pogge: ApJ, 589, 774 (2003)
8. M. Peeples, P. Martini: ApJ, *in press* (2006)
9. S. Ravindranath et al: ApJ, 122, 653 (2001)
10. M.S. Rice, P. Martini et al: ApJ, 636, 654 (2006)
11. K. Sakamoto, S.K. Okumura, S. Ishizuki, & N.Z. Scoville: ApJ, 525, 691 (1999)
12. E. Schinnerer, W. Maciejewski, N. Scoville, & L.A. Moustakas: ApJ, 575, 826 (2002)
13. Y. Sofue et al: PASJ, 55, 17 (2003)
14. P.G. van Dokkum & M. Franx: AJ, 110, 2027 (1995)
15. K. Wada & C.A. Norman: ApJ, 547, 172 (2001)
16. M. Whittle: MNRAS, 213, 1 (1985)

18

Star Formation in the Central Regions of Galaxies

Johan H. Knapen[1], E. L. Allard[1], L. M. Mazzuca[2], M. Sarzi[1], and R. F. Peletier[3]

[1] University of Hertfordshire, Centre for Astrophysics Research, Hatfield, Herts AL10 9AB, UK, j.knapen@herts.ac.uk
[2] NASA Goddard Space Flight Center, Greenbelt, MD 20771, USA
[3] University of Groningen, NL-9700 AV Groningen, The Netherlands

Summary. Massive star formation in the central regions of spiral galaxies plays an important role in the dynamical and secular evolution of their hosts. Here, we summarise a number of recent investigations of the star formation history and the physical conditions of the gas in circumnuclear regions, to illustrate not only the detailed results one can achieve, but also the potential of using state-of-the-art spectroscopic and analysis techniques in researching the central regions of galaxies in general. We review how the star formation history of nuclear rings confirms that they are long-lived and stable configurations. Gas flows in from the disk, through the bar, and into the ring, where successive episodes of massive star formation occur. Analysing the ring in NGC 7742 in particular, we determine the physical conditions of the line emitting gas using a combination of ionisation and stellar population modelling, concluding that the origin of the nuclear ring in this non-barred galaxy lies in a recent minor merger with a small gas-rich galaxy.

1 Introduction

Starbursts, defined as relatively short periods of enhanced massive star formation (SF) activity, are important events in the evolution of galaxies. They enhance the luminosity of the host galaxy, facilitating the detection of those at larger distances, can transform significant quantities of gas into stars, can cause metal injection into, and mixing of, the interstellar medium, and can help the secular evolution of galaxies (e.g., reviews by Kormendy & Kennicutt 2004; Gallagher 2005). We focus here on a particular class of low-luminosity starbursts occurring in nuclear rings in spiral galaxies, which allow the detailed study of their SF histories and of the physical properties of the gas in the circumnuclear region.

2 Cold Gas Flowing in and Feeding the Starburst

The centres of many spiral galaxies show evidence of massive SF, often organised into a nuclear ring or pseudo-ring. Such rings are found in 20% of spiral galaxies (Knapen 2005), are thus relatively common, and almost always occur within a barred host (Knapen 2005). Dynamically, nuclear rings are thought to trace the position of the inner Lindblad resonances (ILRs), where gas driven in under the influence of the large bar slows down (Knapen et al. 1995, hereafter K95, and references therein). M100 (NGC 4321) is a prominent, relatively face-on spiral galaxy with a moderately strong bar, at a distance of 16.1 Mpc (so 1 arcsec corresponds to 70 pc). M100 hosts a well-known nuclear ring with prominent massive SF, which is located near a pair of ILRs induced by the bar (K95).

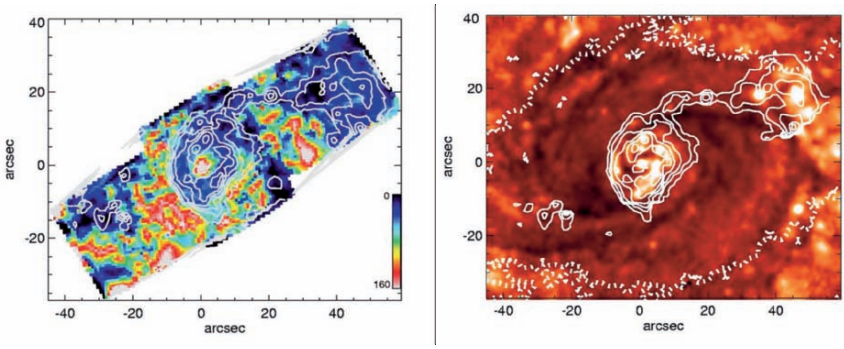

Fig. 1. *Left:* SAURON gas velocity dispersion in the central region of M100 (in $\mathrm{km\,s^{-1}}$), with, overlaid, contours of Hβ line emission at relative levels [0, 0.05, 0.1, 0.2, 0.5, 1, 2, 3]. *Right: B-R* image with the location of the bar indicated by a K_s band contour (thick dashed line) at 18.3 $\mathrm{mag\,arcsec^{-2}}$; H$\beta$ emission line contours as in the *left* panel. Reproduced with permission from Allard et al. (2005).

We have obtained integral-field spectroscopic data with SAURON (Bacon et al. 2001) on the William Herschel Telescope (WHT) of the central region of the barred spiral galaxy M100 (Allard et al. 2005, 2006). These data allow us to derive maps of emission line intensities, line strength indices, and the gas velocity dispersion across the circumnuclear region. Fig. 1 shows how the Hβ emission traces the nuclear ring, broken into hotspots of emission.

The gas velocity dispersion map (Fig. 1, *left* panel) shows clearly that the ring has lower dispersion than the underlying disk, and is thus cooler, exactly where the strongest Hβ emission occurs. This happens within the ring, but in the bar the cold gas is aligned and offset from the dustlanes (Fig. 1, *right* panel). This is confirmation of the gas inflow model of nuclear ring formation, as the low dispersion traces cold gas flowing into the area through the dustlanes, and accumulating into the ring under the influence

of the ILRs. Instabilities within this gas then trigger significant massive SF (Allard et al. 2005).

3 Star Formation Histories: Evidence for Multiple Bursts

3.1 M100

The SAURON observations described in the previous Section not only allow analyses of the kinematics and of the emission line characteristics, but also an in-depth study of the SF history of the circumnuclear region of M100 (Allard et al. 2006). For this, we extracted Hβ, Mgb and Fe5015 absorption line indices across the field of view, where the latter two were subsequently combined into one, MgFe= $\sqrt{\text{Mg}b \cdot \text{Fe5015}}$, which minimises the effect of differing abundance ratios across the galaxy (Falcón-Barroso et al. 2002). The indices vary with time for a single burst stellar population (SSP): the Hβ absorption line index first rises, reaching a peak at an age of around 250 Myr, then decreases gradually, whereas the MgFe index rises monotonically with age.

Comparing SSP model predictions with the data points measured for the nuclear ring and centre of M100 shows that whereas the nucleus can be fitted well and yields an age of some 3 Gyr, the nuclear ring points cannot be fitted at all because the Hβ index values are much lower then expected for any reasonable SSP (Allard et al. 2006). We thus introduce a family of composite models, which are characterised by a combination of an old underlying bulge and/or disk contribution and a series of much more recent SF events. We estimate the age of the bulge/disk as 3 Gyr from our fit of an SSP model to the nuclear data point. Adding a number of recent bursts, 100 Myr apart, and starting a couple of hundred Myr ago so that the latest burst occurs now (to yield the observed Balmer line emission) then produces a grid of model lines, illustrated in Fig. 2, which straddle the observed nuclear ring data points.

Our proposed model (Allard et al. 2006) not only fits the data, but is also phenomenologically attractive: it stipulates the formation of the underlying bulge/disk component and the current SF activity in the ring, but also the long-lived nature of the ring, albeit not constantly forming stars at the same high rate as observed now. Our modelling thus confirms a picture in which the bar in M100, a stable configuration, constantly channels gas into the nuclear region, where it concentrates in the nuclear ring until it reaches a density high enough to collapse gravitationally, and enter the next starburst phase. That phase will last a relatively short time, until either the gas runs out or the negative feedback from the massive SF stops the formation of further stars, after which the process of accretion followed by instability to SF can start again.

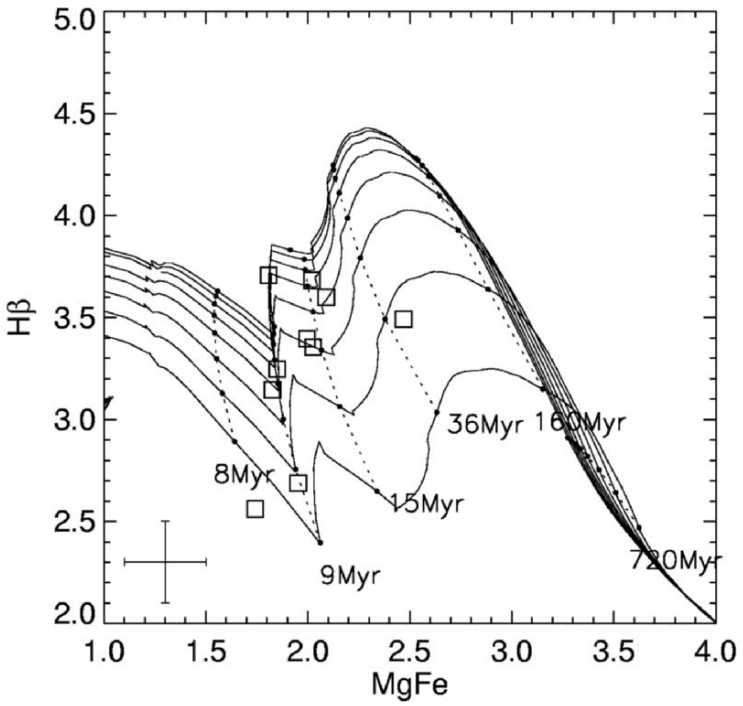

Fig. 2. Measured Hβ and MgFe indices for different points in the nuclear ring of M100 (squares), compared to a family of models which give the time evolution (indicated, in Myr) of the indices in an SSP. The models are combinations of an old (~ 3 Gyr) bulge/disk population with one (bottom) to eight (top) discrete SF episodes within the last ~ 0.5 Gyr, separated by 100 Myr. From Allard et al. (2006).

3.2 Other Nuclear Rings

The model described above for M100 yields a good fit to the data, as well as a convincing interpretational framework which ties the origin and dynamics of the nuclear ring to its SF properties. M100 is often seen as a prototype of a barred galaxy hosting a nuclear ring, and to confirm this further, we analysed the SF history of a sample of seven more nuclear rings (Allard et al. 2007). This analysis is based on long-slit spectra obtained with the ISIS spectrograph on the WHT, covering a wide wavelength range from which we could extract values for the Hβ, MgFe, HδA, and D(4000) line indices for selected points in the rings, as well as in the nuclei of the host galaxies.

We find that the nuclear data points can be reproduced well by a single old SSP model, yielding, as in the case of M100, ages of a couple of Gyr for the underlying bulge and/or disk component. In none of the eight sample galaxies the nuclear ring data points can be fitted by such a model, reproducing again the results for M100 (Sect. 3.1; Allard et al. 2006).

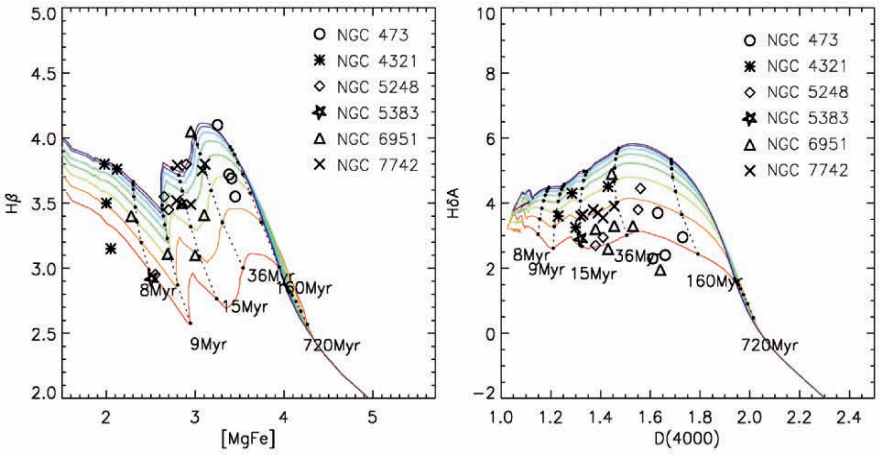

Fig. 3. Evolution of the indices Hβ vs. MgFe (*left*) and HδA vs. D(4000) (*right*) for a family of eight composite stellar population models, compared to the nuclear ring data points measured from ISIS long-slit spectra for six galaxies. The different model lines refer to models with one (bottom) to eight (top) discrete SF episodes within the last ~ 0.5 Gyr, separated by 100 Myr. From Allard et al. (2007).

Figure 3 shows how we can fit the data points for six of the galaxies with composite SSP models very similar to the ones developed for M100. We can thus generalise our conclusion that most nuclear rings are stable configurations, with recurrent episodes of massive SF, the latest of which we are witnessing. The use of the HδA vs. D(4000) plot (Fig. 3), made possible by the wider wavelength range of the ISIS observations compared to the SAURON data set, allows us to exclude with a high degree of certainty a model in which the nuclear ring is only a one-off massive SF event, preceded merely by the SF which formed the bulge and/or disk, some 3 Gyr ago. Such a model could, at a stretch, still explain the M100 SAURON data, but can now be excluded.

The galaxies NGC 4314 and NGC 7217 can be explained by a model representing an old underlying bulge/disk component, of some 10 Gyr old, and only one, current, burst of massive SF. This would imply that the nuclear rings in these galaxies are new to forming massive stars, at least at their current position. So either they have only now entered the first episode where their gas clouds are unstable against gravitational collapse, or the rings have shrunk, and previous SF events have happened at slightly larger radii (Benedict et al. 2002), not covered by our data points as plotted in Fig. 3 (Allard et al. 2007).

4 Physical Conditions of the Gas: The Case of NGC 7742

Another important aspect in deciphering the history and properties of nuclear rings, and, perhaps more importantly, in recognising the role they can play

in tracing the evolution of their host galaxy, is the study of the physical properties of the ionised gas. This can be done by using diagnostic emission line diagrams, such as those introduced by Veilleux & Osterbrock (1987), which plot the ratio between two blue emission lines against that between two red lines, ensuring that the effects of dust on the diagnostics are limited.

We have recently started a programme to use integral-field spectroscopy (IFS) measurements of the circumnuclear regions of galaxies to disentangle not just their SF histories, but also the physical conditions of the gas, in order to constrain the history of these regions and to model the interplay between them and their host galaxies. As a first step, and as a feasibility study, we have combined blue (SAURON, from Falcón-Barroso et al. 2006) and red (DensePak on the WYIN telescope) IFS data of the nuclear ring region in the non-barred galaxy NGC 7742 (Mazzuca et al. 2006). The fields of view of the instrument cover the ring nicely, and the combination of wavelength ranges means that we can deduce information on most of the lines traditionally used in emission line diagnostics.

NGC 7742 is one of the few known cases where the galaxy hosting a star-forming nuclear ring contains no significant bar. The origin of such rings may lie in a previously existing, but now dissolved, bar, in a weak oval, or in a past or present interaction or minor merger (see Knapen et al. 2006 for a literature overview and examples). NGC 7742 is known to have counterrotating gas and stars in the central region (e.g., de Zeeuw et al. 2002), which immediately points to an interactive past.

Our IFS data yield, first of all, a low value for the electron density, $N_{\rm e}$, of order $10\,{\rm cm}^{-3}$, in the ring region, as derived from the ratio of the [SII] lines at 6716 and 6731 Å (assuming $T = 10^4\,{\rm K}$, see Mazzuca et al. 2006). The knowledge of this value allows us to model other line ratios, such as those of [OIII] λ5007 Å/Hβ, [NII] λ6583/Hα, or [NII] λ6583/[SII] $\lambda\lambda$6716, 6731Å, as shown in Fig. 4. In that figure, the different points in and around the ring are indicated by shade and shape, as reproduced in the inset which shows an Hα image of the region, and with the points with the lowest [OIII] λ5007 Å/Hβ ratios corresponding to those located in the ring.

The left panel of Fig. 4 shows a comparison with a set of MAPPINGS III shock and SF models (Kewley et al. 2001), which confirms that SF is the dominant ionisation mechanism within the ring, but that shock ionisation is important both in- and outside the ring. It also indicates that there is little azimuthal variation in line ratios around the ring. The right panel of Fig. 4 yields valuable information on the metallicity, which we find to be very near solar in the nuclear ring region (as indicated by the drawn line going through the nuclear ring points, which is at $Z = Z_{\odot}$).

So what conclusions can we draw about the origin of the nuclear ring? The non-barred nature of its host, NGC 7742, and the counterrotation observed in the central region might indicate that some past interactive event is responsible. For the similar non-barred nuclear ring host galaxy NGC 278, a past minor merger is indeed what we proposed as origin for its ring on the basis of

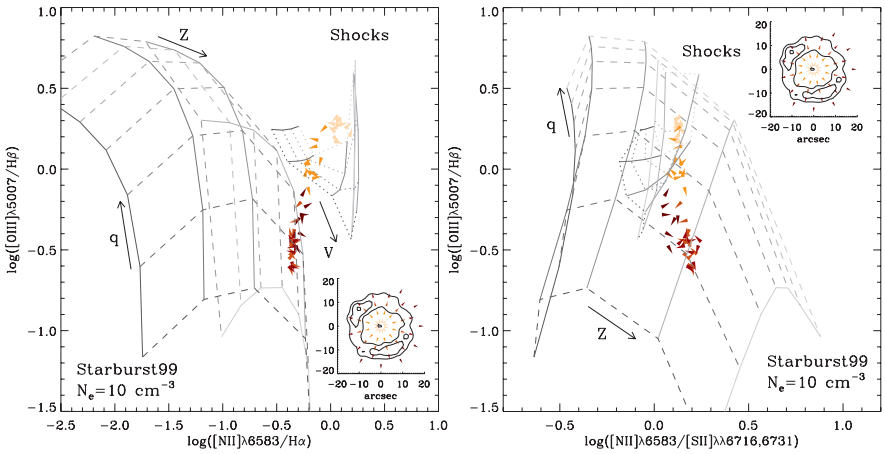

Fig. 4. Diagnostic diagrams of [OIII]λ5007/Hβ vs. [NII]λ6583/Hα (*left*) and [OIII]λ5007/Hβ vs. [NII]λ6583/[SII]$\lambda\lambda$6716, 6731 (*right*). Data points are shown by filled triangles, and the inset shows the location of these points in the ring region, with the contours showing the Hα emission of the circumnuclear ring. Darker symbols refer to points at larger radii; they are oriented according to their position angles. In each panel, MAPPINGS III starburst or shock models are shown by the grid of solid and dashed lines or of solid and dotted lines, respectively. Reproduced with permission from Mazzuca et al. (2006).

the severely disturbed morphology and kinematics of its atomic gas (Knapen et al. 2004). NGC 7742 has a companion galaxy, NGC 7743, but that seems too far away and of too regular morphology to be a candidate for a recent interaction. A minor merger with a small gas-rich galaxy, as in the case of NGC 278, seems the most likely, but this would undoubtedly lead to an influx of low-Z gas, seemingly at odds with our near-solar metallicity measurement.

Here is where the SF history models as described above (Sect. 3) come to our aid: the multiple bursts of SF, for which we found evidence there, would have enriched the gas to near-solar metallicity on timescales which are completely consistent with those modelled above (Mazzuca et al. 2006). We thus conclude that indeed a past minor merger has caused the asymmetry in the gravitational potential which lies at the origin of the nuclear ring. To confirm this further, we are presently pursuing HI observations of NGC 7742: our model predicts non-regular HI morphologies and velocity fields.

5 Closing Remarks

The results highlighted here illustrate the use of integral-field spectroscopic analysis techniques to study key aspects of circumnuclear regions of galaxies: their detailed SF histories, and their physical conditions. We have found strong

evidence for the stability and longevity of nuclear rings, which we model to form massive stars episodically, for the past 0.5 Gyr or so. Using the nuclear ring in the non-barred galaxy NGC 7742 as a showcase for our techniques, we find low electron densities, SF-dominated ionisation and near-solar metallicity in the ring. We postulate that a minor merger with a small gas-rich galaxy has led to the nuclear ring, and that the episodic SF in the ring, as modelled above, has enriched the infallen metal-poor gas to its current metallicity.

Our results show the importance of nuclear rings, being stable, long-lived structures which transform significant amounts of disk gas into inner-kpc stars. The techniques we have outlined here can be applied more widely than to nuclear rings, though, and should lead to important insights on, e.g., nuclear starbursts, or the zones surrounding AGN or composite nuclei.

Acknowledgements We thank our co-workers on the papers as reviewed here. JHK thanks the Leverhulme Foundation for the award of a Leverhulme Research Fellowship, and the Royal Society for the award of a conference grant which allowed him to attend the meeting in Ishigaki.

References

1. Allard, E. L., Knapen, J. H., Peletier, R. F., & Sarzi, M.: MNRAS, 371, 1087 (2006)
2. Allard, E. L., Peletier, R. F., & Knapen, J. H.: ApJL, 633, L25 (2005)
3. Allard, E. L., Sarzi, M., Knapen, J. H., Mazzuca, L. M.: MNRAS, submitted (2007)
4. Bacon, R., et al.: MNRAS, 326, 23 (2001)
5. Benedict, G. F., Howell, D. A., Jørgensen, I., Kenney, J. D. P., & Smith, B. J.: AJ, 123, 1411 (2002)
6. de Zeeuw, P. T., et al.: MNRAS, 329, 513 (2002)
7. Falcón-Barroso, J.: PhD Thesis, University of Nottingham (2002)
8. Falcón-Barroso, J., et al.: MNRAS, 369, 529 (2006)
9. Gallagher, J. S.: In: *Starbursts: From 30 Doradus to Lyman Break Galaxies*, ed by R. de Grijs, R. M. González Delgado (Kluwer, Dordrecht 2005), 11
10. Kewley, L. J., Dopita, M. A., Sutherland, R. S., Heisler, C. A., & Trevena, J.: ApJ, 556, 121 (2001)
11. Knapen, J. H.: A&A, 429, 141 (2005)
12. Knapen J. H., Beckman J. E., Heller C. H., Shlosman I., & de Jong R.S.: ApJ, 454, 623 (1995)
13. Knapen, J. H., Whyte, L. F., de Blok, W. J. G., & van der Hulst, J. M.: A&A, 423, 481 (2004)
14. Knapen, J.H., Mazzuca, L.M., Böker, T, Shlosman, I., Colina, L. Combes, F., Axon, D.J.: A&A, 448, 489 (2006)
15. Kormendy, J., & Kennicutt, R. C., Jr.: ARAA 42, 603 (2004)
16. Mazzuca, L. M., Sarzi, M., Knapen, J. H., Veilleux, S., & Swaters, R.: ApJL, 649, L79 (2006)
17. Veilleux, S., & Osterbrock, D. E.: ApJS, 63, 295 (1987)

19

The Synchrotron Cut-off Frequency of Relativistic Electrons in the Radio Arc and their Acceleration Area

Masato Tsuboi[1], Atsushi Miyazaki[2], and Toshihiro Handa[3]

[1] Nobeyama Radio Observatory, Minamisaku, Nagano, Japan
tsuboi@nro.nao.ac.jp
[2] Shanghai Astronomical Observatory, China amiya@shao.ac.cn
[3] Institute of Astronomy, University of Tokyo, Mitaka, Japan
handa@ioa.s.u-tokyo.ac.jp

We estimated synchrotron cutoff frequency of Radio Arc from continuum maps at 21,45,94 GHz with the Nobeyama 45-m telescope.

1 Introduction

The Galactic Center region is a nearest central region of spiral galaxy. Unique structures which may relate intrinsic activities in the central region have been found. "gRadio Arc" is a most outstanding one of such features. This consists of two parts with different properties. These are non-thermal "Vertical filament" and thermal "Arched filament" [1]. Although the intensity is abruptly decreased at the both ends of Vertical filament, the positive galactic latitude extension corresponds to the base of a famous off-plane feature, "Galactic Center Ω-shaped lobe", which was identified by Sofue and Handa (1986) [2]. The lobe also consists of two parts with different properties. The positive longitude part is highly linear polarized up to 50% at 10 GHz, which is non-thermal, and the negative longitude part is non-polarized, which is presumably thermal [3]. It is controversial that the lobe is a real combined structure or an apparent feature by chance superposition in the line of sight. On the other hand, the negative galactic latitude extension is distinctive only in linear polarization map. Two polarized extensions is called "Polarized Lobe" [3]. Radio Arc and Polarized Lobe are presumably a part of large scale poloidal magnetic field through the Galactic center region. It is, however, an open question how much is the strength of the magnetic field. In addition, several vertical continuum features identified in lower frequency map are also a part of such magnetic field [4]. It is also an open question that such magnetic field exists anywhere in the region or is restricted in smaller region. The synchrotron cut-off frequency

in the Radio Arc and its distribution presumably provide the informations of the acceleration area of relativistic electrons and the acceleration mechanism.

2 Observation and Results

We have made continuum maps of Sgr A*-Radio Arc complex region at 21,45,94 GHz in order to explore synchrotron cutoff frequency with the Nobeyama 45-m telescope. We used the multi-beam receivers except for the 21 GHz observation. The multi beam receivers provide high sensitive observation. The receiver of 100 GHz band has 5×5 grid beams on celestial sphere [5]. The FWHM beam size is 17" and the beam spacing is 40". The receiver of 40 GHz band 2×3 grid beams [6]. The FWHM beam size is 39" and the beam spacing is 100". The system noises during the observation are 300 K at 94 GHz and 200K at 45 GHz, respectively.

Figure 1, 2, and 3 show the results of the observations. Vertical filaments, Arched filaments, sickle HII region, and the counter arch are clearly seen in these maps. The continuum spars around Sgr A are decreased in higher frequency maps. The north part of Vertical filaments, G0.18-0.10, is clearly seen even in the 94 GHz map. The part has flat spectrum up to 94 GHz. The part is disappeared in the 150 GHz data observed with the bolometer of the 45-m telescope [7]. Then there is cutoff frequency between 94 and 150 GHz. On the contrary the south part, G0.16-0.18, is seen in the 45 GHz map and disappeared in the 94 GHz map. There is the cutoff frequency between 45 and 94 GHz. Then the cutoff frequency is decreasing as going to south along Vertical filaments.@

3 Discussion

Our observation provides an estimation for the strength of magnetic field in Vertical filament. From equipartition condition, minimum strength of the magnetic field is given by

$$H_{min} = [6(1+k)C_{12}(L/V)]^{2/7} \tag{1}$$

where $(1+k)$ is a factor depending on the acceleration mechanism of the relativistic electrons, which is the value from 2 to 1000. C_{12} is a factor depending on shape of spectrum, and L/V is volume emissivity [8]. Although this formula includes unknown or not well-determined parameters, weak dependence of the parameters in the formula provides good estimation for the strength. Minimum strength of the magnetic field in Vertical filament is estimated to be $H_{min} = 0.3$ mG for flat spectrum between 10 MHz and 100 GHz. Rigidity of the filament for disturbance provides another estimation, $H = 1 - 3$ mG [1]. Our value is slightly smaller than that from rigidity. Because our estimation

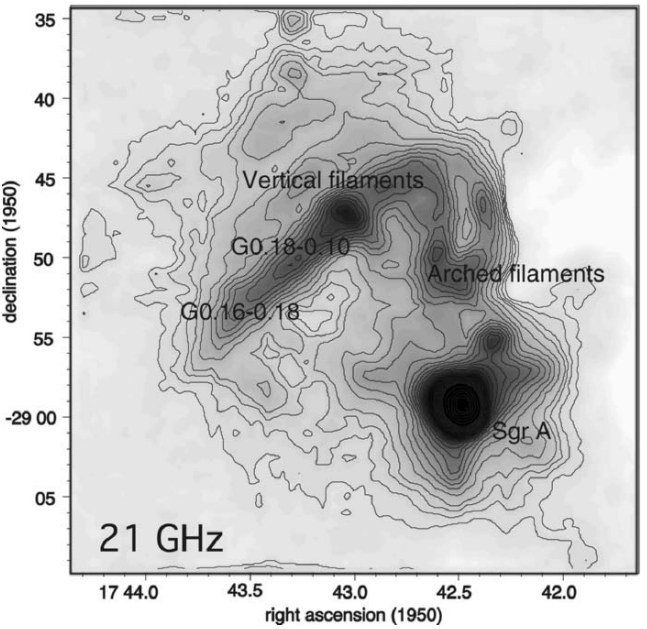

Fig. 1. Sgr A-Radio Arc region at 21 GHz with NRO 45-m telescope

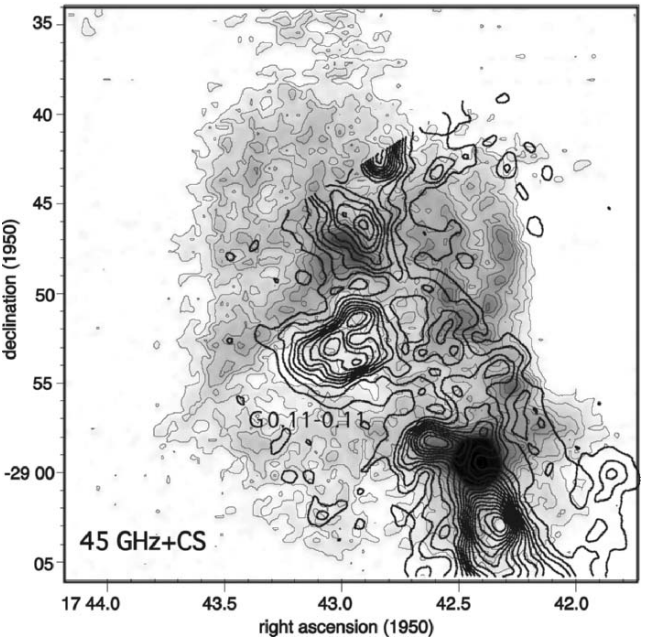

Fig. 2. Sgr A-Radio Arc region at 45 GHz with NRO 45-m telescope and molecular clouds in CS $J = 1 - 0$ (thick contours)

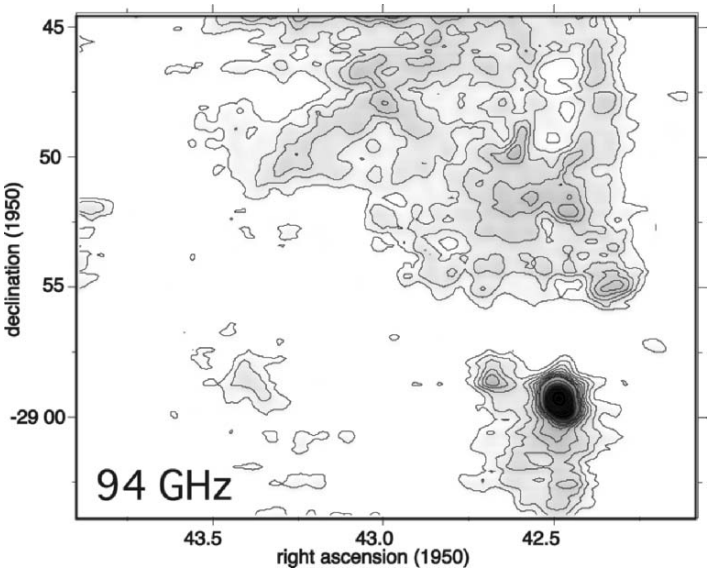

Fig. 3. Sgr A-Radio Arc region at 94 GHz with NRO 45-m telescope

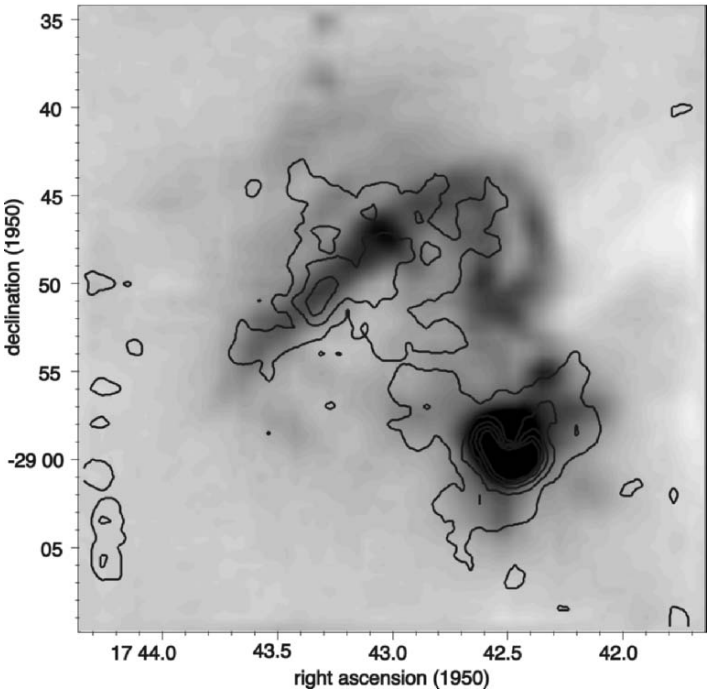

Fig. 4. Sgr A-Radio Arc region at 21 GHz and Stokes V (thick contours)

gives only minimum strength, there is not obvious discrepancy between two values. Life time of the relativistic electrons is given by [8]

$$T_{1/2} = 1/2C_{12}H^{-3/2} \tag{2}$$

The life time is estimated to be $T_{1/2} = 3 \times 10^2 - 3 \times 10^3$ years for 1-5 mG. Although drift velocity along the filaments of the relativistic electrons is not clear, this life time presumably shows they are accelerated in the filaments. On the other hand, the strength of magnetic field in Polarized Lobe is also estimated to be $H_{min} = 0.1$ mG by equipartition condition. The life time is much longer than several 10^5 years. Then the electrons in Polarized Lobe are probably transported from the acceleration area.

We propose a molecular clouds colliding with Vertical filament as the energy source of the relativistic electrons [9]. The molecular cloud is G0.11-0.11 which seems to collide with the filaments (see Fig.2). There is a ridge-like structure parallel to Vertical filaments in the cloud. The structure has velocity width of as large as $50\,kms^{-1}$, which are 10 times larger than those of disk clouds. In addition, Vertical filaments are probably bending at apparent contact area to the cloud. Then they may be interacted physically. The relativistic electron are accelerated by squeezing the magnetic field in the area. And they are drifting to north and south along the filaments. This image is consistent with cut-off frequency change along the filaments.

We will discuss the polarization properties of bending magnetic field in Vertical filament. There is an inversion of Faraday rotation measure at 10 GHz around the galactic plane [3]. This is explained as an inversion of line-of-sight component by bending of the large-scale poloidal magnetic field. In such situation, circular polarization may be made during propagation in Vertical filament by "gre-polarization" mechanism. Linear polarized emission is made by synchrotron radiation. The direction of $\boldsymbol{E}$ is perpendicular to the magnetic field projected on celestial sphere. During the propagation the direction is rotated by Faraday rotation. Then this can be divided to the two polarization components, parallel and perpendicular to the magnetic field on celestial sphere. Because the two have different phase velocities, circular polarization should be made [10]. Fig. 4 shows Stokes V parameter at 21 GHz. The peak in Vertical filament is $0.8 \pm 0.4\%$. This is correspond to highly linear polarized and highly Faraday RM area. The marginal detection suggests that the circular polarization is originated by re-polarization mechanism in Vertical filament.@

References

1. F.Yusef-Zadeh, M. Morris, D. Chance: Nature 310, 557 (1984)
2. Y. Sofue, T. Handa: Nature 310, 568 (1984)
3. M. Tsuboi, M. Inoue, T. Handa et al.: AJ 92, 818 (1986)
4. T. N. LaRosa, N. E. Kassim, T. Lazio et al.: AJ 119, 207 (2000)

5. K. Sunada, C. Yamaguchi,N. Nakai, et al. In: *Radio telescope*, SPIE vol 4015, ed by H. R. Butcher (Netherlands Foundation for Research in Astronomy, Netherlands 2000) pp237–246
6. M. Tsuboi, A. Miyazaki, T. Kasuga et al:PASJ, 56, 711 (2004)
7. W. Reich, Y. Sofue, H. Matsuo:PASJ, 52, 355 (2000)
8. A. G. Pacholcyczyk: *Radio Astrophysics*, (W.H. Freeman and Company, USA 1970)
9. M. Tsuboi, T. Handa, N. Ukita:ApJ 481, 263 (1997)
10. T. W. Jones:ApJ, 332, 678 (1988)

20

The Origin of σ–drops: Mapping Stellar Kinematics and Populations in Spirals

Eric Emsellem[1]

Universit de Lyon 1, CRAL, Observatoire de Lyon, 9 av. Charles André, F-69230 Saint-Genis Laval; CNRS, UMR 5574 ; ENS de Lyon, France
emsellem@obs.univ-lyon1.fr

1 Introduction

The link between nuclear activity and the host galaxy remains elusive. It seems now clear that the galactic environment is not the key, and that there is no significant apparent difference in terms of the presence of bars/spirals between active and non-active galaxies. Nuclear activity nevertheless requires a small central gas reservoir (10^4-10^7 $M_\odot$) which may be only partly consumed during the $\sim 10^6 - 10^7$ yr AGN duty cycle. A possible route towards a better understanding of the involved physical processes is to directly probe the gravitational potential of the host galaxies, with the hope that the corresponding sensitive tracers (stars, gas) will deliver convincing evidence for a kinematic signature associated with the AGN. This is the motivation for an on-going survey of 50 galaxies, for which the two-dimensional kinematics of the (neutral, ionised and molecular) gas and stellar components are being obtained (see Dumas et al., this conference). With only 10 to 15% of Seyfert galaxies in the local Universe, we must also acknowledge the possibility that this activity is a recurrent (but short) process, and that signatures of recent gas accretion associated with the onset of the central activity should be detectable. This paper is a short report on the detection and study of σ–drops which we believe are the result of past gas accretion followed by subsequent star formation.

2 σ-drops: The List is Growing

In the course of an observational program aimed at revealing dynamical evidences for the presence of inner bars in spiral galaxies, we have detected a decrease of the stellar velocity dispersion towards the centre of 3 out of 3 barred galaxies [2] where we could probe the very central region. We suggested that these σ–drops are the result of gas accretion followed by star formation, and therefore indicative of a relatively recent infall of dissipative material.

This idea was successfully tested for the specific case of an infall driven by a large-scale bar [7], although this does not mean that bars are the preferred cause for such a process.

Since this study of a very small sample of barred galaxies, the list of σ–drops has been growing very significantly (and steadily). Fig 1 provides a non-exhaustive list of such objects and shows that σ–drops are indeed a rather common phenomenon. Most of the galaxies listed in Fig 1 contain active nuclei, but this is most certainly due to a bias in the observed sample where reliable stellar kinematics have been obtained.

NGC 1068	SBb	Sy2	Emsellem et al. 2006
NGC 1097	SB(s)b	Sy2	Emsellem et al. 2001
NGC 1138	SBO	?	Simien & Prugniel 2002
NGC 1808	SAB(s:)b	Sy 2/starburst	Emsellem et al. 2001
NGC 2639	SAa	Sy2	Marquez et al. 2003
NGC 2460	SAa	?	Shapiro et al. 2003
NGC 2775	SAab	?	Shapiro et al. 2003
NGC 3021	SAbc		Héraudeau et al. 1999
NGC 3412	SB0		Aguerri et al. 2003
NGC 4030	SAbc	?	Shapiro et al. 2003
NGC 2639	SA(r)a	Sy 1.9	Marquez et al. 2003
NGC 3412	SB0(s)	?	Aguerri et al. 2003
NGC 3593	SA(s)0/a	Sy 2	Bertola et al. 1993
NGC 3623	SAB(rs)a	Liner	De Zeeuw et al. 2002
NGC 3627	SBb	Liner/Sy 2	Héraudeau & Simien 1998
NGC 4303	SBbc	Sy 2	Héraudeau & Simien 1998
NGC 4579	SBb	Liner/Sy 1.9	Héraudeau & Simien 1998
NGC 4725	SBab	Sy 2	Héraudeau et al. 1999
NGC 4477	SB0	Sy 2	Jarvis et al. 1988
NGC 5728	SABb(r)	Sy 2	Emsellem et al. 2001
NGC 6503	SA(s)cd	Liner/HII	Bottema 1993; Bottema & Gerritsen 1997
NGC 6814	SAB(rs)bc	Sy 1.5	Marquez et al. 2003
NGC 6951	SAB(rs)bc	Sy 2	Marquez et al. 2003
IC 184	SB(r)a	Sy 2	Marquez et al. 2003
+ 10			Chung & Bureau 2004

Fig. 1. A (non-exhaustive) list of galaxies exhibiting a σ–drop with associated references. The columns are, from left to right: name of the galaxy, Hubble type, activity type and reference.

3 Formation Scenarios

Numerical simulations including stars, gas and star formation are very helpful in constraining the formation process of σ–drops in the central regions of disc

galaxies. Recent experiments [6] clearly showed that σ–drops can be formed on a relatively short timescale (500 Myr) and are long-lived if star formation is sustained at a level of about 1 $M_{\odot}$/yr in the nuclear region. This easily occurs in a gas-rich spiral galaxy where a bar can funneled gas towards the central 500 pc or so. When star formation stops, the amplitude of the σ–drop starts to significantly decrease, as shown in Fig. 2 [6].

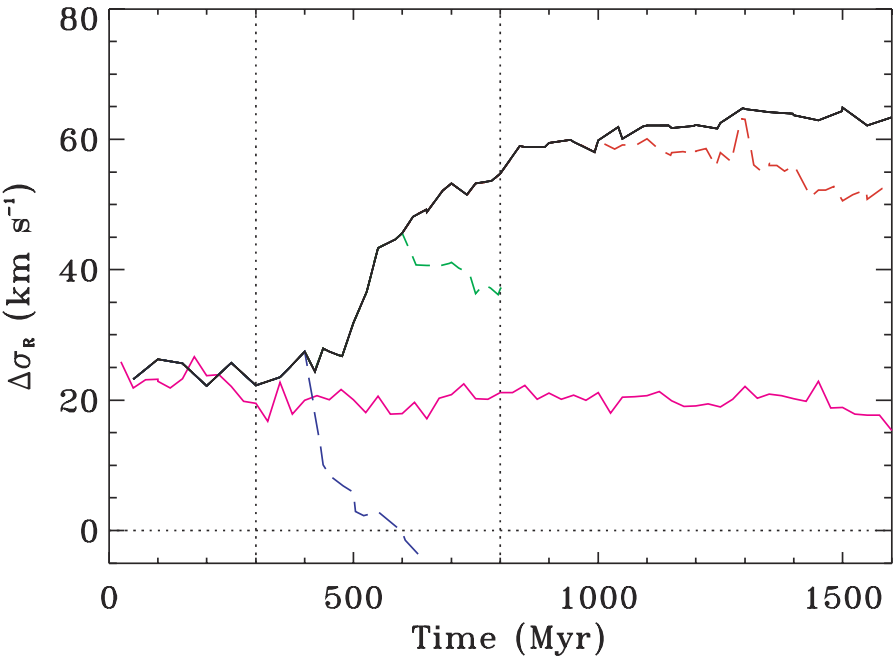

Fig. 2. Amplitude of the σ–drop in numerical simulations of spiral galaxies, where central star formation is sustained via regular gas infall (black curve), or stopped at different times (red, green, blue). The magenta curve corresponds to a similar simulation but where star formation is not turned on. Extracted from [6].

4 A 3D View

Integral-field spectrographs (IFS) are now routinely used in order to probe the full extent and shape of σ–drops, and hence to better understand the stellar component with which they are associated. Recent IFS data obtained on the prototypical Seyfert 2 galaxy NGC 1068 clearly demonstrated how critical is such a detailed mapping of the kinematics in the central region [1, 4]. Surveys of spiral galaxies using integral-field spectrographs [3] are now showing that about one third of spirals are expected to exhibit a σ–drop, this

being a lower limit considering the difficulty of such a detection when dust is at play. This significant fraction of galaxies with σ–drops would suggest the presence of relatively young stars associated with the underlying dynamically cold stellar component. However, there seems to be no direct relation between the presence of a σ-drop and the mean luminosity weighted age of the stellar population. In order to further test this issue, we have obtained high spectral resolution ($R = 12000$) integral-field data of a known σ–drop galaxy, NGC 3623, using FLAMES at the VLT. Fig. 3 shows the corresponding two-dimensional stellar kinematics for this galaxy, emphasizing the presence of the central σ–drop in this galaxy. A preliminary analysis of the stellar populations in that region shows that stars associated with the σ–drop cannot be younger than 1 Gyr, confirming the fact that σ–drops can be long-lived.

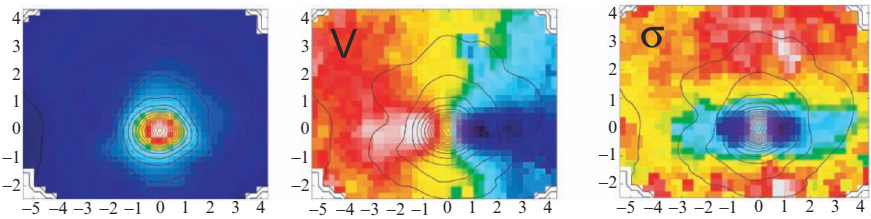

Fig. 3. VLT/FLAMES maps of the galaxy NGC 3623. From left to right: reconstructed image, stellar velocity field and stellar velocity dispersion field. The σ-drop is obvious and associated with the pinching of the (disk-like) isovelocities.

5 Conclusions

σ-drops are ubiquitous in spirals, with a relative fraction of about 30% or more. This suggests that significant episodes of star formation occur recurrently in the central part of these galaxies. This could in fact be linked with the common presence of blue nuclei in late-type galaxies [5]. The detection of a young stellar component associated with a σ-drop is rather difficult and requires high spectral resolution and high signal-to-noise ratio data. We have recently started a more systematic study of these stellar populations using the near-infrared integral-field spectrograph SINFONI. The analysis of these data is on-going, and should help us to constrain the star formation history in the central few hundred parcsecs. This may eventually lead to a better understanding of the chronology/synchronicity between star formation and activity in the nuclear region.

References

1. Emsellem, E., Fathi, K., Wozniak, H., Ferruit, P., Mundell, C. G., & Schinnerer, E.: MNRAS 365, 367 (2006)
2. Emsellem, E., Greusard, D., Combes, F., Friedli, D., Leon, S., Pécontal, E., & Wozniak, H.: A&A 368, 52 (2001)
3. Ganda, K., Falcón-Barroso, J., Peletier, R. F., Cappellari, M., Emsellem, E., McDermid, R. M., de Zeeuw, P. T., & Carollo, C. M.: MNRAS 367, 46 (2006)
4. Gerssen, J., Allington-Smith, J., Miller, B. W., Turner, J. E. H., & Walker, A.: MNRAS 365, 29 (2006)
5. Rossa, J., van der Marel, R. P., Böker, T., Gerssen, J., Ho, L. C., Rix, H.-W., Shields, J. C., & Walcher, C.-J.: AJ 132, 1074 (2006)
6. Wozniak, H., & Champavert, N.: MNRAS 369, 853 (2006)
7. Wozniak, H., Combes, F., Emsellem, E., & Friedli, D.: A&A 409, 469 (2003)

21

Star Formation and Molecular Gas in AGN

Richard Davies[1], R. Genzel[1], L. Tacconi[1], F. Mueller Sánchez[1], and A. Sternberg[2]

[1] Max Planck Institut für extraterrestrische Physik, Postfach 1312, 85741, Garching, Germany
[2] School of Physics and Astronomy, Tel Aviv University, Tel Aviv 69978, Israel

Summary. We present initial results from a survey of nearby AGN using the near infrared adaptive optics integral field spectrograph SINFONI. These data enable us to probe the distribution and kinematics of the gas and stars at spatial resolutions as small as $0.085''$, corresponding in some cases to less than 10 pc. In this contribution we present results concerning (1) the molecular gas in the nucleus of NGC 1068 and its relation to the obscuring torus; and (2) the stars which exist on spatial scales of a few tens of parsecs around the AGN, the evidence for their remarkably young age and extreme intensities, and their relation to the AGN.

1 Introduction

Between 2002 and 2005 we have observed and analysed the central regions of 9 AGN with the following aims in mind:

- determine the extent, intensity, and history of recent star formation and its relation to the AGN;
- measure the distribution and kinematics of molecular gas, and understand its relation to the obscuring material;
- derive black hole masses from spatially resolved stellar kinematics – both to test the $M_{\rm BH} - \sigma_*$ relation for AGN, and also to compare to reverberation masses, perhaps yielding constraints on the broad line region geometry.

The sample was selected according to several criteria, of which the primary constraint was that the nucleus should be bright enough for adaptive optics correction. In addition, we required that the galaxies be close enough that small spatial scales can be resolved at the near infrared diffraction limit of an 8-m telescope. Finally, we wanted the galaxies to be "well known" so that complementary data could be found in the literature. These criteria were not applied strictly, since some targets were also of particular interest for other reasons. Thus, while the sample cannot be considered 'complete', we nevertheless believe it provides a reasonable cross-section of AGN; additional

Table 1. AGN sample

Target	Classification	Dist. (Mpc)	Resolution arcsec	pc
Mkn 231[a]	ULIRG, Sy 1, QSO	170	0.176	145
IRAS 05189-2524	ULIRG, Sy 1	170	0.12	100
NGC 2992	Sy 1	33	0.30	48
NGC 3783	Sy 1	42	0.18	37
NGC 7469[b]	Sy 1	66	0.085	27
NGC 1097	LINER, Sy 1	18	0.245	21
NGC 3227[c]	Sy 1	17	0.085	7
NGC 1068	Sy 2	14	0.085	6
Circinus[d]	Sy 2	4	0.22	4

Detailed studies of individual objects already published: [a] Davies et al. 2004a [2]; [b] Davies et al. 2004b [3]; [c] Davies et al. 2006 [4]. [d] Müller Sanchez et al. 2006 [10].

AGN may be added once the VLT Laser Guide Star Facility is commissioned. The selected targets are listed in Table 1. All the observations have now been performed and, although work concerning the molecular gas and coronal line emission is still in progress, analysis of the nuclear star forming properties – the main subject of this contribution – is complete.

2 Molecular Gas in NGC 1068

As the cornerstone of AGN unification models, NGC 1068 is one of the most studied objects in the night sky, yet many aspects of its nuclear region remain poorly understood, despite its proximity. In particular, the peculiar gas kinematics revealed in 0.7″ CO(2–1) mapping were modelled as a warped disk [13]. It is now apparent from our 2.12 μm H_2 1-0 S(1) maps of the distribution (Fig. 1) and kinematics (Fig. 2), which have a spatial resolution nearly 10 times better, that this picture is too simple (Mueller Sánchez et al. in prep).

What was previously thought to be a ring of gas at an inner Lindblad resonance we now find is comprised of several distinct components. Besides the bright emission east of the AGN, the ring itself is in fact centred 0.6″ (40 pc) to the southwest of the AGN. Its kinematical major axis coincides with its minor axis – suggestive of inflow or outflow – at a position angle of about 135° (significantly different to the 85° of the stars). The offset centre and the fact that 1.64 μm [FeII] emission is seen along the inside edge of the H_2 ring suggests that it is outflowing. Assuming it is intrinsically circular, the geometry implies an outflow speed of 150 km s^{-1}. In addition, the diffuse knot of H_2 near the middle of the ring is moving at 300 km s^{-1} relative to systemic. It is probable that the momentum and energy needed to drive such expansion can only be provided by one or more hypernova [11].

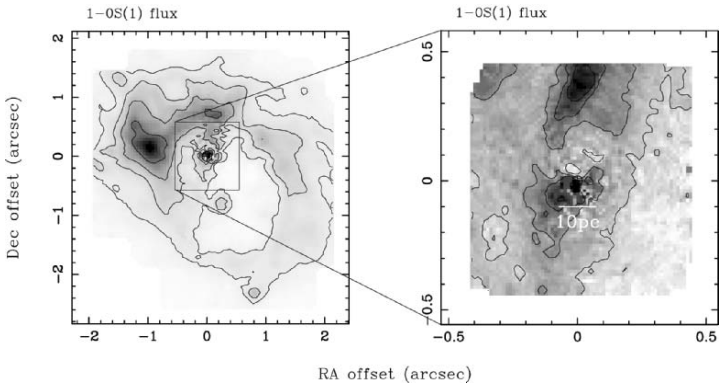

Fig. 1. Map of H_2 1-0 S(1) line emission in NGC 1068 at a resolution of 0.085″. The AGN is at (0,0) offset. There is clear evidence for H_2 at this position with a size scale of 10–20 pc, which we identify with the obscuring molecular torus.

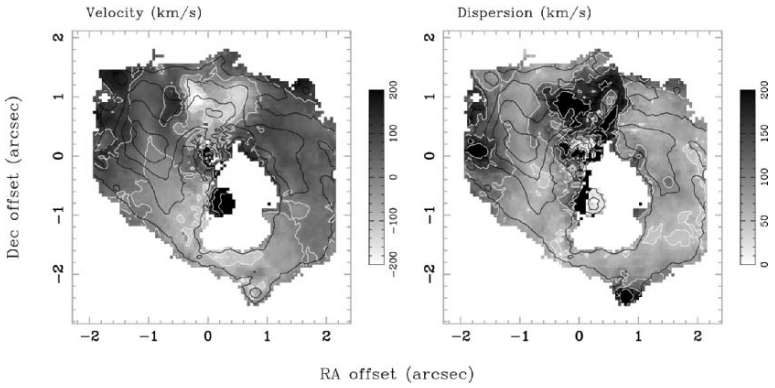

Fig. 2. The kinematics of the H_2 1-0 S(1) emission in NGC 1068 are far more complex than those of the stars, which have PA=85° throughout the field here.

The region north of the AGN is characterised by double-peaked line profiles (hence the large velocity dispersion), where the AGN jet has driven its way through the H_2. There is also a linear structure north and south of the AGN. The tip of the finger extending from the north to within 0.2″ of the AGN coincides with a knot of radio continuum emission [7] – direct evidence of the shock interface between the jet and a molecular cloud that has caused the jet direction to change. Further on, the jet also brightens where it passes through the arc of bright 1-0 S(1) emission to the northeast.

Finally, we have found a knot of H_2 emission at the location of the AGN with a size scale of 10–15 pc. Given that this is consistent with the smaller 3 pc scale of the 300 K dust emission [9] as well as the 5–20 pc scales implied by static torus models [8, 12, 6], we tentatively identify it with the nuclear obscuring material that is hiding the broad line region.

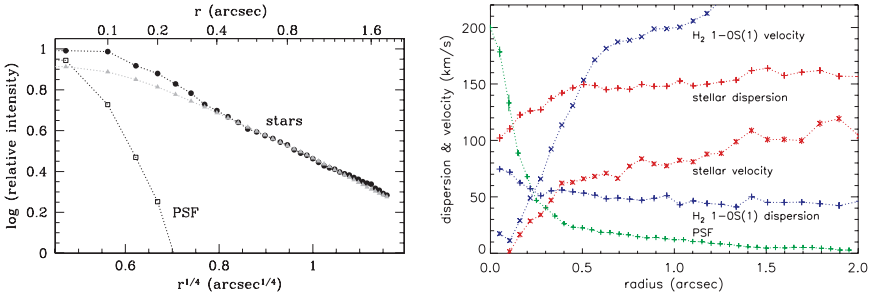

Fig. 3. Left: azimuthally averaged stellar continuum profile of NGC 1097 (circles), with an $r^{1/4}$ fit extrapolated to the centre (triangles). Right: 1D kinematics of the stars and H_2 1-0 S(1) in NGC 1097, extracted from the 2D field using kinemetry. The radial profile of the PSF (arbitrary flux scaling) is shown for comparison.

3 Nuclear Star Formation in AGN

Our AGN sample is rather hetereogeous, including type 1 and 2 Seyferts, ULIRGs, and a QSO. And their range of distances, coupled with varying adaptive optics performance, has led to a wide range of spatial resolutions. Despite this the logarithmic mean resolution of <25 pc is nearly an order of magnitude smaller than that of other large studies [1]. And we have, as far as is possible, analysed all the galaxies in a consistent fashion. After correcting for dilution by the non-stellar continuum associated with the AGN, we make use of: (1) $W_{\mathrm{Br}\gamma}$, Brγ emission associated with star formation ratioed to the stellar continuum; (2) M/L_K, the ratio of the mass (estimated where possible using stellar kinematics) to the K-band stellar luminosity; (3) ν_{SN}, the supernova rate from spatially resolved data in the literature, after accounting for a compact AGN contribution. Davies et al. (in prep) gives details of how these diagnostics are measured and applied, and assesses the general properties of nuclear star formation in AGN. Here we summarise our main results.

Nuclear Disks

Tracing the stellar absorption features (e.g. CO bandheads in H- and K-bands) rather than the broad band continuum, we have resolved a stellar population close around the AGN in every case: the stellar intensity increases towards the nucleus on scales of <100 pc (and in a number of cases <50 pc). In a few objects (e.g. NGC 1097, Fig. 3), we have been able to show explicitly that there is excess stellar continuum in the nucleus above that predicted by an extrapolation of an $r^{1/4}$ law from the surrounding region.

The age of the star formation in these regions comes primarily from ν_{SN} (typically high) and M/L_K (typically low), and lies in the range 10–300 Myr. In most cases we can only estimate a 'characteristic' age, since there may simultaneously be two or more stellar populations that are not co-eval. For example, contamination by the bulge population, although having little effect

on $W_{\mathrm{Br}\gamma}$, could strongly impact M/L_K, driving up the inferred age. Intriguingly, although the star formation is relatively recent, the typically low $W_{\mathrm{Br}\gamma}$ indicates that there is none actually on-going, implying that the star formation occurs in relatively short episodes.

In two cases there is also direct kinematical evidence for young stars through a spatially resolved reduction in the stellar velocity dispersion (on the same ∼50 pc scale as the excess continuum). This has been interpreted as arising from stars which have formed recently from a dynamically cold gas disk, and hence which are themselves dynamically cool [5]. In NGC 1097 (Fig. 3) this coincides with a change in the kinematics of the molecular gas, which, at radii $< 0.5''$, become increasingly similar to the stellar kinematics.

In conclusion, we have found evidence for recent but short-lived star formation occuring on scales of ∼50 pc that is dynamically cooler than the bulge: strong support for the existence of nuclear disks.

Eddington Limited Starbursts

When active, the star formation rate on scales of 0.1–1 kpc is of order 10–50 $\mathrm{M_\odot\,yr^{-1}\,kpc^{-2}}$, increasing to ∼300 $\mathrm{M_\odot\,yr^{-1}\,kpc^{-2}}$ on scales of 10 pc. Consequently the stellar luminosity close around the AGN is, per unit area, very high. In contrast the area itself is small, so that within a few tens of parsecs the luminosity due to star formation is only a few percent of that of the AGN; but on scales of 1 kpc, the two can often be comparable.

Fig. 4 shows the integrated stellar bolometric luminosity $L_{*\mathrm{bol}}$ as a function of radius. This figure is robust, despite assuming that all the K-band light is associated with young stars, because the vertical axis covers nearly 5 orders of magnitude while the ratio $L_{*\mathrm{bol}}/L_K$ varies by no more than ±0.3 dex for almost any star formation scenario. It is remarkable that the curves all roughly follow the same trend, approaching $10^{13}\,\mathrm{L_\odot\,kpc^{-2}}$ on the smallest scales. Both the luminosity density limit and the dependence on radius are similar to those for optically thick starburst disk models of ULIRGs [15]. In these models, ULIRGs radiate at the the Eddington limit for a starburst, defined as when the radiation pressure dominates over self-gravity. Radiation pressure should halt further accretion for star clusters with luminosity-to-mass ratios exceeding $\sim 500\,\mathrm{L_\odot/M_\odot}$, which occurs when the upper end of the mass function becomes populated [14]. Crucially, even if stars form as fast as gas is fed in, this limit can only be exceeded for ∼30 Myr, and less if the efficiency is lower or some of the gas was present at the start. This may explain why we see no evidence for current active star formation: starbursts can only be sustained at this intensity for short periods. We suggest that starbursts in AGN are episodic phenomena, proceeding in a sequence of short and very intense bursts. Whether one finds evidence for recent star formation in an AGN would therefore depend on how much time has passed since the most recent episode.

Starburst-AGN Connection

Given that the star formation we have discussed here occurs on scales of <50 pc, it is inevitable that it and the AGN will have some mutual influence

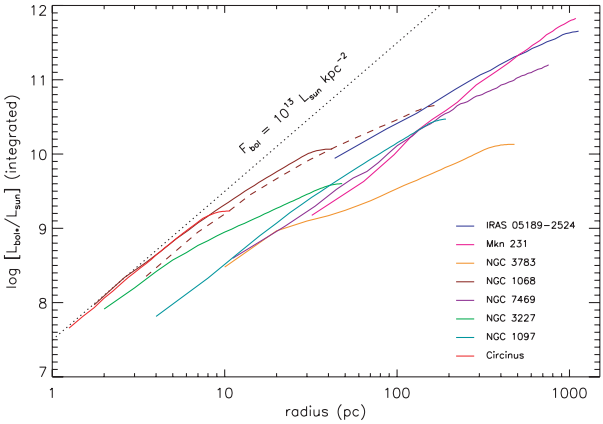

Fig. 4. Stellar bolometric luminosity per unit area as a function of distance from the AGN, showing that in general the stellar intensity increases towards $10^{13}\,L_{\odot}\,kpc^{-2}$ in the central few parsec.

on each other. While the exact form remains elusive, our data do hint at a possible relationship between the characteristic age of the star formation and the accretion rate onto the AGN. The AGN which are radiating at lower efficiency $< 0.1\,L/L_{Edd}$ are associated with starbursts younger than 50–100 Myr; AGN that are accreting and radiating more efficiently $> 0.1\,L/L_{Edd}$ have starbursts older than 50–100 Myr. This implies that there could be a delay between starburst activity and AGN activity. What might cause such a delay is beyond the scope of this contribution, and will be discussed in a future paper.

References

1. Cid Fernandes R., et al.: MNRAS 355, 273 (2004)
2. Davies R., Tacconi L., Genzel R.: ApJ 602, 148 (2004)
3. Davies R., Tacconi L., Genzel R.: ApJ 613, 781 (2004)
4. Davies R., et al.: ApJ 646, 754 (2006)
5. Emsellem E., et al.: A&A 368, 52 (2001)
6. Fritz J., Franceschini A., Hatziminaoglou E.: MNRAS 366, 767 (2006)
7. Gallimore J., Baum S., O'Dea P.: ApJ 464, 198 (1996)
8. Granato G., Danese L., Franceschini A.: ApJ 486, 147 (1997)
9. Jaffe W. et al.: Nature 429, 47 (2004)
10. Mueller Sánchez F., et al., 2006, A&A, 454, 481
11. Nomoto K., et al.: Ap&SS 298, 81 (2005)
12. Schartmann M., et al.: A&A 437, 861 (2005)
13. Schinnerer E., Eckart A., Tacconi L.: ApJ 533, 826 (2000)
14. Scoville N.: JKAS 36, 167 (2003)
15. Thompson T., Quataert E., Murray N.: ApJ 630, 167 (2005)

22

AGN Feeding and AGN Feedback

Santiago García-Burillo[1], F. Combes[2], J. Graciá-Carpio[1] and A. Usero[1]

[1] Observatorio Astronómico Nacional-OAN, Observatorio de Madrid, Alfonso XII, 3, E-28014, Madrid, SPAIN s.gburillo@oan.es
[2] Observatoire de Paris, LERMA, 61, Av. de l'Observatoire, 75014 Paris, FRANCE Francoise.combes@obspm.fr

Summary. CO line maps can be used to study the feeding mechanisms of active galactic nuclei (AGN) and address the issue of how nuclear activity can be sustained in galaxies. The use of other tracers of the dense gas phase can shed light on the feedback influence of activity on the chemistry of molecular gas in galaxies. In this paper we present the results issued from the NUclei of GAlaxies (NUGA) project, a high-resolution (0.5″-1″) CO survey of low luminosity AGNs (LLAGNs) carried out with the IRAM Plateau de Bure Interferometer (PdBI). The efficiency of gravity torques as a possible mechanism responsible for the feeding of LLAGNs can be quantified for the first time on scales (∼10–100 pc) which are known to be critical for the tranfser of angular momentum. We also present the results of a survey which studies the excitation and the chemistry of the dense molecular gas phase in a sample of nearby AGNs and Ultraluminous Infrared Galaxies (ULIRGs) near and far.

1 How to Feed AGN: The NUGA Survey

In high luminosity AGNs (HLAGNs) evidence exists for a correlation between the presence of ∼kpc-scale non-axisymmetric perturbations and the onset of activity. However, the case for a significant similar correlation in LLAGNs is weak if any. The quest of a *universal* mechanism for AGN feeding in LLAGNs is complicated by the fact that the AGN duty cycle ($\sim 10^{7-8}$ yrs) could be shorter than the lifetime of the feeding mechanism itself (e.g., see review by [1]). This time-scale problem translates into a spatial-scale problem: only by probing the scales which are believed to be critical for AGN feeding (∼10–100 pc), the LLAGN fueling problem can be potentially solved. With this in mind, we embarked on a high-resolution (∼0.5”-1”) CO survey of a sample of 25 LLAGNs carried out with the PdBI (fully described by [2, 3]). The CO line maps provided by the NUclei of GAlaxies (NUGA) project can probe the distribution and kinematics of molecular gas in the circumnuclear disks (CND) of these galaxies with unprecedented resolution and sensitivity.

Of particular note, we have also information on the stellar potentials of the majority of NUGA galaxies, obtained through available HST and ground-

based optical/NIR images of the sample. These are used to determine the gravitational torques exerted by the stellar potentials on the gaseous disks and thus derive the characteristic time-scales for gas flows. Furthermore we can investigate whether other mechanisms are required to explain the low level of nuclear activity in the galaxies analyzed thus far [4].

The results obtained by [4] from the analysis of stellar torques in four LLAGNs came out as a surprise. Gravity torques exerted by the stellar potential on the gas disks of four LLAGNs, purposely chosen to represent the whole range of activity classes in the NUGA sample, fail to account for the feeding of the AGN at present. We conclude that gravity torques need to be assisted in due time to drive the gas to the center. In a first step, gravity torques help driving the gas inwards and feeding a nuclear starburst on scales of ∼a few 100 pc. On smaller scales, however, stellar torques have virtually no role in AGN fueling in the current epoch: torques on the gas are not negative all the way to the center, but on the contrary they become positive and quench the feeding (see Figs. 1 and 2 adapted from [4]). This may explain why molecular gas seems to 'avoid' the inner 200-300 pc of NGC 6951 and NGC 4579 where we measured M_{gas} <a few$\times 10^5$–$10^6 M_\odot$. Observational evidence indicates that in NGC 4579 molecular gas on these scales is presently flowing outward (see Fig. 1). In a second step, a mechanism complementary to gravity torques may be required to drive gas inflow on smaller scales, i.e., on scales close to the gravitational influence of the black hole. The gas directly responsible for the Seyfert activity in galaxies like NGC 4579 or NGC 6951 must have been brought to the center during a *previous* phase, while the bar at present is emptying the region inside the nuclear ring, thus regulating the amount of gas available for the active nucleus.

García-Burillo et al. [4] have proposed a new evolutionary scenario in which the onset of nuclear activity can be understood as a recurrent phase during the typical lifetime of any galaxy. In this scenario the recurrence of activity in galaxies is indirectly related to that of the bar instabilities although the various active phases are not necessarily coincident with the maximum strength of a single bar episode. These activity episodes are not expected to be strongly correlated with the phases of maximum strength for the bar, but they may appear at different evolutionary stages of the bar potential, depending on the balance between gravity torques and viscosity. Viscosity can indeed counter-balance positive gravity torques inside the Inner Lindblad Resonance (ILR) region if the bar strength is lowered due to secular evolution. Several (∼3–4) episodes of activity may appear per bar episode. The wide variety of morphologies identified in the CO maps of NUGA targets corroborates that there might not be a universal pattern associated with LLAGNs [2].

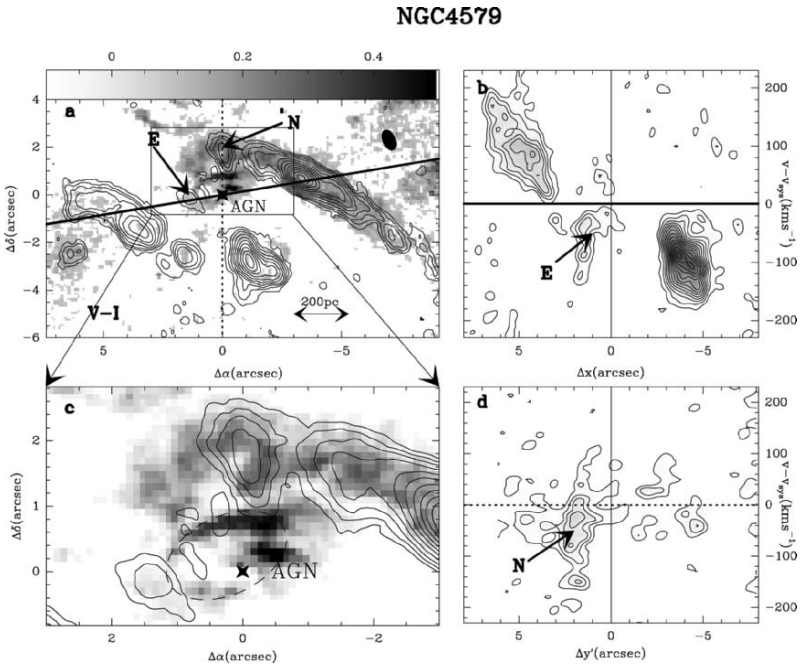

Fig. 1. a) The ^{12}CO(2–1) integrated intensity map obtained with the PdBI (contour levels from 0.4 to 11Jy km s^{-1} beam^{-1}) is overlaid on the V-I color image from HST (grey scale) observed in the nucleus of NGC 4579. Two spiral arcs concentrate the bulk of the molecular gas mass in the central 1 kpc of the galaxy. A close-up view of the inner 200 pc region (**c**) shows a central ringed disk with the AGN lying on its southwestern edge. A gas clump of $\sim 10^6 M_\odot$ (**E**) delimits the disk to the East. The kinematics along the major and minor axes (shown in panels **b** and **d**, respectively) reveal highly non-circular motions. The observed motions are not indicative of ongoing feeding from the central 200 pc disk down to the AGN at present (see discussion in [4]).

2 Probing AGN Feedback Near and Far

The ISM of galaxies showing activity, of the stellar or of the non-stellar variety (i.e., SB or AGN), can suffer the influence of the energies injected into the medium through strong radiation fields and violent mass flows. In particular, molecular gas can be exposed to strong X-ray irradiation close to the central engine of AGN. X-rays can extend their power deep into the clouds by their ability to penetrate huge gas column densities out to A_v=100-1000 [5]. X-ray dominated regions (XDR) manifest themselves by an increase of the gas phase abundances of a certain set of ions, radicals and molecular species [6, 5].

The large HCN/CO intensity and abundance ratios measured in the nucleus of the Seyfert 2 galaxy NGC 1068 by [7] came out as the first observational evidence that molecular gas chemistry could be shaped *somehow* by

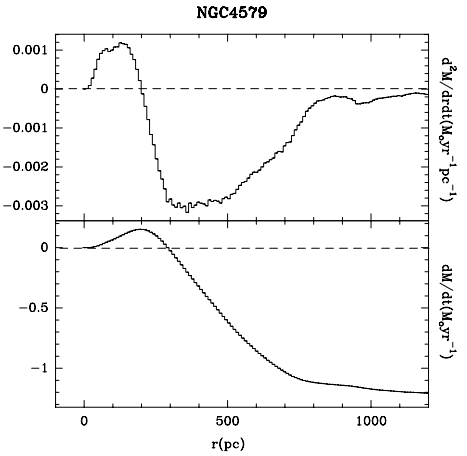

Fig. 2. (**upper panel**): Radial variation of the mass inflow(-) or outflow(+) rate of gas per unit radial length in the nucleus of NGC 4579 due to the action of stellar gravitational torques. Units are $M_\odot$ $yr^{-1}pc^{-1}$. (**lower panel**): Mass inflow/outflow rate integrated inside a certain radius r in $M_\odot$ yr^{-1}.

activity. [8] made complementary observations of the CND of NGC 1068 using the 30m telescope for eight molecular species, purposely chosen to explore the predictions of XDR models for molecular gas. These observations included several lines of CN, HCO, $H^{13}CO^+$, $H^{12}CO^+$, HOC^+, HCN, CS and CO. The first global analysis of the combined survey suggests that the bulk of the molecular gas in the CND of NGC 1068 is highly ionized; this is in agreement with what could be expected for a giant XDR created by the central engine. There is evidence of overluminuous HCN lines in the nuclei of other nearby Seyferts (see e.g., [9]), as well as in some luminous and ultraluminous infrared galaxies (LIRGs and ULIRGs) [10, 11]. The fact that these overluminous HCN lines can be plausibly explained by the enhancement of HCN abundances in the XDRs around AGNs casts doubts on the reliability of HCN as a *true quantitative* tracer of dense molecular gas in galaxies where AGNs are expected to be highly embedded as is the case of LIRGs, ULIRGs and, most particularly, of high redshift galaxies.

Graciá-Carpio et al. [11] completed recently observations with the IRAM 30m telescope in the 1–0 line of HCO^+ of a sample of 16 galaxies including 10 LIRGs and 6 ULIRGs. The results of this HCO^+ survey indicate that the HCN/HCO^+ luminosity ratio increases with L_{IR} for LIRGs and ULIRGs (Fig. 3). This puzzling trend provides indicative evidence that HCN may not be a fair tracer of dense gas in the most extreme LIRGs. In particular, the application to our sample of the diagnostic tool originally designed by [9] to distinguish between 'pure' AGNs and 'composite' starbursts+AGNs in nearby Seyferts, suggests that a large number of embedded AGNs may lie in LIRGs and ULIRGs. A plausible scenario accounting for the observed trends implies

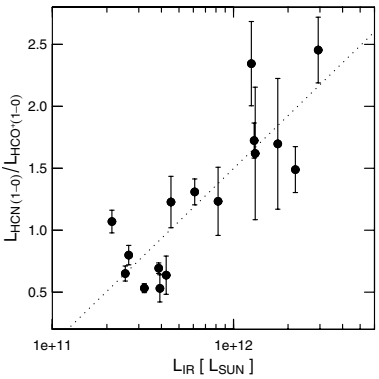

Fig. 3. A intriguing trend between the HCN(1–0)/HCO^+(1–0) luminosity ratio and L_{IR}, identified by [11] in a sample of LIRGs and ULIRGs.

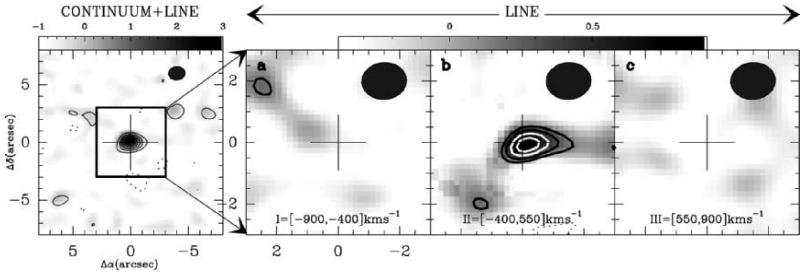

Fig. 4. The first detection of HCO^+ emission at redshift z∼4 in the QSO APM 08279+5255 [14]. We show the continuum+line emission (left panel) and HCO^+(5–4) line emission in the three velocity intervals shown (right panels).

that X-rays may shape the chemistry of molecular gas at $L_{\rm IR} > 10^{12}\,L_{\odot}$. Alternatively, it has also been argued that the abundance of HCN can be enhanced in the molecular gas closely associated with high-mass star forming regions. In this case the reliability of HCN as a straightforward tracer of dense molecular gas in ULIRGs should be equally put on hold, even if the star formation scenario applies here [11].

It is only recently that molecular species other than CO have started to be detected to probe the dense molecular content in gas-rich high-redshift galaxies. The broad absorption line quasar APM 08279+5255 at z=3.9 has been the source of many interesting discoveries lately. Emission of high-J CO lines (J=9–8 and 4–3), mapped by [12], revealed the presence of a circumnuclear disk of hot and dense molecular gas. Wagg et al. [13] reported the detection of HCN (5–4) emission in this quasar using the IRAM PdBI. The exceptionally strong intensity of the HCN (5–4) line with respect to all CO lines measured in APM 08279+5255 came out as a surprise. García-Burillo et al. [14] have recently reported the detection of HCO^+ (5–4) emission in

APM 08279+5255 (See Fig. 4). Most remarkably, the HCN (5–4)/HCO^+ (5–4) luminosity ratio measured by [14] is ∼3 times larger than that predicted by simple radiative transfer models which assume that excitation of the two lines is collisional and that chemical abundances for the two molecular species are comparable. Therefore, inside this scheme, the inferred abundance of HCN in APM 08279+5255 would be *anomalously* high with respect to CO, but, most notably, also with respect to HCO^+: [HCN/CO]∼(1–2)×10^{-2} and [HCN/HCO^+]∼10. Different mechanisms can make for HCN being over-abundant with respect to CO and HCO^+. This includes XDR chemistry or chemical enhancement of HCN in star-forming regions. Alternatively [14] argue that the excitation of HCN and HCO^+ lines in a source like APM 08279+5255 may not be only collisional, but also radiative.

The two scenarios invoked above have completely different but equally relevant implications for the interpretation of high-J molecular line observations of dense gas in other high-redshift galaxies. In either case these observations are a nice illustration of how molecular line probes other than CO can help us to shed light on the nature of the young Universe.

References

1. F. Combes. In: *Active Galactic Nuclei: from Central Engine to Host Galaxy*, ed. by S. Collin, F. Combes & I. Shlosman. ASP (Astronomical Society of the Pacific), Conference Series, Vol. 290, p. 411 (2003)
2. S. García-Burillo, F. Combes, A. Eckart et al. In: *ASP Conf. Ser., Active Galactic Nuclei: from Central Engine to Host Galaxy*, ed. by S. Collin, F. Combes, & I. Shlosman, p. 423 (2003a).
3. S. García-Burillo, F. Combes, L. K. Hunt et al.: A&A, 407, 485 (2003b)
4. S. García-Burillo, F. Combes, E. Schinnerer, F. Boone, & L. K. Hunt: A&A, 441, 1011 (2005)
5. P. R. Maloney, D. J. Hollenbach, & A.G.G.M. Tielens: ApJ, 466, 561 (1996)
6. S. Lepp, & A. Dalgarno: A&A, 306, L21 (1996)
7. L. J. Tacconi, R. Genzel, M. Blietz et al.: ApJ, 426, L77 (1994)
8. A. Usero, S. García-Burillo, A. Fuente, J. Martín-Pintado, & N. J. Rodríguez-Fernández: A&A, 419, 897 (2004)
9. K. Kohno, S. Matsushita, B. Vila-Vilaró et al. In: *ASP Conf. Ser.:The Central Kiloparsec of Starbursts and AGN: The La Palma Connection*, vol 249, p. 672 (2001)
10. Y. Gao, & P. M. Solomon: ApJS, 152, 63 (2004)
11. J. Graciá-Carpio, S. García-Burillo, P. Planesas, & L. Colina: ApJL, 640, L135 (2006)
12. D. Downes, R. Neri, T. Wiklind, D. J. Wilner, & P. A. Shaver: ApJL, 513, L1 (1999)
13. J. Wagg, D. J. Wilner, R. Neri, D. Downes & T. Wiklind: ApJL, 634, L13
14. S. García-Burillo, S., et al.: ApJL, 645, L17 (2006)

23

Suzaku Observations of the Galactic Center: The Origin of Highly Ionized Iron Lines

Yoshiaki Hyodo, Katsuji Koyama

hyodo@cr.scphys.kyoto-u.ac.jp
Department of Physics, Graduate school of Science, Kyoto University, Sakyo-ku, Kyoto 606-8502

Summary. We have made long exposure observations (134 hours in total) of the Galactic Center (GC) region with Suzaku, the 5th Japanese X-ray satellite. With the large effective area, high energy resolution, and low background of X-ray Imaging Spectrometers (XISs; CCD cameras on board Suzaku), we resolved the line complex near the energy of K-shell transitions of iron into 3 Kα lines, 6.4 keV (neutral), 6.7 keV (He-like) and 6.9 keV (H-like), and discovered 6 iron and nickel lines above 7 keV. The center energy of the He-like iron is determined very accurately to be 6680 $\pm$ 1 $\pm$ 5 eV, which favors the hot plasma origin with the predicted center energy of 6685 eV, rather than the charge exchange origin of 6666 eV. The line fluxes are uniformly distributed, in contrast to the clumpy structure of the molecular clouds. This fact is also against the charge exchange origin, because the flux of this process should trace the molecular clouds where donor electrons (neutral hydrogen) are rich. The electron temperature and ionization temperature are determined with the intensity ratio of the 7.9/6.7 keV and 6.9/6.7 keV lines, and are consistent with 6.5 keV, indicating a collisional ionization equilibrium plasma. We hence conclude that the origin of highly ionized iron lines is a hot thin plasma. We discovered five new extended objects from the GC region. They are probably supernova remnants or X-ray reflection nebulae. Further analysis of these objects will reveal the energy injection source of the Galactic center diffuse X-ray emission.

1 Introduction

The Ginga satellite discovered emission lines at about 6.7 keV which are largely extended (150 pc$\times$300 pc) over the Galactic center (GC) region [1], [2]. Subsequently, ASCA found that the 6.7 keV lines are complex with at least 3 lines [3]. The origin of the lines, however has been debatable; whether electron capture (charge exchange (CX) and/or photoionization), or collisional ionization hot plasma. For the collisional ionization case, the best-fit thin thermal plasma temperature of the Galactic center diffuse X-ray emission (GCDX) spectrum was $\sim$10 keV. If the GCDX is really due to a thin hot and uniformly distributed plasma, the total thermal energy is estimated to

be 10^{53-54} erg, or equivalent to 10^2–10^3 supernovae explosions. The temperature of ∼10 keV is higher than that bounded by the Galactic gravity, hence the plasma should escape from the GC region. The time scale estimated by the plasma size (1° or ∼ 150 pc at 8.5 kpc) divided by the sound velocity of the ∼10 keV plasma is $\sim 10^5$ years. Therefore the energy of $\sim 10^{53-54}$ erg should be supplied in the past $\sim 10^5$ years, e.g. 1 SN every 100–1000 year is required in the GC region. This huge energy budget in the GC region suggests that CX recombination may be a more reasonable explanation for the GCDX. In this scenario, during a collision between neutral hydrogen and FeXXVI or FeXXVII, the bound hydrogen electron is captured into an excited state of the iron, and then the excited state decays producing an X-ray. The X-ray spectral signature is distinct from the signature produced by collisional excitation (CE) in a collisional ionization equilibrium (CIE) plasma, such as the high-temperature plasma mentioned above. In the CX case, the forbidden line at $E_{\rm f} = 6636$ eV, is stronger than the resonance line at $E_{\rm r} = 6700$ eV [4, 5, 6], whereas the resonance line is stronger in the case of a plasma in CIE. Thus, even if the resonance and forbidden lines are not completely resolved, the energy centroid of the Kα line of FeXXV produced by CX will be lower than that produced by CE.

2 Observation and Data Reduction

Five pointing observations towards the GC were performed with the XIS at the focal planes of the X-Ray Telescopes (XRT) on board the Suzaku satellite in September and October of 2005, and Feburary and March of 2006. Details of Suzaku, the XRT, and the XIS are found in [7], [8] and [9], respectively. Data taken at elevation angles less than 5° from the Earth rim or during the passage through the South Atlantic Anomaly were discarded. After this filtering, the net exposure times were ∼134 hours.

3 Analysis and Results

3.1 Narrow Band Images

For the spectral analysis, we concentrate on the two field (point 3 and 4 in Fig.3), because these observations were performed at very early phase (September of 2006), hence the CTI-correction and gain-tuning are done very accurately (see [9] for details). We made the X-ray spectrum from the whole two region excluding the corners of the CCD, containing the calibration sources and the central bright object Sgr A East ([11, 12, 13, 14]). The resultant spectrum is given in Fig.1 and 2, where the non-X-ray background is subtructed. Many emission lines are clearly resolved. We co-added the four XIS data sets and made X-ray mosaic maps of the GC region. Figures 3, 4, and

5 show the narrow band maps in the 2.4–2.5 keV (SXV Kα line), 6.3–6.5 keV (FeI Kα line), and 6.6–6.8 keV (FeXXV Kα line) bands, where exposure corrections were applied. The 2.45 keV line traces warm ($\sim 10^7$ K) plasma, while the 6.7 keV line traces hot ($\sim 10^8$ K) plasma. On the other hand, the 6.4 keV line traces cold ($\sim$10 K) matter. CX is a process between cosmic ray ion and neutral matter, therefore the line flux of this process should trace the molecular clouds where donor electrons (neutral hydrogen) are rich. The 6.7 keV line fluxes are however, uniformly distributed, in contrast to the clumpy 6.4 keV structure which traces the cold molecular clouds. This fact is against the CX origin.

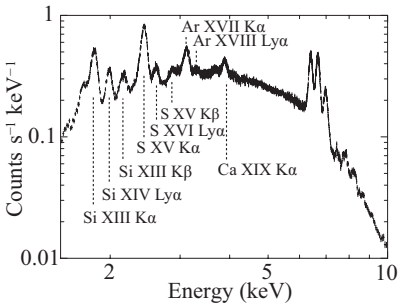

Fig. 1. The averaged spectrum of the 3 FI-CCDs in the 1.5–10.0 keV band. The data are taken from the full FOV excluding the calibration source regions and Sgr A East.

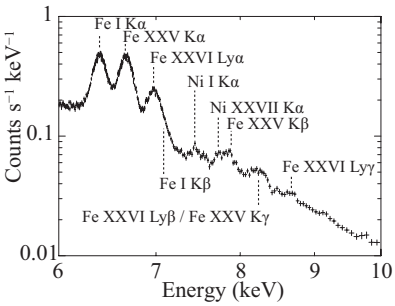

Fig. 2. Same as Fig. 1, but in the 6.0–10.0 keV band.

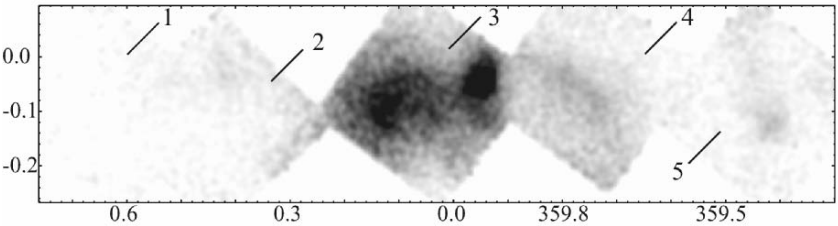

Fig. 3. The narrow band map at the 2.45 keV line (the 2.4–2.5 keV band). Coordinates are galactic l and b in degrees. The size of each XIS FOV is $18' \times 18'$.

3.2 The Center Energy of Kα Line from FeXXV

In order to obtain the center energy, flux and width of each line, we simultaneously fit the spectra from the three FI CCDs and the BI CCD spanning the

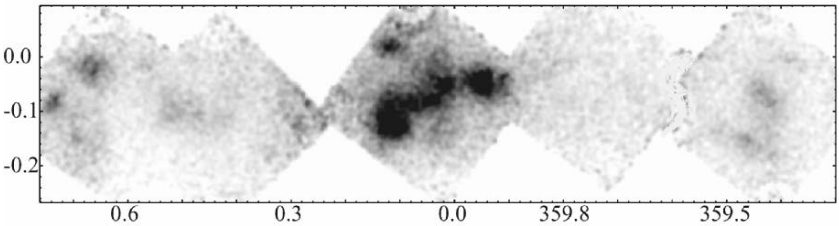

Fig. 4. Same as Fig.3, but for the 6.4 keV line (the 6.3–6.5 keV band)

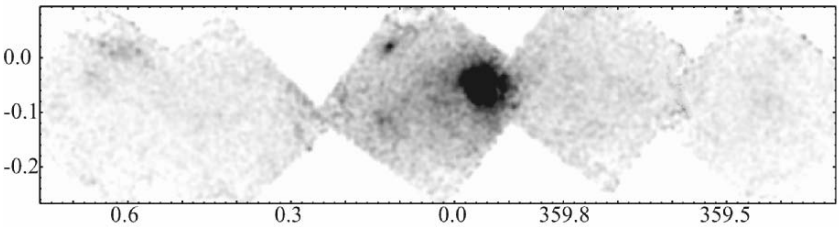

Fig. 5. Same as Fig.3, but for the 6.7 keV line (the 6.6–6.8 keV band)

5.5–11.5 keV band. The model used here is bremsstrahlung absorbed by $N_{\rm Fe}$ for the continuum, adding Gaussians for emission lines.

The best-fit parameters are given in table 1. The Kα line from FeXXV is a blend of the resonance, inter-combination, and forbidden lines of FeXXV (see table 2), and depending on the conditions of the source plasma, may also contain satellite-lines produced by dielectronic recombination and innershell excitation [15, 16]. The fact that the observed line centroid and width of Kα from FeXXV depends on the flux ratio of these lines, which, in turn, are a function of the plasma conditions, make the Kα line feature an excellent diagnostic. As discussed above, a centroid shifted towards lower energy relative to the CIE case is an indication of a recombining plasma. For the GCDX, the observed center energy of Kα of Fe XXV is 6680$\pm$1 eV. We compare our result to the laboratory values produced by the CX recombination, i.e., a recombination dominated plasma, and also to calculations using APEC and MEKAL of the line emission produced by a CIE plasma. The laboratory measured centroid for Kα of FeXXV produced by the CX recombination alone, is 6666 $\pm$ 5 eV [6], significantly lower than the value measure in the GCDX. The APEC and MEKAL predicted centroid for the CIE case are 6685 eV and 6680 eV, respectively, in agreement with the GCDX value of 6680 eV.

Together with the discussion of the previous section, we therefore propose that the 6.7 keV and 6.9 keV lines in the GCDX are likely due to a CIE plasma and would not arise from a CX process.

Table 1. The best-fit parameters of the GCDX.

Emission lines				
Center Energy	Identification		Width[b]	Intensity
(eV)	Line	Energy (eV)[a]	(eV)	(photons s^{-1} cm^{-2})
6409±1	FeI Kα		33^{+2}_{-4}	$4.32^{+0.05}_{-0.08} \times 10^{-4}$
6680±1	FeXXV Kα	6637–6701	39±2	$5.10^{+0.08}_{-0.06} \times 10^{-4}$
6969^{+6}_{-3}	FeXXVI Lyα	6966	15^{+8}_{-15}	$1.66^{+0.09}_{-0.11} \times 10^{-4}$
7069	FeI Kβ		38	$6.91^{+1.12}_{-0.96} \times 10^{-5}$
7490^{+12}_{-14}	NiI Kα		0 (<28)	$3.05^{+0.73}_{-0.57} \times 10^{-5}$
7781^{+24}_{-31}	NiXVII Kα	7735–7805	39	$3.97^{+1.06}_{-0.65} \times 10^{-5}$
7891	FeXXV Kβ	7881	30 (fixed)	$4.69^{+0.81}_{-0.61} \times 10^{-5}$
8220^{+31}_{-22}	FeXXVILyβ	8251	30 (fixed)	$2.29^{+1.35}_{-1.31} \times 10^{-5}$
8264	FeXXV Kγ	8295	30 (fixed)	$3.08^{+1.32}_{-1.34} \times 10^{-5}$
8681^{+33}_{-32}	FeXXVI Lyγ	8700	0 (<91)	$1.77^{+0.62}_{-0.56} \times 10^{-5}$
Calibration source line				
5896^{+1}_{-1}	MnI Kα	5895	31^{+1}_{-1}	
6489^{+1}_{-2}	MnI Kβ	6490	38^{+1}_{-3}	

The errors are at 90% confidence level.

Table 2. Table of He-like Iron triplets

Name	Transition	Energy (eV)[a]
Resonance	$1s^2\ {}^1S_0$–$1s2p\ {}^1P_1$	6701
Intercombination	$1s^2\ {}^1S_0$–$1s2p\ {}^3P_1$	6682
Intercombination	$1s^2\ {}^1S_0$–$1s2p\ {}^3P_2$	6668
Forbidden	$1s^2\ {}^1S_0$–$1s2s\ {}^3S_1$	6637

[a] from [6]

3.3 New Extended Sources

We have discovered 2 new extended sources from the Sgr B region, and designated this source Suzaku J1747.0–2824.5 (G0.61+0.01) and Suzaku J1747.7–2821.2 (M0.74–0.09) from its center position [17]. These objects are possibly a new supernova remnant (SNR) and an X-ray reflection nebula (XRN) candidate [17].

We also found an SNR candidate G359.4–0.1 and XRN candidate 359.4–0.2 from the Sgr C region, and an SNR candidate G0.4+0.0 from the Sgr B1 region.

As mentioned above, the most plausible source of the GCDX is multiple supernovae. The required rate is several × 100 / 10^5 year, hence we expect several × 10 young (< 10^4 years) SNRs which emits X-rays. Further deep X-ray observation with *Suzaku* will discover many new SNRs, and the entire GCDX may be explained by multiple supernovae.

Acknowledgement

Y.H. is supported by JSPS Research Fellowship for Young Scientists. This work is supported by the Grants-in-Aid for the 21st Century COE "Center for Diversity and Universality in Physics" and also by Grants-in-Aid (No 18204015) ofthe Ministry of Education, Culture, Sports, Science and Technology (MEXT).

References

1. Koyama, K., Awaki, H., Kunieda, H., Takano, S., Tawara, Y., Yamauchi, S., Hatsukade, I., & Nagase, F.: Nature, 339, 603 (1989)
2. Yamauchi, S., Kawada, M., Koyama, K., Kunieda, H., Tawara, Y., & Hatsukade, I.: ApJ, 365, 532 (1990)
3. Koyama, K., Maeda, Y., Sonobe, T., Takeshima, T., Tanaka, Y., & Yamauchi, S.: PASJ, 48, 249 (1996)
4. Otranto, S., Olson, R. E., & Beiersdorfer, P.: Phys. Rev. A, 73, 022723 (2006)
5. Beiersdorfer, P., et al.: Phys. Rev. A, 72, 032725 (2005)
6. Wargelin, B. J., Beiersdorfer, P., Neill, P. A., Olson, R. E., & Scofield, J. H.: ApJ , 634, 687 (2005)
7. Mitsuda, K., et al.: PASJ, accepted (2006)
8. Serlemitsos, P., et al.: PASJ, accepted (2006)
9. Koyama, K., et al.: PASJ, accepted (2006)
10. Koyama, K., et al.: PASJ, accepted (2006) (astro-ph/0609215)
11. Maeda, Y., et al.: ApJ, 570, 671 (2002)
12. Sakano, M., Warwick, R. S., Decourchelle, A., & Predehl, P.: MNRAS, 350, 129 (2004)
13. Park, S., et al.: ApJ, 631, 964 (2005)
14. Koyama, K., et al.: PASJ accepted (2006)
15. Beiersdorfer, P., et al.: Phys. Rev. A, 46, No. 7, 3812 (1992)
16. Beiersdorfer, P., et al.: ApJ, 409, 846 (1993)
17. Koyama, K., et al.: PASJ, accepted (2006) (astro-ph/0609310)

24

Nuclear Spirals in Galaxies

Witold Maciejewski

Astrophysics, Denys Wilkinson Bldg, Keble Rd, Oxford OX1 3RH, UK
witold@astro.ox.ac.uk

Summary. Recent high-resolution observations indicate that nuclear spirals are often present in the innermost few hundred parsecs of disc galaxies. My models show that nuclear spirals form naturally as a gas response to non-axisymmetry in the gravitational potential. Some nuclear spirals take the form of spiral shocks, resulting in streaming motions in the gas, and in inflow comparable to the accretion rates needed to power local Active Galactic Nuclei. Recently streaming motions of amplitude expected from the models have been observed in nuclear spirals, confirming the role of nuclear spirals in feeding of the central massive black holes.

1 Introduction

There is an intricate mutual dynamical dependence between the central Massive Black Hole (MBH) and the nuclear region of the host galaxy. Centres of galaxies act as resonant cavities, and the mass of the central MBH contributes to the formation and locations of the resonances [6],[7]. Resonances can either halt or enhance radial gas flow, and thus can control fueling of the nucleus [8]. Among resonantly-induced features, nuclear spirals form naturally as a gas response to non-axisymmetry in the gravitational potential of a galaxy [2],[8]. In fact, recent high-resolution observations often find in the innermost few hundred parsecs of disc galaxies nuclear spirals [13],[10] that are likely to continue inward to within a few parsecs from galaxy's centre [14],[4]. Because of their ubiquity, nuclear spirals were invoked as the mechanism by which material is transported to the central MBH [15]. In this paper, I present implications of [7] and [8] for the diagnostic role of nuclear spirals, and I confront model predictions with the most recent observations.

2 Geometry: Indicator of Central Mass Concentration

Nuclear spirals form naturally as morphology of waves in gas, generated by a rotating asymmetry in the galactic gravitational potential. Generation and

propagation of waves is governed by dynamical resonances, whose presence and positions depend on the central mass distribution in the galaxy. Simple linear approximation enables to describe the morphology of nuclear spiral for most typical rotation curves [7]:
– A, with a linear inner rise, reflecting solid-body rotation in the innermost parts of the galaxy, i.e. constant-density core,
– B, same as A but with a central MBH of mass consistent with the observed correlations (e.g. [16]),
– C, a pure power-law, corresponding to a central density cusp.
These three representative rotation curves are presented in the upper panels of Fig.1, while the shapes of the nuclear spirals generated by a rotating bisymmetry in the potential are shown in the lower panels of Fig.1.

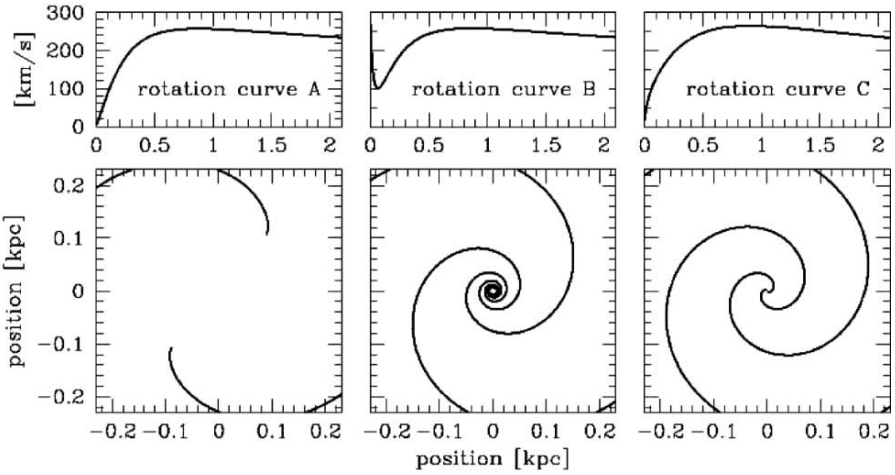

Fig. 1. Rotation curves (upper row), and the corresponding shapes of nuclear spiral (lower row), calculated for isothermal gas with 20 km s^{-1}sound speed for three rotation curves described in the text.

If there is no central MBH, and if the rotation curve rises linearly in its innermost parts (case A), the nuclear spiral will not extend to the centre of the galaxy (Fig.1, left column). If there is a MBH in the centre (case B), the nuclear spiral extends to the centre, and it tightly winds around the central MBH (Fig.1, central column). If there is a central density cusp (case C), the nuclear spiral extends to the centre, but it unwinds towards the centre (Fig.1, right column). Rotation curves A and C appear similar, but their corresponding nuclear spirals are diametrically different. Ubiquity of nuclear spirals in galaxies may indicate that approximating the inner rise of the rotation curve by a straight line is often inadequate. Moreover, nuclear spiral tightly winding around the galactic centre may indicate the presence of a MBH there.

3 Amplitude: Indicator of Asymmetries in the Potential

Nuclear spirals are resonant phenomena, and they can be generated by very small departures from axial symmetry in galaxies. Aside for asymmetries in stellar distribution, other asymmetries may contribute to the overall galactic gravitational potential. If MBHs in centres of galaxies form by merging of smaller black holes, then there should be a few black holes of mass one or two orders of magnitude smaller than that of the central ones, orbiting around the centre of a typical galaxy (e.g. [17],[5]). These black holes constitute a weak perturbation in the gravitational potential, which can generate wave phenomena in gas within a disc close to the centre of a galaxy. A single orbiting black hole about ten times less massive than the central black hole generates a three-arm spiral pattern in the central gaseous disc, with density excess in the spiral arms up to 3-12% ([3]: see Fig.2, left and central panels). Dusty filaments that have been discovered recently in the centres of galaxies (e.g. [10],[14]) have luminosity lower from their surroundings by $5 - 10\%$, therefore spiral patterns in gas generated by the most massive orbiting black holes should be detectable. Interestingly, one of the best investigated nuclear spirals in NGC 1097 ([14],[4]) has three arms (Fig.2, right panel), difficult to generate by the observed bisymmetric bar only.

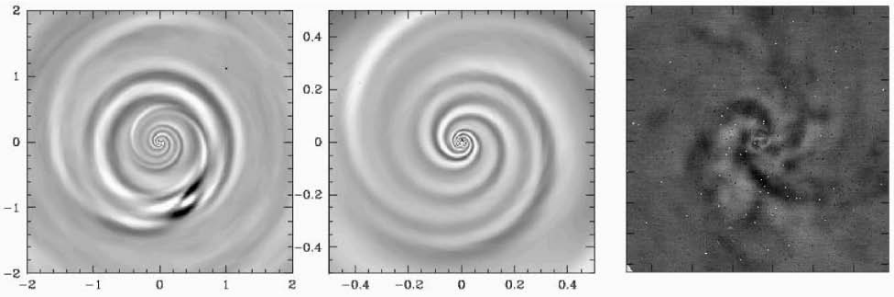

Fig. 2. Left and central panels: the density of gas in galactic plane in model 11 from [3] of a $10^7 M_\odot$ MBH in circular orbit of 1 kpc radius perpendicular to the galactic plane. Darker shading represents higher density. Units on axes are in kpc. Right panel: VLT NACO J-band image of the nuclear spiral in NGC 1097 after subtraction of radial intensity gradient by ellipse fitting. The side of the box is 8 arcsec, corresponding to about 0.55 kpc.

4 Nuclear Spiral as a Feeding Mechanism of the MBH

In the present-day Universe, 10-20 per cent of galaxies show nuclear activity of Seyfert type. This activity is orders of magnitude weaker than that of

quasars, and internal, dynamical factors are likely to play a role in triggering it. Extensive morphological studies had no success in pointing out the mechanism that triggers the nuclear activity, but they might have focused on features on too large scales. A typical local Active Galactic Nucleus (AGN) consumes about 0.01 $M_\odot$ of fuel per year (e.g. [12]), most likely coming from gas inflow. This corresponds to about $10^6 M_\odot$ during its 10^8-yr long activity. Therefore there is no need to transport gas from the outskirts of a galaxy in order to feed a local AGN, but significant redistribution of gas in the innermost tens and hundreds of parsecs should be expected.

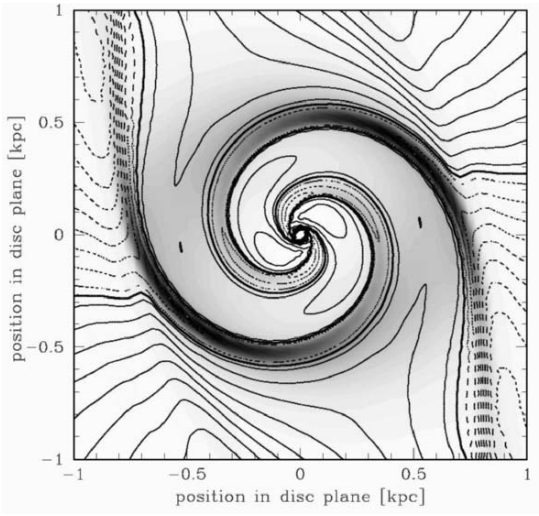

Fig. 3. The density of gas in greyscale in galactic plane in model 8S20 from [8] with nuclear spiral shock. Darker shading represents higher density. Contours outline constant radial velocities, and are spaced every 20 km s^{-1}. Outflow (positive radial velocity) is marked by solid contours, while dashed contours mark inflow (negative radial velocity). Thick solid contour marks zero-radial-velocity line.

In strong bar, the nuclear spiral has the nature of a shock in gas [8], which can trigger gas inflow throughout the spiral. Note however, that analogously to gas flow in the region of straight principal shocks in the bar (e.g. [1],[9]), not all gas in the region of nuclear spiral shows radial inflow (Fig.3). In fact, most of the volume is dominated by outflow of low-density gas, but inflow of dense post-shock gas in the spiral dominates the budget. Therefore exclusive use of tracers of dense gas (e.g. molecular emission) can result in biased estimates of integrated radial flow of galactic gas.

Right panel of Fig.4 shows line-of-sight velocities expected for the standard model 8S20 of nuclear spiral from [8], when viewed at inclination of 60°, and after subtracting contribution of circular motion. Large streaming motions

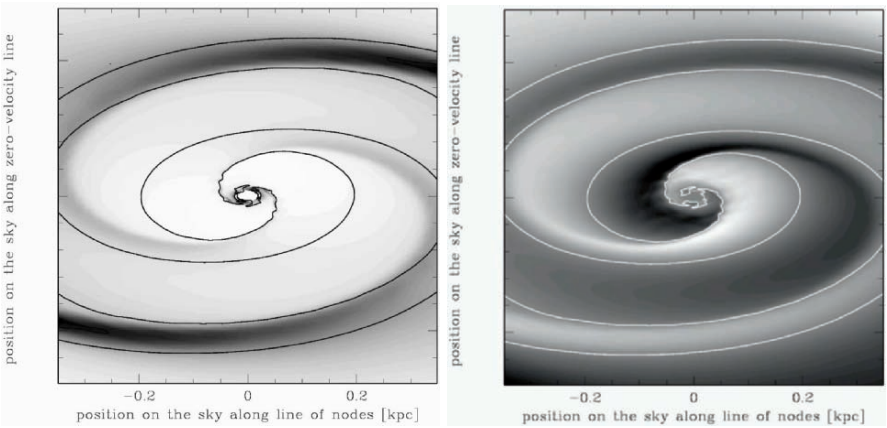

Fig. 4. Left panel: Density in the inner parts of model 8S20 from Fig.3, when viewed at inclination of 60°. Darker shading represents higher densities. Right panel: corresponding residual line-of-sight velocities after subtraction of circular rotation. Darker shading represents negative velocities, brighter one – positive velocities. The solid contours in both panels mark zero velocity, and can be used to guide the eye when comparing shapes of the spirals.

are expected, of amplitude of up to 50 km s^{-1}. This amplitude can only be achieved when shocks in gas are involved. Recently, the same algorithm has been applied to the kinematics of nuclear spiral in NGC 1097 observed with the Integral Field Unit GMOS on the Very Large Telescope [4]. Strong streaming motions of amplitude about 50 km s^{-1} that show spiral morphology, have been observed. *That observation confirms presence of shocks in nuclear spirals.*

Note that the modelled kinematical spiral arms do not overlap with the spiral gas morphology (Fig.4, left panel). This is because the matter distribution is point-symmetric, while the velocity vectors – point-antisymmetric. The shift between the kinematical and morphological spiral arms predicted by the models is consistent with that observed in NGC 1097 [4].

Hydrodynamical models of nuclear spiral shocks indicate the rate of inflow in the innermost parsecs of a galaxy up to 0.03 $M_{\odot}yr^{-1}$[8]. This inflow is sufficient to feed luminous local AGN, and the feeding can continue over long timescales. Nuclear spiral shock is less tightly wound than what the linear theory predicts, hence loosely wound spirals in the classification developed in [10] may indicate spiral shocks. Interestingly, when in that classification one groups together grand-design nuclear spirals (explicitly linked to shocks in bars) and loosely wound spirals, they occur considerably more often in active than in non-active galaxies [10],[11].

This page intentionally blank

5 Discussion and Conclusions

Hydrodynamical models of nuclear spirals presented here assume that galactic gas is a continuous medium, which can be statistically approximated by isothermal fluid. One may expect that this approximation breaks down at scales small enough, but it is still likely to hold on 10-pc scale, because continuous dusty nuclear spiral arms extend down to within that distance from the nucleus. Perhaps this approximation is most appropriate for the dynamic interstellar medium, in which dense clouds continuously form and disperse.

The shape of nuclear spiral can serve as an indicator of the presence of a MBH in a galaxy's centre, and as an estimator of its mass. The amplitude of the spiral can constrain asymmetries in the galaxy's potential, like orbiting remnant black holes left from the time of galaxy formation.

Nuclear spirals in galaxies can either be weak density waves which cannot feed the nucleus, or strong dissipative shocks, which can generate gas inflow large enough to power luminous local AGN. Nuclear spiral shocks should be revealed in kinematical observations by strong streaming motions, and such motions of amplitude consistent with theoretical predictions have been recently observed. This observation makes a sound argument in support of gas inflow in nuclear spirals, which can serve as a mechanism feeding the central MBH and leading the the AGN phenomenon.

This work was partially supported by the Polish Committee for Scientific Research as a research project 1 P03D 007 26 in the years 2004–2007.

References

1. E. Athanassoula: MNRAS 259, 345 (1992)
2. P. Englmaier, I. Shlosman: ApJ 528, 677 (2000)
3. J. Etherington, W. Maciejewski: MNRAS 367, 1003 (2006)
4. K. Fathi, T. Storchi-Bergmann, R.A. Riffel et al: ApJ 641, L25 (2006)
5. R.R. Islam, J.E. Taylor, J. Silk: MNRAS 340, 647 (2003)
6. W. Maciejewski: Gas Dynamics in Central Parts of Galaxies. In: *Galactic & Stellar Dynamics*, EAS Publication Series vol 10, ed by C.M. Boily et al (EDP Sciences, Les Ilis 2003) pp 3–16
7. W. Maciejewski: MNRAS 354, 883 (2004)
8. W. Maciejewski: MNRAS 354, 892 (2004)
9. W. Maciejewski, P.J. Teuben, L.S. Sparke, J.M. Stone: MNRAS 329, 502 (2002)
10. P. Martini, M.W. Regan, J.S. Mulchaey, R.W. Pogge: ApJS 146, 353 (2003)
11. P. Martini, M.W. Regan, J.S. Mulchaey, R.W. Pogge: ApJ 589, 774 (2003)
12. B.M. Peterson: *An Introduction to Active Galactic Nuclei*, (Cambridge Univ. Press, Cambridge 1997)
13. R.W. Pogge, P. Martini: ApJ 569, 624 (2002)
14. M.A. Prieto, W. Maciejewski, J. Reunanen: AJ 130, 1472 (2005)
15. M.W. Regan, J.S. Mulchaey: AJ 117, 2676 (1999)
16. S. Tremaine, K. Gebhardt, R. Bender et al: ApJ 574, 740 (2002)
17. M. Volonteri, F. Haardt, P. Madau: ApJ 582, 559 (2003)

Performance by Yaeyama-Shoko High School

Part III

NEARBY GALAXIES

25

Nobeyama CO Atlas of Nearby Spiral Galaxies

Norio Kuno[1,2], N. Sato[3], H. Nakanishi[1], A. Hirota[4], T. Tosaki[1], Y. Shioya[5], K. Sorai[6], N. Nakai[7], K. Nishiyama[8] and B. Vila-Vilaró[9]

[1] Nobeyama Radio Observatory, Minamimaki-mura, Minamisaku-gun, Nagano 384-1305, Japan
[2] The Graduate University for Advanced Studies (SOKENDI), 2-21-1 Osawa, Mitaka, Tokyo 181-0015, Japan
[3] Wakayama University, Wakayama 640-8510, Japan
[4] The University of Tokyo, Bunkyo-ku, Tokyo 113-0033, Japan
[5] Ehime University, Matsuyama 790-8577, Japan
[6] Hokkaido University, Sapporo 060-0810, Japan
[7] University of Tsukuba, Ten-nodai, 1-1-1 Tsukuba, Ibaraki 305-8577, Japan
[8] Bisei Spaceguard Center, Bisei-cho, Oda-gun, Okayama 714-1415, Japan
[9] National Astronomical Observatory of Japan, 2-21-1 Osawa, Mitaka, Tokyo 181-0015, Japan

Summary. The results of a CO(1–0) mapping survey of 40 nearby spiral galaxies performed with the Nobeyama 45-m telescope are presented. The maps of CO cover most of the optical disk of the galaxies. We investigated the influence of bar on distribution of molecular gas in spiral galaxies using these data. We confirmed that the degree of central concentration is higher in barred spirals than in non-barred spirals as shown by previous works. Furthermore, we show that bars are efficient in driving molecular gas that lies within their radial scales toward the center, while the role in the accumulation from the larger spatial scales on the disks is small. The transported gas accounts for about half of molecular gas within the central region in barred spiral galaxies. We found a correlation between the degree of central concentration and bar strength. Galaxies with stronger bars tend to have higher central concentration. The correlation implies that stronger bars accumulate molecular gas toward the center more efficiently. These results are consistent with long-lived bars.

1 Introduction

Although single dish telescopes are better at measuring total flux, mapping CO in whole disks of external galaxies by large single dishes has been limited so far. This is because a lot of time is needed to map external galaxies with a single-beam receiver with a high angular resolution. The Nobeyama 45-m telescope is one of the most suitable telescopes for such observations, since the 25-Beam Array Receiver System (BEARS) mounted on the telescope has a high performance for mapping observations. Therefore, we performed a CO-mapping survey of nearby spiral galaxies with the 45-m telescope. The data is useful to investigate the relation

between the distribution of molecular gas and galactic structures such as spiral arms and bars.

We investigated the influence of bar on the distribution of molecular gas in spiral galaxies using the CO survey data. Many theoretical studies and numerical simulations have shown that a bar can play an important role for gas fueling toward the central region. Such fueling mechanism is needed for starbursts or AGN activities in the central region. Therefore, it is important to make clear how bars work on the molecular gas. We investigated the relation between distribution of molecular gas and the existence of a bar, and the correlation between the central concentration and the bar strength.

2 Sample Galaxies

We selected our sample of galaxies according to the following criteria. (1) morphological type in the RC3 in the range from Sa to Scd. (2) distance less than 25 Mpc. (3) Inclination angle less than 79°(RC3). (4) flux at 100 μm higher than $\sim$10 Jy. (5) spiral structure is not destroyed by interaction. The number of sample galaxies is 40 (Table 1).

Table 1. Sample galaxies

NGC 253	Mafei 2	NGC 1068	IC 342	UGC 2855	NGC 2903	NGC 3184
NGC 3351	NGC 3504	NGC 3521	NGC 3627	NGC 3631	NGC 4051	NGC 4102
NGC 4192	NGC 4212	NGC 4254	NGC 4303	NGC 4321	NGC 4402	NGC 4414
NGC 4419	NGC 4501	NGC 4535	NGC 4536	NGC 4548	NGC 4569	NGC 4579
NGC 4654	NGC 4689	NGC 4736	NGC 5055	NGC 5194	NGC 5236	NGC 5247
NGC 5248	NGC 5457	NGC 6217	NGC 6946	NGC 6951		

3 Observations

Observations of ^{12}CO(J =1–0) emission were made during 1995 to May 2005 using the 45-m telescope of the Nobeyama Radio Observatory. The SIS focal plane array, BEARS, which consists of 25 beams ([1]), was mainly used as a receiver front-end. The details of observations are described in [2].

4 Results

The CO data of all sample galaxies are presented in [2]. We present here some of them (Figures 1–5).

Most of the barred spirals in our sample have a strong peak at the center and the molecular gas distributes along the bars (e.g., IC 342, Maffei 2). The ridges of the molecular gas along the bars offset toward the leading side as shown by many

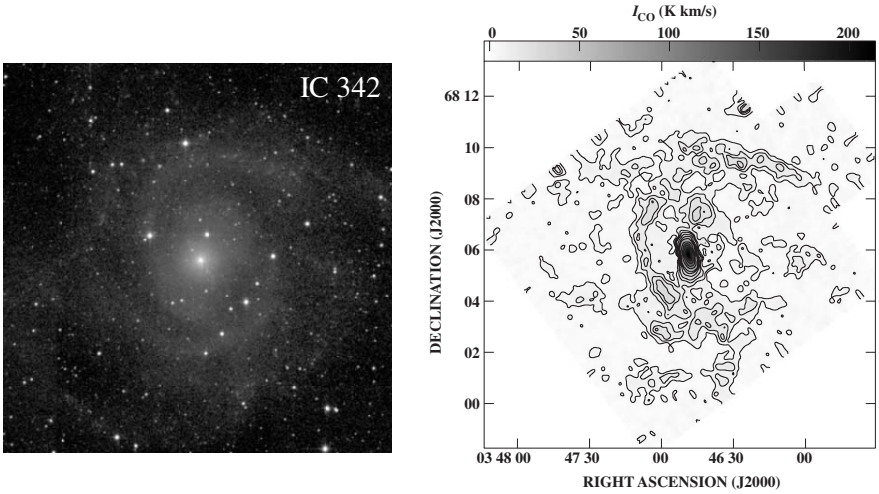

Fig. 1. (left) NIR image of IC 342 from [3]. (right) CO integrated intensity map of IC 342.

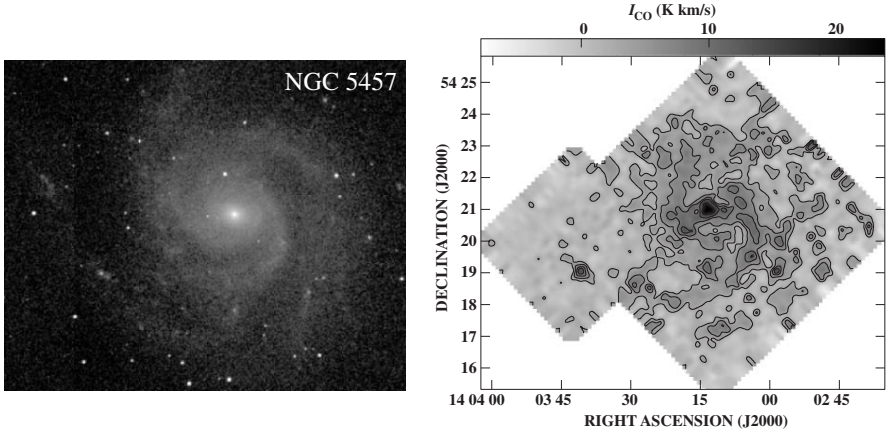

Fig. 2. (left) NIR image of M101 from [3]. (right) CO integrated intensity map of M101.

numerical simulations and previous observations. In some galaxies (e.g., Maffei 2, NGC 2903, NGC 3627, NGC 6951), the bar-ends are the places where molecular gas tends to concentrate. On the other hand, the CO-intensity peak at the center in non-barred spirals except for NGC 5055 is not so prominent. Some galaxies show kiloparsec-scale central gas depletion (NGC 4212, NGC 4414, NGC 4689).

It has been pointed out that the radial distributions of molecular gas in barred spirals show some characteristic features ([4], [5]). Most of the barred spirals have a strong intensity peak at the center, as seen in our CO maps. From the strong peak at the center, the slope of the radial distribution becomes shallower toward the radius

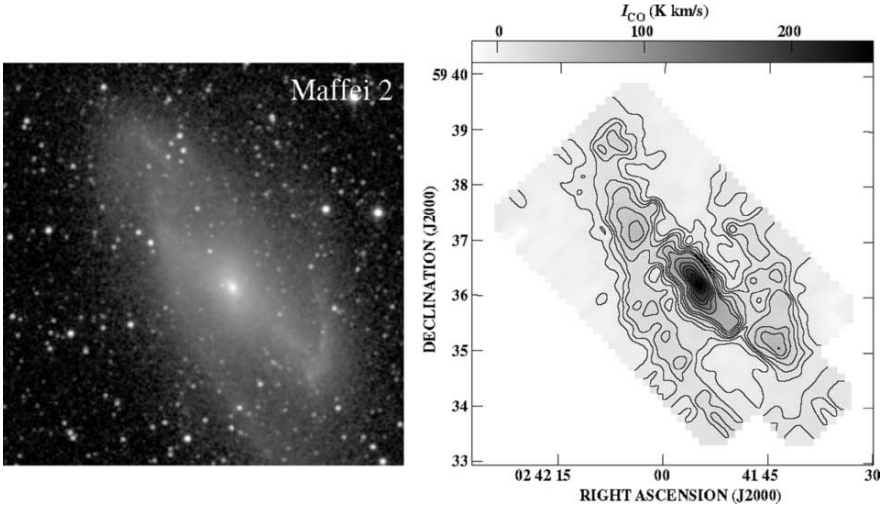

Fig. 3. (left) NIR image of Maffei 2 from [3]. (right) CO integrated intensity map of Maffei 2.

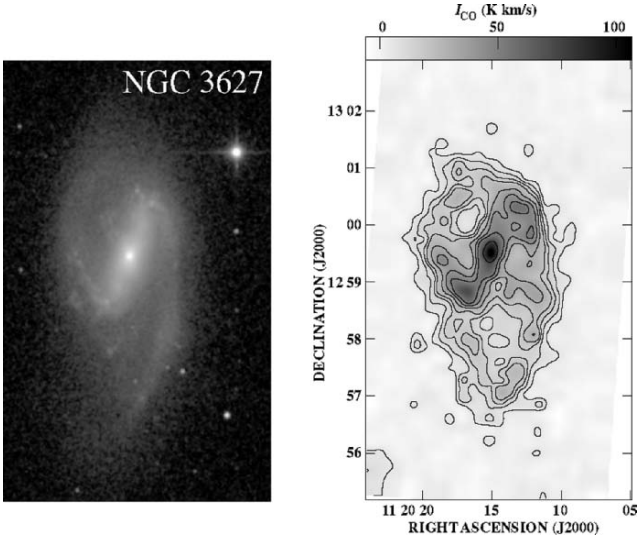

Fig. 4. (left) NIR image of NGC 3627 from [3]. (right) CO integrated intensity map of NGC 3627.

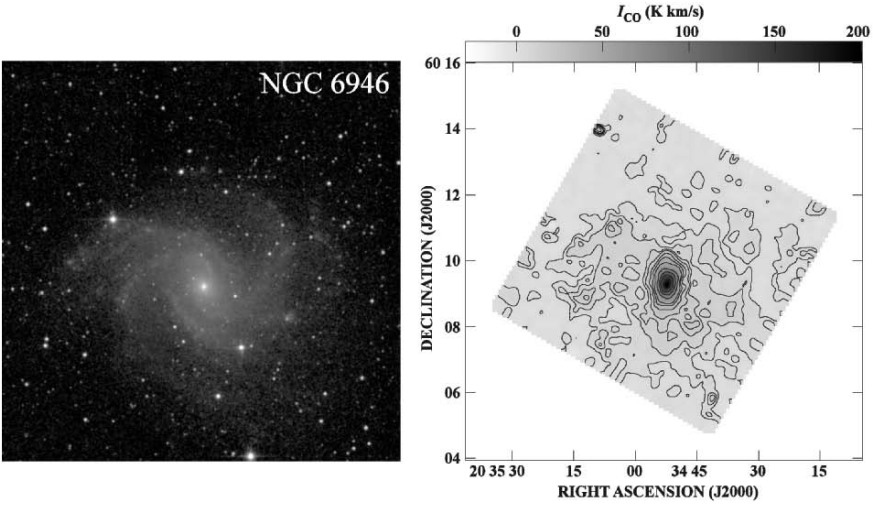

Fig. 5. (left) NIR image of NGC 6946 from [3]. (right) CO integrated intensity map of NGC 6946.

of the bar-ends than the outer region. For some extreme cases, there is a secondary peak near the radius of the bar length. The same trends are seen in our maps. Our data supports the facts that the molecular gas distribution in barred spiral galaxies has distinctive features compared with non-barred spirals.

Using our survey data, [8] investigated environmental effects on the gaseous disks of the Virgo spiral galaxies. [9] derived the pattern speed of the spiral structure of IC 342.

5 Influence of Bar on Distribution of Molecular Gas

5.1 Central Concentration of Molecular Gas

We investigated the degree of central concentration of molecular gas in our sample galaxies. Difference from the previous works by [6] and [7] is that we normalize the areas where we derive molecular gas mass with the size of galaxies. This is important because if we adopt a fixed radius as the central region, there is a possibility that the dependence on the galaxy size appears. Furthermore, it makes it possible to make more detail comparisons. In order to show the role of bars clearer, we compare the accumulations of molecular gas within and from outside of bar region using two indicators. The definition of the indicators, $f_{\rm in}$ and $f_{\rm out}$, are as follows.

$$f_{\rm in} = \frac{M_{\rm H_2}(R_{\rm K20}/8)}{M_{\rm H_2}(R_{\rm K20}/2)} \tag{1}$$

$$f_{\rm out} = \frac{M_{\rm H_2}(R_{\rm K20}/2)}{M_{\rm H_2}(R_{\rm K20})}, \tag{2}$$

where $M_{\rm H_2}(R)$ is molecular gas mass within a radius R and $R_{\rm K20}$ is the radius at the 20 mag arcsec^{-2} in the K_S-band. We used the $R_{\rm K20}$ from the 2MASS Large Galaxy Atlas [3]. We measured the relative bar lengths to $R_{\rm K20}$ of 18 galaxies and found that most of them (17/18) are less than $R_{\rm K20}/2$. Therefore, we selected $R_{\rm K20}/2$ to cover bar region.

Figure 6a shows the distribution of $f_{\rm in}$ in barred (SAB+SB) and non-barred spirals (SA). The averages of $f_{\rm in}$ for non-barred and barred spirals are 0.13 ± 0.03 and 0.20 ± 0.08, respectively. Thus, barred spirals have higher degree of the central concentration and larger dispersion than non-barred spirals. This result is consistent with the previous works by [6] and [7].

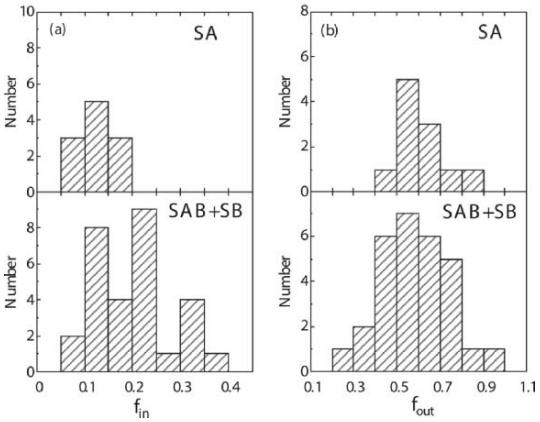

Fig. 6. Histgrams of (a) $f_{\rm in}$ and (b) $f_{\rm out}$ for SA and SAB+SB galaxies.

Our data that cover wide area in the galactic discs are useful to investigate the influence of bars on outside of the bar region. Figure 6b shows the distribution of $f_{\rm out}$ in barred and non-barred spirals. Similar distributions of $f_{\rm out}$ are seen for both groups. The averages of $f_{\rm out}$ of non-barred and barred spirals are 0.60 ± 0.12 and 0.59 ± 0.16, respectively. This result implies that the degree of the gas concentration toward the region within radial distances of the order of the bar is comparable in barred and non-barred spirals and that bars play a little role at larger spatial scales than bars on the disks, while they are efficient in driving molecular gas toward the galactic center. This result seems to be reasonable, since transformation of angular momentum of molecular gas occurs in the bar region. With these results, the characteristic features of the radial distribution of barred spirals can also be explained. Namely, because of the gas flow, the central surface density increases and the radial distribution becomes shallow within the bar region, while the distribution out of the bar is similar to that in non-barred spirals.

We estimated the mass of the molecular gas transported by the bar toward the central region ($R < R_{\rm K20}/8$), although it depends on the size of a galaxy and the total mass of molecular gas. Using the average of $f_{\rm in}$ of SA (0.13), we assume that $M_{\rm H_2}(R_{\rm K20}/8)$ is $0.13 \times M_{\rm H_2}(R_{\rm K20}/2)$ if a galaxy does not have a bar. Then, we regard the excess of the observed $M_{\rm H_2}(R_{\rm K20}/8)$ of barred galaxies from the estimation for non-barred as the transported gas by the bar. For galaxies whose $f_{\rm in}$ is larger than

0.16 (the average of SA plus 1σ), the derived mass is in the range of $6.9 \times 10^6 M_\odot$ to $2.3 \times 10^8 M_\odot$ and the average is $1.1 \times 10^8 M_\odot$. It is difficult to estimate the amount of the gas consumed by star formation until now, since star formation rate changes depending on the amounts of molecular gas. If, however, we assume that a certain fraction of molecular gas is consumed by star formation regardless whether barred or non-barred, the proportion of the transported gas to the observed $M_{\rm H_2}(R_{\rm K20}/8)$ is not altered by them. The proportion is 0.36 to 0.65, and the average is 0.49. Therefore, about half of the molecular gas in the central region ($R < R_{\rm K20}/8$) may have been transported by the bar in these galaxies.

5.2 Correlation Between Central Concentration and Bar Strength

If bars accumulate molecular gas toward the center, it is expected that properties of the bars, especially the bar strength, correlate with the degree of central concentration of the molecular gas. Figure 7 shows the correlation between the bar strength and the degree of central concentration ($f_{\rm in}$), where the bar strengths Q_H were adopted from [10]. 19 galaxies in our sample are included in their sample. They are plotted in Figure 7. It is apparent that galaxies with stronger bar have higher central concentration. The correlation coefficient is 0.69. This correlation can be naturally understood, since strong bars with strong non-axisymmetric forces accumulate molecular gas more efficiently toward the central region. Since, however, sample number is still small, it is not conclusive. Note that the figure indicates that the large dispersion of $f_{\rm in}$ of barred spirals (SAB+SB) shown in Figure 6a is caused by the variation of the bar strength.

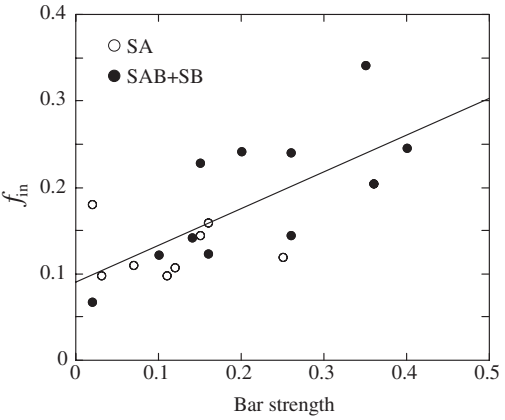

Fig. 7. Comparison of $f_{\rm in}$ with bar strength which is Q_H in [10]. Open and solid circles indicate SA and SAB+SB galaxies, respectively. The solid line is the best fit to the data.

It is still an open question whether bars are short-lived due to destruction by mass transport toward the center or not. Our finding of the correlation between the bar strength and the degree of central concentration seems to support the long-lived

bars, although it is not direct evidence. Such correlation may be hardly seen if bars are dissolved by the gas accumulation and short-lived, since the central concentration weakens the bar strength. If bars are destroyed in 1–2 Gyr ([11]), bars must be reformed to maintain the constant fraction of barred spirals with time. In that case, the bar strength oscillates because of its destruction and reformation, while the central concentration grows with time ([12]). As a result, the correlation between the bar strength and the central concentration dilutes. Therefore, our results seem to be consistent with long-lived bars rather than short-lived ones which are destroyed by gas accumulation toward the center many times in the Hubble time.

6 Conclusion

We made a CO(1–0) mapping survey of 40 nearby spiral galaxies with the Nobeyama 45-m telescope. Using these data we have compared the distribution of molecular gas in barred and non-barred spirals and investigated the influence of the bar. We confirmed that the degree of the central concentration of molecular gas within the radial distances of the order of a bar length ($f_{\rm in}$) in barred spirals is significantly higher than that in non-barred spirals as shown by [6] and [7]. This is contrast with the degree of the concentration of the molecular gas within the radial distances of the order of the bar ($f_{\rm out}$), which is similar for both barred and non-barred spirals. This implies that the bars appear to be efficient in driving gas that lies within their radial scales toward the center of the host galaxies, but that they play quite a smaller role at larger spatial scales on the disks. The accumulated gas by bars accounts for about half of molecular gas within the central region. We also found a correlation between the degree of central concentration of molecular gas, $f_{\rm in}$, and the bar strength. Galaxies with stronger bars tend to have higher central concentrations. The result indicates that stronger bar accumulate molecular gas toward the center more efficiently. The correlation seems to be consistent with long-lived bars rather than short-lived ones which are destroyed by the gas accumulation toward the center many times in the Hubble time.

References

1. K. Sunada, C. Yamaguchi, N. Nakai et al: SPIE 4015, 237 (2000)
2. N. Kuno, N. Sato, H. Nakanishi et al: submitted to PASJ (2006)
3. T.H. Jarrett, T. Chester, R. Cutri: AJ 125, 525 (2003)
4. N. Nakai: PASJ 44, L27 (1992)
5. K. Nishiyama, N. Nakai, N. Kuno: PASJ 53, 757 (2001)
6. K. Sakamoto, S.K. Okumura, S. Ishizuki: ApJ 525, 691 (1999)
7. K. Sheth, S.N. Vogel, M.W. Regan: ApJ 632, 217 (2005)
8. H. Nakanishi, N. Kuno, Y. Sofue et al: ApJ in press (2006)
9. N. Sato: PhD thesis, Hokkaido University (2006)
10. E. Laurikainen, H. Salo: MNRAS 337, 1118 2002
11. F. Bournaud, F. Combes, B. Semelin: MNRAS 364, L18 (2005)
12. F. Bournaud, F. Combes: A&A 392, 83 (2002)

26

CO-Line Rotation Curves, Deep Potential of Massive Cores, and High-density Molecular Nuclei

Yoshiaki Sofue

Institute of Astronomy, University of Tokyo, Mitaka 181-0015, Tokyo Japan
sofue@ioa.s.u-tokyo.ac.jp

Summary. We review observational studies of central rotation curves of spiral galaxies using the Nobeyama mm-wave interferometer in the CO 2.6-mm line emission. The observed high-accuracy rotation curves show universal characteristics: RCs rise steeply in the nuclei, or they start at finite speed, and are flat toward the galaxy edges. Calculated mass distributions are similar to each other: spiral galaxies generally have a massive core of $\sim 10^9 M_\odot$ in the central 100 pc, bulge, disk and a dark halo. We found extremely high-density, single-peaked molecular gas nuclei in many galaxies, which are embedded in deep gravitational potential of the massive core. Although the molecular nuclei is as dense as that of a giant molecular cloud, the gas is kept gravitationally stable because of the high-velocity rotation.

1 Introduction

Mass distributions in the disk and massive halos of spiral galaxies have been derived by rotation curves[1]. However,, the mass structure within bulge and that in the circum-nuclear regions are not well investigated, mainly because of the lack of accurate rotation curves in the central hundred parsecs.

In order to obtain central rotation curves, we need high spatial resolution as well as particular spectral lines that are not contaminated by the bulge light and interstellar extinction. The CO line emission is ideal for this purpose: (1) the CO line is transparent from interstellar dust extinction; (2) CO line is strongest in the central 1 kpc because of high molecular gas concentration; (3) the intrinsic line width is narrow because of low temperature and low velocity dispersion of molecular gas, and hence, radial velocities reflect rotation of the disk better than optical lines emitted by higher-temperature components; (4) high angular resolution is achieved by using mm-wave interferometers; (5) high velocity resolution is achieved by molecular line spectroscopy; and (6) high sensitivity is obtained by using large-aperture antennae.

High sensitivity interferometer CO-line surveys have been, thus, obtained by using OVRO, BIMA, PdB, and Nobeyama mm-wave Arrays [2, 3, 4, 5]. We have performed a CO ($J = 1 - 0$) line survey of Virgo and nearby spirals using the

Nobeyama mm-wave Array (NMA) in order to obtain high-accuracy central rotation curves[6, 7, 8, 9, 10].

2 Rotation Curves and Universal Mass Distribution

We observed fifteen Virgo spirals of normal Sb and Sc types. The reasons why we chose the Virgo galaxies are: that (a) the distance is well determined from Cepheid calibration to be 16.1 Mpc[11]; that (b) galaxies with a variety of types are available at the same distance, (c) a wealth of data sets in other wave ranges are available from the literature, and that (d) Virgo galaxies are visible from ALMA for a more detailed studies in the future based on the present data will be possible.

2.1 Iteration Method

In order to obtain accurate rotation curves, we applied the iteration method, which was developed for deriving RCs as accurate as possible from observed data, so that resultant RCs can reproduce observed PV diagrams, as illustrated in figure 1[12, 7]. Some obtained examples for the Virgo galaxies are shown in figure 2.

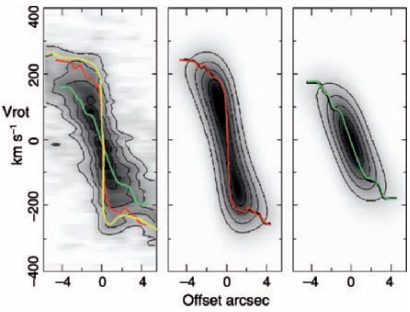

Fig. 1. Iteration method to derive a rotation curves from position-velocity diagram.

2.2 Rotation Curves

The obtained rotation curves of the Virgo galaxies are shown in figure 3a. All RCs have the same characteristics: the rotation speed increases very steeply within a few tens of parsecs of the nuclei, or more appropriately, the rotation velocity starts from a finite value from the nucleus. Then, the rotation velocity remains almost constant till the edges of galaxy disks. This characteristic is commonly observed for nearby spiral galaxies with high-accuracy rotation curves (figure 3b).

As the central rotation curves gets more and more precisely determined such as by using high-resolution interferometers as the present case, it is needed to display an RC in a way so that its nuclear behavior is more appropriately represented. This is particularly crucial for studying the mass structure inside bulges in connection

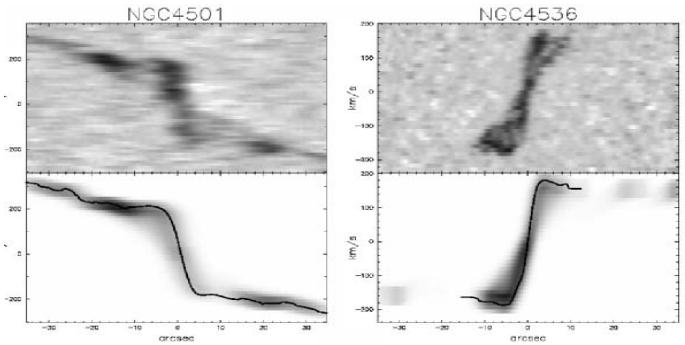

Fig. 2. (a) Observed PV diagrams for two Virgo spiral galaxies (top). (b) Derived rotation curves by iteration method, and reproduced PV diagrams by convolving with the observed intensity distribution (bottom).

to the central black holes. For this purpose, we proposed a logarithmic rotation curves (LRC), as shown in figure 3c. In this logarithmic display, the central high velocity rotation and its connection to the Keplerian law around the black holes are well traced. However, the number of galaxies with such LRC is still limited for observations of velocity structure within an arcsec or subarcsec. Deriving better logarithmic rotation curves and related study of mass distribution in the circum black hole region will be a subject for the future using higher resolution facilities like ALMA.

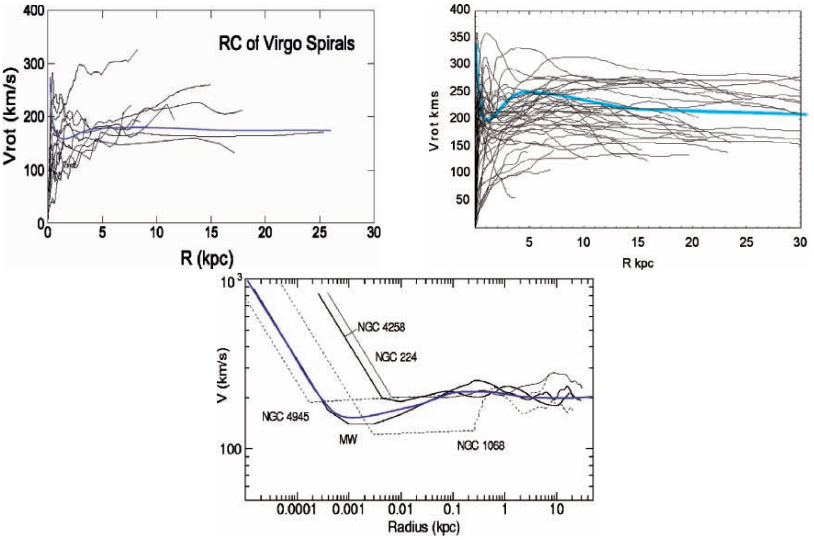

Fig. 3. (a) Rotation curves of Virgo (left) and (b) nearby (right) spiral galaxies. (c) Logarithmic RCs are shown in the bottom panel. Thick lines illustrate typical behavior of the rotation curves.

3 Universal Mass Distribution

Once rotation curves are obtained, we are able to calculate the mass distribution. We have calculated surface mass densities (SMD) by assuming two extreme cases: one for a spherical case, another for a thin disk[13]. Both sphere and disk assumptions give almost the same results within 50% difference except for outer regions, where the sphere assumption loses accuracy for the edge effect.

Figures 4a and 4b show calculated SMD distributions for the whole disk and inner regions of NGC 4536. The mass is highly concentrated in the central 100 pc region, where SMD reaches a value as high as $\sim 10^5 M_\odot \mathrm{pc}^{-2}$, composing a distinguished mass component of total mass $\sim 10^9 M_\odot$, which we call the central massive core. The core is then followed by a bulge component, obeying an exponentially decreasing function with a scale radius of about 0.5 kpc. The bulge is surrounded by an exponential disk of a scale radius of 5 kpc, which is followed by a largely extended dark halo with scale radius greater than 10 kpc. The thick lines schematically indicate these individual components.

The presently obtained mass distribution has been found to be common to all the galaxies including the Virgo as well as the nearby galaxy samples. Namely, the galactic mass distribution can be represented by a fundamental structure comprising a central black hole, a massive core, a bulge, a disk, and a dark halo. This structure appears to be universal, applying even for such irregular galaxy like the Large Magellanic Cloud (figure 5)[14].

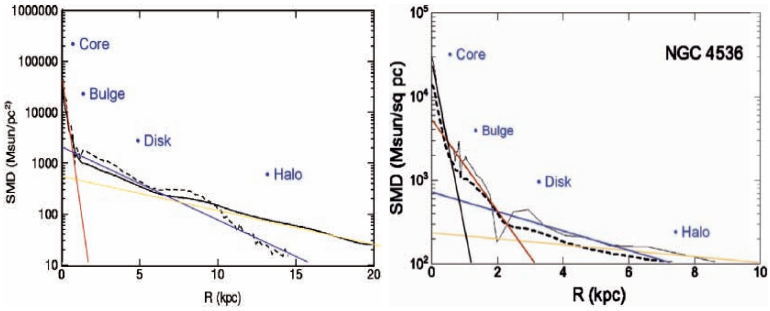

Fig. 4. Typical surface mass density distribution, as observed for the spiral galaxy NGC 4536. Note the existence of a massive core of 100 pc radius with extremely high mass density.

4 High-density Molecular Nuclei

High resolution CO data are useful not only for the dynamics and mass, but also for central interstellar physics such as the gas density distribution. One of the interesting facts we noticed was highly concentrated molecular peaks in the nuclei of several sample galaxies (figure 6).

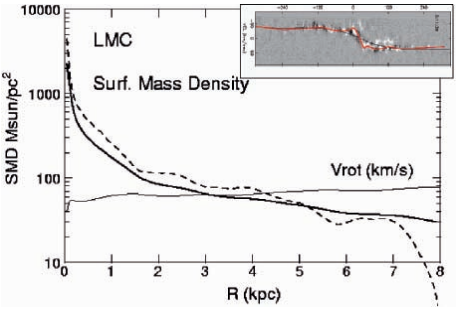

Fig. 5. Rotation curve and mass distribution in the Large Magellanic Cloud. Note the central mass concentration, where no optical counter part is visible: There appears to be a dark bulge.

5 Single Peaks

A high density molecular core was known for NGC 3079[15, 16], which has been thought to be a peculiar case in contrast to more general molecular rings and/or twin-peaks. However, we noticed that centrally peaked molecular peaks are not an exception, but is more generally found than twin peaks: We found five single peaks (NGC 4192, 4212, 4419, 4535, 4536), one semi-single peak (NGC 4501), one twin peaks (NGC 4303) and one ring (NGC 4569) among our fifteen Virgo spirals. Hence, single peaks are more common than twin peaks within the present resolution of ~ 100 pc.

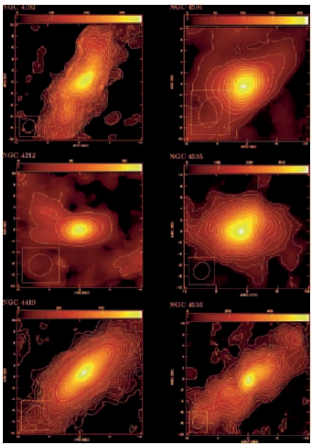

Fig. 6. CO intensity distributions for single peak galaxies at 4-5″ resolution.

In order to investigate the density distribution in and around the single peaks, we used uniform weighting for UV plane of interferometer data analysis to obtain higher resolution maps ($\sim$ 1″ resolution) as shown in figure 7. The central

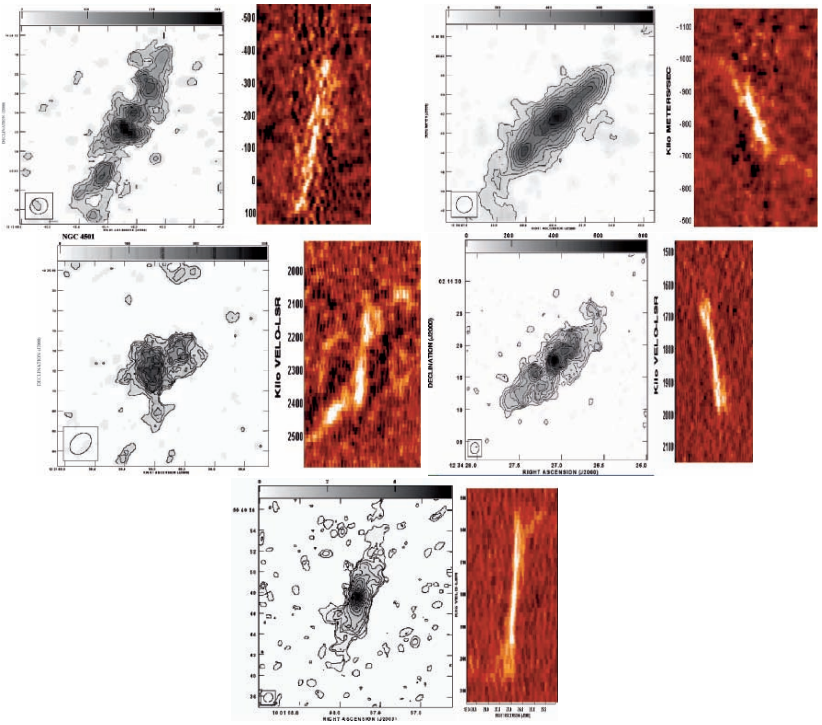

Fig. 7. CO intensity distributions and PV diagrams for the Virgo single peak galaxies NGC 4192, 4419, 4501 (semi-s-peak), 4536, and the typical single peak NGC 3079 at high resolution $\sim 1''$.

intensities indicate that the single peaks have face-on column densities of $N_{\rm H_2} \sim 10^{22} - 10^{23} {\rm H_2 cm^{-2}}$, or surface gas mass density $\Sigma_{\rm gas} \sim 10^2 - 10^3 M_\odot {\rm pc^{-2}}$. Here, we assumed a conversion factor of $1.0 \times 10^{20} {\rm H_2 cm^{-2}/K\ km\ s^{-1}}$. Since the gas is strongly peaked in the center, having very high density, we call these peaks molecular nuclei.

In figure 8 we plotted the CO intensity of the molecular nuclei against dynamical surface mass density (SMD), where triangles denote plots for high resolution analysis with uniform weighting (resolution $\sim 1''$) and circles for natural weighting (resolution $\sim 4''$). The solid line indicates a gas mass equal to 1.5% of the dynamical mass.

5.1 Stability

The high column density of the single peak molecular cores indicates a very high spatial gas density of $n \sim 10^3 - 10^4 {\rm H_2 cm^{-3}}$, if the thickness is several tens of parsecs as in the case of the Milky Way center. This density is comparable to giant molecular cloud. Now, a question arises why such high density gas is stable against gravitational instability for star formation.

Toomre's Q value is defined by $Q = \Sigma_{\rm c}/\Sigma$, where $\Sigma_{\rm c} = \kappa c/\pi G$, $\Sigma = SMD_{\rm gas}$, $\kappa \sim 2\Omega \sim 0.5 {\rm My^{-1}}$ is the epicyclic frequency with Ω being the rotational angular

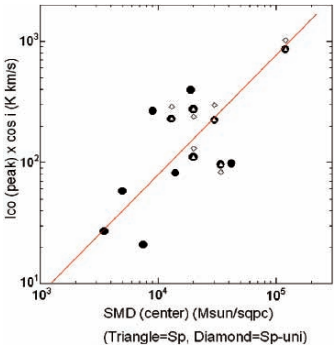

Fig. 8. CO intensity ($I_{\rm co}$) of molecular nuclei plotted against surface mass density (SMD). The solid line indicates the gas mass is 1.5 % of dynamical mass for a conversion factor of $1.0 \times 10^{20} {\rm H_2 cm^{-2}/K\ kms^{-1}}$.

velocity, and $c \sim 30{\rm km\ s^{-1}}$ is the velocity dispersion. Then, we have $\Sigma_{\rm c} = 5 \times 10^3 (V_{200} c_{30}/R_{100}) M_\odot {\rm pc^{-2}}$, where V_{200} is rotation velocity in unit of 200 km s^{-1}, and R_{100} is radius in unit of 100 pc, and c_{30} is velocity dispersion in unit of 30 km s -1. In the molecular cores, we obtain Q values as large $Q \sim 10 - 100$, and hence, the disk is gravitationally stable.

5.2 Formation of Molecular Nuclei

The molecular nuclei are thus gravitationally stable, and therefore, they stay in gas with secularly increasing density until the local gas density exceeds the threshold value $\Sigma_{\rm c}$. It is commonly accepted that the interstellar gas is accumulated by transferring its angular momentum to spiral arms and barred potentials through galactic shocks.

We may draw a possible scenario: The interstellar gas is gathered by two-armed shocked inflow along a bar, temporarily being accumulated on the bar end to form twin-peaked molecular concentration on a ring. Due to internal viscosity as well as to collisions with internal gas on other orbits, the gas is then gradually accumulated to the nuclear region. Since the gas disk is stable as discussed above for the large Q value, it sinks further into the circum-nuclear region to form a centrally peaked high-density molecular nucleus. The inflow will continue until the disk gets denser and gravitationally unstable, until starburst is triggered to exhaust the gas.

6 Summary

We have shown that rotation curves of Virgo and nearby normal spiral galaxies and the calculated mass distributions have the universal characteristics. The mass structure has the central black hole, massive core, bulge, disk, and dark halo. These components may not necessarily be distinguished from each other, but can be considered consist a continuous structure.

High resolution CO imaging revealed that many galaxies have single-peaked central gas concentration, which is more frequently observed than twin peaks and rings. The single peaks, which we called molecular nuclei, are shown to be gravitationally stable, and therefore, are long lived for them to grow to attain sufficiently high density.

Higher resolution mapping of the molecular nuclei and the dynamical structure from velocity information will be a subject to future molecular line observations using ALMA. The Virgo galaxies, well visible from ALMA, would be one of the most promising targets for the future rotation curve projects.

References

1. Sofue, Y. and Rubin, V.: ARAA 39, 137 (2001)
2. Schinnerer, E., Maciejewski, W., Scoville, N.Z., Moustakas, L.A.: ApJ, 575, 826 (2002)
3. Regan, M W., Thornley, M D., Helfer, T T., et al.: ApJ 561, 218(2001)
4. Schinnerer, E., Eckart, A., & Tacconi, L. J.: ApJ 524, L5 (1999)
5. Sakamoto, K., Okumura, S. K., Ishizuki, S., and Scoville, N. Z.: ApJS 124, 403 (1999)
6. Sofue, Y., Koda, J., Nakanishi, H., et al.: PASJ 55,17 (2003)
7. Sofue, Y., Koda, J., Nakanishi, H., Onodera, S.: PASJ 55, 59 (2003)
8. Nakanishi, H., et al.: PASJ 57, 965 (2006)
9. Onodera, S. et al.: PASJ 56, 439 (2004)
10. Koda, J. and Sofue, Y.: PASJ 58, 299 (2006)
11. Ferrarese, L., Freedman, W. L., Hill, R. J., et al.: ApJ. 464, 568 (1996)
12. Takamiya, T, and Sofue, Y.: ApJL 576, L15 (2002)
13. Takamiya, T, and Sofue, Y.: ApJ 534, 670 (2000)
14. Sofue, Y.: PASJ 51, 445 (1999)
15. Sofue, Y., Koda, J., Kohno, K., et al.: ApJL 547, L115 (2001)
16. Koda, K., Sofue, Y., Kohno, K., et al.: ApJ 573, 105 (2002)

27

Gas Kinematics from the Center to the Outer Disk

Eva Schinnerer[1]

MPI for Astronomy, Königstuhl 17, 69117 Heidelberg, Germany schinner@mpia.de

New high resolution sub-arcsecond observations of the molecular gas in the central 300 pc of the two late-type spiral galaxies NGC 6946 and IC 342 are presented. In both galaxies there is evidence for gas inflow in the central 100 pc. While the inflow in NGC 6946 is very likely due to a small-scale secondary bar, it appears that inflow in IC 342 is associated to a density wave driven by the large-scale bar. Despite these differences, the analysis of the gas kinematics in both galaxies strongly suggests that the central gas reservoir can be replenished, thus providing the fuel for repeated massive star formation.

In order to study the gas kinematics from the very nucleus to the outskirts of the galactic disk itself, the HI-NUGA survey was established. The design and aim of this HI survey conducted at the VLA are described and preliminary results are presented.

1 Introduction

A large fraction of nearby spiral galaxies experience intense star formation within a few hundred parsec from their nuclei. Observations with the Hubble Space Telescope (HST) at both optical and near-infrared wavelengths (e.g. Böker et al. 1999a, Carollo et al. 1998) have revealed that a compact ($\sim$ few pc diameter), photometrically distinct star cluster is often present at the photo-center of spiral galaxies of all Hubble types. Surprisingly, most of the nuclear star clusters studied in detail so far turn out to be young. Thus these galaxies must recently have had significant inflow of molecular gas into their central regions in order to trigger the formation of these young clusters. To form a nuclear stellar cluster, which typically has a mass around 10^6 $M_\odot$, at least 10^7 $M_\odot$ of molecular gas must be available within the central few parsecs.

The exact mechanism of how the molecular gas is transported to scales of only a few parsec is not very well understood. Likely, similar mechanisms present at large-scales such as bars, spiral density waves are also at work to produce the high (molecular) gas density required to enable the intense nuclear star formation. In order to test these assumptions sub-arcsecond resolution observations of the (molecular) gas in the central 300 pc are required. Such observations have only recently

become possible with mm-interferometers such as the IRAM Plateau de Bure interferometer or the former Owens Valley Radio Observatory mm-interferometer.

Likelywise, there has been no study so far trying to link the observed nuclear kinematics to the kinematics seen in the outer disk. It is expected that there is a close link between the two; e.g. large-scale bars have been found to be effective in fueling the central activity in spiral galaxies (e.g. Sakamoto et al. 1999, Sheth et al. 2005). Another open issue is the importance of the galactic environmnent for the nuclear activity.

2 Feeding of Nuclear Clusters

2.1 The Late Type Spiral Galaxy IC 342

IC 342 is a prime example of a late-type spiral galaxy with a young luminous nuclear cluster that formed in a short-lived burst about 60 Myr ago (Böker et al. 1997, 1999b). The central region of IC 342 has been mapped in the past in several molecular transitions on scales of a few arcseconds (e.g. Meier & Turner 2001). These maps show that the molecular gas is located in two spiral arms that show strong streaming motions. The spiral arms join to form a ring of about 10" diameter that is the site of massive star formation.

1.2" resolution OVRO observations of the ^{12}CO(2-1) line emission in the central 300 pc of the late-type spiral galaxy IC 342 detected a molecular gas disk (Fig. 1) that coincides with the luminous young ($\sim$ 60 Myr) stellar cluster in the nucleus of IC 342 (Schinnerer, Böker, & Meier 2003). This nuclear CO disk contains a molecular gas mass of M $\sim 2 \times 10^5$ M$_\odot$ and appeared to be connected via two faint CO bridges to the well-known 100 pc diameter circumnuclear gas ring. Both the morphology and the kinematics of the CO gas indicate ongoing inflow of molecular gas into the central few parsecs of IC 342 with an inferred gas inflow rate between 0.003 and 0.14 M$_\odot$ yr^{-1}. Inflow rates of this order can support repetitive star formation events in the nucleus of IC 342 on timescales much smaller than a Hubble time.

Our new 0.5" resolution PdBI CO(2-1) data resolves the nuclear CO disk into thin gas lanes which coincide with the dust lanes seen in optical HST images (Fig. 1; Schinnerer et al., in prep.). In addition, the 'clumpiness' of the molecular gas in the spiral arms becomes more apparent. The dense gas as seen in its HCN(1-0) line emission at $\sim$ 1" resolution has a different distribution than the bulk of the molecular gas traced by the CO(2-1) line: 1) It is significantly stronger at the nucleus, and 2) the southern spiral arm is directly connected to the nucleus. This suggests that new dense gas is currently accumulating at the nucleus. The derived HCN(1-0)/CO(2-1) ratio of $\sim$ 0.3 is at the higher end of ratios observed for star forming nuclei.

2.2 The Nuclear Starburst in NGC 6946

NGC 6946 is a prime example for a late-type spiral galaxy with a prominent nuclear starburst. The starburst history of the inner 8" ($\sim$ 215 pc) can be described by two recent events (about 5 Myrs and 15 Myrs ago) that each converted about (5-10) $\times$ 10^7 M$_\odot$ of molecular gas mass into stars (Engelbracht et al. 1996). These authors

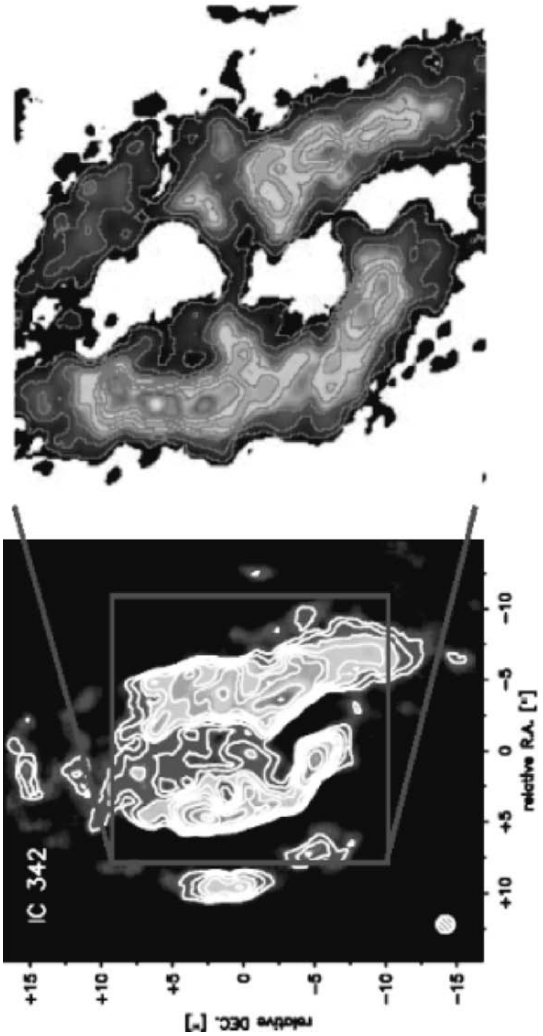

Fig. 1. Intensity maps of the CO(2-1) line emission at 1.2" (OVRO; left) and 0.5" (PdBI; right) resolution. The nuclear disk detected in the OVRO data is resolved into a thin gas lane in the PdBI data. The gas spiral arms break up into numerous giant molecular cloud complexes.

infer a high extinction of $A_V \sim 10$ towards the nuclear region which is surprising given the almost face-on geometry.

As one of the closest galaxies with intense nuclear star formation, NGC 6946 offers a unique opportunity to study the dynamics of its circumnuclear molecular gas disk. A stellar bar with a length of 3.3 kpc has been identified in NIR images. In addition, NGC 6946 harbors a small inner bar with an estimated major axis diameter of $\sim$ 200 pc which is most clearly visible in the NIR (Elmegreen et al. 1998).

PdBI 0.6" (1") resolution observations of the 12CO(2-1) [(1-0)] line emission resolve for the first time the molecular gas distribution in the central 300 pc (Fig. 2) in a spiral with a large concentration of molecular gas $M_{H_2} \sim 1.6 \times 10^7$ $M_\odot$ within the inner 60 pc (Schinnerer et al. 2006). Both the distribution of the molecular gas as well as its kinematics can be well explained by the influence of an inner stellar bar of about 400 pc length. A qualitative model of the expected gas flow shows that streaming motions along the leading sides of this bar are a plausible explanation for the high nuclear gas density. Thus, NGC 6946 is a prime example of molecular gas kinematics being driven by a small-scale, secondary stellar bar.

The nuclear gas spiral was observed in January 2006 using the new PdBI baselines of 760m (Schinnerer et al., sub.). Further analysis using our new 0.35" (9pc) resolution data of the ^{12}CO(2-1) line reveals that the distribution of the emission is very reminiscent of the so-called 'twin peaks' structure (Fig. 2) seen in lower resolution CO(1-0) images of barred galaxies (Kenney et al. 1992) and associated with gas accumulation at the ILR. The kinematics in the central 3" $\times$ 3" are fairly complex showing double line profiles. The decomposition shows, however, that most of the emission is consistent with circular motion. Taken all together this suggests that the inner bar is driving the gas kinematics even in the central 50pc.

3 Linking the Nuclear and the Outer Disk Kinematics

Models of the gas flow in the disks of galaxies suggest a close link between the nuclear gas kinematics and the kinematics in the outer disk (see review by Combes 2003). For example, large-scale stellar bars can drive inflow of molecular gas into the central kiloparsec of spiral galaxies (Sakamoto et al. 1999, Sheth et al. 2005). However, the link between the gas kinematics on the 100 pc to the central parsec, i.e. the black hole, is less clear. As already pointed out, several models have been suggested ranging from dynamical modes with m=1, m=2 to warped disks. The large wealth of nuclear dynamical modes observed in CO line emission of the IRAM NUGA sources (NUclei of GAlaxies; Garcia-Burillo et al. 2003) is adding to this confusing view. In order to identify the main driving mechanism(s) for nuclear fueling it is essential to connect the observed nuclear kinematics in CO line emission to the observed kinematics of the large-scale disk traced by the Hydrogen line of the atomic gas.

To-date no HI survey exists that systematically studies the properties of the atomic gas disk in AGN host galaxies, neither on large or small scales. Recently, two complementary programs using high quality HI data from the VLA were initiated: HI-NUGA and VHIKINGS (VLA Hydrogen Imaging and Kinematics of INactive Galaxies and Seyferts Survey; Mundell et al., in prep.). Both surveys tackle two important issues about the relation of the properties of the large gas disk to the presence of an AGN and are conducted in close coordination.

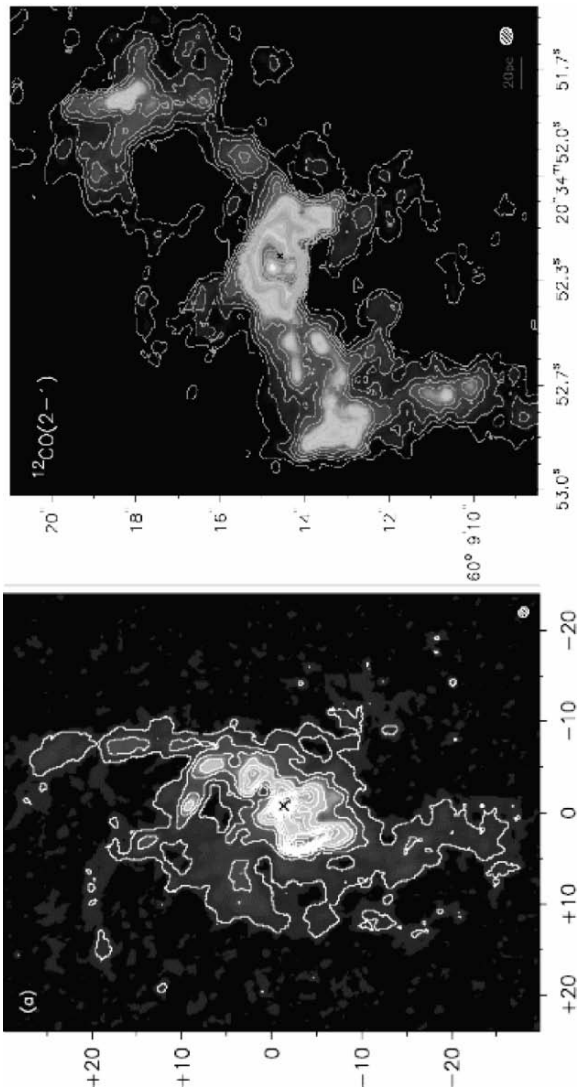

Fig. 2. PdBI intensity maps of the CO(1-0) line emission (left) at 1" resolution. The central gas concentration is resolved into a S-shaped spiral structure which is reminiscent of gas lanes observed along large-scale stellar bars. New PdBI intensity map of the CO(2-1) line emission at ~ 0.35" resolution (right). The nuclear clump is resolved into a 'twin peak' distribution which can be interpreted as barely resolved spirals associated with an inner Lindblad resonance of a stellar bar.

The HI-NUGA survey complements the CO-data of the NUGA project for 16 galaxies to link for the first time the gas kinematics from the outskirts of galaxy disks to the very center covering spatial scales from a few tens of parsec to several tens of kiloparsec. The study is designed to test whether gas instabilities on different scales can decouple or not, and to probe if gas inflow occurs across the entire disk as suggested by dynamical models. The ultimate aim is to tie the central gas kinematics to the overall disk kinematics.

The properties of the atomic gas of the sample were derived and are currently been compared to optical properties (Haan et al., in prep.). The HI morphology displays a large variety of rings, spiral arms, and central concentrations (see Fig. 3). The comparison of optical and HI radial profiles reveals often large discrepancies between the gaseous and stellar distributions within the disk. In addition, the gaseous disks are usually larger than the optical ones with a mean ratio of R_{HI}/R_{25}=1.2. The study of the HI environment yields that 4 galaxies are surrounded by satellites and 8 galaxies exhibit disturbed outer HI disks, likely caused by ram pressure stripping and/or minor mergers (e.g. the interacting system NGC5953/43). The kinematic analysis (Haan et al., in prep.) including rotation curves and kinematic parameters (systemic velocity, inclination, position angle, dynamical mass) is under-way.

The HI-NUGA survey is designed to search for a link between nuclear activity and HI environment, to estimate the gas inflow using gravity torques and to develop a detailed dynamical model of the gas flow in representative sources.

4 Outlook

Observations of the molecular gas on scales of a few parsec provide an unprecedented view of the gas kinematics in the centers of nearby galaxies. As the analysis of the CO data of IC 342 and NGC 6946 have shown, such high-resolution observations are paramount to understand the fueling process associated with nuclear activity (AGN and/or starburst). The Atacama Large Millimeter Array (ALMA) will be essential to conduct similar studies of nearby galaxies in the future.

The combined gas kinematics probed by the CO and HI line emission can be compared to dynamical models over several orders of spatial scales, and thus they will provide an important test of these models.

References

1. Böker, T., Förster-Schreiber, N. M., & Genzel, R. 1997, A.J., 114
2. Böker, T., et al. 1999a, Ap.J.S., 124, 95
3. Böker, T., van der Marel, R. P., & Vacca, W. D. 1999b, A.J., 118, 831
4. Carollo, C. M., Stiavelli, M., & Mack, J. 1998, A.J., 116, 68
5. Combes, F. 2003, ASP Conf. Ser. 290: Active Galactic Nuclei: From Central Engine to Host Galaxy, 290, 411
6. Elmegreen, D. M., Chromey, F. R., & Santos, M. 1998, A.J., 116, 1221
7. Engelbracht, C. W., Rieke, M. J., Rieke, G. H., & Latter, W. B. 1996, Ap.J., 467, 227
8. García-Burillo, S., et al. 2003, A&A, 407, 485

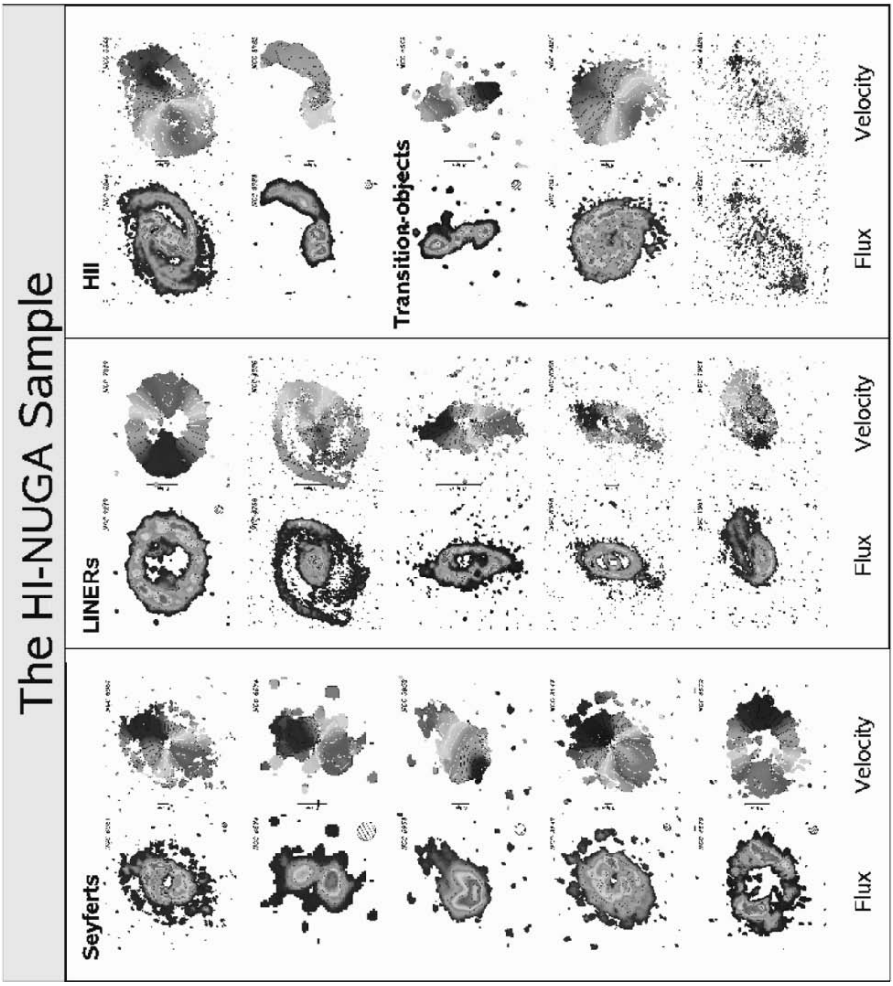

Fig. 3. For the detailed HI study (Haan et al., in prep.), a total of 16 nearby AGN galaxies were selected covering a wide range in nuclear activity (Seyfert, LINERS, HII and transition objects). They were observed in their 21 cm line emission of neutral HI gas using the NRAO Very Large Array (VLA) interferometer in its C- and D-array configuration (20" angular and 5.2 $\mathrm{km\,s^{-1}}$ spectral resolution). All galaxies in our sample are spiral galaxies ranging in Hubble type from Sa to Sbc. For all galaxies high quality mm-interferometric CO data from the NUGA project as well as optical/NIR imaging data are available. The figure shows the intensity maps (left column) and velocity fields (right column) of our HI-NUGA sample sorted by AGN type.

9. Meier, D. S. & Turner, J. L. 2001, Ap.J., 551, 687
10. Sakamoto, K., Okumura, S. K., Ishizuki, S., & Scoville, N. Z. 1999, Ap.J., 525, 691
11. Schinnerer, E., Böker, T., & Meier, D. S. 2003, Ap.J. Letters, 591, L115
12. Schinnerer, E., Böker, T., Emsellem, E., & Lisenfeld, U. 2006, Ap.J., 649, 181
13. Sheth, K., Vogel, S. N., Regan, M. W., Thornley, M. D., & Teuben, P. J. 2005, Ap.J., 632, 217

Osamu Kameya, Eva Schinnerer, Fabian Walter in the receiver room of VERA.

28

Gas Flows and Bars in Galaxies

Françoise Combes

LERMA, Observatoire de Paris, 61 Av. de l'Observatoire, F-75014, Paris, France
francoise.combes@obspm.fr

Summary. Dynamical evolution of spiral galaxies is strongly dependent on non-axisymmetric patterns that develop from gravitational instabilities, either spontaneously or externally triggered. Some evolutionary sequences are described through which a galaxy could possibly concentrate mass and build bulges, how external gas accretion from cosmic filaments could be funneled to the galaxy disks, and intermittently driven to the galaxy center, to form nuclear starbursts and fuel an active nucleus. The frequency of both bars and lopsidedness can be used to constrain the gas accretion rate.

1 Evidence of Gas Flow, Central Star Formation and Pseudo-bulge Formation

1.1 Molecular Gas in Barred Galaxies

Sakamoto et al (1999) from a sample of 20 nearby galaxies were the first to notice that barred galaxies had a larger gas concentration in the central kiloparsec than unbarred galaxies, confirming that bar instabilities were able to drive gas inflow towards the center. Sheth et al (2005) from a sample of about 45 galaxies from BIMA-SONG confirm the larger CO concentration for barred galaxies, and find that the nuclear molecular gas is 4 times more abundant in early-types than late-types, suggesting the gas inflow are larger, possibly due to the existence of inner Lindblad resonances (ILR), expected when the mass is concentrated due to bulges. Jogee et al (2005) further note that barred galaxies have a large circumnuclear surface densities in molecules, and this triggers the nuclear starbursts currently observed there. The observation of non-starbursting gas-rich barred galaxies allows to distinguish several phases of evolution: the first phase reveals gas inflow, non circular motions (since the gas is partly in the bar), and the gas is accumulating at the outer ILR, there is no starburst. In the end-phase, the gas has been driven down to the inner ILR, runs in nearly circular orbits, and the galaxy experiences a nuclear starburst of 3-11 $M_\odot$/yr. Molecular gas surface densities reach up to 500-3500 $M_\odot/pc^2$, or 10-30% of dynamical mass in the center.

1.2 Star Formation in the Center of Spiral Galaxies

Recent work on star formation in the central kpc of galaxies has shown that galaxies with pseudo-bulges are more frequently the host of starbursts. Pseudo-bulges are components intermediate between spheroids and disks, in the sense of light distribution (Sersic index n between 1 and 2) of flattening and kinematics (more rotation than classical bulge, Kormendy & Kennicutt 2004). Fisher (2006) has recently made a star-formation study on a sample of 50 galaxies observed by Spitzer. Pseudo-bulges were identified on HST images from the presence of disky structure in the center, i.e. nuclear disks nuclear bars, and high ellipticity. The star formation was traced from the PAH emission at 8 micron wavelength. As shown in Fig 1, star formation inside 1.5 kpc is clearly larger in pseudo-bulge galaxies, and among them, central starbursts are preferentially in barred galaxies, then in galaxies with oval perturbations. Nuclear star formation in the form of Hα nuclear rings are also preferentially found in barred galaxies (Knapen 2005, and this meeting).

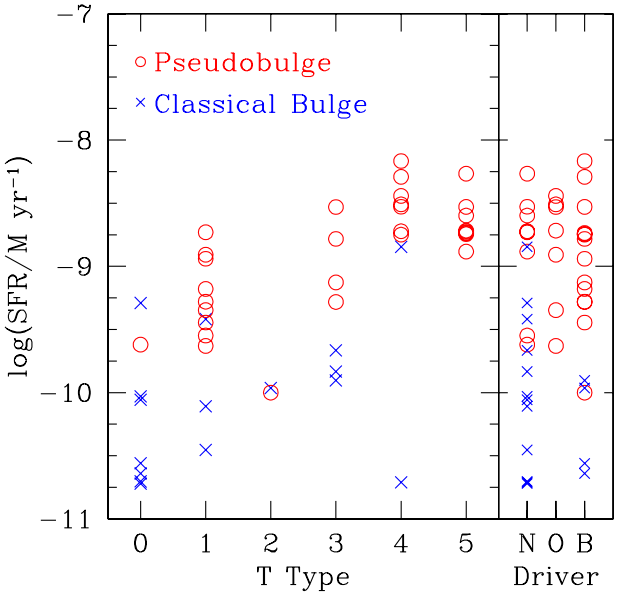

Fig. 1. Specific SFR of the central 1.5 kpc, for a sample of 50 galaxies, from Fisher (2006), as a function of morphological type (left), and as a function of secular driving mechanism (B=bar, O=oval, and N=neither bar no oval). Pseudo-bulge galaxies (red circles) have clearly larger central specific SFR than classical bulge ones (crosses).

Peeples & Martini (2006) study the relation between bar strength (in terms of Q_b) and circumnuclear dust. Dust is distributed preferentially in nuclear rings for barred galaxies. SB(r) galaxies are less strongly barred and have less dust structure than SB(s) galaxies. This can be understood as an evolutionary process, since rings are formed in a second phase in barred galaxies, where first a spiral structure forms.

1.3 Bar Length and Type, Ω_b and Dynamical Friction

In a recent study of about 140 galaxies, Erwin (2005) confirms that bars are longer in early-types than in late-type galaxies, both when normalized with the optical radius R_{25}, or with the exponential scale-length h (see Figure 2). The size of bars does not depend on their strength.

These observational results can be confronted to predictions from numerical models. The length of bars is tightly related to their pattern speed, since stellar orbits support the bar until its corotation only. In the presence of a large mass of dark matter inside the bar radius, bars should slow down through dynamical friction against the dark matter particles (Debattista & Sellwood 2000), and bars should then be too long and slow compared to observations. This puts constraints on the dark matter distribution in spiral galaxies, and favors maximal disks. But in some cases, the transfer of angular momentum to the dark halo can be minimized (Valenzuela & Klypin 2003).

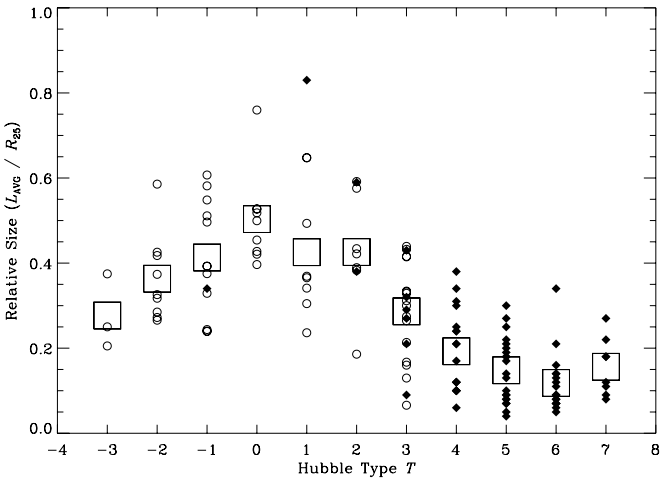

Fig. 2. Sizes of bars (deprojected) relative to their disc radius R_{25}, as a funciton of morphological type, from Erwin (2005). The various symbols correspond to various samples. Large boxes are mean values for each type.

The length of bars is interesting under the point of view of secular evolution, since it is predicted to vary along the successive evolution phases, and is then a tracer of the past history of the galaxy. Bars begin their life with a high pattern speed and a short length (as in late-types) and then slow down and increase their length, as in early-types. This simple scenario is slightly modified when bar destruction and reformation is taken into account: with gas accretion, new bars are generally shorter. They appear late-type just after gas accretion (Bournaud & Combes 2002). Tidal interactions on the contrary can produce longer bars (Holley-Bockelmann et al 2005), depending on mass and distance of the satellites.

In edge-on galaxies, the length of bars can be traced by the size of the peanut-shape. The maximum height of the peanut occurs at the z-resonance with the bar, a function of its pattern speed. When the bar slows down through angular momentum transfer with the halo, the radius of the resonance shifts outwards. Several peanut buckling can occur successively (Martinez-Valpuesta et al 2006).

2 Bar Destruction and Reformation

Along the secular evolution, bars are robust and long-lived features only in pure stellar disks. When gaseous disks are taken into account in numerical simulations, bars are observed to weaken and disappear (e.g. Friedli et al 1994, Bournaud & Combes 2002). This was long attributed to the building of a central mass concentration, due to the gas inflow towards the center (Hasan et al 1993). However, when the central mass concentration is considered alone, it does not destroy the bar (Shen & Sellwood 2004). The details of the evolution are now much better understood: gas is driven inwards by the bar torques. The gas angular momentum is taken up by the bar wave. The latter has a negative angular momentum, being contained inside its corotation (CR). Providing positive angular momentum to the wave is sufficient to weaken or destroy the bar, since the total gas angular momentum from CR to center is of the same order as the bar wave momentum (Bournaud et al 2005a).

Since it is not the central mass concentration which destroys the bar, it is relatively easy to reform a bar, after a bar episode is completed. Substantial gas accretion is required to replenish the disk, and to make it cold and again unstable to bar formation (Block et al 2002). Several bar episodes can then occur in a given galaxy, with a time scales of a few Gyr each, provided that the galaxy mass is doubled in 10 Gyr typically, which is compatible with cosmological accretion rates.

It is interesting to note that the angular momentum transfer mediated by the bar, redistributes the mass in galaxies and produces exponential light profiles, as observed in spiral galaxies. Recently, several exponential components have been identified in galaxy disks, separated by breaks in the density profiles (Pohlen 2002). These could be the consequence of the past activity of several bars along the secular evolution.

Secular evolution with continuous gas accretion can also trigger starbursts, and mimick galaxy interactions. Gas is accreted from CR onto the central regions only intermittently, when the bar is at its maximum strength. Gaseous nuclear disks are then formed in a short time-scale, and starbursts may be triggered. Repeating starbursts have been observed in some barred galaxies (cf Allard et al 2006). In the mean time, external gas continuously accreted accumulates in the outer parts, and can inflow to replenish the disk only when the bar has been weakened. Just after gas accretion, which is in general asymmetric, galaxies look peculiar: lopsidedness and warping structures can not only be due to galaxy-galaxy interactions but also to asymmetric mass accretion.

3 Gas Accretion and $m = 1$ Perturbations

The quantification of observed bar frequency from the near-infrared images of the OSU sample (Eskridge et al 2002) has been used to put constraints on the gas

accretion rate (Block et al 2002). The same can be done for the lopsided perturbations (or Fourier $m = 1$). This asymmetrical perturbation is very frequently observed in galaxies, even in the absence of any companion. Half of the HI profiles in sample of 1700 galaxies have been found asymmetric (Richter & Sancisi 1994), and these perturbations are even more frequent in late-type galaxies (Matthews et al 1998). Stellar disks also participate in those asymmetries (Zaritsky & Rix 1997). About 20% of galaxies have the normalized $m = 1$ Fourier coefficient in near-infrared surface density A1 larger than 0.2, and in about 2/3 of galaxies, an external mechanism is required to explain these asymmetries, that are above the expected amplitude of spontaneous internal perturbations.

The influence of companions however does not appear to be the solution: most lopsided galaxies are isolated (Wilcots & Prescott 2004), and when companions are seen, the A1 parameter is not correlated with the tidal index, computed from the mass ratio between the observed neighbours and the target, and inversely proportional to the cube of their distance. In any case, interactions cannot explain that A1 is higher in late-type galaxies (Bournaud et al 2005b). External gas accretion, which is likely to be asymmetric at a given epoch, is able to explain the asymmetries observed. Fig 3 illustrates the mechanism, with a comparison between an observed asymmetric case and a numerical simulation. Gas accretion can explain the long life-time of the perturbation, and consequently the high frequency of lopsidedness observed, while a minor merger for instance will produce asymmetries on a much shorter time-scale.

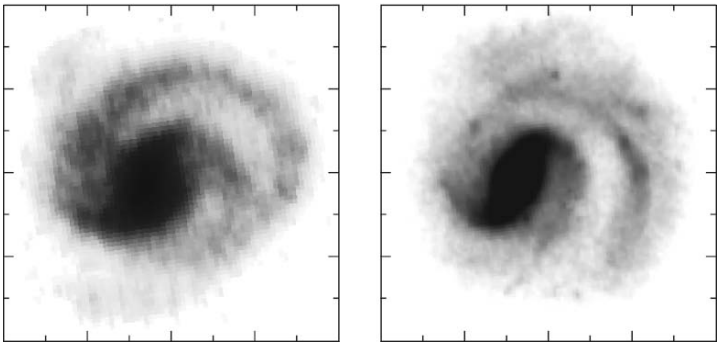

Fig. 3. Comparison between a lopsided isolated galaxy NGC 1637 (right: NIR map from the OSUBGS data, after deprojection), and a numerical simulation of asymmetrical gas accretion (left), producing a strong lopsidedness, from Bournaud et al (2005b). The gas accretion rate is of 6 $M_\odot$ yr^{-1}, and for a galactic mass of 10^{11} $M_\odot$ yr^{-1} correspond to doubling the mass of the galaxy in about one Hubble time.

References

1. Allard, E. L., Knapen, J. H., Peletier, R. F., Sarzi, M.: 2006 MNRAS in press (astro-ph/0606490)
2. Block D., Bournaud F., Combes F. et al : 2002 A&A 394, L35
3. Bournaud F., Combes F.: 2002, A&A 392, 83
4. Bournaud F., Combes F., Semelin B.: 2005a, MNRAS 364, L18
5. Bournaud, F., Combes, F., Jog, C. J., Puerari, I. : 2005b, A&A 438, 507
6. Debattista V.P., Sellwood J.: 2000, ApJ 543, 704
7. Erwin P.: 2005, MNRAS 364, 283
8. Eskridge, P. B., Frogel, J. A., Pogge, R. W. et al.: 2002 ApJS 143, 73
9. Fisher D.B.: 2006 ApJ 642, L17
10. Friedli, D., Benz, W., Kennicutt, R.: 1994 ApJ 430, L105
11. Hasan, H., Pfenniger, D., Norman, C.: 1993, ApJ 409, 91
12. Holley-Bockelmann, K., Weinberg, M., Katz, N.: 2005 MNRAS 363, 991
13. Jogee, S., Scoville, N., Kenney, J. D. P.: 2005, ApJ 630, 837
14. Knapen J.: 2005 A&A 429, 141
15. Kormendy J., Kennicutt R.: 2004, ARAA 42, 603
16. Martinez-Valpuesta, I., Shlosman, I., Heller, .: 2006, ApJ 637, 214
17. Matthews, L. D., van Driel, W., Gallagher, J. S.: 1998, AJ, 116, 2196
18. Peeples M., Martini P.: 2006, ApJ in press (astro-ph/0606460)
19. Pohlen M.: 2002, PhD Thesis, Ruhr-Universität, Bochum, Germany
20. Richter, O., Sancisi, R.: 1994, A&A, 290, 9
21. Sakamoto, K., Okumura, S. K., Ishizuki, S., Scoville, N. Z.: 1999, ApJ 525, 691
22. Shen J., Sellwood J.A.: 2004ApJ 604, 614
23. Sheth, K., Vogel, S. N., Regan, M. W. et al: 2005 ApJ 632, 217
24. Valenzuela O., Klypin A.: 2003, MNRAS 345, 406
25. Wilcots, E. M., Prescott, M. K. M.: 2004, AJ, 127, 1900
26. Zaritsky, D., Rix, H.-W.: 1997, ApJ, 477, 118

29

Molecular Gas in the Andromeda Galaxy: Properties of the Molecular Clouds

Sebastien Muller[1], M. Guélin[2], H. Ungerechts[3], L. Loinard[4], R. Lucas[2], and R. Wielebinski[5]

[1] Academia Sinica Institute of Astronomy and Astrophysics P.O. Box 23-141, Taipei, 106 Taiwan
[2] Institut de Radioastronomie Millimétrique, St Martin d'Hères, France
[3] Instituto de Radioastronomia Millimétrica, Granada, Spain
[4] Centro de Radioastronomiá y Astrofísica, UNAM, Morelia, Mexico
[5] Max-Planck-Institut für Radioastronomie, Bonn, Germany

The closest spiral galaxy, M31, is certainly a key target to study the properties of molecular clouds outside the Milky Way. In this contribution, we use the millimeter CO data obtained with the IRAM 30m telescope and Plateau de Bure interferometer to derive the properties of the GMCs in M31, with a special focus on their mass and on the CO to H_2 conversion factor.

1 IRAM CO Mapping of M31

The molecular disk of M31 has been mapped in the CO(1-0) line with the 30m telescope with unprecedent resolution (FWHM =23″ ∼ 90 pc) and sensitivity (∼30 mK / 1 MHz channel) (see Nieten et al. 2006). Because the big apparent angular size of M31, observations were carried out in an on-the-fly mode, accumulating some 1.7 million spectra during ∼ 500 h. In addition to this CO(1-0) mapping, several portions (hereafter called minimaps) of the arms have also been observed in the CO(2-1) line, with a narrower sampling, and an angular resolution of 12″ (∼ 45 pc).

The 30m CO(1-0) survey allows to trace the large scale distribution of the molecular gas, showing spiral arms and arm-like filaments. The CO arms appear much thinner than in HI and the arm/interarm contrast is also 3–5 times higher. At smaller scales, the arms are clumpy and can be decomposed into molecular complexes (∼ 50 – 100 pc).

To resolve these complexes into molecular clouds (∼ 10 pc), one need the angular resolution of interferometers. Using the Plateau de Bure interferometer (PdBI), we have so far observed 9 positions, selected from their morphology, special kinematics or location, with angular resolution 4″ – 0.8″ (15 – 3 pc) (see Neininger et al. 1998, 2001). We present here two of these fields (Fig.1): a compact narrow line-width complex (D153) located in the inner 6 kpc spiral arm, observed at an angular resolution of 0.8″ in the CO(2-1) line, and an isolated interarm complex at a galactocentric distance of 8 kpc.

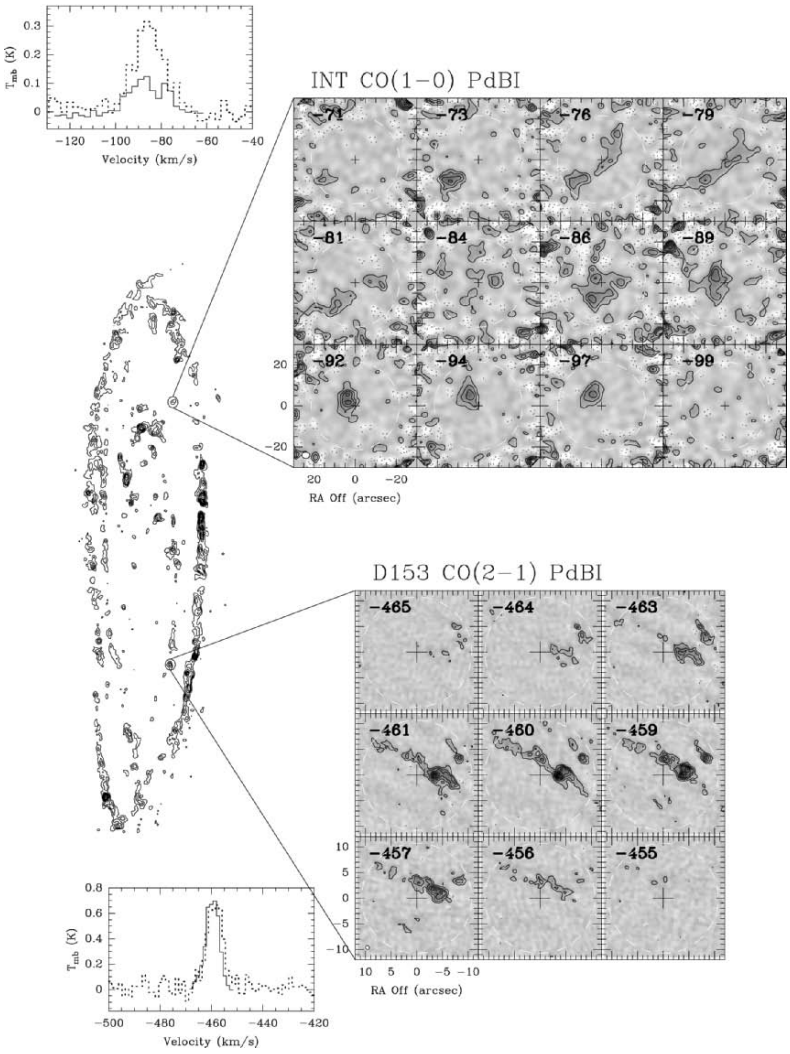

Fig. 1. Two molecular complexes in M31 mapped with the Plateau de Bure interferometer. The interarm complex INT is mapped in a 5-field mosaic (top right). The CO(2-1) emission of the cloud D153 is mapped with a beam resolution of ~ 0.8" (bottom right). The synthesized beam sizes are indicated in the bottom left corner of the channel maps and the dashed white circles show the PdBI primary beam FWHM. The location of the two fields is indicated on the CO(1-0) 30m map on the left. The PdBI maps were smoothed to the 30m beam and the resulting spectra, extracted at the central positions (crosses on the channel maps), are compared to that of the 30m (dotted line) on the left of the channel maps. Despite observations with a very extended configuration, the interferometer recovers all the emission for D153, showing that the CO emission is peaked and compact. In the case of the interarm complex, more than half the CO(1-0) emission was filtered out, indicating that it is more diffusely distributed.

We applied the Gaussclump algorithm (Stutzki & Gusten 1990, Kramer et al. 1998) to decompose the CO emission into 3D (position - position - velocity) gaussian structures. Adopting a threshold of 10σ for the peak signal-to-noise (to avoid fake clouds in the decomposition process), we ended up with a catalog of 389 complexes in the CO(1-0) 30m map. The cumulated mass of these decomposed complexes account for about half the total molecular gas mass (M_{tot} = 3.6 10^8 $M_\odot$) measured on the CO(1-0) 30m map. 47 complexes were decomposed in the CO(2-1) minimaps and 68 clouds in all the CO(1-0) PdBI fields.

2 Mass of the GMCs

There are different methods to derive the mass of the molecular gas in the interstellar medium, but the easiest one is to apply a CO to H_2 conversion factor: $N(H_2)$ = X $I_{CO(1-0)}$, where $N(H_2)$ is the column density of molecular gas and $I_{CO(1-0)}$ the integrated intensity of the CO(1-0) emission. In the Milky Way, a standard value X = 1 – 4 10^{20} $cm^{-2}K^{-1}km^{-1}s$ is observed (e.g. Solomon et al. 1987, Strong & Mattox 1996). In the following, we compare the molecular mass derived from the CO luminosity to the mass calculated from the virial theorem.

Virial mass

Assuming that a molecular cloud is isolated, gravitationally bound and in a stationary state, (the magnetic field and external pressure are assumed to be negligible), one can apply the virial theorem and derive the virial mass (M_{VIR}) of the cloud as:

$$M_{VIR} = kR\Delta V^2 \tag{1}$$

where R is the size and ΔV the (FWHM) velocity dispersion of the cloud. The factor k reflects the density distribution (see e.g. McLaren et al. 1988, Ungerechts et al. 2000). In the case of a gaussian density distribution $\rho(r) \propto \exp\{-r^2/R_g^2\}$, M_{VIR} ($M_\odot$) = 315 R_g (pc) (ΔV (km/s))^2. Using the properties of the clouds decomposed by Gaussclump, we calibrate the factor X' defined as:

$$M_{VIR} = 1.36(M_{HI} + X' M_{H2}) \tag{2}$$

where M_{HI} is the mass of atomic gas and M_{H2} the mass of molecular gas, derived with X = 10^{20} $cm^{-2}K^{-1}km^{-1}s$. We derive X' = 5 $\pm$ 3 for the complexes in the CO(1-0) 30m map, X' = 4 $\pm$ 2 for the complexes in the CO(2-1) minimaps and X' = 10 $\pm$ 5 for the clouds in the PdBI fields (see Fig.2).

The improvement in angular resolution on the CO(2-1) minimaps allows a better estimate of the GMCs size, thus not to overestimate the virial mass. The single-dish data were combined with interferometric visibilities to derive correct CO luminosities. Nevertheless, the average conversion factor is higher for the clouds decomposed on the PdBI fields. This suggests that, as also observed by Heyer et al. (2001) in the MW, the constituent clumps of cloud complexes may not be in self-gravitational equilibrium. From our data, the conversion factor shows no significant trend with galactocentric distance.

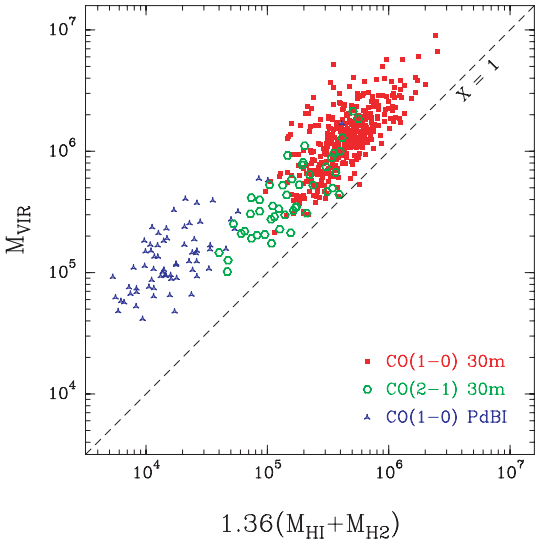

Fig. 2. Comparison of the virial mass and mass derived from the CO luminosity for the complexes on the CO(1-0) 30m map, the CO(2-1) minimaps (the CO luminosity is corrected from the CO(2-1)/CO(1-0) line ratio) and clouds in the PdBI fields.

Ballistic approach

One method to determine the mass of galaxy clusters is to consider galaxy members as point like particles, whose relative positions and velocities trace the gravitational field, hence the total mass. This method led Zwicky to infer the presence of dark matter in clusters of galaxies. We apply the same ballistic approach to derive the mass of molecular complexes. The ballistic mass can be calculated as:

$$M_{BAL} = \frac{3\pi N}{2G} \frac{\sum_i \langle V_{i\perp}^2 \rangle}{\sum_{i<j} \left\langle \frac{1}{R_{\perp,ij}} \right\rangle} \tag{3}$$

where N is the total number of particles in the system, $V_{i\perp}$ the velocity (projected on the line of sight) of the particle i and $R_{\perp,ij}$ the distance between particles i and j, projected on the plane of the sky (see Bahcall & Tremaine 1981, Heisler et al. 1985). This method assumes that the system is in virial equilibrium. The complexes D153 and INT (Fig.1) are good candidates as they appear well isolated and well defined. In addition, D153 shows a relatively narrow linewidth, and is most probably in a quiescient state. For comparison, we also apply the method to a third complex, namely D84, the brightest CO(1-0) emission in M31 and located in the well defined SW spiral arm region, at 10 kpc. The ballistic mass is compared to the H_2 mass (Eq. 2) to obtain a value of the conversion factor (see Table 1).

For the interarm complex, the calculated value of the virial mass is large and would imply a conversion factor ~ 5 times higher. On the other hand, the value X

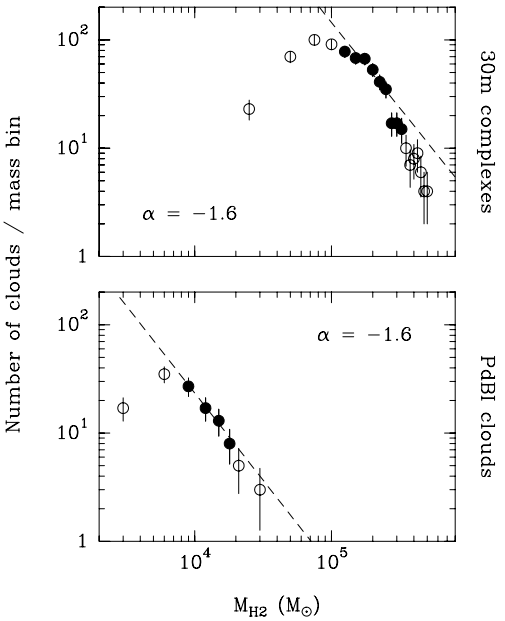

Fig. 3. Mass spectrum of the 30m complexes (up) and Plateau de Bure clouds (down). The mass of the GMCs was estimated from their CO luminosity, using X = 1. The spectral index was fitted from the full dots only.

derived from the ballistic mass does not show discrepancy with other measurements for D153 or D84. We conclude that the conversion factor in M31 is X $\sim$ 3, similar to that measured in the MW.

Complex	Position	ΔV (kpc)	D_{gal} (km/s)	X_{VIR} (10^{20}	X_{BAL} $cm^{-2}K^{-1}km^{-1}s$)
D153	(-18' ; -4')	5.8	7.7	3	2
INT	(30' ; -4.5')	8.2	14.6	20	5
D84	(-16.5' ; -8.7')	9.8	15.3	5	3

Table 1. Conversion factor derived from the virial theorem (X_{VIR}) and the ballistic method (X_{BAL}) for three different complexes observed with the PdBI.

3 Mass Spectrum

One interesting property is the mass distribution, or mass spectrum, of the GMCs. In the MW, it has been shown that the GMCs mass spectrum follows a power law distribution $dN/dM \propto M^{-\alpha}$ with spectral indexes in the range 1.5 – 1.8 (see e.g. Solomon et al. 1987, Heyer et al. 2001, Heithausen et al. 1998, Simon et al. 2001).

The Gaussclump decomposition of the CO(1-0) 30m map allows us to study the properties of a large sample of molecular clouds in M31. We derive a spectral index $\alpha = 1.6 \pm 0.2$ (Fig. 3), similar to that in the MW. Rosolowsky (2006) derives a comparable value from the study of a smaller sample of M31 GMCs observed with the BIMA interferometer. Other results indicate $\alpha = 1.9$ in the LMC (Fukui et al. 2001), and $\alpha = 2.6$ in M33 (Engargiola et al. 2003).

4 Conclusion

We have used CO mapping of the GMCs in M31 to derive their physical properties. In particular, we applied the virial theorem to derive the mass of the molecular complexes and calibrate the CO to H_2 conversion factor. The results indicate that the GMCs in M31 are similar to those of the MW.

Acknowledgments

It is a pleasure to thank the 30m and PdBI IRAM staff for all their work. SM wish to thank the organisers for the nice organisation of the conference and for giving the opportunity to present this work.

References

1. Bahcall, J. N. & Tremaine, S.: ApJ, 244, 805 (1981)
2. Engargiola, G. et al: ApJ Supp., 149, 343 (2003)
3. Fukui, Y. et al: PASJ, 53, L41 (2001)
4. Heisler, J.; Tremaine, S.; Bahcall, J. N.: ApJ, 298, 8 (1985)
5. Heithausen, A. et al: A&A, 331, L65 (1998)
6. Heyer, M. H., Carpenter, J. M. & Snell, R. L.: ApJ, 551, 852 (2001)
7. Kramer, C., Stutzki, J., Rohrig, R. & Corneliussen, U.: A&A, 329, 249 (1998)
8. McLaren, I., Richardson, K. M. & Wolfendale, A. W.: ApJ, 333, 821 (1988)
9. Neininger, N., et al.: Nature, 395, 871 (1998)
10. Neininger, N., et al.: IAU Symp., 205, 352 (2001)
11. Nieten, C., Neininger, N., Guélin, M., et al.: A&A, 453, 459 (2006)
12. Simon, R., Jackson, J. M., Clemens, D. P. & Bania, T. M.: ApJ, 551, 747 (2001)
13. Solomon, P. M., Rivolo, A. R., Barrett, J. & Yahil, A.: ApJ, 319, 730 (1987)
14. Strong, A & Mattox, J.: A&A, 308, 21 (1996)
15. Stutzki, J. & Gusten, R.: ApJ, 356, 513 (1990)
16. Ungerechts, H., Umbanhowar, P. & Thaddeus P.: ApJ, 537, 221 (2000)

30

Atomic and Molecular Gas in Disk Galaxies

Tony Wong[1,2], L. Blitz[3], A. Kawamura[4], H. Iritani[4], and Y. Fukui[4]

[1] CSIRO Australia Telescope National Facility, Epping NSW 1710, Australia
Tony.Wong@csiro.au
[2] School of Physics, University of New South Wales, Sydney NSW 2052, Australia
[3] Astronomy Department, University of California, Berkeley CA 94720, USA
[4] Department of Astrophysics, Nagoya University, Nagoya 464-8601, Japan

Summary. Current knowledge of the radial distributions of atomic and molecular gas in disk galaxies is briefly reviewed. Almost all of our knowledge is based on observations of the HI and CO lines at 21 cm and 2.6 mm wavelength, and some of the caveats associated with these methods are discussed. In nearby spiral galaxies the molecular gas fraction is observed to decrease with radius, which can be understood in terms of a decline in hydrostatic disk pressure. Within the LMC, the CO-HI correlation shows considerable scatter on scales of ∼50 pc, although a binning analysis shows a strong non-linear dependence of CO on HI intensity. The implications for molecular cloud formation and star formation recipes are briefly discussed.

1 Introduction

The structure of the interstellar medium (ISM) is important both as an indicator of astrophysical processes (especially the interaction of turbulence, magnetic fields, radiation, and gravity) and as an important initial condition for the star formation process. However, studying ISM structure is challenging in terms of both observing technique and data interpretation. In particular, most tracers of cold gas emit only at radio wavelengths, requiring time-consuming interferometry to obtain high resolution images—which even so may only sample some of the spatial frequencies present. Chemical and radiative processes also work to prevent a single tracer from being observable at all volume densities, requiring the use of several atomic and molecular probes to study the full range of densities in the ISM.

Here we focus on comparing the two most commonly used tracers of the neutral ISM, the HI line at λ=21 cm and the CO (1–0) line at λ=2.6 mm. In the classical three-phase model of the ISM [16], there is both a warm ($T \sim 10^4$ K) and cold ($T \sim 10^2$ K) component of the HI, with substantially different densities and filling factors so as to be in rough thermal pressure equilibrium. The molecular clouds are even colder and denser, and assumed to be self-gravitating, and thus not in pressure equilibrium with the atomic gas. More recent observations suggest that HI can exist at a wide range of temperatures and pressures and that molecular clouds may be too short-lived to reach virial equilibrium before star formation disrupts

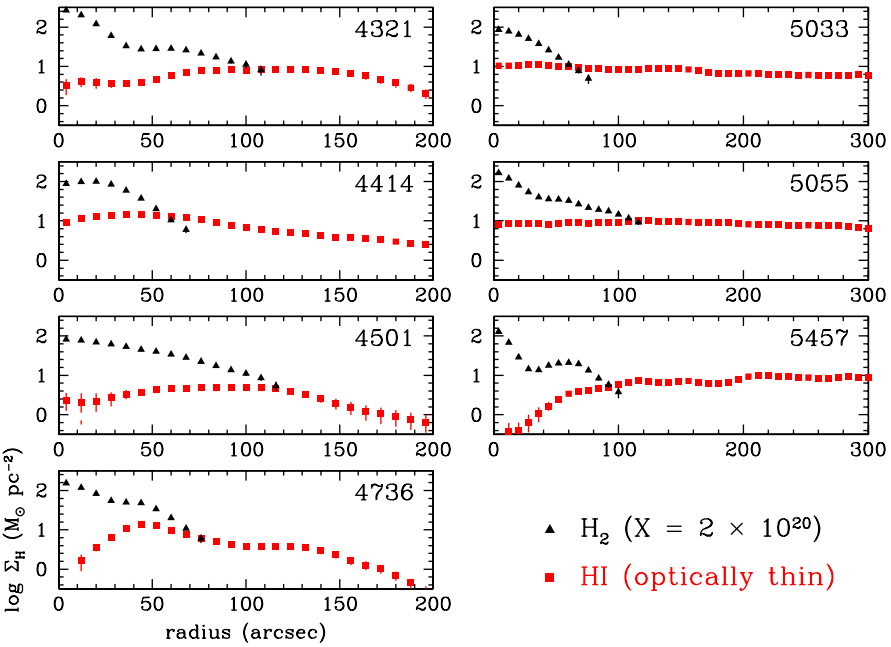

Fig. 1. Radial HI and H_2 profiles for seven spiral galaxies (listed by NGC number) studied by [24]. The profiles are derived from azimuthal averages of BIMA+12m CO and VLA HI images at a resolution of $\sim 15''$.

them. This would tend to blur the distinction between the atomic and molecular gas phases. Hartmann et al. (2001) argue that the cloud formation process occurs mainly in the atomic phase, with a relatively brief period of CO emission just prior to star formation. However, other explanations for apparently short molecular cloud lifetimes have been offered [17].

While the process of forming molecular clouds from atomic clouds has been explored in recent years with numerical simulations (e.g. [14, 11, 1, 19]), observational constraints are still few. This is due to the difficulty of observing the precursors to molecular clouds in the Galaxy in the presence of HI blending and self-absorption, coupled with the difficulty of obtaining arcsecond-resolution observations of both CO and HI in the disks of *external* galaxies. However, recent years have seen substantial progress, particularly in obtaining CO maps of nearby galaxies.

2 Spiral Galaxies

The wide field of view provided by the BIMA interferometer for CO imaging and the angular resolution provided by the VLA for HI imaging have provided new views of the CO-HI relationship in nearby galaxies. Remarkable differences in morphology between CO and HI maps are observed in some galaxies, such as NGC 4736 [23],

yet others exhibit more similarities than differences (e.g. M33, [7]; IC 10, [15]). Differences tend to be most pronounced in the central regions of massive galaxies, which often show a central CO peak filling an HI cavity (Fig. 1). Theoretically this is usually interpreted as being due to the sensitivity of the H_2 formation process to the gas density: gas densities are expected to be higher in the central parts of galaxies where the gravitational potential is deep and thus the hydrostatic midplane pressure is large [5, 6]. Strong correlations between the molecular to atomic gas ratio and the hydrostatic pressure (which depends on both the gaseous and stellar mass surface density) have been pointed out by [24] and [2]. The average power law for the seven galaxies in Fig. 2 is $\Sigma_{\rm mol}/\Sigma_{\rm HI} \propto P^{0.8}$. The higher metallicity and hence dust abundance in galaxy centres may also play a role in increasing the molecular gas fraction there.

A pressure dependence for molecular cloud formation helps to explain a variety of observations, including star formation thresholds in dwarf galaxies and the outer disks of spirals [22, 4], the ability to predict the SFR from the HI and stellar surface density alone [21], and the dependence of star formation history on disk mass surface density seen in the SDSS [12].

On the other hand, the question of how well the HI and H_2 content are sampled by 21-cm and CO line emission remains controversial. In M31, the HI mass is underestimated by ∼1.2 due to optical depth effects [3], although the radial dependence of the correction factor is unclear. Comparisons of CO and ^{13}CO emission in nearby galaxies suggest that the standard CO-to-H_2 conversion factor may overestimate the central ($R < 2$ kpc) H_2 mass by a factor of ∼3 [18]. Thus, optical depth effects could account for a factor of ∼4 change in the inferred H_2/HI ratio, although it is unlikely to account for a factor of ∼10 decrease from galactocentric radii of 2 to 6 kpc.

A key question for future studies is whether the hydrostatic disk pressure has the dominant influence on the H_2/HI ratio compared with more local pressures such as spiral shocks, expanding shells, etc. This is analogous to the debate over whether star

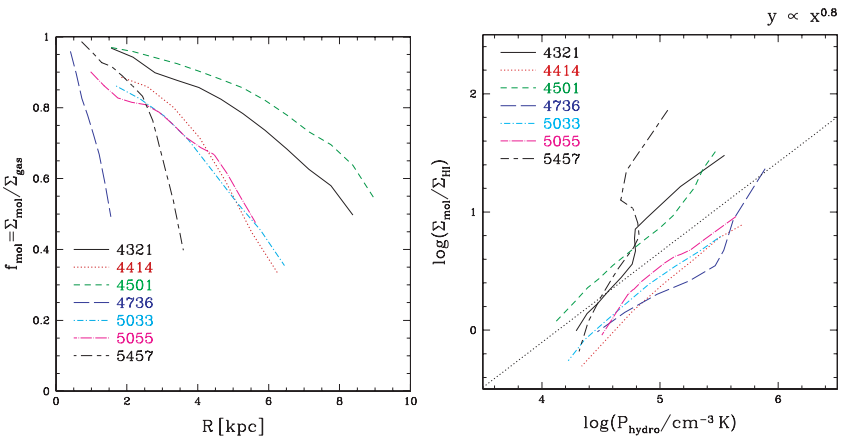

Fig. 2. (*Left*) Molecular gas fraction vs. radius for the seven galaxies in Fig. 1. (*Right*) Ratio of molecular to atomic gas vs. hydrostatic midplane pressure. The dotted line represents a slope of 0.8.

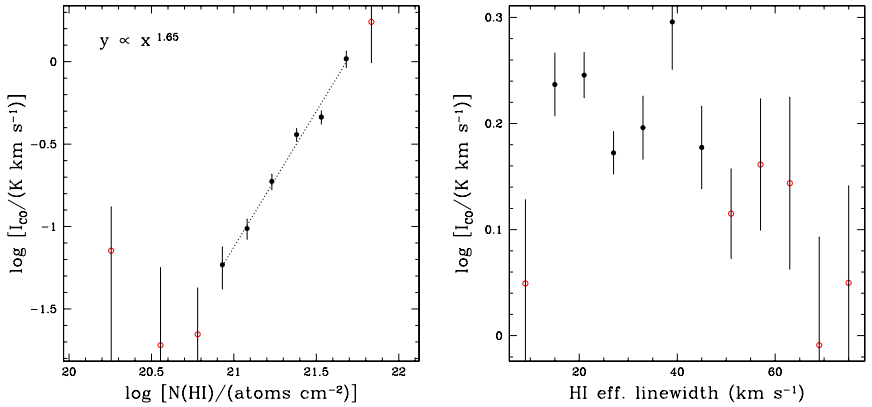

Fig. 3. (*Left*) CO intensity vs. HI column density across the entire LMC as observed by NANTEN. Points with open circles (where the mean value is less than 3σ) are not included in the fit. (*Right*) CO intensity vs. effective HI linewidth, defined as the ratio of the integrated to peak intensity.

formation is primarily spontaneous or triggered. That the star formation rate scales more or less linearly with CO flux suggests that star formation follows directly once molecular clouds are formed. However, the typically *non-linear* relation between CO and HI fluxes leaves open the possibility that molecular clouds in some environments are formed by the collision of atomic clouds (as suggested by [10]), a possibility that is discussed further below.

3 The Large Magellanic Cloud

The Magellanic Clouds, especially the LMC, are ideally situated to study the structure of the ISM across an entire galaxy in detail. However they have the drawbacks of being strongly interacting with the Galaxy (and thus probably not in a steady state) and having a substantially sub-solar metallicity [20], which likely affects the ability of the CO line to trace H_2. If GMCs in the LMC are virialized, the observed relation between CO luminosity and virial mass ($\propto r\sigma_v^2$) should provide a calibration of the CO-to-H_2 conversion factor ("X-factor"). Such an analysis yields an X-factor which is a factor of $\sim$2 larger than in the Milky Way [8]; i.e. twice as much H_2 column density is needed to produce the same CO intensity.

A detailed comparison between the CO and HI maps of the LMC is now possible using the CO data from the NANTEN survey [9] and the HI data from the Parkes and ATCA surveys [13]. At a common resolution of $3'$ (40 pc), it is apparent that despite the large scatter in a pixel-by-pixel comparison, there is an overall correlation between the two images when integrated over velocity. Binning in logarithmic intervals of $I_{\rm HI}$ yields a tight relation of $I_{\rm CO} \propto I_{\rm HI}^{1.7\pm0.1}$ (Fig. 3, *left*). We do not see evidence for a clear "threshold" in HI column density below which CO suddenly disappears; this is not surprising given that the observed column density is averaged over a telescope beam.

The closeness of the observed power law index to 2 suggests that molecular clouds may form by collisions of HI clouds. On the other hand, there is no correlation of $I_{\rm CO}$ with HI linewidth as measured by the ratio of the integrated to the peak intensity (Fig. 3, *right*); in fact, there appears to be a weak *anti-correlation*. Thus, even if turbulent compression is an important process for forming molecular clouds, there appears to be a sufficient time lag before the cloud is easily detected in CO to completely erase any such correlation.

A complete analysis of the CO-HI relation in the LMC in the context of the hydrostatic pressure model in the LMC has yet to be conducted, but if one makes the simplifying assumptions that the pressure is dominated by the gaseous component ($P \propto N_H^2$), as seems plausible outside the LMC bar, and that the gas is mostly atomic, as expected from both CO emission and H_2 absorption studies, then the relation observed in spiral galaxies would yield

$$\frac{\Sigma_{\rm H_2}}{\Sigma_{\rm HI}} \propto P^{0.9} \propto \Sigma_{\rm HI}^{1.8} \Rightarrow \Sigma_{\rm H_2} \propto \Sigma_{\rm HI}^{2.8}$$

This is even steeper than observed, suggesting that the gravitational influence of the stellar or dark matter component may be important to include in the analysis. Alternatively, other sources of pressure besides hydrostatic pressure may be important.

Acknowlegdments. We thank the organisers for a lively and enjoyable meeting, and for allowing this presentation to be given orally at the conference.

References

1. Bergin, E. A., Hartmann, L. W., Raymond, J. C., & Ballesteros-Paredes, J., ApJ, 612, 921 (2004)
2. Blitz, L. & Rosolowsky, E., ApJ, 612, L29 (2004)
3. Braun, R. & Walterbos, R. A. M., ApJ, 386, 120 (1992)
4. de Blok, W. J. G. & Walter, F., AJ, 131, 363 (2006)
5. Elmegreen, B. G., ApJ, 338, 178 (1989)
6. —., ApJ, 411, 170 (1993)
7. Engargiola, G., Plambeck, R. L., Rosolowsky, E., & Blitz, L., ApJS, 149, 343 (2003)
8. Fukui, Y., Kawamura, A., Minamidani, T., Mizuno, Y., Kanai, Y., Mizuno, N., Onishi, T., Yonekura, Y., Mizuno, A., Ogawa, H., & Rubio, M., ApJ, submitted (2006)
9. Fukui, Y., Mizuno, N., Yamaguchi, R., Mizuno, A., & Onishi, T., PASJ, 53, L41 (2001)
10. Hartmann, L., Ballesteros-Paredes, J., & Bergin, E. A., ApJ, 562, 852 (2001)
11. Hidaka, M. & Sofue, Y., PASJ, 54, 223 (2002)
12. Kauffmann, G., Heckman, T. M., White, S. D. M., Charlot, S., Tremonti, C., Peng, E. W., Seibert, M., Brinkmann, J., Nichol, R. C., SubbaRao, M., & York, D., MNRAS, 341, 54 (2003)
13. Kim, S., Staveley-Smith, L., Dopita, M. A., Sault, R. J., Freeman, K. C., Lee, Y., & Chu, Y.-H., ApJS, 148, 473 (2003)

14. Koyama, H. & Inutsuka, S.-I., ApJ, 532, 980 (2000)
15. Leroy, A., Bolatto, A., Walter, F., & Blitz, L., ApJ, 643, 825 (2006)
16. McKee, C. F. & Ostriker, J. P., ApJ, 218, 148 (1977)
17. Mouschovias, T. C., Tassis, K., & Kunz, M. W., ApJ, 646, 1043 (2006)
18. Paglione, T. A. D., Wall, W. F., Young, J. S., Heyer, M. H., Richard, M., Goldstein, M., Kaufman, Z., Nantais, J., & Perry, G., ApJS, 135, 183 (2001)
19. Pelupessy, F. I., Papadopoulos, P. P., & van der Werf, P., ApJ, 645, 1024 (2006)
20. Rolleston, W. R. J., Trundle, C., & Dufton, P. L., A&A, 396, 53 (2002)
21. Ryder, S. D. & Dopita, M. A., ApJ, 430, 142 (1994)
22. Schaye, J., ApJ, 609, 667 (2004)
23. Wong, T. & Blitz, L., ApJ, 540, 771 (2000)
24. —., ApJ, 569, 157 (2002)

31

The Outer Disks of Spiral Galaxies

Jonathan Braine[1]

Observatoire de Bordeaux, Université Bordeaux 1, UMR 5804, BP 89 33270 Floirac, France braine@obs.u-bordeaux1.fr

Molecular gas, via its CO emisssion, is detectable far out in the Milky Way, M33, NGC 4414, and probably all spirals with extended HI. Metallicity is not a great problem for CO detection in regions with a weak radiation field, such as outer disks. The association with HI and star formation is very good but not perfect – giant molecular clouds can be found in zones with little HI. In the outer Galaxy, there is no sharp decrease in CO line intensity despite the lack of obvious heating sources for outer galaxy clouds.

1 What Do We Know and Why Do We Care About the Outer Disk ISM?

One of the basic questions in modern cosmology is how galaxies grow to their current size, morphology, and composition. Where does the mass currently observed come from? How massive is the average spiral at an arbitrary redshift? As the stellar mass is measurable, what is the gaseous mass? The gas mass is a major unknown, and particularly important as it helps unravel the past star formation. As we go back in time, the stellar disks become smaller. Does this imply bigger gaseous disks or does accretion dominate? The bright inner disk is fairly straightforward to study but the outer disk, which contains a lot of gas but is dim and diffuse, has only recently become accessible due to increases in telescope sensitivity. So how do we trace the mass of the interstellar medium (ISM) in the outer disk, and thus the mass of the ISM (the fuel for star formation) as a function of redshift? We first need to understand how to trace the gas mass in the local universe, at $z = 0$. Unfortunately, the most obvious tracer, HI, is very difficult to observe even at intermediate redshifts. What are the other tracers of gas and how can they be used? Again, we first need to test in local objects. Measuring the mass and phases of the ISM in the outskirts of galaxies is the subject of this review.

The outer disk ISM is important for many reasons:
(*i*) as a source of gas for future star formation
(*ii*) as a reservoir of angular momentum
(*iii*) because the outskirts of spirals contain a lot of Dark Matter – could some of it be baryonic and hidden in the disk?

(*iv*) to study a new part of parameter space to understand star formation in subsolar metallicity and low radiation fields (not well studied as the focus has been on bright blue low metallicity environments).

In addition to being exposed to little stellar light, the other main characteristic of the outer disk gas is its low metallicity. Spirals typically show metallicity gradients of order .05dex/kpc, such that 20 kpc from the center the abundances are about 1/10 of the central regions, close to the metallicity of the Magellanic clouds or potentially even lower [10, 6]. The gas in and near galactic nuclei is denser than elsewhere, presumably due to the strong tidal forces which would rip apart less dense clouds. There is some evidence that the dense gas fraction decreases with radius, because the HCN/CO and HCO+/CO ratios (HCN and HCO+ trace dense molecular gas whereas CO is excited at much lower densities) were found to decrease in the Andromeda galaxy [2] – more such observations are necessary to determine whether this is a general trend.

Large spirals frequently have stars well away from the disk and it appears that this is not a spherical component but the remains of accreted objects ([8] for Andromeda, [13] for NGC 5907, Braine et al. in prep. for NGC 4414). At least one small spiral (M33, part of our Local Group and near Andromeda) has been shown *not* to have such a halo (A. Ferguson et al. in prep.). M33 is a blue spiral roughly ten times less massive (or luminous) than the Milky Way and with a subsolar metallicity. In these ways it may resemble intermediate redshift objects before they have been completely assembled. Does the lack of a halo in the smallest of the well-studied objects suggest as well that M33 might be a local universe analog of intermediate redshift objects?

Between redshifts 0 and 0.5, the star formation rate increases by a factor ~ 10 [7] but galaxies were already rich in stars. Today's spirals are about 10% gas. It seems inevitable that the star formation (SF) efficiency (SF rate/Mgas) was higher in the past despite lower metallicities (and thus a possibly lower H_2 fraction). *Why?* This is one of the reasons for trying to understand the ISM and star formation in the widest set of conditions possible. Outer disks, nuclei, Dwarfs of all sorts, and spiral disks all provide different environments.

We are involved in a multi-scale approach, from sub-pc (Milky Way) to single GMC scale (M33, M31) to kpc (NGC 4414) and more (tidal material) to understand the ISM and star formation in outer disks. [4] surveyed part of the outer disk of the Milky Way in the CO(1–0) line with similar objectives to our own, to determine where the molecular gas was no longer visible and understand its relationship to the HI. They found that molecular gas was associated with HI clouds but the CO was not always at the HI maximum. The estimated kinetic temperatures of the clouds ranged from 10 – 25 K but with lower CO luminosities than inner disk clouds. A general problem with studies within the disk of the Galaxy is that continuum data are often difficult to associate with features as several clouds are often present along arbitrary lines of sight. As such, it is difficult to identify heating sources for the gas.

A decade later, we (Braine, Brouillet, Schuster, Gardan, Combes) have started a new survey of a square degree of the outer Galaxy at $l = 148^\circ$ at higher resolution and sensitivity. The new multibeam HERA receiver on the IRAM 30 meter telescope on Pico Veleta (Spain) is being used to map the CO(2–1) emission in the On-the-Fly mode with frequency switching. In the outer galaxy at *e.g.* 10 kpc from the sun, this corresponds to about 200 pc and provides substantial overlap with observations of the local group objects M33 and M31 (resolution $\sim$ 45 pc with the 30 meter and

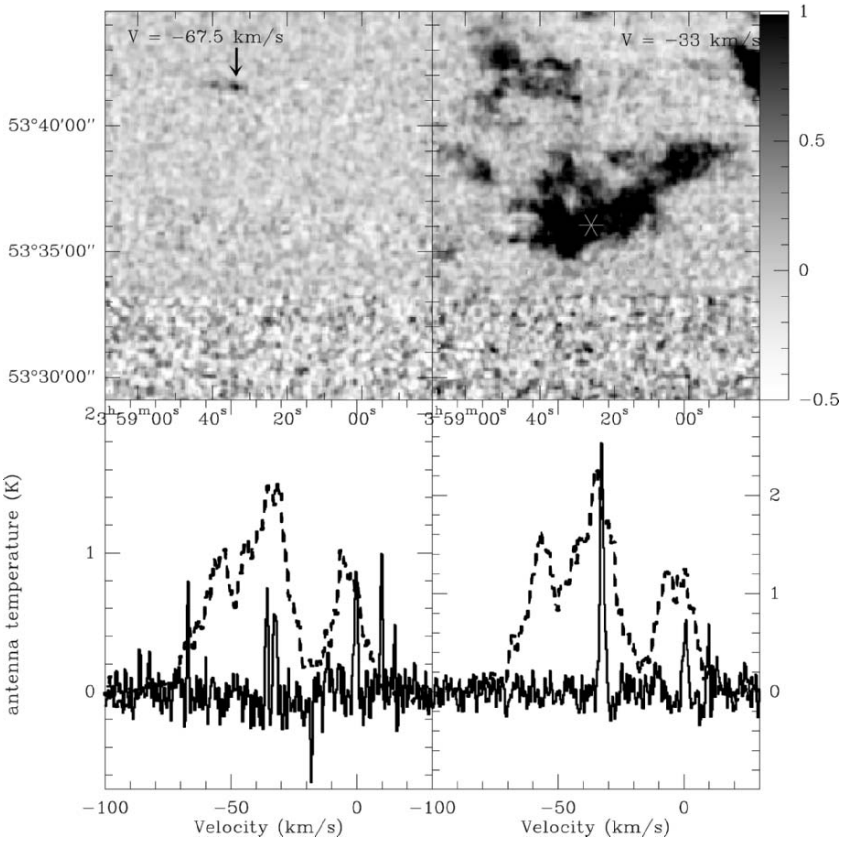

Fig. 1. Upper panels: channel maps as grey scale images of a $\sim 15' \times 15'$ region (about 1/4 of our map) at velocities of −67.5 km/s (left, showing a small and distant cloud indicated by the arrow) and −33 km/s (right, showing the arm at about 13 kpc which has much more CO emission). The grey scale is shown to the right and is the same for both panels, such that temperatures over 1K are black. The lower panels show the CO (solid line) and HI (dashed) spectra towards (left) the cloud indicated by the arrow in the upper left panel and (right) the position indicated by the asterisk in the upper right panel. The CO antenna temperature scale is indicated in K on the y-scales and the HI temperature scale is arbitrary but the same for both panels. In addition to the $v = 7.5$km/s mesospheric CO line, there are several clouds or cloud complexes along the line of sight, and this is true for all sightlines. At least 5 clouds are present towards the distant cloud at RA $3^h\,58^m\,34^s$, Dec 53 41 30 J2000. −67.5 km/s corresponds to a galactocentric distance of just over 20 kpc, beyond the optical "edge" of the Milky Way. The HI data comes from the recent Canadian Galactic Plane Survey, with $1'$ resolution. The lower parts of the images are noisier due to poorer system temperatures. The apparent "absorption" seen at −18 km/s is a poorly subtracted frequency switch "ghost" (Braine et al. in prep.).

better with the Plateau de Bure interferometer). The spatial resolution of the new observations is 11″, some 10 milliparsec for the local gas, and the sensitivity is such that very small clouds ($\lesssim 1$ $M_\odot$) are detectable. As can be seen in Fig. 1, several clouds are typically visible along any line of sight and they correspond in velocity to the HI arms. However, the outer arm is stronger in HI whereas there are many more molecular clouds associated with the local (Perseus) arm. Furthermore, while the HI spectra are rather uniform over the region observed (compare dashed spectra), the molecular gas is organized into small clouds with very narrow linewidths such that several clouds may be present in the same arm along the line of sight. It is very difficult (at best) to associate the molecular clouds with HI concentrations even though the HI observations are at high resolution (1′). The antenna temperatures do not seem to vary greatly with galactocentric distance. The observations are still in progress and we hope to be able to add information from dense gas tracers as well.

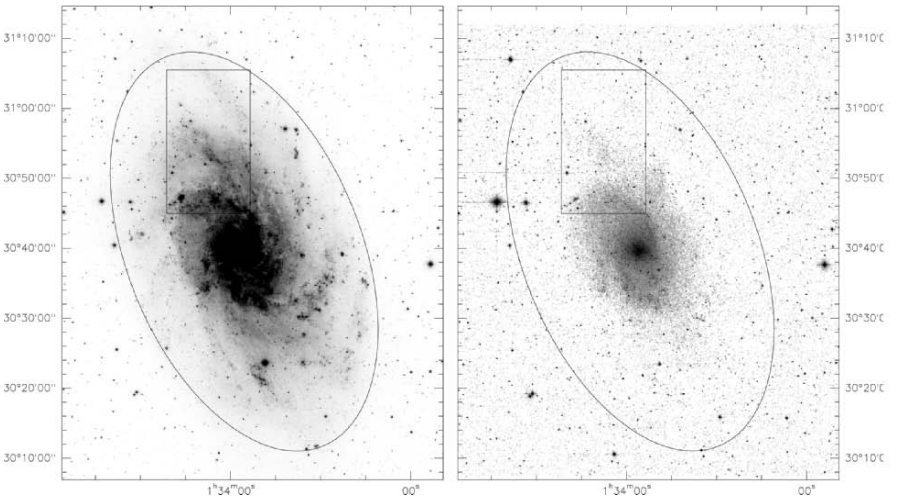

Fig. 2. DSS image (left) and 2MASS K' band image (right) with area surveyed with the IRAM 30meter telescope using HERA in the CO(2–1) line. The ellipse shows the R_{25} contour. While the young stellar population (DSS) is very extended, the K band (old stars) emission, even saturated to reveal emission as far out as possible, becomes very weak well before R_{25}. The region we have observed has a very low stellar mass surface density (Gardan et al. in prep.).

The M33 observations (Gardan et al. in prep.), also with HERA on the IRAM 30 meter telescope, cover much of the northern half of M33 (Fig 2), extending out to R_{25}. For reference, we have included the molecular gas-rich actively star forming region west of NGC 604 in the lower part of the map because these clouds were detected in the complete survey of M33 by [5] but they were the northernmost of their detections.

As can be seen in Fig. 3, the correspondance between CO emission and the other tracers of gas or star formation is excellent (8μm, 24μm, HI, and UV). If

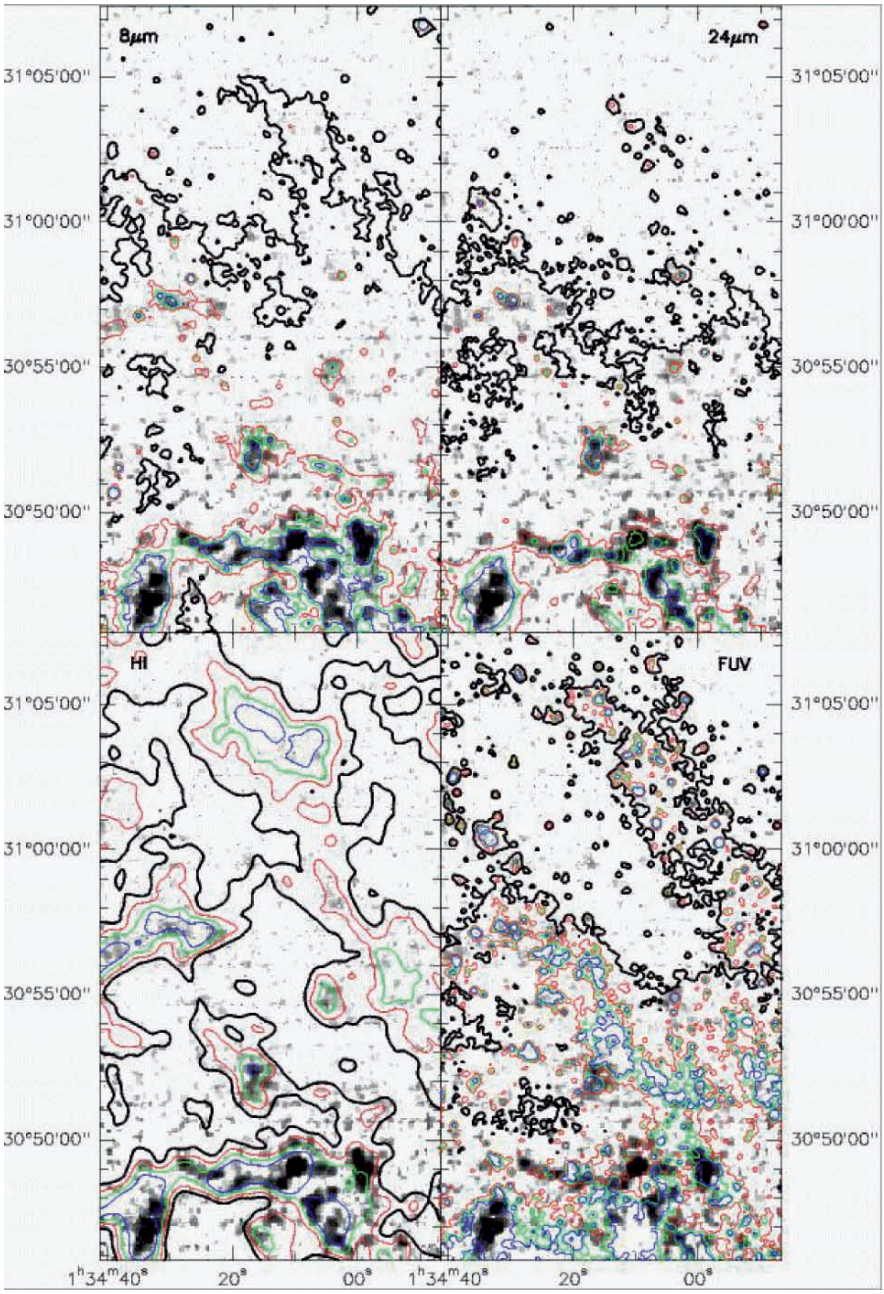

Fig. 3. Comparison of integrated CO intensity (greyscale) with IRAC 8μm, MIPS 24μm, HI, and GALEX FUV emission as contours. The lowest level contour is thick to show the interarm region in the HI [3] and FUV [14] images. Note the presence in the interarm region just below Dec 31° of a molecular cloud with very little HI, FUV, or dust emission associated (Gardan et al in prep.).

the passage from H_2 to stars were not rapid, the spatial correlations would not be so good. One major molecular cloud is however found in the interarm region (just below Dec 31°). Essentially no dust emission is associated and, while there is some HI (present everywhere), the HI column density is low in the region, as is the NUV or FUV emission measured with GALEX. We have tried to calculate the $N(H_2)/I_{CO}$ conversion factor assuming that the cloud is roughly the size of the CO(1–0) beam of the IRAM 30 meter telescope (90pc on M33). Equating the dynamical mass of the cloud from the size and linewidth with the mass calculated from a $N(H_2)/I_{CO}$ factor, we obtain $N(H_2)/I_{CO} \sim (\Delta V^2\, f_H\, R_{cl})/(4G\, m_p I_{co} A_{bm})$. For a linewidth of 4 km/s and assuming a cloud radius of 45pc (half a beam), a beamsize of 90pc, and an integrated intensity of 1.5 Kkm/s, the $N(H_2)/I_{CO} \sim 3 \times 10^{20}$ H_2 cm^{-2}/Kkm/s. f_H is the Hydrogen mass fraction. If the cloud is smaller than the beamsize than the factor would be lower. The [9] size-linewidth relation for galactic clouds suggests that for a linewidth of 4 km/s the cloud would be smaller than 90 pc. Another interesting detection is very far North, above Dec 31°10′, where we measure a linewidth of about 2.8 km/s for $I_{co} \sim 0.8$ Kkm/s, yielding a very similar $N(H_2)/I_{CO}$ factor. The radiation field (ISRF) to which these clouds are exposed is very low and the metallicity is highly subsolar. Extrapolating the metallicity-radius curve to the 31°10′ position, the expected metallicity is about $12 + log(O/H) \sim 7.8$, below that of the Small Magellanic Cloud. We contend that while the $N(H_2)/I_{CO}$ factor may well be a bit higher than in the molecular ring of our galaxy, the low-metallicity/low ISRF environment does not lead to enormously higher $N(H_2)/I_{CO}$ conversion factors, unlike the situation in blue dwarf galaxies. The H_2 mass traced by CO in the outer disk of M33 is only a small fraction of the HI mass and thus not dynamically important.

In another nearby spiral, NGC 4414, CO has been detected well beyond the R_{25} radius [1]. In addition to the fact that molecular gas is present and detectable via CO emission so far out in a normal spiral, the CO detections showed that (*i*) spiral arms are not necessary to provoke the conversion of HI into H_2, (*ii*) the heating of molecular gas is sufficient for detection even at such low surface brightnesses, (*iii*) CO formation may require an HI column density above a threshold of order 3×10^{20} cm^{-2}. Star formation seems to have a similar behavior ([11] but for tidal tails). The molecular gas mass in the outskirts of NGC 4414 appears to be a factor few less than the HI mass. [12] detected thermal emission from dust in the outer parts of the edge-on spiral NGC 891.

Is CO the best tracer of molecular gas? This is generally assumed but in some simulations it appears that CO may have trouble forming in low-density molecular environments (Fig. 4). In future work we will try to explore the formation and destruction mechanisms of CO in order to determine whether or not it is a suitable tracer of molecular gas in the low density environments that may be common in outer disks.

In conclusion, CO is detectable far out in the Milky Way, M33, NGC 4414, and probably all spirals with extended HI. Metallicity is not a great problem for CO detection, despite claims to the contrary. In the outer Galaxy, there is no sharp decrease in CO line intensity despite the lack of obvious heating sources for outer galaxy clouds. All data are consistent with a quick cycling of H_2 into stars. Assuming CO is a better tracer of H_2 than CI, then the H_2 fraction is well below unity in outer disks and thus dynamically unimportant, although very interesting for star

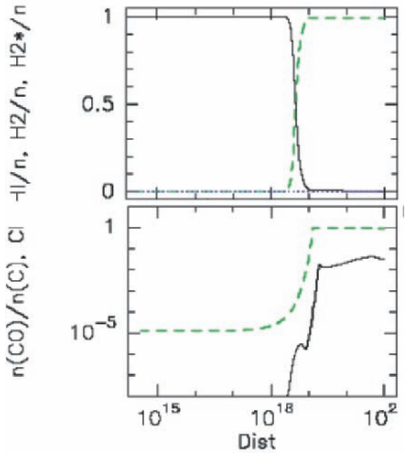

Fig. 4. Upper plot shows HI and H_2 fractions as a function of depth (in cm) into the cloud and lower plot the fraction of Carbon in CI and CO. The green dashed line is respectively the H_2 and CI and the solid line shows the HI and CO fractions. In these simulations of a low density environment, the H becomes molecular but the C remains atomic (Rodriguez-Fernandez et al. in prep.).

formation. Deep CI observations are necessary to investigate whether some H_2 could be hidden through lack of CO formation.

References

1. Braine, J. & Herpin, F.: Nature, 432, 369 (2004)
2. Brouillet, N., Muller, S., Herpin, F., Braine, J., & Jacq, T.: A&A, 429, 153 (2005)
3. Deul, E. R. & van der Hulst, J. M.: A&AS, 67, 509 (1987)
4. Digel, S., de Geus, E., & Thaddeus, P.: ApJ, 422, 92 (1994)
5. Engargiola, G., Plambeck, R. L., Rosolowsky, E., & Blitz, L.: ApJS, 149, 343 (2003)
6. Ferguson, A. M. N., Gallagher, J. S., & Wyse, R. F. G.: AJ, 116, 673 (1998)
7. Heavens, A., Panter, B., Jimenez, R., & Dunlop, J.: Nature, 428, 625 (2004)
8. Ibata, R., Irwin, M., Lewis, G., Ferguson, A. M. N., & Tanvir, N.: Nature, 412, 49 (2001)
9. Larson, R. B.: MNRAS, 194, 809 (1981)
10. Magrini, L., Perinotto, M., Mampaso, A., & Corradi, R. L. M.: A&A, 426, 779 (2004)
11. Neff, S. G., Thilker, D. A., Seibert, M., et al.: ApJL, 619, L91 (2005)
12. Popescu, C. C. & Tuffs, R. J.: A&A, 410, L21 (2003)
13. Sackett, P. D., Morrison, H. L., Harding, P., & Boroson, T. A.: Nature, 370, 441 (1994)
14. Thilker, D. A., Hoopes, C. G., Bianchi, L., et al.: ApJL, 619, L67 (2005)

32

A Complete CO 2-1 Map of M51 with HERA

Carsten Kramer[1], Marc Hitschfeld[1], Karl F. Schuster[2], Santiago Garcia-Burillo[3], and Bhaswati Mookerjea[4]

[1] KOSMA, I. Physikalisches Institut, Universität zu Köln, Zülpicher Straße 77, 50937 Köln, Germany kramer@ph1.uni-koeln.de
[2] IRAM, 300 Rue de la Piscine, F-38406 S^t Martin d'Hères, France schuster@iram.fr
[3] Centro Astronomico de Yebes, IGN, E-19080 Guadalajara, Spain burillo@oan.es
[4] Department of Astronomy, University of Maryland, College Park, MD 20742, USA bhaswati@astro.umd.edu

Summary. The nearby, almost face-on, and interacting galaxy M51 offers an excellent opportunity to study the distribution of molecular gas and the mechanisms governing the star formation rate. We have created a complete map (Fig. 1) of M51 in ^{12}CO 2–1 at a resolution of 11″ corresponding to 450 kpc using HERA at the IRAM-30m telescope. In [1] we have combined these data with maps of HI and the radio-continuum to study the star formation efficiency, the local Schmidt law, and Toomre stability of the disk in radial averages out to radii of 12 kpc. Here, we also discuss the distribution of giant molecular associations and its mass spectrum, in comparison with similar studies in the literature.

1 CO, HI, and the Radio Continuum

M51 is an interacting, grand-design spiral galaxy at a distance of only 8.4 Mpc seen nearly face-on. The emission detected with the 30m telescope (Fig. 1) traces the well known two-armed spiral pattern out to the companion galaxy NGC 5195, which shows up brightly in the north-east at $\sim$ 10.5 kpc radial distance, and out to the south-western tip of the second arm at the opposite side of M51. The outer parts of the two arms in the west and in the east appear more fragmented than the inner parts. The western arm especially is almost unresolved. Inter-arm emission is detected above the 3σ level out to radii of about 6 kpc. Several spoke-like structures connect the spiral arms radially. The large-scale distribution of the 21 cm line of atomic hydrogen in M51 was analyzed by [2] using the VLA. The HI emission at 13″ resolution (Fig. 2) is weak in the inner region while the outer CO arms are clearly delineated in HI. These data have been combined with a new large scale 20cm map of [3] which provides an extinction-free estimate of the star formation rate.

We derive a global star formation rate of $2.56\,M_\odot\,\mathrm{yr}^{-1}$. The total gas surface density $\sum_{\mathrm{gas}} = 1.36(\sum_{\mathrm{H_2}} + \sum_{\mathrm{HI}})$ drops by a factor of $\sim$ 20 from $70\,M_\odot\,\mathrm{pc}^{-2}$ at

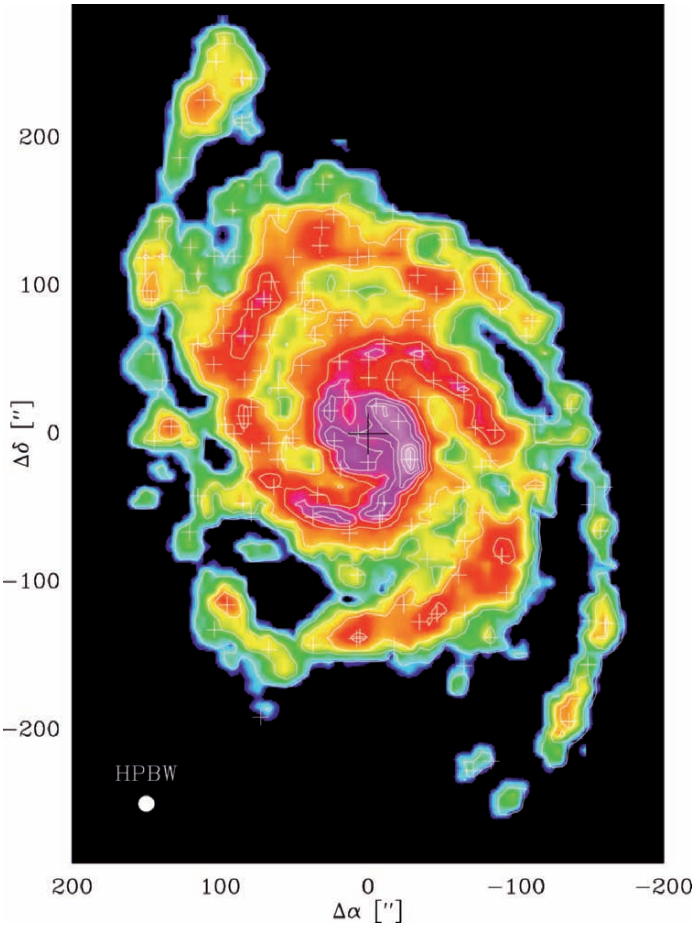

Fig. 1. Map of ^{12}CO 2–1 integrated intensities in Kkms^{-1} showing M51, i.e. NGC 5194 and its companion galaxy NGC 5195 in the north-east. Crosses mark the center positions of the identified 155 giant molecular associations (GMAs).

the center to $3\,M_\odot\,\mathrm{pc}^{-2}$ in the outskirts at radii of 12 kpc. The ratio of HI over H_2 surface densities, $\sum_{\mathrm{HI}} / \sum_{\mathrm{H2}}$, increases from ~ 0.1 near the center to ~ 20 in the outskirts without following a simple power-law. The star formation rate per unit area drops from $\sim 400\,M_\odot\,\mathrm{pc}^{-2}\,\mathrm{Gyr}^{-1}$ in the starburst center to $\sim 2\,M_\odot\,\mathrm{pc}^{-2}\,\mathrm{Gyr}^{-1}$ in the outskirts. $\sum_{\mathrm{gas}}$ and $\sum_{\mathrm{SFR}}$ are well characterized by a local Schmidt law $\sum_{\mathrm{SFR}} \propto \sum_{\mathrm{gas}}^{n}$ with a power-law index of $n = 1.4 \pm 0.6$ (Fig. 3).

The critical gas velocity dispersions needed to stabilize the gas against gravitational collapse in the differentially rotating disk of M51 using the Toomre criterion, vary with radius between 1.7 and 6.8 kms^{-1}. Observed radially averaged dispersions derived from the CO data vary between 28 kms^{-1} in the center and $\sim$8 kms^{-1} at radii of 7 to 9 kpc. They thus exceed the critical dispersions by factors Q_{gas} of 1

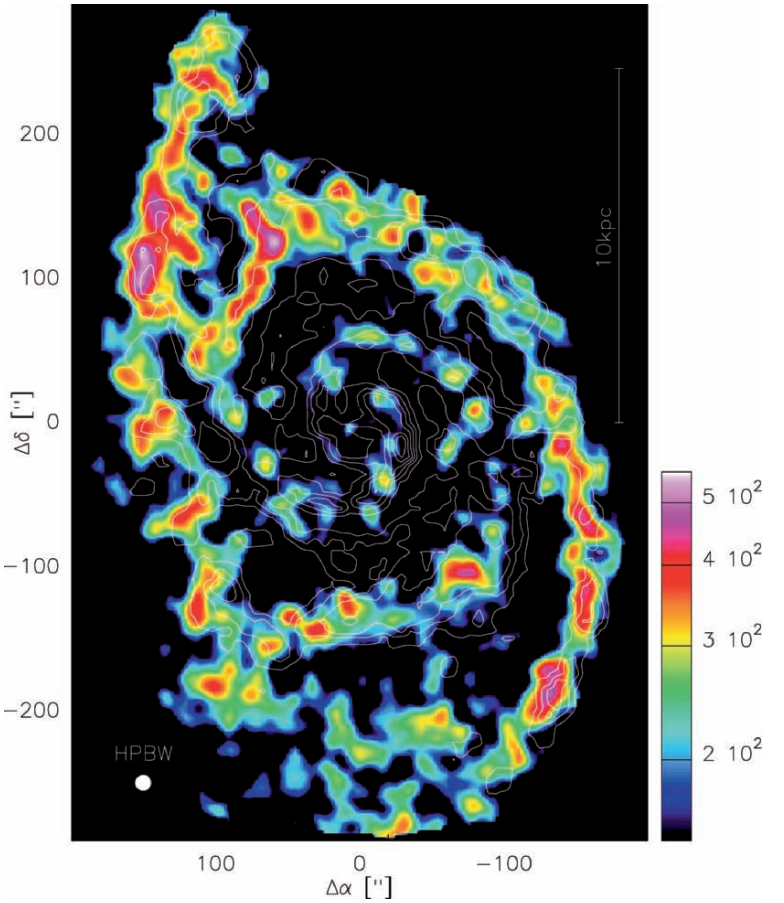

Fig. 2. VLA map of integrated HI intensities [Jy/beam] at 13″ resolution [2] in colors. Contours show integrated ^{12}CO 2–1 intensities (cf. Fig. 1).

to 5. Taking into account, in addition, the gravitational potential of stars, the disk may be critically stable.

2 Distribution of Molecular Gas

Molecular clouds are the sites of all star formation in the Milky Way and also in external galaxies. It is therefore of great interest to study the global distribution of star formation in entire galaxies by studying the distribution of the molecular gas. Nearby face-on galaxies like M51 offer the possibility to study the distribution of molecular gas over their entire surface at high spatial resolution and without the distance ambiguities as encountered for the Milky Way. In M51, the total mass of molecular material derived from the integrated ^{12}CO 2–1 intensities is $2\,10^9\,M_\odot$. The 3σ limit with resolutions of 11″ and $5\,\mathrm{kms}^{-1}$ corresponds to a mass of $1.7\,10^5\,M_\odot$.

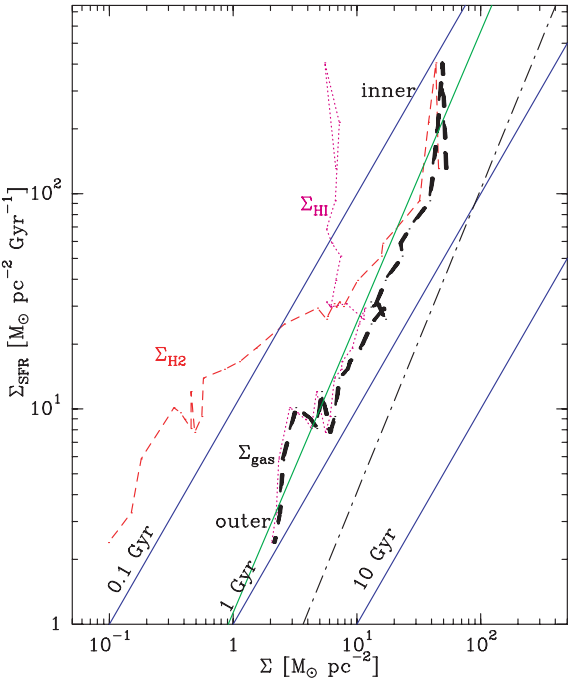

Fig. 3. Radially averaged star formation rate per unit area, $\sum_{\rm SFR}$, versus surface densities of the total gas $\sum_{\rm gas}$, and of H_2 and HI only. The solid green line is the local Schmidt-law found in M51. The dashed-dotted black line is the global Schmidt-law found by [4]. Drawn blue lines represent lines of constant gas depletion time or star formation efficiency.

The spatial resolution of 450 pc resolves structures larger than typical GMCs which we label giant molecular associations. These may be bound clusters of GMCs as suggested by [5] or random superpositions of GMCs [6]. In a first attempt to study the properties of these GMAs, we have decomposed the CO 2–1 data set into Gaussian shaped clouds using the *gaussclumps* algorithm [7]. This algorithm has been developed to study the statistical properties of the structure of molecular clouds as seen in spectral line emission cubes and has been applied to many Galactic clouds, e.g. [8, 15]. It iteratively fits a local Gaussian to the global maximum of the data and subtracts it. The algorithm fits the intrinsic, deconvolved widths to the observed data taking into account the given angular and spectral resolutions. It outputs the clump center positions and widths in the two spatial and in the velocity coordinates. It also outputs the clump peak temperatures, as also their orientations. In the following, we will use the term clouds or GMAs rather than clumps.

In M51, the algorithm decomposes 78% of the total mass into 155 clouds. Their deconvolved, i.e. intrinsic, sizes and FWHMs are larger than 20% of the resolutions. The 16 most massive GMAs with masses between $2\,10^7\,M_\odot$ and $1\,10^8\,M_\odot$ follow the two inner logarithmic spiral arms like beads on a string (Fig. 1). These masses exceed the masses derived by [5] using the three-element Caltech Millimeter Array

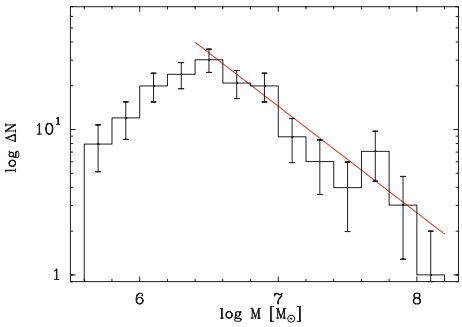

Fig. 4. The mass spectrum of GMAs identified in M51 shows the number of sources per logarithmic mass interval. Errorbars represent $\sqrt{\Delta N}$ statistical errors. The best fitting power law of the form $dN/dM \propto M^{-\alpha}$ has a slope of $\alpha = 2.0 \pm 0.2$.

Table 1. Mass spectra of GMCs and GMAs in external galaxies. The number of identified clouds is given in column 4. $M_{\rm min}$ and $M_{\rm max}$ are the minimum and maximum cloud mass detected. $M_{\rm turn}$ is the mass at the turnover of the spectrum.

Source	Distance	Resol. [pc^2]	No.	α	$M_{\rm min}$ [M$_\odot$]	$M_{\rm turn}$ [M$_\odot$]	$M_{\rm max}$	Lit.
NGC 4038/39	19 Mpc	310×480	100	1.4 ± 0.1	$2\,10^6$	$5\,10^6$	$9\,10^8$	[9]
M51	8.4 Mpc	450	155	2.0 ± 0.2	$5\,10^5$	$3\,10^6$	$1\,10^8$	[10]
M33	850 kpc	50	148	2.6 ± 0.3	$3\,10^4$	$2\,10^5$	$7\,10^5$	[11]
M31	780 kpc	90	389	1.6 ± 0.2	$2\,10^4$	$1\,10^5$	$5\,10^5$	[12]
LMC	54 kpc	41	168	1.9 ± 0.1	$4\,10^4$	$8\,10^4$	$3\,10^6$	[13]

by a factor of ~ 2, presumably due to the slightly larger beam size of the present study and missing short spacing information. Such very massive molecular cloud complexes have also been found in other galaxies. See the compilation by [9] (their Table 3). In our study of M51, GMAs are also identified along the two outer arms extending towards the companions galaxy in the north and to the south. At least five spoke like features connecting spiral arms are decomposed into clouds. Only few clouds are seen in the interarm medium. The least massive clouds have a mass of $5\,10^5$ M$_\odot$.

Figure 4 shows the mass spectrum of all 155 clouds. It follows a linear slope of $\alpha = 2.0 \pm 0.2$ above the turnover mass of $5\,10^6$ M$_\odot$. The turnover is presumably not intrinsic to the GMA distribution but caused by the detection limits, similar as in Galactic clouds [8]. A slope of 2.0 agrees well, within the error, with more recent large-scale mapping studies of Galactic clouds by e.g. [14, 8, 15, 16]. These studies find a rather constant slope of $\alpha = 1.6 - 1.9$ for cloud and clump masses between more than 10^4 M$_\odot$ and 10^{-4} M$_\odot$. Todate, only few studies exist which derive mass spectra of the entire cloud population of external galaxies. In Table 1, we compare the mass spectrum of M51, with those found in NGC 4038/39, M33, M31, and the LMC. The slope which we find in M51 is similar to the slope found in the Andromeda Galaxy using the same algorithm, though the study of M31 covers a lower mass range

due to its proximity. The slope is also similar to the slope found in the nearby dwarf galaxy LMC. The Antennae exhibit a rather flat mass distribution with very massive GMAs while M33 shows a very steep spectrum with $\alpha = 2.6$ similar to the initial mass function.

References

1. K. Schuster, C. Kramer, M. Hitschfeld, S. Garcia-Burillo, B. Mookerjea: accepted for publication in A&A (2006)
2. A.H. Rots, P.C. Crane, A. Bosma, E. Athanassoula, J.M. van der Hulst: ApJ, 100, 387 (1990)
3. I. Patrikeev, A. Fletcher, R. Stepanov, R. Beck, E.M. Berkhuijsen, P. Frick, C. Horellou: A&A in press (2006)
4. R.C. Kennicutt: ApJ, 498, 541 (1998)
5. R.J. Rand, S.R. Kulkarni: ApJL, 349, L43 (1990)
6. S. Garcia-Burillo, F. Combes, M. Gerin: A&A, 274, 148 (1993)
7. J. Stutzki, R. Guesten: ApJ, 356, 513 (1990)
8. C. Kramer, J. Stutzki, R. Roehrig, U. Corneliussen: A&A, 329, 249 (1998)
9. C.D. Wilson, N. Scoville, S.C. Madden, V. Charmandaris: ApJ, 599, 1049 (2003)
10. M. Hitschfeld, C. Kramer, K. Schuster, S. Garcia-Burillo, J. Stutzki, B. Mookerjea: A&A, in prep. (2007)
11. G. Engargiola, R.L. Plambeck, E. Rosolowsky, L. Blitz: ApJS, 149, 343 (2003)
12. S. Muller: "Molecular gas in the Andromeda Galaxy: properties of the molecular clouds", this conference
13. Y. Fukui, N. Mizuno, R. Yamaguchi, A. Mizuno, T. Onishi: PASP, 53, 41 (2001)
14. A. Heithausen, F. Bensch, J. Stutzki, E. Falgarone, J.F. Panis: A&A, 331, 65 (1998)
15. R. Simon, J.M. Jackson, D.P. Clemens, T.M. Bania, M.H. Heyer: ApJ, 551, 747 (2001)
16. M.H. Heyer, J.M. Carpenter, R.L. Snell: ApJ, 551, 851 (2001)

33

Mapping of Nearby Galaxies in [CI] 370 μm and CO (7→6) 371 μm

Thomas Nikola[1], G.J. Stacey[1], C.M. Bradford[2], A.D. Bolatto[3], S.J. Higdon[1], K. Isaak[4] and F. Israel[5]

[1] Cornell University tn46@cornell.edu
[2] JPL
[3] UC Berkeley
[4] Cardiff University
[5] Sterrewacht Leiden

Summary. The fine structure line of [CI] at 370 μm, and the CO (7→6) rotational line at 371 μm are important coolants which can be used to probe the temperature and density of the warm gas component in regions of enhanced star formation. These lines can be used to provide key constrains on the physical properties of the warm molecular gas component and to deduce the excitation mechanism that heats the molecular gas. We have used the Cornell submillimeter spectrometer, SPIFI, on the JCMT to map the [CI] and CO (7→6) line emission from the nuclear regions of the nearby galaxies NGC 253 and M82, and from the overlap region of NGC4038/9. In both NGC 253 and NGC 4038/9 the [CI] emission appears fairly constant, while the CO (7→6) emission peaks at the nucleus and the most active star-forming region, respectively. The observations of NGC 253 suggest that the majority of the nuclear molecular gas is most likely heated by cosmic rays. The spatial distribution of the line emission in the overlap region of NGC 4038/9 is suggestive of a PDR, with a decrease in density from the most active region to the outside. In contrast, in M82 both the CO (7→6) and [CI] line intensities vary over the mapped region, with the line ratios remaining fairly constant. This suggests a change in the beam filling factor of PDRs with a higher PDR number density in the most active regions.

1 [CI] 370 μm and CO (7→6) Line as Probes of the ISM

Far-ultraviolet (FUV) photons ($\sim 6 - 13.6$ eV) from the interstellar radiation field (ISRF) and nearby stars impinging on molecular clouds photodissociate the molecular gas and create a photodissociation region (PDR; e.g. [9]). In regions of enhanced star formation the PDR forms the interface between H II regions surrounding the newly-formed, massive star and their natal molecular cloud. PDRs constitute a large fraction of the interstellar medium (ISM). Emission lines from PDRs are therefore powerful probes of the chemical and the physical properties of the ISM and the ISRF. Far-IR and submillimeter lines from PDRs are particularly important as,

unlike optical or near-IR line emission, they are (almost) impervious to interstellar extinction.

1.1 [CI] 370 μm Emission Line

Atomic carbon has two fine structure lines in the submillimeter wavelength regime: the $^3P_1 \rightarrow ^3P_0$ transition at 609.135 μm and the $^3P_2 \rightarrow ^3P_1$ transition at 370.415 μm. The origin of the [CI] submillimeter lines is well described by PDR models (e.g. [9] [6] and references therein), in which the [CI] emission arises mostly from the surface of molecular clouds between the [CII] emitting region and the bulk of CO gas. The column density of this C$^\circ$ layer is independent of the strength of the FUV flux. However, the strength of the FUV field determines the depth of the C$^+$/C$^\circ$/CO transition. In addition to this peak in the C$^\circ$ abundance a second peak in the neutral carbon abundance occurs at larger depths ($A_V \sim 7$; [6]).

To-date, the majority of the ground-based [CI] observations have been made using the lower-J 609 μm line because of favorable atmospheric conditions. These observations show extended [CI] emission and a good correlation between [CI] and ^{13}CO ($2 \rightarrow 1$) emission (e.g. [10] [5]). The observed abundances are typically C$^\circ$/CO ~ 0.1 within the Galaxy and C$^\circ$/CO ~ 0.5 in starburst nuclei. Models of clumpy PDRs [14] can readily explain these results. Another explanation for the high C$^\circ$ abundances would be the dissociation of carbon bearing molecules by cosmic rays or X-rays deeper inside the molecular cloud. X-rays can generate a similar structure than PDRs, but since they penetrate deeper into a cloud, creating a so called XDR (e.g. [12]), they create a larger column density of C$^\circ$. Similarly, cosmic rays penetrate deeper into the molecular cloud than FUV or X-ray radiation and can alter the chemical composition, leading to a higher C$^\circ$ abundance [4].

Despite worse atmospheric conditions, observation of the [CI] 370 μm line has an advantage over the 609 μm line, since it is a transition between excited levels and thus not affected by cold foreground gas. The [CI] 370 μm line has an excitation temperature of $T_{\rm ex} = 63$ K and a critical density of $n_{\rm crit} = 1.2 \times 10^3$ cm^{-3} compared to $T_{\rm ex} = 24$ K and $n_{\rm crit} = 4.7 \times 10^2$ cm^{-3} for the 609 μm line.

1.2 CO 371 μm Emission Line

The CO (J=7$\rightarrow$6) 371.651 μm rotational transition has a critical density of $n_{\rm crit} = 3.9 \times 10^5$ cm^{-3} and an excitation temperature of $T_{\rm ex} = 155$ K. This line, which is usually optically thin, is a good tracer of hot, dense molecular gas and therefore an excellent probe of the vast amount of warm, dense molecular gas typically found in regions of enhanced star formation. Line excitation mechanisms include mechanical heating due to shocks and supernovae (SN) blast waves, FUV (PDRs) and cosmic rays.

The temperature and density of the molecular gas can be estimated assuming large velocity gradient (LVG) models, which are constraint by observations of multiple transitions of the rotational ladder of, for example, CO. Robust constraints on the denser, warmer gas component can only be achieved through observations of the higher-J transitions which are strongly excited under such conditions.

1.3 Emission Line Comparison

The ratio of the integrated intensities of CO (7→6) to [CI] (370 μm) is a sensitive probe of the density (Fig. 1) over the range found in PDRs in regions of enhanced star formation and it is almost independent of the ISRF over most of the density range.

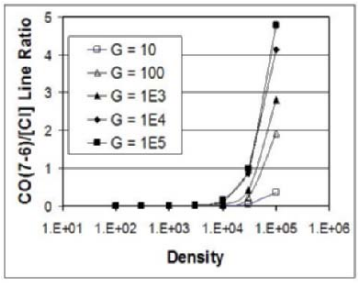

Fig. 1. CO (7→6)/[CI] 370 μm line intensity ratio vs. density for various values for the strength of the ISM (derived from [9])

Adding the [CII] 158 μm line to the comparison of the [CI] and CO (7→6) line intensities provides a tool that can distinguish between excitation by an AGN or by various types of starbursts: (a) in a standard starburst all three lines are strong; (b) in the case of a heavily dust-enshrouded starburst the [CII] line is suppressed due to extinction, reducing the line intensity by factors of 10, while the [CI] and CO (7→6) lines remain strong; (c) in an old starburst both the [CII] and [CI] emission are reduced by factors of 10 due to the lack of energetic FUV photons that are required to dissociate CO, and (d) in an AGN all three tracers are expected to be weak, with line intensities lowered as much as a factor of 100. In the case of an AGN the ISRF is very strong, making the photoelectric heating of the gas very inefficient. In addition, the high energy photons will dissociate most of the CO and carbon will be at much higher ionization states.

We use the [CI] and CO (7→6) lines to map nearby galaxies and to characterize the ISM in the regions of enhanced star formation in order to investigate the interplay between the star formation regions and their environment.

2 Observation

We used the South Pole Imaging Fabry-Perot Interferometer (SPIFI; [1]) at the James Clerk Maxwell Telescope (JCMT) on Mauna Kea, Hawaii, to observe the CO (7→6) and the [CI] 370 μm line emission from selected regions of NGC 253, M82, and NGC 4038/9. SPIFI employs a 5×5 pixel array of silicon bolometers, covering a total field of view of $35'' \times 35''$. We have set the resolution to $R = 1500$ and

scanned the Fabry-Perot Interferometer over a wavelength range of 1700 km/s. The [CI] 370 μm line and the CO (7→6) are 1000 km/s apart. SPIFI can therefore detect both lines in a single scan, resulting in very good relative calibration of the lines. In addition SPIFI obtains a spectrum in each pixel simultaneously. This is important since the correction for atmospheric transmission is the greatest uncertainty in the spectra.

3 NGC 253

NGC 253 is an isolated, nearby ($\sim$ 2.5 Mpc) barred spiral galaxy with a starburst concentrated within about 60 pc of the nuclear region.

We have previously observed NGC 253 in the CO (7→6) [2], revealing a significant quantity of warm molecular gas, more than a factor of 30 higher than that expected from standard PDR models. Our observation ruled out mechanical heating due to shocks/SN blasts, and suggested cosmic rays as the heating source. In our new observation we obtained both the [CI] and CO (7→6) line, enabling us to place much tighter constraints on the mechanism that heats the dense molecular gas.

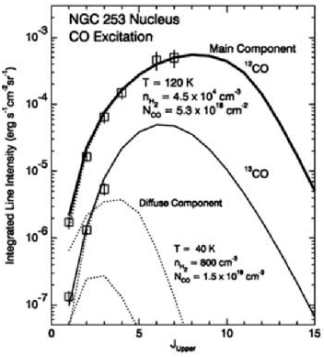

Fig. 2. Run of CO line intensities in NGC 253 [2]

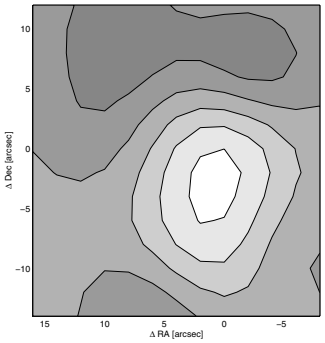

Fig. 3. Integrated CO (7→6) line intensity distribution in the center of NGC 253

The observed CO emission peaks in the nuclear region (Fig. 3) with an integrated line intensity of about 1900 K km/s, which agrees with our previous observation. The strongly peaked emission is suggestive of a very localised region with warm, dense molecular gas. In contrast, the [CI] emission is almost uniform with a slight depression at the center and to the west. The average, integrated intensity is about 1280 K km/s and the deviation from this value is at most 2 sigma over the mapped region. The [CI] integrated intensity is about a factor of 1.5 - 2 higher than that of the [CI] 609 μm line [8]. Such a high ratio suggests that the physical temperature of the emitting gas is at least 120 K, which is in agreement with the temperature required to explain our CO (7→6) observation. Using the [CI] line intensity we derive a mass of the [CI] emitting region of about 10^7 $M_\odot$ within the central 20″. This is about 4 times the derived PDR mass in the center of NGC 253 [3].

The ratio of the CO (7→6) to [CI] 370 μm line peaks at the center of NGC 253 with a value of ∼2 and falls of with distance from the center to a value of ∼1. The decrease in the ratio is suggestive of a decrease in the density of PDRs as illustrated in Fig. 1. The line ratio in the center of NGC 253 indicates a density of roughly 5×10^4 cm^{-3}, in agreement with our previous LVG model [2].

4 M82

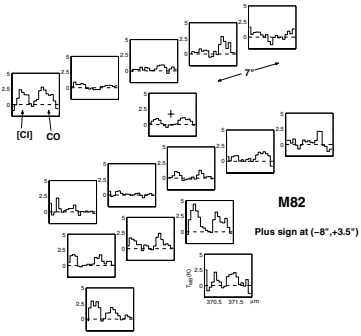

Fig. 4. [CI] and CO (7→6) spectra of a single SPIFI footprint on the nucleus of M82.

M82 is the archetypical starburst galaxy at a distance of 3.5 Mpc. It has an irregular morphology and an extended starburst region. In Fig 4 we show a single SPIFI footprint of the nuclear region. In total we have observed an area of about $55'' \times 45''$ and both lines are detected over a region of ∼ 400 pc. The nuclear region of M82 has been observed extensively in CO [11] [17] [16]. Our observation of the CO (7→6) emission is in general agreement with the CO (7→6) distribution seen by [11]. The [CI] line is typically as strong as the CO (7→6) line, indicating a highly excited and dense medium, which is typical of that found in starburst regions. The [CI] and CO (7→6) line intensities vary over the mapped region, however the line ratio remains fairly constant. This suggests that while the number of PDRs in the beam changes, the physical conditions in the PDRs remain the same.

5 NGC 4038/9

We have observed the overlap region of the strongly interacting galaxies NGC 4038 and NGC 4039, more commonly known as the Antennae. At a distance of about 21 Mpc, the Antennae is one of the most studied interacting systems. Shown in Fig. 5 is the overlay of the SPIFI footprint on an Spitzer/IRAC image of the Antennae: the region observed with SPIFI includes the region with the strongest mid-IR emission and the strongest star formation activity as traced by ISOCAM [13].

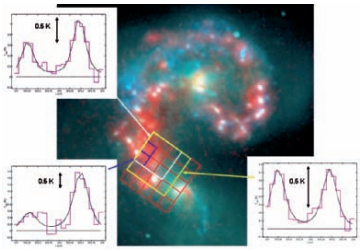

Fig. 5. Combined [CI] and CO spectra and detector footprint [7] overlayed on an Spitzer IRAC image of the Antennae Galaxy [15]

The signal-to-noise of our data is low: by averaging the spectra as shown in Fig. 5 we can see that the integrated intensity of the [CI] line stays constant over the region, while the CO (7→6) peaks sharply at the most active region, where its integrated intensity is a factor of about 3 higher than the equivalent [CI]. In the spectrum averaged over the largest area the [CI] and CO (7→6) lines are about equal. As shown in Fig. 1 a line ratio of about 3 suggests that the ISRF is at least 10^3 $G_\circ$. The observed decrease in the line ratio between the most active region and the averaged overlap region can be attributed to either a decrease in density by a factor of ∼2 (constant ISRF), or decrease by a factor of ∼100 in the ISRF (constant density).

Acknowledgement. This work was supported by NSF grants OPP-0094605, OPP-0338149, and OPP-0126090.

References

1. Bradford, Stacey, Swain, et al.: ApOpt 41, 2561 (2002)
2. Bradford, Nikola, Stacey, et al.: ApJ 586, 89 (2003)
3. Carral, Hollenbach, Lord, et al.: ApJ 423, 223 (1994)
4. Farquhar, Millar, & Herbst: MNRAS 269, 641 (1994)
5. Gerin & Phillips: ApJ 537, 644 (2000)
6. Hollenbach & Tielens: ARA&A 35, 179 (1997)
7. Isaak, K. (in preparation)
8. Israel, White, Baas: A&A 302, 343 (1995)
9. Kaufman, Wolfire, Hollenbach, & Luhman: ApJ 527, 795 (1999)
10. Keene, Lis, Phillips, & Schilke: IAUS 178, 129 (1996)
11. Mao, Henkel, Schulz, et al.: A&A 358, 433 (2000)
12. Meijerink & Spaans: A&A 436, 397 (2005)
13. Mirabel, Vigroux, Charmandaris, et al.: A&A 333, L1 (1998)
14. Spaans: A&A 307, 271 (1996)
15. Spitzer/IRAC image of the Antennae Galaxy; Spitzer Space Telescope, IRAC,; NASA/JPL-Caltech/Z.Wang (Harvard Smithsonian CfA)
16. Ward, Zmuidzinas, Harris, & Isaak: ApJ 587, 171 (2003)
17. Wild, Harris, Eckart, et al.: A&A 265, 447 (1992)

34

Molecular Gas and Star Formation in Nearby Galaxies

Shinya Komugi[1], Yoshiaki Sofue[1], Hiroyuki Nakanishi[2], Sachiko Onodera[1], Fumi Egusa[1], Kazuyuki Muraoka[1], and Judith S. Young[3]

[1] Institute of Astronomy, University of Tokyo skomugi@ioa.s.u-tokyo.ac.jp
[2] Nobeyama Radio Observatory, National Astronomical Observatory of Japan
[3] University of Massachussetts, Amherst

Summary. The quantitative relationship between molecular gas and star formation, or the Schmidt Law, was derived for the central kpc of nearby spiral galaxies using ^{12}CO(J=1-0) line data and Hα imaging. The CO spectra were obtained at the 45m telescope at Nobeyama Radio Observatory (NRO). The derived Schmidt law index is found to be affected significantly depending on galaxy distance, ranging from 0.7 to 1.3. The data covers the densest regions of normal spirals, and overlaps with starburst galaxies. We categorize the Schmidt law according to existence of bars. Barred galaxies are found to display a Schmidt law with higher gas density, but on the same Schmidt law track as non-barred samples.

1 Introduction

Past studies have shown that the Schmidt law, or the power law relation between gas density and star formation rate (SFR), is to some extent a universal characteristic of spiral galaxies in general(Kennicutt 1998)[5]. It is tempting, still, and worthwhile to categorize the Schmidt law by galactic characteristics in a global scale. In other words, it is possible that the relation between gas content and star formation rates may vary depending on morphology, galaxy type, and other possible parameters which are assigned to global characteristics of a target galaxy.

To fulfill the above aim, we conducted a large scale survey of the central regions of nearby galaxies in ^{12}CO (J = 1–0)using the NRO45m telescope. We compared the molecular gas density observed in this survey with a uniform set of Hα data.

2 Data

2.1 CO Observation

The observations of the ^{12}CO(J = 1–0)line at 115GHz were conducted with the 45m telescope at NRO during three observing runs in May 2005, December 2005,

and January 2006. The beamsize at 115GHz is 16". We chose our sample from galaxies observed in Young et al. (1995)[11], with priority on galaxies whose Hα data are accessible and the internal Hα extinction can be corrected via E(B-V) from Ho et al. (1997)[4]. As a result, we were able to observe a sample of 69 galaxies within limited time.

Compiled with previous measurements at NRO45m (Nishiyama & Nakai, 2001)[7] and similar angular resolution (22") single dish data from the IRAM30m telescope (Böker et al. 2003[1], Braine et al. 1993[2], Combes et al. 1988[3], Planesas et al. 1989[8]), our data set is comprised of 189 nearby (mainly spiral) galaxies, of which 162 are detected at a 5 σ level. Morphology and distance distribution of the detected samples are in table 1 and figure 1, respectively.

Table 1. Morphology of the Sample Galaxies. Others include Irregular and Peculiars

	0,a,ab	b,bc	later
S, SA	11	20	28
SAB, SB	14	35	51
Others	3	0	0

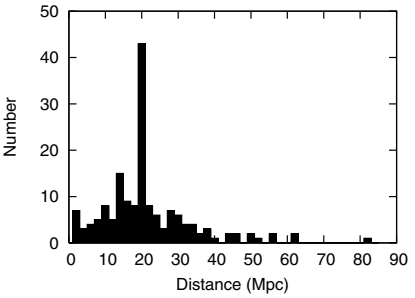

Fig. 1. Distance Distribution of the Sample Galaxies. Most of the galaxies are members of the Virgo cluster, indicated by the peak at 20Mpc. Note that the NRO45m beamsize of 16" corresponds to roughly the central 1 kpc at this distance.

2.2 Hα Data

The SFR, in units of $M_\odot pc^{-2} yr^{-1}$, was derived from narrow band imaging by Young et al. (1996)[12] and the calibration by Kennicutt (1998)[5]. Internal extinction was corrected using $E(B-V)$ for the central regions from spectroscopic data from Ho et al. (1997)[4]. SFR for 66 galaxies observed in CO were corrected using this method.

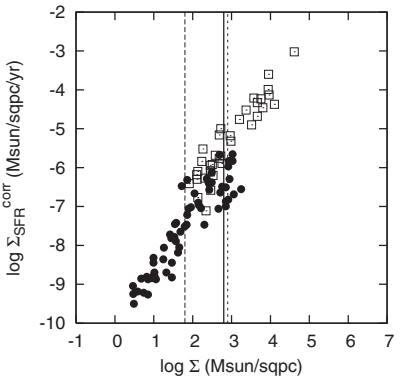

Fig. 2. The Schmidt Law, from Komugi et al. (2005)[6](filled circles; normal nearby spirals) with circumnuclear starburts from Kennicutt (1998)[5] plotted in open squares. The vertical lines correspond to the boundary for spontaneous and cloud-collision as the mechanism for star formation (Komugi et al. 2006, in print).

3 The Schmidt Law

Figure 3 is the obtained relation between SFR and surface gas density $\Sigma_{\rm SMD}$ ($\rm M_\odot pc^{-2}$) assuming a uniform CO-$\rm H_2$ conversion factor of $\rm X_{CO} = 2.8 \times 10^{20}$ ($\rm cm^{-2}$). A linear fit gives a slope of $N = 0.8 \pm 0.1$ for the Schmidt law index. Plots which seem to be deviated are mostly galaxies with irregular morphology. A comparison with figure 2 shows that the plots dominate the densest regions of normal spiral galaxies.

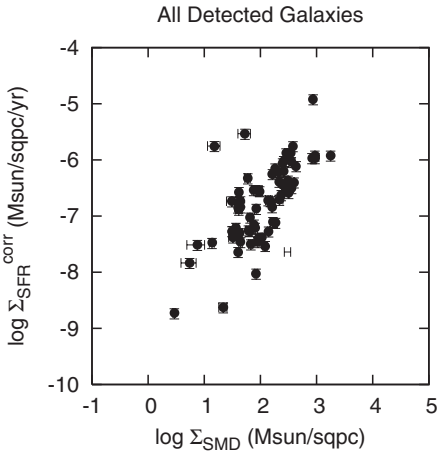

Fig. 3. All the detected samples with $\Sigma_{\rm SFR}$ corrected for extinction. Galaxies which did not have $E(\rm B-V)$ measurements are omitted.

4 Effect of Distance

The single beam of either the NRO45m or the IRAM30m telescope subtends different scales depending on the distance to the galaxy. It is important to know what effect this can have on the gas-SFR relation. Figure 4 shows the same plots as figure 3 but divided by whether the galaxy is closer than an arbitrary distance of 15Mpc or not.

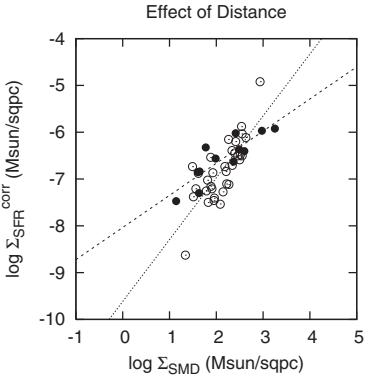

Fig. 4. Effect of distance on the Schmidt law. Samples are the same as figure 3, with irregular galaxies omitted. Galaxies with distance of 15Mpc or less in filled circles, more than 15Mpc in open circles. The broken line is a fit to the closer galaxies with a fixed slope of 1, and the dashed line is a fit to the farther galaxies, with a slope of 1.32

A best fit to the closer galaxies give a slope N of 0.69 ± 0.13, and 1.32 ± 0.19 for the farther galaxies. The two are significantly different.

The arbitrary 15Mpc was chosen so that the NRO45m beam of 16" corresponds to a scale of 1.2 kpc, or 600pc from the nucleus. Sakamoto et al. (1999)[9], Sofue et al.(2003b)[10] and others have shown that many spirals have a central exponential molecular disk, with a characteristic radius of roughly this size. It may be possible, that observing galaxies closer than 15 Mpc will truncate this observed region of exponential structure. Assuming that the star forming nuclear disk is also exponential and about this size, the observed Schmidt law index will be biased towards $N \sim 1$ (Komugi et al. 2007, in prep.), and although the observed slope is 0.69, a fit of $N = 1$ also seems to be reasonable (see figure 4). Galaxies with distances of more than 15 Mpc will give $\Sigma_{\rm SMD}$ and $\Sigma_{\rm SFR}$ of more or less a global scale of this exponential structure. Although this argument alone cannot give a decisive conclusion to the difference in the slope, we categorize these galaxies with different distance regimes in the following analysis.

5 Effect of Bars

One of the primary goals of this study is to see the effect of bars on the Schmidt law sequence. Bars are understood in general to feed gas into the central kpc of galaxies

(Sakamoto et al. 1999[9], Sofue et al. 2003b[10]). Under this assumption, one of two cases may be observed: (1) bars concentrate gas into the central kpc, but a common Schmidt law explains the SFR in the same way as non-barred galaxies, or (2) due to central condensation of gas, bars induce additional star formation than can be predicted by the Schmidt law, in which case the star formation efficiency (SFE) will rise and a different sequence in the Schmidt law can be seen.

The Schmidt law categorized by the existence of bars can be seen in figure 5.

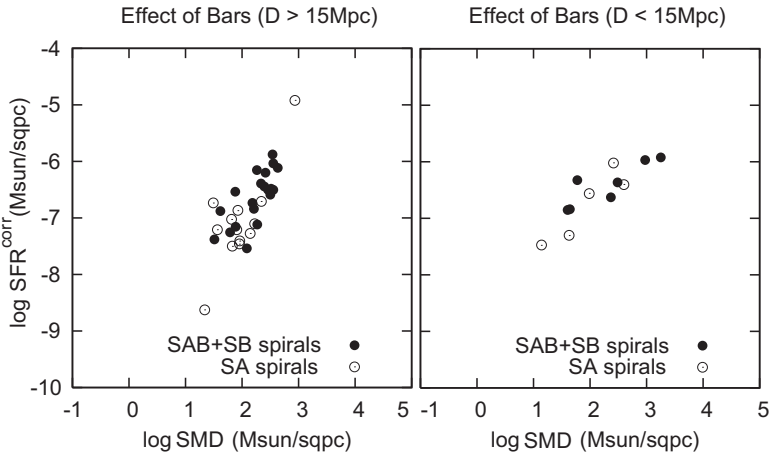

Fig. 5. The Schmidt law categorized by bar/non-barred galaxies. Left: for galaxies with distance of more than 15Mpc. Right: for galaxies closer than 15Mpc.

Apparently, barred galaxies occupy the denser regime cofirming that bars condense gas into the central region. A sequential offset between barred and non-barred galaxies is not seen, however, and the two morphological types seem to follow a common Schmidt law. Case (1) is supported, therefore. This can be further visualized in terms of the SFE, in figure 6. The SFE as a function of $\Sigma_{\rm SMD}$ seem to be independent of the existence of bars, although with considerable dispersion.

We therefore conclude from these observations that in a statistical sense, bars do concentrate gas into the central kpc but does not raise the SFE, and star formation occurs according to a common Schmidt law as non-barred galaxies.

References

1. Böker, T., Lisenfeld, U., & Schinnerer, E.: , A& A, 406, 87 (2003)
2. Braine, J., Combes, F., Casoli, F., Dupraz, C., Gerin, M., Klein, U., Wielebinski, R., & Brouillet, N.: A&AS, 97, 887 (1993)
3. Combes, F., Dupraz, C., Casoli, F., & Pagani, L.: A& A, 203, L9 (1988)
4. Ho, L. C., Filippenko, A. V., & Sargent, W. L. W.: ApJSS, 112, 315 (1997)
5. Kennicutt, R. C., Jr.: ApJ, 498, 541 (1998)

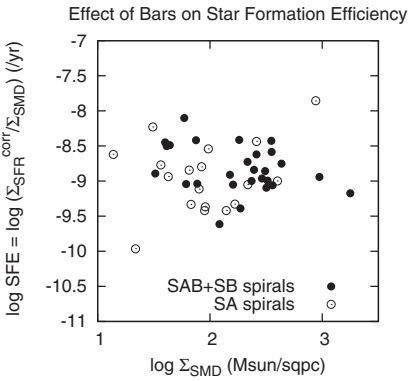

Fig. 6. The SFE, for all the galaxies in figure 5. SFE is derived as $\Sigma_{\rm SFR}/\Sigma_{\rm SMD}$.

6. Komugi, S., Sofue, Y., Nakanishi, H., Onodera, S., & Egusa, F.: PASJ, 57, 733 (2005)
7. Nishiyama, K., & Nakai, N.: PASJ, 53, 713 (2001)
8. Planesas, P., Gomez-Gonzalez, J., & Martin-Pintado, J.: A& A, 216, 1 (1989)
9. Sakamoto, K., Okumura, S. K., Ishizuki, S., & Scoville, N. Z.: ApJSS, 124, 403 (1999)
10. Sofue, Y., Koda, J., Nakanishi, H., & Onodera, S.: PASJ, 55, 59 (2003)
11. Young, J. S., et al.: ApJSS, 98, 219 (1995)
12. Young, J. S., Allen, L., Kenney, J. D. P., Lesser, A., & Rownd, B.: AJ, 112, 1903 (1996)

35

Extragalactic Magnetic Fields

Richard Wielebinski

Max-Planck-Institut für Radioastronomie, Auf dem Hügel 69, 53121 Bonn, Germany
rwielebinski@mpifr-bonn.mpg.de

Summary. Magnetic fields were first discovered by the observation of optical polarization in our Galaxy. Theoretical work suggested that magnetic fields can align dust grains and this then can lead to the observed optical polarization. Soon after this discovery the sensitivity of the observations was improved that allowed the detection of optical polarization in nearby galaxies. Radio polarization is a consequence of the synchrotron emission process, the emission of radio waves by relativistic electrons in magnetic fields. The radio waves are emitted with the E vector normal to the magnetic field direction. In the passage through a magneto-ionic medium the position angle of the emitted linear polarization is rotated (the Faraday effect) and hence we can determine the magnetic field along the line of sight. In my contribution I will concentrate on the results of the radio observations of magnetic fields in nearby galaxies. The present knowledge about distant magnetic fields will be briefly sketched. The results on the magnetic fields of the Galaxy are presented by W. Reich (this volume).

1 Introduction

The earliest indication of the existence of magnetic fields in nearby galaxies came from optical polarization observations (e.g. [23], [1]). At first the optical astronomy community was divided on the question if this polarization was a consequence of dust grain alignment (the Davis–Greenstein effect) or just simply a scattering effect. The first radio polarization observations of nearby galaxies ([38], [5], [6]) showed that indeed the magnetic fields in these extra-galactic objects were present and actually confirmed the earlier optical results. By going to higher radio frequencies (e.g. [28], [29]) observations of many nearby objects followed, showing large-scale magnetic fields. A much cited review by Sofue et al. [41] described the state of knowledge about magnetic fields in galaxies at that time. Magnetic fields have also been detected in radio galaxies as well as in clusters of galaxies.

In trying to understand the morphology of magnetic fields in galaxies, theoretical work by Piddington [35], Tosa & Fujimoto [45] and Sofue et al. [40] investigated the development of a bi-symmetrical spiral field from a primordial intergalactic magnetic field by shear in a galactic rotation. Alternatively the dynamo theory, originally

developed to explain the Earths magnetic field, by Parker [34] and Steenbeck & Krause [42] was extended to be applicable to other cosmic objects. More recently computer simulations of the amplification of magnetic fields by kinetic processes (e.g. [20]) or the solution of full magnetohydrodynamic (MHD) problems (e.g. [9]) showed great promise. The interpretation of details of extragalactic magnetic fields in jets (e.g. [36]) and in large volumes like clusters of galaxies also received attention. A review of the situation in clusters of galaxies can be found in Carilli & Taylor [10]. In this talk I will describe the data on magnetic fields in nearby galaxies and leave the theoretical discussion on the origin of these fields to other speakers.

2 Recent Data on Nearby Galaxies

The accumulation of data about the morphology of galactic magnetic fields in recent years was possible due to a few large radio telescopes. The Effelsberg 100-m radio telescope was instrumental in providing multi-frequency maps of many galaxies at medium angular resolution. The VLA has played a major role in providing the detailed structures. In particular the VLA data in combination with Effelsberg maps gives the best information. The Parkes telescope has been used to map the magnetic fields in the Magellanic Clouds. The Australia Telescope Compact Array has mapped a number of galaxies, also in polarization. An 'Atlas of Magnetic Fields' is available at: `www.mpifr-bonn.mpg.de/div/konti/mag-fields.html`. In the following I will discuss some of the details of selected galaxies in this compendium before coming to a characterization of the magnetic field morphology. Many reviews have been published on this subject (e.g. [47], [7], [18], [2]).

2.1 LMC/SMC

The Large Magellanic Cloud (LMC) and the Small magellanic Cloud (SMC) were mapped by Haynes et al. [21], [22] and the magnetic fields were described by Klein et al. [31]. A surprisingly well organized magnetic field is seen in this irregular galaxy originating in the 30 Doradus complex, rather than from the main nucleus of the LMC. The distribution of the radio polarization is in good agreement with the optical polarization data. Recent observations of Faraday Rotation of sources beyond the LMC by Gaensler et al. [16] confirmed these earlier results. The radio polarization in the SMC is less distinctive, nevertheless the observed radio vectors suggest a field orientation along the bar (Fig. 1).

2.2 M 31

This nearest spiral galaxy has been a subject of many studies. The early low angular resolution observations (e.g. [6]) suggested a 'ring' magnetic field. The analysis of high angular resolution multi-frequency data by Fletcher et al. [14] shows a more complex picture, namely an axisymmetric magnetic field structure with significant radial component. The total equipartition field strength was found to be $B \sim 5\,\mu$G. Polarization observations at the highest angular resolution show structures termed as 'canals' ([39]), probably generated in the Galactic foreground (see W. Reich, this volume).

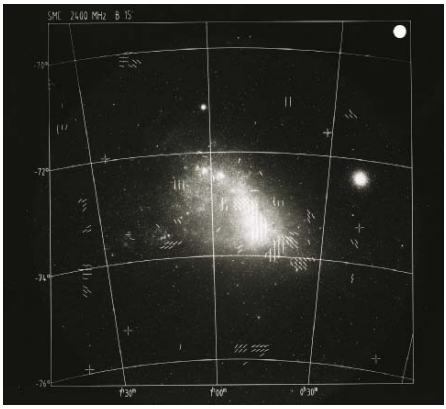

Fig. 1. The B-field in the Small Magellanic Cloud

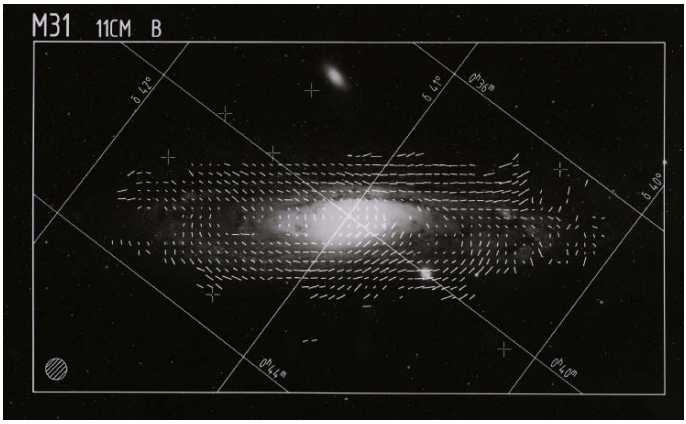

Fig. 2. The B-field of M 31 observed in 1980

2.3 M 51

This classical spiral galaxy was most important in all the studies because of its high radio luminosity. The earliest polarization data came from Segalovitz et al. [38]. High-frequency observations by Klein et al. [29] were obtained, allowing the study of Rotation Measure for M 51. The first combination of Effelsberg and VLA data was made for this object (Fig. 4). The highest angular resolution so far achieved for any object ([15]) was $6''$ giving most interesting insights in the morphology of magnetic fields in this object. By now M 51 has been observed at several frequencies allowing detailed Faraday rotation studies. The turbulent magnetic fields are strongest in the spiral arms with field strength $B \sim 20\,\mu$G. The inter-arm magnetic fields are lower ($B \sim 10\,\mu$G) but well ordered. Comparison of the magnetic field morphology with all other components (e.g. Hi, CO, Hα, IR) shows that the correlation is best between

magnetic field and the 15 μm emission. This suggests a coupling of the magnetic fields to the warm dust and gas component in the galaxy.

2.4 NGC 6946

This galaxy was mapped in polarization by Klein et al. [28] and more recently by Beck & Hoernes [4]. The spiral arm structure is well replicated in the magnetic field morphology but a bi-furcation of the field is seen in the outer reaches of the galaxy. A study of the energy densities in NGC 6946 ([2], p. 45) show that the scale length of the magnetic field is largest with $l \sim 16$ kpc, larger than cold gas ($l \sim 4$ kpc), warm gas ($l \sim 4$ kpc) or cosmic rays ($l \sim 8$ kpc). The bi-furcation of magnetic field in outer spiral arms has also been observed in other galaxies, e.g. in NGC 2997 ([19]).

2.5 NGC 4631 and Other Edge-on Galaxies

The edge-on galaxy NGC 4631 is known to possess a large radio halo. Detailed polarization observations have shown that the magnetic field is along the disc of the galaxy but with prominent vertical components (e.g. [17]) extending into the halo, especially from the nucleus (Fig. 3). These features give often the appearance of an X-shape suggesting that large-scale magnetic fields are present in the halos. Similar vertical features have been observed in other edge-on galaxies like NGC 5775, and M 104 ([32]).

2.6 M 82

This prototype nearby starburst galaxy is an important object whenever first observations are made in any spectral range because of its luminosity. It has been observed

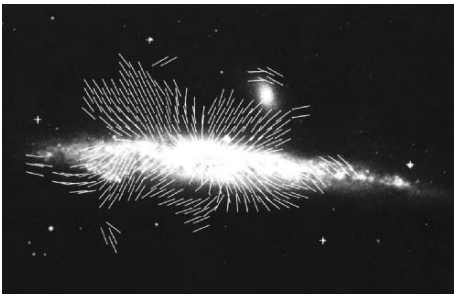

Fig. 3. The B-field in the edge-on galaxy NGC 4631

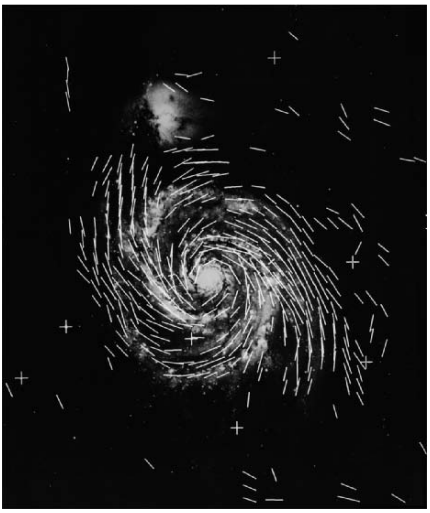

Fig. 4. The B-field of M 51 observed in Effelsberg

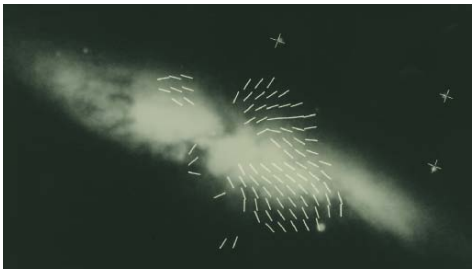

Fig. 5. The B-field of M 82 result of VLA observations

in a very wide spectral range (e.g. [30]). The magnetic field is most intense in this galaxy reaching $B \sim 50\,\mu$G. Magnetic fields along the disc as well as vertical fields originating in the nucleus have been observed by Reuter et al. [37] (Fig. 5) and more recently confirmed by Wielebinski [46]. This morphology has already been mentioned above for edge-on galaxies.

2.7 Barred Galaxies

Most galaxies have some sort of a bar. Well aligned magnetic fields have been detected in many barred galaxies. The most prominent objects that have been studied in detail are NGC 1097 and NGC 1365 ([8]). The results for NGC 1097 show that there is a well aligned magnetic field along the bar which follows the sudden change of direction at the end of the bar. Similar magnetic field morphology is observed in NGC 1365. This discovery has led to considerable theoretical investigations both numerical and analytical. Another spectacular barred galaxy is NGC 3627.

2.8 Irregular and Flocculent Galaxies

The irregular galaxies LMC and SMC were already discussed in Sect. 2.2. The surprisingly regular magnetic field in the LMC noted first by Klein et al. [31] was recently confirmed by Gaensler et al. [16]. Even more surprising was the result for NGC 4449 by Chyży et al. [12] which showed a very regular field, estimated to be $B \sim 10\,\mu$G, for this most irregular object. Also NGC 6822 [13] has a substantial magnetic field of $B \sim 5\,\mu$G. Spiral magnetic fields are also observed in several flocculent galaxies.

2.9 Interacting Galaxies

Magnetic fields have been detected in numerous galaxies in interaction. A classical example is the 'Antennae' system (NGC 4038/39) that shows considerable ($B \sim 50\,\mu$G) tangled magnetic field [11]. Also galaxies in the Virgo cluster show effects of compression due to the cluster mass distribution; this is discussed in detail by B. Vollmer (this volume).

3 A Characterization of Magnetic Fields in Nearby Galaxies

The observations that were described in Sect. 2 can be characterized to give an overview of the morphology of magnetic fields in nearby galaxies.

Both turbulent and regular magnetic fields are present in the observed galaxies. Turbulent magnetic fields are strongest in star-forming regions. Regular magnetic fields dominate in the inter-arm regions of galaxies with prominent spiral arms. In galaxies with known strong density waves (e.g. M 51) the regular field is also seen on the inside of the molecular spiral arm. In barred galaxies strong regular magnetic fields are seen in the bar and in the up-stream regions. The magnetic field lines follow the gas flow in bars. Field lines from spiral patterns, even in irregular and flocculent galaxies. The magnetic fields are strongly concentrated to the discs of galaxies, aligned in them. Regular fields follow the spiral arms showing occasional bi-furcation. Magnetic fields can be strongly distorted by tidal forces or ram pressure.

Observations of edge-on galaxies show that magnetic fields leave the disc and extend into the halo region. The scale height of halo fields is considerable, typically $l \sim 4$ kpc. Halo fields are responsible for depolarization in face-on galaxies by the Faraday effect.

The details of both the scales of magnetic fields in the discs and of halo fields are not observable with present instruments but may be studied in the near future with such instruments as the new E–VLA and in some time with the Square Kilometer Array (see [3]).

4 Distant Magnetic Fields

The fact that magnetic fields are present in the distant universe is a result of the early discovery that synchrotron radiation powers radio galaxies. Polarization observations of radio galaxies (e.g. [24], [26], [33]) have shown that magnetic fields are the basis of the formation of jets and the development of outer lobes. Since most quasars are detectable as synchrotron sources we must conclude that magnetic fields are present in these objects, out to $z \sim 6$. Also clusters of galaxies have been shown to harbour magnetic fields, (e.g. [27], [44]) with field strengths of $B \sim 2\,\mu$G. Recent work on Cosmic Microwave Background polarization (e.g. [43], [25]) suggests that possibly these are the signatures of the most distant magnetic fields.

5 Summary

I have not dealt with the origin of the magnetic fields in this contribution. I did mention some directions that interpretation did take, giving us up till now no final explanation of the role of magnetic fields in the Universe. A recent overview of many aspects of magnetic fields is found in Cosmic Magnetic Fields, Wielebinski & Beck ([48]). I believe that we have come a long way since the initial attempts to interpret the observations by either twisting of a primordial magnetic field or of a simple dynamo action. We have now definite evidence that magnetic fields are present everywhere in the extragalactic Universe and that they interact with the interstellar

medium. One must bear in mind that while gravitation is an omni-directional effect magnetic fields give a very uni-directional coupling. Hence quite weak fields may have a profound effect on dynamics of the ISM. It is not only a question of energy density but of real force on matter. This fact has not been exploited intensely up till now. As put in the discussion in this conference we do not know if magnetic fields are 'the chicken or the egg'; if magnetic fields are the result of the motion of the ISM, or if magnetic fields are guiding the flow of matter. In any case we must study magnetic fields, include them in the simulations to model the whole Universe, not just a part of it.

Acknowledgement. I would like to acknowledge many discussions in our continuum group at the MPIfR, in particular with Dr. Rainer Beck and Dr. Wolfgang Reich.

Richard Wielebinski

References

1. I. Appenzeller: PASP 79, 600 (1967)
2. R. Beck: 2005, In: *Cosmic Magnetic Fields*, Lecture Notes in Physics, vol. 664, ed by R. Wielebinski, R. Beck (Springer, Heidelberg 2005) p. 41
3. R. Beck, B.M. Gaensler: New Astron. Rev. 48, 1289B (2004)
4. R. Beck, P. Hoernes: Nature 379, 47 (1996)
5. R. Beck, E.M. Berkhuijsen, R. Wielebinski: A&A 68, L27 (1978)
6. R. Beck, E.M. Berkhuijsen, R. Wielebinski: Nature 283, 272 (1980)
7. R. Beck, A. Brandenburg, D. Moss et al.: ARA&A 34, 155 (1996)
8. R. Beck, A. Fletcher, A. Shukurov et al.: A&A 444, 739 (2005)
9. M. Camenzind: In: *Cosmic Magnetic Fields*, Lecture Notes in Physics, vol. 664, ed by R. Wielebinski, R. Beck (Springer, Heidelberg 2005) p. 255
10. C.L. Carilli, G.B. Taylor: ARA&A 40, 319 (2002)
11. K.T. Chyży, R. Beck: A&A 417, 541 (2004)

12. K.T. Chyży, R. Beck, S. Kohle et al.: A&A 356, 757 (2000)
13. K.T. Chyży, J. Knapik, D.J. Bomans et al.: A&A 405, 513 (2003)
14. A. Fletcher, E.M. Berkhuijsen, R. Beck, A. Shukurov: A&A 414, 53 (2004a)
15. A. Fletcher, R. Beck, E.M. Berkhuijsen et al.: In: *How does the Galaxy work?*, Astrophys. Space Science Library No. 315, ed by E.J. Alfaro et al. (Kluwer, Dordrecht 2004b) p. 299
16. B.M. Gaensler, M. Haverkorn, L. Staveley-Smith et al.: Science 307, 1610 (2005)
17. G. Golla, E. Hummel: A&A 284, 777 (1994)
18. J.L. Han, R. Wielebinski: Chin. J. A&A 2, 293 (2002)
19. J.L. Han, R. Beck, M. Ehle et al.: A&A 348, 405 (1999)
20. M. Hanasz, G. Kowal, K. Otmianowska-Mazur et al.: ApJ 605, L33 (2004)
21. R.F. Haynes, U. Klein, R. Wielebinski, J.D. Murray: A&A 159, 22 (1986)
22. R.F. Haynes, U. Klein, S.R. Wayte, R. Wielebinski et al.: A&A 252, 10 (1991)
23. W.A. Hiltner: ApJ 128, 9 (1958)
24. J.A. Högbom, I. Carlsson: A&A 34, 341 (1974)
25. K. Ichiki, K. Takahashi, H. Ohno et al.: Science 311, 827 (2006)
26. C.H. Ishwara-Chandra, D.J. Saikia, V.K. Kapahi et al.: MNRAS 300, 269 (1998)
27. K.-T. Kim, P.P. Kronberg, P.E. Dewdey et al.: ApJ 355, 29 (1990)
28. U. Klein, R. Beck, U.R. Buczilowski, R. Wielebinski: A&A 108, 176 (1982)
29. U. Klein, R. Wielebinski, R. Beck: A&A 135, 213 (1984)
30. U. Klein, R. Wielebinski, H. Morsi: A&A 190, 41 (1988)
31. U. Klein, R.F. Haynes, R. Wielebinski, D. Meinert: A&A 271, 402 (1993)
32. M. Krause, R. Wielebinski, M. Dumke: A&A 448, 133 (2006)
33. J. Machalski, M. Jamrozy: A&A 454, 95 (2006)
34. E.N. Parker: ApJ 142, 584 (1965)
35. J.H. Piddington: MNRAS 128, 345 (1964)
36. R.E. Pudritz, C.A. Norman: ApJ 274, 677 (1983)
37. H.-P. Reuter, U. Klein, H. Lesch et al.: A&A 282, 724 (1994)
38. A. Segalovitz, W.W. Shane, A.G. de Bruyn: Nature 264, 222 (1976)
39. A. Shukurov, E.M. Berkhuijsen: MNRAS 342, 496 (2003)
40. Y. Sofue, T. Takano, M. Fujimoto: A&A 91, 335 (1980)
41. Y. Sofue, M. Fujimoto, R. Wielebinski: ARA&A 24, 459 (1986)
42. M. Steenbeck, F. Krause: Zeitschr. f. Naturforsch. 21a, 1285 (1966)
43. K. Subramanian: Astron. Nachr. 327, 403 (2006)
44. M. Thierbach, U. Klein, R. Wielebinski: A&A 397, 53 (2003)
45. M. Tosa, M. Fujimoto: PASJ 30, 315 (1978)
46. R. Wielebinski: Astron. Nachr. 327, 510 (2006)
47. R. Wielebinski, F. Krause: Rev. A&A 4, 449 (1993)
48. R. Wielebinski, R. Beck: *Cosmic Magnetic Fields*, Lecture Notes in Physics, vol. 664, (Springer, Heidelberg 2005)

36

Galactic Winds

Sylvain Veilleux

Department of Astronomy, University of Maryland veilleux@astro.umd.edu

1 Introduction

Galactic winds have become arguably one of the hottest topics in extragalactic astronomy. This enthusiasm for galactic winds is due in part to the detection of winds in many, if not most, high-redshift galaxies. Galactic winds have also been invoked by theorists to (1) suppress the number of visible dwarf galaxies and avoid the "cooling catastrophe" at high redshift that results in the overproduction of massive luminous galaxies, (2) remove material with low specific angular momentum early on and help enlarge gas disks in CDM + baryons simulations, (3) reduce the dark mass concentrations in galaxies, (4) explain the mass-metallicity relation of galaxies from selective loss of metal-enriched gas from smaller galaxies, (5) enrich and "preheat" the ICM, (6) enrich the IGM without disturbing the Lyα forest significantly, and (7) inhibit cooling flows in galaxy clusters with active cD galaxies.

The present paper highlights a few key aspects of galactic winds taken from a recent ARAA review by Veilleux, Cecil, & Bland-Hawthorn (2005; herafter VCBH). Readers interested in a more detailed discussion of this topic are encouraged to refer to the original ARAA article.

2 Basic Physics

Here we summarize the basic physics behind galactic winds. The mechanical energy from a starburst- or AGN-driven wind is injected in the ISM of the host galaxy and transformed into thermal energy ("thermalization"). The expected temperature of this hot gas is $T = \dot{E}/\dot{M} \sim 10^8 \xi \Lambda^{-1}$ K, where ξ is the thermalization efficiency ($\leq$ 1; i.e. % of mechanical energy from the starburst or AGN which goes into heating the wind fluid) and $\Lambda = M_{\rm total}/M_{\rm ejecta}$ = mass loading term ($\geq$ 1). This bubble of hot gas is overpressured with respect to the rest of the ISM and therefore expands at velocity V(bubble) $\sim 100\ (\xi dE/dt_{42})^{0.2} n_0^{-0.2} t_7^{-0.4}$ km s^{-1} where n_0 is the nucleon density of the ISM in cm^{-3}, dE/dt_{42} is the rate of deposition of mechanical energy in units of 10^{42} erg s^{-1} and t_7 is the age of the bubble in units of 10^7 years.

If the energy source is powerful enough, the expanding bubble will burst out of the galaxy ISM and the wind fluid may reach a terminal velocity of up to

$V(\mathrm{wind}) \sim 3000\ \xi^{0.5} \Lambda^{-0.5}$ km s^{-1}. This value should be considered an upper limit to the actual velocity of the outflowing material. Perhaps a more relevant quantity is the terminal velocity of a cloud accelerated by the wind ram pressure $V(\mathrm{cloud}) \sim 600\ dp/dt_{34}^{0.5}\, \Omega_w^{-0.5} r_{0,\mathrm{kpc}}^{-0.5} N_{\mathrm{cloud},21}^{-0.5}$ km s^{-1}, where $N_{\mathrm{cloud},21}$ is the column density of the cloud in units of 10^{21} cm^{-2}, $r_{0,\mathrm{kpc}}$ is the initial radius in kpc at which the cloud enters the wind flow, dp/dt_{34} is the wind momentum flux in units of 10^{34} dynes, and Ω_w is the solid angle of the wind in steradian.

3 Local Galactic Winds

3.1 Milky Way

Only 8.0±0.5 kpc distant, the Galactic Center shows remarkable energetic activity at infrared, radio, X-ray and γ-ray wavelengths. A particular problem with galactic wind studies has been deriving reliable energies from multi-wavelength observations at comparable resolution. Current estimates of the energetics of our Galactic Center span a huge range. Sofue & Handa (1984) discovered the 200 pc diameter Galactic Center radio lobe (GCL), with an implied thermal energy of $\sim 3\times10^{51}$ erg. Chevalier (1992) argued for a higher value ($\sim 2\times10^{52}$ erg) due to winds from hot young stars over the past 30 Myr. Others have argued from the high temperatures implied by the ASCA detection of 6.7 keV Kα emission from He-like Fe XXV (Koyama et al. 1989, 1996; Yamauchi et al. 1990; see Hyodo's contribution at this conference for a discussion of the recent Suzaku results) that an explosive event ($4-8\times10^{53}$ erg) must have occurred. Bland-Hawthorn & Cohen (2003) detected the GCL at mid-IR wavelengths. The association of the lobe with denser material raises the energetics to $10^{54}/\kappa$ erg, where κ is the covering fraction of the dense shell; less energy is needed if there is substantial polycyclic aromatic hydrocarbon (PAH) emission with the mid-IR continuum. These energetics assume a shell velocity of ~ 150 km s^{-1}, a value based on the kinematics of the neighboring molecular gas after correction for bar streaming; this value is uncertain because of our location in the plane. The ROSAT 1.5 keV diffuse X-ray map over the inner 45° provides compelling evidence for this galactic wind interpretation (Bland-Hawthorn & Cohen 2003).

3.2 M82

M82 hosts arguably the best-studied galactic wind. Detailed studies of the warm line-emitting gas has revealed the 3D structure of this outflow and derived deprojected velocities and energetics (e.g., Shopbell & Bland-Hawthorn 1998): v(filaments) $\sim 525-655$ km s^{-1}, M(filaments) $\sim 5.8\times10^6 M_\odot$, and KE(filaments) $\sim 2.1\times10^{55}$ ergs $\sim 1\%$ of the total mechanical energy input from the starburst in M82. Recent X-ray observations of M82 have detected the hot wind fluid in the center of this object and X-ray emitting gas out to ~ 12 kpc, spatially coincident with the Hα cap detected from the ground. The velocity of the warm ionized gas at this location is sufficient to escape the potential well of M82 if halo drag is negligible. Millimetric observations of M82 by Walter et al. (2002) have revealed the presence of a substantial quantity of molecular gas ($\sim 3\times10^8$ M$_\odot$) with kinetic energy $\sim 10^{55}$ ergs entrained in the wind. The molecular gas is therefore a energetically important component of this

wind. Unfortunately, M82 is the only case of wind galaxy where the molecular gas phase has been mapped with good enough precision to unambiguously decompose it into disk versus wind components.

3.3 NGC 3079

The nuclear region of this object harbors a spectacular kpc-scale bubble which is in the process of bursting out of the disk ISM. The line-emitting gas is resolved with HST into streams of filamentary strands and droplets with small volume filling factors (Cecil et al. 2001). CXO data show that the bright, soft X-ray and Hα filaments in NGC 3079 have strikingly similar patterns on both small and large scales ($\sim$ 0.01 – 10 kpc; Cecil et al. 2002). This tight optical-line/X-ray match seems to arise from cool disk gas that has been driven by the wind, with X rays being emitted from upstream, standoff bow shocks or by conductive cooling at the cloud/wind interfaces. The kinematics of the line-emitting gas in NGC 3079 are remarkable. Outflow velocities of ~ 1500 km s^{-1} are directly measured in the bubble region. Gas near the top of the partially ruptured bubble is entrained in a mushroom vortex, as predicted theoretically. Irwin & Sofue (1992) have argued for the presence of entrained molecular gas in this object, but more recent observations by Koda et al. (2002) do not seem to support this conclusion.

3.4 Search for Starburst-Driven Winds

Many other local starburst and active galaxies harbor galactic-scale outflows. In nearly all cases, the wind was discovered spectroscopically (e.g., line splitting). This method is highly reliable but is time-consuming. Recently, tunable filter imaging of local starburst galaxies have revealed the ionization signature of shock-excited galactic winds (Veilleux & Rupke 2002). This method consists in obtaining separate images of the wind candidate at Hα and [N II] λ6583 ([S II] $\lambda\lambda$6716, 6731 could also be used for this exercise) and creating a [N II]/Hα ratio map. The ratio map emphasizes the difference between the star-forming disk with [N II]/H$\alpha < 1$ and the shocked wind material with [N II]/H$\alpha > 1$. In principle, this method could be used to detect shocked-excited starburst-driven winds out to at least $z \sim 1$.

4 Neutral Winds in z = 0 - 0.5 Galaxies

There are now estimates of the frequency of wind occurrence in nearby star-forming galaxies for most wavebands. Detailed studies of extended optical line emission around various starburst and quiescent galaxies reveal a clear trend between starburst strength and the presence of kinematically confirmed winds or extraplanar diffuse ionized gas. Complementary results from systematic searches for blueshifted optical (e.g., Na ID) absorption lines from neutral gas confirm this dependence on starburst strength (e.g., Rupke et al. 2002, 2005ab and references therein). This neutral gas often extends up to several kiloparsec, but morphological constraints are sparse (e.g., Martin 2006). Detailed long-slit spectra show some degree of correlation with the warm ionized gas, although smaller outflow velocities in the neutral gas relative to the ionized components are often seen in LIRGs and ULIRGs. These

systematic kinematic variations with phase temperature are consistent with entrainment of gas clouds by a hot wind if the warmer phase has smaller column densities than the cool gas, perhaps as a result of cloud erosion.

The projected "maximum" velocities in the outflowing neutral components average 300 – 400 km s^{-1}, and attain $\sim$ 600 km s^{-1} (although 1100 km s^{-1} is seen in one object). Outflow and circular velocities correlate positively, but this correlation is mainly due to the dwarf galaxies (Martin 2005, Rupke et al. 2005ab). Escape fraction $f_{\rm esc} \sim 5 - 20\%$ are derived from these data assuming negligible halo drag and truncated isothermal spheres for the potential of the hosts. There is some indication of a trend of increasing outflow velocities with increasing SFR, particularly when data from Schwartz & Martin (2004) on dwarf galaxies are included. These results can be understood in terms of entrainment in an increasingly powerful wind.

Estimates from Na I D profiles suggest that galactic winds entrain considerable neutral material, $\sim 10^4 - 10^7$ $M_\odot$ (0.001 – 1.0 $M_\odot$ yr^{-1}) in dwarfs and $\sim 10^8 - 10^{10}$ $M_\odot$ ($\sim$ 10 – 1000 $M_\odot$ yr^{-1}) in ULIRGs, but these numbers rely on a number of uncertain assumptions. Assuming that these estimates of neutral gas masses are correct, the ratios of $\dot{M}$ to the global SFRs span $\eta \equiv \dot{M}/{\rm SFR} \approx 0.01 - 10$. The parameter η, the mass entrainment efficiency, shows no obvious dependence on SFR except perhaps for a decreasing trend at high SFR ($\gtrsim$10 – 100 $M_\odot$ yr^{-1}). The inferred kinetic energy increases with increasing SFR: $\sim 10^{50} - 10^{54}$ erg among dwarfs but $\sim 10^{56} - 10^{59}$ erg among LIRGs and ULIRGs; corresponding power outputs are $\sim 10^{36} - 10^{39}$ and $10^{41} - 10^{44}$ erg s^{-1}, respectively. Such energies and powers exceed those of the outflowing warm ionized gas, and imply thermalization efficiencies $\gtrsim$10%. Contrary to some expectations (e.g., Silk 2003), the trend with SFR flattens among ULIRGs, perhaps due to the complete evacuation of the gas in the wind's path, a common neutral gas terminal velocity for LIRGs and ULIRGs, and/or a decrease in the efficiency of thermalization of the SN energy.

5 Summary

Galactic winds are detected in galaxies with SFR > a few $M_\odot$ yr^{-1} or SFR / πR_{25}^2 > $0.001 M_\odot$ yr^{-1} kpc^{-2}. Most radio-loud AGN and > 1/3 radio-quiet AGN show some signs of outflows on galactic scales. The wind solid angle are $\Omega_{\rm wind}/4\pi \sim 0.1 - 0.5$. The radial extent of the wind is $R_{\rm wind}$ = few – 50^+ kpc, based on optical, X-ray, and UV absorption-line observations. The wind velocity $V_{\rm outflow} = 25 - 10^{3+}$ km s^{-1} and is a function of SFR and the temperature of the gas phase under consideration. The kinetic energies are $E_{\rm outflow} = 10^{53} - 10^{59}$ ergs $\sim$ (10% - 50%) x (total kinetic energy returned to ISM by starburst). The mass outflow rates are $dM/dt_{\rm outflow} = \eta$ SFR where $\eta \sim 0.01 - 5$. The entrainment efficiency, η, "saturates" at the highest SFRs. The escape fraction is $f_{\rm esc} \sim 5 - 20\%$, but this number is very uncertain since it assumes negligible halo drag. It is almost certainly a function of the temperature of the gas phase under consideration.

6 Observational Challenges

Following VCBH, we list a number of observational challenges which we feel need to be addressed to gain a complete understanding of galactic winds.

This page intentionally blank

1. Hot wind fluid. This component is the driving force behind galactic winds, yet it has been detected in only three objects (Milky Way, M82, and possibly NGC 1569). The metal abundances determined from the X-ray observations are uncertain and therefore the estimate of mass loading is also uncertain.

2. Entrained molecular gas and dust. Entrained molecular gas and dust have been studied in detail in M82 but in very few other objects. On-going observations with the SST will shed some light on the role of the dust in galactic winds, but an effort should also be made to look for deviations from Gaussian profiles in data cubes obtained with current and future (e.g., CARMA) mm-wave facilities. CO studies of galactic winds are very important because so much mass is required to see molecular gas that its detection dramatically increases the inferred energies.

3. Zone of influence and escape efficiency. The current constraints on the zone of influence (and thus escape efficiency) of local winds are limited by the sensitivity of the instruments used for the measurements. Absorption-line studies of bright sources behind galactic winds are a promising avenue of research, but *COS* on HST will be needed to make significant progress in this area.

4. Thermalization efficiency. This efficiency is calculated by comparing energy input from the starburst/AGN with the energy in the wind. This last quantity requires tabulation of the energetics in all phases of the wind, and is therefore uncertain.

5. Wind/ISM interface and magnetic fields. Our knowledge of the microphysics at the interface of the wind and the ISM is still severely limited by the spatial resolution of the observations. The role of magnetic fields on small scale is very poorly constrained.

6. Positive feedback. Examples of positive feedback have been observed in the Milky Way and in M82 (Matsushita et al. 2004). The presence of a ring of H II regions in the disk of NGC 3079 is also intriguing in this context. This issue needs to be understood before we can draw a complete picture of the influence of galactic winds on the evolution of galaxies.

7. Galactic winds in the distant universe. While galactic winds have been detected in many high-z galaxies, very few have been fully quantified in terms of mass and energy outflows and zone of influence. Absorption-line studies will continue to be important in this area of research and the advent of tunable filters on 8-meter class telescopes promises to help survey the moderate-redshift universe in search for galactic winds.

References

1. J. Bland-Hawthorn, M. Cohen: ApJ, 582, 246 (2003)
2. G. Cecil, J. Bland-Hawthorn, S. Veilleux: ApJ, 576, 745 (2002)
3. G. Cecil, et al: ApJ, 555, 339 (2001)
4. R. A. Chevalier: ApJ, 397, L39 (1992)
5. J. A. Irwin, Y. Sofue: ApJ, 396, L75 (1992)
6. J. Koda, et al: ApJ, 573, 105 (2002)
7. K. Koyama, et al: Nature, 339, 603 (1989)
8. K. Koyama, et al.: PASJ, 48, 249 (1996)
9. C. L. Martin: ApJ, 621, 227 (2005)
10. C. L. Martin: ApJ, 647, 222 (2006)

11. S. Matsushita, et al: ApJ, 617, 20 (2004)
12. D. S. Rupke, S. Veilleux, D. B. Sanders: ApJ, 570, 588 (2002)
13. D. S. Rupke, S. Veilleux, D. B. Sanders: ApJS, 160, 115 (2005)
14. D. S. Rupke, S. Veilleux, D. B. Sanders: ApJ, 632, 751 (2005)
15. C. M. Schwartz, C. L. Martin: ApJ, 610, 201 (2004)
16. P. L. Shopbell, J. Bland-Hawthorn: ApJ, 493, 129 (1998)
17. J. Silk: MNRAS, 343, 249 (2003)
18. Y. Sofue, T. Handa: Nature, 310, 568 (1984)
19. S. Veilleux, G. Cecil, J. Bland-Hawthorn: ARAA, 43, 769 (2005)
20. S. Veilleux, D. Rupke: ApJ, 565, L63 (2002)
21. F. Walter, A. Weiss, N. Scoville: ApJ, 580, L21 (2002)
22. S. Yamauchi, et al: ApJ, 365, 532 (1990)

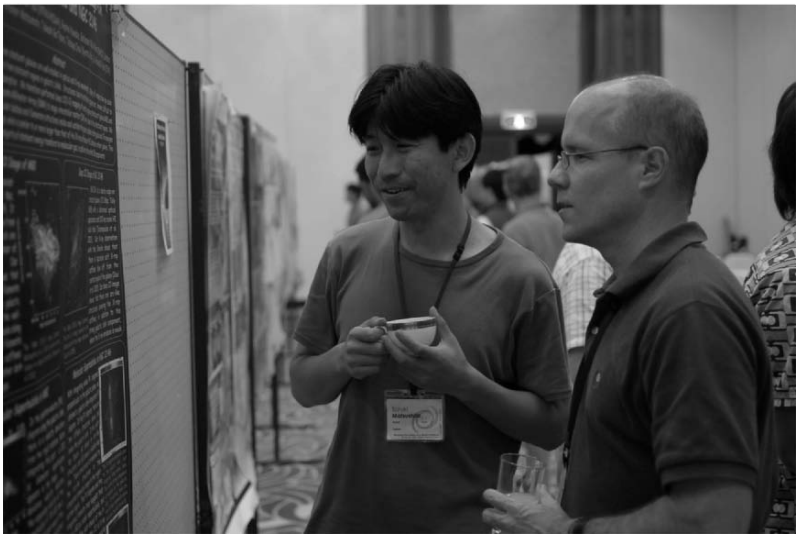

Satoki Matsushita, and Slyvain Veilleux

Part IV

GALACTIC EVOLUTION AND ENVIRONMENT

Eiichiro Kokubo is presenting a 4-D digital universe at VERA observatory.

37

Ram Pressure Stripping in the Virgo Cluster

Bernd Vollmer

CDS, Observatoire astronomique de Strasbourg, 11, rue de l'université, 67000 Strasbourg, France bvollmer@astro.u-strasbg.fr

Summary. The recent advances in understanding the effects of ram pressure on Virgo spiral galaxies is discussed. For a sample of 6 galaxies interaction diagnostics are made by a detailed comparison between observed and simulated gas distributions and velocity fields. Once the interaction is identified (gravitational, ram pressure or a mixture of both), we can estimate its parameters. The importance of a new diagnostic tool, the polarized radio continuum emission, is emphasized. This emission shows a characteristic distribution in cluster spiral galaxies. It directly traces gas compression or shear regions, which both can occur during an interaction of a cluster galaxy with its environment. A first complete time sequence for ram pressure stripping in the Virgo cluster is presented.

1 Introduction

The Virgo cluster of galaxies is the only cluster in the northern hemisphere where we can observe the ISM distribution and kinematics of cluster galaxies with a kpc resolution (1 kpc $\sim 12''$[1]). The Virgo cluster is dynamically young and spiral-rich making it an ideal laboratory for studying the influence of the cluster environment on spiral galaxies. Most of the Virgo spiral galaxies are HI deficient, i.e. they have lost a significant amount of their ISM [5], [7]. Imaging HI observations have shown that these galaxies have truncated HI disks [4]. Thus, the cluster environment changes the HI content and morphology of Virgo cluster spiral galaxies. However, Virgo spiral galaxies are not CO-deficient [9].

The interaction between a galaxy and the cluster environment can be a

- gravitational interaction: with the cluster potential [3], [25] and with other cluster galaxies (galaxy "harassment"; [12], [13]).
- or an interaction of the interstellar medium and the intracluster medium (ram pressure stripping; [8]).

At the outskirts of the cluster where the relative velocities between galaxies are small gravitational interactions are more important than in the inner part of the

[1] We use a distance of 17 Mpc to the Virgo cluster

cluster where the relative velocities between galaxies is of the order of the dispersion velocity of cluster spirals (~ 700 km s^{-1}). On the other hand, ram pressure plays an important role in the cluster core where galaxy velocities are high and the density of the intracluster medium is maximum. Ram pressure is most likely responsible for the HI deficiency of Virgo spiral galaxies showing a symmetric old stellar disk together with a truncated HI disk. The old VLA HI observations [4] did not reveal direct evidence for ram pressure stripping. The observations of the last years compared to detailed simulations gave us new insights how and when ram pressure affects Virgo cluster spiral galaxies.

2 Ram Pressure Models

Several groups have investigated the effects of ram pressure on a gas-rich spiral galaxy. These groups have employed different ways to describe the ISM:

- continuous description: Eulerian hydrodynamics in 2D [17] and 3D [18], [19], [11];
- discrete-continuous hybrid description: smoothed particles hydrodynamics: [1], [20];
- discrete description: sticky particles [26].

These groups studied galaxies with different rotation velocities and different initial gas surface density profiles. In addition, most of the authors used a constant ram pressure except [26] who used realistic time-dependent ram pressure profile for radial galaxy orbits.

Classical momentum transfer stripping [8] with strong ram pressure where the typical interaction timescale is $\sim 10-100$ Myr is different from the effect of constant low ram pressure (turbulent/viscous stripping [14]) where the typical interaction timescale is ~ 1 Gyr.

In the following only strong momentum transfer ram pressure stripping is discussed. Fig. 1 shows the resulting gas stripping radius as a function of maximum ram pressure for the different models. All models agree within a factor of ~ 2. Thus, the end product of ram pressure stripping, i.e. a truncated gas disk, is the same for all models, but the time-dependent removal of mass and angular momentum might be different in these models. In the following I will discuss results based on sticky particle simulations [26].

3 Data

Our group (J. Kenney (PI), J. van Gorkom, A. Chung, H. Crowl, B. Vollmer) has conducted a new HI survey of Virgo cluster spiral galaxies (cf. talk of J. Kenney). Within the Virgo Cluster HI Survey (VIVA) 28 carefully chosen spiral or spiral-like Virgo cluster galaxies were observed in HI at 15" resolution (in the C array configuration). Combined with already existing VLA observations this makes a total sample of 53 galaxies (Fig. 2). The atlas will be presented in Chung et al., in prep. (see also J. Kenney's contribution). This sample is ideal to study the effects of the Virgo cluster environment on spiral galaxies.

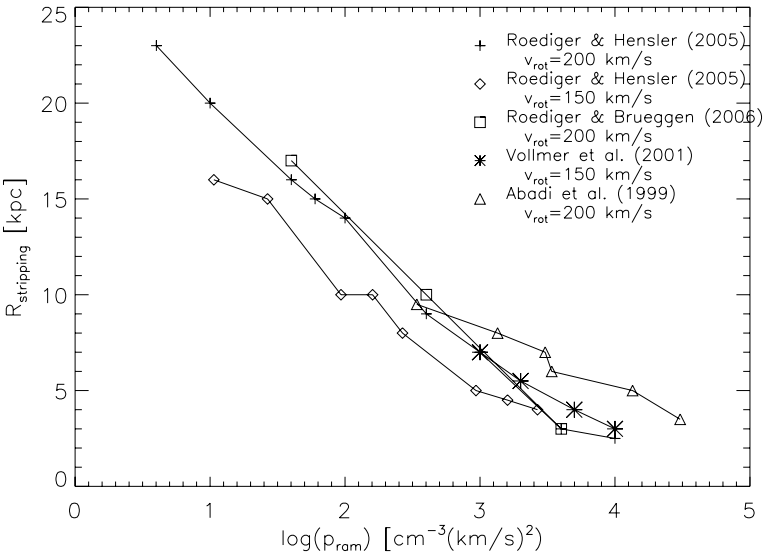

Fig. 1. Comparison between different ram pressure stripping models.

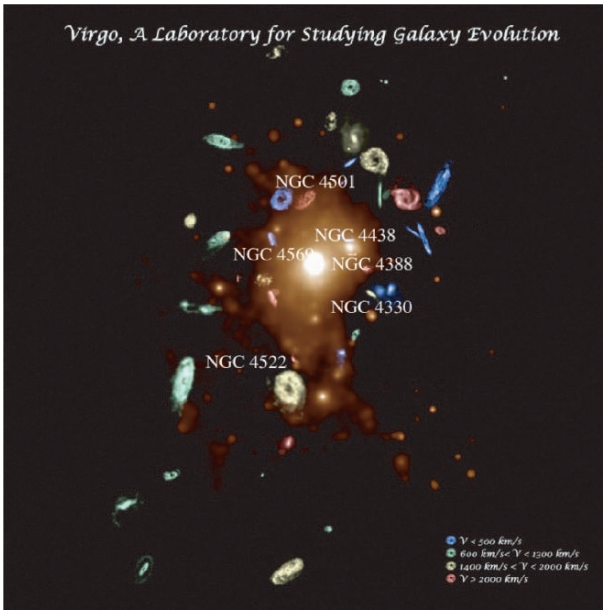

Fig. 2. The VLA Imaging of Virgo in Atomic gas (VIVA) survey (by A. Chung; winning image of the NRAO/AUI Radio Astronomy Image Contest). The further discussed galaxies are marked with their names.

4 Polarized Radio Continuum Emission

Polarized radio continuum emission represents a diagnostic tool for interactions, which is complementary to interferometric HI data. Polarized radio continuum emission $S_{\rm PI}$ is proportional to the density of relativistic electrons $n_{\rm e}$ and the strength of the regular large scale magnetic field B to the power of $2-4$: $S_{\rm PI} \propto n_{\rm e} B^{2-4}$. Large scale means larger than the resolution of the observations which is about $20'' \simeq 1.6$ kpc for the VLA. The total radio emission is sensitive to the turbulent small scale magnetic field which is usually a factor of 2.5–5 larger than the regular large scale magnetic field in spiral arms and 1.25–2 larger in the interarm regions. Whenever there is compression or shear the large scale magnetic field is enhanced and the polarized radio continuum emission increases rapidly.

It is very difficult, if not impossible, to predict the distribution of polarized radio continuum emission on the basis of HI observations, because of the complex evolution of the magnetic field (induction equation) and beam depolarization effects. Therefore, it is necessary to make detailed MHD modelling for direct comparison with observations. In [16] we demonstrated the feasibility of the method and in [29] we applied it successfully to the Virgo spiral galaxy NGC 4522.

4.1 Data

Encouraged by our results on NGC 4522 we observed a sample of 8 bright Virgo spiral galaxies in polarized radio continuum emission at 20 cm (C array) and 6 cm (D array) at a spatial resolution of $\sim 20''$ (PI: B. Vollmer). The sensitivity at 6 cm is ~ 10 mJy/beam.

In a "normal" field spiral galaxy the polarized radio continuum emission is mainly found in regions between the spiral arms, because turbulence linked to star formation in the spiral arms destroys the large scale magnetic field. Only one observed galaxy, NGC 4321, out of 8 shows this characteristic distribution of polarized radio continuum emission (left panel of Fig. 3). All other galaxies show asymmetric distribution of polarized radio emission with ridges at the outer parts of the galactic disks. The middle and left panels of Fig. 3 show 2 examples for this kind of distribution. The asymmetries are tracers of the interactions of Virgo spirals with their environment and can be used as diagnostic tools to determine the kind of interaction (gravitational or ram pressure) and the interaction parameters [29], [22].

4.2 MHD Simulations

The Zeus3D MHD code ([23], [24]) is used in order to solve the induction equation:

$$\frac{\partial \boldsymbol{B}}{\partial t} = \nabla \times (\boldsymbol{v} \times \boldsymbol{B}) - \nabla \times (\eta \, \nabla \times \boldsymbol{B}) \tag{1}$$

where $\boldsymbol{B}$ is the magnetic induction, $\boldsymbol{v}$ is the large-scale velocity of the gas, and η is the coefficient of a magnetic diffusion (see [16]). Realistic, time dependent gas velocity fields are provided by the 3D N-body sticky-particle simulations as in [26].

In order to obtain the simulated polarized intensity maps we rotate the cube of 3D magnetic field according to the orientation of a given galaxy. Next, we integrate the transfer equations of synchrotron emissivities in Stokes I, Q and U parameters

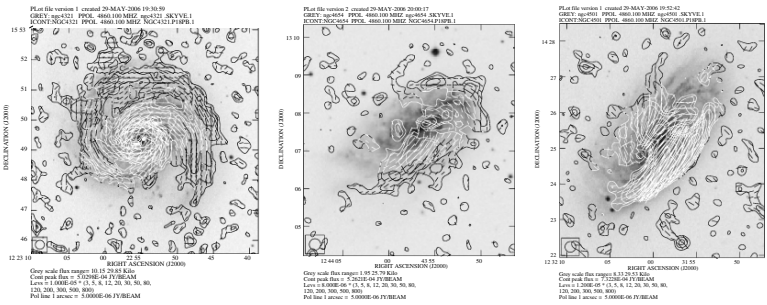

Fig. 3. Three Virgo spiral galaxies observed in polarized radio continuum emission at 6 cm (contours). The magnetic field vectors are shown as lines. Greyscale: DSS image.

along the line of sight. The intrinsic degree of synchrotron polarization is assumed to be $p = 75\%$. Both, thermal and relativistic electron distributions are taken as Gaussians. We neglect Faraday effects by setting $n_{th} = 0$. Finally for direct comparison with radio observations, the model maps of Stokes I, Q and U are convolved with a 2-D Gaussian function of a given HPBW. The final Q and U maps are combined in order to obtain maps of polarized intensity and polarization angle (rotated by 90° to show the magnetic vector).

5 Comparison Between Models and Observations

For the direct comparison between model and observations for a given galaxy the known parameters are: the systemic velocity of the galaxy, its distance from the cluster center, inclination angle, position angle, gas distribution, and velocity field. With the help of the dynamical model we determine the maximum ram pressure, the time to the maximum ram pressure, and the angle between the galactic disk and the ram pressure wind. We have investigated 6 galaxies in detail (the results on NGC 4501 and NGC 4330 are preliminary).

As already stated in section 4.1 all galaxies show asymmetric ridges of polarized radio continuum at the outer galactic disk. Based on our HI and CO observations we can divide Virgo spiral galaxies into 5 groups based on the gas morphology:

- (i) gas disk truncated near the optical radius (R_{25}) and asymmetric outer gas disk with a tail structure (NGC 4501, NGC 4330);
- (ii) strongly truncated gas disk and extraplanar high surface density gas (NGC 4522, NGC 4438);
- (iii) strongly truncated gas disk and low surface brightness gas (NGC 4388);
- (iv) truncated gas disk and perturbed low surface brightness arms (NGC 4569, and perhaps NGC 4548).

These observational groups can be put together to form a time sequence for ram pressure stripping in the Virgo cluster.

6 A First Complete Stripping Sequence

The two galaxies of group (i) (NGC 4501 and NGC 4330) are at the beginning of a ram pressure stripping event, i.e. they approach the cluster center. The outer disk has already been removed and the inner disk just begins to be affected by ram pressure.

NGC 4438 is approximately at its closest distance to the cluster center. Despite the strong tidal perturbation caused by its companion NGC 4435, ram pressure is the dominant effect on the gas distribution and kinematics [30]. NGC 4522 is also close to peak ram pressure. However, this galaxy is located at a distance of about 1 Mpc from the cluster center. The most plausible scenario is that the intracluster medium is moving opposite to the galaxy's motion within the cluster [10], [31]. This can enhance ram pressure significantly. The motion of the intracluster medium is most probably due to the infall of the M49 group of galaxies into the Virgo cluster from behind and from the south (see, e.g., [21]).

After peak ram pressure, i.e when the galaxy leaves again the cluster core, the removed ISM is accelerated and expands. Thus extraplanar gas tail becomes larger and its gas surface density decreases. This is observed in NGC 4388 [15] where the dynamical model yields a time to peak ram pressure of ~ 100 Myr [27].

If one then waits again for two galactic rotations (~ 200 Myr) the gas tail is no more detectable. The only traces of the past interaction are kinematically perturbed low gas surface density arms [28]. At the very end of this sequence stripped spiral galaxies show a truncated symmetric and unperturbed gas disk.

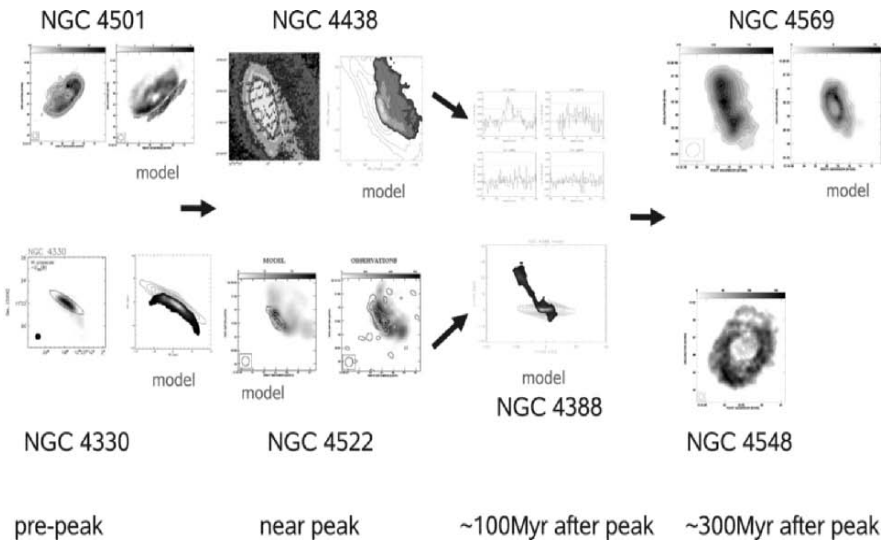

Fig. 4. A first complete ram pressure stripping sequence in the Virgo cluster.

7 Conclusions

In the last years we have gained new insights on how ram pressure acts in detail on Virgo spiral galaxies. This has been possible due to the combination of new deep HI observations, deep polarized radio continuum observations, and detailed dynamical modelling (sticky particles and MHD). The simulations help us to determine which kind of interaction acts on a given galaxy and to determine the interaction parameters. The time to peak ram pressure is of particular interest, because it can be compared to independent estimates based on optical spectra or multiband photometry. For two galaxies the dynamical timescale [28], [31] and the timescale derived from (i) multiband photometry including GALEX UV data (NGC 4569 [2]) and (ii) optical spectroscopy and GALEX UV data (NGC 4522 [6]) coincide.

The dynamical model serves as a guideline, but it is observations which tell us what really happens to these galaxies. We are now at the point where we begin to see the effect of ram pressure stripping on the different ISM phases (ionized, atomic, and molecular). Thus, we hope not only to learn more about ram pressure stripping, but also about the ISM itself.

References

1. Abadi, M.G., Moore B., & Bower, R.G.: MNRAS, 308, 947 (1999)
2. Boselli, A., Boissier, S., Cortese, L. et al.: ApJ, in press; astro-ph/0609020 (2006)
3. Byrd, G. & Valtonen, M.: ApJ, 350, 89 (1990)
4. Cayatte, V., van Gorkom, J.H., Balkowski, C., & Kotanyi C.: AJ, 100, 604 (1990)
5. Chamaraux, P., Balkowski, C., & Gérard, E.: A&A, 83, 38 (1980)
6. Crowl, H.H. & Kenney, J.D.P.: ApJ, in press, astro-ph/0608229 (2006)
7. Giovanelli, R. & Haynes, M.P.: AJ, 88, 881 (1983)
8. Gunn, J.E. & Gott, J.R.: ApJ, 176, 1 (1972)
9. Kenney J.P.D. & Young J.S.: ApJ, 384, 171 (1989)
10. Kenney, Jeffrey D.P., van Gorkom, J.H., Vollmer, B.: AJ, 127, 3361 (2004)
11. Marcolini, A., Brighenti, F., D'Ercole, A.: MNRAS, 345, 1329 (2003)
12. Moore, B., Katz, N., Lake, G., Dressler, A., & Oemler A.: Nature, 379, 613 (1996)
13. Moore, B., Lake, G., & Katz, N.: ApJ, 495, 139 (1998)
14. Nulsen P.E.J.: MNRAS, 198, 1007 (1982)
15. Oosterloo T. & van Gorkom J.H.: A&A, 437, L19 (2005)
16. Otmianowska-Mazur, K. & Vollmer, B.: A&A, 402, 879 (2003)
17. Rödiger E. & Hensler G.: A&A, 433, 875 (2005)
18. Rödiger E. & Brüggen M.: MNRAS, 369, 567 (2006)
19. Rödiger E., Brüggen M., & Höft M.: MNRAS, 371, 609 (2006)
20. Schulz S. & Struck C.: MNRAS, 328, 185 (2001)
21. Shibata, R., Matsushita, K., Yamasaki, N.Y. et al.: ApJ, 549, 228 (2001)
22. Soida, M., Otmianowska-Mazur K., Chyzy K., Vollmer, B.: A&A, in press; astro-ph/0608292 (2006)
23. Stone J.M., Norman M.L.: ApJS 80, 791 (1992)
24. Stone, J. M., Norman, M. L.: ApJS, 80, 791 (1992)

25. Valluri, M.: ApJ, 408, 57 (1993)
26. Vollmer, B., Cayatte, V., Balkowski, C., & Duschl, W.J.: ApJ, 561, 708 (2001)
27. Vollmer B. & Huchtmeier W.: A&A, 406, 427 (2003)
28. Vollmer, B., Balkowski, C., Cayatte, V., van Driel, W., Huchtmeier, W.: A&A, 419, 35 (2004)
29. Vollmer, B., Beck, R., Kenney, J.D.P., van Gorkom, J.H.: AJ, 127, 3375 (2004)
30. Vollmer, B., Braine, J., Combes, F., Sofue, Y.: A&A, 441, 473 (2005)
31. Vollmer, B., Soida, M., Otmianowska-Mazur, K. et al.: A&A, 453, 883 (2006)

38

From Nearby to High Redshift Compact Group of Galaxies

Philippe Amram[1], Chantal Balkowski[2], Claudia Mendes de Oliveira[3], Henri Plana[4], and Benoît Epinat[1]

[1] Laboratoire d'Astrophysique de Marseille, OAMP, Université de Provence, CNRS, France – Philippe.Amram@oamp.fr
[2] GEPI, Observatoire de Paris-Meudon, Université Paris VII, CNRS, France
[3] IAG, Universidade de São Paulo, Brazil
[4] Universidade Estadual de Santa Cruz, Ilhéus, Brazil

1 Introduction

Groups of galaxies are small systems containing a few L_* galaxies. Up to half of all nearby galaxies are in groups or clusters [1] and more than 50% of the nearby structure in the universe lies in groups formed by 3 to 20 members [2]. Nevertheless, only very few of them are compact. Compact Groups of Galaxies (CGs) are isolated entities containing 4 to 7 galaxies close to one another: their mean galaxy-galaxy angular separation is of the same order as the diameters of the galaxies and their velocity dispersions are rather low ($\sim$ 200 $km\ s^{-1}$). Most of CGs are physically bound by gravity as it can be attested by the high fraction of interacting members, they evolve through dynamical friction and may finally merge to form one single galaxy, called a fossil group ([3],[4]).

Studies on CGs may be classified in four different epochs: 1) the first ones were those of "pioneers", namely Stephan and Seyfert who discovered respectively Stephan's Quintet (1877) [5] and the Seyfert's Sextet [6]; the second period was based on visual inspection on the POSS-I and allowed the identification of numerous pairs, triplets, quartets and quintets of galaxies ([7], [8], [9] and [10]); the third epoch started with the construction on objectively defined catalogs ([10],[11],[12],[13]), but still using visual inspection as the search method; and finally the present time, when the searches are mostly done on digital sky surveys. Digital sky surveys are used with two different methodologies. The first approach consists of using the today large galaxy redshift surveys (usually surveys done using fiber spectrographs) for identifying CGs as by-products of the catalogues using the "Las Campanas Redshift Survey (LCRS)" ([14],[15]); using the SLOAN [16] or the 2dF galaxy redshift survey [17] . Due to technical limitations imposed by the minimum separation between two adjacent optical fibers ($\sim 1'$), the efficiency of this approach is rather low because most galaxies within CGs have angular separation smaller than $1'$. For instance, in a work based on the LCRS, among 76 candidate CGs only one has measured redshifts for the group; 23 have measures for 2 galaxies; 52 for one galaxy. Thus, this approach is most suitable to search for loose groups [17]. The second approach consists

of an automatic search on the DPOSS followed by specific redshift determination programs; 122 CGs were discovered [18]; 84 small and high density CGs [19] and [20] ([20] include in their sample that of [19]).

2 The Stephan's Quintet

It is a challenge to recover the history of this nearby CG. This group clearly illustrates the complexity of the formation and evolution of CGs. The Stephan's Quintet was discovered by Edouard Stephan in 1877, using the Foucault 80-cm reflector in Marseille. It consists of 5 members; three of them are strongly interacting, the fourth one is an elliptical galaxy to the southwest of the group and the fifth one, NGC7320 is a foreground galaxy, with a velocity of about 800 km/s. Three of the members have about the same redshift (V(NGC7317) = 6563 km s^{-1}; V(NGC7318A) = 6620 km $s^{-1}$and V(NGC7319) = 6650 km s^{-1}) and there is a fourth concordant redshift galaxy (V(NGC 7320C) = 6000 km s^{-1}), that was not originally in the quintet, but which is definitely part of the system. It is located 3' from the other three objects, and it is thought to be a past intruder which produced an old tidal tail [21] embedded in a very extended HI tail [22]. It is noticeable that there is no detected neutral hydrogen in any galaxy of the CG, while a mass of 10^{10} $M_{\odot}$ of HI is detected in several tails distributed in the intragroup medium. A large cloud of molecular gas detected through ^{12}CO is located at the end of one optical tail, in the middle of the eastern HI tail (BIMA observations [23]; IRAM observations [24]). This large cloud might lead to the formation of a tidal dwarf galaxy candidate. Seven other tidal dwarf candidates have been detected within an optical tail. They were classified as tidal dwarf candidates from the study of their kinematic properties obtained from Hα emission [25]. Four intergalactic HII regions have also be detected in (or closed to) the end of the HI tail, 25 kpc away from the closest bright galaxy member [26]. A plausible scenario explaining the recent history of this CG may be the following [27]: NGC 7318B is entering the group with a different velocity of about 1000 km s^{-1}(V(NGC7318B)=5770 km s^{-1}) and produces a new optical tidal tail and particularly a large scale shock region revealed by *(i)* a 40 kpc non thermal radio continuum region ([28], [29]); *(ii)* the exceptional detection of the molecule H_2 in the IR [30]; *(iii)* the high resolution X-ray emission detected with Chandra [31] coincident with the Hα emission regions [32] and the gas stripped regions detected with XMM [33]. Moreover, the GALEX data in the far and near-UV detected around NGC 7319 and NGC 7318b show a peculiar morphology but a SFR consistent with that of normal Sbc galaxies, meaning that the strength of star formation activity is not enhanced by interactions [34].

3 Interaction and Merging in Compact Groups

One of the best pieces of evidence showing that CGs are physically bound is the high rate of groups which are X-ray loud from where it has been inferred that 75% of the Hickson compact group sample contains X-rays [35]. The X-ray emittig CGs are in most cases dominated by an elliptical galaxy while CGs dominated by spirals do not show X-ray emission [37]. Commonly, the higher activity is found in CGs having

the lowest velocity dispersions. In addition, CGs show a strong velocity dispersion-morphology correlation but no density-morphology correlation. Interactions that do not disrupt galaxies are common in CGs but mergers occur seldom ([38], [39], [40], [41]). The interactions in CGs are revealed by the presence of tidal tails (in which tidal dwarf galaxy candidates are found), by their high IR luminosity, central activity, diffuse intergalactic light, kinematics and dynamics, HI deficiency and central double nuclei. For instance, the diffuse light in the Seyfert's sextet (HCG 79) forms about 46% of the total light, its blue color indicates that the light may come from the stripping of dwarf galaxies (bluer than the galaxies) dissolved into the group potential well [42]. Some apparently rather quite normal-looking CGs show galaxies with almost all the interaction indicators. This is the case for the galaxy HCG 16c who displays a highly disturbed velocity field, a central double nuclei, a double kinematic gas component, a kinematic warp, a gaseous versus stellar major-axis misalignment, a high IR luminosity and central activity [39]. The HI content in CGs is still somewhat controversial: HI deficiency was found in CGs by one team [43] while another one did not find it in CGs while deficiency is found in loose groups [44]. On the other hand, observational evidences show that CGs evolution is different from interacting pairs of galaxies: interactions in pairs trigger an inflow of gas to the galactic nucleus but CGs do not appear to show rates of either activity enhanced beyond that of the field ([45], [14]). Furthermore, traces of mergers are rare in CGs ($\sim$7%, [46]). Nevertheless the expected lifetime is much longer than of a few crossing times. Indeed, CGs have high density and low velocity dispersion so they should merge fast, instead of that their observed merging rate is very low. Why CGs dominated by ellipticals are still observed today? Stellar populations of early-type galaxies in CGs are older than in the field and similar to cluster [47]. This indicates that despite the fact that ellipticals in CGs were formed long ago, the CGs have not yet merge. The crossing time in a CG is a few 0.01 H_0^{-1} while the galaxy/galaxy merging time is only a few crossing times (determined by n-body simulations), then major merging should be faster than one Gyr, which is not the case. Two scenarii have been developed to explain the longevity of CGs. The first one needs a continuous secondary infall of close-by galaxies coming from surrounding loose groups [48] and the second one invokes either specific initial condition or massive halos to stabilize CGs ([49], [50], [51]) allowing to reach dynamical timescales as high as 25 Gyr. Finally, a well known cosmological issue of the ΛCDM theory predicts more satellite galaxies than seen in groups ([52], [53]).

4 Past and Future of Compact Groups

Very little is known on the precursors and the end products of CGs. When extreme cases of dynamical friction occur, fossil groups may be the end products of merging of L_* galaxies in low-density environments [4]. The most massive versions of today's CGs, like HCG 62, are the best candidate precursors of fossil groups [54]. High velocity dispersion CGs, which contain mainly bright ellipticals and extended X-ray halos, embedded in neighborhoods rich in low-luminosity companions may have been the precursors of fossil groups [55]. Due to their high sizes and masses, most of the 15 fossil groups candidate discovered up to now may be in fact poor clusters end-products rather than end-products of CGs. The past history of CGs and their

role in galaxy evolution is not better known. Do galaxies in CGs mimic the early-universe galaxies? The high densities of CGs suggests that it might be the case. Nevertheless, local CGs are long-live structures with a low merging rate even if the interaction rate between their galaxies is high. What is the fraction of galaxies which are in CGs through the age? Local CGs in the nearby universe are isolated and due to the highest density of the universe in the past because the universe was denser, isolated CGs should not have been frequent in the past. The relation between their global properties and the formation and evolution of their galaxies members may be a clue for their understanding. Further searches for high-z CGs will allow better understanding about the evolution of the fraction of CGs and will give the opportunity to learn about the change in their average physical properties (mass, velocity dispersion, radius, star formation rate). Up to z$\sim$0.12 (1.56 Gyr look back time) no change is seen in their properties [56]. A related topic of high interest for the knowledge of the role of CGs in the past is the accretion of CGs by clusters which may be a preprocessing step in galaxy evolution during the high redshift cluster assembly phase. Indeed, ΛCDM theory indicates that galaxy clusters grow by accreting small groups of galaxies falling in along large scale filaments. A blue CG, with a low velocity dispersion ($\sim$150 km s^{-1}), infalling at high speed ($\sim$1700 km s^{-1}) into the dynamically young cluster Abell 1367 was recently discovered ([57], [58]). This example might reproduce, at the present epoch, the physical conditions that were likely to exist in clusters under formation. Tidal interactions produced extended tidal tail ($\sim$150 kpc) as well as stellar shells and weakened the potential wells of the CG, making it easier for ram pressure to strip the galaxies ISM. Tidal forces and ram-pressure fragment this CG and blown out gas and stars through the cluster. Meanwhile, at least ten tidal dwarfs and extragalactic compact HII regions were formed. This produced an unusually high Hα emission associated with the two giant galaxies and made this CG the highest density of star formation activity ever observed in the local clusters [59].

5 Kinematic of High Redshift Galaxies

The forthcoming studies on high-z galaxies in CGs will aim to quantify the effects of galaxy evolution. Due to their large distances, high-z galaxies are unfortunately not observable with the same spatial sampling as low-z galaxies. Thus, first of all, it is necessary to disentangle distance effects from evolution ones. In order to analyze the kinematics of high-z galaxies, control samples of nearby galaxies, with well studied kinematics, are necessary. Nearby samples of galaxies having a broad range of luminosities/masses, morphological types, and environments provide a wide range of kinematical signatures ([60], [61]). Due to the loss of spatial resolution, these signatures are smoothed for high-z galaxies. Spatial resampling of nearby galaxies can be used to simulate distant galaxies [62]. The comparison between "resampled" and distant galaxies can help identifying signatures of mergers, internal features such as bars or even the disk/halo density distributions. A first order use of kinematical analysis is the study of the evolution of the Tully-Fisher relation which only requests the maximum velocity of the rotation curve. Nevertheless, a "believable" rotation curve may be obtained from a 2D velocity field if the ratio between the optical radius of the galaxy and the spatial resolution (called B hereafter) is greater or equal to 10 (B must be larger than 7 in the HI [63]). Thanks to the advent of adaptative

optics, leading to a resolution of typically 0.1", B≥10, for a galaxy having a size ≥ 2". Thus, the determination of the kinematical parameters of the galaxy such as the dynamical center, its inclination, position angle and its maximum rotational velocity (V_{max}) become reliable. When B is large enough, V_{max} may be computed from the rotation curve rather than from the width of the central velocity dispersion, in the center of the galaxy.

Even at low redshift, controversy may exist on the nature and on the history of CGs. It is the case for the nearby HI and Hα gas rich system HCG 31, displaying a low velocity dispersion (∼60 km s^{-1}) and an intense star formation rate. Three scenarios have been put forward to explain the nature of this CG: *(i)* these are two systems that are in a pre-merger phase ([64], [65]), *(ii)* the system is a late-stage merger [66] or *(iii)* it is a single interacting galaxy [67]. What would the observations of such a CG tell us if observed at higher redshift? To tackle this question, we have tested the beam smearing effect on it. The original data cube has been convolved by the mean seeing function (0.62") to simulate a VLT/FLAME/GIRAFFE observation (pixel size=0.52"). On Fig. 1, the group has been projected to redshift z=0.15 and z=0.60, leading respectively to scales of 2.6 and 6.7 kpc per arcsec. At z=0.013 (the actual distance of HCG 31), the kinematical signature of two rotating disks (HCG 31 A and C) producing tidal tails is maybe seen in addition to a very inclined galaxy on the SW side (HCG 31B). At z=0.15, it becomes difficult to count how many galaxies are involved in the system, nevertheless it is still possible to distinguish at least two galaxies (A+C and B). At z=0.60, disentangling the system is a real challenge. At z=0.013, high spatial and spectral Fabry-Perot observations allow to observe that the broader Hα profiles (larger than 30 $km\ s^{-1}$) are located in the overlapping regions between the two galaxies (HCG 31 A and C). This clearly maps the shock between both galaxies and the subsequent starburst regions [64]. At higher redshift, even at z=0.15, this broadening would be interpreted as a indicator of rotating disk and this system should have been catalogued like a rotator instead of a merger [62].

On the other hand, in cases when B≥10, it becomes possible to address the problem of the shape of the inner density profile in spirals (CORE vs CUSPY controversy), which remains one of the five main further challenges to ΛCDM theory [68]. For the largest and brightest galaxies, it will then be possible to trace the mass distribution in separating luminous from dark halo contribution, which has not been done so far; for instance, for the best data observed without adaptative optics (Q2343-BX610 located at $z \sim 2.2$), B<3 [69].

In order to test the systematics induced by the beam smearing effects, we have projected the data cube of the galaxies used to study the local Tully-Fisher (TF) relation for CGs [70] to different redshifts. The results indicate that the high-z galaxies have smoother rotation curves than the ones for the local galaxies. In other words, a "solid-bodyfication" of the rotation curve is observed. The consequence is that there is no indication that the maximum velocity of the rotation curve is reached, leading to uncertainties in the TF relation determination. In addition, the (fine) structures within the galaxies (bars, rings, spiral arms, bubbles, etc.) are attenuated or erased and the determination of the other kinematical parameters (position angle, center, inclination) becomes highly uncertain. For the sample we used [70], we have determined that, up to $z \sim 0.6$, the maximum rotation velocity reached in the rotation curve decreases with redshift, following the empirically derived function:

$$\frac{\Delta V}{V} = \frac{V_z^{max} - V_{z=0}^{max}}{V_{z=0}^{max}} = -(11 \pm 4)\ 10^{-3} z \qquad (1)$$

For instance, at $z \sim 0.6$, a galaxy having an actual rotation velocity V^{max}=200 km s^{-1}, might be observed with V^{max}= 187±5 km s^{-1}, shifting the TF relation determination towards higher luminosity. This estimate is a higher limit for V^{max}, since the simulation has been done using the kinematical parameters determined for $z = 0$. Indeed, a wrong determination of the position angle of the major axis will lower V^{max} even more. In addition to this systematic effect, a wrong determination of the inclination of the disk increases the dispersion of V^{max}. Indeed, inclination is the most complicated kinematical parameter to determine for high-z galaxies due to beam smearing effect and morphological evolution in galaxies. A disk rotating at V^{max}=200 km s^{-1} inclined to 35° with respect to the plane of the sky, might be confused with a disk rotating at V^{max}= 160 or 270 km s^{-1} if the inclination is respectively overestimated by 10% (25°) or underestimated by 10% (45°).

6 Summary/Conclusions

- Nearby Compact Groups of Galaxies (CGs) are very complex systems, tracing their history is a challenge (e.g. Stephan's Quintet).
- The presence of a diffuse X-rays emission that often peaks in the center of CGs shows that CGs are bound structures, they show numerous signs of interaction but their lifetime in much longer than their crossing times.
- Hickson CGs clearly show different stages of evolution, from weakly interacting galaxies to merging systems.
- CGs infalling into clusters may provide a mechanism to form clusters at high redshifts (e.g. in A1367).
- Massive versions of today's CGs may have been the best candidate precursors of fossil groups.
- Do CGs mimic the high redshift universe? This is still an open question. Indeed, their high density and low velocity dispersion should induce a high interaction rate and fast merging, CGs are nevertheless long-lived structures. On the other hand, there is probably no (or a few) isolated CGs in the high z universe. CGs may fuel high z clusters. CGs may produce fossil groups and fossil ellipticals.
- CGs at high z are difficult to detect and are still to be discovered.
- Interpretation of distant kinematics of galaxies may need nearby sample of galaxies to disentangle beam-smearing from evolutionary effects (e.g. HCG 31)
- Beam smearing effects may bias the Tully-Fisher relation (shifted towards lower M/L)

References

1. Geller, M. J., Huchra, J. P.: ApJS 52, 61 (1983)
2. Tully, R. B.: ApJ 321, 280 (1987)
3. Vikhlinin, A., McNamara, B. R., Hornstrup, A. et al.: ApJ 520L, 1 (1999)
4. Jones, L. R., Ponman, T. J., Horton, A., et al.: MNRAS 343, 627 (2003)
5. Stephan, M.: 1877, MNRAS 37, 334 (1877)
6. Seyfert, C.K.: AJ 53, 203 (1948)

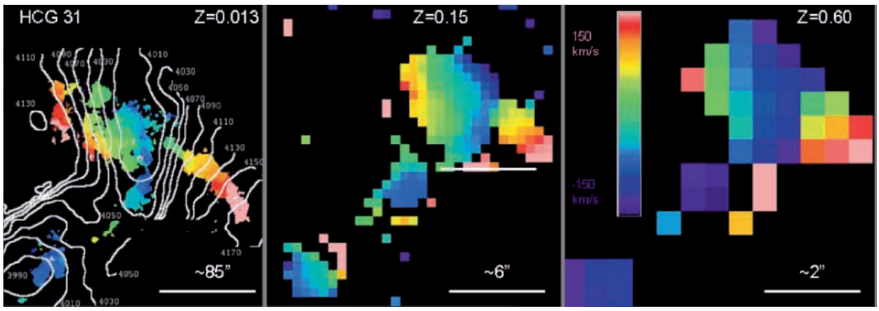

Fig. 1. -Left- Hα Velocity Field of HCG 31 on which is superimposed the HI velocity contours from Verdes-Montenegro et al. - Middle and right - The original data cube of HCG 31 has been convolved by the mean seeing function (0,62") to simulate a VLT/FLAME/GIRAFFE observation (pixel size=0.52"). The group has been projected respectively to redshift z=0.15 (middle image) and z=0.60 (right image), leading respectively to a scale of 2.6 and 6.7 kpc per arcsec ($h_0 = 71$, $\Omega_M = 0.27$, $\Omega_V = 0.73$). The velocity scale is the same for the 3 images [64].

7. Vorontsov-Velyaminov, B.A:. Atlas. Cat. Inter. Gal., I, Mosc. Stern. Inst. (1959)
8. Vorontsov-Velyaminov, B.A.: Atlas. Cat. Inter. Gal., II, A&ASuppl 28, 1 (1977)
9. Arp, H. ApJS 14, 1 (1966)
10. Shakhbasian, R. K.: Astrofizika 9, 495 (1973)
11. Rose, J.A.: ApJ 211, 311 (1977)
12. Hickson, P.: ApJ 255, 382 (1982)
13. Hickson, P.: Astrophys. Lett. Commun. 29, 1 (1993)
14. Allam, S. S., Tucker, D. L., Lin, H., & Hashimoto, Y.: ApJ 522, L89 (1999)
15. Tucker, D. L, et al.: ApJS 130, 237 (2000)
16. Lee, B. C., Allam, S. S., Tucker, D. L. et al.: AJ 127, 1811 (2004)
17. Merchan, M. E., Zandivarez, A.: MNRAS 335, 216 (2002)
18. Prandoni, I., Iovino, A., & MacGillvray, H. T.: AJ 107, 1235 (1994)
19. Iovino, A.: AJ 124, 2471 (2002)
20. de Carvalho, R. R., Goncalves, T. S., Iovino A. et al.: AJ 130, 425 (2005)
21. Arp, H.: ApJ 183, 411 (1973)
22. Williams, B. A., Yun, M. S., & Verdes-Montenegro, L.: AJ 123, 2417 (2002)
23. Gao, Y., & Xu, C.: ApJ 542, L83 (2000)
24. Lisenfeld, U., Braine, J., Duc, P.-A., Brinks, E., et al.: A&A 426, 471 (2004)
25. Mendes de Oliveira, C., Plana, H., Amram, P., et al.: AJ 121, 2524 (2001)
26. Mendes de Oliveira, C., Cypriano, E.S., Sodre, Jr., et al.: ApJL 605, L17 (2004)
27. Sulentic, J.W., Rosado, M., Dultzin-Hacyan, D., et al.: AJ 122, 2993 (2001)
28. van der Hulst, J.M., Rots, A.H.: AJ 86, 1775 (1981)
29. Xu, C.K., Lu, N.Y., Condon, J.J., et al.: ApJ 595, 665 (2003)
30. Appleton, P., Xu, C.K., Reach, W., Dopita, M., et al.: ApJ 639L, 51 (2006)
31. Trinchieri, G., Sulentic, J.W., Breitschwerdt, D. et al.: A&A 401, 173 (2003)
32. Plana, H., Mendes de Oliveira, C., Amram, P., et al.: ApJ 516, L69 (1999)
33. Trinchieri, G., Sulentic, J.W., Pietsch, W. et al.: A&A 444, 697 (2005)
34. Xu, C.K.: ApJ 619, 95 (2005)
35. Ponman, T. J., Bourner, P.D.J., Ebeling, H. et al.: MNRAS 283, 690 (1996)

36. Hickson P.: ARA&A 35, 360 (1997)
37. Zabludoff, A., & Mulchaey, J.: ApJ 496, 39 (1998)
38. Mendes de Oliveira, C. & Hickson, P.: ApJ 427, 684 (1994)
39. Mendes de Oliveira, C., Plana, H., Amram, P., Bolte et al.: ApJ 507, 691 (1998)
40. Amram, P., Plana, H., Mendes de Oliveira, C. et al.: A&A 402, 865 (2003)
41. Plana, H., Amram, P., Mendes de Oliveira, C. et al.: AJ 125, 1736 (2003)
42. Da Rocha, C., de Oliveira, C. Mendes: MNRAS 364, 1069 (2005)
43. Verdes-Montenegro, L., Yun, M. S., Williams et al.: A&A 377, 812 (2001)
44. Stevens, J. B., Webster, R. L., Barnes, D. G. et al.: PASA 21 21, 318 (2004)
45. Pildis, R. A., Bregman, J. N., Evrard, A. E.: ApJ 443, 514 (1995)
46. Zepf, S. E.: ApJ 407, 488 (1993)
47. Proctor, R. N., Forbes, D. A., Hau, G. K. T. et al.: MNRAS 349, 1381 (2004)
48. Ramella, M., Diaferio, A., Geller, M. J., & Huchra, J. P.: AJ 107, 1623 (1994)
49. Athanassoula, E., Makino, J., & Bosma, A.: MNRAS 286, 825 (1997)
50. Athanassoula, E.: APS Conf 209, 245. (2000)
51. Gomez-Flechoso, M. A., Dominguez-Tenreiro, R.: ApJ 549, L187 (2001)
52. Moore, B., Ghigna, S., Governato, F. et al.: ApJ 524, 19 (1999)
53. Klypin, A., Kravtsov, A. V., Valenzuela, O., Prada, F.: ApJ 522, 82 (1999)
54. Mendes de Oliveira, C.: 11^{th} Lat. Am. Reg. Meet. of the Inter. Astro. U. (2005)
55. Mendes de Oliveira, C., Cypriano, E. S. and Sodré, L. Jr.: AJ 131, 158 (2006)
56. Pompei, E., de Carvalho, R.R., & Iovino, A.: A&A 445, 857 (2006)
57. Iglesias-Paramo, J., Boselli, A., Cortese, L. et al.: A&A 384, 383 (2002)
58. Sakai, S., Kennicutt, R. C., van der Hulst et al.: ApJ 578, 842 (2002)
59. Cortese, L., Gavazzi, G., Boselli, A. et al.: A&A 453, 847 (2006)
60. Garrido, O., Marcelin, M., Amram, P. et al.: MNRAS 362, 127 (2005)
61. Hernandez, O., Carignan, C., Amram, P. et al.: MNRAS 360, 1201 (2005)
62. Flores, H., Hammer, F., Puech, M. et al.: A&A 455, 107 (2006)
63. Bosma, A.: PhDT 195 (1978)
64. Amram, P., Mendes de Oliveira, C., Plana, H. et al.: ApJ 612L, 5 (2004)
65. Verdes-Montenegro, L., Del Olmo, A., Yun, M. S. et al.: A&A 430, 443 (2005)
66. Williams, B. A., Mc Mahon, P. M., & van Gorkom, J. H.: AJ 101, 1957 (1991)
67. Richer, M. G., Georgiev, L., Rosado, M. et al.: A&A 397, 99 (2003)
68. Primack, J. R., Astro-ph/0609541
69. Förster Schreiber, N. M., Genzel, R., Lehnert, M. et al.: ApJ 645, 1062 (2006)
70. Mendes de Oliveira C., Amram P., Plana H. et al.: AJ 126, 2635 (2003)

39

The Cosmic Evolution Survey – COSMOS

Nick Scoville[1]

California Institute of Technology, Pasadena, CA 91125, USA
nzs@astro.caltech.edu

Summary. The Cosmic Evolution Survey (COSMOS) is designed to probe the correlated evolution of galaxies, star formation, active galactic nuclei (AGN) and dark matter (DM) with large-scale structure (LSS) over the redshift range $z > 0.5$ to 3. The survey includes multi-wavelength imaging and spectroscopy from X-ray to radio wavelengths covering a 2 square degree area, including HST imaging of the entire field. Given the very high sensitivity and resolution of these datasets, COSMOS will also provide unprecedented samples of objects at $z > 3$. Here I provide a brief overview of the survey strategy, the characteristics of the major COSMOS datasets, and summarize the science goals.

1 Introduction

Our understanding of the formation and evolution of galaxies and their large-scale structures (LSS) has advanced enormously over the last decade – a result of a phenomenal synergy between theoretical and observational efforts. Deep observational studies using the Hubble Space Telescope (HST) and the largest ground based telescopes have probed galaxy and AGN populations back to redshift $z = 6$ when the universe had aged less than 1 billion of its current 13 billion years. Just as remarkable is the enormous success of numerical simulations for ΛCDM models in reproducing many of the current LSS characteristics, all starting from an initial, nearly uniform, hot universe!

The COSMOS survey is the first survey encompassing a sufficiently large area that it can address the coupled evolution of LSS and galaxies, star formation and AGN. COSMOS is the largest HST survey ever undertaken – imaging an equatorial, 2 square degree field with single-orbit I-band exposures to a depth of $I_{AB} = 28$ mag (5σ). Extensive multi-λ ground and space-based observations of this field have been gathered or are anticipated, spanning the entire spectrum from X-ray, UV, optical/IR, mid-infrared, mm/submm and to radio with extremely high sensitivity imaging and spectroscopy. This full spectrum approach is required to probe the coupled evolution of young and old stellar populations, starbursts, the ISM (molecular and ionized components), AGN and dark matter. Each of these cosmic components may be best probed quite differently. The multi-λ approach is also **required** due to

the differential redshifting of cosmic history and the prescence of dust obscuration in many of the most rapidly evolving galactic regions. The large area coverage of COSMOS is motivated to sample the largest structures existing in the local universe – smaller area coverage can lead to severe cosmic variance problems.

COSMOS detects $\simeq 2 \times 10^6$ galaxies and AGN sampling a volume in the high redshift universe approaching that sampled locally by the Sloan Digital Sky Survey (SDSS). In this article, we provide a brief overview of the scientific goals of the COSMOS survey and an overall summary of the survey observational program.

2 COSMOS Science Goals

The COSMOS survey addresses nearly every aspect of observational cosmology over the majority of the Hubble time at z $\geq$ 0.5 to 6:

- the assembly of galaxies, clusters and dark matter up to $2 \times 10^{15}\ M_{\odot}$;
- reconstruction of the dark matter distributions and characteristics out to z $\sim$1 using weak gravitational lensing at z $<$ 1.5;
- the evolution of galaxy morphology, galactic merger rates and star formation as a function of LSS environment and redshift;
- evolution of AGN and the dependence of black hole growth on galaxy morphology and environment; and
- the mass and luminosity distribution of the earliest galaxies, AGN and intergalactic gas at z = 3 to 6 and their clustering.

Over 2 million galaxies are detected in the HST-ACS and Subaru optical imaging and photometric redshifts have been determined for approximately 800,000 galaxies. The COSMOS spectroscopic surveys (VLT and Magellan) will yield 50,000 galaxies with accurate redshifts at $z = 0.5 - 2.5$, all having $0.05''$ HST imaging. Redshift bins can then be constructed, each with tens of thousands of galaxies, to probe evolution of the morphological distribution (E, Sp, Irr, etc.) as a function of both LSS and time. Evolution of the luminosity and spatial correlation functions for type-selected galaxies will be analyzed with unprecedented statistical accuracy. The growth of galaxies, AGN and dark matter structure will be traced over a period corresponding to $\sim$75% of the age of the universe. The largest survey of the local universe (SDSS) samples approximately $\sim 10^7$ Mpc^3 at z $\leq$ 0.1; COSMOS samples equivalent or larger volumes in the earlier universe.

3 Major Observational Components

In this section, I briefly review the major ingredients of the COSMOS survey.

3.1 Galaxy Evolution : HST Imaging and SEDs

The evolutionary status of galaxies can be analyzed from either their morphologies or their spectral energy distributions (SED, characterizing the stellar population).

Morphological parameters for the galaxies are obtained from the HST imaging (e.g. bulge/disk ratios, concentration, asymmetry, size, multiplicity, clumpiness).

The COSMOS I-band ACS images have sufficient depth and resolution to allow classical bulge-disk decomposition for L^* galaxies at $z \leq 2$, while less detailed structural parameters such as compactness, asymmetry, clumpiness and size can be measured for all galaxies down to the spectroscopic limit ($I_{AB} \sim 25$), out to z $\sim$ 5. None of these measures can be obtained from ground-based imaging at these flux levels; ACS imaging is therefore a critical ingredient for understanding the evolution and build-up of galaxies.

In COSMOS, deep imaging (from Subaru, GALEX, UKIRT and NOAO, and SPITZER-IRAC) provides SEDs to characterize the integrated stellar populations of the 2 million galaxies detected with HST. The SEDs are derived self-consistently with the photometric redshift determinations. (For most of the galaxies, the multi-color imaging has insufficient resolution to measure internal population or extinction gradients – this requires two or more bands of imaging with HST.)

3.2 Galaxy Redshifts : Photometric and Spectroscopic

Determining the redshifts or lookback time of individual galaxies is clearly one of the most difficult and time consuming aspects of any cosmological evolution survey. In COSMOS this is even more difficult since the redshifts are needed with sufficient precision not just to determine the cosmic epoch, but also to place the galaxies within or outside of LSS appearing along the line of sight. Without high precision, structures become 'blurred' due to scattering of galaxies to different distances in the line of sight and for specific galaxies, their environment cannot be determined.

In COSMOS, photometric redshifts are obtained from deep (mostly ground-based) imaging – from Subaru, CFHT, UKIRT, and NOAO [2, 12]. At present the photometric-redshift accuracy is $\sigma_z/(1+z) \sim 0.04$ for approximately 2×10^5 galaxies at z < 1.2 (and 0.1 accuracy for 8×10^5 galaxies), enabling initial definition of the LSS, especially for the denser environments [20]. Expected improvements for the sensitivity of the near infrared imaging and the addition of more optical bands should further increase the accuracy and increase the redshift range of the photometric redshifts within the next year.

Very large spectroscopic surveys are now ongoing as part of COSMOS at the VLT and Magellan telescopes [11, 9]. The spectroscopic sample will eventually include approximately 45,000 galaxies and 1000 AGN down to limits of $I_{AB} = 24.5$ and $I_B = 25.5$ mag. These spectroscopic samples will provide very precise definition of the environment, albeit for smaller subsets of the overall COSMOS galaxy population.

3.3 COSMOS Field Selection

The COSMOS field is located near the celestial equator to ensure visibility by all astronomical facilities, especially unique instruments such as the next generation 20 – 30m optical/IR telescope(s). The time requirements for deep imaging and spectroscopy over a total area of 2 square degrees, containing over a million galaxies makes it strategically imperative that the field be readily observable by all large optical/IR telescopes. For radio studies, high-declination fields such as Lockman Hole, HDF-North, Groth strip and CDF-South are ruled out – they can not be easily observed by *both* (E)VLA in the north and ALMA in the south.

3.4 COSMOS Multi-wavelength Surveys

The COSMOS field is accessible to essentially all astronomical facilities, enabling complete multi-λ datasets (x-ray, UV, optical/IR, FIR/submm to radio). The status of these observational programs is continuously updated on the COSMOS web-site:

http://www.astro.caltech.edu/~cosmos/.

The extensive allocations on Subaru, CFHT, UKIRT and NOAO have providing extremely deep photometry for 22 bands from U to K_s, enabling accurate photo-z's, integrated colors and color selection of populations (e.g. LBGs, EROs, AGN, etc) for essentially all objects detected in the 2 square degree ACS field. XMM has devoted 1.4 Ms to a complete x-ray survey of the field [8], and COSMOS was one of the deep-GALEX fields for UV imaging [18]. The COSMOS VLA survey was alllocated 320 hrs for the largest, deep radio survey every done [17]. The XMM, GALEX and VLA surveys are all now complete. Deep mid-infrared observations (IRAC) and far-infrared observations (MIPS) of the full COSMOS field with Spitzer [16] will be carried out in 2006 January. At submm-wavlengths, partial surveys of COSMOS are on-going at the CSO and IRAM-30m telescopes. The COSMOS field will be a prime survey field for Herschel – providing longer wavelength coverage in the far infrared. Submm-λ surveys of the COSMOS field have been initiated to identify the most luminous starbursts at $z > 1$. In the long term, high resolution imaging with ALMA will be a vital capability – providing resolved images of the neutral ISM, luminosity distribution and dynamical masses for virtually all COSMOS galaxies having ISMs equivalent to the Galaxy. The COSMOS field was specifically selected to take advantage of the ALMA capabilities which will provide a fundamental capabilities.

4 Large Scale Structure

The need to sample very large scales arises from the fact that structure occurs on mass scales up to $\geq 10^{14} M_{\odot}$ and existing smaller surveys are likely to be unrepresentative at z $\sim$ 1. Evolution of the luminous-galaxy occupation number in halos as a function of both redshift and halo mass will provide stringent tests of LSS models. COSMOS will also provide critical data on the efficiency of star formation as a function of environment and cosmic epoch – these will be critical inputs/checks for the next generation of simulation models.

In Figure 1 contours of galaxy overdensity are shown for the COSMOS field using photometric redshifts at z $<$ 1.1 to separate galaxies along the line of sight [19]. Structures are seen on scales up to 20 Mpc with stellar masses up to $2{\times}10^{13}$ $M_{\odot}$.

4.1 Assembly and Evolution of Galaxies

Galaxies in the early universe are built up by two major processes: dissipational collapse and merging of lower mass protogalactic and galactic components. Their intrinsic evolution is then driven by the conversion of primordial and interstellar gas into stars, with galactic merging and interactions triggering star formation and starbursts. While there is general agreement over this qualitative picture, the precise

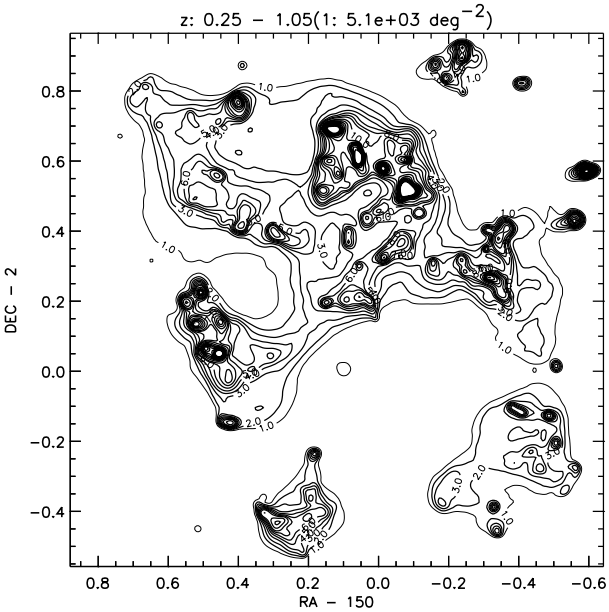

Fig. 1. The galaxy overdensities derived from the adaptive smoothing results, integrated in z from z = 0.25 to 1.05. The contour units are 5.1×10^3 galaxies deg^{-2} and the contours are at 1,2,3,4,5,6,7,8,10,12,14,16,18,20,22 and 24 units.

timing of these events, as well as their relation to local environment, remains to be observationally explored. There is currently much debate as to whether the assembly of massive galaxies takes place at a substantially earlier epoch (z >2) than predicted by the semi-analytic models. Spheroids include the majority of the stellar mass in the local universe [5], and may have formed at very early times (z > 2 – 3 [15, 14]. Their progenitors at $z \sim 3$ are possibly detected as highly clustered, red objects [10]. The Gemini Deep Survey finds massive galaxies out to z ∼ 2; HDF-N has few massive galaxies and those in the HDF-S are at higher z, suggesting strong environmental dependence and underscoring the need for large fields. As for spiral galaxies, their major epoch of formation may be in the range z = 1 – 2 [3]. COSMOS measures all galaxy populations in their large-scale context as a function of redshift, providing essential guidelines for the next generation of theoretical models.

4.2 Environment : Galaxy Overdensities, DM Weak Lensing and Correlation Functions

The environment or LSS in which a given galaxy resides is defined from the local number density of galaxies or from the DM density as determined from weak lensing or the local galaxy velocity dispersion. The COSMOS HST imaging provides measures of the close-in environment (from galaxy multiplicity and merger indicators such as tidal distortions) and larger-scale DM environment . As noted in section 3.2, definition of the environment is critically dependent on moderately high accuracy

spectroscopic (or photometric) redshifts; the integrated, multi-wavelength approach adopted for COSMOS is intended to maximize the impact and utility of each component. Having multiple approaches to environmental determination should also provide added confidence.

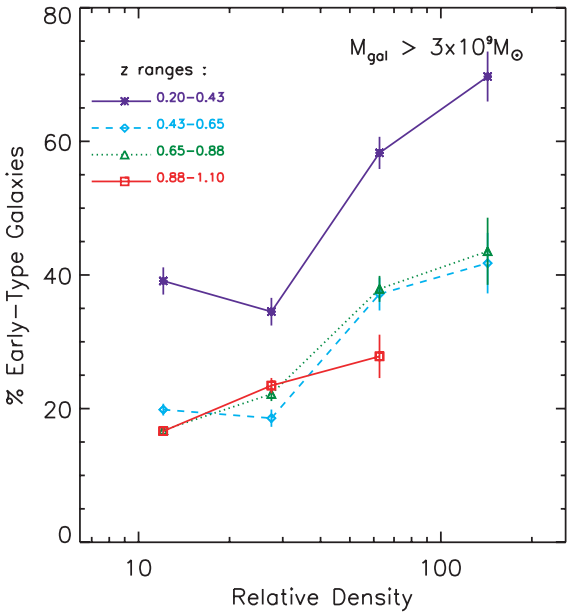

Fig. 2. The median early galaxy fraction (or red galaxy fraction with SED type < 1.9) is shown for galaxies binned in redshift (the curves) as a function of environmental density. The galaxy sample is such that the stellar mass is $M_* > 3 \times 10^9 M_\odot$.

The galaxy SED types shown exhibit very significant variations with both redshift and density – in the sense that earlier type SEDs (E's) are seen at higher density, later types in the lower density regions. The percentage of galaxies of early-type galaxies in COSMOS at $z < 1.1$ is shown in Figure 2. For all environmental densities, the median galaxy type is later (i.e. bluer, star forming) at higher redshifts. The major variation with z occurs between the lowest two redshifts (from z $\sim$ 0.3 to 0.5 or lookback times less than 5.3 Gyr) – all three high z bins have similar SEDs and their variations with density are the same. The major shift in the early-type galaxy fraction occurs beween the lowest two redshift bins shown in Figure 2; all redshifts an increased early-type fraction in seen above environmental density $\sim$50 (see [19]). Figure 2 clearly demonstrates that the galaxy-type correlation with density was clearly in place before $z = 1$ and we have extended this correlation to low densities, as well as the dense clusters.

4.3 Activity : Starbursts and AGN

The COSMOS survey samples ∼45,000 galaxies spectroscopically – providing an enormous sample of emission line tracers of both starbursts and AGN over a broad range of redshift. In addition, complete very high sensitivity radio continuum [17] and X-ray [8] coverage directly probes the population of AGN; the radio sensitivity can detect the starburst population at $z \sim 1 - 2$. Perhaps most importantly, the coverage with Spitzer will detect dust embedded ultraluminous starbursts and AGN out to $z \sim 2 - 3$. Thus, in the near term, COSMOS will sample large samples of galaxies with multiple, independent tracers of luminous activity – which can then be analyzed as a function of both redshift and environment – opening up fundamental investigations of starburst and AGN fueling in the early universe.

4.4 z = 3 – 6 : High Redshift Galaxies, LSS and IGM

The large areal coverage and high sensitivity of the COSMOS survey will result in significant samples of z > 3 objects, selected by multi-band color criteria (e.g. BzK selection), the Lyman-break method [7], or by direct detection of Lyα emission lines [22]. At these higher redshifts, the field subtends over 200 Mpc (comoving) and samples a volume similar to that sampled locally by SDSS.

5 Acknowlegements

First, it is pleasure to acknowledgement the wonderfulplanning of the LOC and SOC which has made this meeting possible; and secondly it is a profound pleasure to acknowledge the enormous and diverse contributions of Professor Sofue to our understanding of galactic structure and evolution.

The major COSMOS datasets become publicly available in staged releases (following calibration and validation) through the web site for IPAC/IRSA:

http://irsa.ipac.caltech.edu/data/COSMOS/

I gratefully acknowledge the contributions of the entire COSMOS colaboration consisting of more than 70 scientists.The HST COSMOS Treasury program was supported through NASA grant HST-GO-09822.

References

1. Bahcall, N. et al., ApJ, 603,1 (2004)
2. Capak, P. et al., ApJSS, (COSMOS special issue – in press) (2007)
3. Conselice, C. et al., ApJL, 600, L139 (2004)
4. Daddi, E., et al. : A& A, 361, 535 (2000)
5. Fukugita, Hogan & Peebles : ApJ, 503, 518 (1998)
6. Giavalisco, M et al., ApJ, 503, 543 (1998)
7. Giavalisco, M. et al., ApJL, (COSMOS special issue – in press) (2007)
8. Hasinger, G. et al., ApJSS, (COSMOS special issue – in press) (2007)
9. Impey, C. D. et al., ApJSS, (COSMOS special issue – in press) (2007)

10. Labbé, I. et al., AJ, 125, 1107 (2003)
11. Lilly, S.. et al., ApJSS, (COSMOS special issue – in press) (2007)
12. Mobasher, B. et al., ApJSS, (COSMOS special issue – in press) (2007)
13. Park, Y. et al., ApJL, 600, 155 (2004)
14. Peebles, J.E.: ASPC, 283, 351 (2002)
15. Renzini, A.: ApSS, 267, 357 (1999)
16. Sanders, D.B. et al., ApJSS, (COSMOS special issue –in press) (2007)
17. Schinnerer, A. et al., ApJSS, (COSMOS special issue –in press) (2007)
18. Schiminovich, D. et al., ApJSS, (COSMOS special issue – in press) (2007)
19. Scoville, N. et al., ApJSS, (COSMOS special issue – in press) (2007)
20. Scoville, N. et al., ApJSS, (COSMOS special issue – in press) (2007)
21. Taniguchi, Y. et al., ApJSS, (COSMOS special issue – in press) (2007)
22. Taniguchi, Y. et al., ApJSS, (COSMOS special issue – in press) (2007)

40

Dynamics of High-z Galaxies

Reinhard Genzel[1] and L.J. Tacconi[1]
on behalf of the SINS and SMG teams

Max-Planck Institute for extraterrestrial Physics, Garching, FRG
genzel@mpe.mpg.de

Summary. We report the first results of two major new efforts of exploring the dynamics of $z \sim 2$ galaxies with spatially resolved imaging spectroscopy at near-infrared (SINS/SINFONI) and millimeter (IRAM PdBI) wavelengths.

1 INTRODUCTION

Over the past two decades observations and theoretical simulations have established a global frame-work of galaxy formation and evolution in the young Universe. Galaxies formed as baryonic gas cooled at the centres of collapsing dark matter halos. Mergers of halos and galaxies led to the hierarchical build-up of galaxy mass. It remains unclear, however, over what time scales galaxies were assembled and when and how bulges and disks, the primary components of present day galaxies, were formed. It is also puzzling that the most massive galaxies were more abundant and were forming stars more rapidly at early epochs than expected from models. A major step forward in understanding these issues requires well resolved physical information on individual galaxies at high redshift. We report here the first results of two major programs of studying the dynamics of $z \sim 2$ galaxies with spatially resolved, near-infrared integral field spectroscopy (with SINFONI on the ESO VLT) and with millimeter interferometry (with the Plateau de Bure millimeter interferometer of IRAM).

2 SINFONI Integral Field Spectroscopy

Imaging spectroscopy of high redshift galaxies at high angular resolution of well understood rest-frame optical spectral diagnostics (Hα, [OIII] etc.) is now becomingz feasible with integral field spectroscopy on 8m-class large ground-based telescopes. This promises new empirical information about the crucial epoch of galaxy evolution near cosmological redshift $z \sim 2$, the peak of activity of QSOs and massive galaxy assembly, when the Universe was about 20% of its current age. We have recently begun a study of a representative sample of $z \sim 2$–3 star forming galaxies, selected based

on their rest-frame ultra-violet/optical fluxes and colors, with the near-infrared integral field spectrometer SINFONI on the Very Large Telescope of the European Southern Observatory (Eisenhauer et al. 2003). At the time of writing our 'SINS' survey has provided data sets on 35 z ∼1.5–3.2 optically/UV bright star forming galaxies (Forster Schreiber et al. 2006, Genzel et al. 2006, and in preparation). In the majority of cases the SINFONI data (spatial resolution ∼0.15–0.5") resolve the Hα/[OIII] emission. For about a dozen galaxies we extract two-dimensional velocity fields. In all of the best cases the gas dynamics appears regular at our resolution and can be accounted for by orbital motion in rotating disks or mergers. Perhaps the most surprising first result is the evidence that fairly large and massive proto-disk galaxies were present already at z ∼2–3. Figure 1 shows the velocity resolved Hα emission in BzK15504 ($z = 2.4$, Genzel et al. 2006). This high quality data set was obtained with adaptive optics delivering a resolution of ∼0.15" (∼1.2 kpc), for the first time fully resolving individual HII region complexes and kinematics of a powerful star forming disk galaxy at high redshift.

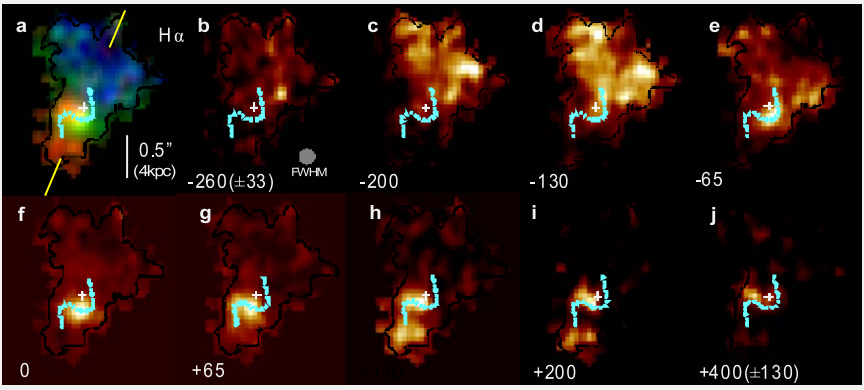

Fig. 1. Velocity channel maps of Hα emission in BzK-15504 ($z = 2.38$). Panel a is an RGB composite color map of the entire Hα emission, with three colours encoding the total velocity range of the emission. Panels (b–i) are velocity maps summed over 65 km/s. Panel j (260 km/s range) displays the highly red-shifted feature east of the nucleus. The velocity maps provide clear evidence for a rotating disk. The crosses in the panels mark the position of the continuum peak. The dotted, thin white curve outlines the shape of the integrated Hα emission at the ∼20% level. The two yellow lines mark the orientation of the major axis of the disk. North is up and East to the left, and a bar marks the length of 0.5" (adopted from Genzel et al. 2006).

The properties of BzK15504 suggest that the proto-disk was assembled rapidly, on a time scale of a few hundred million years, and has been converting a significant fraction of its total baryonic mass to stars on that time scale, with no obvious evidence for a major merger. The dynamical properties and the global and local matter surface densities show that the gas in the proto-disk is globally unstable to star formation. The inferred intrinsic rotation curves of BzK15504 and several other large disks we have studied as part of the SINS program are shown in Figure 2, and are compared to local disk galaxy rotation curves from Sofue & Rubin (2001). The remarkable similarity shows that large disks akin to the modern Milky Way already existed 2–3 billion years after the Big Bang. The angular momenta of these early disks are large. The baryonic gas cannot have lost much of the original angular momentum during the collapse from the ∼100 kpc virial radius to the ∼4 kpc disk scale length, in agreement with the original dissipative disk collapse scenario (Fall & Efstathiou 1980, Mo, Mao & White 1998), and perhaps resolving the 'angular momentum crisis' in numerical simulations.

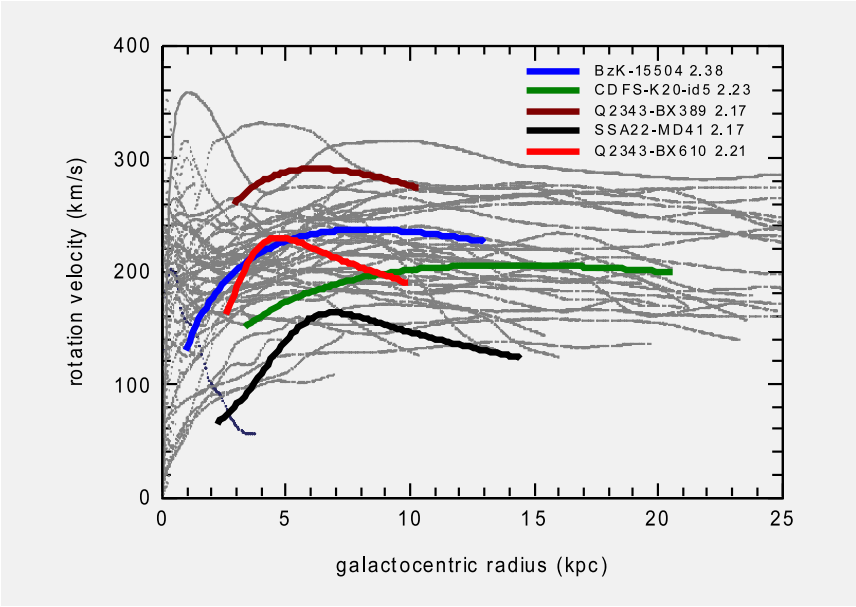

Fig. 2. Inferred intrinsic rotation curve of five $z \sim 2$ optically/UV-bright star forming galaxies from the SINS survey (from Forster Schreiber et al. 2006, Genzel et al. 2006 and in prep.), superposed on a collection of $z \sim 0$ late type disk rotation curves from Sofue & Rubin (2001).

3 Millimeter Interferometry of Submillimeter Galaxies

In the submillimeter galaxy survey at the IRAM Plateau de Bure Interferometer we have been studying a sample of submillimeter bright ($S_{850\mu m} > 5$ mJy), very luminous ($L_{\rm IR} \sim 10^{13} L_{\odot}$) submillimeter galaxies (SMGs) from the radio detected sample of Chapman et al. (2005). To date we have detected about 14 SMGs in the redshift range 1-3.5 (Fig. 3, Genzel et al. 2003, Neri et al. 2003, Greve et al. 2005, Tacconi et al. 2006), thus more than quadrupling the number of CO line detections in high-z dusty galaxies. We also carried out the first sub-arcsecond resolution, mm interferometry of 8 submillimeter galaxies (Tacconi et al. 2006). The results are summarized in Figure 3.

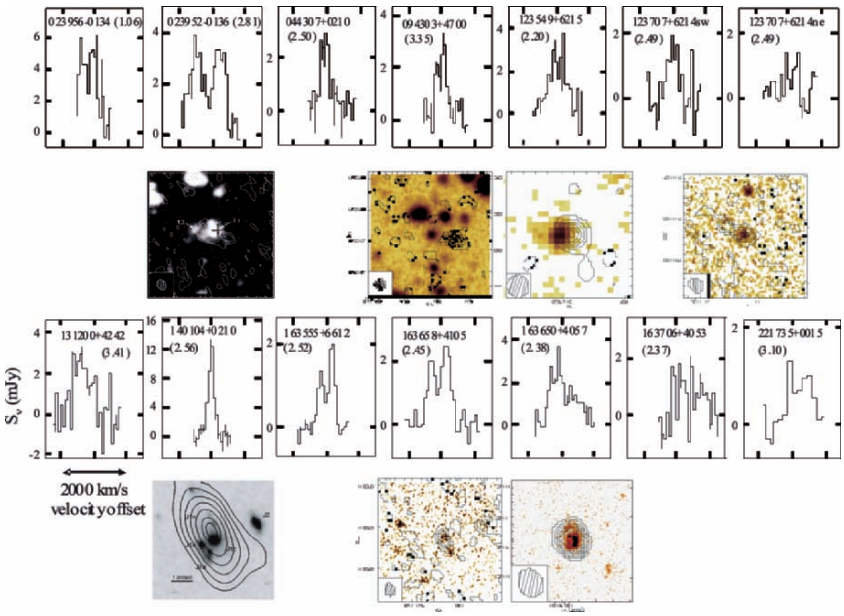

Fig. 3. CO 3–2/4–3 line profiles and high resolution integrated line and 1.2 mm continuum maps of 14 z ∼1-3.4 SMGs (from Genzel et al. 2003, Downes & Solomon 2003, Neri et al. 2003, Greve et al. 2005, Kneib et al. 2004, Tacconi et al. 2006).

There are three key results. First the average velocity width of the SMGs is close to 600 km/s FWHM, corresponding to an inclination corrected circular velocity of 380 km/s (Greve et al. 2005). This is approximately twice that of the optically/UV bright star forming population (Erb et al. 2006). Second, based on their CO fluxes the SMGs are gas rich with a typical gas fraction of ∼40% (Greve et al. 2005, Tacconi et al. 2006). Third, the 1.2mm emission from dust continuum and CO line emission from the 3–2/4–3 and 6–5/7–6 lines is compact; we marginally resolve or obtain tight upper limits to the FWHM sizes in all cases. The characteristic linear source diameters are? 4 kpc (Tacconi et al. 2006). This is about half of the average size of the optically/UV bright population discussed above. Five of the eight sources we have

studied at high resolution exhibit double-peaked line profiles indicative of orbital motion with significant angular momentum, either in a rotating disk, or an advanced merger. Our data are not yet detailed enough to distinguish between these two options. We find that dynamical masses, matter volume and surface densities of the SMG population, are comparable to those in massive local ellipticals and Sa bulges. The SMGs we have studied are similar to local Universe ultra-luminous infrared galaxy mergers (ULIRGs), suitably scaled for their larger masses, luminosities and star formation rates, as well as their greater gas fractions. The SMGs can be self-consistently understood in the framework of 'maximal' starbursts, where most of the available cold gas reservoir (10^{10}–$10^{11} M_{\odot}$) is converted to stars on a time scale $1/\epsilon$ times the characteristic dynamical time scale ($\sim$ 40 –100 Myrs).

4 Consequences for Galaxy Evolution

SMGs and UV/optically selected galaxies have similar dynamical masses and may be drawn from the same halo population, as proposed by Reddy et al. (2005). The differences in dynamical and star forming properties can be plausibly accounted for by the smaller sizes, smaller angular momenta and much larger surface/volume densities of the submillimeter population, in the sense of a 'Kennicutt'-star formation recipe where star formation rate scales with gas surface density and inversely with dynamical time scale. The difference between the two populations may then be whether or not a galaxy has been recently undergoing a major merger, resulting in a large loss of angular momentum, and whether the resulting remnant has been transformed into a dense, spheroidal component. The large differences in the observed kinematic/structural properties of the submillimeter and UV/optically-bright populations may thus indicate that in the former, dissipative major mergers lead to the formation of a compact, dense elliptical-galaxy remnant. The latter may have evolved in a less violent fashion. Possibilities include a series of minor mergers, or rapid and probably cold, gas flows from the halo, leading in a number of cases to the formation of large high-z protodisks. The disks we are observing at $z \sim 2$ obviously cannot continue to grow at the rate inferred from the simple dissipative collapse scenario because otherwise their scale lengths would exceed those observed in the local Universe. It seems likely that the early high-z protodisks were destroyed by subsequent mergers (Forster Schreiber et al. 2006), or by secular evolution (Genzel et al. 2006), or that further growth was inhibited by strong negative feedback due to star formation or active galactic nuclei.

Acknowledgements. The authors thank the SINS and SMG teams whose work we have presented here. We are also grateful to Keiichi Wada and the organizers of the Ishigaki conference. In many ways the work on high-z galaxies we have presented here follows on from the research that Prof. Y. Sofue and his colleagues have carried out for many years in the local Universe.

References

1. Downes, D. & Solomon, P.M.: ApJ, 582, 37 (2003)
2. Eisenhauer, F. et al.: Proc. SPIE, 4841, 1548 (2003)

3. Erb, D. K., Steidel, C. C., Shapley, A. E., Pettini, M, Reddy, N. A.& Adelberger, K. L.: ApJ, 647,128 (2006)
4. Fall, S. M. & Efstathiou, G.: MNRAS, 193, 189 (1980)
5. Forster Schreiber, N. M. et al. 2006, ApJ, 645, 1062
6. Genzel, R., Baker, A. J., Tacconi, L. J., Lutz, D., Cox, P., Guilloteau, S. & Omont, A.: ApJ, 584, 633 (2003)
7. Genzel, R. et al.: Nature, 442, 786 (2006)
8. Greve, T.R., Bertoldi, F., Smail, I., Neri, R., Blain, A.W., Ivison, R.J., Chapman, S.C., Genzel, R., Omont, A., Cox, P. Tacconi, L.J. & Kneib, J.-P.: MNRAS, 359, 1165 (2005)
9. Kneib, J.-P., Neri, R., Smail, I., Blain, A.W., Sheth, K., van der Werf, P., & Knudsen, K.K.: A&A, 614, L5 (2004)
10. Mo, H. J., Mao, S. & White, S. D. M.: MNRAS, 295, 319 (1998)
11. Neri, R., Genzel, R., Ivison, R.J., Bertoldi, F., Blain, A.W., Chapman, S.C., Cox, P., Greve, T.R., Omont, A. & Frayer, D.T. 2003, ApJ, 597, L113 Reddy, N. A., Erb, D. K., Steidel, C. C., Shapley, A. E., Adelberger, K. L., & Pettini, M.: ApJ, 633, 748 (2005)
12. Sofue, Y. & Rubin, V.: AnnRevAstr&Ap, 39, 137 (2001)
13. Tacconi, L. J., Neri, R., Chapman, S. C., Genzel, R., Smail, I., Ivison, R. J., Bertoldi, F., Blain, A., Cox, P., Greve, T. & Omont, A.: ApJ, 640, 228 (2006)

41

Coevolution and Downsizing of Supermassive Black Holes and Galactic Bulges

Masayuki Umemura

Center for Computational Sciences, University of Tsukuba, Ibaraki 305-8577, Japan: umemura@ccs.tsukuba.ac.jp

Summary. We consider recently reported "downsizing" of galaxies as well as SMBHs from a theoretical point of view. If the putative SMBH-to-bulge relation is incorporated, the downsizing of galaxies and SMBHs implies the downsizing of galactic bulges. We propose a physical mechanism to bring the downsizing of galactic bulges with the consideration of galaxy formation in UV background radiation. The star formation efficiency in primordial galaxies is basically regulated by the self-shielding againt UV background radiation. At higher redshift epochs, the self-shielding is stronger, and therefore galaxies form in a dissipationless fashion. As a result, earlier type (higher bulge-to-disk ratio) galaxies form at earlier epochs. Besides, a radiation-hydrodynamic mechanism is proposed to account for the SMBH-to-bulge relation. The growth of SMBHs can be promoted through the mass accretion driven by radiation drag which is exerted on dusty interstellar gas in radiation fields generated by bulge stars. It turns out that the resultant mass of a SMBH is predicted to be in proportion to the bulge mass, and the mass ratio is basically determined by the nuclear energy conversion efficiency from hydrogen to helium, $\varepsilon = 0.007$. In this scenario, the bulge luminosity overwhelms the BH accretion luminosity in the growing phase of SMBH. This phase corresponds to a "proto-QSO", thereafter evolving to a QSO. Also, the proto-QSO phase is preceded by an optically-thick ultraluminous infrared galaxy (ULIRG) phase. This provides a coevolution scheme of SMBHs and bulges. If coupled with the downsizing of bulges, this coevolution scheme leads to the downsizing of SMBHs. The present scenario is a potential solution of the coevolution and downsizing of SMBHs and galactic bulges.

1 Introduction

In a cold dark matter-dominated (CDM) universe, the hierarchical structure in the universe develops in a bottom-up fashion. However, it is pointed out recently that more massive galaxies completed the star formation episodes in earlier epochs [1, 2, 3, 4]. This trend is called "*downsizing*", which appears contrary to the prediction of the CDM universe. Also, it has turns out that more supermassive black holes (SMBHs) in galactic centers acquired their mass in earlier epochs [5, 6, 7, 8]. This implies that the downsizing also occurred in SMBHs.

On the other hand, the recent compilation of the kinematical data of galactic centers in both active and inactive galaxies has shown that a central 'massive dark object' (MDO), which is the nomenclature for a black hole (BH) candidate, correlates with the properties of a hosting bulge (a bulge means a whole galaxy for an elliptical galaxy). The demography of MDOs have revealed the following relations:

1) The BH mass exhibits a linear relation to the bulge mass with the ratio of $f_{\rm BH} \equiv M_{\rm BH}/M_{\rm bulge} \approx 0.002$ as a median value [9, 10, 11, 12, 13, 14, 15, 16]

2) The BH mass correlates with the velocity dispersion of bulge stars with a power-law relation as $M_{\rm BH} \propto \sigma^n$, $n = 3.75$ [17], 4.72 [14, 18] or 4.02 ± 0.32 [19].

3) In disk galaxies, the mass ratio is significantly smaller than 0.01 if the disk stars are included. But, if the bulge is focused, the relation 1) still holds [20, 21]

4) For quasars, the $f_{\rm BH}$ is at a similar level to that for elliptical galaxies [22, 23].

These correlations imply that the formation of a SMBH is physically linked to the formation of a galactic bulge which harbors a supermassive BH.

If the SMBH-to-bulge relation is combined with the downsizing of SMBHs and galaxies, it can be concluded that more massive bulges formed at earlier epochs. In other words, earlier type galaxies formed earlier. In this sense, Hubble's classification has turned out to be physical. In this paper, we propose a potential mechanism to cause the downsizing of SMBHs and galaxies, based on a coevolution scheme for SMBHs and bulges.

2 Formation of Supermassive Black Holes

The rotation barrier by the tidal spin up in a growing density fluctuation in the univers is given by

$$\frac{R_{\rm barr}}{R_{\rm Sch}} \approx 10^7 \left(\frac{M_b}{10^8 M_\odot}\right)^{-2/3} \left(\frac{\lambda}{0.05}\right)^2 (1+z)^{-1} \tag{1}$$

in units of the Schwarzshild radius $R_{\rm Sch}$, where M_b is the baryonic mass, z is the cosmological redshift, and λ is the spin parameter which provides the ratio of circular velocity to velocity dispersion of dark matter. The key physics for the formation of SMBHs is the angular momentum transfer. Furthermore, required mechanisms for BH formation must work effectively in a spheroidal system, since a correlation is found between SMBHs and bulges. The α-viscosity or non-axisymmetric gravitational instabilities would effectively transfer angular momentum once a disk-like system forms, but they are not likely to work in a spheroidal system.

A potential mechanism to remove angular momentum in a spheroidal system is proposed recently by Umemura (2001) [24], based on the radiation hydrodynamics in the galactic centers. In this model, the radiation drag extracts angular momentum from interstellar gas and allow the gas to accrete onto the center. For the total luminosity L_* of a bulge, the mass accretion rate is estimated to be

$$\dot{M} \simeq \eta_{\rm drag} \frac{L_*}{c^2}(1 - {\rm e}^{-\tau}), \tag{2}$$

where $\eta_{\rm drag}$ is the efficiency, c is the light speed and τ is the total optical depth. In an optically-thick regime, this gives simply $\dot{M} = \eta_{\rm drag} L_*/c^2$. Based on the numerical simulation by Kawakatu and Umemura (2002) [25], $\eta_{\rm drag} = 0.34$ maximally. If $L_* \approx$

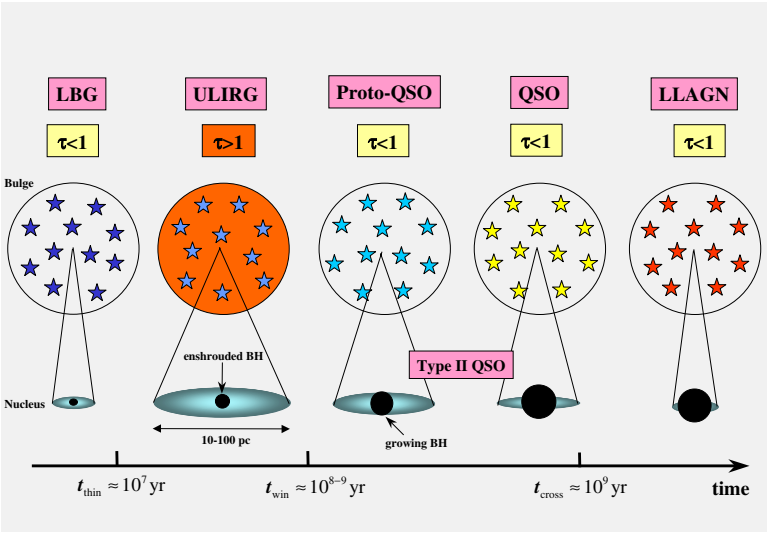

Fig. 1. Schematic sketch for the coevolution of SMBH and galactic bulge.

$10^{12} L_\odot$, this rate is comparable to the Eddington mass accretion rate for a black hole with $10^8 M_\odot$. The timescale of radiation drag-induced mass accretion is estimated to be

$$t_{\rm drag} \simeq 8.6 \times 10^7 {\rm yr} R_{\rm kpc}^2 \left(\frac{L_*}{10^{12} L_\odot} \right)^{-1} \left(\frac{Z}{Z_\odot} \right)^{-1}, \tag{3}$$

where $R_{\rm kpc} = R/{\rm kpc}$ is the galaxy radius and Z is the metallicity of gas. Due to the mass accretion induced by the radiation drag, a massive dark object forms at the center of bulge, eventually evolving into a SMBH. Then, the mass of SMBH is estimated in terms of

$$M_{\rm BH} = \int_0^t \dot{M} dt \simeq \int_0^t \eta_{\rm drag} \frac{L_*}{c^2} (1 - {\rm e}^{-\tau}) dt. \tag{4}$$

In practice, optically-thin surface layers are stripped from optically-thick clumpy clouds by the radiation drag. The stripped gas loses angular momentum and therefore accretes onto the center [26]. In this radiation hydrodnamic mechanism for BH formation, $f_{\rm BH}$ is tightly correlated with a bulge component even in a disk galaxy [27].

3 Coevolution of SMBHs and Galactic Bulges

Here, we construct a picture of the coevolution of SMBH and bulge based on the present mechanism for SMBH formation. The coevolution scheme of a SMBH and a bulge is summarized in Fig. 1. In order to incorporate the chemical evolution of host galaxy, we use an evolutionary spectral synthesis code 'PEGASE' [28], and also employ a galactic wind model with the wind epoch of $t_{\rm win} = 7 \times 10^8$yr to match

the present-day color-magnitude relation. The system is assumed to change from optically-thick to optically-thin phase at $t_{\rm win}$.

At a time $t_{\rm cross}$, all the accreted materials are swallowed by the central BH. The resultant BH fraction becomes $f_{\rm BH}/ \simeq 0.001$, which is just comparable to the observed ratio. The accretion luminosity, $L_{\rm AGN}$, exhibits a peak at $t_{\rm cross}$, it fades out abruptly due to exhausting the fuel. The fading nucleus could be a low luminosity AGN (LLAGN).

It is found that the era of $t_{\rm win} < t < t_{\rm cross}$ can be divided into two phases with a transition time $t_{\rm crit}$ when $L_{\rm bulge} = L_{\rm AGN}$; the earlier phase is the host luminosity-dominant phase and the later phase is the AGN luminosity-dominant phase. The lifetimes of both phases are comparable to each other, which is about 10^8yr. The AGN-dominant phase is likely to correspond to ordinary QSOs, while the host-dominant phase is obviously different from observed QSOs so far. We define this phase as "a proto-QSO" [29]. The observable properties of proto-QSOs are predicted as follows: (1) The width of broad emission line is narrower, which is less than 1500km/s. (2) $f_{\rm BH}$ rapidly increases from $10^{-5.3}$ to $10^{-3.9}$ in $\approx 10^8$ years. (3) The colors of $(B-V)$ at rest bands and $(V-K)$ at observed bands are about 0.5 magnitude bluer than those of QSOs. (4) In both proto-QSO and QSO phases, the metallicity of gas in galactic nuclei is $Z_{\rm BLR} \simeq 8Z_\odot$, and that of stars weighted by the host luminosity is $Z_* \simeq 3Z_\odot$. Such metallicity is consistent with the observations for QSOs and elliptical galaxies. (5) A massive dusty disk ($> 10^8 M_\odot$) surrounds a massive BH, and it may obscure the nucleus in the edge-on view to form a type 2 nucleus. The predicted properties of proto-QSOs are quite similar to those of radio galaxies at high redshifts. Thus, high-z radio galaxies are a key candidate for proto-QSOs.

The proto-QSO phase is preceded by a bright and optically thick phase, which may correspond to a ultraluminous infrared galaxy (ULIRG) phase. Also, the precursor of ULIRGs is an optically-thin and very luminous phase with the lifetime of $\sim 10^7$ years. This may correspond to the assembly phase of LBGs or Lyα emitters. In this phase, the metallicity is subsolar ($Z_* < 0.1Z_\odot$), and the hard X-ray luminosity is $L_{\rm x} \sim 5 \times 10^8 L_\odot$ if $L_{\rm x} = 0.1 L_{\rm AGN}$.

4 Downsizing of Galactic Bulges

From a theoretical point of view, the origin of the Hubble type has been attributed to the dissipativeness of the collapse, which is regulated by the efficiency of star formation. If the star formation proceeds after most of the gravitational energy is dissipated, the pregalactic clouds will evolve into spiral galaxies. This is a paradigm of the so-called *dissipational galaxy formation* (e.g. [30, 31, 32]). On the other hand, an early star formation episode leads to the *dissipationless galaxy formation* (e.g. [33, 34]), ending up with the formation of elliptical galaxies. However, the key mechanism which physically controls the star formation efficiency has been hitherto unsolved.

Recently, Susa & Umemura (2000a) [35] (hereafter SU0a) propose that the self-shielding against UV background radiation regulates the star formation in pregalactic clouds. The star formation processes in primordial gas have been extensively explored (e.g. [37, 38, 39, 40, 41, 42]). The key physics is the radiative cooling by H_2 line emission, because H_2 is the only coolant for primordial gas at $T \lesssim 10^4$ K. SU0a

have studied the efficiency of H_2 cooling in collapsing clouds exposed to UV background radiation, because galactic bulges are thouhgt to form after the reionization of the universe, probably at $z \lesssim 10$ ([43], and references therein). SU0a have found that if a cloud undergoes the first sheet collapse at higher redshifts ($z \gtrsim 4$), then the cloud is quickly shielded against the UV background and consequently cools down due to the efficient formation of H_2. Resultantly, it leads to an early burst of star formation. On the other hand, the shielding is retarded for a later collapsing cloud at $z \lesssim 4$, resulting in the dissipational galaxy formation. As a result, the bifurcation branch of the self-shielding is corresponding to the boundary between the dissipationless and dissipational galaxy formation. If the UV background is constant, the bifurcation mass scale is given as

$$M_{\rm SB}^{\rm max} = 2.2 \times 10^{11} M_\odot \left(\frac{1+z_{\rm c}}{5}\right)^{-4.2} \left(\frac{I_{21}}{0.5}\right)^{0.6}, \tag{5}$$

where I_{21} is the UV background intensity in units of 10^{-21}erg s^{-1}cm^{-2}str^{-1}Hz^{-1}. However, the dark matter potential may affect the evolution in the early phase of collapse. If we take this effect into account maximally, the Jeans length is reduced by a factor of $\sqrt{\Omega_{\rm b}/\Omega}$. With this Jeans scale, the bifurcation mass is changed to be $M_{\rm SB}^{\rm min} = (\Omega_{\rm b}/\Omega)^{1.2} M_{\rm SB}^{\rm max}$. Thus, the practical bifurcation mass would be between $M_{\rm SB}^{\rm max}$ and $M_{\rm SB}^{\rm min}$. This theory predicts that a larger amount of matter in pregalactic clouds collapses in a dissipationless fashion owing to stronger self-shielding at higher redshifts. As a result, galaxies with higher bulge-to-disk ratios form at higher redshifts. Hence, this bifurcation theory leads to the trend that more massive bulge formed at earlier epochs, say *downsizing*.

Based on SU0a, Susa & Umemura (2000b) [36] (hereafter SU0b) confronted the bifurcation theory of galactic morphology with the observations of elliptical and spiral galaxies. SU0a have assumed the UV intensity to be independent of time. Practically, the intensity seems to evolve. SU0b included the effect of the evolution of UV background radiation as $I_{21} = 0.5\left[(1+z)/3\right]^3$ for $z \leq 2$ and $I_{21} = 0.5$ for $2 < z \leq 4$. This dependence is consistent with the UV intensity in the present epoch, and the value inferred from the QSO proximity effects at high redshifts ([44]). As a result, it is shown that the bifurcation theory successfully discriminates between elliptical and spiral galaxies. This suggests that the UV background radiation could play a profound role for the downsizing of galactic bulges.

5 Conclusions

Recently the "downsizing" of galaxies as well as SMBHs are reported by observations of high redshift galaxies and active galactic nuclei. If the putative SMBH-to-bulge relation is incorporated, the downsizing of galaxies and SMBHs implies the downsizing of galactic bulges. We have proposed a physical mechanism to bring the downsizing of galactic bulges with the consideration of galaxy formation in UV background radiation. The star formation efficiency in primordial galaxies is basically regulated by the self-shielding againt UV background radiation. At higher redshift epochs, the self-shielding is stronger, and therefore galaxies form in a dissipationless fashion. As a result, earlier type (higher bulge-to-disk ratio) galaxies form at earlier epochs. Besides, a radiation-hydrodynamic mechanism is proposed to account for

the SMBH-to-bulge relation. The growth of SMBHs can be promoted through the mass accretion driven by radiation drag exerted by stellar radiation in bulges. It turns out that the resultant mass of a SMBH is predicted to be in proportion to the bulge mass, and the mass ratio is basically determined by the nuclear energy conversion efficiency from hydrogen to helium, $\varepsilon = 0.007$. This is a coevolution scheme of SMBHs and bulges. If coupled with the downsizing of bulges, it leads to the downsizing of SMBHs. The present scenario may provide a potential solution of the coevolution and downsizing of SMBHs and galactic bulges.

References

1. Cowie, L. L., Songaila, A., Hu, E. M., & Cohen, J. G. 1996, AJ, 112, 839
2. Kauffmann, G., et al.2003, MNRAS, 341, 54
3. Kodama, T., et al. 2004, MNRAS, 350, 1005
4. Glazebrook, K., et al. 2004, Nature, 430, 181
5. Ueda, Y., Akiyama, M., Ohta, K., & Miyaji, T. 2003, ApJ, 598, 886
6. Hasinger, G. 2003, AIP Conf. Proc. 666: The Emergence of Cosmic Structure, 666, 227
7. Marconi, A., Risaliti, G., Gilli, R., Hunt, L. K., Maiolino, R., & Salvati, M. 2004, MNRAS, 351, 169
8. Merloni, A. 2004, MNRAS, 353, 1035
9. Kormendy, J., & Richstone, D. 1995, ARAA, 33, 581
10. Richstone, D., et al. 1998, Nature, 395A, 14
11. Magorrian, J., et al. 1998, AJ, 115, 2285
12. Gebhardt, K., et al. 2000a, ApJ, 539, L13
13. Ferrarese, L., & Merritt, D. 2000, ApJ, 539, L9
14. Merritt, D., & Ferrarese, L. 2001a, MNRAS, 320, L30
15. McLure, R. J., & Dunlop, J. S. 2002, MNRAS, 331, 795
16. Marconi, A., & Hunt, L. K. 2003, ApJ, 589, L21
17. Gebhardt, K., et al. 2000b, ApJ, 543, L5
18. Merritt, D., & Ferrarese, L. 2001b, ApJ, 547, 140
19. Tremaine, T. et al. 2002, ApJ, 574, 740
20. Salucci, P., et al. 2000, MNRAS, 317, 488
21. Sarzi, M., et al. 2001, ApJ, 550, 65
22. Laor, A. 1998, ApJ, 505, L83
23. Shields, G. A. et al. 2003, ApJ, 583, 124
24. Umemura, M. 2001, ApJ, 560, L29
25. Kawakatu, N. & Umemura, M. 2002, MNRAS, 329, 572
26. Sato, J., Umemura, M., Sawada, K., & Matsuyama, S. 2004, 354, 176
27. Kawakatu, N. & Umemura, M. 2004, ApJ, 601, L21
28. Fioc, M., & Rocca-Volmerrange, B. 1997, A&A, 326, 950
29. Kawakatu, N., Umemura, M., & Mori, M. 2003, ApJ, 583, 85
30. Larson, R. B. 1976, MNRAS, 176, 31
31. Carlberg, R. G. 1985, ApJ, 298, 486
32. Katz, N., & Gunn, J. E. 1991, ApJ, 377, 365
33. Aarseth, S. J., & Binney, J. 1978, MNRAS, 185, 227
34. Aguilar, L. A., & Merritt, D. 1990, ApJ, 354, 33
35. Susa, H., & Umemura, M. 2000, ApJ, 537, 578

36. Susa, H., & Umemura, M. 2000, MNRAS, 316, L17
37. Bromm, V., Coppi, P. S., & Larson, R. B. 1999, ApJ, 527, L5
38. Bromm, V., Coppi, P. S., & Larson, R. B. 2002, ApJ, 564, 23
39. Nakamura, F. & Umemura, M. 1999, ApJ, 515, 239
40. Nakamura, F. & Umemura, M. 2001, ApJ, 548, 19
41. Abel, T., Bryan, G. L., & Norman, M. L. 2000, ApJ, 540, 39
42. Abel, T., Bryan, G. L., & Norman, M. L. 2002, Science, 295, 93
43. Nakamoto, T., Umemura, M., & Susa, H. 2001, MNRAS, 321, 593
44. Umemura, M., Nakamoto, T., & Susa, H. 2001, ASP Conference Series, 222, 143

42

Molecular Gas in the Early Universe

Fabian Walter[1]

Max Planck Institut for Astronomy Heidelberg walter@mpia.de

1 Introduction: QSOs at High z

Over the last few years, the study of high redshift QSOs has been revolutionized in three ways. First, wide field surveys have revealed 100's of high–z QSOs, right back to the epoch of cosmic reionization ($z > 6$; e.g., Fan et al. 2006). Second, it has been shown that most (all?) low redshift spheroidal galaxies have central super-massive black holes (SMBH), and that the black hole mass correlates with bulge velocity dispersion. This M_{BH}–σ_v correlation suggests coeval formation of galaxies and SMBH, thereby making SMBHs a fundamental aspect of the galaxy formation process (Gebhardt et al. 2000). And third, mm surveys of high redshift QSOs find that 30% of the sources are 'hyper-luminous infrared galaxies' ($L_{FIR} = 10^{13}$ $L_\odot$), corresponding to thermal emission from warm dust, and that this fraction is *independent of redshift out to* $z = 6.4$ (Beelen et al. 2004, Omont et al. 2004). If the dust is heated by star formation, the implied star formation rates are extreme ($> 10^3$ $M_\odot$ year^{-1}), consistent with the formation of a large elliptical galaxy on a dynamical timescale of 10^8 years.

2 Molecular Gas in QSO Hosts

Molecular line observations (typically CO) of FIR-luminous high–z QSOs have revealed large gas masses in most cases observed to date (see Carilli et al. 2004; Solomon & Vanden Bout 2005). Molecular gas has now also been detected in numerous high–z FIR-bright submillimeter galaxies (see contribution by Tacconi and Genzel, this volume). Detecting large amounts of warm, extended molecular gas currently provides the strongest evidence that these luminous QSOs are undergoing vigorous star formation. The coeval growth of massive black holes and of massive stellar populations can be examined directly in these unique systems, providing an opportunity to study the cause of the tight correlation between these components that is observed in local spheroidal galaxies. High resolution observations are crucial for this, since the structure of the dense gas which is feeding the starburst and the black hole can reveal the cause of event (e.g. mergers) and the mass of the systems, placing them into the cosmic structure evolution context. Molecular gas has now been detected in more than a dozen $z > 2$ QSO host galaxies. Most sources have

been studied in the higher order transitions ($\geq$ CO 3–2), although at $z \geq 4$ the lower order transitions become accessible to cm telescopes such as the VLA.

The *detection* of CO emission is critical to estimate the reservoir of the molecular gas in these early systems. A second step is then to *spatially resolve the molecular gas distribution*. In particular, given the typical diameters of galaxies of many kpc, a linear resolution of ~ 1 kpc is needed to *resolve the structure* of the underlying host galaxy. Such measurements are needed 1) to get an estimate for the *size of the host galaxy* (and thus a better estimate for the dynamical mass), 2) to resolve potentially merging systems and 3) to better constrain the *physical properties* of the molecular gas by measuring the brightness temperature of the molecular gas in the hosts. A linear resolution of 1 kpc corresponds to a resolution of $0.15''$ at the redshifts under consideration ($1'' \sim 8.5$ kpc at $z = 2$, $1'' \sim 5.8$ kpc at $z = 6$). Such observations can then in turn be used to constrain the predictions by CDM simulations of early galaxy formation, and, if a large sample was available, put limits on the frequency of mergers at high redshift. In addition, such studies can be used to constrain the possible redshift-evolution of the M_{BH}–σ_v relation (as will be discussed below).

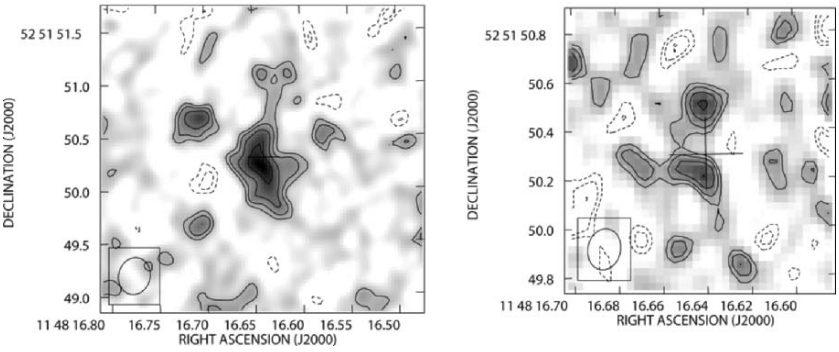

Fig. 1. *left*: CO(3–2) map of J1148+5251 of the combined B- and C-array data sets (covering the total bandwidth, 37.5 MHz or 240 km s^{-1}). Contours are shown at -2, -1.4, 1.4, 2, 2.8, and 4 $\times\sigma$ ($1\sigma = 43$ μJy beam^{-1}). The beam size ($0.35'' \times 0.30''$) is shown in the bottom left corner. *right*: The central region at 1 kpc ($0.17'' \times 0.13''$) resolution ($1\sigma = 45$ μJy beam^{-1}). 2, 2.8, and 4 $\times\sigma$ ($1\sigma = 45$ μJy beam^{-1}). This high–resolution map recovers half of the flux seen in the left panel (see Walter et al. 2004 for more details). New HST ACS imaging suggests that the AGN seen in the optical is associated with the souther CO clump seen in the right panel (White et al. 2005).

It is important to note that the highest resolution imaging of QSO host galaxies can currently only be obtained using the recently upgraded Q–band system at the VLA. In optical/NIR observations the central bright AGN greatly overshines the host galaxy, thus rendering optical/NIR studies of the QSO hosts impossible given current instrumentations (but see Genzel, this volume, for the latest results of NIR observations of z 2–3 submillimeter galaxies). We note that observations of the molecular gas phase at resolutions of $0.15''$ will even be difficult to achieve with ALMA during the 'early science' operations, as they require $\sim$4 km ($\nu \sim 100$ GHz) or

$\sim 2\,\mathrm{km}$ ($\nu \sim 200\,\mathrm{GHz}$) baselines (numbers are for a $z \sim 2.5$ source). For comparison, current mm interferometers typically only observe at baselines up to $\sim 400\,\mathrm{m}$.

3 Previous Work

Over the last few years, the VLA has been used to image a number of high–z sources, e.g., in the case of the strongly lensed source J2322+1944 (z=4.1, Carilli et al. 2003) and the double system BRI1202-0725 (z=4.7, Carilli et al. 2002). Resolved imaging has recently also been obtained for J1148+5251, which is still the redshift record–holder for QSOs (z=6.42). It has been detected in CO(3-2) using the VLA (Walter et al. 2003) and in CO(6–5) and CO(7–6) using the Plateau de Bure interferomter (Bertoldi et al. 2003). Follow–up VLA B and C array observations clearly resolved the the molecular distribution spatially and also in velocity space (Walter et al. 2004, see Fig. 1). The molecular gas distribution in J1148+5251 is extended out to radii of 2.5 kpc. The central region is resolved and shows 2 peaks, separated by 1.7 kpc; they account for about half of the total emission, with the other half present in the more extended molecular gas distribution. Each of these peaks harbors a molecular gas mass of $\sim 5 \times 10^9\,\mathrm{M}_\odot$ within a radius of 0.5 kpc, respectively; this mass is similar to the total mass found in nearby ULIRGS such as Mrk 273 or Arp 220 (Downes & Solomon 1998). The peaks have intrinsic brightnesses of $\sim 35\,\mathrm{K}$ (averaged over the 1 kpc-sized beam), similar to what is found in the centres of nearby active galaxies (Downes & Solomon 1998, assuming constant surface brightness down to the CO(1–0) transition), albeit measured over a larger physical area.

Based on the extent of the molecular gas distribution and the line-width measured from the higher CO transitions we derive a dynamical mass of $\sim 4.5 \times 10^{10}\,\mathrm{M}_\odot$ ($\sim 5.5 \times 10^{10}\,\mathrm{M}_\odot$ if we correct for an inclination of $i \sim 65°$). This dynamical mass estimate can account for the detected molecular gas mass within this radius but leaves little room for other matter. In particular, given a black hole mass of mass $\sim$1-5$\times 10^9$ $\mathrm{M}_\odot$ (Willot et al. 2003), this dynamical mass could not accomodate an order few $\times 10^{12}\,\mathrm{M}_\odot$ stellar bulge which is predicted by the present–day $\mathrm{M_{BH}} - \sigma_{\mathrm{bulge}}$ relation (Ferrarese & Merritt 2000, Gebhardt 2000), if this relation were to hold at these high redshifts. Even if we assume a scenario in which this bulge was 10 times the scale length of the molecular gas emission, we would still expect a bulge contribution of few $\times 10^{11}\,\mathrm{M}_\odot$ within the central 2.5 kpc (assuming a central density–profile of $\rho \sim r^{-2}$, e.g., Jaffe 1983, Tremaine 1994) which can not be reconciled with our results. Our finding therefore suggests that black holes may assemble before the stellar bulges. Depending on the space density of similar sources at these high redshifts, the smaller dynamical masses may be in better agreement with the masses predicted by CDM simulations in the very early universe as a $10^{12}\,\mathrm{M}_\odot$ bulge would imply a rather massive dark matter halo of $> 10^{14}\,\mathrm{M}_\odot$. Regardless, these results show the power of high-resolution CO imaging in sources at the end of cosmic reionization.

4 The Latest from the VLA...

In the following, we present some new observations that we recently obtained at the VLA in B array configuration (D. Riechers, PhD Thesis, MPIA Heidelberg).

APM0827+5255 ($z = 3.9$): The presence of extended CO(1–0) emission in APM0827+5255 was reported by Papadopoulus et al. (2001). Additional CO(2–1)

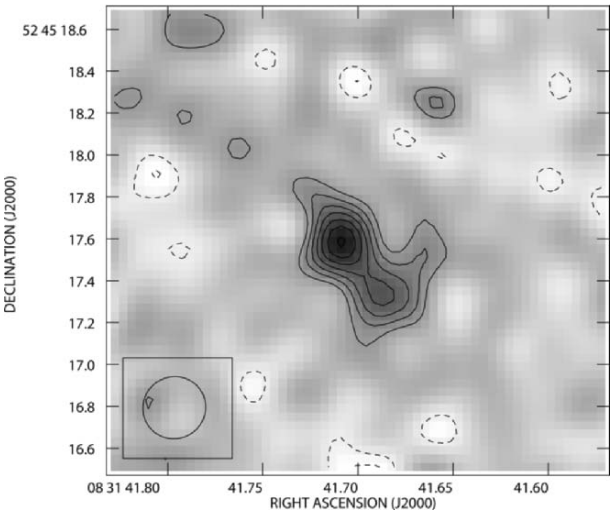

Fig. 2. Image of CO(1–0) towards APM 08729+5255 obtained with the VLA covering a bandwidth of 43.75 MHz, or 560 km s^{-1} (Riechers et al. 2006, in prep.). Contours are shown at -3, -2, 2, 3, 4, 5, 6, 7, and 8 $\times\sigma$ ($1\sigma = 16$ μJy $beam^{-1}$. The beam size ($0.30'' \times 0.30''$) is shown in the bottom left corner. We find no evidence for an extended reservoir of molecular gas around this source.

C–array imaging by Papadopoulus et al. also showed some evidence for an extended envelope around the central QSO. We have have obtained new C and B array observations for this source and do not find evidence for such an extended CO component. In Fig. 2, we show our highest resolution data, where we detect a compact but resolved structure of the lens images. Two clearly separated images can be seen, and their morphology and brightess ratio is very similar to that of the optical QSO. We thus conclude that the CO in this source is indeed extremely compact, and that the lensing magnification is close to the optical magnification i.e., a factor of 100 rather than 7 as derived in previous models (Lewis et al. 2002). Further evidence against an extended CO(1–0) reservoir around APM0827+5255 comes from our multi–CO transition study of this source (Weiss et al. 2006, in prep., see also this volume, and recent single dish observations of this source using the GBT, Riechers et al. 2006, see also this volume).

B1335-0417 ($z = 4.4$): This is one of the first sources detected in CO(2–1) with the VLA in D array (Carilli et al. 1999). We recently re–observed the CO(2–1) transition in the $z = 4.4$ QSO BRI 1335-0417 at high resolution ($0.15''$) with the VLA in B–array (Fig. 3, Riechers et al. 2006, in prep.). The integrated CO map shows a compact but resolved molecular gas reservoir, and our velocity channel maps show, for the first time, the actual dynamics of the molecular gas in a high-z QSO host galaxy at high signal–to–noise. The detected structure shows an interesting morphology which may be interpreted as a close merger or rotation. We are currently modeling the kinematics of this unique dataset.

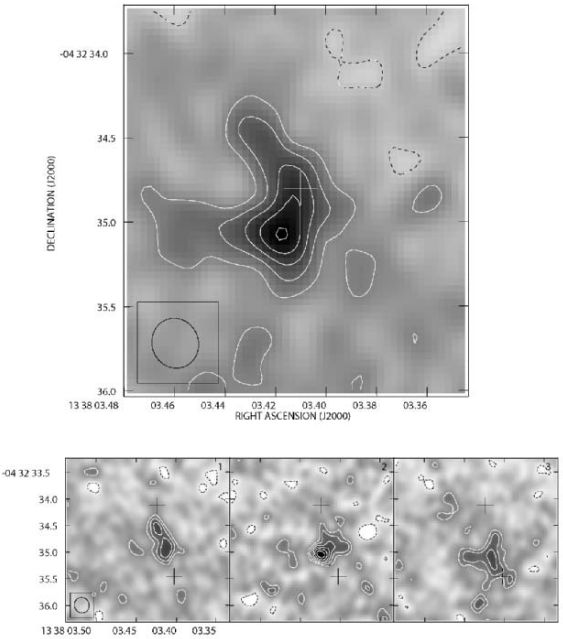

Fig. 3. Image of CO(2–1) towards BRI 1335-0417 obtained with the VLA. *top*: Moment 0 map covering a bandwidth of 43.75 MHz, or 300 km s^{-1} (Riechers et al. 2006, in prep.). Contours are shown at -2, 2, 4, 6, 8, and 10 $\times\sigma$ ($1\sigma = 50$ μJy beam^{-1}. *bottom*: Channel maps with a width of 12.5 MHz, or 85 km s^{-1} each, covering the central 260 km s^{-1} of the emission. Contours are shown at -3, -2, 2, 3, 4, 5, 6, 7, and 8 $\times\sigma$ ($1\sigma = 100$ μJy beam^{-1}). For the first time these observations allow us to study the kinematics in a high-z QSO host galaxy in detail.

5 Concluding Remarks

New observations obtained during the last few years have resulted in fundamental new insights of the molecular gas properties of distant QSOs and submillimeter galaxies. Some of thes recent observations presented here have shown that resolved molecular gas *maps* of objects out to the highest redshifts can already be achieved with today's instrument (i.e. the VLA). Although these observations are time intensive, they have dramatically improved our knowledge of the properties of the molecular gas phase at high redshift. E.g., they have helped to constrain the source sizes and kinematics, which in turn constrain the dynamical masses (e.g. in the case of J1148+5251, and B1335-0417). Also, they have provided clear evidence for coeval starburst and AGN activity (e.g., J2322+1944) and revealed likely interactions with objects that are barely visible in the optical (e.g. B1202-0725). These results show the enormous potential for future studies of the molecular gas content and

dynamical masses in a statistically significant sample of high–redshift galaxies using ALMA, where resolutions of $< 0.1''$ will be achieved routinely.

References

1. Beelen, A., et al.: A&A, 423, 441 (2004)
2. Bertoldi, F., Cox, P., Neri, R., et al.: A&A, 409, L47 (2003)
3. Carilli, C. L., Menten, K. M., & Yun, M. S.: ApJ, 521, L25 (1999)
4. Carilli, C. L., Kohno, K., Kawabe, R., et al.: AJ, 123, 1838 (2002b)
5. Carilli, C. L., Lewis, G. F., Djorgovski, S. G., et al.: Science, 300, 773 (2003)
6. Carilli, C., et al. 2004, astro-ph/0402573
7. Downes, D., & Solomon, P. M.: ApJ, 507, 615 (1998)
8. Fan, X, et al.: AJ, 131, 1203 (2006)
9. Ferrarese, L. & Merritt, D.: ApJL, 539, L9 (2000)
10. Gebhardt, K., et al.: ApJL, 539, L13 (2000)
11. Hu, E., et al.: ApJ, 459, L53 (1996)
12. Jaffe, W.: MNRAS, 202, 995 (1983)
13. Lewis, G. F., Carilli, C., et al.: MNRAS, 330, L15 (2002)
14. Omont, A., et al.: in 'Multiwavelength AGN Surveys',World Scientific, Singapore, 109 (2004)
15. Papadopoulos, P., Ivison, R., et al.: Nature, 409, 58 (2001)
16. Riechers, D. A., Walter, F., Carilli, C. L., et al.: ApJ, 650, 604s (2006)
17. Solomon, P. M., & Vanden Bout, P. A.: ARA&A, 43, 677 (2005)
18. Tremaine, S., Richstone, D. O., Byun, Y., et al.: AJ, 107, 634 (1994)
19. Walter, F., Bertoldi, F., Carilli, C. L., et al.: Nature, 424, 406 (2003)
20. Walter, F., Carilli, C., Bertoldi, F., et al.: ApJ, 615, L17 (2004)
21. White, R. L, Becker, R. H, Fan, X., & Strauss, M. A.: AJ, 129, 2102 (2005)
22. Willott, C. J., McLure, R. J., & Jarvis, M. J.: ApJL, 587, L15 (2003)

43

Galaxy Evolution Viewed as Functions of Environment and Mass

Tadayuki Kodama[1], Masayuki Tanaka[2], Ichi Tanaka[3], and Masaru Kajisawa[1]

[1] National Astronomical Obseravtory of Japan, 2–21–1 Osawa, Mitaka, Tokyo 181-8588, Japan,
kodama@optik.mtk.nao.ac.jp, kajisawa@optik.mtk.nao.ac.jp
[2] Department of Astronomy, University of Tokyo, 7–3–1 Hongo, Bunkyo-ku, Tokyo 113-0033, Japan, tanaka@astron.s.u-tokyo.ac.jp
[3] Subaru Telescope, National Astronomical Observatory of Japan, 650 North Aohoku Place, Hilo, HI 96720, USA, ichi@subaru.naoj.org

We present two large surveys of distant clusters currently being carried out with Subaru, making use of its great capability of wide-field study both in the optical and in the near-infrared. The optical surveys, called PISCES, have mapped out large scale structures in and around 8 distant clusters at $0.4 < z < 1.3$, composed of multiple filaments and clumps extended over 15-30 Mpc scale. From the photometric and spectroscopic properties of galaxies over a wide range in environment, we find that the truncation of galaxies is seen in the outskirts of clusters rather than in the cluster cores. We also see a clear environmental dependence of the down-sizing (progressively later quenching of star formation in smaller galaxies). The near-infrared surveys are being conducted with a new wide-field instrument targeting proto-clusters around high-z radio-loud galaxies up to $z \sim 4$. Most of these field are known to show a large number of Lyα and/or Hα emitters at the same redshifts of the radio galaxies. We see a clear excess of near-infrared selected galaxies (JHK_s-selected galaxies as well as DRG) in these fields, and they are indeed proto-clusters with not only young emitters but also evolved populations. Spatial distribution of such NIR selected galaxies is filamentary and track similar structures traced by the emitters. There is an hint that the bright-end of the red sequence first appeared between $z = 3$ and 2.

1 Panoramic Views of Cluster Evolution at $z \lesssim 1$

1.1 Large scale structures

We are conducting PISCES project (Panoramic Imaging and Spectroscopy of Cluster Evolution with Subaru; [10]) with making use of the wide-field imaging capability of Subaru. We first map out large scale structures and define local envioronments of galaxies therein, and then investigate the variation in galaxy properties as a function of environment and mass. We have completed multi-colour imaging of 8 distant clusters between $0.4 < z < 1.3$ so far, and we have successfully mapped

out filamentary/clumpy structures in and around the clusters across 15–30 Mpc scales based on photometric redshifts [10] (see some examples in Figs. 1). The large scale structures of these two clusters have secure spectroscopic confirmation of their physical association to the main body of the clusters.

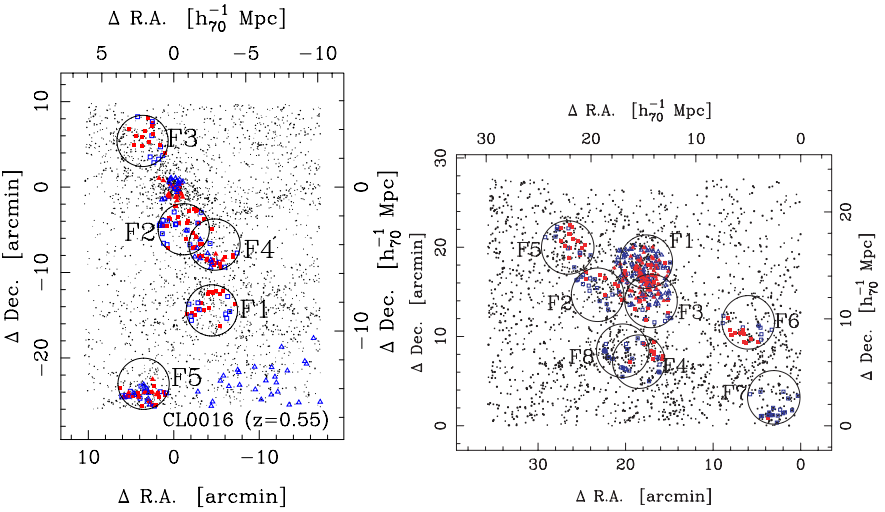

Fig. 1. Large scale structures of the two distant clusters, CL0016+16 at $z = 0.55$ on the left [14] and RXJ0152.7–1357 at $z = 0.83$ on the right [13]. Spectroscopically confirmed cluster members and non-members are shown in filled and open symbols (squares/triangles), respectively. Other member candidates on the basis of photometric redshifts are shown by small dots.

1.2 Environmental dependence of galaxy properties

Colour distribution of faint galaxies along the structures show a sudden change to red at relatively low density (which we call break density) as shown in Figs. 2 [12]. This suggests that galaxies are preprocessed and their star foramtion activities are truncated in group environments in the outskirt of clusters before they eventually enter to the cluster cores. Also, we see a signiture of post star-burst (ie., strong $H\delta$ absorptions) in the composite spectra of red galaxies in groups. Terefore the group environment is the key hisrarchy to process galaxies probably through galaxy-galaxy interactions [8][12]. We also see a clear environmental dependence of the "down-sizing" (delayed or prolonged star formation in small galaxies [4][9]) in the sense that the stage of down-sizing is delayed in lower density environments [12].

2 Proto-Clusters with Evolved Populations at $z \gtrsim 2$

To extend further our panoramic surveys of distant clusters at $z < 1.3$, we now explore proto-clusters around some high-z radio galaxies at $2 \lesssim z \lesssim 3$ based on the

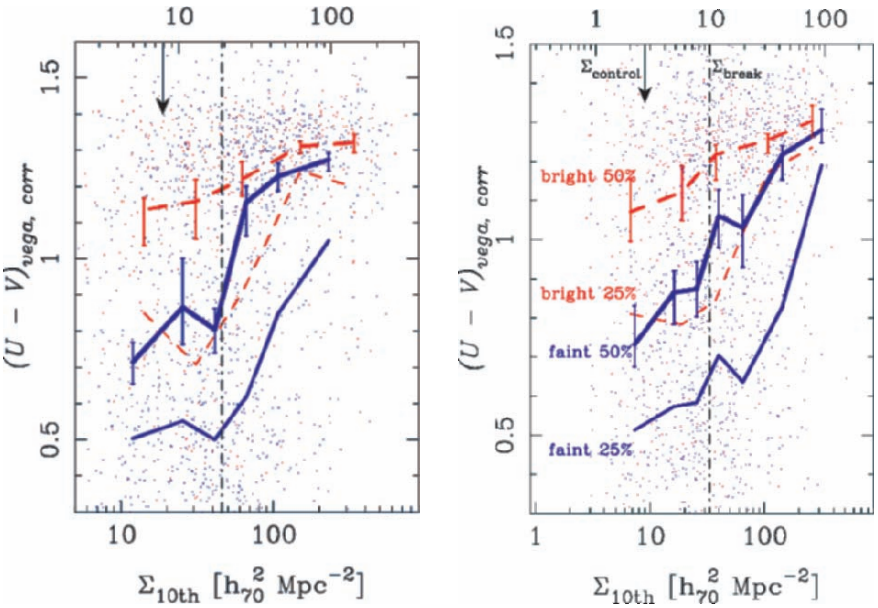

Fig. 2. K-corrected colours of galaxies as a function of 2-D local number density of galaxies for CL0016+16 on the left and RXJ0152.7–1357 on the right [12]. Top and bottom labels indicate comoving and physical densities, respectively. Loci of the 50 and 25 percentiles of the colour distribution are shown by thick and thin lines for bright (dashed) and faint (solid) galaxies separated at M_*+1. Break density indicates where the colour distribution changes drastically especially for faint galaxies.

wide-field near-infrared imaging. Most of our target fields are known proto-clusters on the basis of a large number of emitters located at the same redshifts as the radio galaxies found by narrow-band surveys and spectroscopic follow-up observations [11][15]. We have carried out a deep and wide near-infrared imaging with a new wide-field near-infrared camera, MOIRCS, on Subaru Telescope, on the three targets (PKS1138–262, USS0943–242 and MRC0316–257) to the depth of $K_s \sim 22$ (5σ) over a $4' \times 7'$ area centered on the radio galaxies.

2.1 New selection technique of galaxies at $2 < z < 3$

We apply colour cuts in $J-Ks$ or JHK_s in order to exclusively search for galaxies located at $2 < z < 3$. Our JHK_s selection is a new technique to efficiently select galaxies at $2 < z < 3$ as described in [6] and in Fig. 3 of this article. The advantage of our JHK_s selection is that unlike the single colour DRG selection ($J-K_s > 2.3$) that can pick out only passive or dusty galaxies at $z > 2$, we can also pick out bluer populations with on-going star formation activities with two colours. Furthermore, our method is robust against dust extinction because the reddening vector is almost paralell to the boundary line of our colour criterion (Fig. 3).

To the completeness limit ($K_s \sim 22$), we see a significant excess of NIR selected galaxies by a factor of two to three compared to those found in the general field

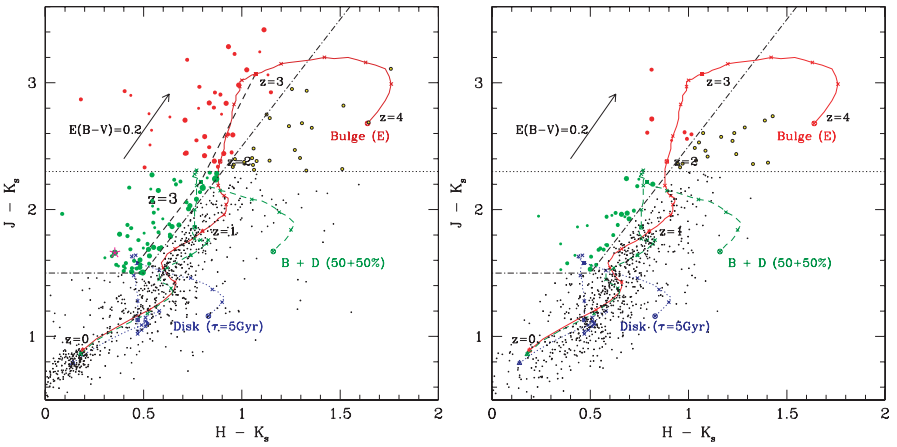

Fig. 3. Colour-colour diagrams of a proto-cluster USS0943–242 at $z \sim 2.9$ (left) and the GOODS-South Field (right) [5]. The horizontal dotted line and the dot-dashed lines show the boundaries of our single colour selection of $J - K_s > 2.3$ and the two-colours selection with JHK_s, respectively. Solid, dashed and dotted curves represent the evolutionary tracks of galaxies over $0 < z < 4$ with different star formation histories (passive, intermediate, and active) formed at $z_{\rm form} = 5$. The thick dashed line connects the model points at $z = 3$, showing that our selection technique works to pick out not only passive galaxies but also star forming galaxies at $2 < z < 3$. Large filled circles indicate our JHK_s-selected galaxies that satisfy our criterion. The size of the symbols for the JHK_s-selected galaxies is scaled according to apparent magnitudes in K_s-band (the bigger, the brighter). A large star indicates the targeted radio galaxies at $z \sim 2.9$. The arrow shows a reddening vector of Calzetti et al.'s law [2] of $\mathrm{E}(B-V) = 0.2$ at $z = 3$. Importantly the vector is almost paralell to the boundary line of our JHK_s selection, and thus our method is robust against dust extinction.

of GOODS-South [5] as shown in Figs. 3. The spatial distribution of these NIR selected galaxies are not uniform and track similar structures to those of the emitters, although individual galaxies rarely overlap between the NIR selected galaxies and the emitters, implying that the former is the evolved population with much higher stellar mass than the young, active emitters.

2.2 First appearance of the colour-magnitude relation

We focus on the build-up of the red sequence at its very first stage in the proto-clusters. Massive elliptical galaxies are seen to dominate cluster cores up to a redshift of $z \sim 1$ with the red sequence firmly in place by that epoch [7][12]. What remains uncertain is whether this holds true at higher redshift and therefore at what epoch did massive, rich clusters first begin to assemble and from which stage do they undergo mostly passive evolution.

We find that the bright-end ($\mathrm{M_{stars}} > 10^{11}\mathrm{M_\odot}$) of the red sequence has been already well populated by $z \sim 2$ but is much less popoulated at $z \sim 3$ (Figs. 4).

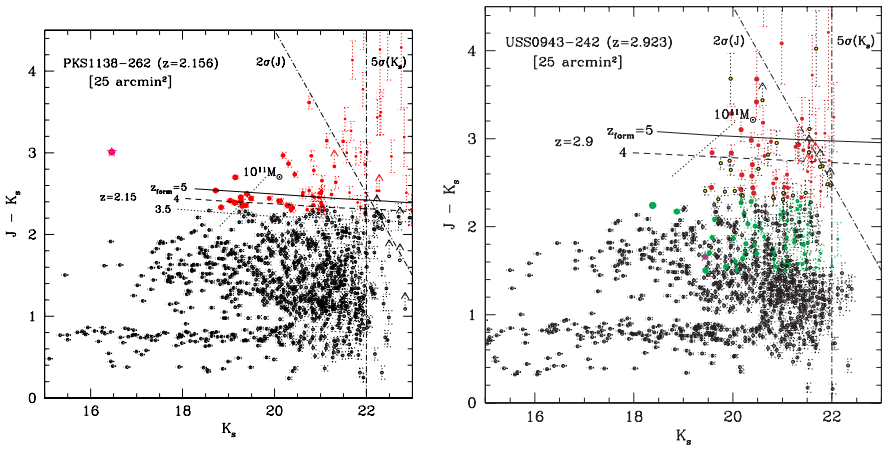

Fig. 4. Colour-magnitude diagrams of the two proto-clusters at $2 < z < 3$. Filled circles indicate proto-cluster member candidates selected with $J-K_s > 2.3$ (PKS1138–262) and JHK_s diagram (USS0943–242), respectively (see Fig. 3 and [6] for our new JHK_s selection technique of passive/active galaxies at $2 < z < 3$). Solid, dashed and dotted lines show the expected location of colour-magnitude relations at the radio galaxies' redshifts in the case of passive evolution [7]. The iso-stellar-mass lines of $10^{11}\mathrm{M}_{\odot}$ are also shown.

This implies that the bright-end of the colour-magnitude sequence first appeared between $z = 3$ and 2 by vigorous star formation and assembly of massive early-type galaxies. Note that this epoch coincides with the peaks of the apearance of Submm galaxies [3] and the cosmic star formation rate [1].

These interesting results on proto-clusters will be confirmed spectroscopically by up-coming spectroscopic surveys both in the optical and near-infrared.

This work was financially supported in part by a Grant-in-Aid for the Scientific Research (No. 15740126) by the Japanese Ministry of Education, Culture, Sports and Science.

References

1. R.J. Bouwens, G.D. Illingworth, R.I. Thompson et al: The Astrophysical Journal Letters, 624, L5 (2005)
2. D. Calzetti, L. Armus, R.C. Bohlin et al: The Astrophysical Journal, 533, 682 (2000)
3. S.C. Chapman, A.W. Blain, I. Smail et al: The Astrophysical Journal, 622, 772 (2005)
4. L.L. Cowie, A. Songaila, A., E.M. Hu et al: Astronomical Journal, 112, 839 (1996)
5. M. Giavalisco et al: The Astrophysical Journal Letters, 600, L93 (2004)
6. M. Kajisawa, T. Kodama, I. Tanaka et al: Monthly Notices of Royal Astronomical Society, 371, 577 (2006)

7. T. Kodama, N. Arimoto, A.J. Barger, A. et al: Astronomy & Astrophysics, 334, 99 (1998)
8. T. Kodama, I. Smail, F. Nakata et al: The Astrophysical Journal Letters, 562, L9 (2001)
9. T. Kodama, T. Yamada, M. Akiyama: Monthly Notices of Royal Astronomical Society, 350, 1005 (2004)
10. T. Kodama, M. Tanaka, T. Tamura, A. et al: Publication of Astronomical Society of Japan, 57, 309 (2005)
11. J.D. Kurk et al: Astronomy & Astrophysics Letters, 358, L1 (2000)
12. M. Tanaka, T. Kodama, N. Arimoto et al: Monthly Notices of Royal Astronomical Society, 362, 268 (2005)
13. M. Tanaka, T. Kodama, N. Arimoto et al: Monthly Notices of Royal Astronomical Society, 365, 1392 (2006)
14. M. Tanaka et al: in preparation
15. B.P. Venemans et al: The Astrophysical Journal Letters, 569, L11 (2002)

44

Structure of Galactic Dark Halos and Observational Prospects for Identifying the Nature of Dark Matter

Naoki Yoshida[1]

Department of Physics, Nagoya University, Furocho, Chikusa, Nagoya 464-8602
nyoshida@a.phys.nagoya-u.ac.jp

Summary. We study the internal structure of galactic size dark matter halos in the standard Λ Cold Dark Matter model under the assumption that cold dark matter consists of light neutralinos whose annihilation cross section is large. We use high resolution cosmological hydrodynamic simulations which include radiative cooling, star-formation and supernova feedback effects. We show that the dissipative processes generally act as steepening the dark matter density profile, whereas supernova feedback mitigates the effect. However, when all of the processes are included, we still find many subhalos that have a steep ($\propto r^{-1.5-2}$) density profiles. Such subhalos may be bright sources of γ-ray via pair-annihilation of neutralinos. We also find poor correlation between the stellar velocity dispersion profile and the underlying dark matter density profiles of subhalos. Observations of stellar velocity dispersions need to be interpreted with caution.

1 Introduction

The nature of dark matter in the Universe is one of the most prominent unsolved questions in cosmology. The best candidates are weakly-interacting massive particles with mass in the range 10 to 10^4 GeV. While it is generally thought that detecting dark matter content in a direct manner (rather than by indirect astronomical observations) is extremely difficult [1], there may be an encouraging possibility of "directly" observing dark matter distribution through annihilation signals [2].

Recently, neutralinos have been drawing particular attention as a dark matter candidate, because self-annihilation of neutralino is expected to produce distinct signatures. Pair annihilation of such particles produces neutrinos, positron, anti-protons and γ-rays. For a spherically symmetric object, annihilation flux (in photons $\mathrm{cm}^{-2}\mathrm{s}^{-1}$) may be written as

$$F = \frac{N_\gamma \langle \sigma v \rangle}{2d^2 m_{\rm DM}^2} \int_0^{r_{200}} \rho_{\rm DM}^2(r) r^2 dr, \tag{1}$$

which diverges if the inner density profile is steeper than $\propto r^{-1.5}$. High-resolution N-body simulations [4] consistently show the inner density profiles of dark matter halos

are as steep as $\propto r^{-1-1.5}$. However, these simulations employ only collisionless dark matter particles. It is important to note that at the innermost regions of galaxies, the so-called baryonic physics, such as radiative cooling, star-formation and supernova feedback, can substantially alter the distribution of dark matter.

We run high-resolution cosmological simulations of galactic-size halo formation. We use three simulations; one with dark matter only, one with gas with radiative cooling, and finally one with star-formation and supernova feedback. By comparing density profiles of dark halos and their substructures, we examine the possibility of detecting dark matter annihilation signals from nearby galaxies.

2 Numerical Simulations

We adopt the concordance ΛCDM cosmology with matter density $\Omega_m = 0.26$, baryon density $\Omega_{\rm b} = 0.04$, cosmological constant $\Omega_\Lambda = 0.7$ and expansion rate at the present time $H_0 = 70$ km s^{-1}Mpc^{-1}. The density fluctuation amplitude is normalized by setting $\sigma_8 = 0.9$. While some of these cosmological parameters are different from those determined most recently from the third-year WMAP, all of our results presented below are robust to slight changes in the values. We use the parallel Tree N-body/SPH solver GADGET2 [3] to evolve the system from $z = 49$ to $z = 1$ when the main target halo is dynamically relaxed and has a mass of $3 \times 10^{12} M_\odot$. In practice, we use a multi-level zooming technique to generate initial conditions for high resolution simulations. In the highest resolution region surrounding the main halo, the mass of dark matter particles is $4 \times 10^6 M_\odot$ and that of gas particles is $6.2 \times 10^5 M_\odot$ and thus there are roughly 0.8 million dark matter particles and a similar number of gas particles within the virial radius at $z = 1$. Hereafter we call the run with dark matter only as Run DM, the run with radiative cooling as Run Cool, and the run with star-formation and supernova feedback as Run SFSN.

3 Simulation Results

3.1 The effect of gas cooling

We first presents the results from the simulation with radiative cooling. Fig. 1 show the radial density profiles of the main halo and those for a subhalo within it. There we compare two cases using Run DM and Run Cool. Baryonic contraction clearly steepens the dark matter density profile. The main halo has a profile that is close to a NFW profile (solid line), while that for Run Cool is close to Moore et al. profile that has an asymptotic slope of $\alpha = 1.5$. Similar effects are seen also in the substructure density profiles. Run Cool produces almost a power law of $\rho \propto r^{-2}$ at the inner 1 kpc region. These results suggest that there will be strong annihilation signals from the center of the main halo and centers of subhalos. Fig. 2 shows the projected square of dark matter density $\propto \rho^2$, so that it represents an image in annihilation radiation. The center of the main halo becomes much brighter owing to the steep density profile caused by baryonic contraction. It is interesting that many of the subclumps also appear much brighter. The peak flux of annihilation signal is 10-100 times greater than in Run DM. Although the contributions from all

This page intentionally blank

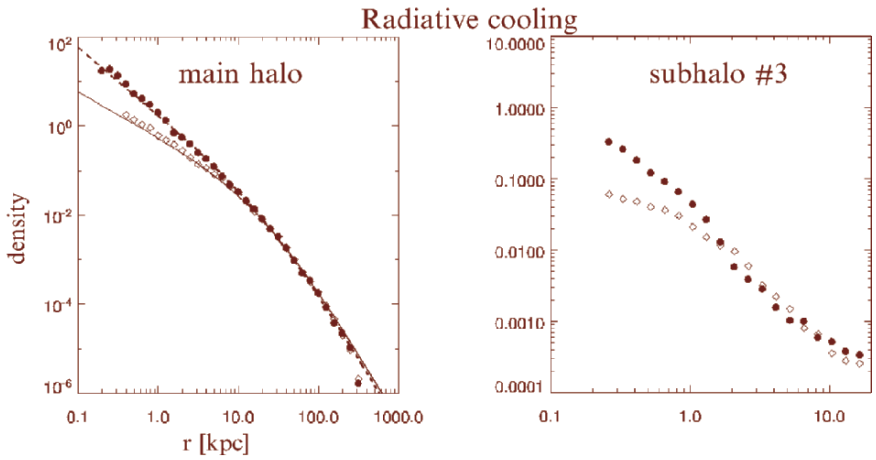

Fig. 1. The dark matter density profiles around the main halo and those for a particular subhalo which has a mass of $\sim 10^{10} M_{\odot}$. The solid line in the left panel is the best fit NFW profile to the result of Run DM (open circles), whereas the dashed line is the Moore et al. profile fit to Run Cool (solid circles). The steepening of the inner density profile owing to baryonic contraction is clearly seen for both the main halo and the subhalo.

the subhalos to the total annihilation radiation flux is small, less than 2 percent in our simulation, their centers are extremely bright, and thus may be a good target for future observation using ground-based ACTs. We mention that the (sub) halos appear somewhat rounder in Run Cool, which is likely owing to more isotropic distribution of gas.

While it is striking that the annihilation signal is enhanced in Run Cool, one can also argue that it is much expected because the run include only a dissipative process (radiative cooling). Indeed, simple analytic models of adiabatic contraction predict the dark matter density profile can be as steep as an isothermal profile when dissipation occurs rapidly. It is still unclear whether or not other, possibly more important baryonic physics such as star-formation and feedback can significantly affect the above results.
It is expected that theses processes can counter-act and can redistribute the matter at the center to make a shallower profile. To this end, we use an additional simulation in which star-formation and supernova feedback are implemented in a widely-used manner.

The resulting annihilation radiation maps are shown in Fig. 3. Despite the complicated process of star-formation with collisionless particles generated, and supernova feedback that expell some of the gas, there are still many subhalos whose centers have larger densities, i.e., they are brighter in annihilation radiation. However, the increase in the total flux from the region (approximately with a radius twice the halo's virial radius) is only a few percent. It will be necessary to probe the substructure signal by a high angular resolution observations.

It may be worth mentioning that the CACTUS team recently presented preliminary findings of $\sim$ 150GeV γ-ray excess from the region of Draco, possibly indicating

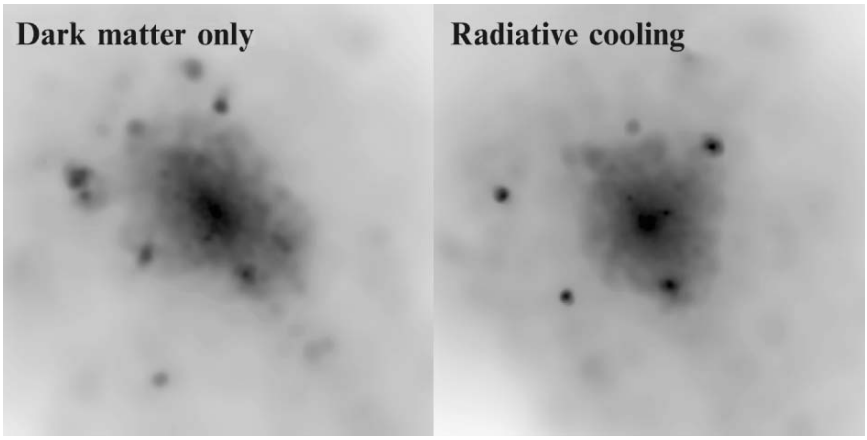

Fig. 2. The projected dark matter distribution weighted by local dark matter density. Hence the brightness scales as annihilation radiation flux. The region has a proper 100 kpc on a side. Run DM (left) and Run Cool (right). The center and subhalos appear brighter in Run Cool. Note that we use a logarithmic scale for this picture.

that the signal is due to dark matter annihilation. Since then there have been many papers discussing the indication and the viability of dark matter candidates within super-symmetric models. Our simulations suggest that there should be at leaset some subhalos whose density profiles are as steep as $\propto r^{-1.5}$ and hence can produce a strong annhilation signal.

Finally we discuss the structure of stellar systems from observational point of view. Stellar velocity dispersions and the profiles are often used to infer the distribution of underlying dark matter near the centers of small satellite galaxies. Recently, Wilkinson et al. measured the velocity dispersions of Draco and Ursa Minor and argue that the sudden decrease at the outer most radii are explained by a larger mass of the host halo than used to be believed.

In order to study the relation of the subhalo mass and stellar velocity dispersions, we measured the both quantities for 20 most massive subhalos in our main halo. Surprisingly we found a very poor correlation between the shape of the velocity dispersion profiles and the host's virial mass and dark matter density profiles. This is probably because of the stars are formed at various different epochs in the hierarchical model, and some of the systems are still going mergers and relaxation. Hence the stellar velocity dispersion may not be a robust measure for dark matter distribution. Observations need to be interpreted with caution. Detailed studies based on the formation history are clearly needed.

References

1. G. Bertone, D. Hooper, J. Silk : Physics Reports, 405, 279 (2005)
2. L. Bergstrom, P. Ullio, J. H. Buckley : Astroparticle Physics, 9, 137 (1998)

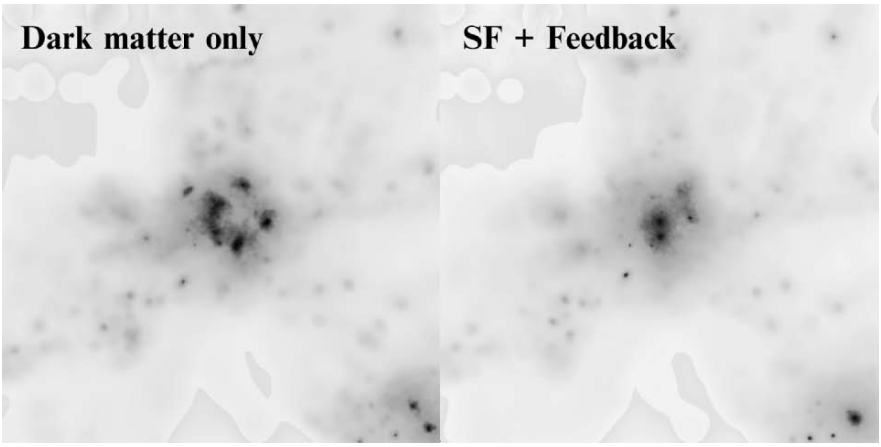

Fig. 3. The projected dark matter distribution weighted by local dark matter density for Run DM (left) and for Run SFSN (right). The region has a proper 300 kpc on a side.

3. V. Springel : MNRAS, 6, 79 (2005)
4. F. Stoehr, S. D. M. White, V. Springel, G. Tormen, N. Yoshida : MNRAS, 345, 1313 (2003)
5. Wilkinson, M. I. et al. : preprint astro-ph/0602186

Part V

POSTER PAPERS

PDF images of the poster presentations are compiled in the supplement CD-ROM.

Jeff Kenney and Hiroyuki Nakanishi

Joshua G. Peek, Marijke Haverkorn, Evan Levine, and Ettore Carretti

Star Formation Morphology in a Sample of Local Galaxies

Ruyman Azzollini[1] and John E. Beckman[2]

[1] Instituto de Astrofisica de Canarias (C/Via Lactea, s/n, 38200 La Laguna, S/C de Tenerife, Spain) ruyman@iac.es
[2] Instituto de Astrofisica de Canarias (Spain) & Centro Superior de Investigaciones Cientificas (Spain) jeb@iac.es

We present a morphological study of a sample of 95 star forming, late type, local galaxies. The objects are a sub-sample of "The $H\alpha$ Galaxy Survey" by James et al., 2004 (J04 hereafter), which are also present in the 4th Data Release of the SDSS (York et al., 2000).
We measured (mainly following Lotz et al. 2004), five morphological parameters related to several aspects of the distribution of light: the radial concentration ("C", "Concentration", Bershady et al., 2000), asymmetry ("A", "Asymmetry", Abraham et al., 1996), clumpiness ("S", "Clumpiness", Conselice 2003), spatial "unevenness" ("Gini parameter", Abraham et al., 2003), and degree of spatial dispersion of the brightest pixels ("M20/90", inspired by the M_{20} parameter defined in Lotz et al., 2004).
We used broad-band images from SDSS and in $H\alpha$ from J04, aiming to compare the spatial distribution of the old and young (high mass) stars in the galaxies. We present a brief analysis of the main observational biases which affect these parameters, and simulate the observational effects of increasing the distances to the objects. Our goal is to establish a fiducial database of the spatial distribution of the massive star formation in local galaxies, to compare with the analogous distributions in galaxies at increasing redshift.

References

1. Abraham, R. G. et al.: MNRAS 279, L47 (1996)
2. Abraham, R., van den Bergh, S. & Nair: ApJ 588, 218 (2003)
3. Bershady, M., Jangren, A. & Conselice C.: AJ 119, 2645 (2000)
4. Conselice, C.: ApJS 147, 1 (2003)
5. James, P. A. et al.: A&A 414, 23 (2004) [J04]
6. Lotz, J. M., Primack, J. & Madau, P.: AJ 128, 163 (2004)
7. York, D. G. et al.: AJ 120, 1579 (2000)

The External Zones of Spiral Galaxies: Truncations, No Truncations and Antitruncations

John E. Beckman[1,2], Peter Erwin[3], Michael Pohlen[4], Leonel Gutiérrez[1,5], Rebeca Aladro[1,6] and Ignacio Trujillo[7]

[1] Instituto de Astrofísica de Canarias, La Laguna, Tenerife, Spain. jeb@iac.es
[2] Consejo Superior de Investigaciones Científicas,Spain.
[3] Max Planck Institut fuer Astrofysik, Garching, Germany.
[4] Kapteyn Institut,Universitit te Groningen, Netherlands.
[5] Universidad Nacional Autónoma de México, Campus Ensenada, México.
[6] Departamento de Astrofísica, Universidad de La Laguna, Tenerife, Spain.
[7] School of Physics and Astronomy, University of Nottingham, U. K.

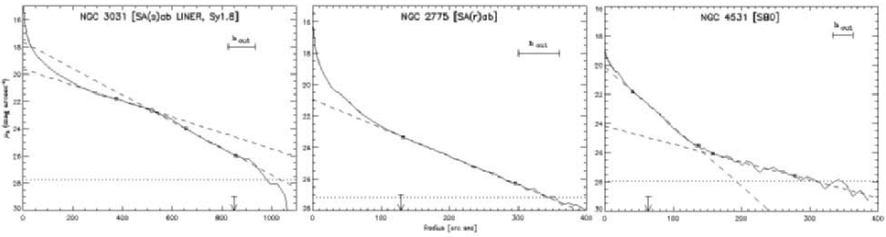

Fig. 1. Radial surface brightness profiles of three disk galaxies showing characteristic behaviour in the outer disk: (a) a "classically" truncated profile with a steeper outer exponential decline; (b) a profile with no observable truncation, i.e. a single exponential with unchanging slope to large radii; (c) an "antitruncated" profile, where the outer exponential is shallower than the inner. Using face-on galaxies we have shown that the majority of galaxy discs (notably for early types) are not truncated, and have established a comprehensive classification of which the three types in the figure are a subset (see references for details).

References

1. Erwin, P.; Beckman, J.E.; Pohlen, M., 2005, ApJ 626L, 81
2. Erwin, P.; Pohlen, M.; Beckman, J.E., 2006a, A&A (In preparation)
3. Erwin, P.; Gutiérrez, L.; Pohlen, M.; Beckman, J.E.; Aladro, R., 2006b, A&A (In preparation)
4. Freeman, K.C., 1970 ApJ 160, 811
5. Pohlen, M.; Dettmar, R.-J.; Lutticke, R.; Aronica, G., 2002 A&A 392, 807
6. Pohlen, M.; Trujillo, I., 2006 A&A (In press) astro-ph/0603682
7. van der Kruit, P. C.; Searle, L., 1981 A&A 95, 116

Tracing Galaxy Evolution in the Field: the UV Emission in Shell Galaxies Mapped by GALEX

Daniela Bettoni[1], A. Marino[1], L. M. Buson[1], C. Chiosi[2], G. Galletta[2], R. Rampazzo[1], R. Tantalo[2] and M. Rich[3]

[1] INAF - Osservatorio Astronomico di Padova daniela.bettoni, lucio.buson, antonietta.marino, roberto.rampazzo@oapd.inaf.it
[2] Dipartimento di Astronomia, Universitá di Padova cesare.chiosi, giuseppe.galletta, rosaria.tantalo@unipd.it
[3] Physics & Astronomy Department, UCLA rmr@astro.ucla.edu

Nearby early-type galaxies (ETGs) showing shells inhabit low density regions. Whatever their origin is, either a weak interaction [1] or a merging/accretion between galaxies [2, 3], the event should have triggered a secondary burst of star formation. We imaged with *Galaxy Evolution Explorer (GALEX)* in far (FUV) and near (NUV) ultraviolet three nearby shell galaxies, namely NGC 2865, NGC 5018 and NGC 7135, whose optical line-strength indices [4] suggest that they host recent ($\leq$2 Gyr) star formation. Their FUV emission is always confined in the innermost regions while the NUV emission shows fine structures very similar to those detected in the optical band. Remarkable in NGC 7135 is the coincidence between the optical and NUV fine structures which give to the galaxy a "medusa-like" morphology in both bands. NUV and FUV emissions likely have different origins [5]. The NUV emission in a passively evolving galaxy is dominated by the turnoff and sub-giant stars. The FUV emission traces one (or more) hot, plausibly high-metallicity, stellar components (e.g. hot-HB and/or post-AGB and AGB manquè stars) giving origin to their well-known UV-upturn phenomenon. At the same time, the UV light is also a sensitive tracer of the *residual star formation* in ETGs, a necessary ingredient to constrain the galaxy *rejuvenation* suggested by the optical line-strength indices which suffer from age-metallicity degeneracy effects.

References

1. Thomson R.C.: MNRAS, 253, 256 (1991)
2. Dupraz C., Combes F.: AAS, 166, 53 (1986)
3. Hernquist L., Quinn P.: ApJ, 312, 1 (1987)
4. Longhetti, M., Bressan, A., Chiosi, C., Rampazzo, R.: A&A, 345, 419 (1999)
5. Dorman, B., Rood, R.T., O'Connell, R.W.: ApJ, 591, 878 (2003)

Star Formation in Nearby Early-Type Galaxies: Mapping in UV, Optical, and CO

Martin Bureau[1], R. Bacon[2], M. Cappellari[3], F. Combes[4], R.L. Davies[1], P.T. de Zeeuw[3], E. Emsellem[2], J. Falcón-Barroso[5], H. Jeong[6], D. Krajnović[1], H. Kuntschner[7], R.M. McDermid[3], R.F. Peletier[8], M. Sarzi[9], K.L. Shapiro[10], G. van de Ven[11], S.K. Yi[6] and L.M. Young[12]

[1] Sub-Department of Astrophysics, University of Oxford, United Kingdom
[2] Centre de Recherche Astronomique de Lyon – Observatoire, France
[3] Sterrewacht Leiden, Universiteit Leiden, The Netherlands
[4] Observatoire de Paris, France
[5] European Space Research and Technology Centre, The Netherlands
[6] Department of Astronomy, Yonsei University, South Korea
[7] ST-ECF, European Southern Observatory, Germany
[8] Kapteyn Astronomical Institute, Universiteit Groningen, The Netherlands
[9] Centre for Astrophysics Research, University of Hertfordshire, United Kingdom
[10] Department of Astronomy, University of California Berkeley, U.S.A.
[11] Department of Astrophysical Sciences, Princeton University, U.S.A.
[12] Department of Physics, New Mexico Institute of Mining and Technology, U.S.A.

The SAURON integral-field survey reveals that small ($\sim 0.1\,R_e$) kinematically decoupled cores (KDCs) in early-type galaxies are increasingly young toward the center and typically found in fast-rotating galaxies, while large KDCs ($\sim 0.5\,R_e$) have homogeneously old stars in non-rotating galaxies [1]. *GALEX* UV imaging further allows the direct identification of regions of recent (≤ 0.5 Gyr) star formation (SF). In e.g. NGC 2974, young stars are identified in the center and an outer ring [2]. Nuclear and inner ionised-gas rings [3] then suggest that current SF is bar-driven. The CO detection rate of SAURON early-type galaxies is $\approx 40\%$ (Combes et al, in prep.). Synthesis imaging reveals that it is generally contained in a well-ordered central disk, both in galaxies with a (young) central stellar disk (e.g. NGC 4459, 4526) or a (young) KDC (e.g. NGC 3032, 4150) (Young et al, in prep.). CO also traces well the ionised gas and young stellar populations, but not always the stellar kinematics [3, 4, 5].

References

1. R.M. McDermid, E. Emsellem, K.L. Shapiro et al: MNRAS, submitted
2. H. Jeong, M. Bureau, S.K. Yi et al: MNRAS, submitted
3. M. Sarzi, R. Bacon, M. Bureau et al: MNRAS **366**, 1151 (2006)
4. H. Kuntschner, E. Emsellem, R. Bacon et al: MNRAS **369**, 497 (2006)
5. E. Emsellem, M. Cappellari, R.F. Peletier et al: MNRAS **352**, 721 (2004)

The Effect of Cosmological Large–scale Structure on the Orientation of Galaxies

Conrado Carretero[1], Ignacio Trujillo[2] and Santiago Patiri[1]

[1] Instituto de Astrofisica de Canarias. Via Láctea s/n. 38200 La Laguna, Tenerife, Spain. cch@iac.es, spatiri@iac.es
[2] University of Nottingham, UK. Ignacio.Trujillo@nottingham.ac.uk

Galaxies are not distributed randomly throughout space but are instead arranged in an intricate "cosmic web" of filaments and walls surrounding bubble-like voids. There is still no compelling observational evidence of a link between the structure of the cosmic web and how galaxies form within it. However, such a connection is expected on the basis of our understanding of the origin of galaxy angular momentum: disk galaxies should be highly inclined relative to the plane defined by the large-scale structure surrounding them. Using the two largest galaxy redshift surveys currently in existence (2dFGRS and SDSS) we show at the 99.7% confident level that these alignments do indeed exist: spiral galaxies located on the shells of the largest cosmic voids have rotation axes that lie preferentially on the void surface.

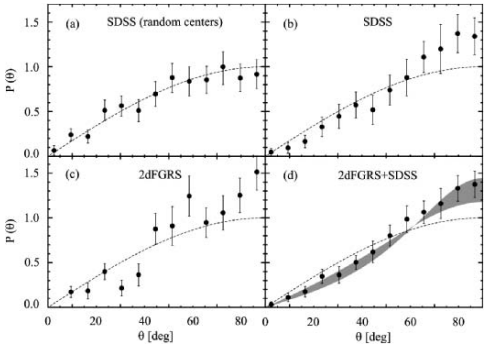

Fig. 1. Probability density distribution of the angles θ between the rotation axes of the galaxies and the vectors normal to the planes defined by their surrounding matter. Dashed line: null hypothesis. Panel (a) results from using random centres for the voids within the survey volume. Panel (b) and (c) shows the output when the centres of the large voids are used in SDSS and 2dFGRS. Panel (d) shows the angle distribution when the full data set is used. The grey region in panel (d) corresponds to the Tidal Torque Theory predictions. From Trujillo, Carretero & Patiri (2006).

A Physical Classification Scheme for Disk Galaxies

Bernardo Cervantes-Sodi[1] and X. Hernandez[2]

Instituto de Astronomía, Universidad Nacional Autónoma de México A. P. 70–264, México 04510 D.F., México bcervant@astroscu.unam.mx

We present a model of the dynamical structure of a disk galaxy where only two parmeters fully determine the solution, mass and angular momentum. We show that once the mass has been fixed, the angular momentum parameter λ is expected to regulate such critical galactic disk properties as colour, thickness of the disk and disk to bulge ratio. It is hence expected to be the determinant physical ingeredient resulting in a given Hubble type. A simple analytic estimate of λ for an observed system is provided. This estimate is then used to obtain a distribution of λ for a real sample of galaxies that shows a behaviour consistent with numerical simulations.

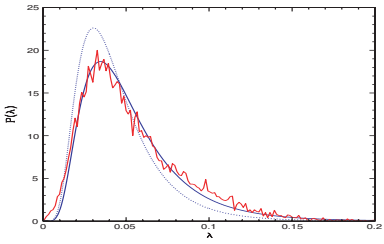

Fig. 1. Distribution of values of λ for 11,597 spirals plus ellipticals, binned into 150 intervals, broken curve. Best log-normal fit to the data, having parameters $\lambda_0 = 0.046$ and $\sigma_\lambda = 0.535$, solid curve. Maximum likelihood underline distribution with parameters $\lambda_0 = 0.0394$ and $\sigma_\lambda = 0.509$ dotted curve, once estimate errors are considered.

References

1. Hernandez, X. & Cervantes-Sodi, B., 2006, MNRAS, 368, 351
2. Hernandez, X., Park, C., Choi, Y. & Cervantes-Sodi, B., 2006, astro-ph/0607605

Evolution of dE Galaxies in Abell 496

Igor Chilingarian[1,2], T. Ferraz Lagana[3], V. Cayatte[3,4], F. Durret[3], C. Adami[5], C. Balkowski[4], L. Chemin[6], and P. Prugniel[2]

[1] Sternberg Astronomical Institute, 13 Universitetski prospect, Moscow, 119992, Russia chil@sai.msu.su
[2] Observatoire de Lyon, 9 ave. Charles André, 69230 St.Genis Laval, France
[3] Institut d'Astrophysique de Paris, 98bis, bd. Arago, 75014 Paris, France
[4] Observatoire de Paris-Meudon, 5, place Jules Janssen, 92195 Meudon, France
[5] Laboratoire d'Astrophysique de Marseille, Traverse du Siphon, 13012 Marseille, France
[6] Université de Montréal, C. P. 6128, Montréal, Québec, Canada H3C 3J7

We present the studies of a sample of 46 galaxies in the Abell 496 cluster, 28 of which are dE's and dS0's with velocity dispersions as low as 20 km/s, based on deep 4-band CFHT Megacam imaging and VLT Giraffe multi-object spectroscopy. We use Lick indices to obtain [Mg/Fe] abundance ratios. We apply a new conceptual technique for extracting internal kinematics and stellar population characteristics from line-of-sight integrated spectra, giving better precision than the traditional approach based on Lick indices. Small galaxies appear to be younger than large ones – we found a correlation between luminosity weighted age and absolute magnitude. There is a tight dependency between [Mg/Fe] and σ_0 for relatively massive objects ($\sigma_0 > 60$ km/s). Dwarfs of Abell 496 are located exactly on the fundamental plane, coinciding with the locus of known dE galaxies and theoretical predictions. We discuss the origin of dE galaxies, metal enrichment mechanisms and environmental effects on their chemical and dynamical evolution: star forming episodes must be long enough to lower [Mg/Fe] to solar values as observed even in very low-mass objects; thus the popular theory of metal removal by supernova driven winds experiences difficulties explaining observational properties of dE's: we do not see an anti-correlation between the metallicity and [Mg/Fe].

References

1. Chilingarian et al.: MNRAS, submitted (2006)
2. De Rijcke et al.: A&A, 438, 491 (2005)
3. Durret et al. 2002, A&A, 356, 815
4. Prugniel et al.: proc. of IAUC, 198, 73 (astro-ph/0510398) (2005)

Kinematics and Morphology of Peculiar Virgo Cluster Galaxies

Juan R. Cortés[1,2], Jeffrey D. P. Kenney[3] and Eduardo Hardy[4]

[1] Departamento de Astronomía, Universidad de Chile
[2] National Astronomical Observatory of Japan
[3] Astronomy Department, Yale University
[4] National Radio Astronomy Observatory

We present the morphology and kinematics of 13 bright peculiar Virgo cluster galaxies. R-band and Hα images, and 2-D maps of the stellar velocity, stellar velocity dispersion and ionized gas velocity are presented for the sample galaxies. The results show that most galaxies display disturbed stellar isophotes, and truncated Hα distribution. The kinematics reveals misalignments between the optical and kinematical major axis in at least five galaxies due to bars or warps. Kinematical distinct components are found in at least two galaxies; a cold circumnuclear stellar disk in NGC 4429, and orthogonally rotating core in NGC 4698. Two galaxies (NGC 4698 and NGC 4424) exhibit extremely low V/σ values, indicating that they are the result of major-intermediate mergers. Most galaxies reveal signatures that can be associated with gravitational interactions and ICM-ISM stripping. Thus, the evolution of a significant fraction of cluster galaxies is likely strongly impacted by both effects.

The Outskirts of Milky Way

Leonidas Dedes[1] and P. Kalberla[1]

Argelander Institute for Astronomy, University of Bonn
ldedes@astro.uni-bonn.de

We investigate the disk-halo connection in the Milky Way and analyze the thick disk layer of HI gas which surrounds the Milky Way. To extract this part of the HI gas we determine first the global properties of the neutral gas disk. We use the Leiden/Argentine/Bonn (LAB) HI survey (Kalberla et al. 2005) to determine the shape of the disk. We first convert our dataset to Galactocentric coordinates. Then the first and second moments are used to infer the Warp and the flaring of the disk, respectively. Finally we subtracted from the data modes W0, W1, W2 and we fitted the residuals for possible modes $3 < n < 20$ to search for scalloping in the disk. The disk flares with scale height 600pc at $R \sim 20$kpc. We find three well defined modes for the warp, out to R = 40kpc. Higher modes have relative power 1-3% and the mode frequency is not constant through out the rings. So we are unable to detect scalloping in the Milky way disk, concluding that if present, it is a local phenomenon.

The determination of the properties of the Milky Way disk, together with a Milky Way mass model (Kalberla 2003), enable us to disentangle disk from the halo. In the LAB database we mask those parts which, according to the model, are expected to originate from the disk. After filtering, we derive maps representing the expected emission from the disk-halo interface. We observed at $\lambda = 21$cm an number of interesting regions using the 100-m Effelsberg Radio Telescope. A number of unresolved clumps were detected. They are at $R \sim 12.5$kpc and $z \sim 2.5$kpc, having $T_{\rm K} \sim 200$K and showing a core-envelope structure. Follow up observations with WSRT resolved the clump into a number of arc-min cores column densities several times $10^{19}\mathrm{cm}^{-2}$.

References

1. Kalberla, P. M. W.: ApJ, 588, 805 (2003)
2. Kalberla, P. M. W., Burton, W. B., Hartmann, D., Arnal, E. M., Bajaja, E., Morras, R., Pöppel, W. G. L.: A&A, 440, 775 (2005)

Seyferts in 3D: Probing the Kinematic Signatures of Gas Fueling

Gaelle Dumas[1 2], Eric Emsellem[1], and Carole G. Mundell[2]

[1] Universit de Lyon 1, CRAL, Observatoire de Lyon, 9 av. Charles André, F-69230 Saint-Genis Laval; CNRS, UMR 5574 ; ENS de Lyon, France.
[2] Astrophysics Research Institute, Liverpool John Moores University, Twelve Quays House, Egerton Wharf, Birkenhead CH41 1LD, UK.

We present prelimary results from our 3D imaging spectroscopic survey of 15 nearby Seyfert and inactive control galaxies, using the SAURON IFU on the WHT. A goal of the project is to search for dynamical triggers of nuclear activity. To this end, detailed analysis of the stellar and gaseous kinematics is underway. All galaxies show disk-like rotation in their stellar and gaseous velocity fields, with some showing significant misalignments between the stellar and gaseous components.

We first compared the average global orientation of the gaseous and stellar velocity fields, by deriving the symmetrized velocity fields and the corresponding average position angle of the line of nodes. Although the Seyferts show a larger range of kinematic misalignments in the gas with respect to the stars, we find no statistically-significant difference in global kinematics between Seyferts and their controls for this sample size.

To further investigate the kinematic misalignments, a more refined kinematic analysis was performed. Using a simple model for a rotating inclined disc, we used the tilted-ring method to derive disc parameters as follows: $V_{los}(R,\phi) = V_{sys} + V_{rot}(R) \times cos(\phi) \times sin(i)$, where V_{sys} is the systemic velocity, i is the disc inclination, and V_{rot} represents the rotational velocity. Residual velocity maps, derived by subtracting the model circular velocity fields, reveal deviations from circular motion that may be consistent with gaseous streaming.

Further analysis in underway to quantify the observed velocity fields via harmonic decomposition in order to fully quantify and physically interpret these non-circular motions in the context of gas fueling of AGN.

Galaxies with Nested Bars: Constraining Their Formation Scenarios

Adriana de Lorenzo-Cáceres[1], Alexandre Vazdekis[1] and J. Alfonso L. Aguerri[1]

Instituto de Astrofísica de Canarias, C/ Vía Láctea s/n, 38200 La Laguna, Spain
adlcr@iac.es

We have carried out a complete kinematical and stellar population analysis of the double-barred S0 galaxy NGC 357, in order to see if the nuclear bar is transporting gas to the central regions where it may trigger the star formation needed to generate galactic bulges.

Stellar population analysis based on absorption line strengths measured on extremely high quality spectra lead to old and similar ages for all the structural components of NGC 357 (see Fig. 1), suggesting that the nuclear bar has not played an important role in the star formation history of this galaxy. Moreover, the [Mg/Fe] overabundance of the bulge is similar to that found for elliptical galaxies of similar masses and indicate that the bulk of the stellar population was formed in less than 1 Gyr.

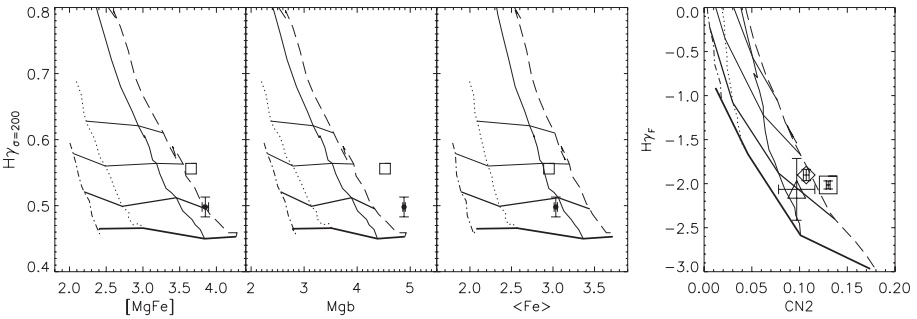

Fig. 1. The age indicators Hγ_σ (Vazdekis & Arimoto, 1999, ApJ, 525, 144) and Hγ_F vs. the metallicity indicators [Mg/Fe], Mg, Fe and CN2 of the Lick system. The grids were obtained by using the Vazdekis 1999 (ApJ, 513, 224) stellar population models, smoothed to match the σ measurements for the bulge of this galaxy (i.e. ~ 180). The solid lines represent different ages (from top to bottom: 4, 6, 10 and 18 Gyr). The metallicity increases from left to right ([Fe/H] -0.7, -0.4, 0.0 and 0.2). The symbols represent the structural components of NGC 357: the bulge (square), the nuclear bar (diamond), the outer bar (triangle) and a reference Virgo galaxy of similar σ (NGC 4473; filled dot).

Determination of Pattern Speed and Star Formation Timescale in Nearby Spiral Galaxies

Fumi Egusa[1], Yoshiaki Sofue[1], Hiroyuki Nakanishi[2] and Shinya Komugi[1]

[1] Institute of Astronomy, the University of Tokyo
[2] Nobeyama Radio Observatory, National Astronomical Observatory of Japan

In spiral galaxies, molecular arms are often offsetted to upstream side of young and massive stellar arms. We propose a method using these offsets to determine the pattern speed ($\Omega_{\rm P}$) and timescale for star formation ($t_{\rm SF}$) from molecular clouds in spiral galaxies. With simple assumptions, an angular offset θ can be written as $\theta = (\Omega - \Omega_{\rm P}) \times t_{\rm SF}$, while Ω is an angular rotation velocity of materials. Since we can measure Ω and θ directly from observations, the rest two parameters, $\Omega_{\rm P}$ and $t_{\rm SF}$, can be determined by plotting θ against Ω and then fitting this plot with a line[1].

This method has been successfully applied to two grand-design spirals, M 51 (NGC 5194) and M 99 (NGC 4254). Results are listed in Table 1. For both galaxies, comparisons between CO and K-band images supported the resultant value of $\Omega_{\rm P}$, which located the corotation resonances beyond the CO arms. Derived $t_{\rm SF}$ for two galaxies were about 5 Myr, corresponding to the Jeans timescale of typical molecular clouds. From this results, a dominant mechanism for star formation in spiral arms might be a gravitational collapse.

Table 1. Results for M 51 and M 99

	M 51	M 99
$t_{\rm SF}$ (Myr)	4.0 ± 0.5	4.8 ± 1.8
$\Omega_{\rm P}$ (km/s/kpc)	19^{+4}_{-3}	26^{+17}_{-8}
$R_{\rm CR}$	$210''$ (10 kpc)	$79''$ (6.2 kpc)

References

1. F. Egusa, Y. Sofue, H. Nakanishi: PASJ 56, L45 (2004)

Contribution of Gas-rich Low Surface Brightness Galaxies to the Local Universe

Diego A. Garcia-Appadoo[1] and Andrew A. West[2]

[1] Argelander-Institute for Astronomy, Auf dem Huegel 71, 53121, Bonn, Germany
dgarcia@astro.uni-bonn.de
[2] University of California Berkeley, Berkeley, CA, 94720-3411, USA
awest@astro.berkely.edu

The Equatorial Strip is a unique sample which comprises 1077 galaxies selected purely by their HI signature. This sample covers a large area of sky, is free from optical selection effects and has complete, very high quality, optical data (SDSS) for a subsample of 201 galaxies. The combination of the HI data with optical data allows us to make a comprehensive analysis of the properties of HI selected extragalactic sources and investigate vital global correlations which improves our understanding of gas-rich and Low Surface Brightness galaxies. The Equatorial Strip runs along the celestial equator from $-6^\circ < \delta < +10^\circ$ and through all R.A.s out to a distance of ~ 170 Mpc. The Equatorial Strip sample represents $\sim 14\%$ of the whole sky, covering an area of 5738 deg^2 and a total volume of $\sim 2.76 \times 10^6$ Mpc^{-3}. LSB galaxies make up 12% of the sample, however, no high luminosity or high HI mass LSB galaxies have been found. Consequently, LSB galaxies make up no more than 6% of the high luminosity, gas-rich population, and massive LSB galaxies contribute no more than 13% of the population, at the 95% confidence level. The Bivariate Brightness Distribution and the Luminosity Function for the sample have been calculated and relationships found between surface brightness and optical luminosity, HI, baryonic and dynamical mass. From these results I find that LSB galaxies contribute $35^{+29}_{-20}\%$ to the number density of gas-rich galaxies in the Universe but only $7^{+3}_{-2}\%$ to the luminosity density. They also contribute $21^{+7}_{-6}\%$ and $12 \pm 3\%$ respectively to the neutral hydrogen (HI) and baryon density of gas-rich galaxies in the Universe. The Equatorial Strip sample has unveiled many objects not found in optical surveys, ranging from very low surface brightness, very blue galaxies to extremely gas-rich galaxies.

References

1. D.A. Garcia-Appadoo. PhD Thesis, Cardiff University (2005)

New Catalogs of Radio Compact HII Regions in the Milky Way

Uriel Giveon[1], R. H. Becker[1,2], D. J. Helfand[3], R. L. White[4] and M. J. Richter[1]

[1] University of California - Davis, 1 Shields Ave., Davis, CA 95616, USA
[2] Lawrence Livermore National Laboratory, Livermore, CA 94566, USA
[3] Columbia Astrophysics Laboratory, 538 West 120th St., New York, NY 10027, USA
[4] Space Telescope Science Institute, 3700 San Martin Dr., Baltimore, MD 21218, USA

We utilize new 6cm and 20cm VLA maps [6] covering portions of the first two Galactic quadrants in conjunction with the MSX Galactic plane catalog [1] to construct a large sample of compact HII regions (CHIIs). The matching resulted in 650 6cm matches and 500 20cm matches, showing red MSX colors and thermal radio spectra. Their latitude distribution is very narrow [$\mathrm{FWHM}_{6cm} = 16'$ or 40pc for a distance of 8.5 kpc], indicative of population I sources, most of which are previously uncataloged [2, 3]. We also identify a population of 70 radio sources with flat or decreasing mid-IR spectrum - possibly Wolf-Rayet stars.

For 18 CHIIs we present dust temperature and optical depth maps from recent diffraction-limited Keck observations at 11.7, 17.65, and 24.5 μm [4]. We determine the sizes, luminosities, and morphologies of dust that is directly heated by the stellar sources. We find a correlation between IR diameters and the central source ionizing photon rates, suggesting that the more compact sources result from later spectral types rather than young age, which might alleviate the 'age problem' of CHIIs. The new data may also suggest a revision to color selection criteria of CHIIs at resolutions $\lesssim 1''$. Our radio maps overlap the Spitzer program GLIMPSE that have better angular resolution ($2''$) compared to MSX ($18.3''$). This will reduce problems of confused matching created by the large difference in resolution compared to the radio surveys ($5''$) and allow us to compare the IR and radio shapes of the matching sources and see if the emission is coming from the same material. We are in the process of incorporating new 20 cm maps from the Multi-Array Galactic Plane Imaging Survey (MAGPIS; [5]) with unprecedented spatial information and sensitivity into the matching analysis. Combining the radio data and GLIMPSE creates a unique dataset that will improve our understanding of the distribution and properties of Galactic massive star-formation.

References

1. Egan, M.P., Price, S.D., & Kraemer, K.E. 2003, AAS, 203, 5708
2. Giveon, U., Becker, R.H., Helfand, D.J. & White, R.L. 2005a, AJ, 129, 348
3. Giveon, U., Becker, R.H., Helfand, D.J. & White, R.L. 2005b, AJ, 130, 156
4. Giveon, U., Richter, M.J. Becker, R.H. & White, R.L. 2006, AJ, submitted
5. Helfand, D.J, Becker, R.H., White, R.L., Fallon, A. & Tuttle, S. 2006, AJ, 131, 2525
6. White, R.L., Becker, R.H. & Helfand, D.J. 2005, AJ, 130, 586

Revealing Cosmic Magnetism with the Square Kilometre Array

Bryan M. Gaensler[1], Rainer Beck[2], Luigina Feretti[3], and Wolfgang Reich[2]

[1] School of Physics A29, The University of Sydney, NSW 2006, Australia
bgaensler@usyd.edu.au
[2] Max-Planck-Institut für Radioastronomie, Auf dem Hügel 69, 53121 Bonn, Germany rbeck,wreich@mpifr-bonn.mpg.de
[3] Istituto di Radioastronomia INAF, Via P. Gobetti 101, 40129 Bologna, Italy lferretti@ira.cnr.it

The Square Kilometre Array (SKA, *www.skatelescope.org*) will be the major radio telescope for the 21st century, with more than fifty times the sensitivity of any existing facility. The SKA concept is currently under development by a consortium of 16 countries, with operations expected to begin in 2015–2020. Vigorous technological developments in computing and antenna design make such a telescope possible. Operating between 100 MHz and 25 GHz, the SKA will probe fundamental physics, the origin and evolution of the Universe, the structure of the Milky Way Galaxy, and the formation and distribution of planets. *Cosmic magnetism* has been identified as one the five SKA key science projects. The evolution, structure and origin of magnetic fields are fundamental and unsolved problems in physics and astrophysics. The SKA will carry out an all-sky survey of rotation measures, in which Faraday rotation toward more than 10^7 background sources will provide a dense "rotation measure grid" for probing magnetism in the Milky Way, nearby galaxies, in distant galaxies, clusters and protogalaxies. Using these data, we can map out the evolution of magnetized structures from redshifts $z > 5$ to the present, and can thus reveal what cosmic magnets look like, how they formed, and what role they have played in the evolving Universe. With SKA's unprecedented capabilities, the window to the Magnetic Universe can finally be opened.

References

1. R. Beck, B.M. Gaensler: New Astr. Review 48, 1289 (2004)
2. B.M. Gaensler: AN 327, 387 (2006)
3. B.M. Gaensler, R. Beck, L. Feretti: New Astr. Review 48, 1003 (2004)

Maps of the Galaxy in HI with GALFA

Joshua E. G. Peek[1], Snežana Stanimirović[2], Mary E. Putman[3], Carl Heiles[4], Kevin Douglas[5], Eric J. Korpela[6] and Steven J. Gibson[7]

[1] Department of Astronomy, University of California, Berkeley, CA 94720 goldston@astro.berkeley.edu
[2] Department of Astronomy, University of Wisconsin, 475 N. Charter Street, Madison, WI 53706 sstanimi@astro.wisc.edu
[3] Department of Astronomy, University of Michigan, 500 Church Street, Ann Arbor, MI 48109 mputman@umich.edu
[4] Department of Astronomy, University of California, Berkeley, CA 94720 heiles@astro.berkeley.edu
[5] Space Sciences Laboratory, University of California, Berkeley, CA, 94720 douglas@ssl.berkeley.edu
[6] Space Sciences Laboratory, University of California, Berkeley, CA, 94720 korpela@ssl.berkeley.edu
[7] National Astronomy and Ionosphere Center, HC03 Box 53995 Arecibo, Puerto Rico 00612 gibson@naic.edu

Over the last year Galactic HI studies with the new 7-beam focal plane array at Arecibo (GALFA-HI) have come into their own. We have already mapped over 30% of the Arecibo sky, observing for more than 500 hours, and we plan to map the entire Arecibo Galactic sky in the coming years. The unprecedented quality of the rapidly-growing GALFA-HI data set has tremendous implications for all areas of Galactic astronomy, including explorations of the disk-halo interface and the interactions between HVCs and the halo. The early findings of this large-scale, high-resolution Galactic mapping project include the discovery of new, very low column-density HVCs, and the development of a quantitative technique for measuring halo gas density by observing the details of the disruption and destruction of HVCs by halo drag forces. This metric may help us understand the processes by which HVCs are destroyed and the relative importance of gravity, gas drag and magnetic forces in the shaping of the HVC population. We also report on the discovery of small, cold clouds in the Galactic anti-center region inhabiting the disk-halo transition region [1].

References

1. S. Stanimirović, M.E. Putman, J.E.G. Peek et al: ApJ, in press

TCS-CAIN: NIR Survey of the Galactic Plane

Carlos González Fernández[1], A. Cabrera Lavers[1,2], F. Garzón[1,3],
P. L. Hammersley[1], M. López Corredoira[1] and B. Vicente[1]

[1] Instituto de Astrofísica de Canarias, carlos.gonzalez@iac.es
[2] GTC Project Office
[3] Universidad de La Laguna

This poster describes TCS-CAIN [1], a NIR survey of the Galactic plane, recently made public at the Instituto de Astrofsica de Canarias, along with some results, and a spectroscopical follow-up program to the survey.

The body of the catalogue comprises about 500 4.25'x4.25' fields, obtained using JHKs photometry with the TCS Telescope (1.5m, Tenerife, Spain), and yielding 10 million source points, with limiting magnitudes of 17 (J), 16.5 (H) and 15.2 (Ks), with a photometric precision of 0.1 mag and astrometric errors of 0.15", both measured against 2MASS data.

With this data, a distinct structure was discovered [2], spanning from l=27° to l=5°, by means of isolating red giant stars over differents lines of sight. This structure can be traced further using these very same stars as distance indicators [3], [4] resulting in an elongated, wide and flat structure, forming an angle of 43° with the line Earth-Galactic center.

To further understand Milky Way's inner structure, we need spectral coverage, in order to obtain chemical information of the stars forming the bar and the bulge. With this aim, a spectroscopical follow-up has been carried using the TNG telescope at La Palma, obtaining low resolution ($R = 500$) spectra of ≈ 100 stars on selected fields. With this spectra, measures of metallicity an spectral type can be obtained.

This spectroscopical survey will evolve into a central observing program of EMIR [5], the MOS NIR spectrograph/imager to be installed in GTC, the 10m Spanish telescope.

References

[1] Cabrera-Lavers, A., Garzón, F., Hammersley, P. L., Vicente, B., & González-Fernández, C.: A&A, 453, 371 (2006)
[2] Hammersley, P. L., Garzón, F., Mahoney, T. J., López-Corredoira, M., & Torres, M. A. P.: MNRAS, 317, L45 (2000)
[3] Lopez-Corredoira, M., Cabrera-Lavers, A., Mahoney, T. J., Garzon, F., Hammersley, P. L., & González-Fernández, C.: AJ, in press. (2006)
[4] Nishiyama, S., et al.: ApJ, 621, L105 (2005)
[5] Garzón, F., et al.: SPIE, 6269, 40 (2006)

Young Stellar Clusters in the Southern Spiral Arm of NGC 2997

Preben Grosbøl[1], H. Dottori[2], and R. Gredel[3]

[1] European Southern Observatory, Karl-Schwarzschild-Str. 2, 85748 Garching, DE, pgrosbol@eso.org
[2] Instituto de Física, Univ. Federal do Rio Grande do Sul, Av. Bento Gonçalves 9500, 91501-970 Porto Alegre, RS, BR, dottori.voy@terra.com.br
[3] Max-Planck Institut für Astronomie, Königstuhl 17, 69117 Heidelberg, DE, gredel@mpia-hd.mpg.de

1 Abstract

Near-infrared K-band images of grand-design spiral galaxies frequently display bright knots along the spiral arms. Their compactness and alignment suggest that they are related to the spiral structure such as large scale fronts in the gas associated to a density wave. To investigate their nature, low resolution K-band spectra of a string of knots in the southern arm of the grand design, spiral galaxy NGC 2997 were obtained with ISAAC/VLT (Grosbøl et al. 2006).

The spectra show strong Brγ emission while some having H_2 (2.122μ) and HeI (2.059μ) emission. A few knots have indications of CO absorption. With sizes of less than 50 pc (marginally resolved with a seeing of 0.8″) and absolute K magnitudes exceeding -12 mag (assuming a distance modulus of -30 mag), they are likely to be very compact, young stellar clusters.

The knots are strikingly aligned along about 4 kpc, suggesting a well-synchronized mechanism of piling up the material of which they were formed and for the triggering of star formation that is consistent with a scenario of density wave propagation.

Agreement between large-scale, synchronously triggered star formation and knot age differences requires several bursts or continuum SF instead of a single burst within the knots. The youngest of the knots is about 7 Myr old, has a mass of approximately 5×10^4 $M_\odot$, and needs about 200 O7V ionizing stars to explain the Brγ line flux. The oldest are about 10 Myr old.

References

1. P. Grosbøl, H. Dottori and R. Gredel: A&A, 453, L25 (2006)

Gas Feeding to the Galactic Center Region within 10 pc in Our Galaxy

Asao Habe[1], Daisuke Namekata[2], and Hidenori Matsui[3]

[1] Hokkaido University, Sapporo, JAPAN habe@astro1.sci.hokudai.ac.jp
[2] Hokkaido University, Sapporo, JAPAN name@astro1.sci.hokudai.ac.jp
[3] Hokkaido University, Sapporo, JAPAN hidenori@astro1.sci.hokudai.ac.jp

Gas feeding to the Galactic center is important for active phenomena in the Galactic center. In the Galactic center, there are various active phenomena and related objects, such as many young stars, active x-ray sources, massive molecular gas ($3 \times 10^7 M_\odot$ in 300pc) and a super massive black hole. We investigate possible role of an inner bar on gas feeding process, since evidence of an inner bar in G.C. is reported [1].

We assume an inner bar model which is not conflict with the galactic stellar disk, the major bar, the spiral potential and the dark halo of our galaxy [2] [3]. Its pattern speed is larger than that of the major bar.

Our model of an inner bar is a Ferres ellipsoid with $n = 1$, ($M = 10^8 M_\odot$, $a = 200pc$, and $b = 150pc$). We use a 2-D, isothermal AUSM hydrodynamic code with logarithmic (r, θ) meshes in the range of $r = 5pc \sim 15kpc$.

From our numerical results, we find that 1) formation of a gas ring ($r \sim 300pc$) with $M_{gas} \sim 9 \times 10^7 M_\odot$, 2) formation of a small nuclear gas disk ($r \sim 20pc$) with $M \sim 8 \times 10^6 M_\odot$, 3) two narrow gas ridges connecting the ring and the small nuclear gas disk, and 4) mass supply rate frm the gas ring to the small nuclear gas disk $\leq 0.05 M_\odot/yr$.

Our numerical results show that pattern speed is an important parameter for the mass supply rate that is large for the pattern speed as high as the inner Lind Blad resonance appears near the inner bar edge.

References

1. C. Alard: Astronomy and Astrophysics 379, L44 (2001)
2. N. Bissantz, P. Englmaier and O. Gerhard: Monthly Notice of the Royal Astronomical Society 340, 949 (2001)
3. R. Launhardt, R. Zylka, P. G. Mezger: Astronomy and Astrophysics 384, 112 (2001)

Water Maser Sources in the Outer Galaxy

Kazuya Hachisuka[1], Nanako Mochizuki[2] and Tomofumi Umemoto[3]

[1] Max-Planck-Institut für Radioastronomie, Germany
hkazuya@mpifr-bonn.mpg.de
[2] Institute of Space and Astronautical Science, Japan
nanakom@vsop.isas.jaxa.jp
[3] Nobeyama Radio Observatory, Japan umemoto@hotaka.mtk.nao.ac.jp

A size of optical disk of the Galaxy is still unknown, probably the size is less than a Galactrocentric radius of 15 kpc (e.g. [1]). Galactic maser sources in a star forming region are distributed in the Galaxy and their truncation radii should be related to the size of the optical disk. Methanol maser sources have been found at the Galactrocentric distance of up to 13 kpc (e.g. [2]) which is less than or equal to the radius of optical disk. On the other hand, beyond the optical disk where is called the far-outer-Galaxy (FOG; radius $>$ 15 kpc), there are water maser sources which might be truncated at a radius of around 17 kpc (e.g. [3]). We searched a new water maser sources beyond 17 kpc with Effelsberg 100m telescope, however no maser sources were found.

If these maser distributions show true truncation radii, why is the truncation radius of water maser sources larger than methanol masers? One possibility is the water maser sources in the FOG are associated with a low/intermediate mass protostars since methanol masers are associated with only high mass stars. In fact, it is more difficult to form a star in the FOG than the inner Galaxy, especially high mass stars (e.g. [4]). There are water maser source clusters in the Perseus arm which are also methanol maser source. Probably these methanol masers arise from the most massive protostar in the cluster. On the other hand, there is no water maser source cluster in the FOG. Perhaps they are not the high mass protostars.

References

1. Freudenreich, H. T.: ApJ, 492, 495 (1998)
2. Pestalozzi, M. R., Minier, V. & Booth, R. S.: A&A, 432, 737 (2005)
3. Valdettaro, R., Palla, F., Brand, J., Cesaroni, R. & Comoretto, G. et al.: A&A, 368, 845 (2001)
4. Brand, J., Wouterloot, J. G. A., Rudolph, A. L.: and de Geus, E.J.: A&A, 377, 644 (2001)

Mapping Galactic Magnetism through Faraday Rotation of Polarized Extragalactic Sources

Marijke Haverkorn[1], Bryan M. Gaensler[2], and Jo-Anne C. Brown[3]

[1] Jansky Fellow NRAO/UC-Berkeley marijke@astro.berkeley.edu
[2] Alfred P. Sloan Fellow, The University of Sydney bmg@usyd.edu.au
[3] University of Calgary jocat@ras.ucalgary.ca

Magnetic field strength and structure in the Milky Way are studied using rotation measures (RMs) from extragalactic point sources in the Galactic plane. The data come from the Canadian (Taylor et al 2003) and Southern (McClure-Griffiths et al 2005, Haverkorn et al 2006) Galactic Plane Surveys, which have already provided more than 500 RM sources in the second and fourth quadrants, with another 1000 sources expected as the surveys are completed.

Structure function analysis of RMs indicate a difference in typical outer scale l for spiral arms ($l < 10$ pc) and interarm regions ($l \approx 100 - 200$ pc). The difference is possibly due to H II regions dominating in the spiral arms, whereas turbulence dominates in the interarm regions (Haverkorn et al 2006).

The strength and direction of the regular magnetic field are derived from comparison with RMs from magnetic field models. SGPS observations confirm a previously observed magnetic field reversal on Galactic scale inside the solar radius. However, claims of additional reversals in the inner or outer Galaxy cannot be substantiated (Brown et al 2006, Brown et al in prep).

RMs from extragalactic sources are also used to probe the magnetic field of the Large Magellanic Cloud (LMC). The RMs indicate a regular spiral or circular magnetic field of approximately 1 μG in combination with a stronger ($B_{\rm ran} \approx 5$ μG) random magnetic field component. Given the LMC's recent violent star forming history, the existence of a regular magnetic field points to a rapid dynamo mechanism (Gaensler et al 2005).

References

1. J.C. Brown, M. Haverkorn, B.M. Gaensler et al: ApJ, submitted (2006)
2. B.M. Gaensler, M. Haverkorn, L. Staveley-Smith et al: Science 307, 1610 (2005)
3. M. Haverkorn, B.M. Gaensler, N. McClure-Griffiths et al: ApJS in press (2006)
4. M. Haverkorn, B.M. Gaensler, J.C Brown et al: ApJ 637, 33 (2006)
5. N.M. McClure-Griffiths, J.M. Dickey, et al: ApJS 551, 394 (2005)
6. A.R. Taylor, S.J. Gibson, M. Peracaula et al: AJ 125, 3145 (2003)

$H^{13}CO^+$ and Thermal SiO Observations of G0.11−0.11; an Extremely Large Column Density Cloud

Toshihiro Handa[1], Masaaki Sakano[2], Seiichiro Naito[3], Masaaki Hiramatsu[3], and Masato Tsuboi[4,5,3]

[1] Institute of Astronomy, the University of Tokyo handa@ioa.s.u-tokyo.ac.jp
[2] the University of Leicester
[3] Department of Astronomy, the University of Tokyo
[4] Nobeyama Radio Observatory tsuboi@nro.nao.ac.jp
[5] Graduate University for Advanced Studies(Soken-Dai)

A molecular cloud G0.11−0.11, which is located between the Galactic Center Arc (GCA) and Sgr A, was found from the NRO CS survey of the Galactic Center region [1]. Its morphology and velocity structure suggests that this cloud is interacting with GCA [2]. However, line intensity ratio of CS lines suggests they are optically thick ($\tau = 2 - 3$) in the Galactic Center region [1]. To investigate the actical physical parameters and structure observations in optically thin line is required.

Here, we observed the first view in $H^{13}CO^+$ and in thermal SiO lines of G0.11−0.11 [3]. Using comparison of line intensities, we found the $H^{13}CO^+$ line is optically thin, whereas the thermal SiO lines are optically thick.

In the souther part the cloud has large column density up to $N(H_2) = (6 - 7) \times 10^{23}\mathrm{cm}^{-2}$, which corresponds to about $640 - 740$ mag in A_V or 10-12 mag in $A_{25\mu m}$. This is the largest known any even in the Galactic Center region.

The intensity ratio of SiO to CS lines suggests that emitting gas is highly inhomogeneous for SiO abundance on a scale smaller than the beam with about 35".

References

1. M. Tsuboi, T. Handa, N. Ukita, ApJ, 120, 1 (1999)
2. M. Tsuboi, N. Ukita, T. Handa, ApJ, 481, 263 (1997)
3. T. Handa, M. Sakano, S. Naito et al, ApJ,636, 261 (2006)

A Possible Detection of CO (J = 3–2) Emission from the Host Galaxy of GRB 980425 with the Atacama Submillimeter Telescope Experiment

Bunyo Hatsukade[1], Kotaro Kohno[1], Akira Endo[1,2], Tomoka Tosaki[3], Kouji Ohta[4], Seiichi Sakamoto[2], Nobuyuki Kawai[5], Juan R. Cortés[6], Kouichiro Nakanishi[3], Takeshi Okuda[1,3], Kazuyuki Muraoka[1], Takeshi Sakai[2], Hajime Ezawa[2], Nobuyuki Yamaguchi[2], Kazuhisa Kamegai[1] and Ryohei Kawabe[2]

[1] Institute of Astronomy, the University of Tokyo
[2] National Astronomical Observatory of Japan
[3] Nobeyama Radio Observatory
[4] Department of Astronomy, Kyoto University
[5] Department of Physics, Tokyo Institute of Technology
[6] Departamento de Astronomia, Universidad de Chile

We observed ^{12}CO (J = 3–2) line emission from the host galaxy of GRB 980425 using the Atacama Submillimeter Telescope Experiment (ASTE). Five points were observed covering the entire region of the galaxy, and we find possible emission features (S/N $\sim 3\,\sigma$) at the velocity range corresponding to the redshift of the galaxy. After combining all spectra of five points, we obtain a global spectrum with a $\sim$4 σ emission feature. If the features are real, this is the first detection of CO among GRB host galaxies. We derive the total gas mass of $M(\mathrm{H_2}) = 7 \pm 1 \times 10^8\ M_\odot$ assuming a CO-to-H_2 conversion factor of $\alpha_{\mathrm{CO}} = 8.0\ M_\odot\ (\mathrm{K\ km\ s^{-1}\ pc^2})^{-1}$. The dynamical mass is calculated to be $M_{\mathrm{dyn}} = 2 \times 10^{10}\ M_\odot$, and $M(\mathrm{H_2})/M_{\mathrm{dyn}} \sim 3\%$ is consistent with those of nearby dwarfs and normal spirals. The derived star formation rate is $0.4 \pm 0.1\ M_\odot\ \mathrm{yr^{-1}}$ based on the Schmidt law. This SFR agrees with the results of previous Hα observations (SFR = $0.35\ M_\odot\ \mathrm{yr^{-1}}$; Sollerman et al. 2005), suggesting that there is no significant obscured star formation in this host galaxy. This result implies that there is a variety of GRB hosts in terms of the presence of obscured star formation.

References

1. Hatsukade et al.: submitted to PASJ (2006)
2. Sollerman, J., Östlin, G., Fynbo, J. P. U., Hjorth, J., Fruchter, A., Pedersen, K.: New Astronomy, 11, 103 (2005)

Formation of the Comet Cloud by the Galactic Tide

Arika Higuchi[1] and Eiichiro Kokubo[2]

[1] National Astronomical Observatory of Japan higuchi@th.nao.ac.jp
[2] National Astronomical Observatory of Japan kokubo@th.nao.ac.jp

The Oort Cloud is a spherical comet reservoir surrounding the solar system. It is generally accepted that it consists of more than 10^{12} comets and its size is on the order of 10^4-10^5 AU. The standard scenario of the Oort Cloud formation consists of two dynamical stages: (1) giant planets raise aphelia of residual planetesimals of planet formation to the outer region of the solar system, and (2) the galactic tide and perturbations from passing stars and giant molecular clouds pull their perihelia out of the planetary region and randomize their inclinations. The galactic tide is the major perturbation on the second stage [1]. We investigate the effect of the galactic tide on the evolution of orbits of planetesimals. We assume the galactic potential to be axisymmetric and consider the dominant vertical component of the galactic tide. We derive the analytical solutions of the time evolution of orbital elements of planetesimals by using the secular perturbation theory [1, 2]. Due to the galactic tide, the eccentricity and inclination of some planetesimals with small angular momentum conversely oscillate a great deal. Also some planetesimals show the libration of the argument of perihelion ω around ω=90° or 270° (the Kozai mechanism [3]). We find that due to the galactic tide, planetesimals with the semimajor axes >1,000 AU raise the perihelion distances to the outside of the planetary region (>100 AU) and planetesimals with the semimajor axes >20,000 AU spread the inclination to the galactic plane over the range 0° to 90° in 5 Gyr.

References

1. Heisler, J. & Tremaine, S. 1986, Icarus, 65, 13
2. Kinoshita, H. & Nakai, H. 1999, CMDA, 75, 125
3. Kozai, Y. 1962, AJ, 67, 591

Radio–Far-Infrared Spectral Energy Distribution of Young Starbursts

Hiroyuki Hirashita[1] and Leslie K. Hunt[2]

[1] Center for Computational Sciences, University of Tsukuba, Tsukuba 305-8577, Japan hirasita@ccs.tsukuba.ac.jp
[2] Istituto di Radioastronomia, Largo E. Fermi, 5, 50125 Firenze, Italy

We investigate the radio spectral energy distributions of young star-forming galaxies [1]. The radio energy emitted per supernova remnant (fluence) is constrained by using the observational radio data of SBS0335−052 ("active") and I Zw 18 ("passive"), which are the two lowest-metallicity blue compact dwarf galaxies. The typical radio fluence is estimated to be higher than previous estimates by nearly an order of magnitude and may depend on gas density. We have also predicted the time dependence of the radio spectral index for both the active and passive cases [2] (Fig. 1). We also predict the evolution of the radio–far-infrared (FIR) relation by using our FIR radiation models [2] (Fig. 1).

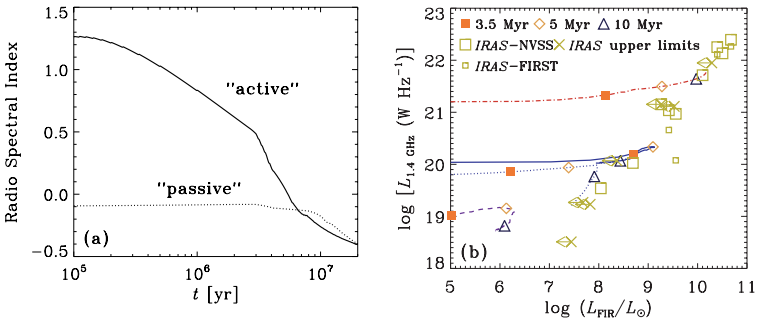

Fig. 1. Evolution of (a) radio spectral index [1] and (b) radio-FIR relation.

References

1. H. Hirashita, L. K. Hunt: A&A in press (2006)
2. H. Hirashita, L. K. Hunt: A&A **421**, 555 (2004)

GMCs in the Nearby Galaxy IC 342

Akihiko Hirota[1], N. Kuno[2], N. Sato[3], T. Tosaki[2], H. Nakanishi[2], and K. Sorai[4]

[1] the University of Tokyo, Bunkyo-ku, Tokyo 11-0033, Japan
[2] Nobeyama Radio Observatory, Minamimaki-mura, Minamisaku-gun, Nagano 384-1305, Japan
[3] Wakayama University, Wakayama 640-8510, Japan
[4] Hokkaido University, Sapporo 060-0810, Japan

Large scale distribution of massive star forming region in spiral galaxy is thought to be controlled by galactic density wave (Roberts 1969). Since GMCs are progenitor of massive star formation, observation of GMCs in external galaxies is cruicial to know the relationship between density wave and massive star formation.
IC 342 is one of the nearest molecular-rich galaxies. We made a full mapping observation of IC 342 in the ^{12}CO(1–0) line with the NRO 45 m telescope (HPBW$\sim$15$''$, Sato 2002). With the NMA, we observed the north-east arm segment 2 kpc away from the center, where major axis of the galaxy crosses the spiral arm and offset between dust lane and Hα emission is seen. The spatial resolution of the observation is $\sim$50 pc (3.1$''$x4.1$''$), which is comparable to the size of GMC. The molecular arm is resolved into clumpy structures with the NMA. Since the amount of missing flux is large (about 60%), combination of the NMA and the 45 m data is cruicial.
From the combined data, we identifed a number of molecular clouds which have properties comparable to those of GMCs in the Milky Way. Our data also detect the steep velocity gradient across the arm with respect to the galatic circular rotation ($\sim$300 km s^{-1} kpc^{-1} on galactic plane, which is in agreement with the tangential streaming motion caused by the density wave. Assuming that the position of the steep velocity gradient is the location of the galactic shock, we classified GMCs into two categories: pre-shock and post-shock clouds. Comparison between luminosity estimated mass and virial estimated mass suggest that the pre-shock clouds are more gravitationally unbound and diffuse than the post-shock clouds.

References

1. Roberts, W. W.: ApJ, 158, 123 (1969)
2. N, Sato: PhD thesis, Hokkaido University (2006)

Observations of H_2O Maser Sources in Nearby Molecular Clouds with VERA

Tomoya Hirota[1] and VERA team[1,2]

[1] Mizusawa-VERA Observatory, National Astronomical Observatory of Japan
tomoya.hirota@nao.ac.jp
[2] Department of Physics, Kagoshima University

We presented the first results of multi-epoch VLBI observations of H_2O maser sources in nearby molecular clouds with VERA. Observed sources were SVS13A in NGC1333, TMR-1 in the Taurus Molecular Cloud, Orion KL, HH1, and Mon R2 in the Orion-Monoceros Molecular Cloud Complex. Using the VERA dual-beam receiving system (Honma et al. 2003), we carried out phase-referencing VLBI and measured absolute proper motion and annual parallax of H_2O maser features. We successfully detected the annual parallax of Orion KL, 2.4 ± 0.4 mas, corresponding to the distance of 410 ± 50 pc from the Sun (Fig. 1). In addition, the annual parallax of SVS13A was also determined to be 4.4 ± 0.9 mas (230 ± 50 pc), although the life time of the maser feature was only 100 days. We will continue monitoring observations of these sources with VERA to determine their annual parallax more precisely.

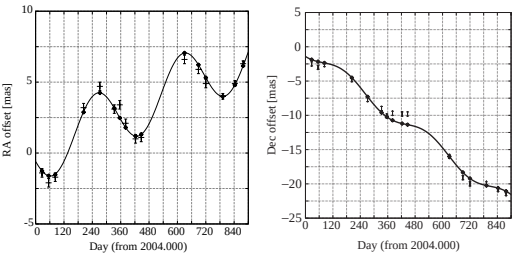

Fig. 1. Movements of a maser spot in Orion KL as a function of time. Each solid line represents the best fit model with linear proper motion and the annual parallax.

References

1. Honma, M. et al. 2003, PASJ, 55, L57

A Systematic Infrared Spectroscopic Study of Nuclear Starbursts in Seyfert Galaxies – Implications for an AGN Fueling Mechanism –

Masatoshi Imanishi

National Astronomical Observatory, 2-21-1, Osawa, Mitaka, Tokyo 181-8588, Japan masa.imanishi@nao.ac.jp

We report on the results of systematic infrared 3–4 μm spectroscopy of 23 Seyfert 1 and 32 Seyfert 2 galaxies. The putative nuclear starbursts in dusty tori of Seyfert galaxies are investigated through the 3.3 μm polycyclic aromatic hydrocarbon (PAH) emission feature. The 3.3 μm PAH emission is detected in roughly a half of the observed Seyfert galaxies. Since dust extinction is insignificant at infrared 3–4 μm, we can *quantitatively estimate* the magnitudes of the nuclear starbursts from the *observed* 3.3 μm PAH emission luminosities.

Figure 1 compares the luminosities of nuclear starbursts and AGNs. We find that (1) nuclear starburst to AGN luminosity ratios are similar between Seyfert 1 and 2 galaxies, and that (2) nuclear starburst luminosity positively correlates with AGN power in both types of Seyfert galaxies [1],[2]. Our results suggest that nuclear starbursts are physically closely related to AGNs and control the mass accretion rate onto the central AGNs, through the increased turbulence of molecular gas in the tori and/or increased radiation effects.

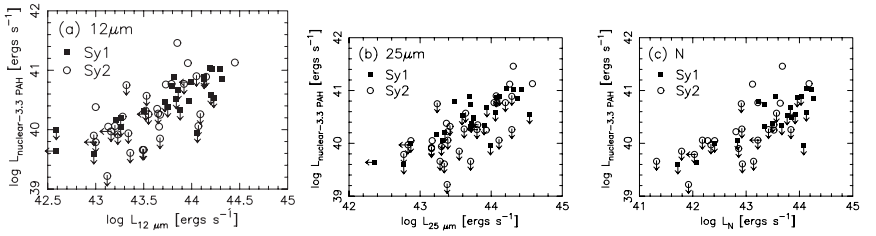

Fig. 1. Comparison of nuclear starburst (ordinate) and AGN (abscissa) luminosities.

References

1. Imanishi, M. 2003, ApJ, 599, 918
2. Imanishi, M., & Wada, K., 2004, ApJ, 617, 214

Ultraviolet Colours and Dust Properties of Nearby Normal Galaxies

Akio K. Inoue

College of General Education, Osaka Sangyo University
akinoue@las.osaka-sandai.ac.jp

Observed ultraviolet (UV) colours of nearby disc galaxies show a reddening relative to their expected intrinsic colours. Since the 2175 Å bump found in the Milky Way's dust extinction law blues the UV colours, it might suggest that dust in nearby disc galaxies does not have the bump and that the Milky Way is exceptional. However, this conclusion can be modified by the effect of the radiarive transfer: (1) configuration of dust and stars and (2) scatteirngs. If young stars are embedded deeply in thin disc and gas clouds, which is exactly observed in the Milky Way, observable UV colours become red because blue young stars are selectively extinguished by dust. If the scattering albedo decreases towards shorter wavelengths, observable UV colours also become red. An extensive comparison between observed UV colours and those expected from radiative transfer simulations shows two types of dust suitable for nearby disc galaxies: (1) dust with a bump and a smaller albedo for a shorter wavelength (except for the bump range), and (2) dust without any bump but with an almost constant albedo. If very small carbonaceous grains responsible for the common unidentified infrared emission band are also the bump carrier, the former dust is favorable. See Inoue et al. (2006) for more details.

References

1. A. K. Inoue, V. Buat, D. Burgarella, P. Panuzzo, T. T. Takeuchi, J. Iglesias-Paramo: MNRAS, 370, 380 (2006)

Possible Detection of Outer Plasma Around AGN Jets

Makoto Inoue[1], A. Haba[1], K. Asada[1], H. Nagai[1], Y. Murata[2], and P. Edwards[2]

[1] National Astronomical Observatory of Japan
[2] Institute of Space and Astronautical Science

We point out a possible way to investigate a plasma cocoon which has been revealed recent Faraday rotation studies of AGN jets. A high spatial resolution observation of VSOP suggests a sharp absorption feature which suggests free-free absorption by the plasma cocoon. The spiral jet configuration could provide, in general, an opportunity to investigate nature of plasma cocoon surrounding AGN jets.

Polarimetric observations have been revealing the existence of thermal plasma around AGN jets. It is interpreted that the gradient of Faraday rotation measure across the jets is due to helical magnetic field (e.g., [1]). However, it is not clear the nature of the thermal plasma responsible for the Faraday rotation. Although the thermal plasma is suggested to surround the jets like cocoon [2], observation to detect it is difficult, as the synchrotron emission from the jets may be too bright to see the thermal emission, if any. Here, we propose a possible way to investigate the thermal plasma around jets, showing one example of it.

When a jet trajectory is spiral in shape like a precessing jet, we could observe absorption features against the jet itself, which is probably produced by the thermal plasma surrounding the jet. In general, spiral jets could provide a new opportunity to study thermal plasma surrounding AGN jets. The new space VLBI 'VSOP-2' should be a powerful tool to investigate such phenomena.

References

1. Asada, K. et al: PASJ 54, 39 (2002)
2. Inoue, M., Asada, K., and Uchida, U.: ASPC 300, 141 (2003)

Candidate Streams of the Galactic Globular Clusters

Biwei Jiang[1], Shuang Gao[1] and Yongheng Zhao[2]

[1] Department of Astronomy, Beijing Normal University, Beijing 100875
bjiang@bnu.edu.cn,sgao@mail.bnu.edu.cn
[2] National Astronomical Observatories of China, Beijing 100012
yzhao@lamost.org

There are two opinions on the formation of the Galactic halo: the rapid collapse of a relatively uniform proto-galactic cloud, and the growth by accreting nearby dwarf galaxies over an extended period. The later fits the scenario of the cold dark matter model, and has obtained more and more observational support such as the discovery of the Sagittarius stream (Ibata et al 1994). The globular clusters, as one of the oldest and major halo component, are consequently suggested to originate from the accretion of satellite galaxies. Lynden-Bell & Lynden-Bell (1995) analyzed the kinematics of the globular clusters in the outer halo and nearby galaxies, and found some of the Galactic globular clusters could be classified as the members of the merging streams.

This work aims to retrieve the possible streams under the pre-assumption that all the globular clusters were formed in the very early merge events. The analysis was based on two assumptions: (1) the specific energy and angular momentum of the globular clusters after merging are not changed in the Galactic evolution, and (2) the globular clusters with common origin would stay in the same orbit plane. From the positions, velocities and distances, and the calculated orbital parameters, five candidate streams were derived. The total number of streams is consistent with previous results from others (see e.g. Mackey & Gilmore (2004)). Three of the four well established members of the Sagittarius stream were found to be in one of our streams. Several other globular clusters in our result were also thought to come from accretion by previous research. Whether these streams are true or imaginary needs further investigations.

References

1. R. Ibata, G. Gilmore, M.J. Irwin: Nature 370, 194 (1994)
2. D. Lynden-Bell, R.M. Lynden-Bell: MNRAS 275, 425 (1995)
3. A. Mackey, G. Gilmore: MNRAS 355, 504 (2004)

Distances to Streams of High Velocity Clouds

Shoko Jin and D. Lynden-Bell

Institute of Astronomy, University of Cambridge, Madingley Road, Cambridge, CB3 0HA, UK
shoko@ast.cam.ac.uk

We present a geometrodynamical method for determining distances to orbital streams of neutral hydrogen gas in the Galaxy. The method makes use of the Sun's offset from the Galactic centre and assumes that the gas comprising the stream nearly follows a planar orbit about the Galactic centre. Here, we provide a brief description of its application to the Magellanic Stream, which allows distances to be determined along the entire length of the stream. These distances are determined independently of information on the Magellanic Clouds, in other words they are not extrapolated from the positions of these Clouds.

We begin by writing down the energy equation for a generic point on the stream; assuming a simple logarithmic form for the Galactic potential allows the equation to be written purely as a function of r, the distance from the Galactic centre. A value for the angular momentum can be derived from the point (with distance $r_{\rm H}$) of the stream which has the largest radial velocity. (In this method, we initially assume that the line-of-sight velocity corrected to the Galactic Standard of Rest is a good approximation to the actual radial velocity $\dot{r}$.)

We select a fiducial point on the stream, whose direction from the Sun is known and its distance from the Galactic centre, as a fraction of $r_{\rm H}$, is also known for a given $r_{\rm H}$. Using three such fiducial points, the value of $r_{\rm H}$ can be fixed by requiring the plane of the stream to go through the Galactic centre. This in turn allows r to be calculated for each point. Since the distance d from the Sun is also known as a function of r and $r_{\rm H}$, values for d can also be determined once $r_{\rm H}$ is fixed. We then have a method of finding distances to all points along the stream.

According to this method, the perigalacticon is located at 45 kpc and the end of the stream at 70 kpc from the Galactic centre. The centre of mass of the Magellanic Clouds is independently determined to be at approximately 47 kpc, in agreement with observationally determined values. The method described here is also applicable to other long streams of high-velocity clouds, provided they also nearly follow planar orbits; this would allow otherwise unconstrainable distances to be determined.

Atomic Carbon in the Southern Galactic Plane

Kazuhisa Kamegai[1,2], T. Oka[2], M. Hayashida[2], M. Nagai[2], M. Ikeda[3,4], N. Kuboi [2], K. Tanaka[2], L. Bronfman[5] and S. Yamamoto[2]

[1] Institute of Astronomy, University of Tokyo, 2-21-1 Osawa, Mitaka, Tokyo 181-0015, Japan, e-mail: kamegai@ioa.s.u-tokyo.ac.jp
[2] Research Center for the Early Universe and Department of Physics, University of Tokyo
[3] National Astronomical Observatory of Japan (NAOJ)
[4] Institute of Physical and Chemical Research (RIKEN)
[5] Departamento de Astronomia,Universidad de Chile

In order to investigate formation processes of molecular clouds, it is essential to study the large-scale spatial distribution and kinematics of molecular cloud forming regions in the Galaxy. For this purpose, we have performed the first Galactic plane survey in the neutral atomic carbon emission line ([CI] $^3P_1 - ^3P_0$; 492 GHz) toward the southern Galactic plane ($l = 300^\circ - 354^\circ$, $b = 0^\circ$) with the Portable 18 cm Submillimeter-wave Telescope (POST18) at Atacama, Chile in 2003 (Oka et al. 2005).

The coarsely sampled $l - V$ map ($\Delta l = 1^\circ$) shows that the distribution of the [CI] emission resembles closely that of the CO $J = 1 - 0$ emission, suggesting a widespread distribution of atomic carbon (C^0) on the Galactic scale. The ratio of the antenna temperature of [CI] to that of CO concentrates on the narrow range $(0.05 - 0.3)$.

An LVG analysis reveals that the [CI] emission from the Galactic disk is dominated by a population of neutral gas with high abundance ratios of atomic carbon to CO, $N(C^0)/N(CO)$, and moderate column densities, which can be categorized as diffuse translucent clouds. The ratio of bulk emissivity indicates a systematic trend across the Galactic disk, suggesting that the bulk $N(C^0)/N(CO)$ abundance ratio increase with the Galactic radius. Two groups of high $T_{MB}([CI])/T_{MB}(CO)$ intensity ratio areas are found in the $l - V$ loci several degrees inside of tangential points of the Galactic spiral arms. These areas could be gas condensations just accumulated in the potential well of spiral arms and be in the early stages of molecular cloud formation.

References

1. Oka, T., et al.: ApJ, 623, 889 (2005)

Delectability of Massive Tori in Proto-QSOs with ALMA

Nozomu Kawakatu[1], P. Andreani[2], G. L. Granato[3] and L. Danese[4]

[1] National Astronomical Observatory of Japan kawakatu@th.nao.ac.jp
[2] European Southern Observatory, Germany
[3] NAF-Ossevatorio Astronomica di Padova, Italy
[4] SISSA/ISAS, Italy

We examine the detectability of ∼100 pc scale massive tori with $10^{8-9}M_{\odot}$ with the Atacama Large Millimeter Array (ALMA). Such massive tori are predicted to lie in the centre of elliptical galaxy progenitors by a model of a supermassive black hole growth coeval to the spheroidal population of the host galaxy [1]. We propose that submillimeter galaxies (SMGs) are the best targets to test our predictions. In order to assess the observational feasibility, we estimate the expected number counts of SMGs with massive tori and check the detectability with the ALMA instrument, the unique facility which can resolve the central region of high redshift objects. Our work shows that ALMA will be able to resolve and detect high-J ($J > 4$) CO emissions from massive tori up to $z \approx 2$ at 5σ in twelve hours on-source integration time and a velocity resolution of 25 km/s (please see our poster). In addition, we predict the number count of SMGs with a massive torus (more than $10^8 M_{\odot}$) ≈ 100 deg^{-2} at the redshift $1 < z < 3$. We stress the relevance of studying with ALMA samples of gravitationally lensed SMGs. It can allow a much higher spatial resolution, which can be a crucial piece of information in inferring the gas distribution in the very central regions around the growing SMBHs. Moreover, it is worth to discuss the possible detection of molecular clouds along the line of sight – associated with .. – not belonging to the massive central torus. CO lines in massive tori have likely very large velocity width (a few hundreds of km/s) because of their rotation around the central BH. Normal molecular clouds in star-forming region can move randomly with much less than 100 km/s.Velocity mapping is therefore the crucial observational tool to distinguish among the two cases (Kawakatu et al. 2006 in preparation).

References

1. N. Kawakatu, M. Umemura, M. Mori: ApJ, 583, 85 (2003)

Molecular Clouds and Star Formation in the Magellanic Clouds

Akiko Kawamura[1], T. Minamidani[1], Y. Mizuno[1], H. Iritani[1], N. Mizuno[1], T. Onishi[1], A. Mizuno[2] and Y. Fukui[1]

[1] Department of Astrophysics, Nagoya Univ., Chikusa-ku, Nagoya 464-8602
kawamura@a.phys.nagoya-u.ac.jp
[2] Solar-terrestrial Environment Lab., Nagoya Univ., Chikusa-ku, Nagoya 464-8601

The Large and Small Magellanic Clouds (LMC and SMC), at a distance of $\sim$ 50 kpc, are one of the nearest galaxies to our own. Studies of the LMC and SMC provide invaluable information to understand the evolution of interstellar matter and stars formation. More than 300 H II regions (e.g., [1]) and Stellar clusters called "populous clusters" with masses $\sim 10^4$–$10^5\,M_\odot$, are identified in the Magellanic system (e.g., [2]). There are populous clusters significantly younger, i.e., a few Myr–10 Gyr, than the Galactic globular clusters, enable us to study massive stars and cluster formation.

Survey of the molecular clouds in the LMC and SMC, as well as the Magellanic Bridge were carried out by NANTEN (e.g., [3]). Comparisons of 230 giant molecular clouds (GMCs) in the LMC with young clusters and H II regions show the following results: A study of the distance of H II regions and clusters measured from the nearest GMCs shows that a large number of the young clusters($\tau < 10$ Myr) and H II regions are found within 100 pc of the GMCs. On the other hand, older clusters show almost no correlation with the GMCs. We found that about a half of the H II regions and young clusters are associated with the GMCs. It is found that $\sim$ 24 % of the GMCs are starless, while 52 % and 24 % are associated with H II regions and young clusters, respectively. It is also shown that the number ratio of massive GMCs is higher in Class III than those in the other two, and the mass of Class I GMCs tends to be smaller than the rest.

References

1. R. D. Davies, K. H. Elliott, & J. Meaburn: MemRAS, 81, 89 (1976)
2. E. Bica, J. J. Clariá, H. Dottori, J. F. C. Jr. Santos, & A. E. Piatti: ApJS, 102, 57 (1996)
3. Y. Fukui, A. Kawamura, T. Minamidani, Y. Mizuno, Y. Kanai, N. Mizuno, T. Onishi, Y. Yonekura, A. Mizuno & H. Ogawa: ApJS, *submitted* (2006)

The Angstrom Project

Eamonn Kerins, on behalf of The Angstrom Project Team

Astrophysics Research Institute, Liverpool JMU, Twelve Quays House,
Egerton Wharf, Birkenhead CH41 1LD, UK
ejk@astro.livjm.ac.uk

The Andromeda Galaxy Stellar Robotic Microlensing (Angstrom) Project is a long-term microlensing survey of the bulge of the Andromeda Galaxy (M31). Microlensing describes the transient magnification of starlight by the gravitational field of a foreground compact object passing close by the line of sight. The spatial distribution of microlensing events is sensitive to the three-dimensional stellar mass distribution whilst the duration of each event is statistically sensitive to the mass of the intervening lensing star. The science goals of the Angstrom Project are to use the observed sample of microlensing events to contrain the three-dimensional structure of the M31 bulge and the low-mass end of the M31 bulge stellar mass function. More information on the project can be found in our poster contained on the CD-ROM and on our wiki web site [1].

References

1. The Angstrom Project wiki: http://www.astro.livjm.ac.uk/angstrom/

Mid-*J* CO Emissions from the Star Forming Complexes in the Milky Way and the Large Magellanic Cloud

Sungeun Kim[1]

Astronomy and Space Science Department, Sejong University, Seoul, 143-747, South Korea sek@sejong.ac.kr

A more complete picture of the thermodynamic state of the molecular gas can be gained through observations of other, higher-J transitions of CO and the various rotational transitions of the isotopically-substitued species ^{13}CO and C^{18}O. The Large Magellanic Cloud (LMC) and the Milky Way can be mapped with a high spatial resolution in higher-J excitation of ^{12}CO lines by the Antarctic Submillimeter Telescope and Remote Observatory (AST/RO). AST/RO is located at 2847 m altitude at the Amundsen-Scott South Pole Station and is capable of observing at wavelengths between 200 μm and 1.3 mm (Stark et al. 2001). This site is very dry, and thus very good for submillimeter observations (Lane & Stark 1996). We have studied the inner 500 pc in the Galactic Center regions (Kim et al. 2002; Martin et al. 2004) and the massive, southern star-forming region NGC 6334 (Kim & Narayanan 2006) in the CO $J = 7 \rightarrow 6$, CO $J = 4 \rightarrow 3$, and 809 GHz [C I] transitions. These lines were observed with the AST/RO. Almost all of the molecular cloud has now been imaged in these high-J transitions. The data show that high excitation temperatures exist throughout most of the cloud volume. X-rays emitted by embedded pre-main sequence stars (PMSs) in the molecular cloud may have profound effects on the molecular cloud evolution and star formation therein. X-rays can penetrate electrons via photoionization of the clouds. Detailed comparison of the observed line intensities and ratios with the thermal and chemical model of the X-ray dissociated regions in progress. CO $J = 4 \rightarrow 3$, CO $J = 7 \rightarrow 6$, and [C I] line observations of the molecular clouds in the LMC show anticorrelations between CO and [C I] in the low metallicity photodissociation regions (PDRs) of the LMC. We also mapped the molecular clouds interacting with X-ray superbubble in the LMC in submillimeter lines, [C I], CO $J = 2 \rightarrow 1$, CO $J = 4 \rightarrow 3$, and CO $J = 7 \rightarrow 6$ lines using the AST/RO (Kim, Walsh, & Xiao 2004; Kim et al. 2005; Kim 2006). We apply the X-ray dissociation regions (XDRs) model on dense molecular clouds illuminated by an incident X-ray flux (Kim et al., in preparation).

Dust Lanes and Starburst Rings in Barred-spiral Galaxies

Lien-Hsuan Lin[1], David Chien-Chang Yen[2] and Chi Yuan[3]

[1] Department of Physics, National Taiwan niversity, Taiwan, R.O.C.
[2] Department of Mathematics, Fu-Jen Catolic University, Taiwan, R.O.C.
[3] Institute of Astronomy and Astrophysics, Academia Sinica, Taiwan, R.O.C.

Many nearby spiral galaxies with a major bar, such as NGC1300 and NGC1097, are featured with a set of straight dust lanes and a central star formation ring. It is well known that these dust lanes are shock waves. In this study, we show that such observations can be reproduced by imposing a strong bar to a gaseous disk system. In our numerical simulations, we use the Antares code which we have developed. It is a code which adopts Cartesian coordinates and uses the high-order Godunov scheme [1] with unsplit flux calculated from the exact Riemann solver. We find the numerical results are very sensitive to the strength of a bar potential and grid sizes. The stronger the bar potential and the smaller the grid size, the more straight the shock waves and the smaller the starburst ring in the center will result. We have applied our numerical results to the major-bar galaxies NGC1300. With proper choice of these parameters, we can reproduce dust lanes and the central starburst ring which are in excellent agreements with the observations.

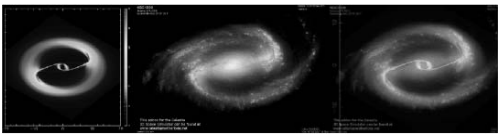

Fig. 1. The figures are from left to right the numerical results, observations, and their superposition respectively. The superimpositions show that the dust lanes obtained in our simulation match remarkably well with the data.

References

1. R.J. LeVeque *Finite Volume Methods for Hyperbolic Problems*, (Cambridge, Cambridge New York Melbourne Madrid Cape Town 2002)

Molecular Gas and Star Formation in M 83

Andreas A. Lundgren[1]

ESO, Casilla 19001, Santiago 19, Chile alundgre@eso.org

Summary. We have compared star formation rates and efficiencies, obtained from different star formation tracers, before and after compensation for internal extinction due to gas and dust, in the barred spiral galaxy M 83. The star formation tracers that we used were far-UV, B-band, radio thermal and non-thermal continuum, and Hα line emission. We calculated both SFRs and SFEs at 25″ resolution. We use total gas map, derived from CO(J=1-0) and HI data to compensate for internal extinction.

As an example of the results, the images below show median SFE(τ_8) maps. (**Left:** not corrected for extinction, **right:** corrected for extinction). The scale is logarithmic, and contours range from −2.5 to 0 with an increment of 0.25 (first white at −1.5) in units of $(10^8\,\mathrm{yr})^{-1}$.

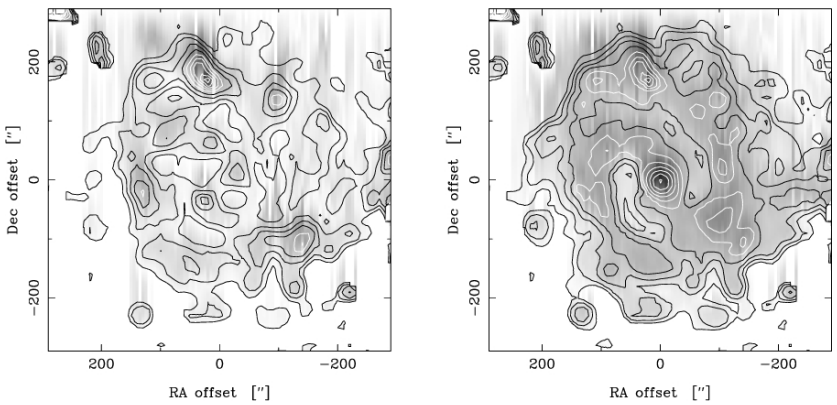

References

1. Lundgren, A. A., Olofsson, H., Wiklind, T., & Beck, R. A&A, submitted, (2006)
2. Lundgren, A. A., Wiklind, T., Olofsson, H., & Rydbeck, G. A&A, **413**, (2004)

Mapping the Inner Boxy Bulge of the Milky Way

Terry J. Mahoney, M. López-Corredoira, A. Cabrera-Lavers, P. L. Hammersley
F. Garzón, and C. González-Fernández

Instituto de Astrofísica de Canarias, E-38205 La Laguna, Tenerife, Spain
tjm@iac.es

Historically, star count analyses have been vitiated by heavy extinction in the visible, but even in the infrared Galactic structure (especially for the inner ∼4 kpc) is especially complicated by the multiplicity of distinct stellar and gaseous/dusty components (a typical line of sight will include spiral arms, rings and bulge or bar). We have adopted a Bayesian strategy devised by Lucy [5] to extract bulge parameters from the data rather than making prior guesses at the parameters.

We used the Lucy algorithm to invert the equation of star counts in order to recover 3D information on the structure of the inner Galaxy. This method enabled us to obtain both the stellar density distribution and the luminosity function with no need for prior assumptions [3]. Using 2MASS star counts [4], we obtained the 3D density distribution and K-band luminosity of the Galactic bulge. The result is a boxy bulge with axial ratios 1:0.5:0.4, the major axis making an angle of 20–35 deg w.r.t. the Sun–Galactic Centre radius vector. We set our results for the bulge into the wider context of the Tenerife model of the inner Galaxy, in which what has sometimes been referred to as the Galactic bar is identified with the boxy bulge described here in contradistinction to the long Galactic bar ([2], [1], [6]).

References

1. Benjamin, R. A. et al.: ApJ 630, L149 (2005)
2. Hammersley, P. L. et al.: MNRAS 317, L45 (2000)
3. López-Corredoira, M. et al.: MNRAS 313, 392 (2000)
4. López-Corredoira, M., Cabrera-Lavers, A. & Gerhard, O. E.: A&A 439, 107 (2005)
5. Lucy, L. B.: AJ 79, 745 (1974)
6. Weinberg, M. D.: ApJ 384, 18 (1992)

Revealing the three dimensional structure of the ISM in the Galaxy

Douglas J. Marshall[1 2], A. C. Robin[1], C. Reylé[1], M. Schultheis[1], A. Jones[2], F. Boulanger[2], M. Compigne[2] and S. Picaud[1 3]

[1] CNRS UMR6091,Observatoire de Besançon, BP 1615, 25010 Besançon Cedex, FRANCE
[2] CNRS UMR8617, Institut d'Astrophysique Spatiale, 91405 ORSAY Cedex, FRANCE
[3] Instituto de Astronomia e Geofísica (IAG/USP), São Paulo, Brazil

A technique using the Besançon model of the Galaxy [4] has been developed to extract the reddening information locked up in stellar observations from the visible to the near infrared. This has been done for the entire Galactic plane, a large fraction of these results are available online [3].

Using the resulting map, dust has been detected in the Galactic bulge, or bar, and indicates that the stellar bar and dust bar are not aligned. This non alignment, interpreted as dust lanes, has been observed in external galaxies but has never been confirmed for the Milky Way.

Furthermore, it has enabled the creation of a three dimensional map of dust emission. Using the dust map, a dust model [1] and a model for the interstellar radiation field [2], this has been accomplished and shows very good agreement with IRAS observations at 100μm.

Finally, the dust mapping technique has been used in the localisation of Infrared Dark Clouds (IRDCs). By using a catalogue of the positions and sizes of these clouds [5], it is possible to obtain the dust distribution along the line of sight to the cloud. This provides the distance to as well as the mass of the cloud.

References

1. F.X. Désert, F. Boulanger, J.L. Puget A&A 237, 215 (1990)
2. T.J. Sodroski, N. Odegard, R.G. Arendt et al. ApJ 480, 173 (1997)
3. D. J. Marshall, A.C. Robin, C. Reylé et al. A&A 435, 635 (2006)
4. A.C. Robin, C. Reylé, S. Derrière et al. A&A 409, 523 (2003)
5. R. Simon, J.M Jackson, J.M. Rathborne et al. ApJ 639, 227 (2006)

Effects of a Supermassive Black Hole Binary on a Nuclear Gas Disk

Hidenori Matsui[1], Asao Habe[2] and Takayuki R. Saitoh[3]

[1] Division of Physics, Graduate School of Science, Hokkaido University, Sapporo 060, Japan hidenori@astro1.sci.hokudai.ac.jp
[2] Division of Physics, Graduate School of Science, Hokkaido University, Sapporo 060, Japan habe@astro1.sci.hokudai.ac.jp
[3] National Astronomical Observatory of Japan, Mitaka, Tokyo 181-8588, Japan saitoh.takayuki@nao.ac.jp

We study effects of a suppermassive black hole (SMBH) binary on a nuclear gas disk, considering the dynamical friction between field stars and SMBHs by using high-resolution SPH+N-body simulations, in which we use 100000 SPH particles for a gas disk and 2-500000 N-body particles for field stars.

In our previous study [1], it has been shown that a SMBH binary enhances star formation in a nuclear gas disk due to resonances between the binary potential and gas motion. If orbital decay of the SMBH binary due to the dynamical friction which was not considered in the previous study, resonance positions will change and gas in the disk may be highly affected. In this study we investigate this case.

Our numerical results show that during SMBHs approaching to the galactic center, much gas is affected by the resonances and is concentrated into the galactic central region. As a result, star formation becomes very active in the central region and its star formation rate is comparable to that in the nuclear region of ultra luminous infrared galaxies. The active star formation decreases gas mass in the central region. However, our numerical results show that when SMBHs approach to the galactic central region, gas is carried to the central region. As a result, much gas can be supplied to the central region. The massive gas will have an important role in meging of SMBHs.

References

1. H. Matsui, A. Habe, and T. R. Saitoh: astroph/0606140 accepted for the publication in ApJ (2006)

The Distribution of Mira Variables in the Galactic Bulge

Noriyuki Matsunaga

Institute of Astronomy, School of Science, the University of Tokyo, 2-21-1 Osawa, Mitaka, Tokyo 181-0015, Japan; matsunaga@ioa.s.u-tokyo.ac.jp

Mira variables provide promising chances of mapping the stellar component in the galaxy since their period-luminosity relation can be used as a distance indicator. We can directly discuss the distribution of individual stars and their motions. Matsunaga, Fukushi, and Nakada [2] used 1968 Mira variables, extracted from the OGLE-II database [6], to obtain their space distribution. We detected the paucity of nearby stars at the negative galactic longitude, supporting the well-known asymmetry of the bar-like bulge. In this contribution, I will present further discussions about the structure of the galactic bulge.

First, I obtained the distance to the galactic center, 7.74 ± 0.06 kpc, from the distance histogram of the Mira variables in four OGLE-II fields at around ($l \sim 0^\circ, b \sim -1.5^\circ$). The result agrees well with recent studies based on other methods ([3], and references therein). Then, I found that the surface density of Mira variables follows de Vaucouleurs' law: $\sigma = \exp(20.4 - 4.5 r^{1/4})$, where $r^2 = l^2 + 4b^2$. The obtained effective radius of 0.6 kpc is larger than those for the outer part of the bulge (see Table 1 in [1]). Finally, I collected the proper motions of the Mira variables from the catalog obtained by Sumi et al [5]. The result was that distant stars (> 9kpc) are shifting toward the negative galactic longitude by 1.7 ± 0.3 mas/yr against the near side ones (< 7kpc) on the average. This is consistent with the result for red clump giants [4].

The author acknowledges the financial support from the Japan Society for the Promotion of Science through the fellowship for Young Scientists.

References

1. J. A. Frogel: ARA&A 26, 51 (1988)
2. N. Matsunaga, H. Fukushi, Y. Nakada: MNRAS 364, 117 (2005)
3. S. Nishiyama, T. Nagata, S. Sato et al: ApJ 647, 1093 (2006)
4. T. Sumi, L. Eyer, P. R. Woźniak: MNRAS 340, 1346 (2003)
5. T. Sumi, X. Wu, A. Udalski et al: MNRAS 348, 1439 (2004)
6. P. R. Woźniak, A. Udalski, M. Szymanski et al: Acta Astron. 52, 129 (2002)

Molecular Bubbles and Outflows in the Edge-on Starburst Galaxies M82 and NGC 2146

Satoki Matsushita[1], A.-L. Tsai[1], R. Kawabe[2], K. Nakanishi[2], B. Vila-Vilaro[2], K. Kohno[3], T. Inui[4], H. Matsumoto[4], T. G. Tsuru[4], and A. B. Peck[5]

[1] Academia Sinica, Institute of Astronomy and Astrophysics
[2] National Astronomical Observatory of Japan
[3] University of Tokyo
[4] Kyoto University
[5] Harvard-Smithsonian Center for Astrophysics

We performed deep CO(1-0) mapping of the central 60″ regions of nearby edge-on starburst galaxies M82 and NGC 2146 with the Nobeyama Millimeter Array. Both galaxies show kpc-scale Hα and/or soft X-ray outflows emanating from starburst regions within the galactic disks [1, 2]. We succeeded in imaging molecular bubbles and filamentary structures inside and outside the galactic disks in both galaxies. The mass and energy of the molecular bubbles show $\sim 1.8\times10^{8}$ $M_{\odot}$ and $\sim (0.5-2)\times10^{55}$ ergs for M82 [3] and $\sim 1.5 \times 10^{8}$ $M_{\odot}$ and $\sim (2-5) \times 10^{54}$ ergs for NGC 2146, respectively. The total thermal energies of Hα and X-ray outflows in M82 are $\sim 7 \times 10^{54}$ ergs [1] and $\sim 4 \times 10^{55}$ ergs [4], respectively, and that of X-ray outflows within the central 60″ of NGC 2146 is $\sim 3 \times 10^{54}$ ergs [5], assuming the filling factor of the Hα and X-ray is 0.01. These results indicate that the energy of a molecular bubble almost corresponds to that of the whole Hα or X-ray outflows in a galaxy. Note that the energy of a HI bubble in other galaxies is much smaller, $< 10^{54}$ ergs [6]. Although our result is based only on two galaxies (but typical starburst galaxies), it suggests that the molecular gas is one of the dominant components of outflows in starburst galaxies in terms of the energetics.

References

1. P. L. Shopbell, J. Bland-Hawthorn: ApJ 493, 129 (1998)
2. T. Inui, H. Matsumoto, T. G. Tsuru et al: PASJ 57, 135 (2005)
3. S. Matsushita, R. Kawabe, H. Matsumoto et al: ApJ 545, L107 (2000) 891 (2002)
4. D. K. Strickland, T. J. Ponman, I. R. Stevens: A&A 320, 378 (1997)
5. L. Armus, T. M. Heckman, K. A. Weaver, M. D. Lehnert: ApJ 445, 666 (1995)
6. G. Tenorio-Tagle, P. Bodenheimer: ARAA, 26, 145 (1988)

The Star Formation Properties of HI Selected Galaxies from SINGG

Gerhardt R. Meurer[1] and the SINGG Team

The Johns Hopkins University, Department of Physics and Astronomy
meurer@pha.jhu.edu

The star formation properties of a sample of 93 HI selected targets observed in Hα and the R band are examined. The data are from the Survey of Ionization in Neutral Gas Galaxies (SINGG) and cover a broad range of surface brightness, mass and morphologies. Distance independent normalized star formation indicators correlate in the expected sense - higher star formation intensity corresponds to a higher star formation rates per unit R luminosity (equivalent width) and per unit HI mass (inverse gas cycling time). The star formation indicators have a larger scatter about the mean for dwarf galaxies compared to normal galaxies, in agreement with expectations from the Stochastic Self-Propagating Star Formation (SSPSF) scenario. However, the lack of significant numbers of non-detections is contrary to the expectations of SSPSF models. Star formation intensity and the gas cycling time show a very strong dependence on the R band effective surface, confirming earlier results from Dopita and Ryder (1994). In contrast the dependence on a pseudo HI surface brightness ($\mathcal{M}_{\rm HI}/\pi r^2_{\rm opt}$) is rather weak. These results highlight the importance of the existing stellar populations for binding the ISM and inducing star formation.

More information on the SINGG survey including access to public data can be found at http://sungg.pha.jhu.edu/.

Dense Clouds and Star Formation on Spiral Arm in M33 -deep CO and HCN Observation in NGC604-

Rie Miura[1,2], Yoichi Tamura[1,2], Sachiko K. Okumura[2], Ryohei Kawabe[2], Tomoka Tosaki[2], Nario Kuno[2], Kouichiro Nakanishi[2], Seiichi Sakamoto[2], and Takashi Hasegawa[3]

[1] the University of Tokyo
[2] National Astronomical Observatory of Japan
[3] Gunma Astronomical Observatory

We investigated properties of giant molecular clouds (GMCs) in the massive star forming region NGC604 on the spiral arm in M33. CO(J=1-0), HCN and 90G Hz continuum emissions were observed at the two field toward NGC604 with the Nobeyama Millimeter Array (NMA). Eight clouds are identified from our high-resolution CO images using the CLFIND algorithm, with similar masses and sizes ($M\sim 0.2-2.9\times10^5 M_\odot$, D∼21-38pc). The physical properties of these clouds follow the Larson's law and are comparable to those of Galactic GMCs. Several of these clouds compose two large complexes. From our HCN and continuum results as well as the CO results, we classify these clouds into 4 categories; the clouds which have (1) no sign of star formation (2) association with dense gas but no HII region, (3) association with both dense gas and star cluster formation, and (4) association with HII regions. Category (3) has a larger rotation velocity than that predicted by the galactic rotation curve and that of category (2), although both categories locate at the same galactic radius. The reason is likely to be the acceleration by the galactic potential. In fact there are intensive star formation activity in category (3), which suggest that the molecular gas is being accumulated at the bottom of the gravitational potential. This scenario is also supported by a rough estimate of the time scale from category (2) to (3).

References

1. Bonnell, I. A.; Dobbs, C. L.; Robitaille, T. P.; Pringle, J. E.: MNRAS 365, 37B (2006)

Flux Variability of Sgr A* at Short Millimeter Wavelengths

Atsushi Miyazaki[1,2], Z.-Q. Shen[1], M. Miyoshi[3], M. Tsuboi[4], and T. Tsutsumi[3]

[1] Shanghai Astronomical Observatory, Chinese Academy of Sciences
[2] Mizusawa VERA Observatory, National Astronomical Observatory of Japan
[3] National Astronomical Observatory of Japan
[4] Nobeyama Radio Observatory, National Astronomical Observatory of Japan
amiya@miz.nao.ac.jp

Since 1996, we performed the flux monitoring observations of Sagittarius A* (Sgr A*), which is a compact source located at the dynamical center of the Galaxy and is associated with a supermassive black hole, at mm-wavelengths using the Nobeyama Millimeter Array (NMA) [1, 2]. The monitoring observations were carried out in the 3- & 2-mm (100 & 140 GHz) bands over one to several months at each NMA observing season. We detected at least four flares of Sgr A* with the duration of a few weeks. In the flares, the increase of the flux densities reached to 100-200% at 100 GHz and 200-400% at 140 GHz. We also detected some intraday variations (IDVs) of Sgr A* at both 100 and 140 GHz bands. These IDVs have the twofold increase timescale of a few hours. The shortest timescale of the IDVs, $\sim$1.5 hrs, suggests that the physical size is on a scale at or below about 12 AU (150 $R_{\rm s}$). These IDVs has a similar increase timescale as those known in the X-ray and infrared flares, but has smaller amplitude [3, 4]. Our result is consistent with the radio IDVs recently reported by some investigators (e.g., [5]).

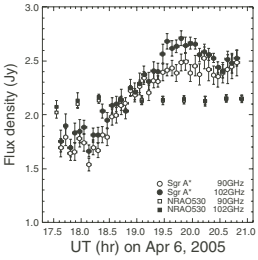

Fig. 1. Light curves of Sgr A* (*circles*) and the calibrator (NRAO530; *squares*) in the 100 GHz band on April 6, 2005.

References

1. Miyazaki, A., Tsutsumi, T., & Tsuboi, M.: ApJL, 611, L97 (2004)
2. Miyazaki, A., et al.: in the proceedings of the GC workshop 2006, in press
3. Porquet, D., et al.: A&A, 407, L17 (2003)
4. Genzel, R., et al.: Nature, 425, 934 (2003)
5. Mauerhan, J.C., et al.: ApJL, 623, L25 (2005)

The Feedback Between the Starburst and the ISM in NGC 1569

Stefanie Mühle[1], E. R. Seaquist[1], S. Hüttemeister[2], U. Klein[3] and E. M. Wilcots[4]

[1] Department of Astronomy and Astrophysics, University of Toronto, 50 St. George St., Toronto, Ontario, M5S 3H8, Canada, muehle@astro.utoronto.ca,
[2] Astronomisches Institut, Ruhr-Universität Bochum, Universitätsstr. 150, 44780 Bochum, Germany,
[3] Argelander-Institut für Astronomie, Universität Bonn, Auf dem Hügel 71, 53121 Bonn, Germany
[4] Washburn Observatory, University of Wisconsin, 475 N. Charter St., Madison, Wisconsin 53706, USA

The nearby metal-poor dwarf galaxy NGC 1569 has experienced a tremendous starburst, which has lead to numerous Hα filaments, a strong metal-rich galactic wind and a region of shocked gas at the position of the western Hα arm [1, 2]. The velocity structure of the neutral atomic hydrogen is highly disturbed with evidence for gas having been pushed outwards to larger radii [3, 4]. As a result, the neutral atomic gas now seems to be concentrated in a torus, which is punctured in its southern part by a pronounced HI chimney at the position of two very bright super-star clusters (SSCs). The complex HI halo structure surrounding the dwarf galaxy may consist of the remnants of a tidally disrupted intergalactic HI cloud currently being accreted by NGC 1569 and thus feeding the starburst. Our fully-sampled CO($1 \rightarrow 0$), CO($2 \rightarrow 1$) and CO($3 \rightarrow 2$) single-dish maps agree very well with previous interferometric observations [5] and suggest a depletion of the CO emission close to the SSCs as well as a large amount of low-density molecular gas. Including new spectra of faint ^{13}CO emission, the first results of our non-LTE line ratio analysis suggest an unusually high average kinetic temperature of the molecular gas near the SSCs at a moderate average gas density.

References

1. C.L. Martin, H.A. Kobulnicky & T.M. Heckman: ApJ 574, 663 (2002)
2. S. Mühle: PhD Thesis, University of Bonn, Cuvillier Verlag Göttingen (2003)
3. S. Mühle, U. Klein, E.M. Wilcots, S. Hüttemeister: AJ 130, 524 (2005)
4. S. Mühle, U. Klein, E.M. Wilcots, S. Hüttemeister: AJ 132, 443 (2006)
5. C.L. Taylor, S. Hüttemeister, U. Klein, A. Greve: A&A 349, 424 (1999)

CO(3-2) Wide Area Imaging of M 83 with ASTE: Correlation between CO(3-2)/CO(1-0) Ratios and Star Formation Efficiencies

Kazuyuki Muraoka[1], Kotaro Kohno[1], Tomoka Tosaki[2], Nario Kuno[2], Kouichiro Nakanishi[2], Kazuo Sorai[3] and Seiichi Sakamoto[4]

[1] Institute of Astronomy, the University of Tokyo
[2] Nobeyama Radio Observatory
[3] Hokkaido University
[4] National Astronomical Observatory of Japan

We present CO($J = 3 - 2$) emission observations with the Atacama Submillimeter Telescope Experiment (ASTE) toward the $5' \times 5'$ (or 6.6×6.6 kpc at the distance D = 4.5 Mpc) region of the nearby barred spiral galaxy M 83. We successfully resolved the major structures, i.e., the nuclear starburst region, bar, and inner spiral arms in CO($J = 3 - 2$) emission at a resolution of $22''$ (or 480 pc), showing a good spatial coincidence between CO($J = 3 - 2$) and 6 cm continuum emissions.

From a comparison of a CO($J = 3 - 2$) data with CO($J = 1 - 0$) intensities measured with Nobeyama 45-m telescope, we found that the radial profile of CO($J = 3 - 2$)/CO($J = 1 - 0$) integrated intensity ratio $R_{3-2/1-0}$ is almost unity in the central region ($r < 0.25$ kpc), whereas it drops to a constant value, 0.6–0.7, in the disk region. The radial profile of star formation efficiencies (SFEs), determined from 6 cm radio continuum and CO($J = 1 - 0$) emission, shows the same trend as that of $R_{3-2/1-0}$.

At the bar-end ($r \sim 2.4$ kpc), the amounts of molecular gas and the massive stars are enhanced when compared with other disk regions, whereas there is no excess of $R_{3-2/1-0}$ and SFE in that region. This means that a simple summation of the star forming regions at the bar-end and the disk cannot reproduce the nuclear starburst of M 83, implying that the spatial variation of the dense gas fraction traced by $R_{3-2/1-0}$ governs the spatial variation of SFE in M 83.

Kinematic Aging and Spectral Aging in Young Radio Galaxies

Hiroshi Nagai[1,2], M. Inoue[2], K. Asada[2], S. Kameno[3] and A. Doi[4]

[1] The Graduate University for Advanced Studies hiroshi.nagai@nao.ac.jp
[2] National Astronomical Observatory of Japan
[3] Kagoshima University
[4] Yamaguchi University

1 Introduction

Compact symmetric objects (CSOs), which are a new sub-class in extra-galactic radio sources, are found by recent VLBI observations. Their radio morphologies are similar to giant radio galaxy such as Cygnus A, but their sizes are $\sim 10^3$ times smaller. They are candidates for young radio galaxies (the youth scenario). To estimate the source age is crucial test for the youth scenario. We present a study of kinematic and spectral ages of the compact radio source CTD 93 (Nagai et al. 2006). As well, we report a preliminary result of spectral age measurement for 3C 84.

2 Results

Muti-epoch VLBA observations revealed hot-spot advancing of CTD 93. The advance speed is $0.17\pm0.06c$ (H_0=72 km s^{-1} Mpc^{-1}), which results in a kinematic age of 2200±700 yr. The radio lobe spectra show a high frequency steepening. The spectral break decreases with the distance from the hot spot. This tendency is expected from the basic scenario of radio lobe evolution (Scheuer 1974; Blandford & Rees 1974). Preliminary results for 3C 84 also revealed similar tendency of spectral break distribution. Sufficient resolution across the lobe will allow a detail analysis of spectral age.

References

1. Blandford, R. D., & Rees, M. J.: MNRAS, 169, 395 (1974)
2. Nagai, H., Inoue, M., Asada, K., Kameno, S., & Doi, A.: ApJ, 648, 148 (2006)
3. Scheuer, P. A. G.: MNRAS, 166, 513 (1974)

A High-velocity [CI] Wing Emission Toward the M17 Molecular Cloud

Makoto Nagai[1], T. Oka[1], S. Yamamoto[1], Y. Moriguchi[2], Y. Fukui[3] and Y. Sekimoto[4]

[1] Research Center for the Early Universe and Department of Physics, The University of Tokyo`nagai@taurus.phys.s.u-tokyo.ac.jp`
[2] Max-Planck Institut für Kernphysik
[3] Department of Astrophysics, Nagoya University
[4] National Astronomical Observatory of Japan

Recent observations with the portable 18 cm submillimeter-wave telescope (POST18; [1]) have revealed a prominent high-velocity wing emission in the $C^0\ ^3P_1$–$^3P_0$ ([CI]) line profile from M17. The wing emission has a large velocity width ($\sim$40 km s^{-1}) and occupies about one third of the [CI] integrated intensity.

Follow-up observations with the Mt. Fuji submillimeter-wave telescope have confirmed the presence of the [CI] wing emission and have shown its large spatial extent and mapping observations of CO lines with the NRO 45 m telescope have shown that the high-velocity gas emitting the wing has large turbulent motion. An LVG analysis of emission lines including CO J=1–0 and J=3–2 have revealed that the high-velocity gas has a high C^0/CO abundance ratio (2.6–5.4) and a low column density, $N(H_2) \sim 4{\times}10^{21}$ cm^{-2}.

A possible explanation for the origin of the high-velocity gas in M17 is that it is the remains of rapid cloud formation by an expanding supershell formed by the previous generation of massive star formation. A large-scale CO survey have shown that M17 molecular clouds are on the edge of a supershell with a diameter of 200 pc [2]. Diffuse gas just accumulated by a supershell is mainly atomic, and it can have large velocity width since an energy injection had activated turbulent motion. This picture can explain the physical and chemical properties of the high-velocity gas in M17.

References

1. Oka, T. et al.: ApJ 623, 889 (2005)
2. Moriguchi, Y. et al.: The Proceedings of the IAU 8th Asian-Pacific Regional Meeting, II, 173 (2002)

Evaporation of Tiny HI Clouds: Possible Probes of Physical State of the Galactic Gas Disk

Masahiro Nagashima[1,3], Hiroshi Koyama[2] and Shu-ichiro Inutsuka[3]

[1] Faculty of Education, Nagasaki University, Nagasaki 852-8521
[2] Department of Earth and Planetary Science, Kobe University, Kobe 657-8501
[3] Department of Physics, Kyoto University, Kyoto 606-8502

We computed the evaporation rate of HI clouds, assuming that they consist of the cold neutral medium (CNM) surrounded by the warm neutral medium (WNM) under pressure equilibrium. The two phases are thermally stable balancing the heating rate with the cooling rate.

Performing numerical simulations for spherical clouds, we found that clouds of 0.01 pc evaporate in $\sim$ 1Myr almost irrespective of the ambient pressure, and the evolution of clouds larger than 0.1 pc depends strongly on the pressure. The evaporation rate for the saturation pressure, $p_{\rm sat}$, is proportional to the cloud size, R_c. Although this is the same scaling as that of [1], the value is about a factor of four smaller [2][3].

Applying a pattern formation theory of non-equilibrium statistical physics, we obtained a new formula for evaporation. The evaporation rate should consist of two parts as $\dot{M} = \dot{M}_{\rm p} + \dot{M}_c$, where $\dot{M}_{\rm p}$ and $\dot{M}_{\rm c}$ are the "pressure" and "curvature" terms, respectively, and

$$\dot{M}_{\rm p} = -4\pi R_c^2 \rho_{\rm CNM} c(p) \propto R_c^2, \tag{1}$$

$$\dot{M}_{\rm c} = 4\pi R_c^2 \rho_{\rm CNM} f \frac{\gamma - 1}{\gamma} \frac{\mu}{k_B} \frac{2}{R_c} \frac{\kappa_R}{\rho_{R_c}} \propto R_c. \tag{2}$$

When $p = p_{\rm sat}$, $\dot{M}_{\rm p} = 0$. When $p > p_{\rm sat}$, $\dot{M}_{\rm p} < 0$. Therefor, when the pressure is high enough and the cloud size is sufficiently large, the evaporation rate becomes negative, which means condensation. Thus the evaporation timescale scales as $t_{\rm evap} \sim M/\dot{M}_{\rm c} \propto R_c^2$ for small clouds and $t_{\rm evap} \sim M/\dot{M}_{\rm p} \propto R_c$ for large clouds. This explains well the simulation results.

References

1. C.F. McKee, L.L. Cowie: ApJ 215, 213 (1977)
2. M. Nagashima, H. Koyama, S. Inutsuka: MNRAS 361, L25 (2005)
3. M. Nagashima, S. Inutsuka, H. Koyama: ApJL in press (2006)

A Wide Survey in NH_3 Lines of the Central 200 pc Around the Galactic Center with Kagoshima 6 Meter Radio Telescope

Takumi Nagayama[1], Toshihiro Omodaka[1], Toshihiro Handa[2], Tsuyoshi Sawada[3], Hayati Bebe Iahak[1] and Naohito Matsuyama[1]

[1] Faculty of Science, Kagoshima University, 1-21-30 Korimoto, Kagoshima 890-0065 nagayama@astro.sci.kagoshima-u.ac.jp
[2] Institute of Astronomy, University of Tokyo, 2-21-1 Osawa, Mitaka, Tokyo 181-0015 handa@ioa.s.u-tokyo.ac.jp
[3] Nobeyama Radio Observatory, National Astronomical Observatory of Japan, Minamimaki, Minamisaku, Nagano 384-1305 sawada@ioa.s.u-tokyo.ac.jp

NH_3 lines are useful to estimate the temperature of molecular gas. Although many observations have been done toward the Galactic center, they covered much smaller region than the Central Molecular Zone (CMZ). Here we present a map of the major part of the CMZ by simultaneous observations in NH_3 $(1,1)$ and $(2,2)$ lines with the Kagoshima 6 meter telescope. The mapped area is -1.000 deg $< l <$ 1.625 deg, -0.375 deg $< b <$ 0.250 deg with 0.125 deg spacing, which is closer than the telescope beamsize, 9.5 arcmin. The overall distribution well traces in other molecular emission such as CO and CS. From the l-b-v data cube we identify and investigate 4 clouds, which correspond Sgr A 20 km s^{-1} cloud, 40 km s^{-1} cloud, Sgr B2 cloud, and the 1.3-deg region cloud. We find a high velocity wing at $l = 0.8$ deg, a part of which is seen in the previous observations. The $(2,2)$ to $(1,1)$ intensity ratio is uniform over most of the observed region and is about 0.7-0.8, which corresponds 36-42 K in optically thin case and 24-34 K in optically thick case. Comparison with the CO survey by Sawada et al. (2001), NH_3 emitting region is surrounded by the high pressure region on l-v plane. High pressure region is not traced by NH_3 emission. It is at the edge of NH_3 emitting region. Therefore, the high pressure region is less dense and hotter. In the Galactic center molecular cloud complex has a "core" of dense and warm cloud which is traced in NH_3 emission, and an "envelope" of less dense and hotter gas clouds.

References

1. Sawada, T., et al.: ApJS 136, 189 (2001)

Inclination Angle of the LMC Disk

Yoshikazu Nakada[1], N. Matsumoto[1], T. Tanabe[1], N. Matsunaga[1], H. Fukushi[1], Y. Nakajima[2], D. Kato[3] and IRSF Team

[1] Univ.Tokyo nakada@kiso.ioa.s.u-tokyo.ac.jp
[2] NAOJ
[3] Nagoya Univ.

Red clump stars (hereafter RCs) are a useful tool as a distance indicator. However, it turned out that their luminosities and colors change with their metallicities and ages. It is necessary to select a suitable pair of these two parameters for the RCs. The recent photometric and spectroscopic observations showed that the LMC red clump is dominated by the stars with the metallicity [Fe/H] $= -0.4$ and the age of a few Gyr. Fortunately, the recent optical and near-infrared surveys (Zaritsky 2002, Kato 2006) are deep enough to reach the LMC RCs.

Here we report a preliminary analysis of the colors and magnitudes of the RCs in the LMC from these catalogues. First, we adapt their intrinsic color of $(J-H)_0 = 0.42$ and their absolute magnitude of $M_H = -1/02$. Next, we make the H-band luminosity function the (J-H) color distribution in each 0.5 degrees square areas over the LMC disk. The peak colors show a slight variation which is interpreted as the extinction distribution. The standard Galactic extinction law is adapted for the reddening correction. Then, the distances to the disk areas are derive from the peak magnitude togather with the reddening correction. The derived distances to the total of more than one hundreds mesh points over the disk are least-square-fitted to the plane with the inclination angle 34 degrees which is coincident with the recently obtained values by other authors. The V and I photometric data is also analyzed but it turns out difficult to fit the optical data to the plane.

References

1. D. Zaritsky, J. Harris, I. Thompson et al: AJ 128, 1606 (2004)
2. D. Kato: Private communication (2006)

Three-Dimensional HI and H_2 Gas Maps of the Milky Way Galaxy

Hiroyuki Nakanishi[1] and Yoshiaki Sofue[2]

[1] Nobeyama Radio Observatory, 462-2 Nobeyama, Minamimaki, Minamisaku, Nagano, 384-1305, Japan hnakanis@nro.nao.ac.jp
[2] Institute of Astronomy, the University of Tokyo, 2-21-1 Osawa, Mitaka, Tokyo 181-0015, Japan sofue@ioa.s.u-tokyo.ac.jp

We created three-dimensional HI and H_2 gas maps of the Milky Way Galaxy using the latest HI and CO survey data [1, 2, 3, 4], and rotation curves [5, 6], based on the kinematic distance.

The total gas map (HI plus H_2) revealed clear logarithmic spiral arms; the Outer arm, Perseus arm, the Orion arm, the Sagittarius-Carina arm, the Scutum-Crux arm, and the Norma arm. The Norma and the Outer arms can be identified as the same spiral arm considering pitch angle of $11 - 15^\circ$.

Plotting HI or H_2 gas densities against the total gas density, we found following characteristics of the HI and H_2 phases. In the case of small total density ($n < 0.4$ cm^{-3}), all the gas is in HI phase. However, the HI density is constant in the case of $n > 0.4$ cm^{-3}. There seems to exist HI saturation density.

References

1. Hartmann, D., & Burton, W. B.: *Atlas of Galactic Neutral Hydrogen* (Cambridge University Press 1997)
2. Kerr, F. J., Bowers, P. F., Jackson, P. D., & Kerr, M.: A&AS, 66, 373 (1986)
3. Burton, W. B., & Liszt, H. S.: A&AS, 52, 63 (1983)
4. Dame, T. M., Hartmann, D., & Thaddeus, P.: ApJ, 547, 792 (2001)
5. Clemens, D. P.: ApJ, 295, 422 (1985)
6. Dehnen, W., & Binney, J.: MNRAS, 294, 429 (1998)

Radio Continuum and Water Vapor Maser Monitoring Toward the Luminous Infrared Galaxy NGC 6240

Kouichiro Nakanishi[1], Naoko Sato[2], Nario Kuno[1], Sachiko K. Okumura[1], Ryohei Kawabe[3], Kotaro Kohno[4], Aya Yamauchi[5] and Naomasa Nakai[5]

[1] Nobeyama Radio Observatory, National Astronomical Observatory of Japan
[2] Center for Education and Research of Lifelong Learning, Wakayama University
[3] ALMA Project Office, National Astronomical Observatory of Japan
[4] Institute of Astronomy, University of Tokyo
[5] Institute of Physics, University of Tsukuba

We have carried out monitoring observations of 87 GHz (3.4 mm) continuum toward the center of the luminous infrared galaxy NGC 6240 with the Nobeyama Millimeter Array during the year of 2000-2006, and significant time variations of continuum flux density have been detected (continuum flux flare up by 150-200%). The time-scales of flare event are about a few to several months. The size of area corresponded to the time variations of continuum flux should be smaller than 0.2 pc. NGC 6240 is also known as a time-variable water vapor maser emitter. Water vapor maser emission from NGC 6240 ware also monitored with Nobeyama 45-m Telescope at 22 GHz (1.3 cm), and relatively short time-scale variations (may be less than a few month) of the emission peak flux have been detected at the beginning of the year of 2005.

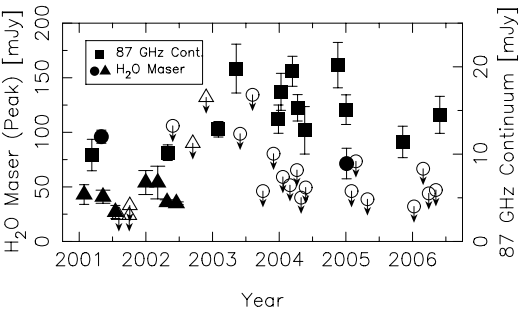

Fig. 1. Time variations of 87 GHz continuum flux (squares) and H_2O maser peak flux density (circles and triangles).

Structure of the Galactic Bulge and Near Infrared Interstellar Extinction Law

Shogo Nishiyama[1], Tetsuya Nagata[2] and Koji Sugitani[3]

[1] National Astronomical Observatory of Japan, Mitaka, Tokyo 181-8588, Japan
shogo@optik.mtk.nao.ac.jp
[2] Kyoto University, Kyoto 606-8502, Japan
[3] Nagoya City University, Nagoya 467-8501, Japan

The IRSF/SIRIUS Galactic center survey project is a deep near-infrared (J, H, K_S) survey of the central region of our Galaxy with the 1.4 m telescope IRSF and the infrared camera SIRIUS [1, 2]. The pixel scale of SIRIUS is $0\farcs45$, and the limiting magnitudes of our survey are 17.0 (J), 16.6 (H), and 15.6 (K_S), which are 2−3 mag deeper than 2MASS at the Galactic center.

Using these data sets, we find a distinct structure, which is probably a secondary bar, inside the primary bar of our Galaxy [3]. To understand the detailed bar structure, we surveyed a strip extending over $| l | < 10\fdg5$ at $b = +1\fdg0$. Bulge red clump (RC) stars, the horizontal branch stars for metal rich population, can be used as a good standard candle, and thus we estimated extinction-corrected magnitude of them. In this process, we have used the infrared extinction law in the J, H, and K_S bands toward the Galactic center newly determined from our survey [4]. The dependence of the magnitude on the Galactic longitude shows clear bar structure (see [3], Fig. 4) in support of previous studies. However, at $| l | < 5^\circ$, the dependence is much weaker, suggesting the presence of an inner structure inside the large-scale bar. Since the inner structure has weak and linear dependence on the Galactic longitude, we suggest that the inner structure is an inner bar.

References

1. C. Nagashima, et al. 1999, in Star Formation 1999, ed. T. Nakamoto (Nobeyama : Nobeyama Radio Obs.), 397
2. T. Nagayama, et al. 2003, Proc. SPIE, 4841, 459
3. S. Nishiyama, T. Nagata, D. Baba et al: ApJ, 621, L105 (2005)
4. S. Nishiyama, T. Nagata, N. Kusakabe et al: ApJ, 638, 839 (2006)

Si and Fe Depletion in Star-forming Regions Probed by Infrared Spectroscopy

Yoko Okada[1], Takashi Onaka[2], Takashi Miyata[2], Itsuki Sakon[2], Hidenori Takahashi[3], Yoshiko K. Okamoto[4], and Hiroshi Shibai[5]

[1] Institute of Space and Astronautical Science (ISAS), Japan Aerospace Exploration Agency (JAXA), Japan okada@ir.isas.jaxa.jp
[2] University of Tokyo, Japan onaka@astron.s.u-tokyo.ac.jp
[3] Gunma Astronomical Observatory, Japan
[4] Ibaraki University, Japan
[5] Nagoya University, Japan

Si and Fe are major constituents of silicate and their gas phase abundance are 5% and 0.5% solar, respectively, in cool clouds [3]. We made observations of 11 Galactic star-forming regions by Infrared Spectrograph (IRS) on board the Spitzer Space Telescope to examine the depletion pattern of Si and Fe. We detected [Si II]35 μm emission for all the observed positions and [Fe II]26 μm and [Fe III]23 μm in most regions. For the regions with NII122 μm or [O I]146 μm data available by previous observations, we derived the gas-phase Si and Fe abundance relative to N or O from line ratios such as [Si II]35 μm/NII 122 μm. The derived Si abundance is 20% solar or larger in HIIregions and 10–20% solar in photodissociation regions (PDRs). From the results of all the observed regions, the gas phase Si abundance in HIIregions is found to be several tens of percent in a wide range of exciting energy. This suggests that a significant fraction of Si-bearing dust grains are destructed in HIIregions. Since large Si abundance in PDRs is reported in this work and in [1, 2], Si-bearing dust is more easily destroyed than silicate. In some regions gas phase Fe abundance is compatible with that in cool interstellar clouds, whereas some other regions have Fe abundance larger by about one order of magnitude than that in cool clouds. The ratio of Fe atoms released from dust grains to those remaining in dust is smaller than that of Si atoms. This suggests that a fraction of Si and Fe atoms reside in different components of interstellar dust.

References

1. Okada, Y., Onaka, T., Shibai, H., & Doi, Y.: A& A, 412, 199 (2003)
2. Okada, Y., Onaka, T., Nakagawa, T., et al.: ApJ, 640, 383 (2006)
3. Savage, B. D., & Sembach, K. R.: ARA&A, 34, 279 (1996)

Simulations of Coevolving Galaxies and Supermassive Black Holes

Takashi Okamoto

Department of Theoretical Astronomy, National Astronomical Observatory of Japan, 2-21-1, Osawa, Mitaka, Tokyo 181-8588 Japan okamoto@th.nao.ac.jp

Observations suggest that every galaxy with a bulge also harbors a supermassive black hole (SMBH) and there is a direct relationship between the mass of the SMBH and the total mass of the bulge. On the other hand, observations that most cooling flow clusters host radio galaxies at their centers suggest that active galactic nuclei (AGNs) activity must give rise to strong heating effects through injection of energy in the form of jets. Recent semi-analytic models of galaxy formation invoke AGN feedback in order to shut off cooling in large halos and to reproduce the observed luminosity functions ([1][2]).

We investigate coevolution of a galaxy and its central SMBH using a cosmological simulation of galaxy formation. The initial condition and the model of the star formation and stellar feedback are the same as [4]. In this work, we assume that (i) gas is funneled due to radiation drag exerted by formed stars and (ii) accretion flows have two modes, that is, the standard thin accretion flow and the radiatively inefficient accretion flow (RIAF). Observations and theories suggest that only the latter is responsible for production of outflows or jets.

As seen in Fig. 2 of the poster, the star formation rate of this galaxy has a peak at $z \sim 2$. During this bursting star formation, the SMBH rapidly increases its mass (Fig. 3). When gas is used up by the star formation, accretion rate begins to decreases and eventually the accretion flow becomes a RIAF whose accretion rate is below $\dot{m}_{\rm crit} \sim 0.01 \dot{m}_{\rm Edd}$. At this stage, jet energy is much more important than the feedback energy from supernovae (Fig. 5).

References

1. R.G. Bower, A.J. Benson, R. Malbon et al: MNRAS 370, 645 (2006)
2. D.J. Croton, V. Springel, S.D.M. White et al: MNRAS 367, 864 (2006)
3. N. Kawakatu, M. Umemura: MNRAS 329, 572 (2002)
4. T. Okamoto, V.R. Eke, C.S. Frenk, A. Jenkins: MNRAS 363, 1299 (2005)

Nuclear Molecular Gas and Star Formation in Nearby Early-type Spiral Galaxies

Takeshi Okuda[1], J. Koda[2], K. Nakanishi[3], K. Kohno[1], S. Ishizuki[4], N. Kuno[3] and S. K. Okumura[3]

[1] Institute of Astronomy, University of Tokyo okuda@ioa.s.u-tokyo.ac.jp
[2] California Institute of Technology
[3] Nobeyama Radio Astronomy, National Astronomical Observatory of Japan
[4] National Astronomical Observatory of Japan

In order to understand nuclear star formation in nearby early-type spiral galaxies, we carried out a ^{12}CO(J=1–0) imaging survey of early-type spiral galaxies with HII nuclei using the Nobeyama Millimeter Array (NMA). We obtained ^{12}CO maps in nuclear regions (central a few kpc regions) of 12 early-type galaxies with a typical spatial resolution of 4 arcsec and a typical spectral resolution of 10 km s^{-1}. These characteristics of the sample enable us to make extensive studies of the distribution, kinematics, and the roles of molecular gas on star formation in the nuclear regions of early-type galaxies at few 100 pc resolution. This is the first systematic imaging survey of the CO emission from nuclear regions of early-type spiral galaxies with HII nuclei.

From our newly observed data set of high resolution ^{12}CO(J=1–0) 3D-images for early-type spiral galaxies, combined with those in late-type spiral galaxies, we find following observational evidence.

We found that early-type spiral galaxies have lower $M_{\rm gas}/M_{\rm dyn}$ ratios than late-type galaxies within a radius of 500 pc. A mean value of $M_{\rm gas}/M_{\rm dyn}$ ratio is only 0.039 for early-type galaxies in our sample. This is surprisingly small given the fact that the almost all observed early-type spirals host significant nuclear star formation.

Late-type barred galaxies have higher nuclear SFEs than late-type unbarred galaxies, and some early-type spiral barred galaxies have small time scales of molecular gas consumption ($< 10^8$ yr).

A standard criterion for the onset of star formation (Toomre's Q) does not explain the star formation properties of our early-type spiral galaxies, where nuclear star formation occurs even if a $M_{\rm gas}/M_{\rm dyn}$ ratio is small or gaseous disk is apparently stable according to Toomre's Q analysis. In fact, most of the observed early-type spiral galaxies with nuclear star formation show Q values much larger than unity.

Macrolens Toward the Galactic Center

Kouji Ohnishi[1], Hosokawa Mizuhiko[2] and Toshio Fukushima[3]

[1] Nagano National College of Technology, Nagano, 381-8550, Japan
kouji.ohnishi@nao.ac.jp
[2] National Astronomical Observatory, Mitaka, Tokyo 181-8588, Japan
[3] Communications Research Laboratory, Tokyo 184-8795, Japan

The motion of Sgr A* has been measured by referring to QSOs in the direction of Galactic Center. The observed magnitude is 6.0mas/yr, which is consistent with the expected value computed from the galactic rotation. The QSOs referred in the observations are close to Sgr A* on the celestial sphere. This means that we observe these QSOs through the core, the bulge, and the disk of the Galaxy where stars are very densely distributed. Therefore, the observed position of QSOs may vary due to the gravitational deflection by foreground objects [1] [2].

To measure the distance to the Galactic Center with the relative error of a few %, in addition to the astrometric microlensing by individual stars in the Galaxy, we have to consider the macro lens effect, the collective gravitational deflection by the core and the bulge of the Galaxy [3]. This effect is important because it has a secular component. Its magnitude is 0.4 μas/yr in the case of internal motion of QSOs by the core and reaches 0.6 μas/yr in the case of the collective motion produced by both the core and the bulge. This will be detected by measuring the relative motion of QSOs near Sgr A* to those far away from the galactic center. Apart from the magnitude, the most important nature of this effect is being secular. This enhances the possibility of its detection when we observe continuously in the long term. The measurement of these effects will provide us valuable information on the density and mass function of the Galactic Center.

References

1. Hosokawa, M., Ohnishi, K., & Fukushima, T. 1997,AJ, 114, 1508
2. Hosokawa, M., Jauncey, D., Reynolds, J., Tzioumis, A., Ohnishi, K., & Fukushima, T. 2002, ApJL,
3. Ohnishi, K.; Hosokawa, M.; Fukushima, T. 2003, in The Proceedings of the IAU 8th Asian-Pacific Regional Meeting, Volume I. ASP Conference Proceedings, Vol. 289. Edited by Satoru Ikeuchi, John Hearnshaw and Tomoyuki Hanawa. p. 461-464

Barstrength and Circumnuclear Dust Structure

Molly S. Peeples and Paul Martini

The Ohio State University, Department of Astronomy, 140 W. 18th Avenue, Columbus, OH 43210, U.S.A. molly, martini@astronomy.ohio-state.edu

As discussed in [1], our goal is to systematically investigate how circumnuclear dust morphology varies with barstrength. We have a sample of 75 nearby spiral galaxies with archival HST data and a measured barstrength Q_b, a measure of a galaxy's maximal tangential-to-radial force ratio determined from near-infrared images. We examine the dust structure of the central 5% of each galaxy, as defined by the diameter of the 25th B-band magnitude isophote, using the structure map technique of [2]. This technique enhances structures on the scale of the PSF (1–15 pc) without the need for data in two bands.

Several nuclear dust morphologies are observed in the most strongly barred galaxies. There is often a large grand design (LGD) spiral whose two prominent symmetric arms lose coherence before extending to the galaxy nucleus, perhaps ending at a circumnuclear starburst ring. In general, galaxies with LGD structure are more strongly barred (have higher Q_b) than those without, with a 0.4% probability of their Q_b distributions being the same. All eight galaxies in our sample with circumnuclear starburst rings have LGD structure that ends at the ring. Within the rings, there is a coherent loosely wound spiral or an incoherent chaotic spiral. In the absence of LGD structure, however, the nuclear dust in the most strongly barred galaxies either forms an incoherent chaotic spiral or is simply fairly chaotic, potentially hosting star formation.

In contrast, structure maps of the weakly barred galaxies (small Q_b) reveal that these galaxies have a much smoother central dust distribution and a higher frequency of tightly wound (TW) nuclear spirals. Galaxies with TW nuclear spirals (pitch angle $\leq 10^\circ$) are more weakly barred than typical galaxies, with a 2.4% probability of their Q_b distributions being the same.

References

1. Peeples, M. & Martini, P., astro-ph/0606460 (2006)
2. Pogge, R. W. & Martini, P., ApJ, 569, 624 (2002)

Spatially-Dependent Metal Abundances in M82

Piero Ranalli[1]

RIKEN, Cosmic radiation laboratory, 2-1 Hirosawa, Wako, Saitama, 351-0198 Japan piero@crab.riken.jp

We report on the preliminary analysis conduced on the outflows, making use of the EPIC camera. To study the different properties of the hot gas as it flows from the central starburst towards the intergalactic space, we divided both outflows in five regions each. Each region has a rectangular shape, the larger side being parallel to the galaxy major axis. The regions are numbered from N1 to N5, and from S1 to S5 with increasing height above the galactic plane. The spectra were extracted from the MOS and PN data. Moreover, a circular region centred on the galaxy nucleus is defined. All regions have been fitted with a thermal plasma model. A powerlaw accounting for point sources is added for the central region only, while point sources in the outflow are sufficiently apart to be excluded when extracting spectra.

We find that all elements are more concentrated in the outflow than in the centre (see Fig. 1). The centre/outskirt abundance ratio ranges from $\sim 1/10$ for O to $\sim 1/3$ for the heavier elements (Mg, Si, S). This is possibly an effect of the different supernova yields for progenitors with different mass. Broadly speaking, one could say that the more massive the progenitor, the larger the yields. An other possibility is that the wind in proximity of the centre is more mass loaded than the wind further away: in this case the mixing of the wind with ambient material would decrease the metallicity.

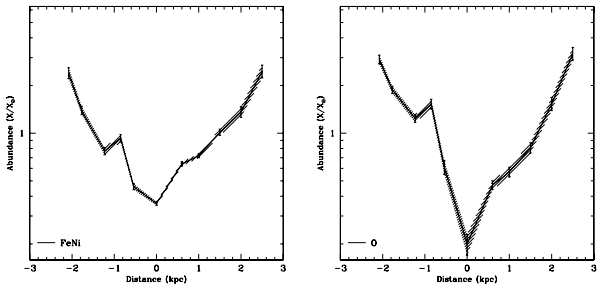

Fig. 1.

Anomalous Absorption Towards the Galactic Anticenter: A Blind Search for Dense Molecular Clouds

Mónica Ivette Rodríguez[1,2], Ronald J. Allen[1], Vladimir Escalante[2], Laurent Loinard[2] and Tommy Wiklind[1]

[1] 1 Space Telescope Science Institute, 3700 San Martin Drive, Baltimore, MD 21218, USA monica, rjallen, wiklind@stsci.edu

[2] Centro de Radiostronomía y Astrofísica, Universidad Nacional Autónoma de México, Apartado Postal 72 3 (Xangari), 58089 Morelia, Michoacán, México m.rodriguez, l.loinard@astrosmo.unam.mx

We have carried out a blind search in the general direction of the Galactic Anticenter for absorption of the Cosmic Microwave Background (CMB) radiation near 4.83 GHz by molecular clouds containing gaseous ortho-formaldehyde (H_2CO). The observations covers strips in Galactic latitude $-1^\circ \leq b \leq +1^\circ$ at severals longitudes in the region $170^\circ \leq l \leq 190^\circ$. Successfully we have dectected H_2CO CMB absorption at $\approx 10\%$ of the survey.

We have mapped these regions in more detail and compared the H_2CO absorption to existing maps of CO(1–0) emission. There appears to be a rough correlation between the velocity-integrated line strength of the CO(1–0) emission and that of the H_2CO absorption, but the larger scatter in our data suggest that there are important differences of detail wich lead to variations of these tracers in different locations and the effects of different optical dephts for each tracers. The distances toward these regions seems to be between 1.5 and 3.0 kpc.

Tidal Disruption of Dark Matter Halos Around Proto-globular Cluster

Takayuki R. Saitoh[1], Jin Koda[2], Takashi Okamoto[1], Keiichi Wada[1] and Asao Habe[3]

[1] National Astronomical Observatory of Japan
[2] California Institute of Technology
[3] Hokkaido University

Globular clusters (GCs) in the Galaxy do not have extended dark matter (DM) halos. Recent observations of extra-galactic GCs whereas indicate self-enrichment of bright metal-poor GCs and therefore such GCs once could possess DM halos to enrich their gas [1, 2]. We hypothesized that the tidal disruption of extended halos would convert proto-GCs to GCs observed at $z = 0$.

With a numerical simulation of galaxy formation, we investigate the role of galactic tidal force on the evolution of globular clusters. The exceedingly high resolution suffices to reproduce the gravitational collapse of very small structures, globular clusters, in their formation [3].

Because of a radiative cooling, each clump immediately forms a 'core-halo' structure which consists of a baryonic core and a DM halo. Due to the tidal force from the host galaxy, the DM halos of the clumps are stripped off; as a result, the clumps are transformed to baryon dominated systems (see Fig. 3). The mass of the DM halos drastically decreases at each pericenter passage. More than half of the clumps become baryon dominated systems by $z = 2$ (baryon mass/total mass > 0.5) (see Fig. 4).

Our results support the tidal evolution scenario of the formation of GCs in the context of the CDM dominated universe.

References

1. Strader, J. Brodie, J. P., Spitler, L., & Beasley, M.A. astro-ph/0508001
2. Brodie, J. P., & Strader, J. ARAA, 44, 193 (2006)
3. Saitoh, T. R., Koda, J., Okamoto, T., Wada, K., & Habe, A. ApJ, 640, 22 (2006)

NRO/CSO/ASTE Galactic Plane CO Survey

Tsuyoshi Sawada[1], Jin Koda[2], Toshihiro Handa[3], Masahiro Sugimoto[4], and Tetsuo Hasegawa[4]

[1] Nobeyama Radio Observatory sawada@nro.nao.ac.jp
[2] California Institute of Technology
[3] Institute of Astronomy, University of Tokyo
[4] National Astronomical Observatory of Japan

How the gas dynamics around the spiral arms (compression, shock, expansion) affects the internal structure of molecular clouds and physical conditions of the gas? We are carrying out a CO survey of the Galactic plane. The distribution of the molecular gas in the Galactic spiral arms and interarm is observed in ^{12}CO and ^{13}CO at three rotational transitions (J = 1–0, 2–1, and 3–2) using the Nobeyama Radio Observatory (NRO) 45-m, the Caltech Submillimeter Observatory (CSO) 10-m, and the Atacama Submillimeter Telescope Experiment (ASTE) 10-m telescopes.

A pilot region ($0\overset{\circ}{.}8 \times 0\overset{\circ}{.}8$ in the J = 1–0, $0\overset{\circ}{.}3 \times 0\overset{\circ}{.}5$ in the 2–1 and 3–2) at $l \simeq 38^\circ$ has been observed at a spatial resolution of 15–30″ (0.5–1 pc at 8 kpc). The arm and interarm regions are simultaneously sampled at different radial velocities in the line of sight. We find that the molecular gas in the arm is confined mostly in dense clumps and filaments, while the interarm gas shows a featureless, extended distribution. The extension of the interarm gas is greater than the survey coverage, 90 pc × 90 pc, exceeding the size of the largest giant molecular cloud. Additionally, the interarm gas has no small-scale, internal structure over the large extension, indicating a new molecular gas component in the Galaxy. The observed ^{12}CO J = 3–2/^{12}CO J = 1–0 intensity ratio, $R_{3-2/1-0}(^{12}\mathrm{CO})$, is higher in the arm ($0.37 \pm 0.03$) than in the interarm ($0.28 \pm 0.02$). The arm gas, even the ambient gas between clumps, exhibits higher line ratio than the interarm gas. The large-velocity-gradient model indicates that $R_{3-2/1-0}(^{12}\mathrm{CO})$ tightly correlates with the kinetic temperature of the gas: the arm molecular gas is warm (warmer than 10 K, up to several × 10 K), while the interarm gas is cooler than 10 K.

Structure and Kinematics of CO (J=2-1) Emission in the Central Region of NGC 4258

Satoko Sawada-Satoh[1], P. T. P. Ho[1,2], S. Muller[1], S. Matsushita[1], and J. Lim[1]

[1] Academia Sinica Institute of Astronomy and Astrophysics, P.O. Box 23-141, Taipei 10617, Taiwan
[2] Harvard-Smithsonian Center for Astronphysics, 60 Garden Street, Cambridge, MA 02138, USA

We present ^{12}CO (J =2-1) observations towards the central region of the Seyfert 2 galaxy NGC 4258 with the Submillimeter Array [3]. (SMA ; Ho, Moran and Lo 2004) Our interferometric maps show two arm-like elongated components along the major axis of the galaxy, with no strong nuclear concentration. The CO (2-1) morphology and kinematics are similar to previous CO (1-0) results (Plante et al. 1991, Helfer et al. 2003, Krause et al. 2005). The velocity field of the components agrees with the general galactic rotation, except for the east elongated component, which shows a significant velocity gradient along the east-west direction. because the trend of the gradient is the same. In order to account for the velocity field, we propose the kinematical models where the warped rotating disk is also expanding. The line ratio of CO(2-1)/CO(1-0) reveals that the eastern component with the anomalous velocity gradient appears to be warmer and denser. This is consistent with the gas in this component being closer to the center, being heated by the central activities, and possibly interacted by expanding motions from the nuclear region.

References

1. Helfer, T. T., Thornley, M.D., Regan, M.W., Wong, T., Sheth, K., Vogel, S.N., Blitz, L., Bock, D. C.-J. 2003, ApJS, 145, 259
2. Ho, P. T. P., Moran, J. M., Lo, F., 2004, ApJ 616, L1
3. Krause, M., Löhr, A., Fendt, C., Neininger, N., 2005,
4. Plante, R. L., Lo, K. Y., Roy, J.-R., Martin, P., Noreau, L., 1991, ApJ, 381, 110

[3] The Submillimeter Array is a joint project between the Smithsonian Astrophysical Observatory and the Academia Sinica Institute of Astronomy and Astrophysics, and is funded by the Smithsonian Institution and the Academia Sinica.

Stellar Populations in the Galactic Bulge

Mathias Schultheis[1], S. Ganesh[2], A. Omont[3], B. Aringer[4], and A. C. Robin[1]

[1] Observatoire de Besançon, France mathias@obs-besancon.fr
[2] Physical Research Laboratory, Ahmedabad shashi@prl.ernet.in
[3] Institut d'Astrophysique de Paris omont@iap.fr
[4] Institut fuer Astronomie der Universitaet Wien aringer@astro.univie.ac.at

In the last decade much progress has been achieved in the understanding of the galactic Bulge while on the other hand a lot of open questions concerning the "heart of our Galaxy" still remain. The galactic Bulge with its wide metallicity range is the ideal place to study stellar and galactic evolution. The understanding of our galactic Bulge is crucial to understand the formation and evolution of our Galaxy.

1 The sample

We used 120 near-IR spectra close to the GC which have an IR excess at 7 and 15 μm. The resolution of the spectra is $\sim$ 1000 and the wavelength range is from 1.55 μm up to 2.55 μm. For our sources we have additional IR photometric data coming from DENIS, 2MASS and ISOGAL and the extinction map of Schultheis et al. ([1]).

2 Results

80% of our objects are mass-losing AGB stars. We could identify also a couple of young stellar objects (YSOs), supergiants and red giant stars below the RGB tip. Combining the equivalent widths of the CO bands (2.3 μm) and the water bands together with photometric data allows to separate the different stellar populations. Atomic lines of Na (2.21 μm) and CaI (2.26 μm) can be used to derive metallicities. However, as shown by Vanhollebeke et al. ([2]) the CaI line is depressed by water absorption and dust for high mass-losing objects such as OH/IR stars. For quantitative metallicity studies synthetic spectra of M giants are needed.

References

1. M. Schultheis, S. Ganesh, G. Simon et al: A&A 349, L69 (1999)
2. Vanhollebeke E, J.A.D.L. Blommaert, M. Schultheis et al: A&A 455, 645 (2006)

Nearby Galaxy Imaging with WFGS2 and SIRIUS

Koji Sugitani[1], H. Hatano[2], M. Uehara[2] C. Nagashima[2], M. Watanabe[3], T. Nagayama[4], M. Tamura[5], WFGS2 Team and IRSF/SIRIUS Team

[1] Graduate School of Natural Sciences, Nagoya City University, Mizuho-ku, Nagoya 467-8501, Japan sugitani@nsc.nagoya-cu.ac.jp,
[2] Department of Astrophysics, Nagoya University, Nagoya 464-8602, Japan
[3] Subaru Telescope, NAOJ, Hilo, HI 96720, USA
[4] Department of Astronomy, Kyoto University, Sakyo-ku, Kyoto 606-8502, Japan
[5] National Astronomical Observatory of Japan, Mitaka, Tokyo 181-8588, Japan

1 WFGS2 (Wide Field Grism Spectrograph 2)

For optical imaging/spectroscopy, we recently have constructed WFGS2 for the 2.2 m telescope of the University of Hawaii. This instrument is suitable for studies of nearby galaxies with a moderately wide field of view and SDSS filters, and provides long-slit (11.5 arcmin.) spectroscopy as well as imaging and slit-less spectroscopy. The spectral coverage is 380 - 970 nm and the field of view is about 11.5 arcmin × 11.5 arcmin with a pixel scale of 0.34 arcsec [1].

2 SIRIUS (Simultaneous Three-Color Infrared Imager for Unbiased Survey)

For near-infrared imaging, we have been operating SIRIUS at the Infrared Survey Facility (IRSF) 1.4 m telescope of SAAO since 2000. SIRIUS has three 1024 × 1024 HgCdTe (HAWAII) arrays and provides simultaneous three-band (J, H, and Ks) images. This instrument is also suitable for studies of nearby galaxies with a moderately wide field of 7.7 arcmin × 7.7 arcmin and a pixel scale of 0.45 arcsec [2, 3].

References

1. M. Uehara, C. Nagashima, K. Sugitani et al: SPIE 5492, 661 (2004)
2. C. Nagashima et al: Pro. of Star Formation 1999 (NRO), p. 397 (1999)
3. T. Nagayama, C. Nagashima, Y. Nakajima et al: SPIE 4851, 459 (2003)

Radio Atlas of Supernova Remnant at 8.38 GHz

Teppei Tamaki[1] and Kenta Fujisawa

Yamaguchi University kenta@yamaguchi-u.ac.jp

We are producing radio atlas of supernova remnant (SNR) at 8.38 GHz using the Yamaguchi 32 m radio telescope. This project aims to offer homogeneous images and data of about 30 SNRs that were listed in Green (2004).
The observation has started since 2005 October, and we have already obtained several maps of the noise level of 10 mK or less ($W44, IC443, DR4, CTB109$, etc). Yamaguchi 32 m has no switching system but amount of observing time. Since it is a single dish observation, the image resolution is relatively low (4 arcmin) but sensitive to diffuse structure.
The observing frequency of 8.38 GHz is almost the highest radio frequency for SNR observation. Such higher frequency observation is known to be sensitive to synchrotron emission from fresh electrons. According to the recent SNR studies with X-ray observations (such as ASCA, Chandra, XMM/Newton, and SUZAKU), our maps will be useful in the research of acceleration of Cosmic Rays etc. The outline of the observation and same maps are shown in the presentation.
The 36 observation source is satisfying of the following selection among 231 SNRs that listed in D.A.Green (2004).

1. Source size $\geq$ 10 arcmin^2
2. Brightness $\geq$ 0.01 Jy arcmin^{-2}
3. Dec $\geq$ -20 deg

References

1. Y. SOFUE, E. REICH, A&A. Suppl. 38. 251-263. (1979)
2. D.A. Green, BULL. Astr. Soc. India. 355-370. (2004)
3. D.Leahy, W. Tian, A&A. 440. 929-936. (2005)
4. X. H. Sun et al, A&A. 447. 937-947. (2006)

HCN and HCO^+ Imaging of the Antennae Galaxies: Distribution and Evolution of Dense Molecular Gas in a Colliding Galaxy System

Yoichi Tamura[1,2], Kouichiro Nakanishi[2], Kotaro Kohno[1], Ryohei Kawabe[2] and Sachiko K. Okumura[2]

[1] Department of Astronomy, The University of Tokyo yoichi.tamura@nao.ac.jp
[2] National Astronomical Observatory of Japan

The Antennae galaxy system (NGC 4038/39) is one of the nearest major merger at the early phase of a galaxy merging sequence. Therefore it is a favorable target to understand the distribution and evolution of molecular gas and formation of massive stars triggered by galactic collision.

Our high spatial resolution ($5'' \times 8''$) HCN and HCO^+ (1–0) imaging of the Antennae obtained with the Nobeyama Millimeter Array (NMA) reveals that dense molecular gas ($n_{H_2} > 10^5$ cm^{-3}) is strongly concentrated around the northern nucleus and the disk overlap region between the two nuclei. The spatial distribution of intensity ratios HCN/HCO^+ and HCN/CO is strikingly different at each nucleus and the overlap region.

HCN/HCO^+ ratio can vary through the starburst history since many authors have pointed out that interstellar shock and/or strong radiation field could enhance HCO^+ abundance (e.g. DeNoyer & Frerking, 1981; Johansson et al., 1994). The northern nucleus is accompanied with nuclear starburst and it has large amount of dense gas and higher HCN/HCO^+ ratio ($\simeq 1$). It implies that the nuclear starburst is relatively young. In the overlap region, known as the anomalous off-nuclear starburst region, the distribution of dense gas agrees well with the on-going starburst regions, where extended mid-infrared (MIR) sources and compact radio sources are found. The lower HCN/HCO^+ ratio ($\simeq 0.5$) of some super giant molecular clouds (SGMCs) in this region suggests that the molecular gas is currently forming a lot of massive stars and exposed to supernova wind. Star formation in this region is probably at the more advanced stage of a starburst than star formation in the northern nucleus region. The southern nucleus has a small fraction of dense molecular gas (HCN/CO $\simeq 10^{-2}$), and elder star clusters and hot plasma have already been found around it. This suggests that it lacks star-forming gas, and is probably at the final stage of its starburst activity.

Kinematics of Molecular Gas in the Bar of Maffei 2

Kazuo Sorai[1], Nario Kuno[2], Naomasa Nakai[3], Hidenori Matsui[1] and Asao Habe[1]

[1] Institute of Fundamental Physics, Department of Cosmosciences, Graduate School of Science, Hokkaido University
sorai@astro1.sci.hokudai.ac.jp
[2] Nobeyama Radio Observatory
[3] Institute of Physics, The University of Tsukuba

We made ^{12}CO $J = 1 - 0$ observations of nearby barred spiral galaxy Maffei 2 with Nobeyama 45-m telescope and Nobeyama Millimeter Array. Molecular gas concentrates on the central region and the bar, which is seen in the 2MASS K-band image, as previous studies shown [1]. A pair of offset ridges and ends of the bar are remarkable.

Position-velocity diagrams crossing the bar indicate abrupt velocity changes and wide velocity width, which suggests that molecular gas moves outward in spray regions [2]. High resolution data show that there are three different components in a position-velocity diagram crossing the bar along the bar minor axis on the galactic disk. The components correspond to spraying gas, rushing one into the leading edges, and moving intensively along the edges. The leading edge component has velocity width of $\sim$ 120 km s^{-1}, and $\sim$ 230 pc in width, which makes velocity gradient of 520 km s^{-1} kpc^{-1}.

The specta in the bar are wider than those in the spiral arms or interarm region. Such wide spectrum caused by intense gas motion in the leading edges may make emission relatively optically thin, which may cause overestimation of molecular gas in the bar.

References

1. A.M. Mason, C.D. Wilson et al: ApJ 612, 860 (2004)
2. D. Downes, D. Reynaud, P.M. Solomon et al: ApJ 461, 186 (1996)

A Subaru/Suprime-Cam Survey of the Andromeda Giant Stream: Constraints of the Dwarf Galaxy as the Stream's Progenitor

Mikito Tanaka[1], Masashi Chiba[2], Yutaka Komiyama[1], Masanori Iye[1], and Puragra Guhathakurta[3]

[1] National Astronomical Observatory of Japan
[2] Astronomical Institute, Tohoku University
[3] University of California Observatories/Lick Observatory

Andromeda Galaxy (M31) is a most nearby spiral galaxy similar to Milky Way. Basically, detailed studying of the M31 halo directly connects to understanding the structure and the formation of our Galaxy. Very interested substructures of the M31 halo were described by the stellar density map [1]. For instance, the stream of metal-rich stars discovered by Ibata et al. (2001) [2] is evidence for the on-going hierarchical formation process and good substance to constrain a galaxy-formation scenario.

We conducted a deep V-band and I_c-band imaging survey of the giant tidal stream of the Andromeda Galaxy using the Suprime-Cam on the Subaru Telescope, down to 50 % completeness limit of $I_c \approx 24.9$ (mag). We present a Color-Magnitude Diagram (CMD) for a field in the stream. The most prominent features of the CMD are a metal-rich Red Giant Branch (RGB) and a Red Clump. And also we detect a very clear AGB bump through detailed analysis for the first time. The metallicity distribution, obtained by comparison of quite a number of the RGB stars with the galactic globular cluster templates, shows the very clear high-metallicity peak ([Fe/H] ~ -0.3) and the broad distribution. Based on its mean metallicity ([Fe/H] ~ -0.55) and luminosity of the AGB bump and the Red Clump, we conclude that the origin of the stream is recent accretion of a dwarf galaxy with stellar mass of $\sim 10^9 M_\odot$. The dwarf galaxy experienced a star burst 10 billion years ago and had completed star formations before 6-8 billion years.

References

1. Ferguson et al. 2002, AJ, 124, 1452
2. Ibata et al. 2001, Nature 412, 49

Giant Molecular Association in Spiral Arms of M 31: Evidence for Dense Gas Formation via Spiral Shock Associated with Density Waves?

Tomoka Tosaki[1], Y. Shioya[2], N. Kuno[1], T. Hasegawa[3], K. Nakanishi[1], S. Matsushita[4] and K. Kohno[5]

[1] Nobeyama Radio Observatory tomoka@nro.nao.ac.jp
[2] Ehime University
[3] Gunma Astronomical Observatory
[4] Institute of Astronomy and Astrophysics, Academia Sinica
[5] Institute of Astronomy, University of Tokyo

We present the high-resolution ^{12}CO($J = 1 - 0$), ^{13}CO($J = 1 - 0$) and ^{12}CO($J = 3 - 2$) maps toward a Giant Molecular Associations(GMA) located on the southern arm region of M 31 using Nobeyama 45 m and ASTE 10 m telescopes. Our main interest is to understand the physical process of star formation inside GMAs along the spiral arms, i.e., physical and evolutional links among GMAs (a few 100 pc), GMCs (a few 10 pc), and dense cores (≤ 1 pc). The GMA consists of two velocity-components, i.e., red and blue. The blue component shows a strong and narrow peak, whereas the red one shows a weak and broad profile. The red component has a lower ^{12}CO($J = 1 - 0$)/^{13}CO($J = 1 - 0$) ratio (~ 5) than that of the blue one (~ 16), indicating that the red component is denser than the blue one. The red component could be the decelerated gas if we consider the galactic rotational velocity in this region. We suggest that the red component is "post shock" dense gas decelerated due to a spiral density wave. This could be observational evidence of dense molecular gas formation due to galactic shock by spiral density waves.

We also present on-going high-resolution observations toward this GMA using Nobeyama Millimeter Array (NMA). NMA observations show a highly clumpy internal structure of the GMA. Their masses and sizes are very similar to those of Galactic GMCs, suggesting that the GMA consists of the "GMC-like cores" and "diffuse envelope" surrounding around them.

SLUGS: Dust along the Hubble Sequence

Catherine Vlahakis[1], Loretta Dunne[2] and Stephen Eales[3]

[1] Argelander Institut Für Astronomie, Universität Bonn, Germany
vlahakis@astro.uni-bonn.de
[2] School of Physics and Astronomy, University of Nottingham, UK
[3] School of Physics and Astronomy, Cardiff University, UK

The SCUBA Local Universe Galaxy Survey (SLUGS) is the first large systematic submm survey of the local Universe. Since our initial survey of a sample of 104 *IRAS*-selected galaxies ([1]) we have now completed a survey of a sample of 81 optically selected galaxies ([3]). Since SCUBA is sensitive to the 90% of dust too cold to radiate significantly in the *IRAS* bands our new sample represents the first unbiased submm survey of dust along the whole length of the Hubble sequence. We find little change in the properties of dust in galaxies along the Hubble sequence, and detected 6 out of 11 ellipticals. As in our earlier work on *IRAS* galaxies we find that the *IRAS* and submm fluxes are well fitted by a two-component dust model with dust emissivity index β=2. The major difference from our earlier work is the ratio of the mass of cold dust to the mass of warm dust, which is much higher for our optically selected galaxies, reaching values of $\sim$1000. Comparison of the results for the *IRAS* and optically selected samples shows that there is a population of galaxies containing a large proportion of cold dust that is unrepresented in the *IRAS* sample. We derive local submm luminosity and dust mass functions, both directly from our optically selected SLUGS sample, and by extrapolation from the *IRAS* PSCz survey using the method of Serjeant and Harrison ([2]), and find excellent agreement between the two. They are well fitted by Schechter functions except at the highest luminosities. We find that as a consequence of the omission of cold dusty galaxies from the *IRAS* sample the luminosity function presented in our earlier work is too low by a factor of 2, reducing the amount of cosmic evolution required between the low-z and high-z Universe.

References

1. L. Dunne et al.: MNRAS 315, 115 (2000)
2. S. Serjeant, D. Harrison: MNRAS 356, 192 (2005)
3. C. Vlahakis, L. Dunne, S.A. Eales: MNRAS 364, 1253 (2005)

Beyond the Unified Theory: Evolution of Active Galactic Nuclei Driven by Starburst Events

Yasuyuki Watabe and Masayuki Umemura

University of Tsukuba watabe@ccs.tsukuba.ac.jp

The origin, structure of obscuring material of AGNs have not been understood both theoretically and observationally. Recent observations suggested that the obscuration of AGNs could be physically related to the starburst event. So we pursue the dynamics of dusty gas clouds that spurt out from the circumnuclear starburst, including the radiation forces by an AGN and a starburst[1].

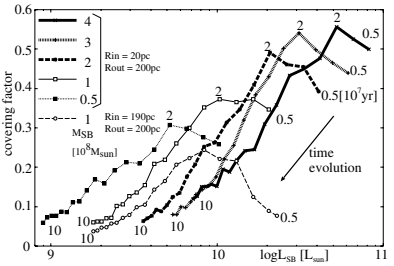

Fig. 1. Time evolution of the covering factor (Horizontal axis: starburst luminosity)

As a result, in the case of starburst-dominant case (Fig. 1), it is shown that the covering factor rises (maximum: $50 \sim 60\%$) if the starburst regions are massive or the extent of starburst regions is small. So the starburst-origin gas clouds contribute to the obscuration of AGN and it may be thought that the structure of the obscuring material is the clumpy. Moreover, the velocity dispersion and the ionization parameter of gas clouds are several 100 kms^{-1}, $10^{-4} \sim 10^{-2}$, respectivelly, which are just comparable that found in NLRs.

References

1. Watabe, Y., & Umemura, M.: 618, 649 (2005)

Water-Vapor Maser Disk at the Nucleus of the Seyfert 2 IC 2560

Aya Yamauchi[1], Naomasa Nakai[1], Yuko Ishihara[2], Philip Diamond[3], and Naoko Sato[4]

[1] University of Tsukuba yamauchi@physics.px.tsukuba.ac.jp
[2] Koriyama City Fureai Science Center
[3] Jodrell Bank Observatory
[4] Wakayama University

We observed the H_2O maser at the nucleus of IC 2560 using the Very Long Baseline Array (VLBA) and the phased Very Large Array (VLA) on 10 April 2006. The systemic, red- and blue-shifted maser features have been detected. The velocities relative to the systemic velocity are 325 km s^{-1} for a red-shifted feature, and 220 km s^{-1} for a blue-shifted. The isotropic luminosities are $L = 0.5L_\odot$, $1L_\odot$, and $45L_\odot$ for the blue-shifted, red-shifted, and systemic features, respectively, at the distance of 26 Mpc.

A continuum component have been detected $\sim$ 0.2 pc southwest of the systemic features (Ishihara et al., private communication). The blue-shifted feature we detected is located on the continuum component. We consider that the blue-shifted feature is emitted due to stimulation by continuum radiation from the background source. We suggest a nearly edge-on maser disk which contains systemic and red-shifted features with the position angle of $PA = -47°$. The thickness of the disk is $2H < 0.025$ pc. The binding mass is $(3.5 \pm 0.5) \times 10^6 M_\odot$. A continuum component is considered as a jet ejected from the nucleus, with an angle of 70° from the disk.

In single-dish observations, blue- and red-shifted features are detected at the $V_{\rm LSR} = 2458$–2661 km s^{-1} and 3089–3222 km s^{-1} [1]. If the features are emitted from a maser disk and the disk rotation is Keplerian, the radii become to be $r = 0.087$–0.335 pc. The mean density within the inner radius is $(1.3 \pm 0.6) \times 10^9 M_\odot$ pc^{-3}. This is as large as the density of NGC 4258 ($3.4 \times 10^9 M_\odot$ pc^{-3} [2]), suggesting a massive black hole at the center.

References

1. Y. Ishihara, N. Nakai, N. Iyomoto et al: PASJ 53, 215 (2001)
2. M. Miyoshi, J, Moran, J. Herrnstein et al: Nature 373, 127 (1995)

Structure, Evolution and Instability of a Self-gravitating Disk Subject to a Rapidly Rotating Bar

David Chien-Chang Yen[1] and Chi Yuan[2]

[1] Department of Mathematics, Fu Jen Catholic University, Taiwan, R.O.C.
[2] Institute of Astronomy and Astrophysics, Academia Sinica, Taiwan, R.O.C.

A rapidly rotating central bar can simultaneously drive spiral density waves in the gas disk of the galactic central regions, at both the outer Lindblad resonance (OLR) and the inner Lindblad resonance (ILR). It is shown that these spiral density waves are responsible for the observed starburst ring outside (at OLR) and the formation of the dense central molecular disk (CMD) near the center (at ILR), see Figure 1. They also reproduce the observed gas depression region between them. The fact that the CMD owes its existence to the ILR is confirmed by the computation in which ILR does not exist, see the last panel on the right in Figure 1. Furthermore, the interaction of spiral waves excited at ILR and OLR may give rise to a diamond-shaped structure, in close resemblance to that observed in NGC6782. When the self-gravity of the disk is included, the disk becomes unstable once Toomre's criterion is violated. The instability happens only at the spiral-ring structure associated with the OLR, not in the CMD, see the middle two panels in Figure 1. This explains why starburst rings should occur while the CMD can exist despite extremely high surface density.

Fig. 1. The first two panels on the left show the numerical results of the ring-like spiral outside with a diamond-shaped double ring and a central molecular disk (CMD) in the center. The next tow panels show the spiral-ring under goes Toomre instability when self-gravity is included. The last panel shows no CMD (no ILR).

Kazuo Sorai, Norio Kuno, and Wofgang Reich

Index